

'Lab in a cell'

**Developing yeast-based systems for rapid *in vivo*
characterization of redox enzymes**

Kumulative Dissertation

zur Erlangung des Grades
des Doktors der Naturwissenschaften
der Naturwissenschaftlich-Technischen Fakultät
der Universität des Saarlandes

von

Jannik Zimmermann

Saarbrücken

2021

Tag des Kolloquiums: 25. November 2021

Dekan: Prof. Dr. Jörn Erik Walter

Berichterstatter:
Prof. Dr. Bruce Morgan
Prof. Dr. Marcel Deponte
Prof. Dr. Markus Hoth

Vorsitz: Prof. Dr. Uli Müller
Akad. Mitglied: Dr. Jens Neunzig

Danksagung

Mein größter Dank gilt Prof. Dr. Bruce Morgan, der mir die Anfertigung dieser Dissertation in seiner Gruppe ermöglicht hat. Vielen Dank für deine Geduld und die intensive wissenschaftliche Betreuung. Danke auch für die Motivation und dafür, dass deine Tür buchstäblich immer offen stand für Fragen und Gespräche aller Art. Ich hoffe und freue mich weiterhin auf gute Zusammenarbeit.

Ebenso bedanke ich mich bei Prof. Dr. Marcel Deponte für seine unzähligen Ideen und Anregungen für vergangene und zukünftige Projekte. Deine Ideen haben maßgeblich zum Gelingen dieser Dissertation beigetragen. Vielen Dank auch für die Übernahme des Zweitgutachtens.

Ein herzliches Dankeschön ebenfalls an meine aktuellen und ehemaligen Arbeitskollegen Marie Mai, Julian Oestreicher, Gurleen Khandpur und Prince Amponsah für die Zusammenarbeit und die konstruktiven Diskussionen. Ich danke Marie und Julian für das Korrekturlesen der Arbeit. Julian und Gurleen danke ich dafür, dass sie die Pendelei erträglicher gemacht haben. Wenn sie mal nicht geschlafen haben.

Ich danke Antje Eiden-Plach und Birgit Heider-Lips für die Hilfe beim Klonieren, die Organisation des Labors und für die sowohl netten als auch lustigen Gespräche. Ich danke auch Gabi Schon für die Hilfsbereitschaft bei bürokratischen Angelegenheiten. Danke auch an Dr. Frank Hannemann für seine Ratschläge. Ich freue mich auf eine gute Zusammenarbeit bei zukünftigen, gemeinsamen Projekten.

Weiterhin danke ich meinen ehemaligen Studenten Shamala Riemann, Hugo Laporte, Antoine Demoulin und Tobias Sukmann, deren Zuarbeit bei verschiedenen Projekten sehr geholfen hat. Besonders danke ich Halie Rae Ropp für das Korrekturlesen der Arbeit.

Ich danke auch meiner ehemaligen Nachbarin, Dipl.-Biol. Elke Schindler, die mir während des Studiums und dem Großteil meiner Promotion mit Tipps und Ratschlägen weitergeholfen hat.

Ganz besonders danke ich meinen Eltern und meinem Bruder für die bedingungslose Unterstützung in allen Belangen während meines Studiums und der Promotionszeit. Vielen Dank für alles!

Abschließend danke ich von ganzem Herzen Svenja. Du warst in jeder Hinsicht mein größter Rückhalt. Ich kann mir nicht vorstellen, wie ich diese, oftmals stressige Zeit ohne dich bewältigt hätte.

Content

Danksagung	I
Content	II
Scientific contributions	III
List of publications and poster presentations	IV
Abbreviations	V
Summary	VI
Zusammenfassung	VII
1. Introduction	1
1.1. Thioredoxin-fold enzymes have versatile functions	1
1.1.1. Glutaredoxins can function as glutathione-dependent oxidoreductases	1
1.1.2. Peroxiredoxins are peroxide scavengers and signal mediators	5
1.1.3. The role of peroxiredoxins in the yeast metabolic cycle.....	7
1.2. Measurements of redox-active molecules using fluorescence-based sensors ...	8
1.2.1. Measurements of the glutathione redox couple	9
1.2.2. Measurements of endogenous H ₂ O ₂ changes.....	10
1.3. Towards <i>in vivo</i> measurements of redox enzyme activity	12
1.3.1. <i>In vitro</i> characterization of the glutaredoxin oxidoreductase activity	12
1.3.2. <i>In vivo</i> approaches for protein analyses in <i>Saccharomyces cerevisiae</i>	13
1.3.3. Novel fluorescence- and yeast-based approaches for redox enzyme analyses..	15
1.4. Aim of this work	16
2. Scientific articles	18
2.1. Liedgens et al., 2020, <i>Nature Communications</i>	18
2.1.1. Supplementary information	37
2.2. Zimmermann et al., 2021, <i>Free Radical Biology and Medicine</i>	102
2.2.1. Supplementary information	113
2.3. Zimmermann et al., 2020, <i>Redox Biology</i>	120
2.3.1. Supplementary information	133
2.4. Amponsah et al., 2021, <i>Nature Chemical Biology</i>	143
2.4.1. Supplementary information	159

3. General discussion and perspective	186
3.1. Development of a fluorescence-based screen to monitor glutaredoxin activity <i>in vivo</i>	186
3.2. Establishment of a roGFP2-based screen to monitor ScGrx7 structure-function relationships	190
3.3. Interconversion analyses of redox-active and -inactive glutaredoxins	193
3.4. ScOPT1 overexpression allows for direct application of GSSG	198
3.5. Monitoring oxidoreductase-mediated reduction of endogenous proteins	202
3.6. Using roGFP2-Tsa2ΔC_R to assess peroxiredoxin-mediated coupling between metabolism and cell division	206
References	VIII

Scientific contributions

This dissertation is based on four research papers. These were reproduced in chapter 2 with kind permission of *Nature Springer* (Nature Communications, Liedgens *et al.*, 2020 and Nature Chemical Biology, Ampontsah *et al.*, 2021) and *Elsevier* (Redox Biology, Zimmermann *et al.*, 2020 and Free Radical Biology and Medicine, Zimmermann *et al.*, 2021). Outlined below are (i.) the expanded contribution of the author of this dissertation, as well as (ii.) the contribution of all authors reprinted from the respective publication.

(1) Liedgens et al., 2020

Liedgens, L. [§], **Zimmermann, J.** [§], Wäschenbach, L. [§], Geissel, F., Laporte, H., Gohlke, H., Morgan, B. and Deponte, M. Quantitative assessment of the determinant structural differences between redox-active and inactive glutaredoxins. *Nature Communications*, (2020) 11(1), 1-18.

[§]Equally contributing authors

(i.) Glutaredoxin structure-function analyses were carried out using *in vitro*, *in vivo* and *in silico* approaches. The author contributed by developing and performing the roGFP2-based *in vivo* experiments. This also required cloning of all roGFP2 fusion constructs and subsequent site-directed mutagenesis of *HsGrx5* for the interconversion study. The author further contributed by analyzing and interpreting the corresponding data.

(ii.) 'L.L. generated the point mutants of ScGrx7, performed the steady-state kinetic measurements and analyzed the kinetic data except for the interconversion mutants which were analyzed by F.G. J.Z. and H.L. performed and analyzed the roGFP2 measurements. L.W. performed and analyzed the molecular dynamics simulations. M.D. conceived the study design and supervised the *in vitro* experiments. B.M. conceived and supervised the roGFP2 experiments. H.G. conceived and supervised the molecular dynamics simulations. M.D., B.M., and H.G. wrote the paper. All authors discussed the results and gave approval to the final version of the paper.'

(2) Zimmermann et al., 2021

Zimmermann, J. [§], Oestreicher, J. [§], Geissel, F., Deponte, M. and Morgan, B. An intracellular assay for activity screening and characterization of glutathione-dependent oxidoreductases. *Free Radical Biology and Medicine*, (2021) 172, 340-349

[§]Equally contributing authors

(i.) The author contributed by developing the novel approach of measuring glutathione-dependent oxidoreductase activity with its natural substrate i.e., GSSG. Furthermore, the author designed experiments, performed and analyzed all *in vivo* roGFP2 measurements and helped interpreting the corresponding data.

(ii.) ‘B.M. and M.D. conceived the study, helped design the experiments and wrote the manuscript. J.Z., J.O. and F.G. performed experiments, analyzed data and helped write the manuscript.’

(3) Zimmermann et al., 2020

Zimmermann, J., Oestreicher, J., Hess, S., Herrmann, J. M., Deponte, M., and Morgan, B. One cysteine is enough: A monothiol Grx can functionally replace all cytosolic Trx and dithiol Grx. *Redox Biology*, (2020) 101598.

(i.) The author generated the quadruple deletion yeast strain, which was the basis of this publication. Furthermore, the author performed and analyzed all plasmid-shuffling and roGFP2 assays, helped design experiments and interpret the data. The author also contributed writing the manuscript.

(ii.) ‘B.M. and M.D. conceived the study, helped design and supervise the experiments, analyzed and interpreted experimental data and wrote the manuscript. J.M.H. supervised experiments and helped to write the paper. J.Z. helped design and perform experiments, analyzed data and helped to write the manuscript. J.O. performed the measurements of glutathione content in cell lysates. S.H. performed all growth curve experiments.’

(4) Amponsah et al., 2021

Amponsah, P.S., Yahya, G., **Zimmermann**, J., Mai, M., Mergel, S., Mühlhaus, T., Storchova, Z. and Morgan, B. Peroxiredoxins couple metabolism and cell division in an ultradian cycle. *Nature Chemical Biology*, (2021) 17(4), 477-484

(i.) The author helped to finalize the publication during the revision by performing fermenter- and fluorescence-based experiments. The author added oxidants and reductants at different stages during the YMC to predictably manipulate a synchronized, continuous culture with simultaneous monitoring of the roGFP2-Tsa2 Δ C_R redox state. The author further took samples from the fermenter vessel for subsequent flow cytometry-based monitoring of DNA content and budding index analyses.

(ii.) 'B.M., P.S.A. and Z.S. designed all experiments and wrote the manuscript. P.S.A., J.Z., M.M. and S.M. performed metabolic cycle and online roGFP2-Tsa2 Δ C_R-based measurements, as well as experiments to assess the impact of redox compounds on oxygen and roGFP2-Tsa2 Δ C_R cycling. They also performed the experiments to assess the impact of genetic and chemical perturbation of the YMC on cell division using flow cytometry-based analysis of DNA content. P.S.A. performed tetrad dissection and the experiments associated with auxin degron-based regulation of peroxiredoxin level. G.Y. performed all budding index experiments and western blot analyses of cell cycle markers. P.S.A., T.M. and B.M. performed the correlation analyses and statistical analyses of all datasets. All authors contributed to data interpretation.'

List of publications and poster presentations

(1) Participation in the 2019 international SPP1710 conference in San Feliu de Guixols (Spain) on ‘Thiol-based Switches and Redox Regulation’ and winning the ‘Best Poster Award’ presenting the poster: *Establishment of a roGFP2-based screen to monitor glutaredoxin structure-function relationships.*

(2) Liedgens, L. [§], **Zimmermann, J.** [§], Wäschenbach, L. [§], Geissel, F., Laporte, H., Gohlke, H., Morgan, B. & Deponte, M. (2020). Quantitative assessment of the determinant structural differences between redox-active and inactive glutaredoxins. *Nature Communications*, 11(1), 1-18.

[§]Equally contributing authors

(3) **Zimmermann, J.**, Oestreicher, J., Hess, S., Herrmann, J. M., Deponte, M., & Morgan, B. (2020). One cysteine is enough: A monothiol Grx can functionally replace all cytosolic Trx and dithiol Grx. *Redox Biology*, 101598.

(4) Amponsah, P.S., Yahya, G., **Zimmermann, J.**, Mai, M., Mergel, S., Mühlhaus, T., Storchova, Z. & Morgan, B. (2021). Peroxiredoxins couple metabolism and cell division in an ultradian cycle. *Nature Chemical Biology*, 17(4), 477-484

(5) **Zimmermann, J.**[§], Oestreicher, J.[§], Geissel, F., Deponte, M. & Morgan, B. (2021). An intracellular assay for activity screening and characterization of glutathione-dependent oxidoreductases. *Free Radical Biology and Medicine*, 172, 340-349

[§]Equally contributing authors

(6) **Zimmermann, J.** & Morgan, B. (2021). Chapter: Thiol-based redox probes
Alvarez, B., Comini, M., Salinas, G., Trujillo, M., Redox Chemistry and Biology of Thiols. Elsevier, currently under revision (by submission of this dissertation)

- (7) Duarte, M., Ferreira, C., Khandpur G. K., **Zimmermann, J.**, Castro, H., Morgan, B. & Tomás, A.M. (2021). *Leishmania* type II dehydrogenase is essential for parasite viability and renders complex I activity dispensable. *PNAS*, currently under revision (by submission of this dissertation)
- (8) **Zimmermann, J.**, Laporte, H., Ampontsah, P.S., Michalk, C., Sukmann, T., Oestreicher, J., Tursch, A., Owusu, T., Prates Roma, L., Riemer, J. & Morgan, B. Tsa1 is the dominant peroxide scavenger and a major source of H₂O₂-dependent GSSG production in yeast. *unpublished*

Abbreviations

5-FOA	5-Fluoroorotic acid
CDC	Cell division cycle
<i>Cg</i>	<i>Candida glabrata</i>
<i>cpFP</i>	Circularly permuted fluorescent protein
C_P	Peroxidatic cysteine residue
C_R	Resolving cysteine residue
DNA	Desoxyribonucleic acid
DTT	Dithiotreitol
Grx	Glutaredoxin
GSH, glutathione	Reduced γ -glutamylcysteinylglycine
GSSCys	<i>L</i> -cysteine-glutathione disulfide
GSSG, glutathione disulfide	Oxidized γ -glutamylcysteinylglycine
H_2O_2	Hydrogen peroxide
HC	Hartwell Complete
HEDS	Bis(2-hydroxyethyl) disulfide
HOC	High oxygen consumption
<i>Hs</i>	<i>Homo sapiens</i>
<i>HsGrx5</i> ^{Active}	<i>HsGrx5</i> ^{loop+G68P+R97Q}
LOC	Low oxygen consumption
NAD(P)H	Nicotinamide adenine dinucleotide (phosphate)
<i>N,N,N',N'</i> -tetramethylazodiacaboxamide	Diamide
<i>Pf</i>	<i>Plasmodium falciparum</i>
PKA	Protein kinase A
PTM	Posttranslational modification
roGFP2	Reduction-oxidation sensitive green fluorescent protein 2
rxYFP	Redox-sensitive yellow fluorescent protein
<i>Sc</i>	<i>Saccharomyces cerevisiae</i>
<i>Sp</i>	<i>Schizosaccharomyces pombe</i>
<i>Tb</i>	<i>Trypanosoma brucei</i>
<i>t</i> -BuOOH	<i>tert</i> -butyl hydroperoxide
TTFL	Transcription-translation feedback loop
YMC	Yeast metabolic cycle

Summary

The thioredoxin superfamily contains a large number of proteins, including thiol-disulfide oxidoreductases. Many of these proteins remain uncharacterized and it is unclear if they are redox active or not. Classic *in vitro* characterization with recombinant proteins has several limitations such as initial time-consuming protein purification and the inactivity of some proteins in these assays. Therefore, the development of new methods is highly desirable.

Here, assays utilizing genetically engineered yeast cells, expressing genetic fusion constructs between redox sensitive fluorescent proteins and thioredoxin superfamily members, were developed to monitor enzymatic activity *in vivo*. Importantly, the oxidation kinetics of roGFP2 were found to directly correlate with the *in vitro*-determined enzymatic activity of a range of thioredoxin proteins and mutants thereof. These novel assays were applied as high-throughput screens to address unanswered questions relating to glutaredoxin structure-function relationships and catalytic mechanisms. We were able to (i.) identify the key structural determinants of glutaredoxin enzymatic activity. (ii.) Demonstrate that endogenous and artificial protein disulfides can be reduced by monothiol glutaredoxins, in contradiction to prevailing mechanistic models. (iii.) Reveal that glutaredoxins can catalyze GSNO-dependent oxidation of roGFP2 *in vivo*. This new methodology should accelerate future research into redox protein mechanisms and function.

Zusammenfassung

Der Thioredoxin-Superfamilie (TSF) gehört eine Vielzahl von Proteinen an. Davon sind einige noch kaum erforscht und es ist oftmals unklar ob sie redox-aktiv sind oder nicht. Meist werden diese Proteine *in vitro* charakterisiert. Zu den Limitationen dieser Methode gehören die zeitintensive Aufreinigung sowie darauffolgende Inaktivität einiger Proteine. Daher ist die Entwicklung neuer Methoden von großer Bedeutung.

In dieser Arbeit wurden genetisch veränderte Hefezellen verwendet, die Fusionskonstrukte zwischen roGFP2 und TSF Proteinen exprimieren, um deren enzymatische Aktivität *in vivo* zu bestimmen. Dabei wurde herausgefunden, dass roGFP2-Oxidationskinetiken die Aktivität des fusionierten Proteins widerspiegeln und mit den *in vitro*-Daten korrelieren. Die neuartigen Methoden erlauben dabei ein Hochdurchsatz-Screening, welches genutzt wurde, um Fragen hinsichtlich der Struktur-Funktions-Beziehungen und katalytischer Mechanismen von Glutaredoxinen zu adressieren. Dies ermöglichte (i.) die Identifikation der wichtigsten strukturellen Unterschiede zwischen redox-aktiven und -inaktiven Glutaredoxinen. (ii.) Entgegen bestehender Modelle konnte demonstriert werden, dass Disulfide in endogenen Proteinen durch monothiole Glutaredoxine reduziert werden können. (iii.) Weiter wurde gezeigt, dass Glutaredoxine die GSNO-abhängige Oxidation von roGFP2 *in vivo* katalysieren. Diese neue Methodik wird die zukünftige Erforschung der Mechanismen und Funktion von Redox-Proteinen beschleunigen.

1. Introduction

1.1. Thioredoxin-fold enzymes have versatile functions

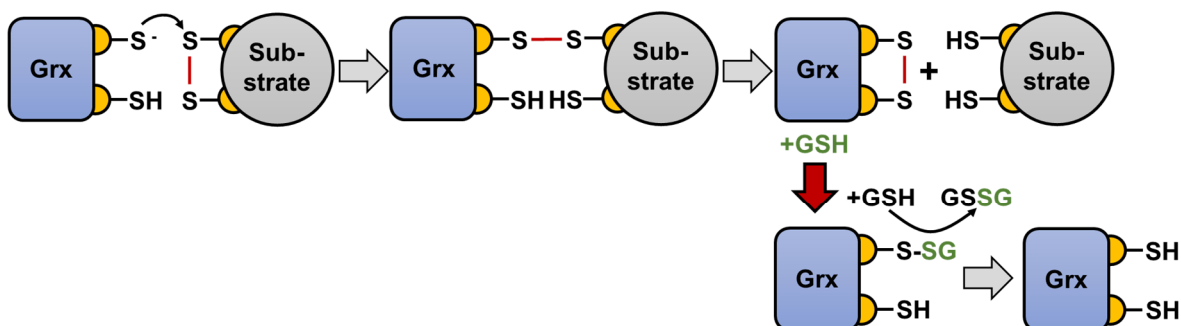
The thioredoxin superfamily is highly diverse and contains a large number of proteins (Höög *et al.*, 1983; Nilewski *et al.*, 2021). They appear in basically all living organisms and often have multiple isoforms in different subcellular compartments (Carvalho *et al.*, 2006). Although the degree of sequence similarity is low between different classes, structurally they all share the so-called thioredoxin fold (Holgrem *et al.*, 1975). The thioredoxin fold was first described for thioredoxins and consists of a four- or five-stranded β -sheet flanked by at least three α -helices (Sousa *et al.*, 2019). Many members of this huge family are enzymatically active redox proteins e.g., glutathione-dependent thiol-disulfide oxidoreductases or thiol peroxidases (Zimmermann *et al.*, 2021). Often, the active site in these proteins contains two cysteine residues separated by two amino acids in a -CxxC- motif (Martin, 1995). However, the family also contains enzymatically inactive members e.g., iron-sulfur (Fe-S) cluster binding glutaredoxins. (Deponte, 2013; Lu, Holgrem, 2014). The thioredoxin superfamily still contains many uncharacterized proteins with unknown enzymatic activity, substrates and cellular functions. This dissertation predominantly focuses on glutaredoxins and peroxiredoxins, which are introduced in more detail in the following sections.

1.1.1. Glutaredoxins can function as glutathione-dependent oxidoreductases

Glutaredoxins were first described in 1976. Lysates made from *Escherichia coli* cells lacking thioredoxins could still reduce ribonucleotide reductase in the presence of NADPH, reduced γ -glutamylcysteinylglycine (glutathione; GSH) and glutathione reductase. The finding suggested an alternative reduction pathway for disulfide substrates apart from the known thioredoxin system. Due to the preference for reduced glutathione as an electron donor, the enzyme facilitating the reduction was called ‘glutaredoxin’ (Holgrem, 1976). Since then, glutaredoxins were found in almost all lifeforms (Couturier *et al.*, 2014). Oxidoreductase activities of glutaredoxins and related proteins are typically determined *in vitro* with recombinant proteins. However, not all glutaredoxins are enzymatically active oxidoreductases. Others are inactive and were shown to coordinate Fe-S clusters (Wingert *et al.*, 2005, Mieyal *et al.*, 2008; Rodríguez-Manzaneque *et al.*, 2002). Based on their activity *in vitro*, these proteins are divided into two major classes, often referred to as enzymatically active class I or inactive class II glutaredoxins.

Dithiol glutaredoxins harbor a typical -CxxC- active site motif and tend to be enzymatically active. According to the traditional model for glutathione-dependent catalysis, these glutaredoxins reduce disulfide substrates via a dithiol mechanism (**Figure 1A**), while glutathionylated substrates are reduced via a monothiol mechanism (**Figure 1B**) (Holgrem, Aslund, 1995, Lillig *et al.*, 2008). The second active site cysteine residue is dispensable for the monothiol mechanism. Therefore, these reactions can also be performed by active class I monothiol glutaredoxins. In agreement with the traditional model, the native glutaredoxin disulfide substrate, ribonucleotide reductase from *E. coli*, is not reduced by engineered monothiol *E. coli* glutaredoxins (Bushweller *et al.*, 1992). However, recombinant mouse ribonucleotide reductase was efficiently reduced by an engineered monothiol Grx2, suggesting that reduction of disulfide bonds does not exclusively require the dithiol mechanism (Zahedi Avval, Holgrem, 2009).

A Dithiol mechanism



B Monothiol mechanism

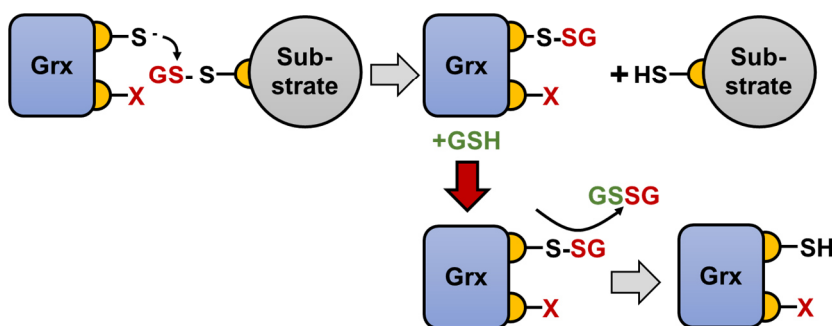


Figure 1. Traditional model of the glutathione-dependent catalysis of glutaredoxin. (A) Dithiol mechanism for reduction of disulfide substrates. The disulfide exchange mechanism involves both active site cysteine residues of the glutaredoxin. The disulfide bond in glutaredoxins is reduced with two molecules GSH. (B) Monothiol mechanism for reduction of glutathionylated substrates. The second cysteine is dispensable for catalysis. Red arrows in (A) and (B) indicate transition from the oxidative into the reductive half-reaction (Deponte, 2013).

The glutaredoxin catalysis requires binding of both glutaredoxin substrates, the glutathionyl moiety of the glutathionylated substrate and GSH. However, the traditional model does not explain how the glutathionyl moiety during the oxidative half-reaction and GSH during the reductive half-reaction are bound. Therefore, refined catalytic concepts were proposed (Eckers *et al.*, 2009; Deponte, 2013). These models distinguish between protein areas

contributing to either of the half-reactions. Thus, the 'glutathione scaffold site' maintains the correct orientation of the glutathionyl moiety of the glutathionylated substrate. The 'glutathione activator site' mediates the interaction and binding of GSH as the reducing agent (**Figure 2**). Previous *in vitro* studies on *Saccharomyces cerevisiae* ScGrx7 have demonstrated and confirmed the contribution of two distinct glutathione interaction sites to the oxidoreductase activity (Begas *et al.*, 2017).

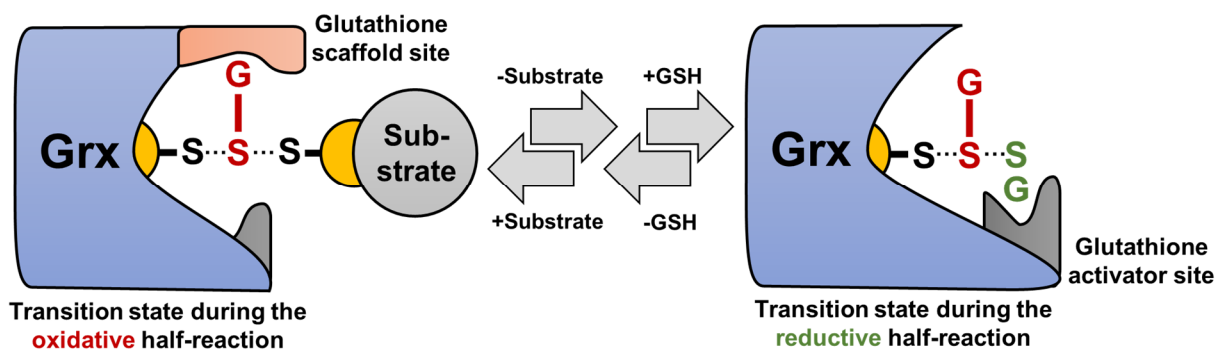


Figure 2. Schematic illustration of the refined models for the glutaredoxin-dependent catalysis for both glutathione moieties. The glutathione scaffold site stabilizes the glutathionyl moiety of the glutathionylated substrate during the oxidative half-reaction (left). The glutathione activator site binds reduced glutathione for the reductive half-reaction (right). Shown are transition states for both half-reactions. The models discriminate between the glutathionyl moieties of both glutaredoxin substrates. Conformational changes upon glutathionylation of the glutaredoxin could make the activator site accessible for GSH. (Eckers *et al.*, 2009; Deponte, 2013)

Often, oxidoreductase activity correlates with the number of cysteine residues in the active site. Naturally occurring monothiol glutaredoxins with -CxxS- active site motifs tend to be inactive *in vitro* and often have other functions i.e., transfer and binding of Fe-S clusters using glutathione as a ligand (Herrero *et al.*, 2007; Couturier *et al.*, 2015). However, there are exceptions regarding the activity of mono- and dithiol glutaredoxins. Dithiol human GRX2 is described as a hybrid protein. It can efficiently reduce disulfides when not coordinating Fe-S clusters. Consequently, binding of the Fe-S cluster impairs the oxidoreductase activity of the enzyme (Lillig *et al.*, 2005). ScGrx6 and ScGrx7 are both monothiol glutaredoxins. However, both are enzymatically active *in vitro*. Unlike ScGrx7, ScGrx6 can also bind Fe-S clusters. Furthermore, these isoforms were the first described glutaredoxins related to the secretory pathway (Mesecke *et al.*, 2008; Izquierdo *et al.*, 2008).

Besides ScGrx6 and ScGrx7, *S. cerevisiae* harbors six other glutaredoxins distributed throughout the cell. Three are dithiol isoforms located in the cytosol, namely ScGrx1, ScGrx2 and ScGrx8. ScGrx1 and ScGrx2 most likely arose from whole genome duplication and share high sequence similarity (Discola *et al.*, 2009). Due to a second in-frame start codon ScGrx2 can also be translocated to the mitochondrial matrix. ScGrx2 is the most abundant glutaredoxin in yeast (Ghaemmaghami *et al.*, 2003).

ScGrx8 is far less active *in vitro* with bis(2-hydroxyethyl) disulfide (HEDS) as substrate in comparison to *ScGrx1* and *ScGrx2* (Eckers *et al.*, 2009; Tang *et al.*, 2014). This might result from the unusual Trp14-type -SWCPDC- motif. *ScGrx8* is often considered to be a glutaredoxin/thioredoxin hybrid protein. However, its physiological function remains unclear. Monothiol *ScGrx3* and *ScGrx4* are located in the cytosol and in the nucleus, while *ScGrx5* functions in the mitochondrial matrix (Herrero *et al.*, 2006). *ScGrx3* and *ScGrx4* share similar cellular functions and probably arose from genome duplication (Wolfe, Shields, 1997). Both are involved in iron trafficking (Mühlenhoff *et al.*, 2014). *ScGrx5* was the first glutaredoxin with proven important implications for iron metabolism. Deletion of *ScGRX5* results in accumulation of iron and inactivation of proteins requiring Fe-S clusters (Rodríguez-Manzaneque *et al.*, 2002). Noteworthy, the function of *ScGrx5* in Fe-S cluster biogenesis and assembly was shown to be conserved throughout species as indicated by studies with recombinant human *GRX5* or expression of *Grx5* homologs in zebrafish and mice (Vilella *et al.*, 2004; Herrero *et al.*, 2006; Wingert *et al.*, 2005).

Physiological functions and substrates of glutaredoxins seem to overlap with those of thioredoxins. Unlike thioredoxins, glutaredoxins show a preference for GSH as an electron donor, while thioredoxins are reduced by thioredoxin reductases (Grant, 2001). Glutaredoxins and thioredoxins also share common disulfide substrates. As mentioned previously, both classes can facilitate the essential reduction of the disulfide bond in certain ribonucleotide reductase isoforms (Bushweller *et al.*, 1992; Zahedi Avval, Holgrem, 2009). Therefore, these enzymes are crucial for DNA synthesis as ribonucleotide reductase catalyzes the production of deoxyribonucleotides from ribonucleotides (Elledge *et al.*, 1992). Altered glutaredoxin abundance and activities within certain tissues or cells were also shown to have implications on the neuronal development and medical implications including diabetes, cardiovascular diseases, lung diseases and cancer (Mieyal *et al.*, 2008; Gorelenkova *et al.*, 2018). Glutathionylation of proteins as posttranslational modification can further alter their activity or affect signaling transduction (Cabiscol *et al.*, 1996; Mohr *et al.*, 1999; Adachi *et al.*, 2004 Song *et al.*, 2003).

Altogether, not all glutaredoxins function as glutathione-dependent oxidoreductases, as certain isoforms show poor oxidoreductase activity *in vitro* and facilitate Fe-S cluster binding and trafficking. The mechanism by which active class I glutaredoxins exert their function is not yet fully understood. Especially the contribution of residues to the glutathione activator site remains elusive. Based on the proposed models for the glutathione-dependent redox catalysis, structurally altered glutathione interaction sites might explain the uncoupling from the glutathione pool in inactive class II glutaredoxins, which will be discussed later in this dissertation.

1.1.2. Peroxiredoxins are peroxide scavengers and signal mediators

Peroxiredoxins are among the most abundant proteins in pro- and eukaryotes (Winterbourn, 2008; Netto *et al.*, 2014). These members of the thioredoxin superfamily are highly conserved and often distributed across multiple cellular compartments. They fulfill various functions including hydroperoxide detoxification and signaling transduction. Further they were shown to act as chaperones during heat- and oxidative stress (Jang *et al.*, 2004; Perkins *et al.*, 2015).

Generally, all peroxiredoxins share a peroxidatic cysteine residue (C_P). The C_P in peroxiredoxins is among the most reactive thiols within cells and react with H_2O_2 with second order rate constants of $\sim 10^5\text{-}10^7 \text{ M}^{-1} \text{ s}^{-1}$ (Ogusucu *et al.*, 2006; Trujillo *et al.*, 2007; Peskin *et al.*, 2007). Presence or absence of a second, so-called resolving cysteine (C_R), alters the catalytic mechanism and determines classification into either 1-Cys or 2-Cys peroxiredoxins. The latter are further divided into typical and atypical isoforms which are both active as dimers. Two subunits are either covalently (typical 2-Cys) or non-covalently (atypical 2-Cys) bound to each other in a head-to-tail fashion (Chae *et al.*, 1994; Wood *et al.*, 2003).

The C_P in either of the classes is oxidized to a sulfenic acid (S-OH) upon peroxide exposure (Rhee, 2016). The sulfenic acid is then either directly reduced (observed in 1-Cys peroxiredoxins) or resolved by the C_R from the same (intramolecular disulfide bond; observed in atypical 2-Cys peroxiredoxins) or another peroxiredoxin subunit (intermolecular disulfide bond; observed in typical 2-Cys peroxiredoxins) (Nelson *et al.*, 2011; Hall *et al.*, 2011). The disulfide bond is then reduced via a disulfide exchange mechanism with thioredoxins, which are recycled in a NADPH-dependent process by thioredoxin reductases (Lu, Holgrem, 2014).

S. cerevisiae harbors different peroxiredoxin isoforms within different subcellular compartments. The most abundant is the cytosolic typical 2-Cys peroxiredoxin ScTsa1 (Ghaemmaghami *et al.*, 2003; Tairum *et al.*, 2012). ScTsa1 has a homolog probably arisen from genome duplication, ScTsa2 (Wolfe, Shields, 1997). Atypical 2-Cys ScAhp1 is the third cytosolic peroxiredoxin. Besides the cytosolic isoforms there is also the nuclear ScDot5 and mitochondrial 1-Cys ScPrx1. An important function of peroxiredoxins is the detoxification of peroxides. However, they also achieved growing importance in H_2O_2 -dependent signaling (Rhee, 2016). Until recently, H_2O_2 was considered an exclusively unwanted, yet unavoidable (by-) product of biological processes including respiration, oxidative protein folding or β -oxidation of fatty acids (Zito, 2015; Hashimoto, Hayashi, 1990). Relevance of H_2O_2 as a signaling molecule was shown for regulation of kinase driven pathways and other mechanisms including cell proliferation and migration, cell survival and apoptosis (Gough, Cotter, 2011).

However, the high activation energy barrier makes it rather unreactive with biological molecules. Therefore, H₂O₂ signaling and general reactions with H₂O₂ are rather kinetically than thermodynamically driven and often mediated by proteins with highly reactive thiols (Winterbourn, 2013).

Interestingly, peroxiredoxins can form sulfinic (S-O₂H) or sulfonic acids (S-O₃H) on their C_P upon further reaction with peroxide. Formation of higher oxidation states is called hyperoxidation. In yeast and mammals, ATP-dependent sulfiredoxins can slowly reduce sulfinic acids, while formation of sulfonic acids is irreversible (Veal *et al.*, 2018). Hyperoxidation leads to inactivation of the C_P and therefore also inactivation of the enzyme. The accessibility of peroxiredoxins to hyperoxidation is an important feature of these enzymes regarding their function as signaling transducers. There are two directly opposing models for the role of peroxiredoxins in H₂O₂ signaling and oxidation of thiols in target proteins (**Figure 3**).

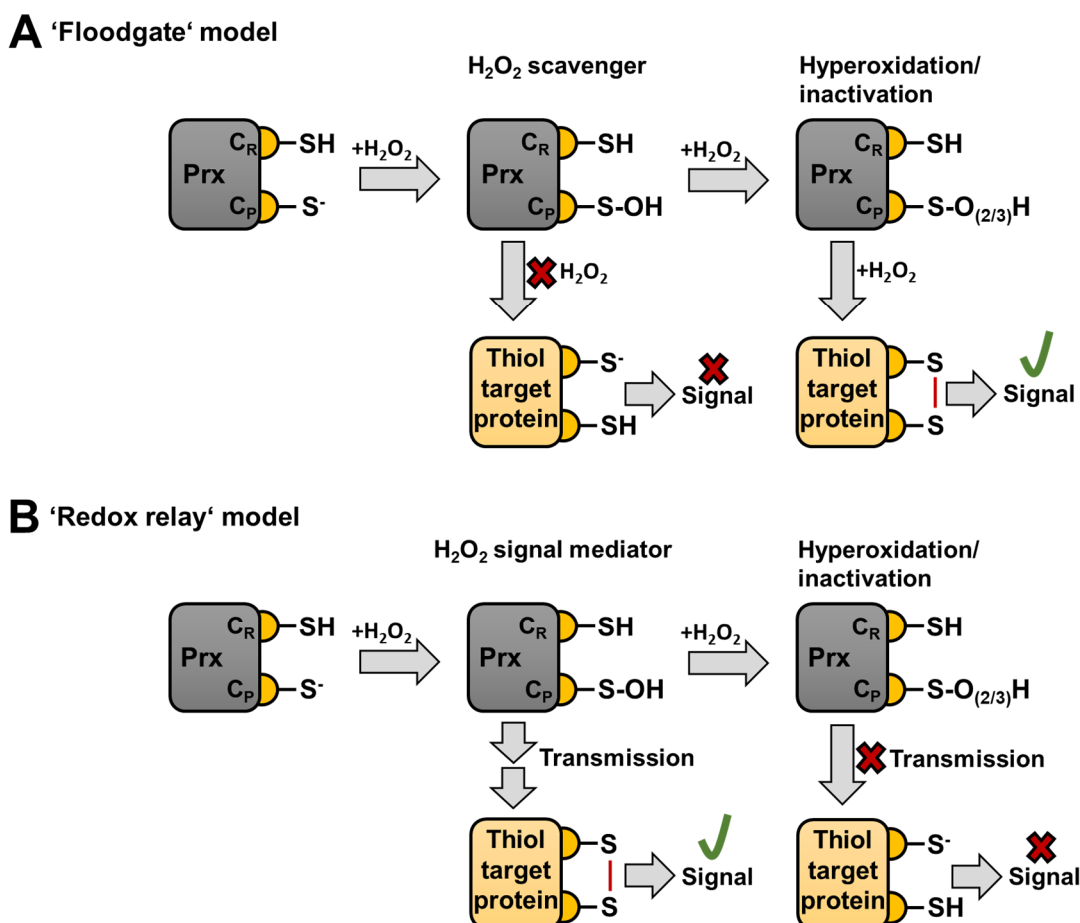


Figure 3. Opposing models for H₂O₂ signaling via peroxiredoxin inactivation. (A) In the 'floodgate' model, peroxiredoxin-mediated peroxide scavenging prevents direct oxidation of target proteins and therefore signal transmission. Inactivation by hyperoxidation enables oxidation of less reactive thiols. (B) In the 'redox relay' model, peroxiredoxins are signaling mediators. Contrarily, their inactivation disrupts H₂O₂-signal transmission.

The ‘floodgate’ model proposes that H₂O₂ temporarily accumulates at the site of generation at such high amounts that hyperoxidize and therefore inactivate peroxiredoxins as potent peroxide scavengers. When peroxide scavenging is impaired, H₂O₂ could accumulate and directly oxidize thiols in target proteins (**Figure 3A**; Wood *et al.*, 2003). According to this model, peroxiredoxin inactivation leads to protein thiol oxidation. Localized inactivation of membrane-associated Prx1 by phosphorylation, and Prx2 by hyperoxidation in mice was shown to allow accumulation of H₂O₂ in proximity of membranes promoting sustained H₂O₂ signals (Woo *et al.*, 2010). Contrarily, the ‘redox relay’ model proposes highly reactive thiols e.g., the C_P of peroxiredoxins, as mediators of H₂O₂ signals to less reactive protein thiols. In this model, hyperoxidation and inactivation of the peroxiredoxins would inhibit the relay and switch off signaling transduction instead of promoting it (**Figure 3B**; D’Autreux, Toledano, 2007). For instance, such relays were shown in *S. cerevisiae* for oxidation and activation of the transcription factor ScYap1 by the thiol peroxidase ScOrp1 and in humans for HsPRDX2-mediated oxidation and activation of the transcription factor HsSTAT3 (Delaunay *et al.*, 2002; Sobotta *et al.*, 2015).

1.1.3. The role of peroxiredoxins in the yeast metabolic cycle

Biological clocks are ubiquitous in all lifeforms. Often, circadian rhythms underly transcription-translation feedback loops (TTFL) (Reddy, Rey, 2014). However, oscillations independent of TTFL were also shown. For instance, persistent circadian timekeeping during inhibition of gene expression was demonstrated in the algae *Ostreococcus tauri* by periodic cycles in peroxiredoxin hyperoxidation (O’Neill *et al.*, 2011). Oscillations in peroxiredoxin hyperoxidation were also shown in human red blood cells within persistent 24h cycles (O’Neill, Reddy 2011). This is particularly interesting as red blood cells do not harbor nuclei and are therefore also independent of TTFL. Furthermore, involvement of peroxiredoxins and posttranslational modifications by formation of sulfinic or sulfonic acids were also demonstrated to correlate with circadian rhythms in mice and flies (O’Neill *et al.*, 2011; Edgar *et al.*, 2012). Redox changes were shown to affect the expression of clock-related genes and *vice versa* as demonstrated in different organisms (Hirayama *et al.*, 2007; Yoshida *et al.*, 2011; Ivleva *et al.*, 2005; Kondratov *et al.*, 2006). Besides their well-known function in peroxide detoxification, all these studies suggest further implications of peroxiredoxins in redox sensing and signaling in respect to cellular timekeeping.

S. cerevisiae does not possess a circadian but rather an ultradian clock i.e., periodic oscillations shorter than 24h. The hallmark are high amplitude periodic oscillations in oxygen consumption that occur over several hours in continuous, synchronized and glucose-limited

cultures. The periodic change in oxygen demand was termed ‘yeast metabolic cycle’ (YMC). Two phases are exceptional and characteristic for the YMC. First, a phase of high oxygen consumption (HOC), indicated by low dissolved oxygen within the culture medium. Second, a phase of low oxygen consumption (LOC), where the oxygen saturation in the medium is high (see publication 2.4. Figure 1a). During these metabolic oscillations, microarray studies demonstrated cyclical expression changes in ~50% of all cellular genes. Furthermore, metabolism and cellular processes including cell cycle and division are coupled and occur in synchrony (Tu *et al.*, 2005).

In *S. cerevisiae*, deletion of both typical 2-Cys peroxiredoxins *ScTSA1* and *ScTSA2* was shown to heavily perturb these metabolic cycles (Causton *et al.*, 2015). Besides the genetic perturbation, chemical perturbation can also affect the YMC e.g., by application of H₂O₂ into the culture vessel (Causton *et al.*, 2015; Tu *et al.*, 2007). Despite the known crosstalk between metabolism, gene expression and redox changes, the mechanisms behind this remains, thus far, elusive. On this basis, cyclical changes in oxygen consumption of synchronized yeast cultures are a suitable model to further investigate the role and mechanism in which peroxiredoxins maintain the YMC and couple metabolism to cell cycle and division.

1.2. Measurements of redox-active molecules using fluorescence-based sensors

Detection of reactive oxygen species inside living cells was and still is extremely challenging. While certain redox species can be monitored with dyes or fluorometric probes (Mohanty *et al.*, 1997; Robinson *et al.*, 2006; Rastogi *et al.*, 2010; Daudi, Brien, 2012), intracellular redox active molecules are usually short-lived, and their concentrations often change quickly, making direct, real-time detection almost impossible. Thus, genetically encoded fluorescent sensors are considered a huge breakthrough in the field, enabling real-time monitoring of specific redox species inside living cells (Björnberg *et al.*, 2006; Belousov *et al.*, 2006). Generally, fluorescent sensors function by coupling changes in certain redox species to changes in the fluorescent properties of the probe. The most commonly used sensors are based upon *circularly permuted* fluorescent proteins (cpFP) or genetic fusions between a sensor protein and a fluorescent reporter protein or Förster resonance energy transfer (FRET) within a specific fluorescent FRET pair (Belousov *et al.*, 2006; Dooley *et al.*, 2004; Enyedi *et al.*, 2013; Langford *et al.*, 2018).

The relevant redox sensors used in this dissertation harbor a sensor moiety fused to the redox sensitive green fluorescent protein, roGFP2. The probe responds sensitively to changes in a certain endogenous redox species and then induces structural changes in the chromophore of

roGFP2. The fluorescent reporter protein contains two cysteine residues adjacent to the GFP chromophore. Reversible formation of an intramolecular disulfide bond changes its protonation state. The anionic chromophore, predominantly in reduced roGFP2, has a fluorescence excitation maximum at ~490 nm, while in the neutral chromophore, predominantly in oxidized roGFP2, this maximum is shifted to ~405 nm. In both protonation states the chromophore emits at ~510 nm (Hanson *et al.*, 2004; Dooley *et al.*, 2004). The shift in fluorescence excitation allows for ratiometric measurements i.e., the fluorescence excitation ratio correlates with the degree of roGFP2 oxidation making the probe independent of varying expression levels.

1.2.1. Measurements of the glutathione redox couple

The laboratory of Jakob R. Winther introduced a pair of cysteine residues into a yellow fluorescent protein (YFP). Upon disulfide bond formation, fluorescence intensity and therefore the redox state of this redox sensitive YFP (rxYFP) could be followed *in vitro* and *in vivo* in yeast (Østergaard *et al.*, 2001). They also found that rxYFP expressed in the cytosol of *S. cerevisiae* equilibrates with the cytosolic glutathione pool catalyzed by endogenous glutaredoxins i.e., ScGrx1 and ScGrx2 (Østergaard *et al.*, 2004). Based on their previous results, they directly tethered ScGrx1 to rxYFP which improved the oxidation rates. These were further elevated by mutation of the second active site cysteine residue of ScGrx1 (Björnberg *et al.*, 2006). The fusion was applied to gain mechanistic insights into the glutaredoxin-dependent redox catalysis but proved to be an important step towards the development of sensitive and highly specific redox probes. Nowadays, rxYFP is predominantly replaced by roGFP2 as it allows for ratiometric rather than intensiometric measurements (Dooley *et al.*, 2004), but the principle of genetic fusions was adapted to generate the HsGrx1-roGFP2 sensor (Gutscher *et al.*, 2008). Interestingly, this probe was not capable of translocation into the mitochondria of plants and *Drosophila melanogaster*. This problem was overcome by inversion of the domains to roGFP2-HsGrx1 (Albrecht *et al.*, 2014). Moreover, this probe shows slightly enhanced reduction and oxidation kinetics and was the probe of choice for creation of the fusions in this dissertation. The sensors have been applied in many different organisms and subcellular compartments (Maughan *et al.*, 2010; Heller *et al.*, 2012; Back *et al.*, 2012; Morgan *et al.*, 2013). As outlined previously, endogenous glutaredoxins facilitate the equilibration of unfused roGFP2 with the intracellular 2GSH/GSSG redox couple (**Figure 4A**). Equilibration kinetics are improved in genetic fusions between glutaredoxins and roGFP2 as the fusion increases the effective glutaredoxin concentration relative to roGFP2 (Meyer, Dick, 2010). GSSG is sensed by the recombinant glutaredoxin in the fusion via glutathionylation of the more N-terminally located active site cysteine residue.

Subsequently, one of the engineered, redox-active cysteine residues in roGFP2 nucleophilically attacks the sulfur atom of the glutathionyl moiety. Release of GSH by the attack of the second engineered cysteine residue leads to formation of an intramolecular disulfide bond in roGFP2 (**Figure 4B**).

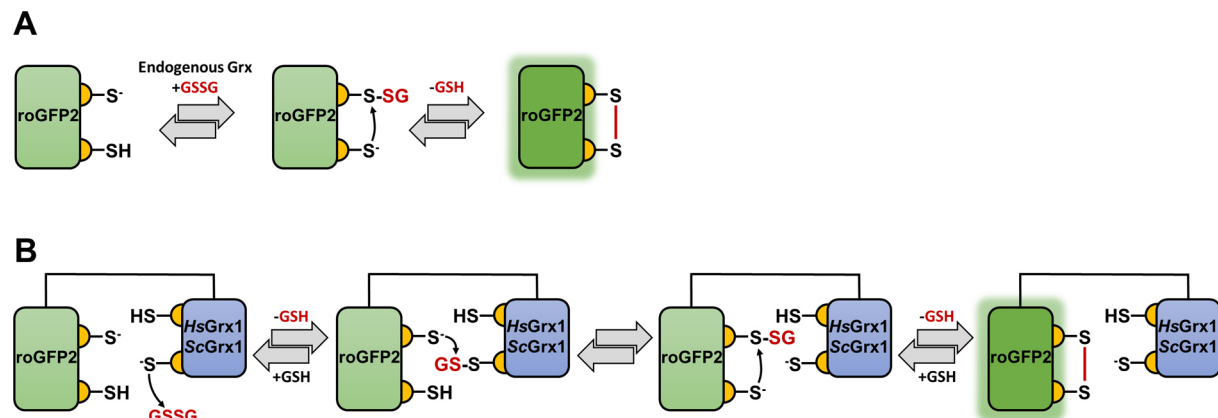


Figure 4. Mechanism of glutaredoxin-dependent equilibration of roGFP2. (A) Equilibration of unfused roGFP2 is mediated by endogenous glutaredoxins. (B) Fusion between roGFP2 and glutaredoxins enhance the oxidation and reduction kinetics making the reaction independent of endogenous glutaredoxins. The second cysteine residue in dithiol glutaredoxins is dispensable for roGFP2 glutathionylation and subsequent disulfide bond formation. Therefore, this mechanism also applies for monothiol active class I glutaredoxins as later discussed (Zimmermann, Morgan, unpublished).

1.2.2. Measurements of endogenous H₂O₂ changes

The idea of fusing roGFP2 to an active class I glutaredoxin facilitating the efficient equilibration with the glutathione redox couple was adapted and applied to other proteins for sensing peroxides. First, the glutathione peroxidase-like thiol peroxidase ScOrp1 (also known as ScGpx3) was fused to roGFP2. The redox relay introduced earlier between ScOrp1 and ScYap1 is the bases for functionality of this sensor (Delaunay *et al.*, 2002). The roGFP2 moiety in the fusion to ScOrp1 replaces ScYap1 in the redox relay as the receiving end of oxidative equivalents from H₂O₂ and ScOrp1. The direct fusion between these two proteins promotes their efficient interaction. The probe responded sensitively to peroxides *in vitro* and *in vivo* (Gutscher *et al.*, 2009). Further optimization of the roGFP2-based peroxide sensor was accomplished by fusing each of the eight thiol-peroxidases from *S. cerevisiae* to roGFP2 and test their sensitivity towards H₂O₂ (Morgan *et al.*, 2016). Although ScTsa1 and ScTsa2 contain extremely reactive thiols with second order rate constants of $2.2 \times 10^7 \text{ M}^{-1} \text{ s}^{-1}$ and $1.3 \times 10^7 \text{ M}^{-1} \text{ s}^{-1}$ respectively for the reaction with H₂O₂ at pH 7 (Ogusucu *et al.*, 2007), they showed similar sensitivity compared to roGFP2-ScOrp1. The reason was efficient competition of the endogenous thioredoxins for the disulfide bond formed in the fused thiol peroxidases (**Figure 5A**).

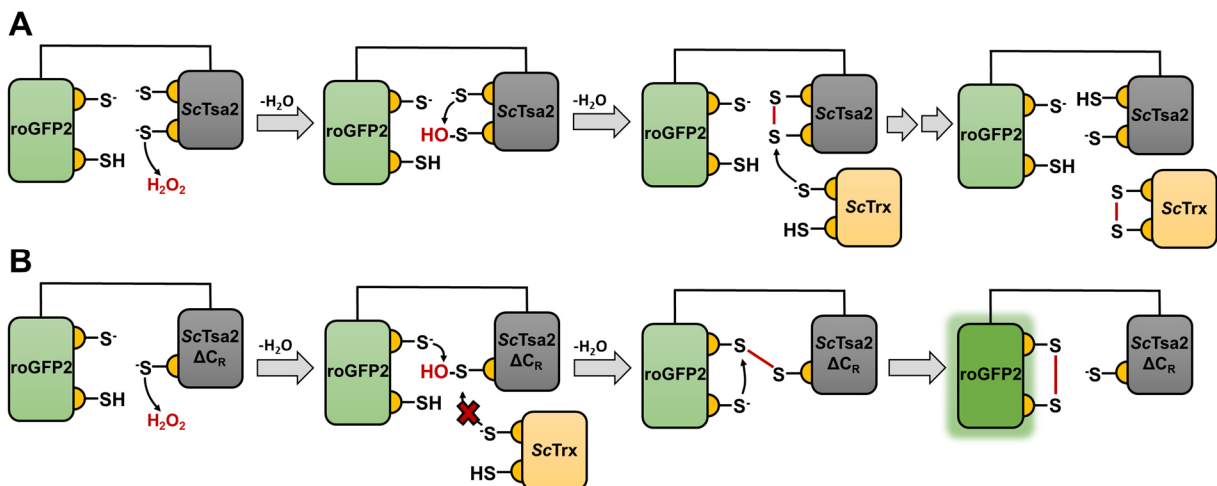


Figure 5. Deletion of the resolving cysteine in ScTsa2 eliminates competition with endogenous thioredoxins. (A) The peroxidatic cysteine residue attacks H_2O_2 forming a sulfenic acid. Subsequently, the resolving cysteine residue nucleophilically attacks the sulfenic acid resulting in an intramolecular disulfide bond. Endogenous thioredoxins can efficiently compete with roGFP2 for reduction of ScTsa2 decreasing the sensitivity of the probe. (B) In roGFP2-ScTsa2 ΔC_R the sulfenic acid on the Tsa2 ΔC_R moiety is directly attacked by one of the cysteines of roGFP2, forming an intermolecular disulfide bond. Subsequently, roGFP2 forms the intramolecular disulfide bond changing its fluorescence properties. The sensor is based on the principle of a redox relay. (Zimmermann, Morgan, unpublished)

Site-directed mutagenesis of the C_R solved the problem of efficient thioredoxin competition resulting in the ultrasensitive peroxide probe roGFP2-Tsa2 ΔC_R (**Figure 5B**; Morgan *et al.*, 2016). The probe was further adapted for measurements in fission yeast *Schizosaccharomyces pombe* in the peroxide sensor roGFP2-*SpTpx1* C169S (Carmona *et al.*, 2019). Both versions were more sensitive to H_2O_2 than their *cpYFP*-based counterpart, HyPer1. In *cpYFP*, N- and C-termini are arranged near the YFP chromophore decreasing the stability of the β -barrel. HyPer sensors harbor fragments of the H_2O_2 -sensitive regulatory domain from the bacterial transcription factor OxyR (Belousov *et al.*, 2006). These fragments are attached to the newly arranged N- and C-termini of *cpYFP*. Disulfide bond formation between both H_2O_2 -sensitive OxyR fragments induces slight structural changes in the YFP chromophore. Recently, the most optimized HyPer version, HyPer7, was developed (Pak *et al.*, 2020). First studies in yeast indicate lower peroxide sensitivity compared to roGFP2-Tsa2 ΔC_R in *S. cerevisiae* or roGFP2-*SpTpx1* C169S in *S. pombe*, respectively (Kritsiligkou *et al.*, 2021; Cubas *et al.*, 2021). However, HyPer7 is brighter and can further be used in mammalian cell systems, where roGFP2-Tsa2 ΔC_R was not successfully applied, yet. The reasons why roGFP2-Tsa2 ΔC_R cannot be expressed in higher plants or mammalian cells remain unclear. Due to the very recent publication of HyPer7 and the advantages of having an engineered redox relay within the probe itself, roGFP2-Tsa2 ΔC_R was the sensor of choice for measurements of endogenous H_2O_2 changes for this dissertation.

1.3. Towards *in vivo* measurements of redox enzyme activity

In vitro characterization of thioredoxin fold proteins mainly contributed to the current understanding of this versatile family. These measurements enable quantitative assessment of the catalytic activity of thioredoxin superfamily proteins. However, inactivity of certain proteins and their initial purification limit broad *in vitro* studies with many different proteins. Analyses of redox proteins in *S. cerevisiae* does not require initial purification. Characterization often involves interpretation and comparison of phenotypes or measurements of metabolites in whole-cell lysates e.g., upon genomic manipulation of yeast cells or chemical treatments. Finding a balance between quantitative *in vitro* and rather qualitative *in vivo* approaches could provide novel insights into thioredoxin superfamily proteins and accelerate their characterization. The recent application of fluorescence-based redox sensors to monitor different characteristics regarding the thiol peroxidase catalysis in living yeast cells might permit a way to ‘bridge this gap’.

1.3.1. *In vitro* characterization of the glutaredoxin oxidoreductase activity

In vitro kinetic measurements for studies on *ScGrx7*, *HsGrx5* and mutants thereof were performed in the laboratory of Prof. Dr. Marcel Deponte at the University of Kaiserslautern. Two different low molecular weight disulfide substrates were used in these assays (see publication 2.1.). Either the non-glutathione substrate bis(2-hydroxyethyl) disulfide (HEDS) (Nagai, Black, 1968), or *L*-cysteine-glutathione disulfide (GSSCys) as a glutathionylated substrate were employed to assess structure-function relationships of different glutaredoxins (Mesecke *et al.*, 2008; Begas *et al.*, 2015; Begas *et al.*, 2017). HEDS first reacts with GSH forming a mixed disulfide between GSH and 2-mercaptoethanol (GSSEtOH). The glutathionyl moiety of GSSEtOH or GSSCys are then attacked by the glutaredoxin of interest. Subsequently, glutathionylated glutaredoxins react with GSH as an electron donor. Both assays rely on the enzyme-dependent formation of GSSG and the subsequent NADPH-dependent reduction by glutathione reductase (Begas *et al.*, 2015). Glutaredoxin activity is monitored spectrophotometrically by consumption of NADPH. Alternative assays also involve the glutaredoxin-dependent reduction of oxidized model proteins e.g., ribonucleotide reductase or PAPS reductase. These alternative approaches play an important role for the development of novel *in vivo* methods as discussed later in this dissertation (see publication 2.3.) (Lillig *et al.*, 1999). In publication 2.2., stopped-flow kinetic measurements for S-nitrosoglutathione- (GSNO) and glutaredoxin-dependent oxidation of roGFP2 were monitored in a spectrofluorometer.

Therefore, a syringe contained either roGFP2 alone or in combination with the glutaredoxin in question. A second syringe contained GSNO. Oxidation of roGFP2 upon mixing of the protein(s) with GSNO was subsequently monitored.

Thioredoxin fold proteins are commonly studied *in vitro*. Although the approach advanced the understanding of this huge family, it still harbors limitations. The initial effort of protein purification and subsequent confirmation of the protein quality is both, time-consuming and labor-intensive. This limits the number of enzymes or mutants that can be studied simultaneously. Bacterial strains are commonly used as expression systems for recombinant proteins. If necessary, proteins can also be expressed in yeast, plants or mammalian cells. However, low yield of recombinantly expressed proteins, or proteins that are generally inactive when analyzed outside their native environment, further limit the *in vitro* characterization. For instance, land plant-specific class III glutaredoxins could not be purified as recombinant proteins thus far. The reason for that is a functionally important, hydrophobic motif at the C-terminal end that prevents expression in *E. coli* (Couturier *et al.*, 2010). Furthermore, *in vitro* assays rely on the reaction with certain model substrates or proteins e.g., HEDS or GSSCys as described previously. Therefore, inactivity of purified proteins *in vitro* does not exclude activity with specific, perhaps unknown substrates *in vivo*. Moreover, essential interactions with other proteins or possible posttranslational modifications, which are generally challenging to assess *in vitro*, are neglected. Consequently, novel assays are needed to overcome these limitations and complement existing *in vitro* approaches.

1.3.2. *In vivo* approaches for protein analyses in *Saccharomyces cerevisiae*

The budding yeast, *S. cerevisiae*, is a unicellular, eukaryotic organism that can exist in haploid or diploid states. Baker's yeast harbors 6275 genes of which ~800 are essential (Goffeau *et al.*, 1996). Many of these have homologs in the human genome which enable complementation and gene function studies (Botstein *et al.*, 1997; Liu *et al.*, 2017). Among the biggest advantages of yeast as a model organism is the accessibility of the yeast genome to genetic manipulations.

In this dissertation, genes were replaced by an antibiotic resistance cassette or a gene encoding an auxotrophic marker protein using a homologous recombination-based technique or tetrad dissection (Janke *et al.*, 2004; Papazian, 1952; Escoria, Forsburg, 2018). Homologous recombination can also be used to apply tags or fluorescent proteins for immunoblotting or microscopic identification of the subcellular localization (Wach *et al.*, 1994; Knop *et al.*, 1999). Furthermore, yeast cells can be readily transformed with plasmids.

The roGFP2-based sensors in publications 2.1., 2.2. and 2.3. were expressed from plasmids in the cytosol of yeast cells. In this dissertation complementation studies in yeast were performed in the context of ‘plasmid shuffling’ (Boeke *et al.*, 1987). Plasmid shuffling is particularly useful when investigating essential genes that cannot be deleted from the genome. For this, two different plasmids are transformed into yeast cells. The first plasmid is selected by an uracil auxotrophic marker and encodes a viability supporting protein. The second plasmid harbors a certain gene encoding the protein in question. Subsequently, yeast cells grow under counter-selective pressure induced by application of 5-fluoroorotic acid (5-FOA) to the growth medium. In presence of functional uracil biosynthesis, 5-FOA is converted into toxic 5-fluorouracil which is lethal after incorporation into the RNA. Hence, yeast cells are counter-selected against the first plasmid and viability or growth phenotypes on 5-FOA depend upon the protein encoded on the second plasmid (Forsburg, 2001).

Very basic, but still commonly used, are growth assays e.g., drop dilution assays or automated measurements of the optical density for growth curves. These methods are often combined with growth on media with different carbon sources or chemical treatments to assess the impact of genomic manipulations in a certain yeast strain. Falsely, it is often assumed that the physiological relevance of a specific protein directly correlates with phenotypes observed in these indirect assays as outlined above. However, these phenotypes might actually be caused by perturbations of downstream processes, where the protein in question participates. For instance, peroxide sensitivity of thiol peroxidase deletion strains is often postulated to result from impaired peroxide scavenging (Jacobson *et al.*, 1989; Chae, *et al.*, 1994; Hofmann *et al.*, 2002). However, it is known that these proteins are also involved in other processes besides peroxide detoxification i.e., H₂O₂ signaling or protein folding (Sobotta *et al.*, 2015; Jang *et al.*, 2004; Teixeira *et al.*, 2019). Recently, it was demonstrated that deletion of *ScTSA1* affected regulation of the protein kinase A subunit *ScTpk1*, which was shown to be the cause of the growth phenotypes on plates containing H₂O₂. Therefore, they postulated that sensitivity of a $\Delta tsa1$ strain does not result from impaired peroxide scavenging *per se* but rather from protein kinase A hyperactivity due to its misregulation in absence of *ScTsa1* (Roger *et al.*, 2020; Bodvard *et al.*, 2017). Further insights into the diverse function of peroxiredoxins are given in publication 2.4. Adaptation of yeast deletion strains or suppressor mutations as a response to the loss of a certain gene can lead to variations in phenotypes (Liu, Zhang, 2019). In many cases it remains unknown if a certain gene deletion causes an overexpression of another protein or leads to other compensatory mechanisms (Zeyl, 2004). The readout of these genomic manipulation-based *in vivo* approaches often relies on phenotypes. How can living yeast cells be used to complement quantitative *in vitro* approaches for monitoring redox enzymes activity or even use them to assess structure-function relationships within a certain protein?

1.3.3. Novel fluorescence- and yeast-based approaches for redox enzyme analyses

The development of genetically encoded redox sensors enabled measurements of intracellular redox species. Sensors are available for reliable monitoring of the major redox-active molecules including H₂O₂ (Belousov *et al.*, 2006; Gutscher *et al.*, 2009; Morgan *et al.*, 2011), glutathione (Gutscher *et al.*, 2008), NADH (Zhao *et al.*, 2011; Hung *et al.*, 2011; Zhao *et al.*, 2015) and NADPH (Tao *et al.*, 2017). These sensors are continuously optimized in respect to their sensitivity and specificity to certain redox species. Since their development, such sensors have predominantly been used to monitor changes in these species with subcellular resolution. However, recently it was demonstrated that roGFP2-based sensors can assess structure-function relationships and activity of thiol peroxidases. Interestingly, the first advances regarding this novel use of these sensors were gained relatively early. In 2006, Björnberg and colleagues employed fusions between rxYFP and ScGrx1. These were the first fusions that permitted rapid equilibration between a redox-sensitive fluorescent protein and the glutathione redox couple. Moreover, they fused an engineered monothiol ScGrx1 variant to rxYFP to gain insights into the glutaredoxin catalysis. They found that the cysteine mutant was capable of oxidizing roGFP2 more efficiently. Consequently, they postulated elevated oxidoreductase activity of an engineered monothiol ScGrx1 mutant in accordance with *in vitro* data (Björnberg *et al.*, 2006). Although the idea of fluorescence-based measurements of redox enzyme activity was born about 15 years ago, it was followed up in detail just recently. Staudacher and colleagues demonstrated in 2018 that roGFP2 oxidation depends upon the activity of the fused thiol peroxidase. Using these fusions, they tested multiple gain- and loss-of-function mutations regarding hyperoxidation of *Plasmodium falciparum* PfAOP *in vivo* and *in vitro* (Djika *et al.*, 2013; Staudacher *et al.*, 2018). Fusions between roGFP2 and ScPrx1 were employed in combination with established glutathione sensors to gain insights into the mitochondrial glutathione homeostasis. They demonstrated ScPrx1-dependent oxidation of the matrix glutathione pool and engineered less hyperoxidation-sensitive variants of ScPrx1 (Calabrese *et al.*, 2019). Hetero-oligomerization of peroxiredoxins was shown using a cysteine-less Tsa2 moiety fused to roGFP2 i.e., roGFP2-Tsa2ΔC_PΔC_R. Intriguingly, roGFP2 was still oxidized in wild-type yeast cells upon H₂O₂ application. The probe was observed to assemble into oligomeric complexes with endogenous cytosolic ScTsa1 and ScTsa2 mediating the oxidation of roGFP2. In contrast, in ScTsa1 and ScTsa2 double deletion cells, roGFP2-Tsa2ΔC_PΔC_R responses upon H₂O₂ treatment were absent (Morgan *et al.*, 2016). These studies all demonstrated different ways of how roGFP2-based fusions were used to gain insights into properties of thiol peroxidase redox catalysis or structure-function relationships *in vivo*.

1.4. Aim of this work

Thioredoxin superfamily proteins are predominantly characterized *in vitro* with purified proteins. *In vitro* protein characterization harbors several limitations including time-consuming protein purification, inactivity of certain proteins in these assays or analysis of enzymes outside their ‘native’ environment. In order to overcome these limitations, alternative approaches are needed to accelerate and improve on characterization of thioredoxin fold proteins. Since their development, fluorescence-based redox sensors were almost exclusively used to monitor intracellular redox species (**Figure 6A**). Recently, advances were made regarding the application of roGFP2-based probes to monitor several aspects of the thiol peroxidase catalysis, including hyperoxidation and hetero-decamerization. Whether these approaches are applicable to other thioredoxin superfamily enzymes remains to be shown.

The goal is to complement and improve upon existing *in vitro* approaches by rapidly screening through many different redox enzymes or mutants thereof. Consequently, the present work aims to develop, establish and apply novel assays that permit rapid monitoring of the glutaredoxin oxidoreductase activity in living yeast cells. The cytosol of these yeast cells serves as an in-cell ‘test tube’. Genomic manipulations by deletion or overexpression of specific genes permit an engineered and fine-tuned environment. This allows for accurate monitoring of the enzyme-dependent roGFP2 oxidation. Yeast cells can readily be transformed with plasmids containing fusions between roGFP2 and many different redox enzymes or mutants thereof. This avoids the initial effort of protein purification for enzyme analyses and is therefore less labor-intensive. Together with automated, fluorescence plate reader-based measurements, the approach enables high-throughput screening of many constructs and conditions in parallel.

The study also aims to provide a deeper understanding of both, the roGFP2-based readout of oxidoreductase activity and glutaredoxin structure-function relationships. To ‘bridge the gap’ between *in vitro* and *in vivo* approaches, relative differences in roGFP2 oxidation kinetics of various constructs will be measured in the cytosol of living yeast cells (**Figure 6B**). In collaboration with Prof. Dr. Marcel Deponte at the University of Kaiserslautern, the respective recombinant proteins and mutants will be characterized *in vitro* allowing for side-by-side comparison. Subsequent studies will then aim to dissect the important structural motifs that determine classification into either class I or class II glutaredoxins. Furthermore, another in-cell system will be developed for monitoring reduction of essential and non-essential endogenous disulfide substrates. Together, both approaches aim for a comprehensive understanding of the glutaredoxin-dependent catalysis. The presented screens will certainly be applied in future experiments to assess the function of even more, potentially uncharacterized thioredoxin superfamily proteins.

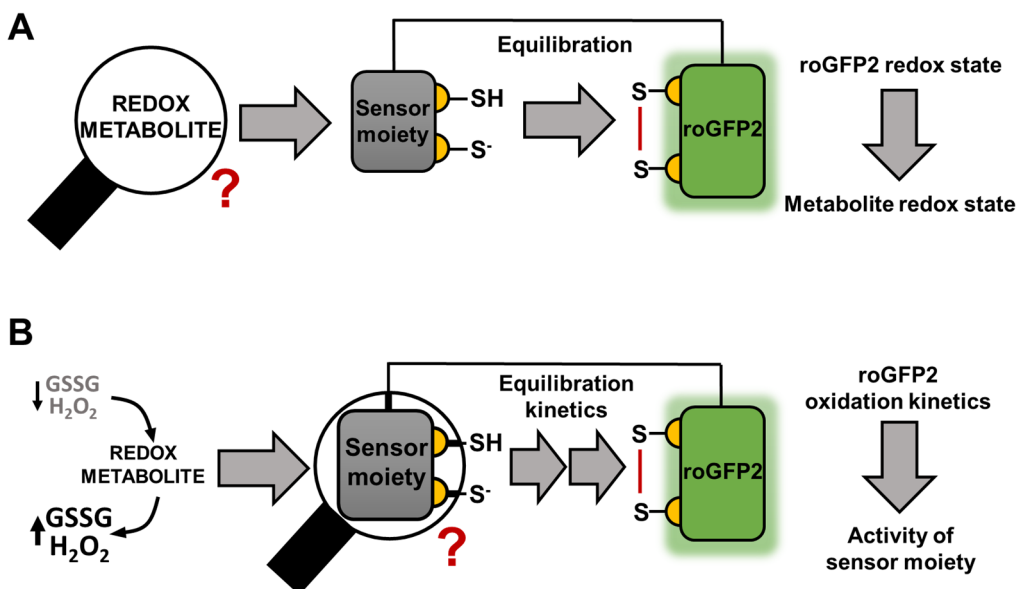


Figure 6. Schematic illustration for common and novel application of roGFP2-based redox sensors.

(A) Thus far, roGFP2 fusions have predominantly been used to monitor a certain redox metabolite. Therefore, the specific sensor moiety mediates the thermodynamic equilibration between this redox species and roGFP2. Monitoring the roGFP2 redox state provides information about the redox state of the endogenous redox metabolite.

(B) In contrast to **(A)**, the sensor equilibrates roGFP2 to an induced change in a certain metabolite. Kinetics of roGFP2 equilibration to that change depend upon the activity of the fused sensor moiety. Hence, relative differences in oxidation kinetics between different sensor moieties reflect changes in their activity.

2. Scientific articles

2.1. Liedgens et al., 2020, *Nature Communications*

Quantitative assessment of the determinant structural differences between redox-active and inactive glutaredoxins.

Liedgens, L.[§], Zimmermann, J.[§], Wäschenbach, L.[§], Geissel, F., Laporte, H., Gohlke, H., Morgan, B. and Deponte, M.

Nature Communications. 2020 April; 11(1), 1-18

DOI: 10.1038/s41467-020-15441-3

[§]Equally contributing authors

Reprinted from *Nature Communications*: Liedgens, L., Zimmermann, J., Wäschenbach, L., Geissel, F., Laporte, H., Gohlke, H., Morgan, B. and Deponte, M. *Quantitative assessment of the determinant structural differences between redox-active and inactive glutaredoxins*. 11(1), 1-18 © (2020), with permission from Nature Springer (*Nature Communications*).

All rights reserved.

ARTICLE



<https://doi.org/10.1038/s41467-020-15441-3>

OPEN

Quantitative assessment of the determinant structural differences between redox-active and inactive glutaredoxins

Linda Liedgens^{1,5}, Jannik Zimmermann^{1,6}, Lucas Wäschenbach^{1,3,5}, Fabian Geissel¹, Hugo Laporte^{1,2}, Holger Gohlke^{1,3,4}, Bruce Morgan^{1,2} & Marcel Deponte¹

Class I glutaredoxins are enzymatically active, glutathione-dependent oxidoreductases, whilst class II glutaredoxins are typically enzymatically inactive, Fe-S cluster-binding proteins. Enzymatically active glutaredoxins harbor both a glutathione-scaffold site for reacting with glutathionylated disulfide substrates and a glutathione-activator site for reacting with reduced glutathione. Here, using yeast ScGrx7 as a model protein, we comprehensively identified and characterized key residues from four distinct protein regions, as well as the covalently bound glutathione moiety, and quantified their contribution to both interaction sites. Additionally, we developed a redox-sensitive GFP2-based assay, which allowed the real-time assessment of glutaredoxin structure-function relationships inside living cells. Finally, we employed this assay to rapidly screen multiple glutaredoxin mutants, ultimately enabling us to convert enzymatically active and inactive glutaredoxins into each other. In summary, we have gained a comprehensive understanding of the mechanistic underpinnings of glutaredoxin catalysis and have elucidated the determinant structural differences between the two main classes of glutaredoxins.

¹ Fachbereich Chemie, Abteilung Biochemie, Technische Universität Kaiserslautern, D-67663 Kaiserslautern, Germany. ² Institut für Biochemie, Zentrum für Human- und Molekularbiologie (ZHMB), Universität des Saarlandes, D-66123 Saarbrücken, Germany. ³ Mathematisch-Naturwissenschaftliche Fakultät, Institut für Pharmazeutische und Medizinische Chemie, Heinrich-Heine-Universität Düsseldorf, D-40225 Düsseldorf, Germany. ⁴ John von Neumann Institute for Computing (NIC), Jülich Supercomputing Centre (JSC) & Institute of Complex Systems, ICS-6: Structural Biochemistry, Forschungszentrum Jülich GmbH, D-52425 Jülich, Germany. ⁵These authors contributed equally: Linda Liedgens, Jannik Zimmermann, Lucas Wäschenbach. email: gohlke@uni-duesseldorf.de; bruce.morgan@uni-saarland.de; deponte@chemie.uni-kl.de

ARTICLE

Canonical glutaredoxins (Grx), also referred to as class I Grx, are enzymatically active in standard *in vitro* oxidoreductase assays. On the contrary, Grx-like proteins, also referred to as class II Grx, bind iron-sulfur clusters and have very little or no oxidoreductase activity (reviewed in refs. 1–7). For the sake of simplicity, hereinafter we classify the two protein subfamilies as “enzymatically active Grx” or “inactive Grx”, respectively. However, we do not exclude the possibility that inactive Grx might, in some cases, catalyze redox reactions with specialized substrates *in vivo*.

Enzymatically active Grx use glutathione as a substrate^{3,4,7–10} (Fig. 1a, b), whereas inactive Grx use glutathione as a ligand for their iron-sulfur cluster^{1,2,5,6} (Fig. 1c). How both Grx subfamilies exert their nonredundant physiological functions in redox catalysis and iron metabolism remains puzzling, and the underlying structure-function relationships are only partially understood. We recently confirmed that enzymatically active Grx have two distinct glutathione-interaction sites, one glutathione-scaffold site that interacts with glutathionylated disulfide substrates (GSSR)

during the oxidative half-reaction, and one glutathione-activator site that interacts with reduced glutathione (GSH) during the reductive half-reaction^{7,11,12} (Fig. 1a). Based on these results, we hypothesized that modified glutathione interactions underlie the enzymatic inactivity of class II Grx and kinetically uncouple these proteins from the glutathione pool^{7,12,13}. Kinetic studies revealed that the glutathione-scaffold site reflects the glutathione interaction that was previously identified in numerous X-ray and nuclear magnetic resonance (NMR) structures of both Grx subfamilies^{4,12}. In contrast, the glutathione-activator site remains predominantly uncharacterized except for a highly conserved lysine residue¹². The relevance of this residue as an activator was recently corroborated by a study on the lysine-deficient *Trypanosoma brucei* homolog TbGrx1 which reacts with GSSG but does not accept GSH as a reducing agent¹⁴.

The aim of this work therefore was, first, to identify protein areas that are relevant for redox catalysis and that are modified in enzymatically inactive Grx and, second, to quantitatively assess the contribution of these protein areas toward the oxidoreductase

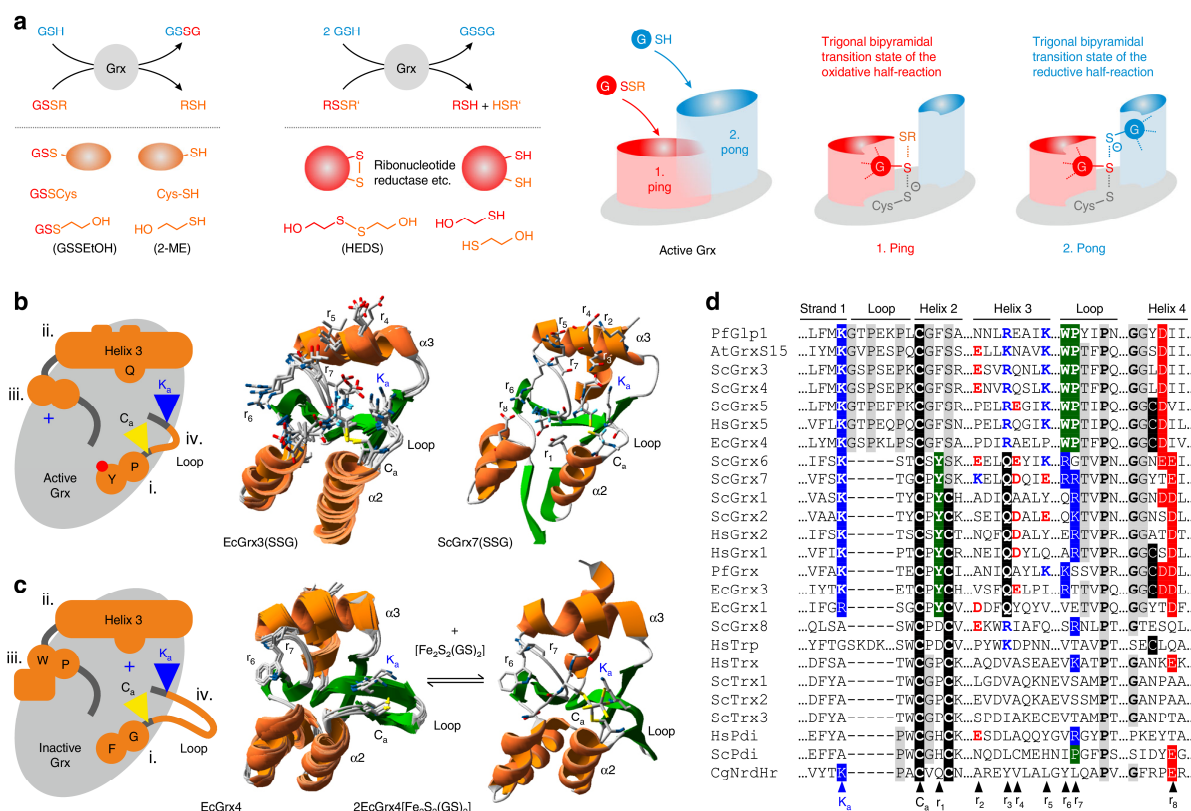


Fig. 1 Structural differences between enzymatically active and inactive Grx. **a** Enzymatically active glutaredoxins (Grx) use reduced glutathione (GSH) as an electron donor for the reduction of high- and low-molecular weight glutathione disulfide substrates (GSSR) or non-glutathione disulfide substrates (RSSR') as highlighted in the left half of the panel. The Grx-catalyzed reduction of GSSR by GSH is separated into an oxidative and reductive half-reaction as highlighted by the two predicted transition states and glutathione interaction sites in the schematic representations in the right half of the panel.

b Structure of enzymatically active Grx. A schematic representation of four specialized protein areas, NMR solution structures of the glutathionylated C14S mutant of enzymatically active EcGrx3 (PDB entry 3GRX), and a model of glutathionylated ScGrx7 are shown from left to right. Please note that the glutathione moiety as well as the conserved active-site cysteine (C_a) and lysine (K_a) residue adopt several alternative positions in the NMR structures. **c** Structure of enzymatically inactive Grx. A schematic representation of four specialized protein areas, NMR solution structures of enzymatically inactive EcGrx4 (PDB entry 1YKA), and the crystal structure of EcGrx4 in complex with an iron-sulfur cluster (PDB entry 2WCI, one EcGrx4 subunit and one GS-ligand were omitted for clarity) are shown from left to right. Please note the conformational change of the elongated loop and the repositioning of the active-site cysteine and lysine residue upon iron-sulfur cluster binding. **d** Sequence alignment of glutaredoxin isoforms and comparison with other proteins of the thioredoxin superfamily from *A. thaliana* (At), *S. cerevisiae* (Sc), *Homo sapiens* (Hs), *E. coli* (Ec), *P. falciparum* (Pf), and *C. glutamicum* (Cg). Established as well as potential glutathione-interacting residues r_{1–8} are highlighted.

activity. At least four protein areas differ between enzymatically active and inactive Grx (Fig. 1b–d): (i) The active site of all Grx contains an essential cysteine residue for catalysis or iron–sulfur cluster binding at the N-terminus of helix 2. This residue is followed in most enzymatically active Grx by a proline, a tyrosine and a second cysteine residue in a CPYC-motif, whereas a glycine, a phenylalanine and a serine residue are usually found in a CGFS-motif in inactive Grx. With the exception of the poorly active hybrid protein ScGrx8 from yeast¹¹, the second cysteine residue of enzymatically active Grx is dispensable for the reduction of glutathionylated substrates and the low-molecular weight model substrate bis(2-hydroxyethyl)disulfide (HEDS)^{15–25}. Accordingly, attempts to activate the Grx-like protein 1 from *Plasmodium falciparum* by simply introducing a second cysteine residue failed²⁶. In contrast to glutathionylated substrates, the reduction of specific, non-glutathionylated protein disulfides such as *Escherichia coli* ribonucleotide reductase requires the second cysteine residue of active Grx^{10,17,27,28}. The second cysteine might also help to resolve kinetically trapped enzyme conformations^{4,11}. The proline residue in the CPYC-motif prevents iron–sulfur cluster binding. It is replaced in a few enzymatically active Grx that can also bind [Fe₂S₂] clusters^{19,21,29–32}. The tyrosine hydroxyl group of the CPYC-motif, which is absent in the CGFS-motif of inactive Grx, protrudes from the protein surface and was hypothesized to contribute to the glutathione-activator site¹². The residue is replaced by aspartate in poorly active ScGrx8, by histidine in protein disulfide isomerases and by proline in thioredoxins^{11,12,33}. (ii) Helix 3 is part of the glutathione-scaffold site and differs significantly between both Grx subfamilies^{4,12,34,35}. It harbors a conserved glutamine residue and also comprises residues that protrude from the protein surface and that might contribute to the glutathione-activator site¹². (iii) A conserved WP-motif in the loop between helix 3 and strand 3 is characteristic of inactive Grx and is usually replaced by one or two basic residues in enzymatically active Grx^{4,19,26,34–37}. (iv) The most striking feature of enzymatically inactive Grx is an elongated loop between the highly conserved lysine residue and the active-site cysteine residue^{4,34,36}. Comparisons between the structures of monomeric apoprotein and homodimeric holoprotein of EcGrx4 from *E. coli* as well as HsGrx5 from human revealed significant rearrangements of this insertion and a repositioning of the cysteine and lysine residue upon [Fe₂S₂] cluster binding^{34,36,38}. The insertion was hypothesized to be the major cause for the enzymatic inactivity of class II Grx¹⁹.

Here, we systematically analyzed protein areas (i)–(iv) for recombinant mutant proteins in steady-state kinetic assays in vitro, for redox reporter-tagged constructs in yeast, and for molecular dynamics simulations in silico. Using the enzymatically active CPYS-type model protein ScGrx7 from yeast as well as the inactive CGFS-type homolog HsGrx5, we further characterized the glutathione-scaffold and glutathione-activator site. We show that protein areas (i)–(iv) all contribute to Grx catalysis and demonstrate that the flanking lysine and tyrosine residue do not affect the thiol pK_a value of the active-site cysteine residue but rather stabilize the transition states. Furthermore, our data suggests that the elongated active-site loop acts as an off-switch in enzymatically inactive Grx. Finally, as a proof-of-principle, we show that by replacing key structural motifs we could interconvert enzymatically active and inactive glutaredoxins, respectively.

Results

The hydroxyl group of Tyr110 is dispensable for catalysis. Most active Grxs harbor a conserved tyrosine residue in their catalytic CPY(C/S)-motif. This residue is typically replaced by

phenylalanine in most inactive Grxs (r₁ in Fig. 1). We first therefore purified recombinant wild-type ScGrx7 as well as the ScGrx7 mutant Y110F. In addition, we prepared the ScGrx7 mutant Y110H to investigate the requirement for an aromatic side chain and the mutant Y110A, which lacks any aromatic side chain or possibility for hydrogen bonding, as a control (Fig. 2, Supplementary Figs. 1–6, Supplementary Tables 1–3). Replacement of Tyr110 by phenylalanine had rather minor effects on the k_{cat}^{app} and K_m^{app} values in the GSSCys assay (Fig. 2a, b). The catalytic efficiencies (k_{cat}^{app}/K_m^{app}) and reciprocal Dalziel coefficients (1/Φ) of the Y110F mutant were almost identical or even slightly increased as compared with the wild-type enzyme (Fig. 2c–e). These parameters can be interpreted as the second order rate constant for the oxidative half-reaction with GSSCys, yielding glutathionylated enzyme and cysteine, and the reductive half-reaction with GSH, yielding reduced enzyme and glutathione disulfide (GSSG)^{12,39} (Fig. 2f). Thus, both half-reactions appeared to be unaffected by the removal of the hydroxyl group. In contrast to the GSSCys assay, catalytic efficiencies and reciprocal Dalziel coefficients of Y110F in the HEDS assay were decreased by 20–56% (Supplementary Fig. 4). In this assay, ScGrx7 can directly react with HEDS, yielding 2-mercaptoethanol (2-ME) and a mixed disulfide between GSH and 2-mercaptoethanol (GSSEtOH). GSSEtOH must change its orientation at the active site before it can be reduced by a second GSH molecule, yielding 2-ME and GSSG^{12,25}. In summary, the hydroxyl group of the conserved active-site tyrosine residue is dispensable for the GSH-dependent reduction of GSSCys and does not play a general role as a GSH activator. However, the hydroxyl group can affect the turnover of non-glutathione disulfide substrates.

Tyr110 forms part of the glutathione-scaffold site. In accordance with preliminary results¹², replacement of Tyr110 of ScGrx7 by alanine decreased the catalytic efficiency and reciprocal Dalziel coefficient for GSSCys to 18–23% and for GSH to 9–15% of the wild-type enzyme (Fig. 2). Catalytic efficiencies and reciprocal Dalziel coefficients of Y110A in the HEDS assay were decreased to 3–6% of the wild-type enzyme (Supplementary Fig. 4). Removal of the bulky aromatic side chain therefore affected both the oxidative and the reductive half-reaction of the enzyme. An intermediate effect was observed for the mutant Y110H, which had an approximately three to four times lower catalytic efficiency and reciprocal Dalziel coefficient for GSSCys, but an almost unchanged catalytic efficiency and reciprocal Dalziel coefficient for GSH (Fig. 2). Thus, replacement of the phenyl moiety by the basic imidazole side chain in Y110H impaired the interaction with GSSCys during the oxidative half-reaction but not with GSH during the reductive half-reaction. As a result, the oxidative half-reaction became rate-limiting for Y110H. In summary, the side chain of Tyr110 plays an important structural role and contributes to the glutathione-scaffold site as revealed for mutants Y110H and Y110A. The unaffected reaction rate between Y110F/H and GSH appears to be based on the bulky aromatic side chain that keeps the glutathione moiety of the glutathionylated enzyme and its transition state in a correct orientation. Removal of the aromatic side chain in Y110A presumably alters this orientation and, therefore, indirectly decreases the rate constant with GSH during the reductive half-reaction.

Lys105 and Tyr110 do not affect the thiol pK_a value of Cys108. Based on studies on human Grx1 and NrdH from *Corynebacterium glutamicum*^{40,41}, we previously suggested that Lys105 (residue K_a in Fig. 1) might also stabilize the thiolate of the active-site cysteine residue of ScGrx7 (ref. ¹²). We now tested this hypothesis for wild-type ScGrx7 as well as the mutants

ARTICLE

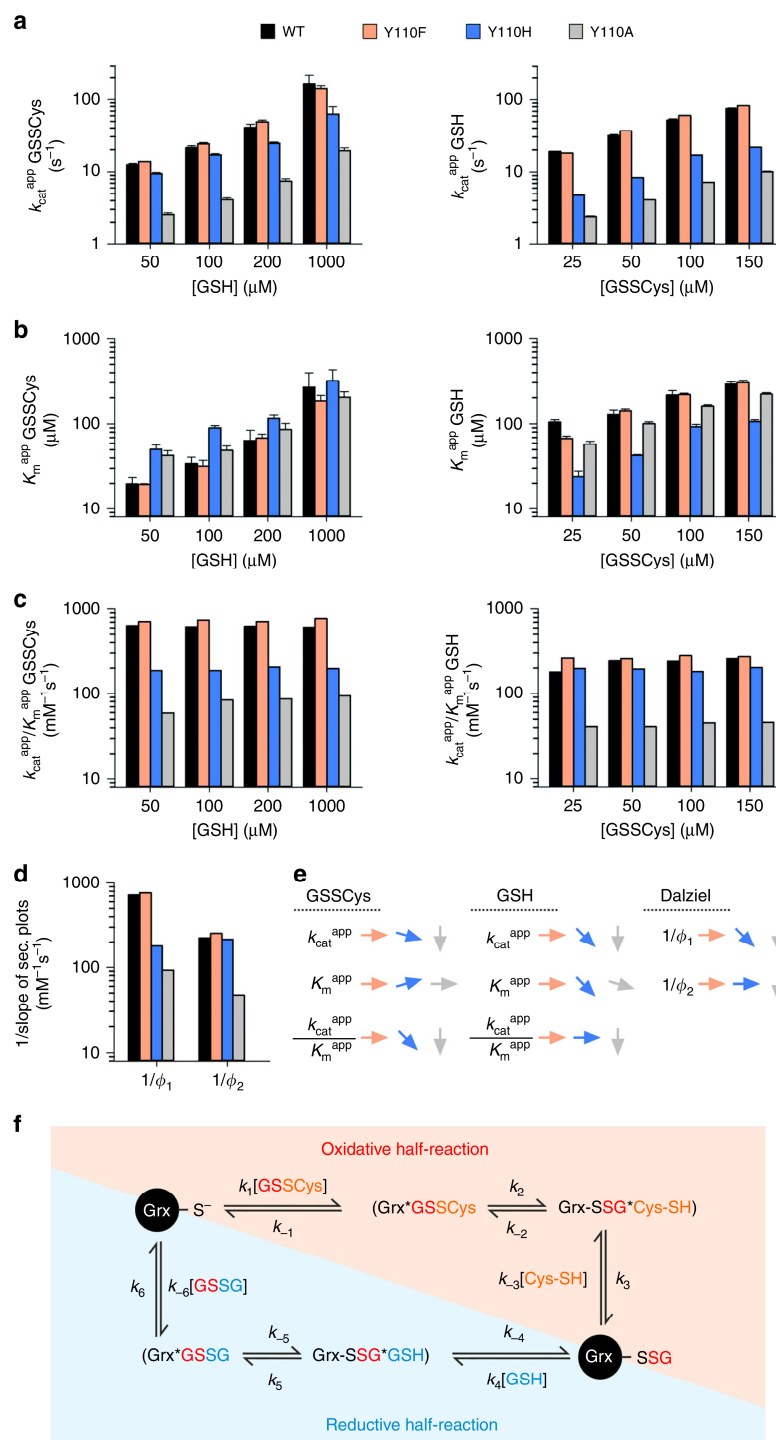


Fig. 2 Tyr110 of ScGrx7 is part of the glutathione-scaffold site in the GSSCys assay. **a, b** Selected $k_{\text{cat}}^{\text{app}}$ and K_m^{app} values of ScGrx7 wild-type enzyme and Y110F/H/A mutants for GSSCys and GSH. **c** Calculated catalytic efficiencies from panels (a) and (b). **d** Reciprocal Dalziel coefficients, which probably reflect the second order rate constants of the oxidative and reductive half-reaction with GSSCys and GSH, respectively. **e** Summary of the altered kinetic parameters for Y110F/H/A. **f** Reaction sequence for the GSSCys assay in accordance with the observed ping-pong kinetics. Please note that the K_m^{app} values are not solely defined by the ratios k_{-1}/k_1 and k_{-4}/k_4 but are also affected by other rate constants. Hence, the K_m^{app} values do not reflect true substrate affinities as shown previously¹². Source data are provided in the Supplementary Information: original plots and kinetic parameters for panels a–c are shown in Supplementary Fig. 2 and Supplementary Table 2. Statistical analyses and P values for the $k_{\text{cat}}^{\text{app}}$ and K_m^{app} values from panels a and b are listed in Supplementary Table 11. Error bars are the calculated standard error from the curve fits in SigmaPlot 13. Reciprocal Dalziel coefficients for panel d were obtained from Supplementary Fig. 3 and are listed together with the true k_{cat} values in Supplementary Table 1.

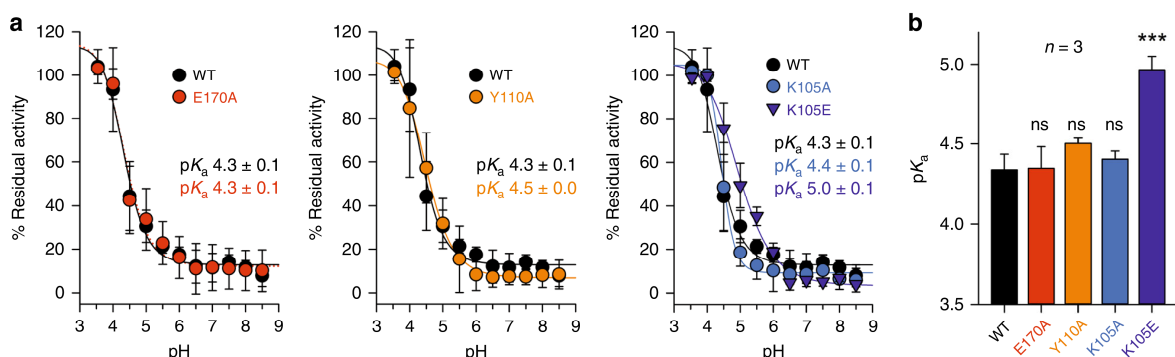


Fig. 3 The side chains of Tyr110 and Lys105 do not affect the pKa-value of the ScGrx7 active site thiol group. Freshly reduced wild-type ScGrx7 (black symbols) and selected mutants (colored symbols) were incubated with 150 μM iodoacetamide at 23 °C for 180 s in a three-buffer system at pH 3.5–8.5. Residual activities were measured in a standard HEDS assay and normalized against mock controls that were incubated in parallel without iodoacetamide. **a** Data for wild-type ScGrx7 (WT) and the mutants E170A, Y110A, K105A, and K105E. Samples containing iodoacetamide were apparently more stable at lower pH values than the mock controls resulting in residual activities slightly above 100%. The pKa values from the sigmoidal fits are indicated. Data points and error bars represent the mean ± s.d. of three independent experiments. **b** Summary and statistical analyses of the pKa values from panel (a). Sigmoidal fits using the four parameter Hill function and P values from one way ANOVA analyses followed by a Holm-Sidak test were calculated in SigmaPlot 13 ($P > 0.05$: ns; $P \leq 0.001$: ***). Source data are provided as a Source Data file.

K105A/E and Y110A. Following incubation of the recombinant ScGrx7 mutants with iodoacetamide at a range of different pH values, the residual enzymatic activity was determined in a standard HEDS assay (Fig. 3). Residue Glu170 (r_8 in Fig. 1), which contributes to the glutathione-scaffold site and is far away from Cys108 (ref. 12), was replaced by alanine and served as a negative control. Replacement of Lys105 or Tyr110 by alanine had no significant effect on the pKa value of the thiol group of Cys108, whereas the replacement of Lys105 by glutamate increased the pKa value from 4.3 ± 0.1 to 5.0 ± 0.1 . In summary, the thiol pKa value of the free enzyme is unaffected by the positive charge of Lys105 or the side chain of Tyr110, and even the introduction of an additional negative charge in the proximity of the active-site cysteine residue has only a moderate effect on its protonation state. We therefore suggest that both residues rather stabilize the conformation of the free and glutathionylated enzyme as well as its negatively charged transition states.

The basic loop following helix 3 is part of the scaffold site. Residue Arg153 (r_7 in Fig. 1) in the loop between helix 3 and strand 3 of ScGrx7 also protrudes from the protein surface and is therefore a candidate for the recruitment of GSH. We therefore analyzed the ScGrx7 mutants R153A/E in the GSSCys assay in vitro (Fig. 5, Supplementary Figs. 1, 11, and 12, Supplementary Tables 4 and 6). Wild-type ScGrx7 was studied in parallel and served as a control for systematic variations. The alanine replacement of Arg153 reduced the catalytic efficiency and reciprocal Dalziel coefficient for GSSCys by 60% but had only a minor effect on the catalytic efficiency and reciprocal Dalziel coefficient for GSH. In contrast, the charge inversion in R153E also affected the reductive half-reaction with GSH. The reductive half-reactions of both mutants were as fast as their oxidative half-reactions, suggesting that the glutathionylation of the mutants became the rate-limiting step for catalysis. In summary, residue Arg153 plays a crucial role for the glutathione-scaffold site and its replacement can result in a rate-limiting oxidative half-reaction.

Helix 3 contributes to the scaffold site and GSH recruitment. Residues Asp144 and Glu147 (r_4 and r_5 in Fig. 1) in helix 3 of ScGrx7 were suggested to contribute to the glutathione-activator site because they protrude from the protein surface on top of the glutathione-scaffold site¹². We addressed this hypothesis for the mutants D144A/K and E147A/K in the GSSCys assay in vitro (Fig. 4, Supplementary Figs. 1 and 7–10, Supplementary Tables 4 and 5). Wild-type ScGrx7 was studied in parallel and served as a control for systematic variations. Replacement of Asp144 by alanine and lysine slightly decreased the reciprocal Dalziel coefficient for GSSCys by 17–20%, whereas replacement of Glu147 by alanine and lysine had no effect on the catalytic efficiency and reciprocal Dalziel coefficient for GSSCys (Fig. 4). The alanine replacement of Asp144 and Glu147 in D144A and E147A also had no effect on the catalytic efficiency and reciprocal Dalziel coefficient for GSH. In contrast, lysine replacements in D144K and E147K yielded gain-of-function mutants with 1.7- and 2.5-fold increased reciprocal Dalziel coefficients for GSH. In summary, the charge-inversion mutants D144K and E147K have an accelerated reductive-half-reaction with GSH in accordance with the hypothesis that helix 3 not only contributes to the glutathione-scaffold site but also plays a role for the recruitment of GSH by surface-exposed residues.

Interconversion studies of active and inactive Grx. Next, we analyzed the predicted relevance of the WP-motif and the elongated active-site loop for enzyme inactivation¹⁹ with the intention to convert enzymatically inactive and active Grx into each other. We therefore replaced either residues Arg152/Arg153 (r_6 and r_7 in Fig. 1) of ScGrx7 by a WP-motif or the short TG loop of ScGrx7 with the elongated GTPEQPQ loop of HsGrx5. In addition, we generated mutants that contained both replacements. The recombinant mutants ScGrx7^{WP}, ScGrx7^{loop}, and ScGrx7^{WP+loop} were subsequently compared with wild-type ScGrx7, which was studied in parallel and served as a control for systematic variations. Likewise, we replaced the WP-motif of HsGrx5 by the RR-motif of ScGrx7, the elongated GTPEQPQ loop of HsGrx5 by the TG loop of ScGrx7 and both features in a combined HsGrx5 mutant. Residue Cys122 of HsGrx5, which is part of a moderately conserved GGC-motif in the proximity of the reaction center⁴, was replaced by serine to avoid unwanted side reactions^{26,42,43}. The three mutants HsGrx5^{RR}, HsGrx5^{loop}, and HsGrx5^{RR+loop} were subsequently compared with wild-type HsGrx5 (Fig. 6, Supplementary Figs. 1 and 13–16, Supplementary Tables 7–9). The insertion of the elongated active-site loop in ScGrx7^{loop} decreased the catalytic efficiencies and reciprocal Dalziel coefficients for GSSCys and GSH by more than two orders of magnitude. In contrast, replacement of the

ARTICLE

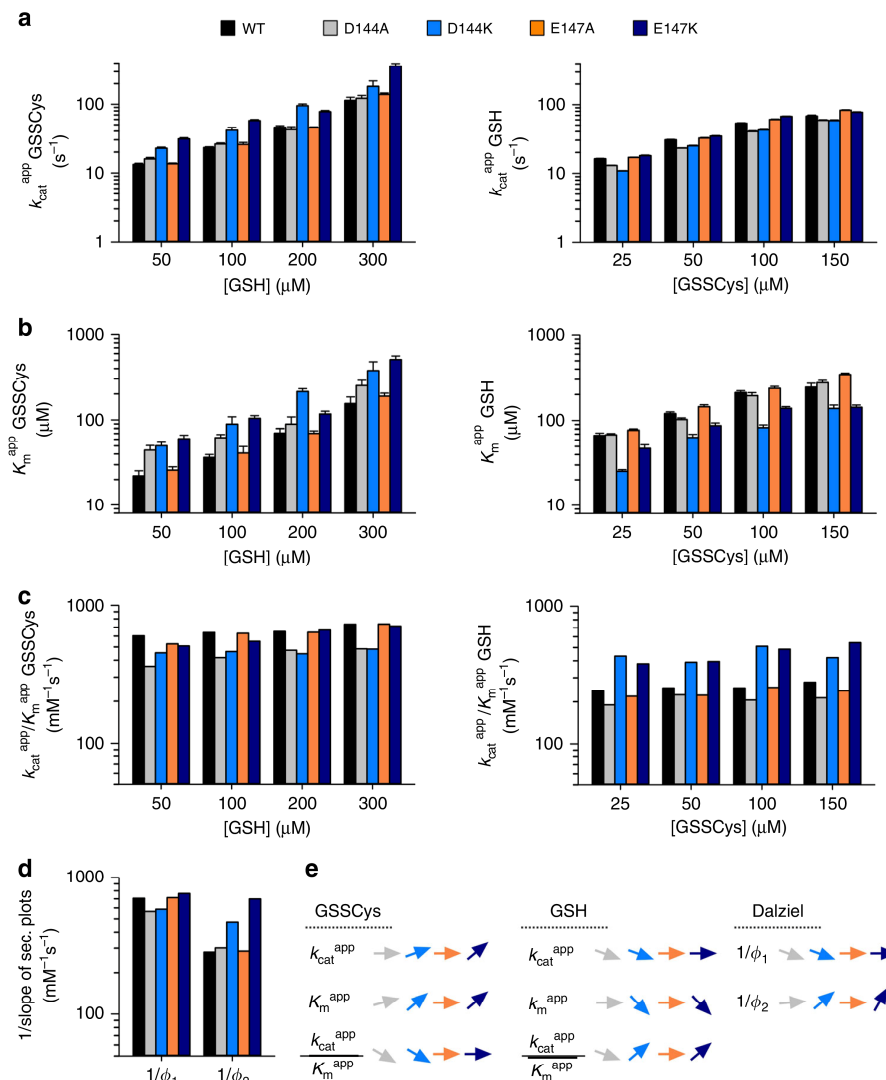


Fig. 4 Lysine replacements of Asp144 or Glu147 in helix 3 of ScGrx7 accelerate the reductive half-reaction in the GSSCys assay. **a, b** Selected $k_{\text{cat}}^{\text{app}}$ and K_m^{app} values of ScGrx7 wild-type enzyme as well as D144A/K and E147A/K mutants for GSSCys and GSH. **c** Calculated catalytic efficiencies from panels (a) and (b). **d** Reciprocal Dalziel coefficients, which probably reflect the rate constants of the oxidative and reductive half-reaction with GSSCys and GSH, respectively. **e** Summary of the altered kinetic parameters for D144A/K and E147A/K. Source data are provided in the Supplementary Information: original plots and kinetic parameters for panels **a–c** are shown in Supplementary Figs. 7 and 9 and Supplementary Table 5. Statistical analyses and P values for the $k_{\text{cat}}^{\text{app}}$ and K_m^{app} values from panels **a** and **b** are listed in Supplementary Table 11. Error bars are the calculated standard error from the curve fits in SigmaPlot 13. Reciprocal Dalziel coefficients for panel **d** were obtained from Supplementary Figs. 8 and 10 and are listed together with the true k_{cat} values in Supplementary Table 4.

RR-motif in ScGrx7^{WP} predominantly affected the catalytic efficiency and reciprocal Dalziel coefficient for GSSCys, resulting in a rate-limiting oxidative half-reaction in accordance with the results from Fig. 5. The oxidative half-reaction became also rate-limiting for ScGrx7^{WP+loop}, which had an even lower activity than ScGrx7^{loop}. Freshly purified recombinant wild-type HsGrx5 contained an iron–sulfur cluster (as indicated by its brown color and absorbance maxima at 321, 412, and 455 nm) as reported previously^{37,38}. For activity measurements, the iron–sulfur cluster was removed by EDTA and subsequent gel filtration chromatography. In contrast, recombinant HsGrx5^{RR}, HsGrx5^{loop}, and HsGrx5^{RR+loop} were colorless, suggesting that the WP-motif and the elongated active-site loop are both crucial for iron–sulfur cluster binding. Shortening the active-site loop in HsGrx5^{loop} activated the protein, resulting in reciprocal Dalziel coefficients for

GSSCys and GSH around $2 \times 10^3 \text{ M}^{-1} \text{s}^{-1}$ and $5 \times 10^3 \text{ M}^{-1} \text{s}^{-1}$, respectively. The activities of the other HsGrx5 constructs were too low ($\leq 10^2 \text{ M}^{-1} \text{s}^{-1}$) to determine reliable kinetic constants. The intermediate activity of HsGrx5^{loop} exemplifies the necessity of a combination of structural features for the enzymatic activity of class II Grx. In summary, while ScGrx7 is inactivated by the elongated active-site loop of HsGrx5 but not by its WP-motif, HsGrx5 can be transformed into a moderately active enzyme by shortening its elongated active-site loop but not by replacing its WP-motif. The length of the active-site loop is therefore a determinant structural difference between both Grx classes.

Intracellular mechanistic assessment of ScGrx7 mutants. Fusion constructs between Grx and a redox-sensitive yellow

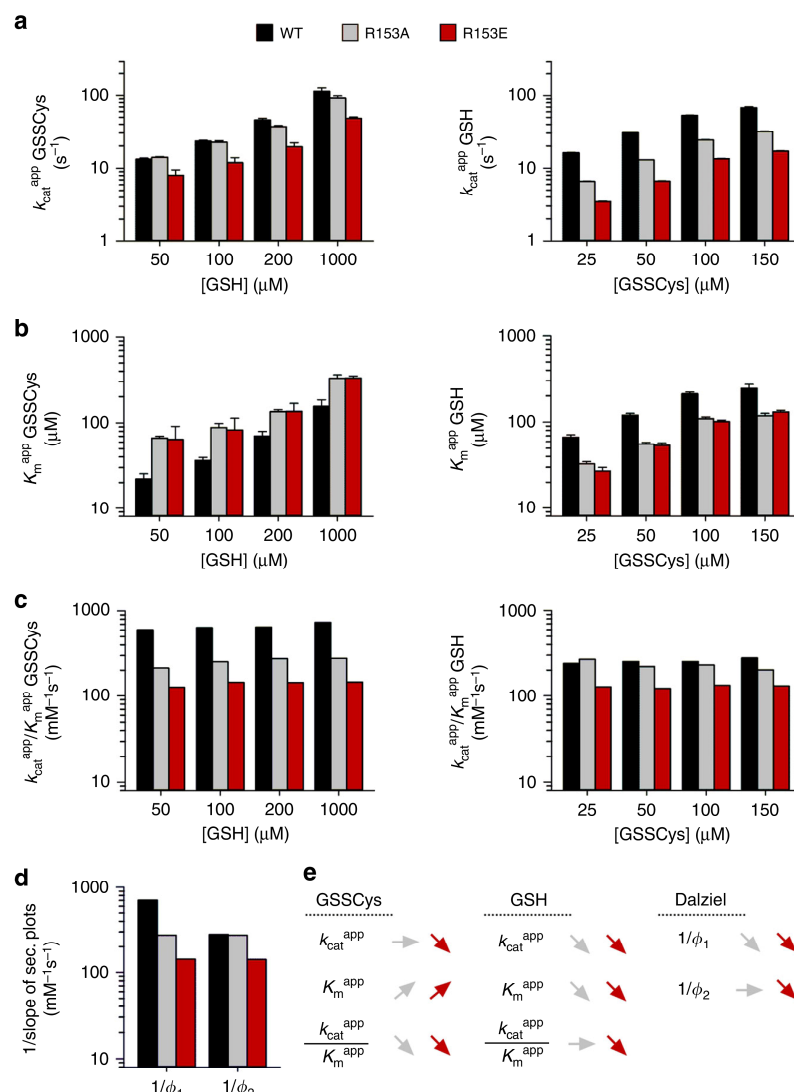


Fig. 5 Arg153 of ScGrx7 is part of the glutathione-scaffold site in the GSSCys assay. **a, b** Selected $k_{\text{cat}}^{\text{app}}$ and K_m^{app} values of ScGrx7 wild-type enzyme and R153A/E mutants for GSSCys and GSH. **c** Calculated catalytic efficiencies from panels **(a)** and **(b)**. **d** Reciprocal Dalziel coefficients, which probably reflect the rate constants of the oxidative and reductive half-reaction with GSSCys and GSH, respectively. **e** Summary of the altered kinetic parameters for R153A/E. Source data are provided in the Supplementary Information: original plots and kinetic parameters for panels **a–c** are shown in Supplementary Fig. 11 and Supplementary Table 6. Statistical analyses and P values for the $k_{\text{cat}}^{\text{app}}$ and K_m^{app} values from panels **a** and **b** are listed in Supplementary Table 11. Error bars are the calculated standard error from the curve fits in SigmaPlot 13. Reciprocal Dalziel coefficients for panel **d** were obtained from Supplementary Fig. 12 and are listed together with the true k_{cat} values in Supplementary Table 4.

fluorescent protein have previously been used to gain mechanistic insight into glutaredoxin catalysis *in vitro*¹⁸, as well as to dynamically monitor the redox state of the intracellular glutathione pool^{44,45}. Recently, we successfully established fusion constructs between redox-sensitive green-fluorescent protein 2 (roGFP2) and peroxidases for monitoring their catalytic mechanism and inactivation in living cells^{46,47}. We thus asked if roGFP2 fusion constructs could also be adapted for the noninvasive assessment of Grx structure–function relationships inside living cells. To this end, we sought to establish a yeast-based system to permit the rapid screening of roGFP2–Grx constructs.

Equilibration of the roGFP2 dithiol/disulfide redox couple with the 2GSH/GSSG redox couple depends upon Grx-mediated catalysis. Therefore, by monitoring the kinetics of roGFP2 oxidation

in response to perturbation of the cytosolic glutathione pool we hoped to be able to observe the impact of specific mutations on glutaredoxin activity. Our assay required that we could readily perturb the cytosolic glutathione pool by the addition of exogenous oxidants and that roGFP2 oxidation is specific for the genetically fused glutaredoxin. To fulfill both of these requirements we generated a yeast strain which lacked the genes encoding glutathione reductase and the two enzymatically active cytosolic Grx ($\Delta grl1 \Delta grx1 \Delta grx2$). This strain was complemented with cytosolic fusion constructs between roGFP2 and various Grx mutants as described previously⁴⁵. Fusion constructs with wild-type ScGrx7 or its redox-inactive mutant C108S served as a positive and negative control, respectively. Wild-type roGFP2–ScGrx7 was found to be ~60% oxidized at steady state and readily responsive,

ARTICLE

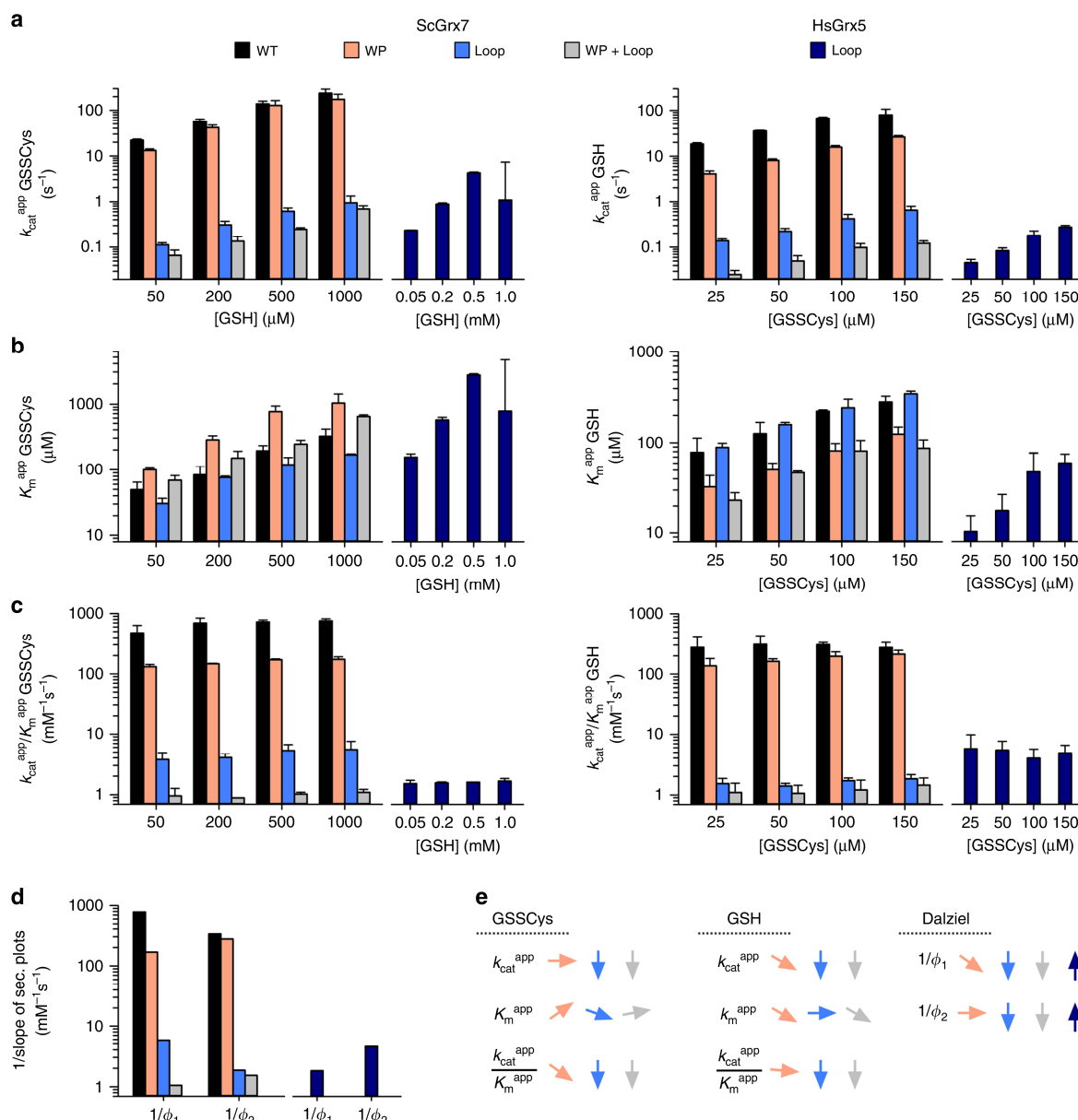
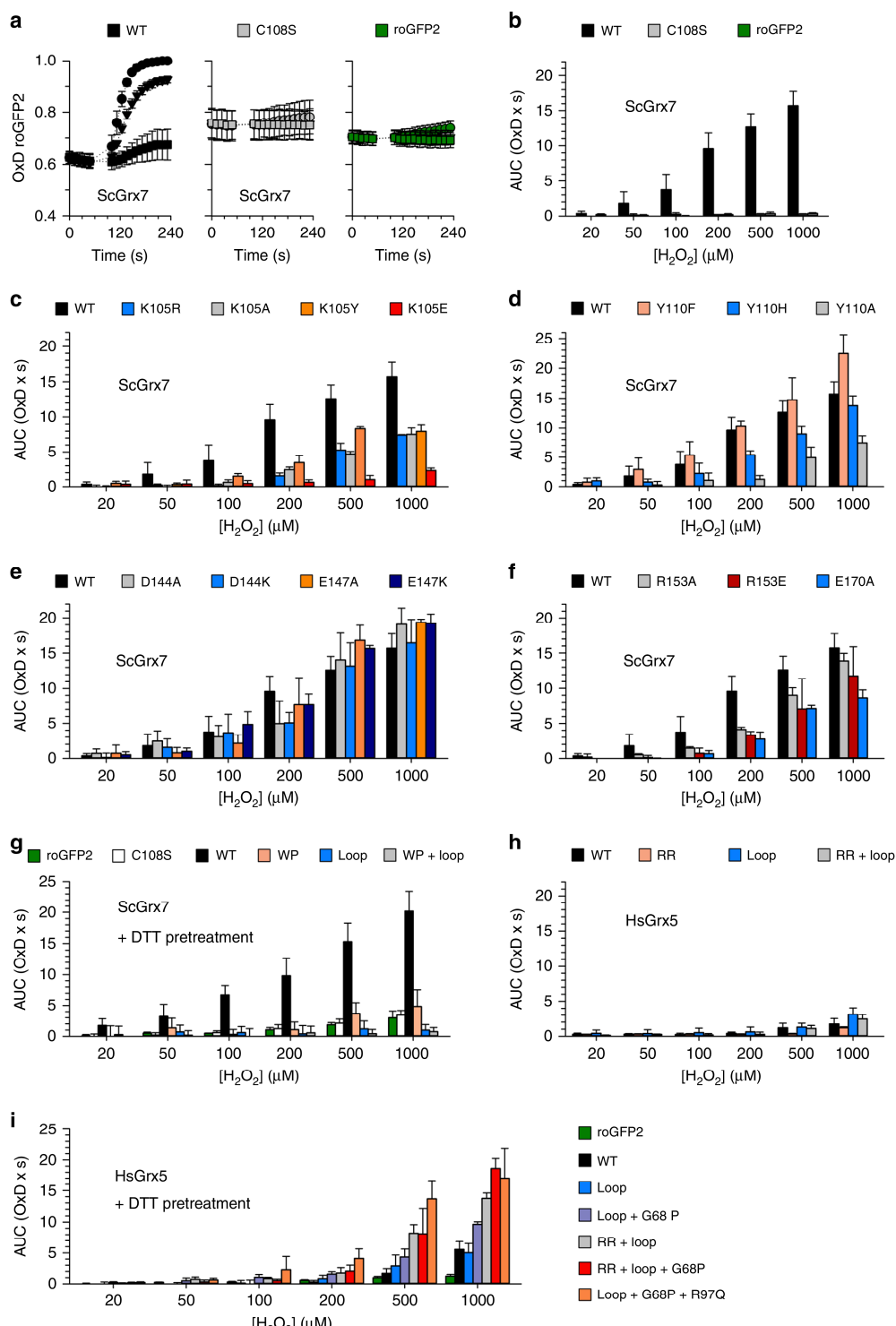


Fig. 6 The active-site loop is a determinant structural difference between enzymatically active and inactive Grx. **a, b** Selected k_{cat}^{app} and K_m^{app} values of ScGrx7 wild-type enzyme, ScGrx7^{WP}, ScGrx7^{loop}, ScGrx7^{WP+loop}, and HsGrx5^{loop}. **c** Calculated catalytic efficiencies from panels (a) and (b). **d** Reciprocal Dalziel coefficients, which probably reflect the rate constants of the oxidative and reductive half-reaction with GSSCys and GSH, respectively. **e** Summary of the altered kinetic parameters. Source data are provided in the Supplementary Information: original plots and kinetic parameters for panels a–c are shown in Supplementary Figs. 13 and 15 and Supplementary Tables 8 and 9. Statistical analyses and P values for the k_{cat}^{app} and K_m^{app} values from panels a and b are listed in Supplementary Table 11. Error bars are the calculated standard error from the curve fits in SigmaPlot 13. Reciprocal Dalziel coefficients for panel d were obtained from Supplementary Figs. 14 and 16 and are listed together with the true k_{cat} values in Supplementary Table 7.

in a concentration-dependent manner, to the exogenous addition of H_2O_2 at concentrations ranging from 0.02 to 1 mM. In contrast, both roGFP2-ScGrx7^{C108S} and unfused roGFP2 were about 70–80% oxidized at steady state and almost completely unresponsive to exogenous H_2O_2 (Fig. 7a). To simplify further analyses, we developed a standardized measure of probe response. First, we subtracted the baseline of an untreated probe response (0 μM H_2O_2) from all H_2O_2 -treated probe responses. Secondly, we then calculated the integrated area under the curve (AUC) for the first 48 s of the “corrected” probe responses. We subsequently plotted the

AUC against the H_2O_2 concentration for all constructs tested (Fig. 7b).

The intracellular roGFP2 responses of the ScGrx7 fusion constructs correlated very well with the in vitro data for the oxidative half-reaction, suggesting that GSSG is rapidly sensed as glutathionylated Grx, which subsequently glutathionylates roGFP2 so that it can form an intramolecular disulfide bond. Strongest effects were observed for the charge inversion mutant K105E and for Y110A, followed by intermediate effects for mutants K105R/A/Y and Y110H (Fig. 7c, d). Mutant Y110F



appeared to be slightly more active than wild-type ScGrx7 in accordance with the in vitro data. No significant differences were detected between mutants D144A/K or E147A/K and wild-type ScGrx7 (Fig. 7e) in accordance with the predominantly unaffected reaction rates of these mutants with GSScys. In contrast, lowered roGFP2 responses were detected for fusion constructs with

mutants R153A/E and the mutant E170A, which served as a reference for the glutathione-scaffold site¹² (Fig. 7f). These results further support our interpretation that the altered roGFP2 responses reflect changes during the oxidative half-reaction of the ScGrx7 mutants. In other words, the transfer of oxidation from ScGrx7 to the fused roGFP2 moiety does not appear to be

ARTICLE

Fig. 7 Noninvasive intracellular assessment of Grx structure-function relationships using roGFP2. **a** Time-dependent ratiometric degree of roGFP2 oxidation (OxD) for yeast cells with genetically encoded fusion constructs between roGFP2 and ScGrx7. The results for bolus treatments with 1 mM (circles), 0.2 mM (triangles), and 0.05 mM (squares) H₂O₂ are shown. Cells with wild-type roGFP2–ScGrx7 (WT) responded rapidly in contrast to the active-site mutant roGFP2–ScGrx7^{C108S} (C108S) and roGFP2 alone (roGFP) which served as negative controls. **b** Integrated dose-response curves from panel (a). The area under the OxD curves (AUC) was determined for the first 48 s following the addition of H₂O₂. **c, d** Integrated dose-response curves for ScGrx7 mutants of residues Lys105 and Tyr110. These residues flank the active-site cysteine residue and the glutathione moiety in glutathionylated Grx. **e, f** Integrated dose-response curves for ScGrx7 mutants of residues r₄, r₅, r₇, and r₈ from Fig. 1. **g–i** Integrated dose-response curves for ScGrx7 and HsGrx5 interconversion mutants under standard conditions (panel h) or after pretreatment and subsequent washout of DTT (panels g and i). RoGFP2 alone (roGFP2) as well fusion constructs with inactive ScGrx7^{C108S} (C108S) or wild-type ScGrx7 (WT) served as negative and positive controls. All experiments were repeated at least three times and data were reported as mean AUCs with error bars representing the standard deviation. Source data are provided as a Source Data file. Statistical analyses and P values are listed in Supplementary Table 12.

rate-limiting, rather, the rate of oxidation of ScGrx7 by GSSG appears to dictate the kinetics of roGFP2 oxidation.

Intracellular assessment of Grx interconversion mutants. We also addressed the interconversion of enzymatically active and inactive Grx in yeast using roGFP2-based fusion constructs. In the fusion construct between roGFP2 and ScGrx7^{WP}, the roGFP2 moiety was found to be almost fully oxidized at steady state. RoGFP2 was ~80% oxidized at steady state in fusion constructs involving ScGrx7^{loop} or ScGrx7^{WP+loop}. In all three constructs roGFP2 oxidation appeared to be robust against further oxidation upon exogenous H₂O₂ addition, however, the high steady-state oxidation limited the possibility for further roGFP2 oxidation and confounded interpretation of oxidation kinetics (Supplementary Fig. 17). Therefore, to gain further insight into the functionality of these ScGrx7 constructs we first pretreated the cells with 50 mM DTT to fully reduce roGFP2, followed by a washing step to remove DTT, and then subsequently monitored kinetics of roGFP2 oxidation upon H₂O₂ addition. In all constructs, around 10–20% of roGFP2 molecules were oxidized after the DTT pretreatment and subsequent washing steps. The exception was wild-type roGFP2–ScGrx7, which was ~40% oxidized. Importantly, after addition of exogenous H₂O₂, we still observed very little response of all constructs, except wild-type roGFP2–ScGrx7, which responded rapidly (Fig. 7g). Again, except for ScGrx7^{WP}, the loss of function of the interconversion mutants ScGrx7^{loop} and ScGrx7^{WP+loop} in yeast correlated very well with the in vitro data.

We next asked about the response of fusion constructs between roGFP2 and HsGrx5, HsGrx5^{RR}, HsGrx5^{loop}, or HsGrx5^{RR+loop}. In all cases, the constructs were poorly active and required high H₂O₂ concentrations to detect a roGFP2 oxidation response under standard conditions without DTT pretreatment. However, replacement of the elongated GTPEQPQ loop of HsGrx5 by the TG loop of ScGrx7 in HsGrx5^{loop} resulted in an up to twofold increase of the AUC as compared with wild-type roGFP2–HsGrx5 (Fig. 7h). Thus, replacement of the loop of HsGrx5 slightly increased its activity, though neither the loop nor the WP-motif (alone or in combination) is enough to impart a high oxidoreductase activity to HsGrx5 using roGFP2 as a substrate. We therefore screened for additional HsGrx5 mutations that might increase the oxidoreductase activity using our more sensitive DTT treatment and washout protocol. Under these conditions, we were able to identify positive additive effects for the short TG loop in combination with a replacement of residue Gly68 in the CGFS motif by proline, the replacement of the WP-motif by the RR-motif, and/or replacement of Arg97 (residue r₃ in Fig. 1) by the conserved glutamine residue in helix 3 (Fig. 7i). HsGrx5 triple mutants of these protein areas were, at the highest H₂O₂ concentrations, almost as active as ScGrx7.

In summary, roGFP2 can be used for the noninvasive intracellular assessment of Grx structure–function relationships yielding similar patterns for glutathione-scaffold site mutants

in vitro and in yeast. Furthermore, the intracellular roGFP2 assay can be used to rapidly screen a set of potential loss- or gain-of-functions mutants of a variety of Grx isoforms. A screen for HsGrx5 gain-of-function mutants revealed that protein areas (i)–(iv) from Fig. 1 synergistically contribute to the oxidoreductase activity of Grx.

Simulation of the interaction between GS[–] and ScGrx7-SSG. We previously showed that conserved residue Lys105 of ScGrx7 (K_a in Fig. 1) serves as a glutathione activator for the reductive half-reaction between GSH and the glutathionylated enzyme¹². To gain insights into the first step of the reductive half-reaction of ScGrx7 at an atomistic level and to identify the residues that form the glutathione-activator site, we performed four replications of molecular dynamics simulations each of wild-type ScGrx7 and the variants K105R, K105E, and E147K. We focused only on the substrate access of the reductive half-reaction by simulating the binding of deprotonated glutathione (GS[–]) in the presence of oxidized ScGrx7, i.e., ScGrx7 that is glutathionylated at Cys108 (Fig. 8). We defined binding events of GS[–] with a distance cutoff of 5.5 Å between the sulfur atom of one of the freely diffusing GS[–] molecules and the center of mass of the sulfur atoms of the disulfide bond between the active-site cysteine and the covalently bound glutathione moiety. Overall, the protein structure of ScGrx7 in all simulations was structurally stable and exhibited no major movements of secondary structure elements (Supplementary Figs. 18 and 19). With respect to the fraction of bound GS[–] states, we observed a ~2-fold increase for K105R and a significant decrease to ~34% for K105E compared to wild-type ScGrx7 (Fig. 8a). For the E147K variant, the fraction of bound states increased by 2.2-fold. These results are in good agreement with those of substitutions of Lys105 by arginine or glutamate that were previously shown to accelerate or decelerate the reductive half-reaction in vitro¹².

To understand these differences at the structural level, we only considered snapshots that fulfill our distance-based criterion for GS[–] binding in the following analyses. The representative conformations of the first two clusters of binding poses revealed clear differences in the active sites and binding poses of GS[–] among the different variants (Fig. 8b). In addition, the occupation density of glutathione (Fig. 8c), its binding pathway (Fig. 8d), and the distance and angular distributions of the encounter complex between GS[–] and Cys108-SSG (Fig. 8e) were analyzed. The side chain of residue 105 interacts with the glycine carboxyl group of the covalently bound glutathione in wild-type ScGrx7 and the K105R variant, but with the backbone of Cys108 in the K105E variant (Fig. 8b). This conformational change is accompanied by a rotation of the glycine carboxyl group away from the active site toward the solution in the K105E variant. As a consequence, in the binding pose of GS[–] in the K105E variant, the glycyl moiety of GS[–] is positioned near Tyr110, and the γ-glutamyl moiety points away from the protein surface, in contrast to wild-type

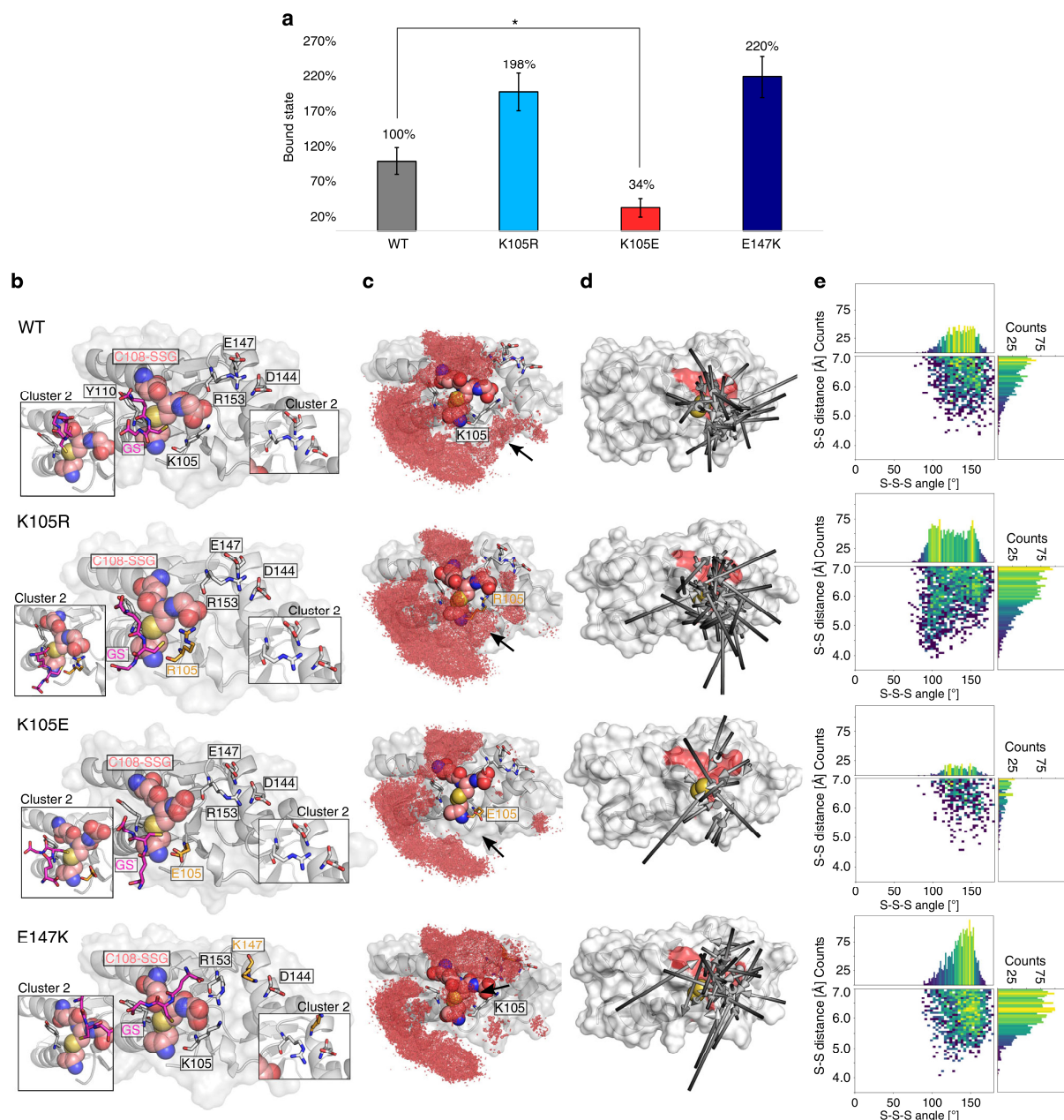


Fig. 8 Molecular dynamics simulations of GS⁻ binding to glutathionylated ScGrx7. **a** Fraction of bound states with the value for wild-type ScGrx7 (WT) normalized to 100%. Error bars show the standard error of the mean over four replications for each system. Datasets were tested with a two-tailed *t* test assuming unequal variances; *: null-hypothesis of equal means can be rejected with $P < 0.05$. For WT and K105R $P = 0.13$; for WT and E147K $P = 0.15$ (see also Supplementary Table 13). **b** For each of the systems of the WT and the variants K105R, K105E, and E147K, bound states were clustered with respect to the structural deviation of the active site and the closest GS⁻ from the solution. The structure representing the most populated cluster is shown in the middle and important areas of the structure representing the second most populated cluster (cluster 2) are shown in the boxes next to it. The covalently bound glutathione moiety at Cys108 is depicted in salmon, the freely diffusing GS⁻ in pink. Residues marked in orange show the mutated residues in the variants. All residues with labels were also studied experimentally. **c** The occupation density of the diffusing GS⁻ is shown as a red grid on the structure of each ScGrx7 variant. Bound states were combined across replications for this analysis, and the threshold of the density grids is the same for all variants. **d** Arrows show the binding pathways of GS⁻. For each binding event, an arrow shows the linearized trajectory of the GS⁻ molecule right before the binding event going from black (start of the pathway) to gray (bound). The active site is shown as a red surface and the sulfur atoms of the mixed disulfide bond are shown in yellow. **e** Histograms show the distance between the sulfur atom of GS⁻ and the center of mass of the sulfur atoms of Cys108-SSG ("S-S-distance") and the angle created by the three sulfur atoms ("S-S-S angle") over all four replications each. The color of the bins ranges from dark blue (lowest populated bin) over green to yellow (highest populated bin). See Supplementary Table 14 for results of the correlation analysis.

ARTICLE

ScGrx7 and the K105R variant. These changes are reflected in differences in the occupation densities of GS⁻ (Fig. 8c) in that in the K105R variant a patch above residue 105 and toward Cys108-SSG is more frequently occupied than in wild-type ScGrx7, but less frequently occupied in the K105E variant.

Substitution of Glu147 with lysine leads to a rearrangement of the side chain of Arg153 toward the glycine carboxyl group of the covalently bound glutathione, in accordance with a changed binding pose of GS⁻ where the molecule is rotated by about 90° so that either the carboxyl group of its γ-glutamyl moiety or its glycyl moiety interacts with the Arg153 guanidinium group (Fig. 8b). This alternative conformation of Arg153 is stable over the whole simulation time for E147K, while it is less frequently sampled for the other variants (Supplementary Fig. 20). As a consequence, the E147K variant exhibits a different pattern of occupation density of GS⁻ across the active site, with the patch of higher occupation across Cys108-SSG now being shifted towards the glutathione moiety and Arg153 (Fig. 8c).

The analysis of binding paths revealed that GS⁻ mostly directly approaches Cys108-SSG from the solvent rather than it exploring the surface near the active site (Fig. 8d). In line with this, there is no single most preferred binding pathway. However, GS⁻ only rarely approaches from the direction of Tyr110, while pathways crossing Lys105 and helix 3 below Glu147 and Asp144 are more common. A contact analysis for GS⁻ revealed several patches, for example, including the covalently bound glutathione moiety and residues Lys105, Thr106, and Gly107 from protein area (iv) in Fig. 1 (Supplementary Fig. 21, Supplementary Table 15). The distance between the sulfur atom of GS⁻ and the center of mass of the sulfur atoms of Cys108-SSG ("S-S distance") and the angle created by the three sulfur atoms ("S-S-S angle") (Fig. 8e) are uncorrelated for wild-type ScGrx7 and the K105E variant and only weakly correlated for the E147K variant ($R^2 = 0.08, P = 0.001$). By contrast, both parameters are fairly correlated in the K105R variant ($R^2 = 0.42, P < 0.001$) (Supplementary Table 14).

In summary, we were able to relate changes in rate constants of the reductive half-reaction upon substitutions in ScGrx7 to differential GS⁻ access to the active site and the covalently bound glutathione in the molecular dynamics simulations. The observed higher fraction of bound states of GS⁻ to the K105R and E147K variants is caused by conformational changes in the binding sites, which lead to differential population of specific binding site regions. In the K105R variant, furthermore, there is a fair correlation between S-S distances and S-S-S angles, which may impact the turnover rate of the reaction. In the E147K variant, by contrast, the fraction of bound states is indirectly increased by changing the conformation of the Arg153 side chain, leading to an increase in overall positive charge at the active site.

Simulation of the interaction between GS⁻ and HsGrx5-SSG. We performed molecular dynamics simulations and subsequent analysis of wild-type HsGrx5 (WT) as described for ScGrx7, i.e., with a glutathionylated Cys67 and freely diffusing GS⁻ in the solution. We also chose the variants HsGrx5^{RR}, HsGrx5^{loop}, and HsGrx5^{RR+loop} for comparison with the in vitro and in vivo experiments. The fraction of bound GS⁻ states was lower for all variants of HsGrx5 than the WT (Fig. 9a) although not statistically significantly. Compared to ScGrx7 (Fig. 8b), clustered binding poses of GS⁻ at the active site exhibit a larger heterogeneity (Fig. 9b), and GS⁻ is oriented more towards conserved Lys59. Notably, residue Arg97 is able to interact with the glycine carboxyl group of Cys67-SSG in some of the clusters. Concordant with the diverse binding poses, the occupation density for HsGrx5 (Fig. 9c) shows different patches across the surface compared to ScGrx7, with no sampling between helix 2 and

helix 4 but primarily across helix 3 and its N-terminal loop. In HsGrx5^{RR} and HsGrx5^{RR+loop}, the density is markedly extended across and around the surface of the RR motif, while this area is rarely sampled in the cases of WT and HsGrx5^{loop}. In HsGrx5^{loop} and HsGrx5^{RR+loop}, the occupation density extends along helix 2.

A comparison of EcGrx4 structures with and without iron–sulfur cluster^{34,36} revealed conformational changes of the N-terminal part of helix 2 and the following elongated loop (Fig. 1c). Secondary structure analysis of helix 2 across all simulations of HsGrx5 variants revealed conformational changes in terms of an increased propensity of turn/bend or β -helix formation in that region only for the WT (Fig. 9d, e). This conformational change was seen only in one of the four replications (not shown), concordant with the slow unfolding kinetics of helices compared to our simulation time scales⁴⁸. Only short-lived (~20 ns) conformational changes of Gly68 were observed for the other variants of HsGrx5, while the corresponding Pro109 residue in ScGrx7 remained α -helical throughout the simulations (Fig. 9e). A marked difference between ScGrx7 and HsGrx5 is the interaction between the conserved lysine residue at the active site and Cys-SSG. In all HsGrx5 variants, Lys59 forms mostly transient interactions to the glycine carboxyl group of Cys-SSG (Supplementary Fig. 22a), whereas Lys105 in ScGrx7 always forms a stable salt bridge in the WT and E147K variant (Supplementary Fig. 22a, b). With respect to differences among HsGrx5 variants, in HsGrx5^{loop} and HsGrx5^{RR+loop}, Lys59 is consistently closer to the disulfide with a distance of ~6 Å than in WT and HsGrx5^{RR}, where distances ~9–11 Å are sampled as well (Supplementary Fig. 22c, d). In summary, the increased activity of HsGrx5^{loop} and HsGrx5^{loop+RR} in vitro correlates with increased occupation densities of GS⁻ near the active site. The increased occupation may result from an improved Lys59-dependent attraction of GS⁻ from the solution because the residue is consistently closer to the active-site disulfide.

Discussion

We established redox-sensitive GFP2 as a tool for the noninvasive intracellular assessment of Grx structure–function relationships yielding similar patterns for glutathione-scaffold site mutants in vitro and in yeast. This novel technique can now be used, for example, to perform initial structure–function analyses by rapidly screening multiple Grx mutants or isoforms from a variety of species without needing to go to the initial effort of purifying recombinant proteins. Furthermore, in combination with classic yeast genetics, the method might be also adopted to screen for gain- or loss-of-function mutants as well as specific protein–protein interactions or post-translational modifications.

In our roGFP2 assays we choose to use H₂O₂ to initiate GSSG formation. Whilst yeast do not harbor any bona fide glutathione peroxidase, it was recently shown that GSH and/or Grx can reduce both 1-Cys and typical 2-Cys peroxiredoxins thereby leading to GSSG production^{42,46,47,49,50}. Furthermore, GSSG was shown to readily accumulate in $\Delta grx1$ cells following H₂O₂ treatment⁴⁵. We used $\Delta grx1\Delta grx1\Delta grx2$ cells for our assay, which lack any endogenous cytosolic glutaredoxin activity. Thus, the expressed roGFP2–Grx fusions will likely play a role in cytosolic GSSG production in our assays following H₂O₂ treatment. It is therefore possible that Grx mutants with impaired activity will affect GSSG production as well as roGFP2 oxidation. Consequently, with this assay, it is not possible to strictly separate the impact of Grx mutants on the capacity to reduce glutathionylated peroxiredoxins on the one hand and the ability to transfer this oxidation to roGFP2 on the other hand. Nonetheless, we consider that the consistent and robust correlation between our in vitro assays and in cellulo roGFP2 assays fully supports the conclusion

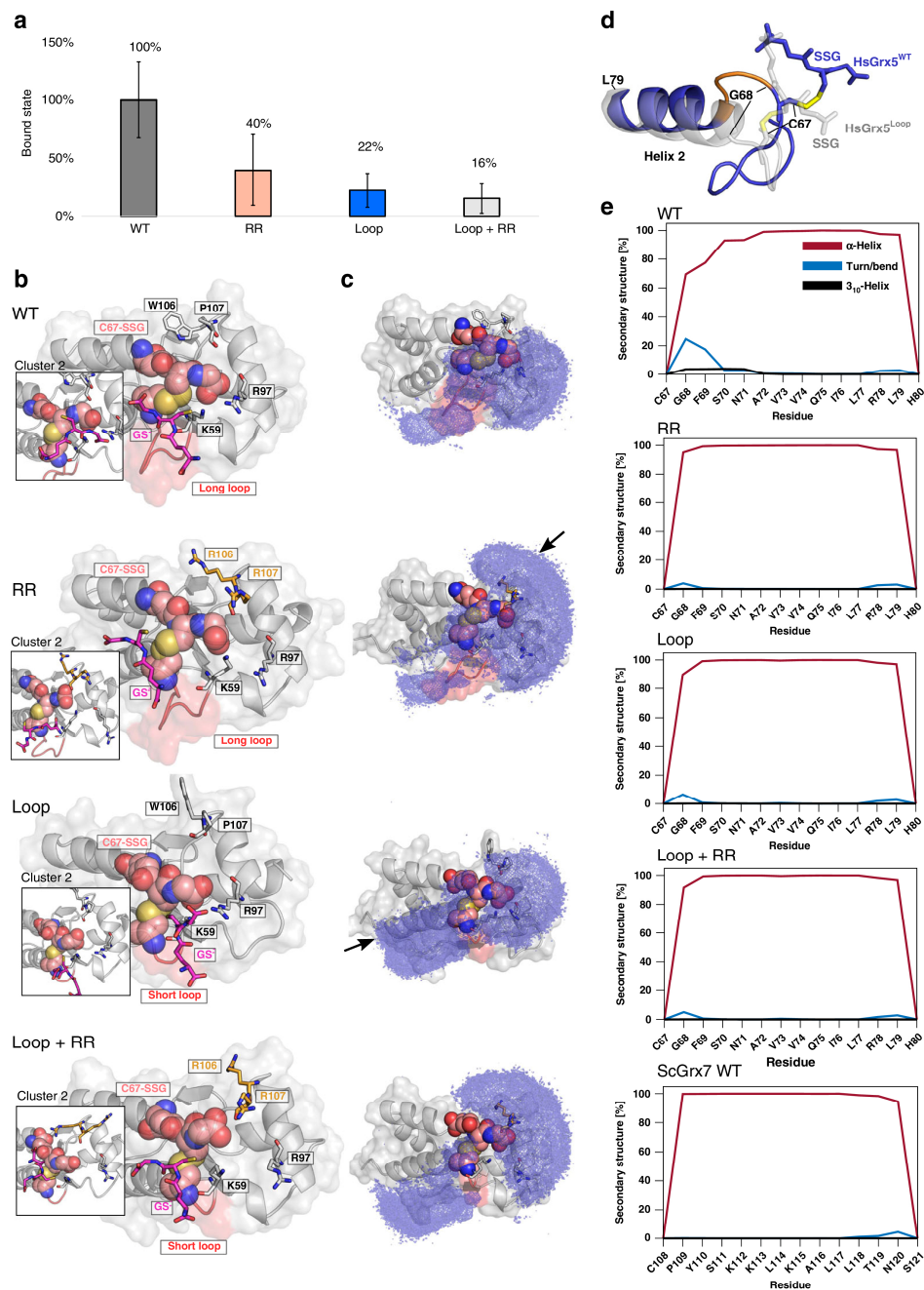


Fig. 9 GS⁻ binding to and conformational changes of glutathionylated HsGrx5 variants. **a** Fraction of bound states with the value for wild-type HsGrx5 (WT) normalized to 100%. Error bars show the standard error of the mean over four replications for each system. Datasets were tested with a two-tailed *t* test assuming unequal variances; null-hypothesis of equal means could not be rejected with $P < 0.05$. For WT and HsGrx5^{RR} $P = 0.17$; for WT and HsGrx5^{loop} $P = 0.10$; for WT and HsGrx5^{RR+loop} $P = 0.08$. **b** For each of the systems of the WT and the variants HsGrx5^{RR}, HsGrx5^{loop}, and HsGrx5^{RR+loop}, bound states were clustered with respect to the structural deviation of the active site and the closest GS⁻ from the solution. The structure representing the most populated cluster is shown in the middle, and important areas of the structure representing the second most populated cluster are shown in the boxes next to it. The covalently bound glutathione moiety at Cys67 is depicted in salmon, the freely diffusing GS⁻ in pink. Residues marked in orange show the mutated residues in the variants; the active site loop is colored red. Residue are numbered always according to the WT sequence. **c** The occupation density of the diffusing GS⁻ is shown as a blue grid on the structure of each HsGrx5 variant. Bound states were combined across replications for this analysis, and the threshold of the density grids is the same for all variants. Arrows show the additional patterns emerging for the RR and loop variants compared to the WT, respectively. **d** Partial unfolding of helix 2 (residues marked orange) was observed in one of the replications of HsGrx5 WT (blue), HsGrx5^{loop} is shown for comparison of the helical conformation (gray). **e** Residue-wise fraction of secondary structure content averaged over the four MD replications of the HsGrx5 variants and the ScGrx7 WT for helix 2. Only relevant secondary structure types are shown: α -helix in red, turn or bend in blue, and 3_{10} -helix in black. Adjacent residues Cys67/Cys108 and His80/Ser121 have a coil conformation.

ARTICLE

that roGFP2-based assays allow rapid assessment of glutaredoxin activity, mechanism and structure–function relationships in living cells.

Which protein areas are crucial for Grx catalysis? All four protein areas in Fig. 1 directly or indirectly affect the reactivity of Grx with GSSCys and GSH. In addition to residue Glu170, which was characterized previously¹², our kinetic analyses reveal that residues Tyr110, Asp144, Arg152, and Arg153 (r_1, r_4, r_6 , and r_7 in Fig. 1) form parts of the glutathione-scaffold site. Based on the effect of alanine mutations on the rate constants for the oxidative half-reaction, the relevance of these glutathione-scaffold site residues is ranked as follows: Tyr110 > Arg152/Arg153 > Arg153 > Glu170 > Asp144. Furthermore, the roGFP2 assay with the HsGrx5 gain-of-function mutants confirms an important role for the active-site proline residue and for the conserved glutamine residue in helix 3 (r_3 in Fig. 1). Regarding protein area (i) in Fig. 1, the hydroxyl group of Tyr110 is dispensable for catalysis and its removal could even accelerate the reaction with GSSCys. These results are in accordance with previous activity measurements of poplar Grx mutants at a single substrate concentration⁵¹. The conservation of the tyrosine residue might point towards a post-translational modification or the recognition of a specialized substrate. While molecular dynamics simulations suggest a direct role of protein area (i) for the interaction with GS[−], replacement of Tyr110 (or Arg153) can also indirectly affect the reductive half-reaction, as observed for mutants Y110A and R153E. Thus, positioning of the glutathione moiety in glutathionylated Grx is crucial for the reactivity with GSH and significantly contributes to the glutathione-activator site, although it still remains puzzling how Grx use GSH much more efficiently than cysteinylglycine or other thiols^{22,52}.

The side chains of the conserved active-site residues Lys105 and Tyr110 do not affect the cysteine thiol pK_a value of free ScGrx7. Even a charge inversion of Lys105, which was shown to slow down the reaction with GSSCys by two orders of magnitude¹², has only moderate effects on the cysteine protonation state. These findings correspond well with experimental data for human Grx1, but differ from studies on the inverse D35Y mutant of yeast ScGrx8 as well as calculations for Lys19 of human Grx1 and Lys8 of NrdH-redoxin from *C. glutamicum*^{33,40,41}. Since Lys105 and Tyr110 do not alter the thiol pK_a value of free ScGrx7, we suggest that these flanking residues stabilize the conformation of the free and glutathionylated enzyme and/or its negatively charged transition states. Further studies are needed to unravel these nonexclusive contributions in addition to the relevance of Lys105 as a GSH activator and potential stabilizer for the thiolate leaving group of the first product¹².

Regarding protein area (ii) in Fig. 1, helix 3 not only contributes to the glutathione-scaffold site but also to the charge-dependent recruitment of GSH, as exemplified by the molecular dynamics simulations and the accelerated reductive half-reaction of the gain-of-function mutants D144K and E147K. The results confirm that geometric and electrostatic complementarity are both crucial for glutathione catalysis^{4,12,13,53}. A minus-plus-plus charge distribution along the side chains of helix 3 is frequently found in enzymatically inactive Grx in contrast to the much more variable charge distribution in active Grx (Fig. 1d). The gain-of-function mutants D144K and E147K refute the hypothesis that additional positive charges in helix 3 prevent a productive interaction with GSH. The potentially missed option for ScGrx7 optimization by a simple point mutation *in vivo* might point toward alternative helix 3-dependent physiological substrate interactions, as previously demonstrated for the complementary surfaces between EcGrx1 and a peptide from ribonucleotide reductase²⁸.

Regarding protein area (iii) in Fig. 1, replacement of Arg153 or the introduction of the WP-motif decelerates the oxidative but not the reductive half-reaction of ScGrx7 *in vitro* and in yeast.

Thus, the WP-motif does not prevent the interaction with GSH but might stabilize the loop between helix 3 and strand 3 and decelerate the unwanted glutathionylation of enzymatically inactive Grx. This interpretation is in accordance with the detected gain-of-function of selected HsGrx5 mutants in the intracellular roGFP2 assay. The relevance of this loop as a crucial part of the glutathione-scaffold site is also supported by previous studies on a conserved TV-motif and its replacement in ScGrx8 (Fig. 1d)³³. An additional function of the WP-motif might be to facilitate or to block the interaction of enzymatically inactive Grx with a specific protein. Substrate- and conformation-dependent altered reduction and oxidation kinetics might explain why ScGrx7^{WP} is active with GSSCys *in vitro* whereas bulky roGFP2 is predominantly oxidized in yeast. Likewise, HsGrx5 and *Arabidopsis thaliana* GrxS15 cannot efficiently reduce roGFP2 in yeast and *in vitro*, respectively¹². An inactivating WP-motif also makes sense from a physiological perspective, because it might allow the stabilization of a modified sensor and/or avoid the accumulation of trapped Grx-SS-protein species in the absence of a resolving cysteine^{7,11,13}. For example, ScGrx3 and ScGrx4 both have a WP-motif and were shown to deglutathionylate very slowly the histone deacetylase Sir2 in a redox-dependent signaling cascade⁵⁴.

How is the Grx-dependent synthesis or sensing of iron–sulfur clusters kinetically uncoupled from redox catalysis at millimolar GSH concentrations^{12,13}, in particular, taking into account that class II Grx can be glutathionylated *in vitro*^{26,55,56}? The active-site loop in protein area (iv) in Fig. 1 seems to affect an important GS[−]–interaction pathway according to molecular dynamics simulations. Furthermore, modification of this loop had the strongest effect on the oxidative and the reductive half-reaction of ScGrx7 and HsGrx5 and allowed a partial interconversion between enzymatically active and inactive Grx. The variable loop before the active-site cysteine residue is therefore a determinant structural difference between both Grx classes and seems to act as an on/off switch. Nevertheless, our data reveal that protein areas (i)–(iv) together determine and fine-tune the oxidative and reductive half-reaction of Grx. An appropriate loop conformation near the active site is necessary to convert an enzymatically inactive Grx to an active one, but such a conformation alone is not sufficient, and additional replacements, for example, of Gly68 and/or Arg97 in HsGrx5 can further increase the enzymatic activity. A kinetic uncoupling mechanism because of a loop-dependent on/off switch is supported by the NMR solution structures of EcGrx4 (Fig. 1c)³⁴. Helix 2 in the apoprotein is partially unfolded so that the active-site cysteine and lysine residue are repositioned and point away from the glutathione-scaffold site. This protein conformation obviously has to be enzymatically inactive. In contrast, EcGrx4 adopts a potentially functional conformation in the presence of the iron–sulfur cluster³⁶, however, the cysteine residue of the holoprotein is now blocked and therefore remains enzymatically inactive. If we assume that the conformational change in class II Grx is triggered or stabilized by the iron–sulfur cluster, we can explain the enzymatic inactivity, because the effective concentration of free enzyme in the active conformation is too low. Conformational changes at the N-terminus of helix 2 and the active-site loop are less pronounced in the apo- and holoprotein NMR solution structures of HsGrx5, however, the local unfolding of helix 2 and the crucial repositioning of the active-site cysteine residue in the apoprotein (PDB entry 2MMZ)³⁸ are similar to EcGrx4. Furthermore, while our molecular dynamics simulations did not reveal an increase of bound GS[−] for loop mutants of HsGrx5, a conformational transition from the proposed active conformation to a presumably inactive state with a partially unfolded helix 2 and rearrangement of the Cys-SSG disulfide was observed for wild-type HsGrx5. In contrast, the N-terminal part of helix 2 of ScGrx7 always remained α -helical during the simulations. Subtle conformational changes

around the active-site proline, serine or glycine residue in protein area (i) are also in agreement with structural and kinetic data on HsGrx1, HsGrx2, ScGrx1, ScGrx2, and ScGrx6-8^{4,11,19,29,40,57}. For example, ScGrx6 with its CSYS-motif has a ~40 times lower k_{cat}^{app} value than CPYS-containing ScGrx7¹⁹. In summary, we propose an active-site loop-dependent conformational switch that parks the apoprotein of class II Grx in an enzymatically inactive state when no iron–sulfur clusters are present. This conformational switch, in addition to combined structural variations around the substrate interaction sites, kinetically uncouple the Grx-dependent synthesis or sensing of iron–sulfur clusters from redox catalysis at millimolar GSH concentrations.

In conclusion, we established and applied a roGFP2-based assay to rapidly screen for gain- or loss-of-function mutants of Grx isoforms in yeast, quantified the relevance and contribution of four crucial protein areas for the oxidative and reductive half-reaction of Grx catalysis, show that the flanking lysine and tyrosine residue do not affect the thiol pK_a value of the active-site cysteine residue but rather stabilize the transition states, and propose an active-site loop-dependent conformational on/off switch that inactivates class II Grx in the absence of iron–sulfur clusters.

Methods

Materials. GSH, GSSG, diamide, H₂O₂, and yeast glutathione reductase (ScGR) were from Sigma-Aldrich, HEDS was obtained from Alfa Aesar, GSSCys from Toronto Research Chemicals, DTT from AppliChem, and NADPH was from Gerbu. Polymerase chain reaction (PCR) primers were purchased from Metabion.

Site-directed mutagenesis, gene synthesis, and cloning. Point mutations were introduced by PCR with *Pfu* polymerase (Promega) using the mutagenesis primers listed in Supplementary Table 10 and the double stop-codon construct of pQE30/*SCGRX7* (ref. ¹¹) as template. Following the digestion of the methylated template DNA by *DpnI* (NEB), plasmids were transformed into chemically competent *E. coli* XL1-Blue cells. Correct mutations and sequences were confirmed for all constructs by sequencing both strands (SEQ-IT). Codon- and mRNA structure-optimized genes *SCGRX7^{WP}*, *SCGRX7^{loop}*, *SCGRX7^{WP+loop}*, *HSGRX5^{C122S}*, *HSGRX5^{RR}*, *HSGRX5^{loop}*, and *HSGRX5^{RR+loop}* were synthesized (Genscript) and either subcloned into the *EcoRI* and *Xhol* restriction sites of p416TEF/roGFP2 (ref. ⁴⁵) for roGFP2 measurements in yeast or PCR-amplified using the primers in Supplementary Table 10 and subcloned into the *BamHI* and *HindIII* restriction sites of pQE30 for heterologous expression in *E. coli*. Please note that all *HSGRX5* constructs encode C122S mutants that lack the mitochondrial presequence and start with residue Ala32.

Heterologous expression and protein purification. *E. coli* strain XL1-Blue was transformed with the according pQE30 plasmid for the expression of wild-type and mutant *SCGRX7* and *HSGRX5^{C122S}*. Recombinant N-terminally MRGS(H)₆-tagged wild-type and mutant ScGrx7 and HsGrx5^{C122S} (without their N-terminal targeting sequences¹⁹) were purified after lysozyme treatment and sonication by Ni-NTA affinity chromatography using an elution buffer containing 200 mM imidazole, 300 mM NaCl, and 50 mM sodium phosphate, pH 8.0^{11,19,25,42}.

GSSCys and HEDS oxidoreductase assays. Steady-state kinetics of wild-type and mutant ScGrx7 and HsGrx5^{C122S} in the GSSCys and HEDS assays were determined spectrophotometrically by monitoring the consumption of NADPH at 340 nm and 25 °C using a thermostated Jasco V-650 UV/vis spectrophotometer^{11,19,25}. Fresh stock solutions of NADPH, GSH, GR, and GSSCys or HEDS were prepared in assay buffer containing 0.1 M Tris/HCl, 1 mM EDTA, pH 8.0 before each experiment. Both assays were performed with 0.1 mM NADPH and 1 U/ml ScGR. The following final protein concentrations were used for Y110F/H/A (5–150 nM), D144A/K (10 nM), E147A/K (10 nM), R153A/E (25–50 nM), ScGrx7^{WP} (20 nM), ScGrx7^{loop} (up to 1.4 μM), ScGrx7^{WP+loop} (up 2.6 μM), HsGrx5^{C122S} (up to 15 μM), HsGrx5^{RR} (up to 12 μM), HsGrx5^{loop} (up to 1.6 μM), and HsGrx5^{RR+loop} (up to 4.0 nM). For the GSSCys assays, GSH was varied between 50 μM and 1.5 mM at fixed GSSCys concentrations (25, 50, 100, and 150 μM). NADPH, GSH, and GR were mixed in assay buffer before Grx was added and a baseline was recorded for 30 s. All GSSCys assays were started by the addition of GSSCys. The absorbance of a reference cuvette containing all components but no Grx was measured in parallel and subtracted from the obtained Grx activity. For the HEDS assays, GSH was varied between 100 μM and 2.0 mM at fixed concentrations of HEDS (0.18, 0.37, 0.55, and 0.74 mM). NADPH, GSH, and HEDS were preincubated in assay buffer for 2 min before GR was added and a baseline was recorded for 30 s. All HEDS assays were started by the addition of enzyme. Kinetic data were analyzed in

Excel and SigmaPlot 13 by nonlinear and linear regression according to Michaelis–Menten, Lineweaver–Burk, Eadie–Hofstee, and Hanes theory^{11,19,25}.

Determination of the thiol pK_a value of ScGrx7. The protocol was modified from Mieyal et al.⁵⁸ and Gallogly et al.²² and is based on the pH-dependent alkylation of the cysteine thiolate of ScGrx7 followed by determination of the residual enzyme activity in a standard HEDS assay. Freshly purified protein (0.3 mM) was reduced with a 20-fold molar excess of NaBH₄ for 2 h on ice following a previous established protocol⁴². Subsequently, 6 μM wild-type or mutant ScGrx7 was incubated for 180 s with 150 μM iodacetamide at 23 °C in a three-buffer system⁵⁹ containing 100 mM KCl, 50 mM potassium acetate, 50 mM MES, and 100 mM Tris at pH values between 3.5 and 8.5. A mock control without iodacetamide was incubated in parallel and the activity of this control was used for normalization. Enzyme activities after incubation with or without iodacetamide were determined in standard IIES assays as described above. The percentage of the normalized residual activity after alkylation was calculated in Excel and plotted in SigmaPlot13. A sigmoidal fit (Hill equation, 4 parameter) was used to determine the pK_a values of ScGrx7 and the different mutants.

Yeast strains and growth conditions. All experiments were performed in a YPH499 strain background (*MATa ura3-52 lys2-801 amber ade2-101 ochre trp1-Δ63 his3-Δ200 leu2-Δ1*). Yeast were grown in Hartwell's complete (HC) medium lacking the appropriate amino acids for plasmid selection with 2% glucose as carbon source.

Generation of yeast strains. Deletion of the genes encoding glutathione reductase (*GLR1*), glutaredoxin 1 (*GRX1*), and glutaredoxin 2 (*GRX2*) were performed using a standard homologous recombination-based technique. Antibiotic resistance markers were amplified using primers with homologous regions up- and downstream of the gene of interest. PCR products were transformed into yeast cells using a standard lithium acetate-based method.

Gene deletions were confirmed by PCR on chromosomal DNA using primers designed to bind ~200 bp up- and down-stream of the gene of interest. Furthermore, PCR reactions were performed using primers designed to bind up- or down-stream of the gene of interest in combination with primers designed to bind inside the antibiotic resistance marker genes.

Intracellular roGFP2-based monitoring of Grx activity. RoGFP2 has been engineered to contain two cysteines residues on parallel β-strands adjacent to the GFP chromophore. The two cysteines can form a disulfide bond. The roGFP2 dithiol/disulfide redox couple readily equilibrates with the cellular 2GSH/GSSG redox couple in a manner dependent upon glutaredoxin activity. RoGFP2 exhibits two major fluorescence excitation maxima at ~400 and ~490 nm, with one major emission maximum at ~510 nm. The intensity of the two excitation maxima changes in opposite directions upon the formation of the disulfide bond. Ratio-metric fluorescence measurements therefore allow the real-time monitoring of the roGFP2 oxidation state.

YPH499 *Aglr1Δgrx1Δgrx2* yeast cells were transformed with p416TEF plasmids for the expression of roGFP2–Grx fusion constructs containing either wild-type or mutant *GRX* variants. Cells were grown at 30 °C in HC media, lacking uracil for plasmid selection, to a $D_{600} \approx 3.0$. Subsequently, the response of the roGFP2–Grx fusion constructs to exogenous H₂O₂, applied at concentrations ranging from 0 to 1000 μM, was monitored^{45,60}. Briefly, cells were harvested from the growth media by centrifugation at 800 g, 3 min, room temperature, and resuspended in 100 mM MES/Tris pH 6.0 buffer to a $D_{600} \approx 7.5$. Subsequently, 200 μl aliquots of cells suspension were transferred to the wells of a 96-well plate. Control samples were treated with either 100 mM DTT or 20 mM diamide to yield fully reduced and oxidized roGFP2, respectively. These samples allow for determination of the degree of probe oxidation (OxD), according to Eq. (1).

$$\text{OxD}_{\text{roGFP2}} = \frac{(I_{400\text{sample}} * I_{480\text{red}}) - (I_{400\text{red}} * I_{480\text{sample}})}{(I_{400\text{sample}} * I_{480\text{red}}) + (I_{400\text{sample}} * I_{480\text{ox}}) + (I_{400\text{ox}} * I_{480\text{sample}}) - (I_{400\text{red}} * I_{480\text{sample}})}, \quad (1)$$

where “I” represents fluorescence emission following excitation at 400 or 480 nm, for the fully oxidized (ox), fully reduced (red) and experimental samples (sample), respectively.

The 96-well plates were centrifuged at 30 g, 5 min, room temperature to create loose pellets of yeast cells at the bottom of the wells. Subsequently, H₂O₂ was added at the required concentration and the fluorescence response was monitored using a BMG Labtech CLARIOstar fluorescence plate-reader. All experiments were performed at least three times using cells from independent cultures. In addition, pre-reduction experiments were performed for constructs that had a too high steady-state roGFP2 oxidation to perform kinetic analyses. Briefly, cells expressing the relevant constructs were incubated with 50 mM DTT for 5 min, isolated by centrifugation, washed once with 100 mM MES/Tris pH 6.0 buffer, and then treated as described above for all other roGFP2 constructs.

Data analysis and statistics. RoGFP2 responses were analyzed by calculating the integrated area under the roGFP2 response curves, which had been corrected by

ARTICLE

subtraction of an untreated sample. The area was determined for the first 48 s following addition of H₂O₂. All experiments were repeated at least three times and data were reported as mean AUCs with error bars representing the standard deviation. Statistically significant differences between samples were determined using one-way ANOVA analyses followed by a Holm-Sidak test were calculated in SigmaPlot 13 ($P > 0.05$: ns; $P \leq 0.05$: * $P \leq 0.01$: ** $P \leq 0.001$: ***).

Molecular dynamics simulations. We used the TopModel program^{61,62} to build a homology model of ScGrx7. The crystal structure of HsGrx5 (PDB-ID: 2WUL)³⁷ was used to prepare the simulations for HsGrx5 WT and HsGrx5^{RR}, while for HsGrx5^{loop} and HsGrx5^{RR+loop}, models were created with TopModel. The ScGrx7 mutants K105E, K105R, and E147K as well as HsGrx5^{RR} were created by deleting the side-chain atoms of the wild-type residue and rebuilding the respective variant with LEaP. To mimic the reductive half reaction, a glutathione moiety was covalently attached to the active-site cysteine via a disulfide bond in all systems.

From the models of ScGrx7 and HsGrx5, solvated systems were built using PACKMOL Memgen⁶³ with 100 mM of GS⁻ molecules in a TIP3P water box⁶⁴; K⁺ ions^{65,66} were added to neutralize the charge of the system. All MD simulations were performed using the GPU implementation⁶⁷ of the AMBER 18 suite of programs, with the ff14SB force field for the proteins⁶⁸. Since the bond between glutamate and cysteine in glutathione is not a regular peptide bond but a γ -peptide bond for which no corresponding residue exists in the ff14SB force field, we first derived force field parameters for the N-terminal γ -glutamyl residue. To this end, we derived atom-centered point charges for γ -glutamylmethionamide by first performing a gas phase geometry optimization at the HF/6-31G(d) level with GAUSSIAN 09, Revisión B.01. To ensure invariance of the molecular electrostatic potential (MEP) with respect to the molecular orientation, the subsequent calculation of the MEP (level of theory: HF/6-31G(d)) and the fitting of the point charges to reproduce the MEP were performed on the R.E.D. server⁶⁹, which uses a rigid-body reorientation algorithm⁷⁰ before calculating the electrostatic potential. The MEP was calculated on four layers defined by scaling the atomic van der Waals radii by factors of 1.4, 1.8, 2.0, and 2.2, respectively, and a point density of 0.28 points Å^{-2} ($1 \text{ pt } \text{Å}^{-2}$). Charge fitting was performed using the RESP procedure with two fitting stages (hyperbolic constraint values: 0.0005/0.001, and intramolecular charge constraints on the N-methionamide fragment of γ -glutamylmethionamide with a target value of zero were employed for charge derivation^{71,72}. Lastly, the charge constrained atoms were removed to obtain the γ -glutamyl residue. Force field parameters for the γ -glutamyl residue were fully assigned by the R.E.D. server⁷³ using the ff14SB force field. The γ -glutamyl residue was then used in the disulfide glutathione as well as the free GS⁻ molecules in the solution.

Minimization, equilibration, and thermalization were carried out as described previously⁷³. In the production simulations, the particle mesh Ewald method⁷⁴ was used to treat long-range electrostatic interactions, and bonds involving hydrogen atoms were constrained using the SHAKE algorithm. A time step of 4 fs was used in accordance with the hydrogen mass repartitioning scheme⁷¹. The direct-space, non-bonded cutoff was 10 Å. Four independent replications of each system were simulated for 500 ns each in NVT (constant number of particles, constant volume, constant temperature) conditions. The system state was saved every 20 ps. This setup allowed us to observe the unbiased diffusion^{72,75} of GS⁻ around the Grx proteins. Binding frequencies were calculated as the fraction of frames with a binding event of all the frames per simulation replication. Binding events were then clustered with the agglomerative hierarchical clustering algorithm of cpptraj⁷⁶ included in the AMBER 18 program suite. Further geometric analyses, including side chain dihedrals and density grids of GS⁻ diffusion, were also performed with cpptraj⁷⁶.

Reporting summary. Further information on research design is available in the Nature Research Reporting Summary linked to this article.

Data availability

All relevant data are included in the paper or its Supplementary information and are available from the authors upon request. The source data underlying Figs. 3 and 7 as well as Supplementary Fig. 17 are provided as a Source Data file. The MD simulations data underlying Figs. 8 and 9 have been deposited at <https://doi.org/10.25838/d5p-10> and <https://doi.org/10.25838/d5p-11>.

Received: 30 October 2019; Accepted: 4 March 2020;

Published online: 07 April 2020

References

1. Herrero, E. & de la Torre-Ruiz, M. A. Monothiol glutaredoxins: a common domain for multiple functions. *Cell Mol. Life Sci.* **64**, 1518–1530 (2007).
2. Lillig, C. H., Berndt, C. & Holmgren, A. Glutaredoxin systems. *Biochim. Biophys. Acta* **1780**, 1304–1317 (2008).
3. Mieyal, J. J., Gallogly, M. M., Qanungo, S., Sabens, E. A. & Shelton, M. D. Molecular mechanisms and clinical implications of reversible protein S-glutathionylation. *Antioxid. Redox Signal.* **10**, 1941–1988 (2008).
4. Deponte, M. Glutathione catalysis and the reaction mechanisms of glutathione-dependent enzymes. *Biochim. Biophys. Acta* **1830**, 3217–3266 (2013).
5. Outten, C. E. & Albelot, A. N. Iron sensing and regulation in *Saccharomyces cerevisiae*: Ironing out the mechanistic details. *Curr. Opin. Microbiol.* **16**, 662–668 (2013).
6. Couturier, J., Przybyla-Toscano, J., Roret, T., Didierjean, C. & Rouhier, N. The roles of glutaredoxins ligating Fe-S clusters: sensing, transfer or repair functions? *Biochim. Biophys. Acta* **1853**, 1513–1527 (2015).
7. Liedgens, L. & Deponte, M. The catalytic mechanism of glutaredoxins. in Glutathione (ed. Flohé, L.) 251–261 (CRC Press, 2019).
8. Nagai, S. & Black, S. A thiol-disulfide transhydrogenase from yeast. *J. Biol. Chem.* **243**, 1942–1947 (1968).
9. Axelsson, K., Eriksson, S. & Mannervik, B. Purification and characterization of cytoplasmic thioltransferase (glutathione:disulfide oxidoreductase) from rat liver. *Biochemistry* **17**, 2978–2984 (1978).
10. Holmgren, A. Glutathione-dependent synthesis of deoxyribonucleotides. Purification and characterization of glutaredoxin from *Escherichia coli*. *J. Biol. Chem.* **254**, 3664–3671 (1979).
11. Eckers, E., Bien, M., Stroobant, V., Herrmann, J. M. & Deponte, M. Biochemical characterization of dithiol glutaredoxin 8 from *Saccharomyces cerevisiae*: the catalytic redox mechanism redux. *Biochemistry* **48**, 1410–1423 (2009).
12. Begas, P., Liedgens, L., Moseler, A., Meyer, A. J. & Deponte, M. Glutaredoxin catalysis requires two distinct glutathione interaction sites. *Nat. Commun.* **8**, 14835 (2017).
13. Deponte, M. The incomplete glutathione puzzle: just guessing at numbers and figures? *Antioxid. Redox Signal.* **27**, 1130–1161 (2017).
14. Manta, B. et al. Kinetic studies reveal a key role of a redox-active glutaredoxin in the evolution of the thiol-redox metabolism of trypanosomatid parasites. *J. Biol. Chem.* **294**, 3235–3248 (2019).
15. Yang, Y. F. & Wells, W. W. Catalytic mechanism of thioltransferase. *J. Biol. Chem.* **266**, 12766–12771 (1991).
16. Yang, Y. et al. Reactivity of the human thioltransferase (glutaredoxin) C7S, C25S, C78S, C82S mutant and NMR solution structure of its glutathionyl mixed disulfide intermediate reflect catalytic specificity. *Biochemistry* **37**, 17145–17156 (1998).
17. Nordstrand, K., Slund, F., Holmgren, A., Otting, G. & Berndt, K. D. NMR structure of *Escherichia coli* glutaredoxin 3-glutathione mixed disulfide complex: implications for the enzymatic mechanism. *J. Mol. Biol.* **286**, 541–552 (1999).
18. Björnberg, O., Ostergaard, H. & Winther, J. R. Mechanistic insight provided by glutaredoxin within a fusion to redox-sensitive yellow fluorescent protein. *Biochemistry* **45**, 2362–2371 (2006).
19. Mesecke, N., Mittler, S., Eckers, E., Herrmann, J. M. & Deponte, M. Two novel monothiol glutaredoxins from *Saccharomyces cerevisiae* provide further insight into iron-sulfur cluster binding, oligomerization, and enzymatic activity of glutaredoxins. *Biochemistry* **47**, 1452–1463 (2008).
20. Mesecke, N., Spang, A., Deponte, M. & Herrmann, J. M. A novel group of glutaredoxins in the *cis*-Golgi critical for oxidative stress resistance. *Mol. Biol. Cell* **19**, 2673–2680 (2008).
21. Izquierdo, A., Casas, C., Muñehoff, U., Lillig, C. H. & Herrero, E. *Saccharomyces cerevisiae* Grx6 and Grx7 are monothiol glutaredoxins associated with the early secretory pathway. *Eukaryot. Cell* **7**, 1415–1426 (2008).
22. Gallogly, M. M., Starke, D. W., Leonberg, A. K., Ospina, S. M. & Mieyal, J. J. Kinetic and mechanistic characterization and versatile catalytic properties of mammalian glutaredoxin 2: implications for intracellular roles. *Biochemistry* **47**, 11144–11157 (2008).
23. Zahedi Avval, F. & Holmgren, A. Molecular mechanisms of thioredoxin and glutaredoxin as hydrogen donors for Mammalian s phase ribonucleotide reductase. *J. Biol. Chem.* **284**, 8233–8240 (2009).
24. Couturier, J. et al. Structure-function relationship of the chloroplastic glutaredoxin S12 with an atypical WCSYS active site. *J. Biol. Chem.* **284**, 9299–9310 (2009).
25. Begas, P., Staudacher, V. & Deponte, M. Systematic re-evaluation of the bis(2-hydroxyethyl)disulfide (HEDS) assay reveals an alternative mechanism and activity of glutaredoxins. *Chem. Sci.* **6**, 3788–3796 (2015).
26. Deponte, M., Becker, K. & Rahlf, S. Plasmodium falciparum glutaredoxin-like proteins. *Biol. Chem.* **386**, 33–40 (2005).
27. Bushweller, J. H., Aslund, F., Wuthrich, K. & Holmgren, A. Structural and functional characterization of the mutant *Escherichia coli* glutaredoxin (C14–S) and its mixed disulfide with glutathione. *Biochemistry* **31**, 9288–9293 (1992).
28. Berardi, M. J. & Bushweller, J. H. Binding specificity and mechanistic insight into glutaredoxin-catalyzed protein disulfide reduction. *J. Mol. Biol.* **292**, 151–161 (1999).
29. Lillig, C. H. et al. Characterization of human glutaredoxin 2 as iron-sulfur protein: a possible role as redox sensor. *Proc. Natl. Acad. Sci. USA* **102**, 8168–8173 (2005).
30. Feng, Y. et al. Structural insight into poplar glutaredoxin C1 with a bridging iron-sulfur cluster at the active site. *Biochemistry* **45**, 7998–8008 (2006).

31. Johansson, C., Kavanagh, K. L., Gileadi, O. & Oppermann, U. Reversible sequestration of active site cysteines in a 2Fe-2S-bridged dimer provides a mechanism for glutaredoxin 2 regulation in human mitochondria. *J. Biol. Chem.* **282**, 3077–3082 (2007).
32. Luo, M. et al. Structural and biochemical characterization of yeast monothiol glutaredoxin Grx6. *J. Mol. Biol.* **398**, 614–622 (2010).
33. Tang, Y. et al. Structure-guided activity enhancement and catalytic mechanism of yeast grx8. *Biochemistry* **53**, 2185–2196 (2014).
34. Fladvad, M. et al. Molecular mapping of functionalities in the solution structure of reduced Grx4, a monothiol glutaredoxin from *Escherichia coli*. *J. Biol. Chem.* **280**, 24553–24561 (2005).
35. Picciocchi, A., Saguez, C., Boussac, A., Cassier-Chauvat, C. & Chauvat, F. CGFS-type monothiol glutaredoxins from the cyanobacterium Synechocystis PCC6803 and other evolutionary distant model organisms possess a glutathione-ligated [2Fe-2S] cluster. *Biochemistry* **46**, 15018–15026 (2007).
36. Iwema, T. et al. Structural basis for delivery of the intact [Fe2S2] cluster by monothiol glutaredoxin. *Biochemistry* **48**, 6041–6043 (2009).
37. Johansson, C. et al. The crystal structure of human GLRX5: iron-sulfur cluster co-ordination, tetrameric assembly and monomer activity. *Biochem J.* **433**, 303–311 (2011).
38. Banci, L. et al. [2Fe-2S] cluster transfer in iron-sulfur protein biogenesis. *Proc Natl Acad Sci USA* **111**, 6203–6208 (2014).
39. Dalziel, K. Initial steady state velocities in the evaluation of enzyme-coenzyme-substrate reaction mechanisms. *Acta Chem. Scand.* **11**, 1706–1723 (1957).
40. Jao, S. C. et al. Computational and mutational analysis of human glutaredoxin (thioltransferase): probing the molecular basis of the low pKa of cysteine 22 and its role in catalysis. *Biochemistry* **45**, 4785–4796 (2006).
41. Van Laer, K., Oliveira, M., Wahni, K. & Messens, J. The concerted action of a positive charge and hydrogen bonds dynamically regulates the pKa of the nucleophilic cysteine in the NrdH-redoxin family. *Protein Sci.* **23**, 238–242 (2014).
42. Djuika, C. F. et al. Plasmodium falciparum antioxidant protein as a model enzyme for a special class of glutaredoxin/glutathione-dependent peroxiredoxins. *Biochim. Biophys. Acta* **1830**, 4073–4090 (2013).
43. Tamarit, J., Belli, G., Cabrisol, E., Herrero, E. & Ros, J. Biochemical characterization of yeast mitochondrial Grx5 monothiol glutaredoxin. *J. Biol. Chem.* **278**, 25745–25751 (2003).
44. Gutscher, M. et al. Real-time imaging of the intracellular glutathione redox potential. *Nat. Methods* **5**, 553–559 (2008).
45. Morgan, B. et al. Multiple glutathione disulfide removal pathways mediate cytosolic redox homeostasis. *Nat. Chem. Biol.* **9**, 119–125 (2013).
46. Staudacher, V. et al. Redox-sensitive GFP fusions for monitoring the catalytic mechanism and inactivation of peroxiredoxins in living cells. *Redox Biol.* **14**, 549–556 (2016).
47. Calabrese, G. et al. Hyperoxidation of mitochondrial peroxiredoxin limits H₂O₂-induced cell death in yeast. *EMBO J.* **38**, e101552 (2019).
48. Munoz, V. & Cerminara, M. When fast is better: protein folding fundamentals and mechanisms from ultrafast approaches. *Biochem. J.* **473**, 2545–2559 (2016).
49. Peskin, A. V. et al. Glutathionylation of the active site cysteines of peroxiredoxin 2 and recycling by glutaredoxin. *J. Biol. Chem.* **291**, 3053–3062 (2016).
50. Staudacher, V. et al. Plasmodium falciparum antioxidant protein reveals a novel mechanism for balancing turnover and inactivation of peroxiredoxins. *Free Radic. Biol. Med.* **85**, 228–236 (2015).
51. Rouhier, N., Gelhay, E. & Jacquot, J. P. Exploring the active site of plant glutaredoxin by site-directed mutagenesis. *FEBS Lett.* **511**, 145–149 (2002).
52. Srinivasan, U., Mieyal, P. A. & Mieyal, J. J. pH profiles indicative of rate-limiting nucleophilic displacement in thioltransferase catalysis. *Biochemistry* **36**, 3199–3206 (1997).
53. Berndt, C., Schwenn, J. D. & Lillig, C. H. The specificity of thioredoxins and glutaredoxins is determined by electrostatic and geometric complementarity. *Chem. Sci.* **6**, 7049–7058 (2015).
54. Vall-Laura, N. et al. Reversible glutathionylation of Sir2 by monothiol glutaredoxins Grx3/4 regulates stress resistance. *Free Radic. Biol. Med.* **96**, 45–56 (2016).
55. Fernandes, A. P. et al. A novel monothiol glutaredoxin (Grx4) from *Escherichia coli* can serve as a substrate for thioredoxin reductase. *J. Biol. Chem.* **280**, 24544–24552 (2005).
56. Filser, M. et al. Cloning, functional analysis, and mitochondrial localization of *Trypanosoma brucei* monothiol glutaredoxin-1. *Biol. Chem.* **389**, 21–32 (2008).
57. Yu, J., Zhang, N. N., Yin, P. D., Cui, P. X. & Zhou, C. Z. Glutathionylation-triggered conformational changes of glutaredoxin Grx1 from the yeast *Saccharomyces cerevisiae*. *Proteins* **72**, 1077–1083 (2008).
58. Mieyal, J. J., Starke, D. W., Gravina, S. A. & Hocevar, B. A. Thioltransferase in human red blood cells: kinetics and equilibrium. *Biochemistry* **30**, 8883–8891 (1991).
59. Ellis, K. J. & Morrison, J. F. Buffers of constant ionic strength for studying pH-dependent processes. *Methods Enzymol.* **87**, 405–426 (1982).
60. Morgan, B. et al. Real-time monitoring of basal H₂O₂ levels with peroxiredoxin-based probes. *Nat. Chem. Biol.* **12**, 437–443 (2016).
61. Mulnaes, D. & Gohlke, H. TopScore: using deep neural networks and large diverse data sets for accurate protein model quality assessment. *J. Chem. Theory Comput.* **14**, 6117–6126 (2018).
62. Widderich, N. et al. Molecular dynamics simulations and structure-guided mutagenesis provide insight into the architecture of the catalytic core of the ectoine hydroxylase. *J. Mol. Biol.* **426**, 586–600 (2014).
63. Schott-Verdugo, S. & Gohlke, H. PACKMOL-Memgen: a simple-to-use, generalized workflow for membrane protein-lipid-bilayer system building. *J. Chem. Inf. Model.* **59**, 2522–2528 (2019).
64. Jorgensen, W. L., Chandrasekhar, J., Madura, J. D., Impey, R. W. & Klein, M. L. Comparison of simple potential functions for simulating liquid water. *J. Chem. Phys.* **79**, 926–935 (1983).
65. Joung, I. S. & Cheatham, T. E. III Molecular dynamics simulations of the dynamic and energetic properties of alkali and halide ions using water-model-specific ion parameters. *J. Phys. Chem. B* **113**, 13279–13290 (2009).
66. Joung, I. S. & Cheatham, T. E. III Determination of alkali and halide monovalent ion parameters for use in explicitly solvated biomolecular simulations. *J. Phys. Chem. B* **112**, 9020–9041 (2008).
67. Le Grand, S., Götz, A. W. & Walker, R. C. Speed without compromise—a mixed precision model for GPU accelerated molecular dynamics simulations. *J. Comput. Phys. Commun.* **184**, 374–380 (2013).
68. Maier, J. A. et al. ff14SB: improving the accuracy of protein side chain and backbone parameters from ff99SB. *J. Chem. Theory Comput.* **11**, 3696–3713 (2015).
69. Vanqualef, E. et al. R.E.D. Server: a web service for deriving RESP and ESP charges and building force field libraries for new molecules and molecular fragments. *Nucleic Acids Res.* **39**, W511–W517 (2011).
70. Dupradeau, F. Y. et al. The R.E.D. tools: advances in RESP and ESP charge derivation and force field library building. *Phys. Chem. Chem. Phys.* **12**, 7821–7839 (2010).
71. Hopkins, C. W., Le Grand, S., Walker, R. C. & Roitberg, A. E. Long-time-step molecular dynamics through hydrogen mass repartitioning. *J. Chem. Theory Comput.* **11**, 1864–1874 (2015).
72. Bhatia, S. et al. Targeting HSP90 dimerization via the C terminus is effective in imatinib-resistant CML and lacks the heat shock response. *Blood* **132**, 307–320 (2018).
73. Klinker, S. et al. Phosphorylated tyrosine 93 of hepatitis C virus nonstructural protein 5A is essential for interaction with host c-Src and efficient viral replication. *J. Biol. Chem.* **294**, 7388–7402 (2019).
74. Cheatham, T. E., Miller, J. L., Fox, T. D., Darden, T. A. & Kollman, P. A. Molecular-dynamics simulations on solvated biomolecular systems—the particle mesh ewald method leads to stable trajectories of DNA, RNA, and proteins. *J. Am. Chem. Soc.* **117**, 4193–4194 (1995).
75. Gohlke, H. et al. Binding region of alanopine dehydrogenase predicted by unbiased molecular dynamics simulations of ligand diffusion. *J. Chem. Inf. Model.* **53**, 2493–2498 (2013).
76. Roe, D. R. & Cheatham, T. E. III PTRAJ and CPPTRAJ: software for processing and analysis of molecular dynamics trajectory data. *J. Chem. Theory Comput.* **9**, 3084–3095 (2013).

Acknowledgements

This work was funded by the DFG priority program SPP 1710 (grant DE 1431/8-2 to M. D., grant GO 1367/3-1 to H.G., and grant MO 2774/2-1 to B.M.). H.G. is grateful for computational support and infrastructure provided by the “Zentrum für Informations- und Medientechnologie” (ZIM) at the Heinrich Heine University Düsseldorf and the computing time provided by the John von Neumann Institute for Computing (NIC) on the supercomputer JUWELS at Jülich Supercomputing Center (JSC) (user IDs: HKF7, HDD19; project IDs: 12723, 14449). We thank Michele Bonus for assistance in parameterizing the γ-glutamyl residue. In memory of Arne Holmgren (1940–2020).

Author contributions

L.L. generated the point mutants of ScGrx7, performed the steady-state kinetic measurements and analyzed the kinetic data except for the interconversion mutants which were analyzed by F.G. J.Z. and H.L. performed and analyzed the roGFP2 measurements. L.W. performed and analyzed the molecular dynamics simulations. M.D. conceived the study design and supervised the in vitro experiments. B.M. conceived and supervised the roGFP2 experiments. H.G. conceived and supervised the molecular dynamics simulations. M.D., B.M., and H.G. wrote the paper. All authors discussed the results and gave approval to the final version of the paper.

Competing interests

The authors declare no competing interests.

ARTICLE

NATURE COMMUNICATIONS | <https://doi.org/10.1038/s41467-020-15441-3>**Additional information**

Supplementary information is available for this paper at <https://doi.org/10.1038/s41467-020-15441-3>.

Correspondence and requests for materials should be addressed to H.G., B.M. or M.D.

Peer review information *Nature Communications* thanks Caryn Outten, and the other, anonymous, reviewer(s) for their contribution to the peer review of this work. Peer review reports are available.

Reprints and permission information is available at <http://www.nature.com/reprints>

Publisher's note Springer Nature remains neutral with regard to jurisdictional claims in published maps and institutional affiliations.



Open Access This article is licensed under a Creative Commons Attribution 4.0 International License, which permits use, sharing, adaptation, distribution and reproduction in any medium or format, as long as you give appropriate credit to the original author(s) and the source, provide a link to the Creative Commons license, and indicate if changes were made. The images or other third party material in this article are included in the article's Creative Commons license, unless indicated otherwise in a credit line to the material. If material is not included in the article's Creative Commons license and your intended use is not permitted by statutory regulation or exceeds the permitted use, you will need to obtain permission directly from the copyright holder. To view a copy of this license, visit <http://creativecommons.org/licenses/by/4.0/>.

© The Author(s) 2020

2.1.1. Supplementary information

Liedgens, et al., 2020, *Nature Communications*

Quantitative assessment of the determinant structural differences between redox-active and inactive glutaredoxins.

Liedgens, L. [§], Zimmermann, J. [§], Wäschenbach, L. [§], Geißel, F., Laporte, H., Gohlke, H., Morgan, B. and Deponte, M.

Nature Communications. 2020 April; 11(1), 1-18

DOI: 10.1038/s41467-020-15441-3

[§]Equally contributing authors

Reprinted from *Nature Communications*: Liedgens, L., Zimmermann, J., Wäschenbach, L., Geissel, F., Laporte, H., Gohlke, H., Morgan, B. and Deponte, M. *Quantitative assessment of the determinant structural differences between redox-active and inactive glutaredoxins*. 11(1), 1-18 © (2020), with permission from Nature Springer (*Nature Communications*).

All rights reserved.

Supplementary Information

Quantitative assessment of the determinant structural differences between redox-active and inactive glutaredoxins

Linda Liedgens^{1§}, Jannik Zimmermann^{2§}, Lucas Wäschenbach^{3§}, Fabian Geissel¹, Hugo Laporte², Holger Gohlke^{3*}, Bruce Morgan^{2*} & Marcel Deponte^{1*}

¹ Fachbereich Chemie, Abteilung Biochemie, Technische Universität Kaiserslautern, D-67663 Kaiserslautern, Germany

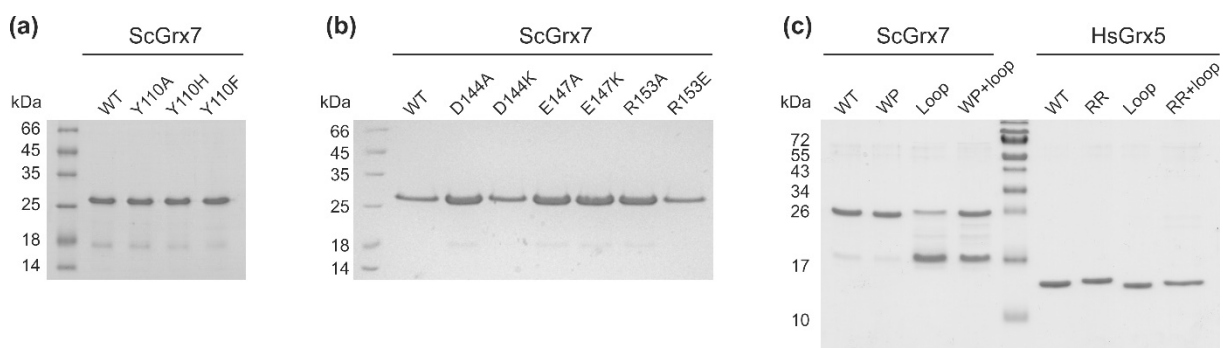
² Institut für Biochemie, Zentrum für Human- und Molekularbiologie (ZHMB), Universität des Saarlandes, D-66123 Saarbrücken, Germany

³ Mathematisch-Naturwissenschaftliche Fakultät, Institut für Pharmazeutische und Medizinische Chemie, Heinrich-Heine-Universität Düsseldorf, D-40225 Düsseldorf, Germany.

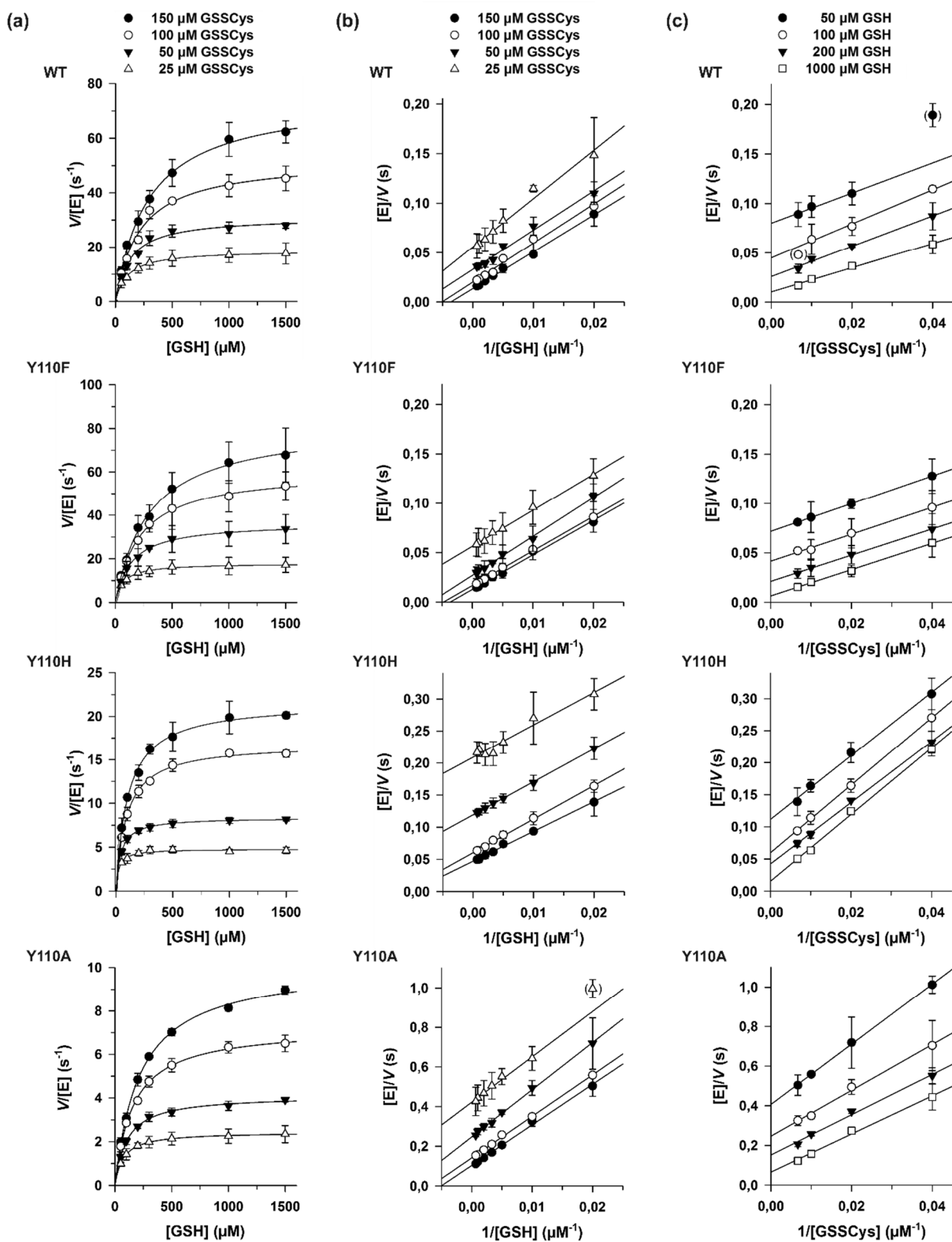
⁴ John von Neumann Institute for Computing (NIC), Jülich Supercomputing Centre (JSC) & Institute of Complex Systems, ICS-6: Structural Biochemistry, Forschungszentrum Jülich GmbH, D-52425 Jülich, Germany

§These authors contributed equally to this work.

*Correspondence and requests for materials should be addressed to M.D. (deponte@chemie.uni-kl.de), B.M. (bruce.morgan@uni-saarland.de) and H.G. (gohlke@uni-duesseldorf.de)

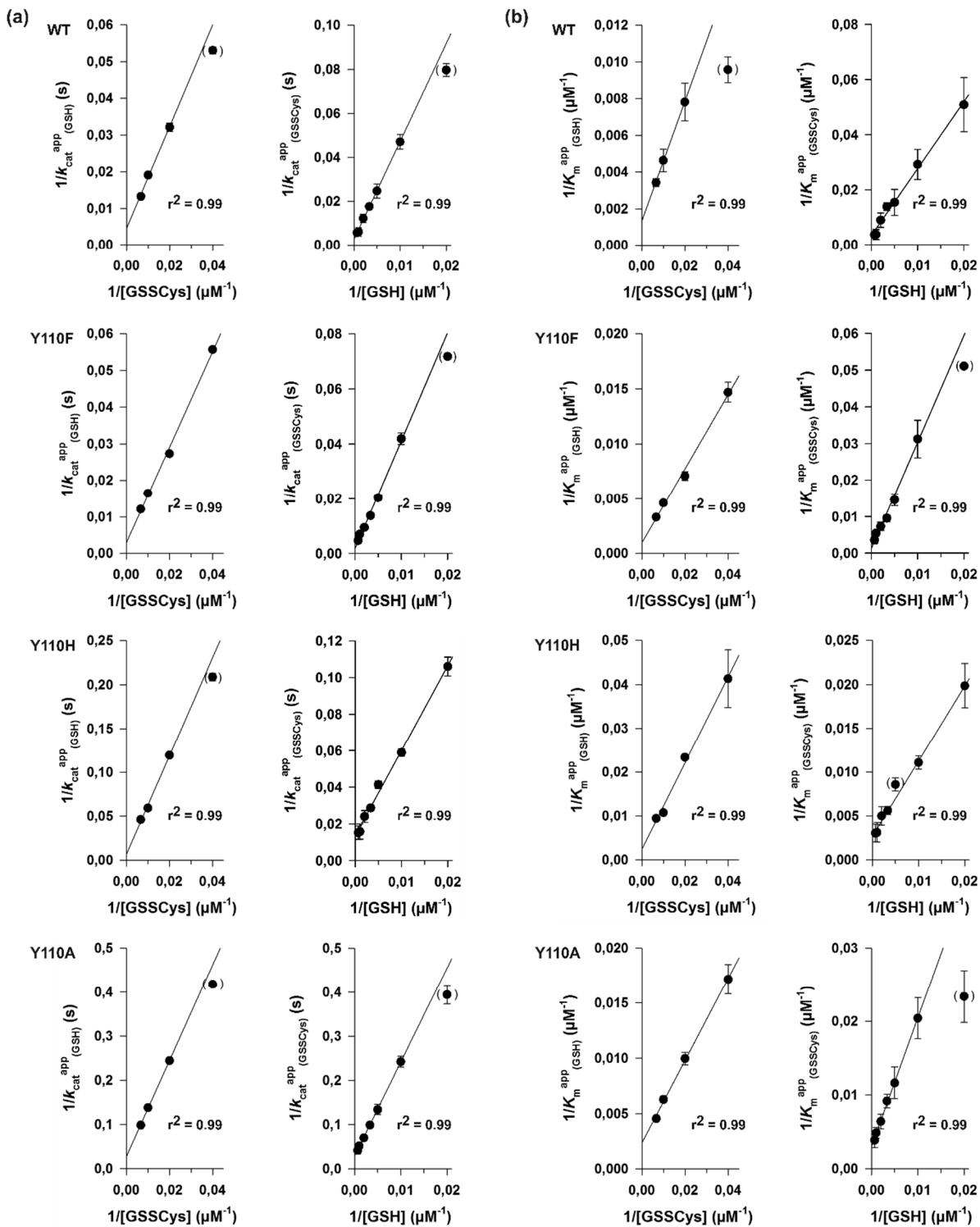
Supplementary Figure 1**Supplementary Figure 1 | Purification of recombinant wild-type and mutant enzymes.**

SDS-PAGE analyses of representative eluates on 15% gels after protein purification by Ni-NTA affinity chromatography. (a) Tyr110 mutants of ScGrx7. ScGrx7 wild-type enzyme, WT; ScGrx7^{Y110A}, Y110A; ScGrx7^{Y110H}, Y110H; ScGrx7^{Y110F}, Y110F. (b) Asp144, Glu147 and Arg153 mutants of ScGrx7. ScGrx7 wild-type enzyme, WT; ScGrx7^{D144A}, D144A; ScGrx7^{D144K}, D144K, ScGrx7^{E147A}, E147A; ScGrx7^{E147K}, E147K; ScGrx7^{R153A}, R153A; ScGrx7^{R153E}, R153E. Average yields from up to seven independent protein purification experiments for each mutant were highly reproducible and ranged from 12.6 ± 4.1 to 53.7 ± 5.1 mg of recombinant ScGrx7 per liter of *E. coli* culture depending on the mutant. (c) Interconversion mutants of ScGrx7 and HsGrx5. Left side: ScGrx7 wild-type enzyme, WT; ScGrx7^{WP}, WP; ScGrx7^{loop}, Loop; ScGrx7^{WP+loop}, WP+loop. Right side: Wild-type HsGrx5, WT; HsGrx5^{RR}, RR; HsGrx5^{loop}, Loop; HsGrx5^{RR+loop}, RR+loop. The calculated molecular masses of recombinant wild-type ScGrx7 and HsGrx5 are 20.2 and 15.1 kDa, respectively. ScGrx7 runs at approximately 26 kDa as reported previously. The exchange of the active site loop in ScGrx7 results in partial proteolysis. Average yields from three independent protein purification experiments for each mutant were highly reproducible and ranged from 2.2 to 16.2 mg of recombinant protein per liter of *E. coli* culture depending on the mutant.

Supplementary Figure 2

Supplementary Figure 2 | GS-SSCys assay steady-state kinetics of ScGrx7 wild-type enzyme and Y110X mutants. (a) Michaelis-Menten plots of the GSH-dependent reaction velocity at different initial concentrations of GS-SSCys. (b) Lineweaver-Burk plots of the GSH-

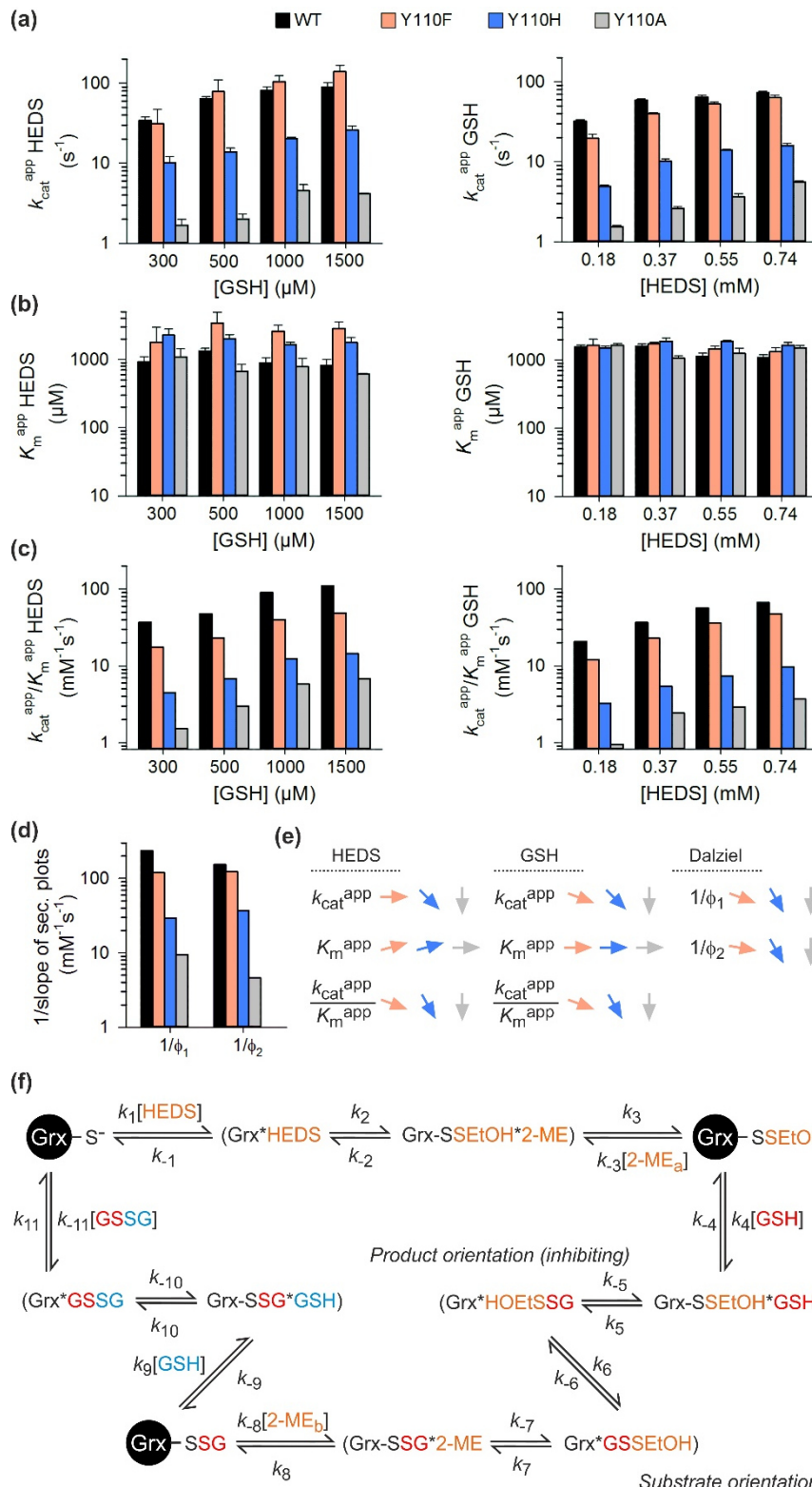
dependent reaction velocity at different initial concentrations of GS_{Cys} revealing ping-pong kinetic patterns. **(c)** Lineweaver-Burk plots of the GS_{Cys}-dependent reaction velocity at different initial concentrations of GSH. Data points and error bars are the mean \pm s.d. from three independent protein purification experiments and were plotted and fitted in SigmaPlot 13 according to Michaelis-Menten, Lineweaver-Burk, Eadie-Hofstee and Hanes theory (the latter two plots are not shown). Calculated k_{cat}^{app} and K_m^{app} values from the four different plots usually varied by less than 10%. Data points in brackets were omitted from the regression analysis when the k_{cat}^{app} or K_m^{app} values from all four plots varied by more than 10% and converged after removal of the outlier. True kinetic constants were estimated from secondary plots in Supplementary Fig. 3 and are listed in Supplementary Table 1. Selected apparent kinetic constants from non-linear regression analyses of Michaelis-Menten plots are listed in Supplementary Table 2.

Supplementary Figure 3

Supplementary Figure 3 | GSSCys assay secondary plots for ScGrx7 wild-type enzyme and Y110X mutants. (a) Secondary plots of the $k_{\text{cat}}^{\text{app}}$ values at different concentrations of GSSCys (left panels) and GSH (right panels) allowing the estimation of the true k_{cat} value from the y-axis intercept ($1/k_{\text{cat}}$) and of the true K_{m} value from the x-axis intercept ($-1/K_{\text{m}}$). Estimated

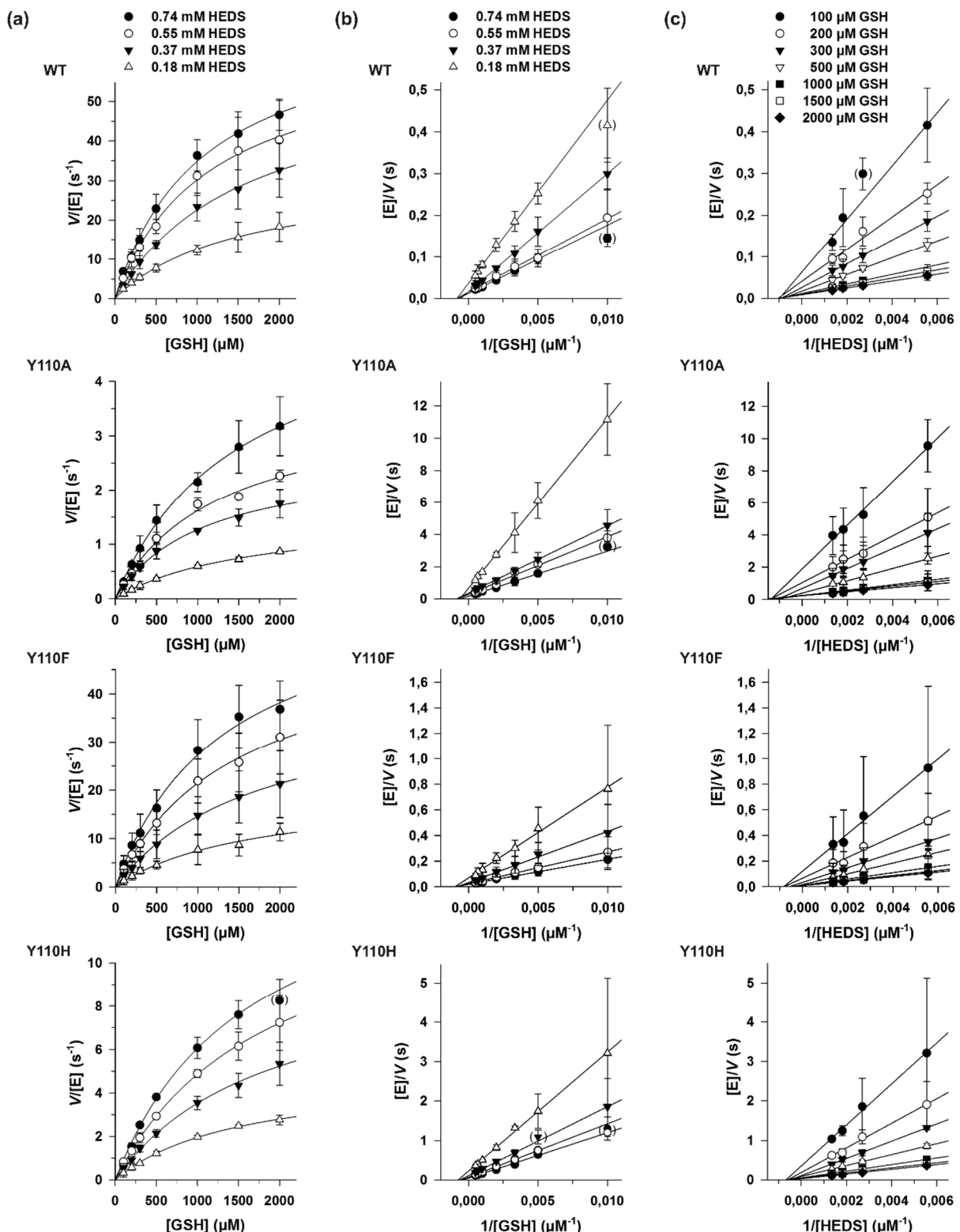
true kinetic constants have to be interpreted with care because of the proximity of the intersection points to the origin of the graphs. Dalziel coefficients were obtained from the slopes. (b) Secondary plots of the K_m^{app} values at different concentrations of GSSCys (left panels) and GSH (right panels). K_m^{app} and k_{cat}^{app} values were obtained from non-linear regression analyses of Michaelis-Menten plots (Supplementary Fig. 2). Error bars are the calculated standard error from the hyperbolic curve fits in SigmaPlot 13. Outliers in brackets were identified based on the r^2 values and omitted from the linear regression analysis in SigmaPlot 13. Estimated true kinetic constants and Dalziel coefficients are listed in Supplementary Table 1.

Supplementary Figure 4



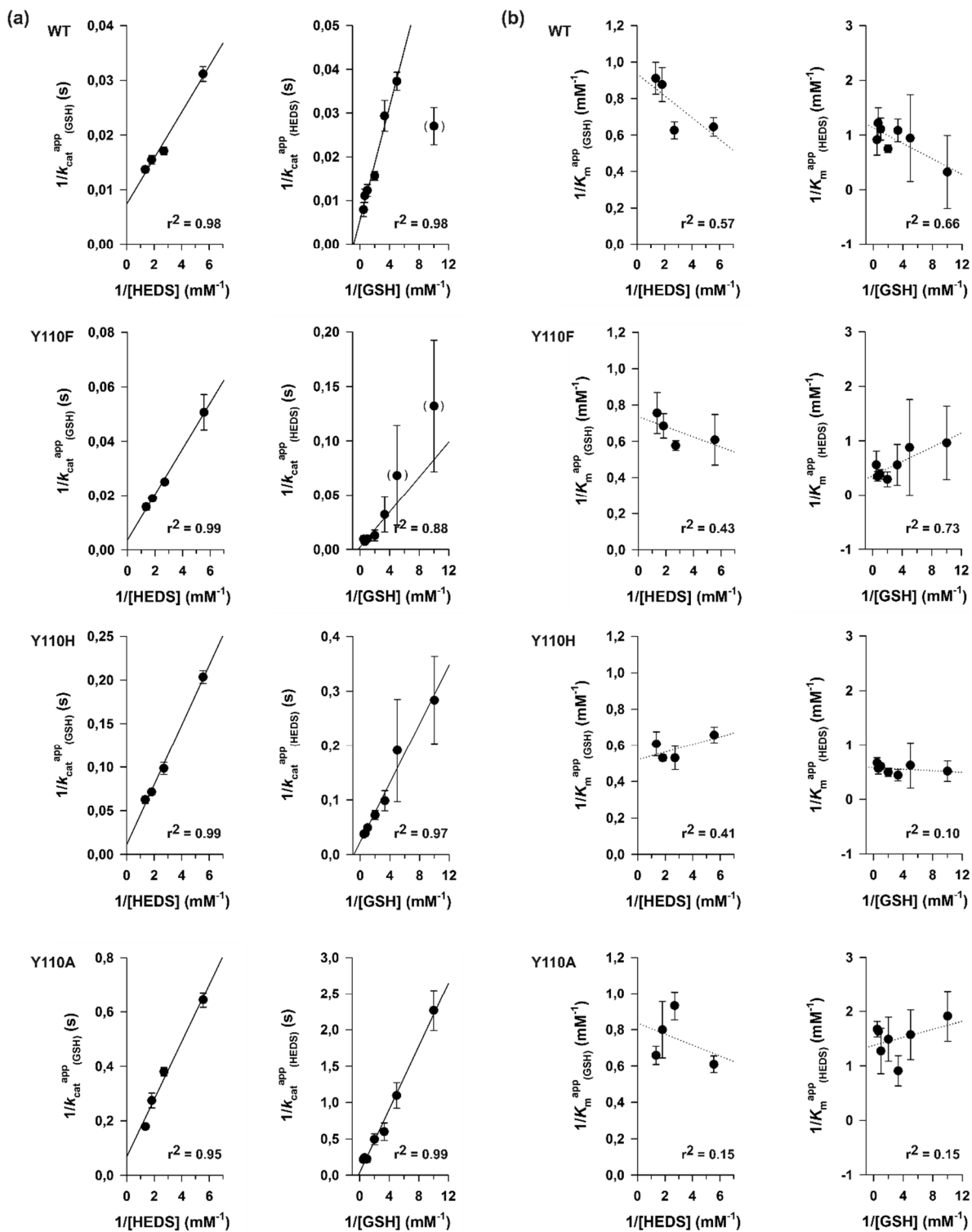
Supplementary Figure 4 | Replacement of Tyr110 in ScGrx7 slows down the turnover of both substrates in the HEDS assay. (a) and (b) Selected k_{cat}^{app} and K_m^{app} values of ScGrx7 wild-type enzyme and Y110X mutants for HEDS and GSH. (c) Calculated catalytic efficiencies

from panels **a** and **b**. Original plots and kinetic parameters for panels **a-c** are shown in Supplementary Fig. 5 and Supplementary Table 3. Error bars are the calculated standard error from the curve fits in SigmaPlot 13. (**d**) Reciprocal Dalziel coefficients obtained from Supplementary Fig. 6. The reciprocal Dalziel coefficients and true k_{cat} values are also listed in Supplementary Table 1. (**e**) Summary of the altered kinetic parameters. (**f**) Potential reaction sequence for the HEDS assay. Please note that GSSEtOH is a product and substrate that can bind in two orientations at the Grx active site. This could explain the sequential kinetic patterns with a common x-axis intercept in the Lineweaver-Burk plots (Supplementary Fig. 5) as discussed previously¹². Statistical analyses and *P*-values for the $k_{\text{cat}}^{\text{app}}$ and K_m^{app} values from panels **a** and **b** are listed in Supplementary Table 11.

Supplementary Figure 5

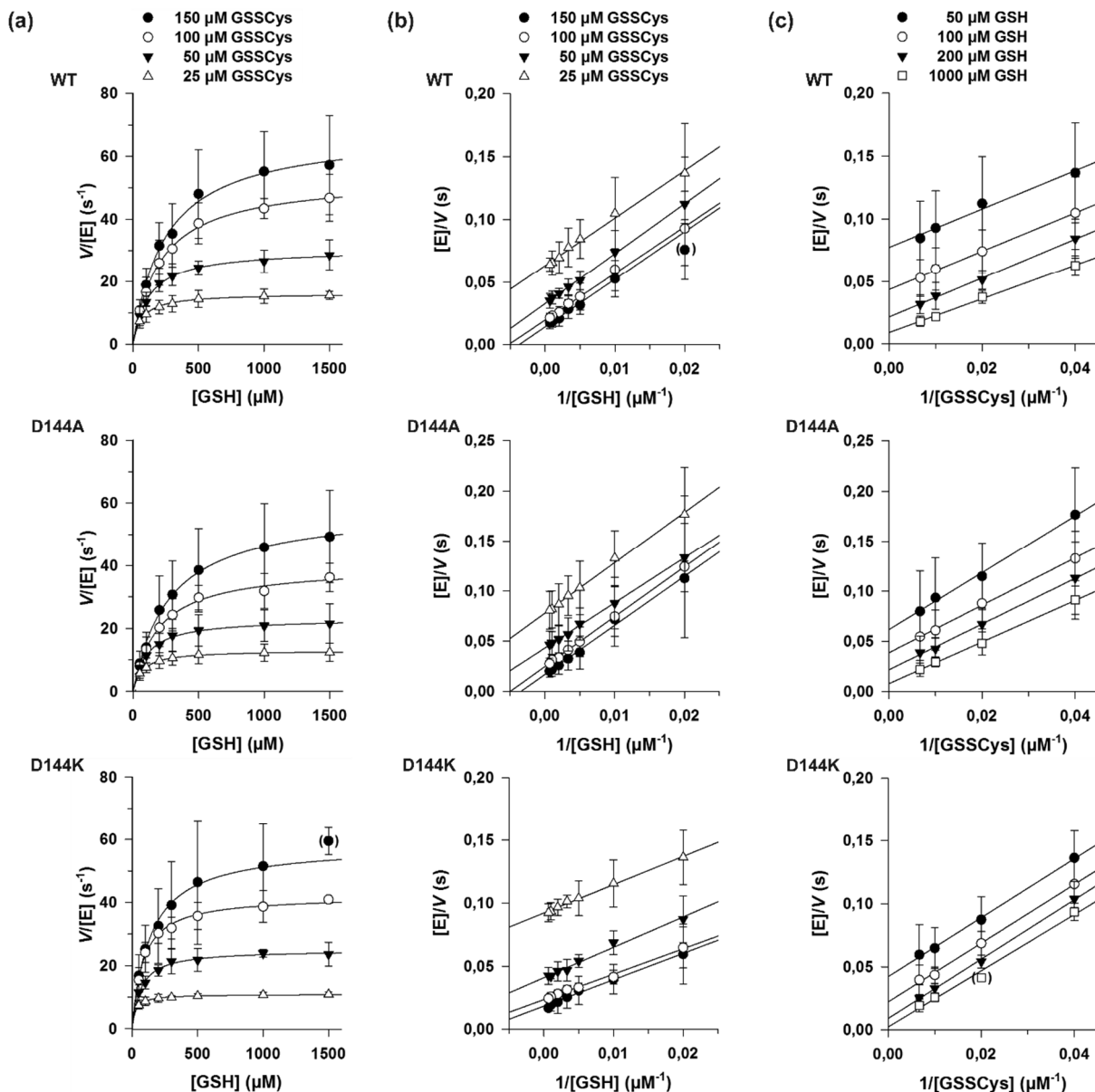
Supplementary Figure 5 | HEDS assay steady-state kinetics of ScGrx7 wild-type enzyme and Y110X mutants. (a) Michaelis-Menten plots of the GSH-dependent reaction velocity at different initial concentrations of HEDS. (b) Lineweaver-Burk plots of the GSH-dependent

reaction velocity at different initial concentrations of HEDS revealing sequential kinetic patterns. (c) Lineweaver-Burk plots of the HEDS-dependent reaction velocity at different initial concentrations of GSH. Data points and error bars are the mean \pm s.d. from three independent protein purification experiments and were plotted and fitted in SigmaPlot 13 according to Michaelis-Menten, Lineweaver-Burk, Eadie-Hofstee and Hanes theory (the latter two plots are not shown). Calculated $k_{\text{cat}}^{\text{app}}$ and K_m^{app} values from the four different plots usually varied by less than 10%. Data points in brackets were omitted from the regression analysis when the $k_{\text{cat}}^{\text{app}}$ or K_m^{app} values from all four plots varied by more than 10% and converged after removal of the outlier. True kinetic constants were estimated from secondary plots in Supplementary Fig. 6 and are listed in Supplementary Table 1. Selected apparent kinetic constants from non-linear regression analyses of Michaelis-Menten plots are listed in Supplementary Table 3.

Supplementary Figure 6

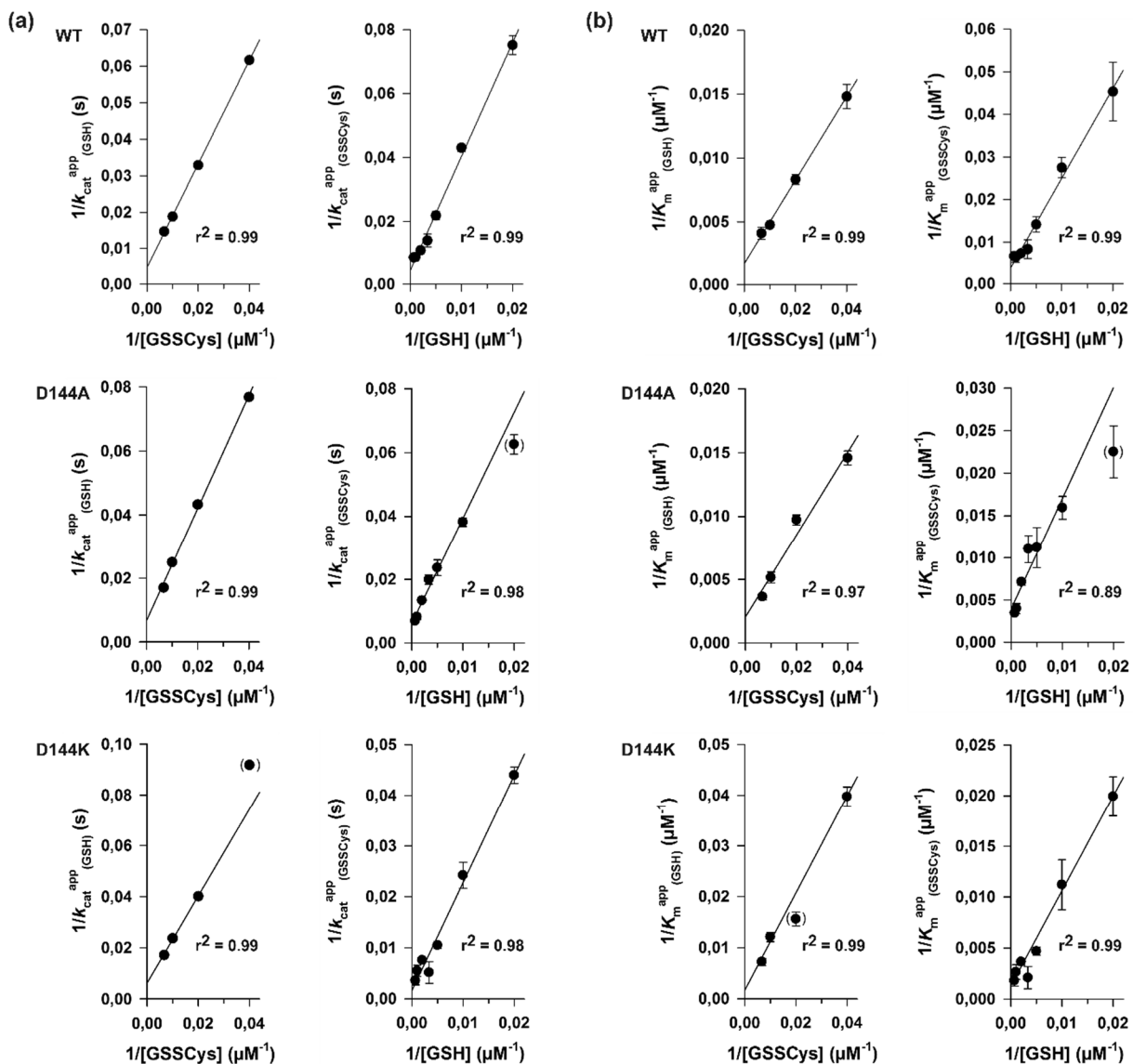
Supplementary Figure 6 | HEDS assay secondary plots for ScGrx7 wild-type enzyme and Y110X mutants. K_m^{app} and $k_{\text{cat}}^{\text{app}}$ values were obtained from non-linear regression analyses of Michaelis-Menten plots (Supplementary Fig. 5). Error bars are the calculated standard error from the hyperbolic curve fits in SigmaPlot 13. **(a)** Secondary plots of the $k_{\text{cat}}^{\text{app}}$

values at different concentrations of HEDS (left panels) and GSH (right panels) allowing the estimation of the true k_{cat} value from the y-axis intercept ($1/k_{\text{cat}}$) and of the true K_m value from the x-axis intercept ($-1/K_m$). Outliers in brackets at the lowest substrate concentration were identified based on the r^2 values and omitted from the linear regression analysis in SigmaPlot 13. Estimated true kinetic constants have to be interpreted with care because of the proximity of the intersection points to the origin of the graphs. The Dalziel coefficients were obtained from the slopes. (b) Secondary plots of the K_m^{app} values at different concentrations of HEDS (left panels) and GSH (right panels). Please note that the differences for K_m^{app} values among independent measurements and mutants are mostly not statistically significant (see also Supplementary Table 3). Estimated true kinetic constants and Dalziel coefficients are listed in Supplementary Table 1.

Supplementary Figure 7

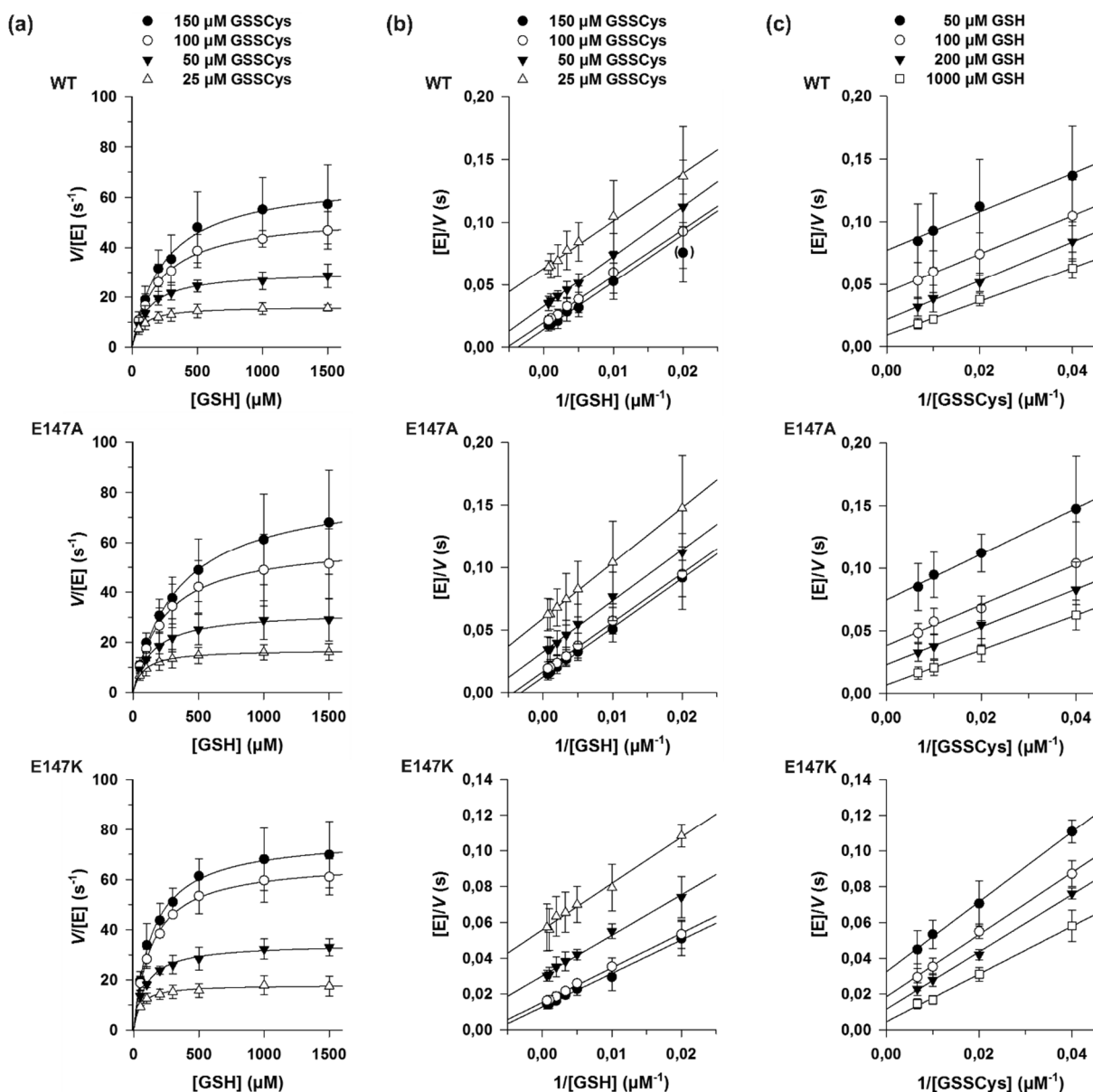
Supplementary Figure 7 | GSSCys assay steady-state kinetics of ScGrx7 wild-type enzyme and D144X mutants. (a) Michaelis-Menten plots of the GSH-dependent reaction velocity at different initial concentrations of GSSCys. (b) Lineweaver-Burk plots of the GSH-dependent reaction velocity at different initial concentrations of GSSCys revealing ping-pong kinetic patterns. (c) Lineweaver-Burk plots of the GSSCys-dependent reaction velocity at different initial concentrations of GSH. Data points and error bars are the mean \pm s.d. from three independent protein purification experiments and were plotted and fitted in SigmaPlot 13 according to Michaelis-Menten, Lineweaver-Burk, Eadie-Hofstee and Hanes theory (the latter

two plots are not shown). Calculated $k_{\text{cat}}^{\text{app}}$ and K_m^{app} values from the four different plots usually varied by less than 10%. Data points in brackets were omitted from the regression analysis when the $k_{\text{cat}}^{\text{app}}$ or K_m^{app} values from all four plots varied by more than 10% and converged after removal of the outlier. True kinetic constants were estimated from secondary plots in Supplementary Fig. 8 and listed in Supplementary Table 4. Selected apparent kinetic constants from non-linear regression analyses of Michaelis-Menten plots are listed in Supplementary Table 5.

Supplementary Figure 8

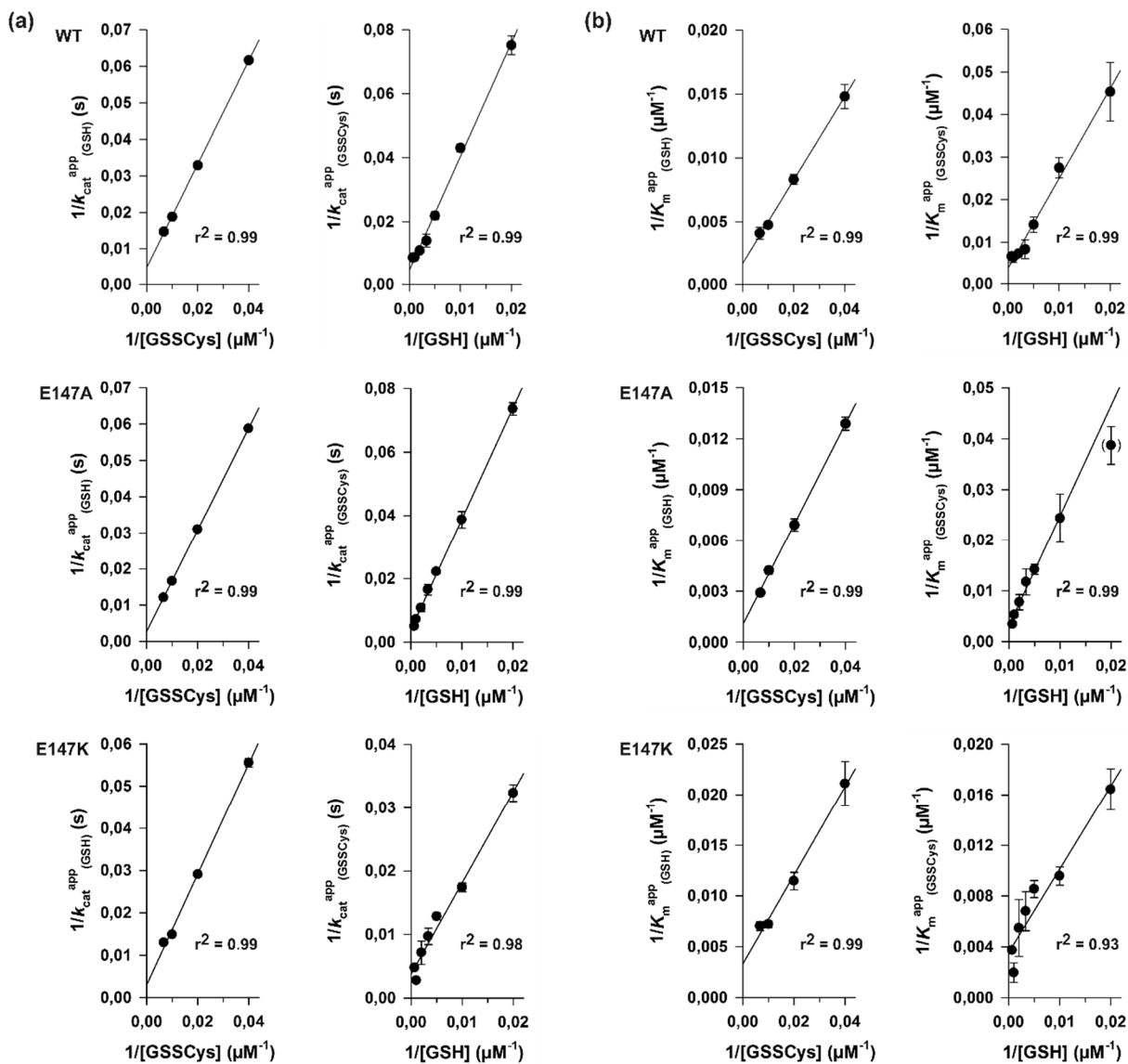
Supplementary Figure 8 | GSSCys assay secondary plots for ScGrx7 wild-type enzyme and D144X mutants. (a) Secondary plots of the k_{cat}^{app} values at different concentrations of GSSCys (left panels) and GSH (right panels) allowing the estimation of the true k_{cat} value from the y-axis intercept ($1/k_{cat}$) and of the true K_m value from the x-axis intercept (- $1/K_m$). Estimated true kinetic constants have to be interpreted with care because of the proximity of the intersection points to the origin of the graphs. Dalziel coefficients were obtained from the slopes. (b) Secondary plots of the K_m^{app} values at different concentrations of GSSCys (left panels) and GSH (right panels). K_m^{app} and k_{cat}^{app} values were obtained from non-linear regression analyses of Michaelis-Menten plots (Supplementary Fig. 7). Error bars are the

calculated standard error from the hyperbolic curve fits in SigmaPlot 13. Outliers in brackets were identified based on the r^2 values and omitted from the linear regression analysis in SigmaPlot 13. Estimated true kinetic constants and Dalziel coefficients are listed in Supplementary Table 4.

Supplementary Figure 9

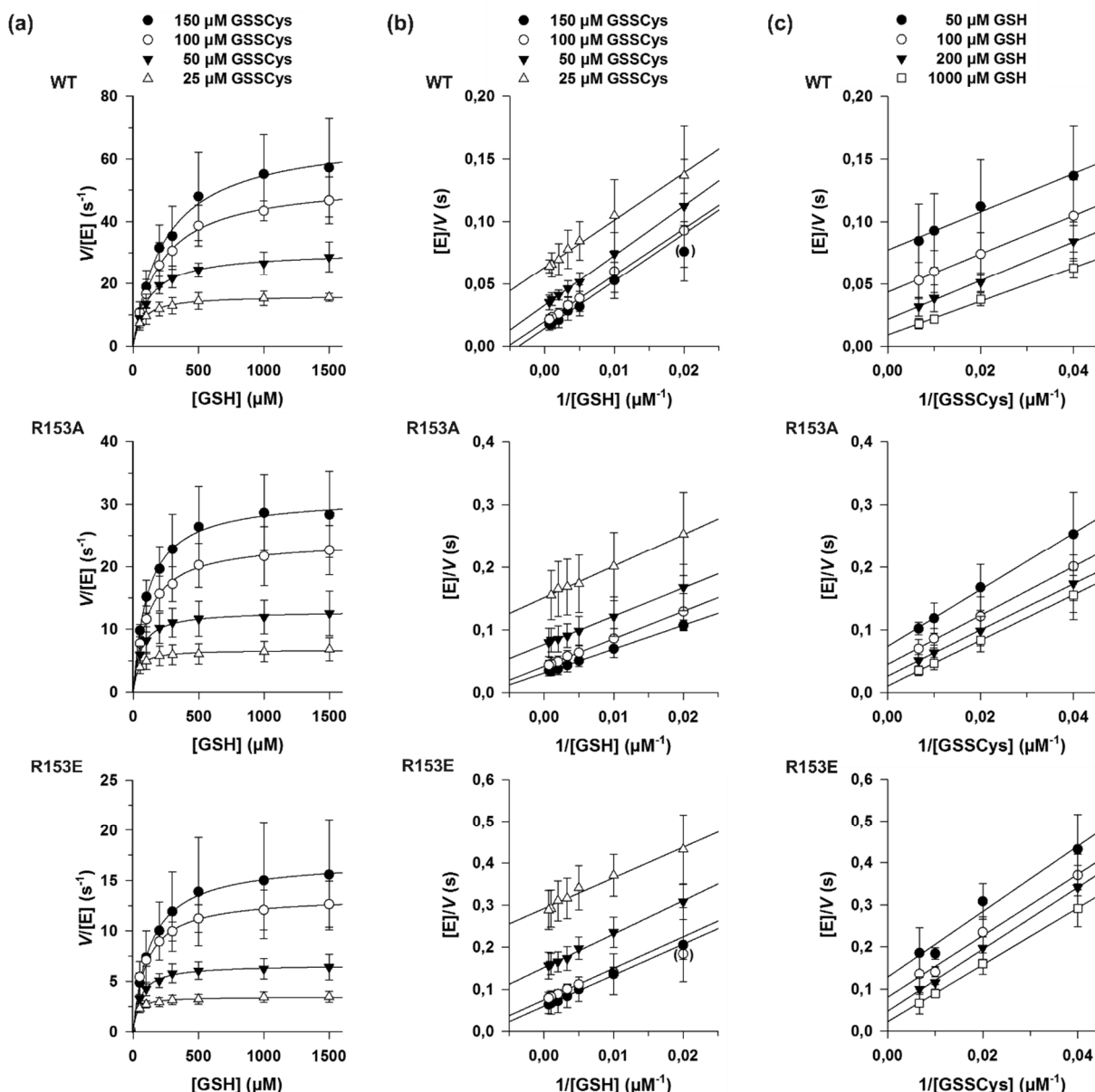
Supplementary Figure 9 | GSSCys assay steady-state kinetics of ScGrx7 wild-type enzyme and E147X mutants. (a) Michaelis-Menten plots of the GSH-dependent reaction velocity at different initial concentrations of GSSCys. (b) Lineweaver-Burk plots of the GSH-dependent reaction velocity at different initial concentrations of GSSCys revealing ping-pong kinetic patterns. (c) Lineweaver-Burk plots of the GSSCys-dependent reaction velocity at different initial concentrations of GSH. Data points and error bars are the mean \pm s.d. from three independent protein purification experiments and were plotted and fitted in SigmaPlot 13 according to Michaelis-Menten, Lineweaver-Burk, Eadie-Hofstee and Hanes theory (the latter

two plots are not shown). Calculated $k_{\text{cat}}^{\text{app}}$ and K_m^{app} values from the four different plots usually varied by less than 10%. Data points in brackets were omitted from the regression analysis when the $k_{\text{cat}}^{\text{app}}$ or K_m^{app} values from all four plots varied by more than 10% and converged after removal of the outlier. True kinetic constants were estimated from secondary plots in Supplementary Fig. 10 and are listed in Supplementary Table 4. Selected apparent kinetic constants from non-linear regression analyses of Michaelis-Menten plots are listed in Supplementary Table 5.

Supplementary Figure 10

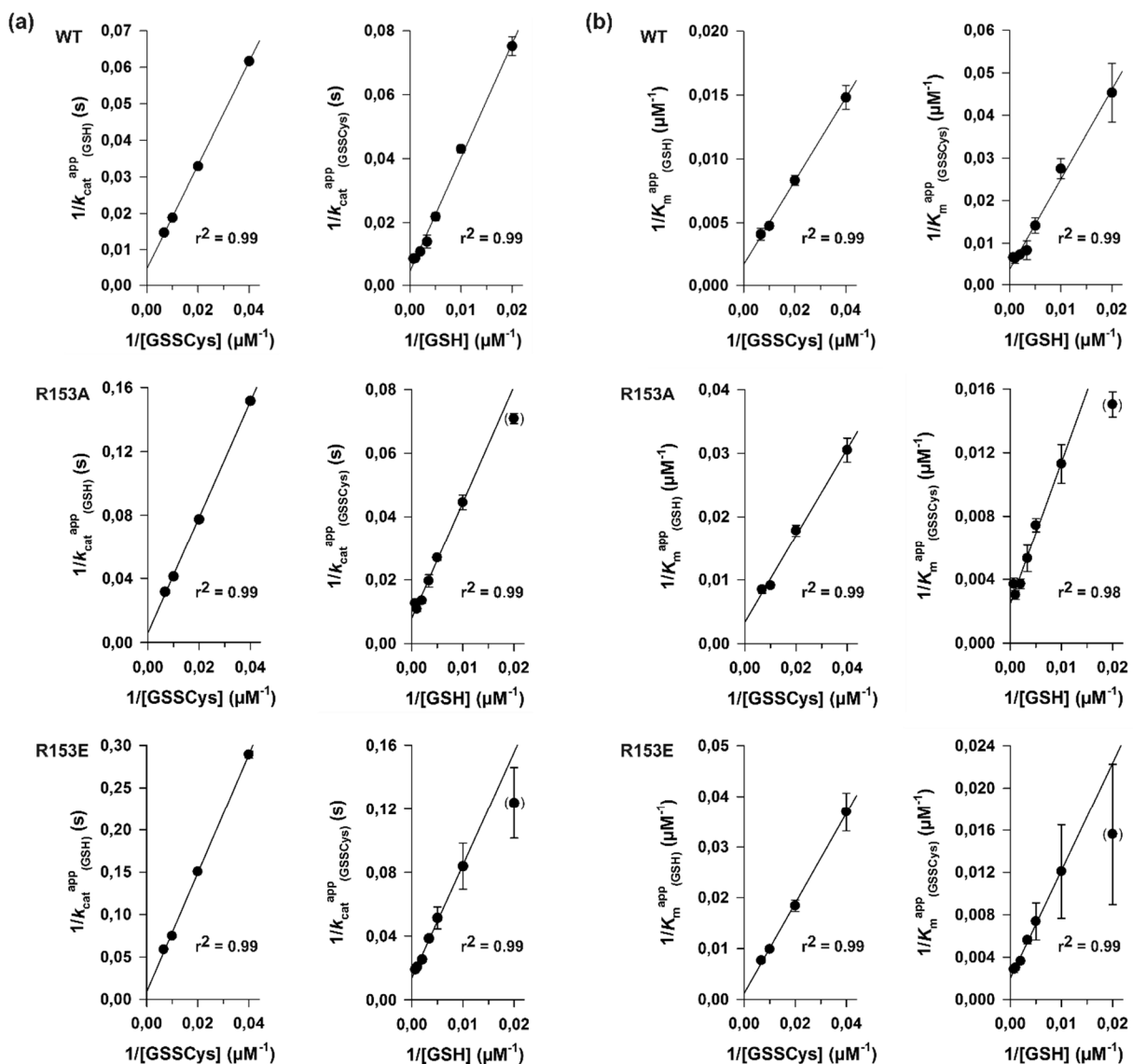
Supplementary Figure 10 | GSSCys assay secondary plots for ScGrx7 wild-type enzyme and E147X mutants. (a) Secondary plots of the $k_{\text{cat}}^{\text{app}}$ values at different concentrations of GSSCys (left panels) and GSH (right panels) allowing the estimation of the true k_{cat} value from the y-axis intercept ($1/k_{\text{cat}}$) and of the true K_m value from the x-axis intercept (- $1/K_m$). Estimated true kinetic constants have to be interpreted with care because of the proximity of the intersection points to the origin of the graphs. Dalziel coefficients were obtained from the slopes. (b) Secondary plots of the K_m^{app} values at different concentrations of GSSCys (left panels) and GSH (right panels). K_m^{app} and $k_{\text{cat}}^{\text{app}}$ values were obtained from non-linear regression analyses of Michaelis-Menten plots (Supplementary Fig. 9). Error bars are the

calculated standard error from the hyperbolic curve fits in SigmaPlot 13. Outliers in brackets were identified based on the r^2 values and omitted from the linear regression analysis in SigmaPlot 13. Estimated true kinetic constants and Dalziel coefficients are listed in Supplementary Table 4.

Supplementary Figure 11

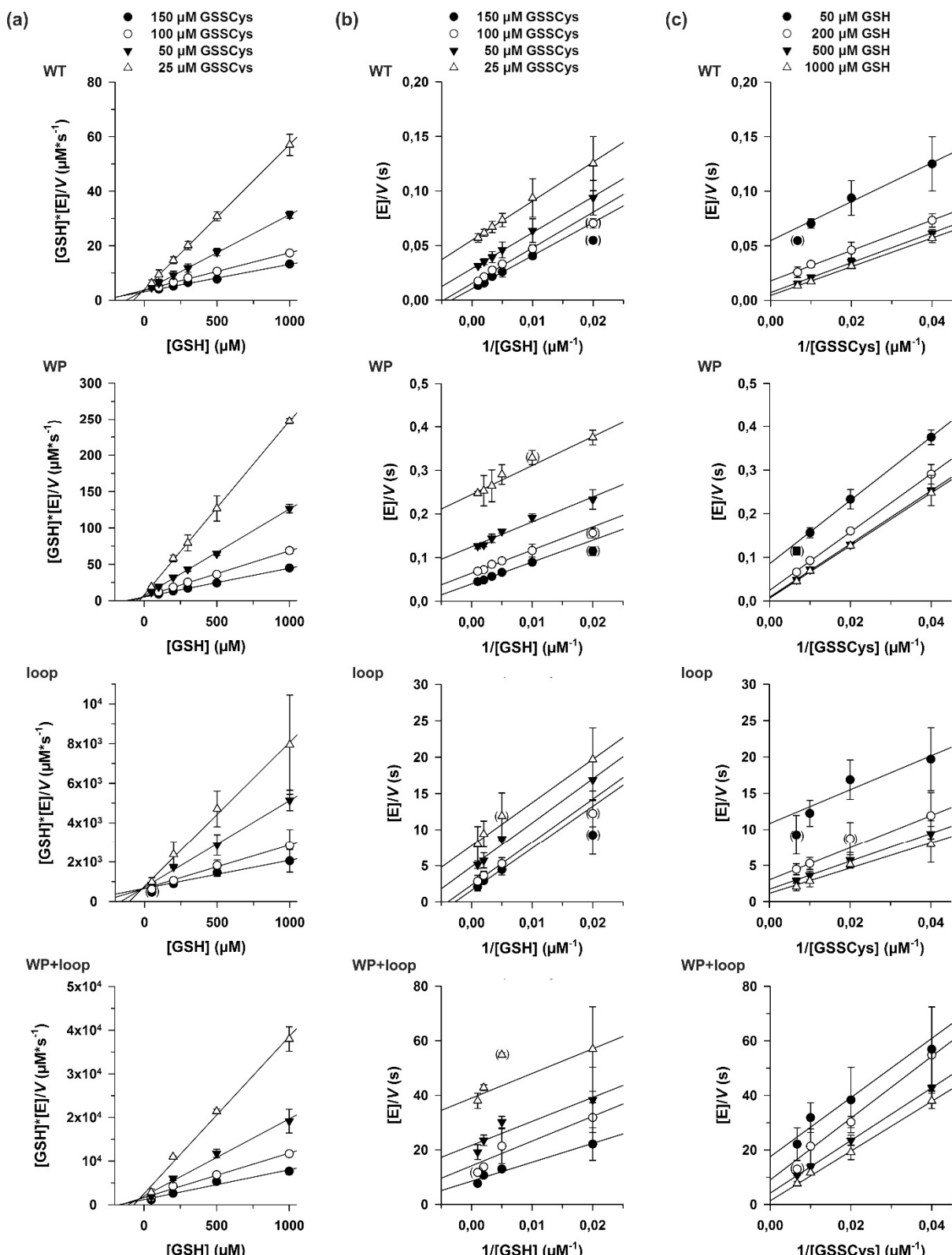
Supplementary Figure 11 | GSSCys assay steady-state kinetics of ScGrx7 wild-type enzyme and R153X mutants. (a) Michaelis-Menten plots of the GSH-dependent reaction velocity at different initial concentrations of GSSCys. (b) Lineweaver-Burk plots of the GSH-dependent reaction velocity at different initial concentrations of GSSCys revealing ping-pong kinetic patterns. (c) Lineweaver-Burk plots of the GSSCys-dependent reaction velocity at different initial concentrations of GSH. Data points and error bars are the mean \pm s.d. from three independent protein purification experiments and were plotted and fitted in SigmaPlot 13 according to Michaelis-Menten, Lineweaver-Burk, Eadie-Hofstee and Hanes theory (the latter two plots are not shown). Calculated K_{cat}^{app} and K_m^{app} values from the four different plots usually

varied by less than 10%. Data points in brackets were omitted from the regression analysis when the $k_{\text{cat}}^{\text{app}}$ or K_m^{app} values from all four plots varied by more than 10% and converged after removal of the outlier. True kinetic constants were estimated from secondary plots in Supplementary Fig. 12 are listed in Supplementary Table 4. Selected apparent kinetic constants from non-linear regression analyses of Michaelis-Menten plots are listed in Supplementary Table 6.

Supplementary Figure 12

Supplementary Figure 12 | GSSCys assay secondary plots for ScGrx7 wild-type enzyme and R153X mutants. (a) Secondary plots of the k_{cat}^{app} values at different concentrations of GSSCys (left panels) and GSH (right panels) allowing the estimation of the true k_{cat} value from the y-axis intercept ($1/k_{cat}$) and of the true K_m value from the x-axis intercept (- $1/K_m$). Estimated true kinetic constants have to be interpreted with care because of the proximity of the intersection points to the origin of the graphs. Dalziel coefficients were obtained from the slopes. (b) Secondary plots of the K_m^{app} values at different concentrations of GSSCys (left panels) and GSH (right panels). K_m^{app} and k_{cat}^{app} values were obtained from non-linear regression analyses of Michaelis-Menten plots (Supplementary Fig. 11). Error bars are the

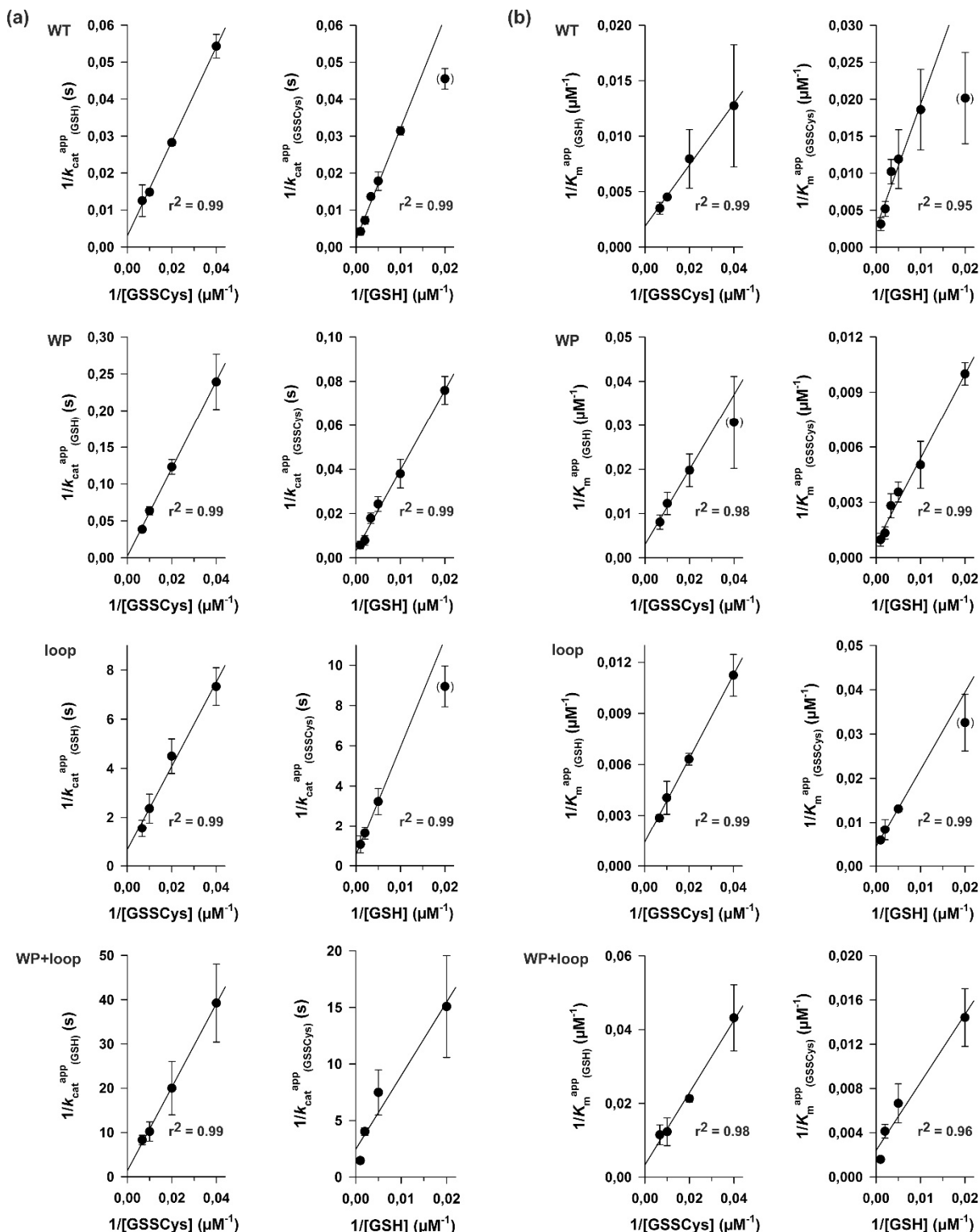
calculated standard error from the hyperbolic curve fits in SigmaPlot 13. Outliers in brackets were identified based on the r^2 values and omitted from the linear regression analysis in SigmaPlot 13. Estimated true kinetic constants and Dalziel coefficients are listed in Supplementary Table 4.

Supplementary Figure 13

Supplementary Figure 13 | GSSCys assay steady-state kinetics of ScGrx7 wild-type enzyme and mutants ScGrx7^{WP}, ScGrx7^{loop} and ScGrx7^{WP+loop}. (a) Hanes plots of the GSH-dependent reaction velocity at different initial concentrations of GSSCys. (b) Lineweaver-Burk

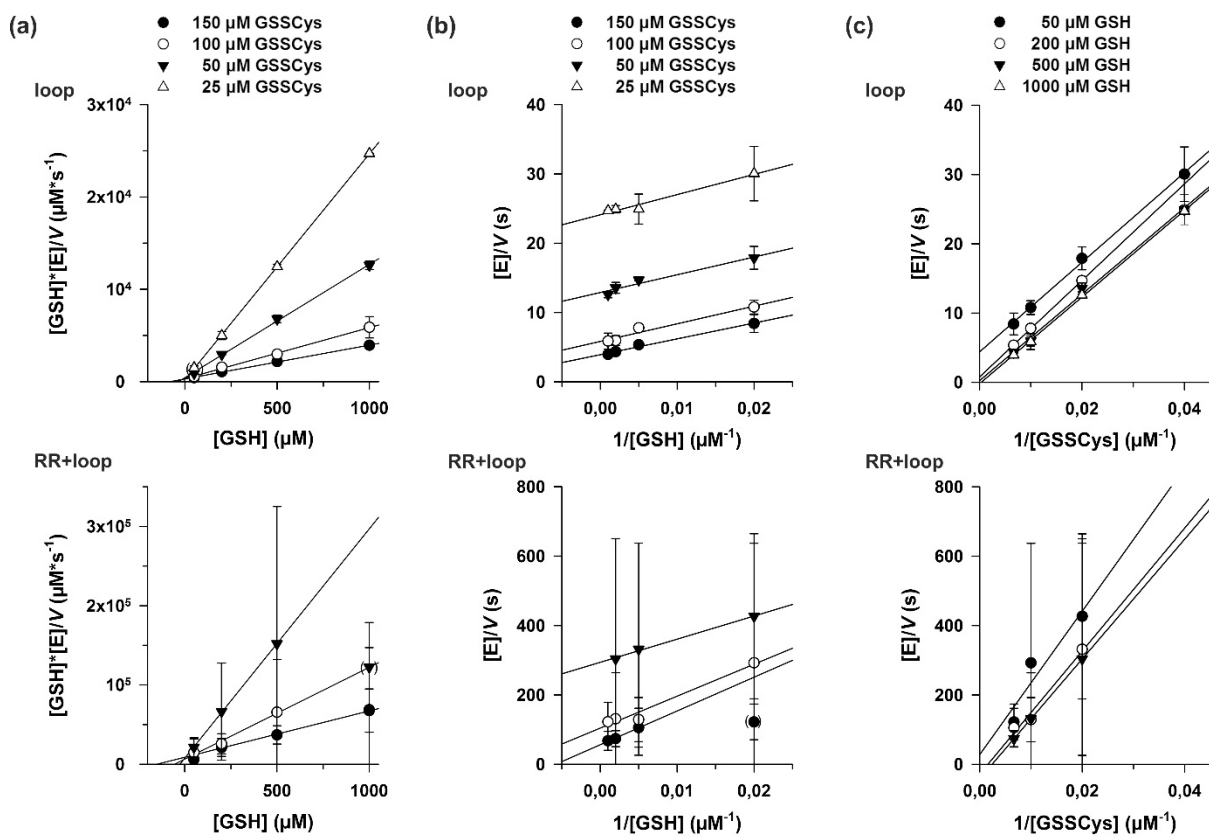
plots of the GSH-dependent reaction velocity at different initial concentrations of GSSCys revealing ping-pong kinetic patterns. (c) Lineweaver-Burk plots of the GSSCys-dependent reaction velocity at different initial concentrations of GSH. Data points and error bars are the mean \pm s.d. from three independent protein purification experiments and were plotted and fitted in SigmaPlot 13 according to Hanes, Lineweaver-Burk and Eadie-Hofstee theory (the latter plots are not shown). Calculated $k_{\text{cat}}^{\text{app}}$ and K_m^{app} values from the three different plots usually varied by less than 10%. Data points in brackets were omitted from the regression analysis when the $k_{\text{cat}}^{\text{app}}$ or K_m^{app} values from all four plots varied by more than 10% and converged after removal of the outlier. True kinetic constants were estimated from secondary plots in Supplementary Fig. 14 and are listed in Supplementary Table 7. Selected apparent kinetic constants from linear regression analyses of Hanes plots are listed in Supplementary Table 8.

Supplementary Figure 14

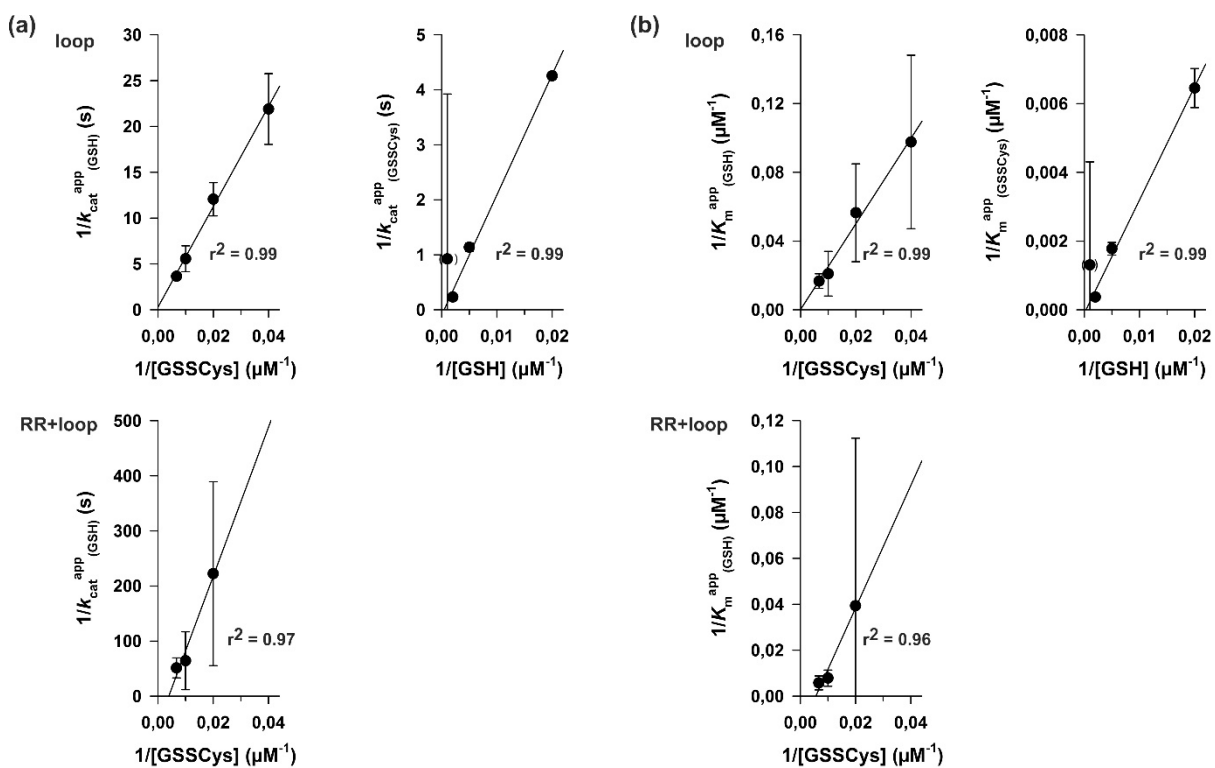


Supplementary Figure 14 | GSSCys assay secondary plots for ScGrx7 wild-type enzyme and mutants ScGrx7^{WP}, ScGrx7^{loop} and ScGrx7^{WP+loop}. (a) Secondary plots of the k_{cat}^{app} values at different concentrations of GSSCys (left panels) and GSH (right panels) allowing the

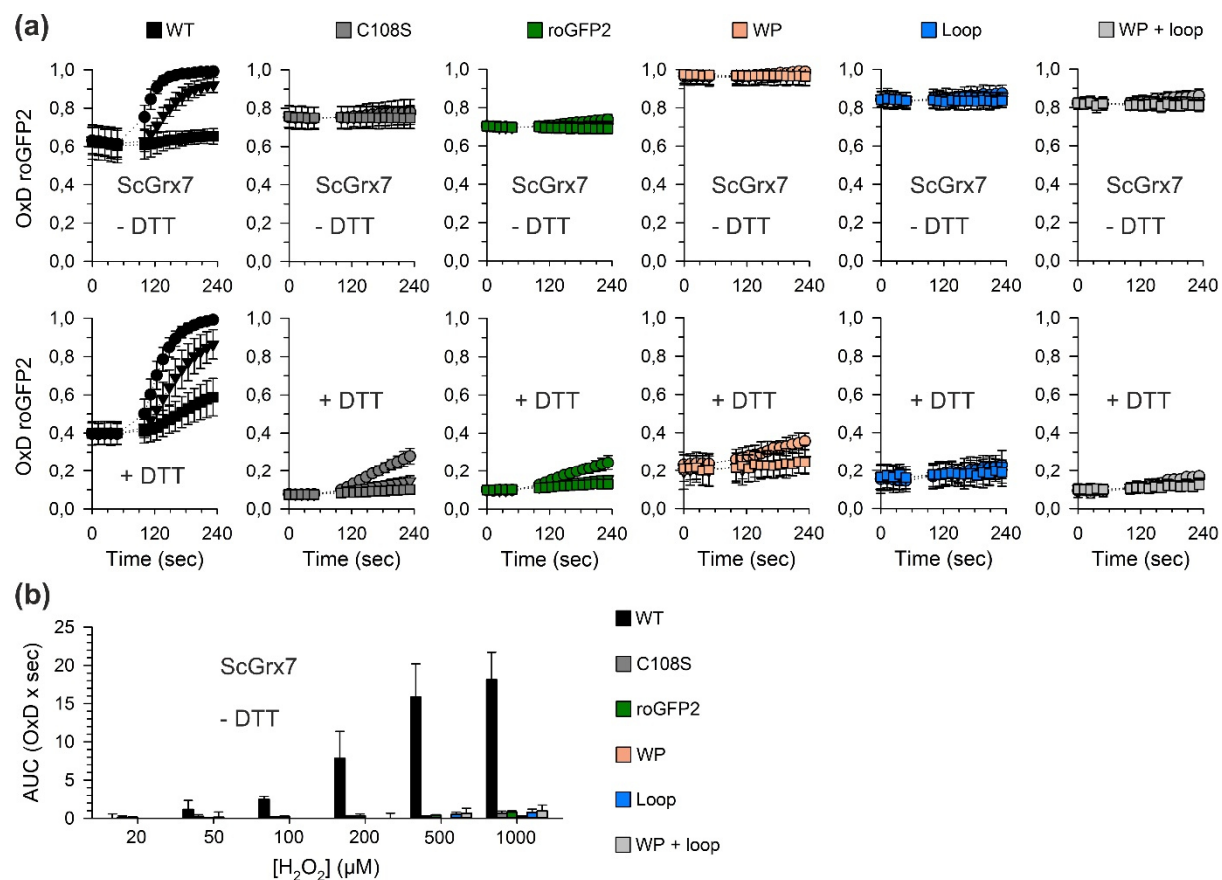
estimation of the true k_{cat} value from the y-axis intercept ($1/k_{\text{cat}}$) and of the true K_m value from the x-axis intercept ($-1/K_m$). Estimated true kinetic constants have to be interpreted with care because of the proximity of the intersection points to the origin of the graphs. Dalziel coefficients were obtained from the slopes. **(b)** Secondary plots of the K_m^{app} values at different concentrations of GSSCys (left panels) and GSH (right panels). K_m^{app} and $k_{\text{cat}}^{\text{app}}$ values were obtained from linear regression analyses of Hanes plots (Supplementary Fig. 13). Error bars are the calculated standard error from the hyperbolic curve fits in SigmaPlot 13. Outliers in brackets were identified based on the r^2 values and omitted from the linear regression analysis in SigmaPlot 13. Estimated true kinetic constants and Dalziel coefficients are listed in Supplementary Table 7.

Supplementary Figure 15

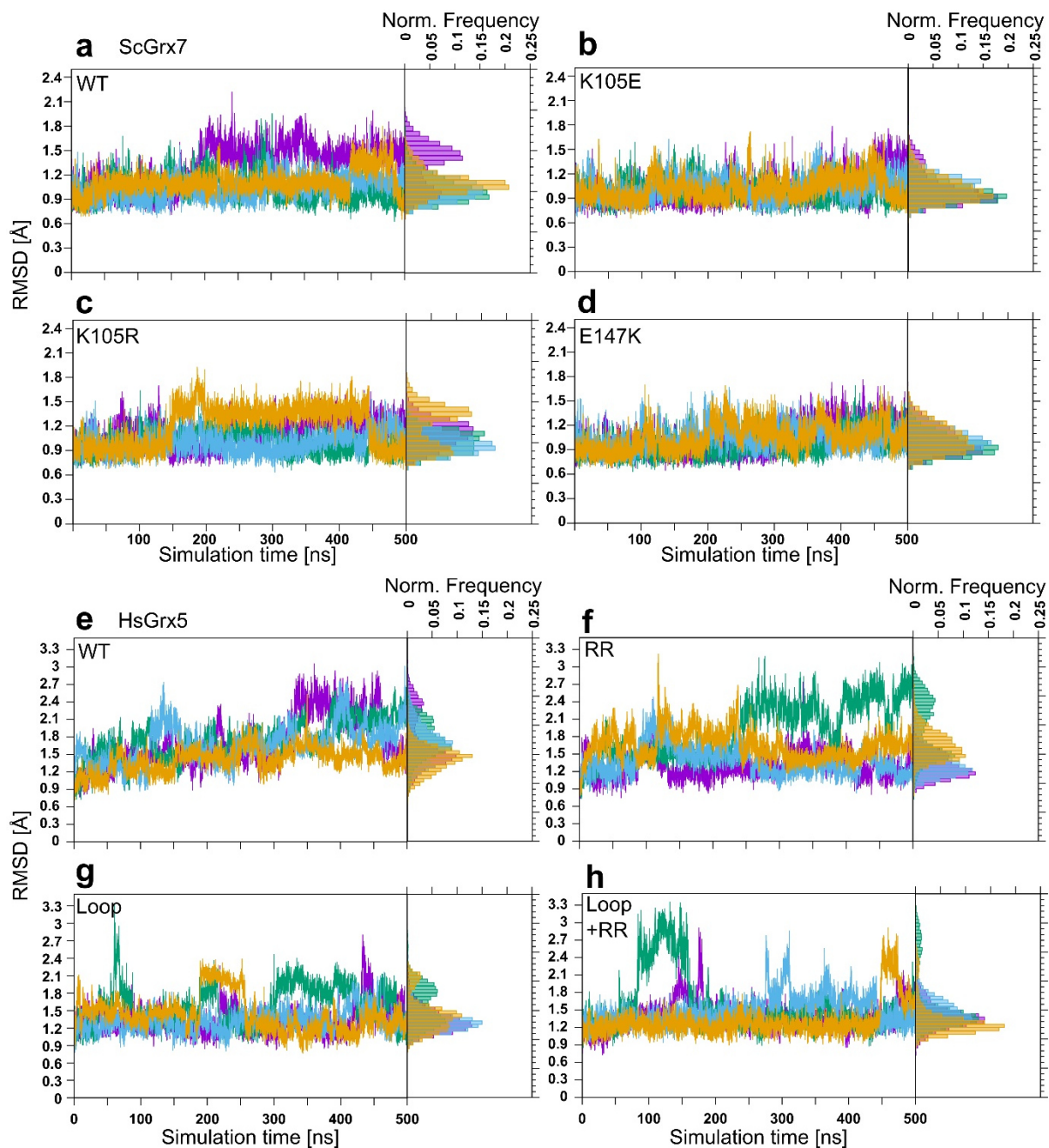
Supplementary Figure 15 | GSSCys assay steady-state kinetics of HsGrx5^{loop} and HsGrx5^{RR+loop}. (a) Hanes plots of the GSH-dependent reaction velocity at different initial concentrations of GSSCys. (b) Lineweaver-Burk plots of the GSH-dependent reaction velocity at different initial concentrations of GSSCys revealing ping-pong kinetic patterns. (c) Lineweaver-Burk plots of the GSSCys-dependent reaction velocity at different initial concentrations of GSH. Data points and error bars are the mean \pm s.d. from three independent protein purification experiments and were plotted and fitted in SigmaPlot 13 according to Hanes, Lineweaver-Burk and Eadie-Hofstee theory. Data points in brackets were omitted from the regression analysis when the k_{cat}^{app} or K_m^{app} values from all four plots varied by more than 10% and converged after removal of the outlier. True kinetic constants were estimated from secondary plots in Supplementary Fig. 16 and are listed in Supplementary Table 7. Selected apparent kinetic constants from linear regression analyses of Hanes plots are listed in Supplementary Table 9. The activities of HsGrx5 and HsGrx5^{RR} were similar to the NADPH consumption of negative controls without enzyme and could not be analyzed.

Supplementary Figure 16

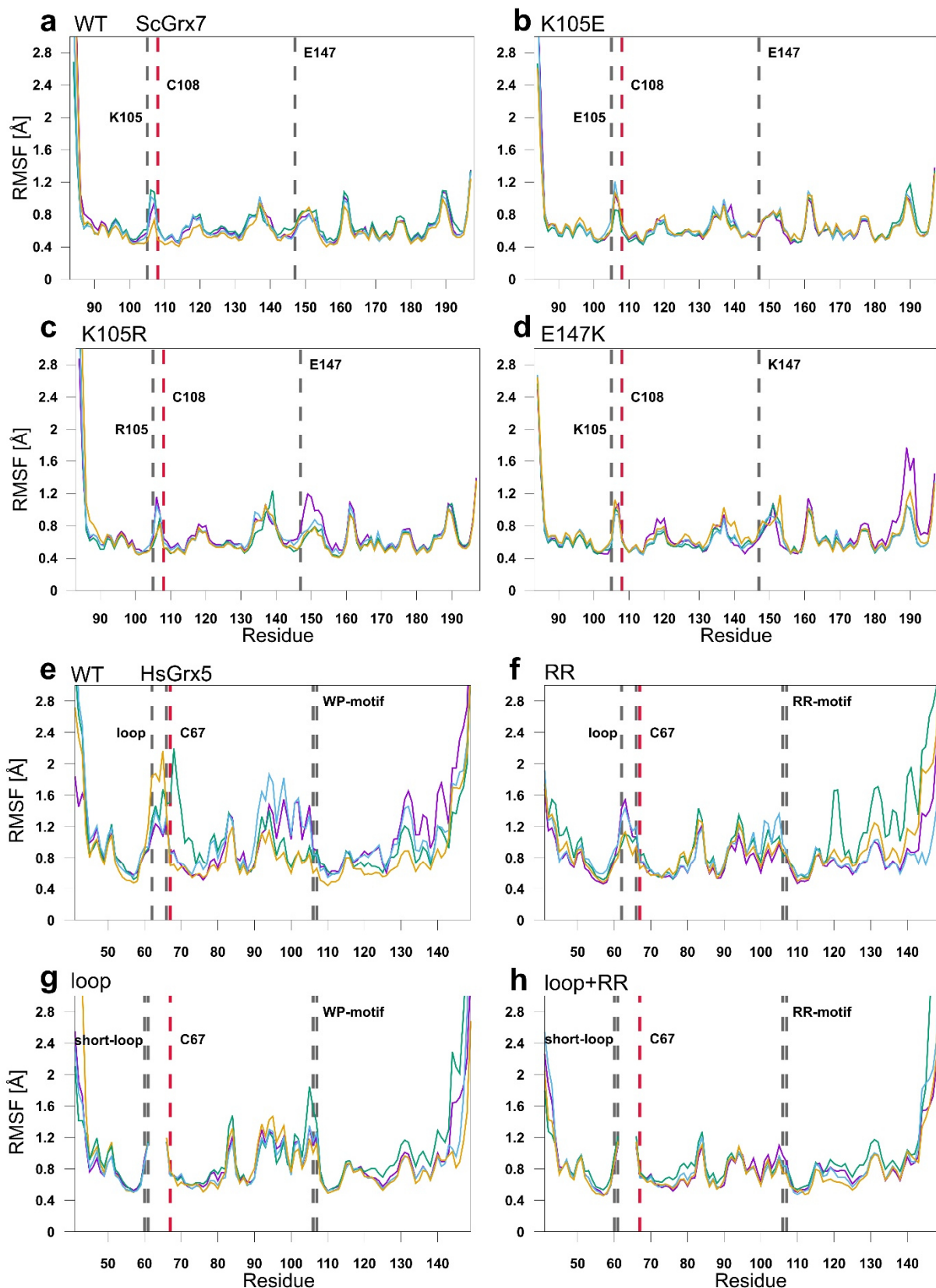
Supplementary Figure 16 | GSSCys assay secondary plots for HsGrx5^{loop} and HsGrx5^{RR+loop}. (a) Secondary plots of the $k_{\text{cat}}^{\text{app}}$ values at different concentrations of GSSCys (left panels) and GSH (right panels) allowing the estimation of the true k_{cat} value from the y-axis intercept ($1/k_{\text{cat}}$) and of the true K_m value from the x-axis intercept ($-1/K_m$). Estimated true kinetic constants have to be interpreted with care because of the proximity of the intersection points to the origin of the graphs. Dalziel coefficients were obtained from the slopes. (b) Secondary plots of the K_m^{app} values at different concentrations of GSSCys (left panels) and GSH (right panels). K_m^{app} and $k_{\text{cat}}^{\text{app}}$ values were obtained from linear regression analyses of Hanes plots (Supplementary Fig. 15). Error bars are the calculated standard error from the hyperbolic curve fits in SigmaPlot 13. Outliers in brackets were identified based on the r^2 values and omitted from the linear regression analysis in SigmaPlot 13. Estimated true kinetic constants and Dalziel coefficients are listed in Supplementary Table 7.

Supplementary Figure 17

Supplementary Figure 17 | Noninvasive intracellular assessment of ScGrx7 interconversion mutants with or without pretreatment with DTT. **(a)** Time-dependent ratiometric degree of roGFP2 oxidation (OxD) for yeast cells with genetically encoded fusion constructs between roGFP2 and interconversion mutants of ScGrx7 under standard conditions (upper row) or after pretreatment and subsequent washout of DTT (lower row). Representative results for bolus treatments with 1 mM (circles), 0.2 mM (triangles) and 0.05 mM (squares) H₂O₂ are shown. **(b)** Integrated dose-response curves for interconversion mutants ScGrx7^{WP} (WP), ScGrx7^{loop} (Loop) and ScGrx7^{WP+loop} (WP + loop) under standard conditions. The area under the OxD curves was determined for the first 48 seconds following the addition of H₂O₂. RoGFP2 alone (roGFP2) as well fusion constructs with inactive ScGrx7^{C108S} (C108S) or wild-type ScGrx7 (WT) served as negative and positive controls. All experiments were repeated at least three times and data were reported as mean AUCs with error bars representing the standard deviation. Source data are provided as a Source Data file. Statistical analyses and *P*-values are listed in Supplementary Table 12.

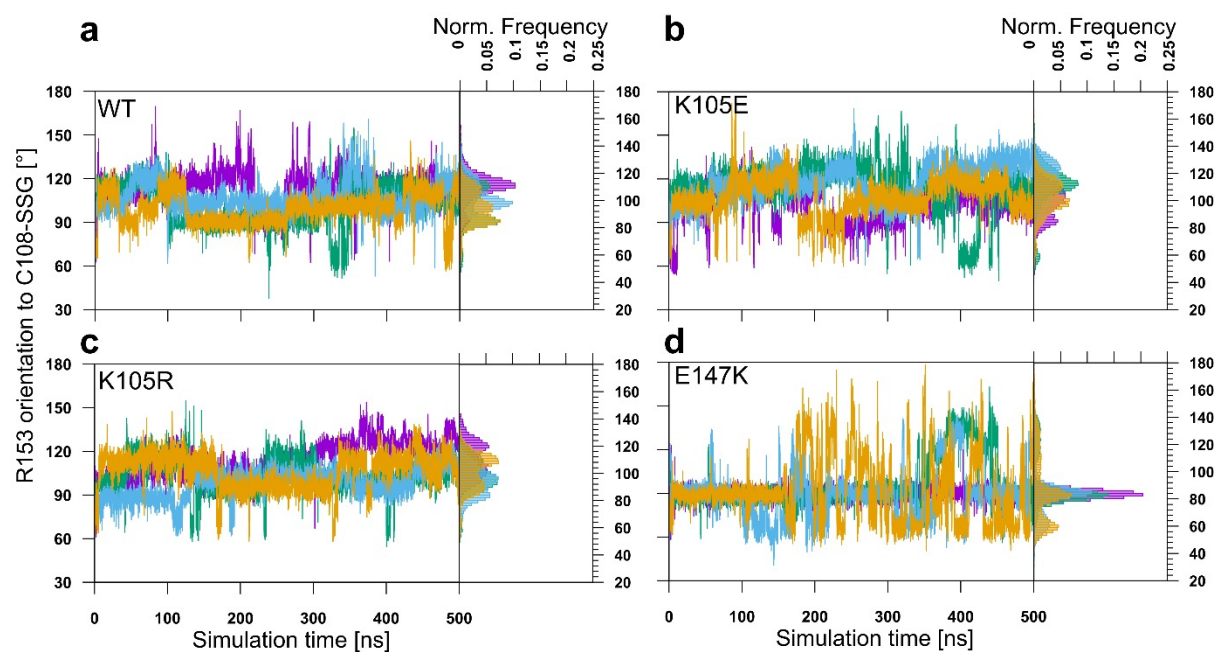
Supplementary Figure 18

Supplementary Figure 18 | RMSD time series of ScGrx7 and HsGrx5. The RMSD of the peptide backbone atoms of ScGrx7 to the starting structure was calculated for the wild-type ScGrx7 (**a**), the K105E variant (**b**), K105R variant (**c**), and E147K variant (**d**) as well as for HsGrx5 WT (**e**), HsGrx5^{RR} (**f**), HsGrx5^{loop} (**g**) and HsGrx5^{RR+loop} (**h**) over the simulation time of 500 ns. For each protein, the four independent replications of the simulation are colored purple, blue, green, and yellow, respectively. The frequency distributions of the RMSD time series were normalized to a total sum of 1 per replication.

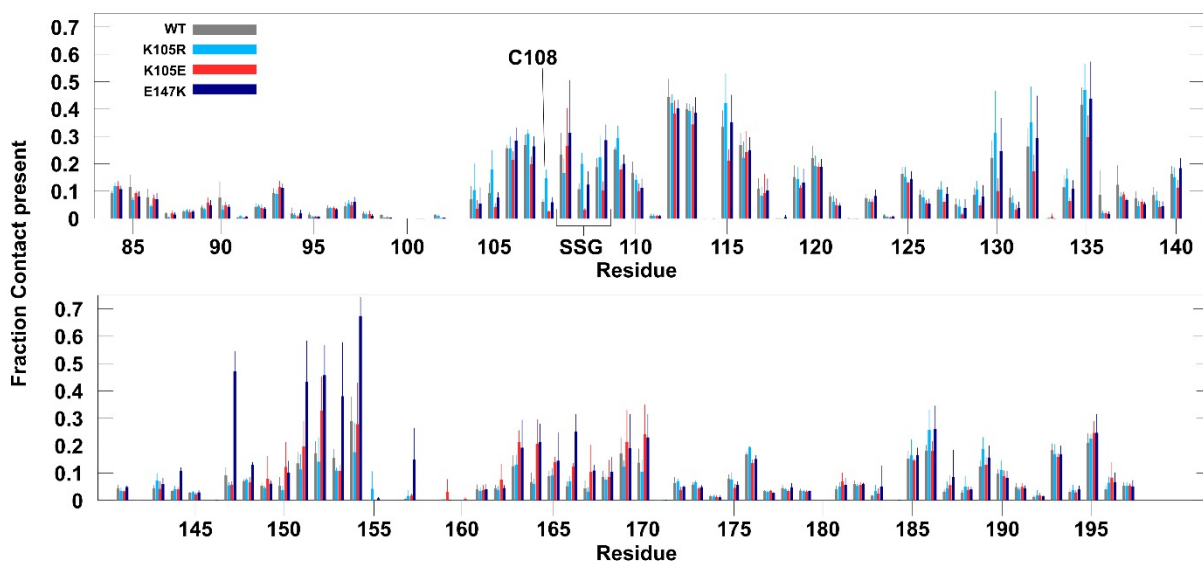
Supplementary Figure 19

Supplementary Figure 19 | Structural fluctuations of ScGrx7 and HsGrx5. Per-residue root mean square fluctuations (RMSF) of protein backbone atoms over the MD trajectories of

500 ns are shown per replication (purple, blue, green, and yellow) for ScGrx7 WT (**a**), K105E (**b**), K105R (**c**), and E147K (**d**) as well as for HsGrx5 WT (**e**), HsGrx5^{RR} (**f**), HsGrx5^{loop} (**g**) and HsGrx5^{RR+loop} (**h**). The active cysteine residue is marked with a red line and important positions of the variants are marked with grey lines. The gap in the sequence for short-loop variants of HsGrx5 is plotted to maintain the residue numbering of the WT.

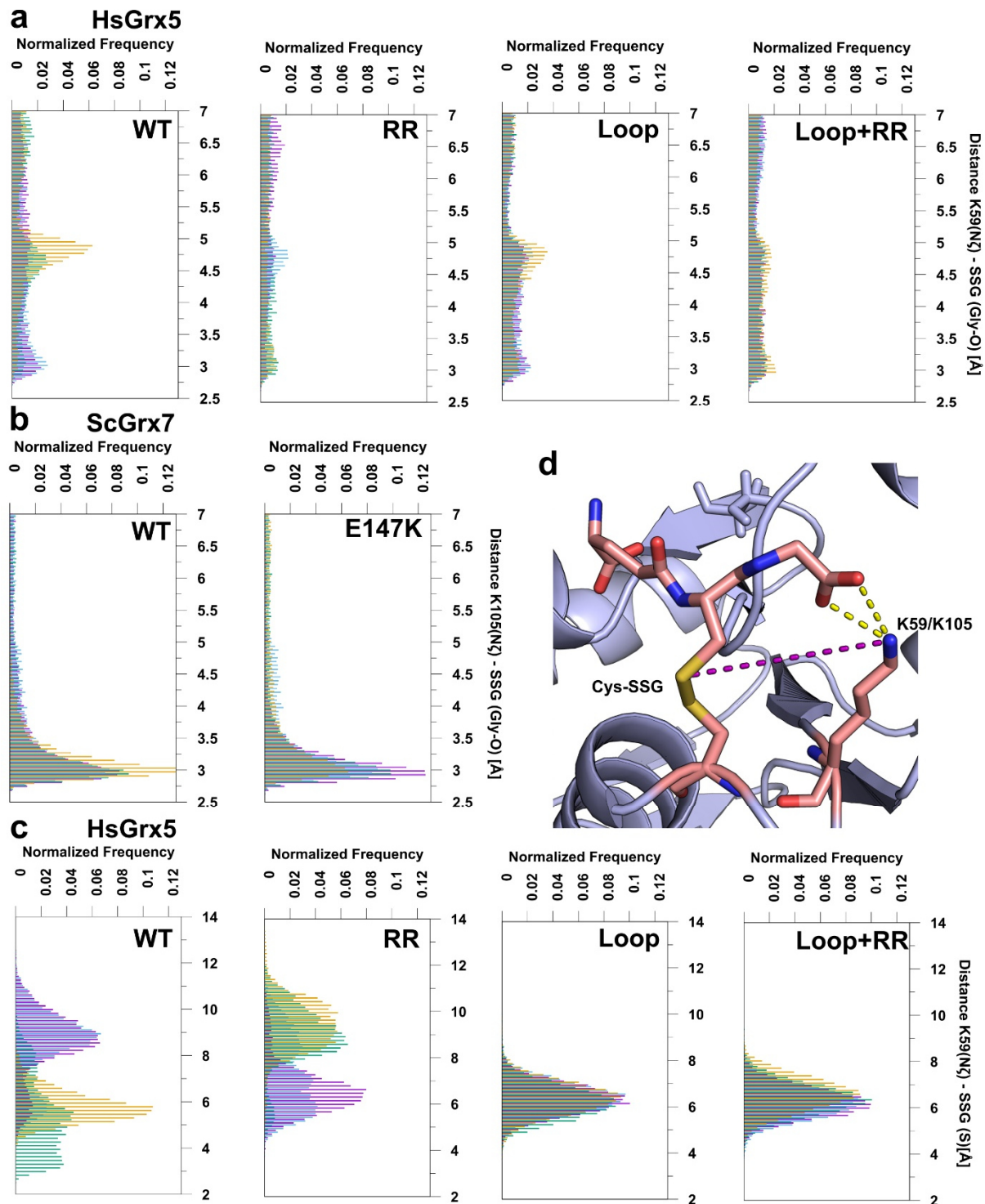
Supplementary Figure 20

Supplementary Figure 20 | Orientation of R153 in the ScGrx7 variants. The angle between the sulfur atom of the bound glutathione (SSG), the Ca-carbon of R153 and the carbon of the guanidino group of its side chain was chosen to show the differential orientation of R153 towards the SSG moiety. In the WT (a), the K105E (b) and K105R variants (c), the angle is mainly distributed between 90° and 130°. For the E147K (d) variant, the angle predominantly shows a narrow distribution around 90°. For each ScGrx7 variant, the four independent replications of the simulation are colored purple, blue, green, and yellow, respectively. The frequency distributions were normalized to a total sum of 1 per replication.

Supplementary Figure 21

Supplementary Figure 21 | Contact analysis of GS⁻ with ScGrx7. Bars show the fraction of the molecular dynamics simulations where a contact between a residue of ScGrx7 and a freely diffusing GS⁻ was present for the WT (grey), the K105R variant (light blue), K105E variant (red), and E147K variant (dark blue) with error bars showing the standard deviation over the four replications. Contacts were counted when the distance between the Cy of the glutamyl moiety of a GS⁻ and a specific atom of the residue was below 8 Å. For each residue type, a specific atom of the side chain was selected for the contact definition such that there is no bias against residues with longer side chains. The glutathione disulfide (SSG) bound to Cys108 was not counted in the residue numbering and is represented following Cys108 as three residues: γ-glutamyl, cysteine, and glycine.

Supplementary Figure 22



Supplementary Figure 22 | Interactions of the conserved active-site lysine residue in HsGrx5 and ScGrx7. (a) Distributions of the distances of Lys59 N ζ of HsGrx5 variants to the closer oxygen atom of the glycine carboxyl group of the covalently bound glutathione for each of the four replications. (b) For ScGrx7, the equivalent residue Lys105 was used in the

analysis. **(c)** Distance distributions of Lys59 N ζ to the sulfur atom of bound glutathione. **(d)** Structural representation of the measured distances (yellow for the distance to the carboxyl group as in panels **(a)** and **(b)**, purple for the distance as in panel **(c)**).

Supplementary Table 1. Comparison of estimated true k_{cat} and K_m values and Dalziel coefficients Φ_1 and Φ_2 of wild-type ScGrx7 and Y110X mutants in the GSSCys and HEDS assay.

GSSCys assay						
ScGrx7	$1/\Phi_1^a$ (M⁻¹s⁻¹)	$1/\Phi_2^a$ (M⁻¹s⁻¹)	$k_{\text{cat}}(\text{GSSCys})^{\epsilon}$ (s⁻¹)	$k_{\text{cat}}(\text{GSH})^a$ (s⁻¹)	$K_m(\text{GSSCys})^a$ (μM)	$K_m(\text{GSH})^a$ (μM)
WT	7.2×10^5	2.2×10^5	380	219	292	762
Y110F	7.7×10^5	2.5×10^5	554	346	784	1067
Y110H	1.8×10^5	2.2×10^5	74	154	375	422
Y110A	9.2×10^4	4.7×10^4	35	36	332	426

HEDS assay						
ScGrx7	$1/\Phi_1^b$ (M⁻¹s⁻¹)	$1/\Phi_2^b$ (M⁻¹s⁻¹)	$k_{\text{cat}}(\text{HEDS})^b$ (s⁻¹)	$k_{\text{cat}}(\text{GSH})^b$ (s⁻¹)	$K_m(\text{HEDS})^c$ (mM)	$K_m(\text{GSH})^c$ (mM)
WT	2.4×10^5	1.5×10^5	185	136	1.3 ± 0.3	1.3 ± 0.8
Y110F	1.2×10^5	1.2×10^5	485	275	1.5 ± 0.2	2.1 ± 0.9
Y110H	2.9×10^4	3.7×10^4	43	92	1.7 ± 0.2	1.8 ± 0.3
Y110A	9.5×10^3	4.6×10^3	30	15	1.4 ± 0.3	0.7 ± 0.2

^a Estimated Dalziel coefficients, k_{cat} and K_m values were obtained from Supplementary Fig. 3. The true k_{cat} and K_m values have to be interpreted with care because of the proximity of the intersection points to the origin of the graphs.

^b Estimated Dalziel coefficients and k_{cat} values were obtained from Supplementary Fig. 6a. The true k_{cat} values have to be interpreted with care because of the proximity of the intersection points to the origin of the graphs.

^c Estimated K_m values were averaged from Supplementary Fig. 5.

Supplementary Table 2. Selected k_{cat}^{app} and K_m^{app} values from GSSCys assays with ScGrx7 wild-type enzyme and Y110X mutants obtained from Supplementary Fig. 2.

ScGrx7	[GSSCys]	$k_{cat}^{app(GSH)}^a$		$K_m^{app(GSH)}^a$		$k_{cat}^{app}/K_m^{app(GSH)}$	
	(μM)	(s^{-1})		(μM)		($mM^{-1}s^{-1}$)	
WT	25	18.8 \pm 0.3	100	104 \pm 7.6	100	180	100 %
Y110F	25	17.9 \pm 0.2	95 %	68.1 \pm 4.2	65 %	264	147 %
Y110H	25	4.8 \pm 0.1	26 %	24.8 \pm 3.8	24 %	198	110 %
Y110A	25	2.4 \pm 0.0	13 %	58.2 \pm 4.5	56 %	41	23 %
WT	50	31.1 \pm 1.1	100	128 \pm 16.8	100	243	100 %
Y110F	50	36.6 \pm 0.5	118	141 \pm 7.7	110	259	107 %
Y110H	50	8.4 \pm 0.0	27 %	42.8 \pm 0.9	33 %	196	81 %
Y110A	50	4.1 \pm 0.1	13 %	100 \pm 5.7	78 %	41	17 %
WT	100	52.3 \pm 2.2	100	215 \pm 28.5	100	243	100 %
Y110F	100	60.7 \pm 1.0	116	216 \pm 10.8	101	280	115 %
Y110H	100	16.9 \pm 5.0	32 %	93.0 \pm 5.0	43 %	181	74 %
Y110A	100	7.2 \pm 0.1	14 %	159 \pm 7.1	74 %	46	19 %
WT	150	75.2 \pm 1.6	100	291 \pm 17.6	100	258	100 %
Y110F	150	82.5 \pm 2.0	110	302 \pm 20.1	104	273	106 %
Y110H	150	21.6 \pm 0.3	29 %	105 \pm 6.4	36 %	204	79 %
Y110A	150	10.1 \pm 0.1	13 %	219 \pm 9.6	75 %	46	18 %
ScGrx7	[GSH]	$k_{cat}^{app(GSSCys)}^a$		$K_m^{app(GSSCys)}^a$		$k_{cat}^{app}/K_m^{app(GSSCys)}$	
	(μM)	(s^{-1})		(μM)		($mM^{-1}s^{-1}$)	
WT	50	12.6 \pm 0.5	100	19.7 \pm 3.8	100	639	100 %
Y110F	50	13.9 \pm 0.03	110	19.6 \pm 0.2	99 %	712	111 %
Y110H	50	9.4 \pm 0.5	75 %	50.4 \pm 6.4	256	187	29 %
Y110A	50	2.5 \pm 0.1	20 %	42.8 \pm 6.5	217	60	9 %
WT	100	21.2 \pm 1.5	100	34.2 \pm 6.4	100	621	100 %
Y110F	100	23.9 \pm 1.2	113	32.0 \pm 5.2	94 %	746	120 %
Y110H	100	17.0 \pm 0.6	80 %	90.3 \pm 6.1	264	188	30 %
Y110A	100	4.1 \pm 0.2	19 %	48.9 \pm 6.7	143	84	14 %
WT	200	40.4 \pm 5.2	100	64.7 \pm 19.7	100	624	100 %
Y110F	200	49.1 \pm 2.4	122	68.6 \pm 7.6	106	716	115 %
Y110H	200	24.2 \pm 1.1	60 %	116 \pm 10.3	180	207	33 %
Y110A	200	7.5 \pm 0.7	19 %	85.9 \pm 15.9	133	87	14 %
WT	1000	163 \pm 54.8	100	266 \pm 129	100	612	100 %
Y110F	1000	142 \pm 13.7	87 %	202 \pm 28.3	76 %	753	123 %
Y110H	1000	63.1 \pm 16.3	39 %	319 \pm 113	120	198	32 %
Y110A	1000	19.2 \pm 1.9	12 %	204 \pm 30.7	77 %	94	15 %

^a Mean \pm s.d. from Michaelis-Menten plots of three independent protein purifications. Percentages are relative to wild-type enzyme. P-values are listed in Supplementary Table 11 'Statistics'.

Supplementary Table 3. Selected k_{cat}^{app} and K_m^{app} values from HEDS assays with ScGrx7 wild-type enzyme and Y110X mutants obtained from Supplementary Fig. 5.

ScGrx7	[HEDS] (mM)	$k_{cat}^{app(GSH)}^a$		$K_m^{app(GSH)}^a$		$k_{cat}^{app}/K_m^{app(GSH)}$	
		(s ⁻¹)		(mM)		(mM ⁻¹ s ⁻¹)	
WT	0.18	32.1 ± 1.4	100	1.55 ± 0.12	100	20.7	100 %
Y110F	0.18	19.7 ± 2.5	61 %	1.64 ± 0.38	106	12.0	58 %
Y110H	0.18	4.9 ± 0.2	15 %	1.52 ± 0.10	98 %	3.2	15 %
Y110A	0.18	1.6 ± 0.1	5 %	1.64 ± 0.12	106	0.9	4 %
WT	0.37	58.6 ± 2.4	100	1.60 ± 0.12	100	36.7	100 %
Y110F	0.37	39.9 ± 1.0	68 %	1.73 ± 0.08	108	23.0	63 %
Y110H	0.37	10.2 ± 0.7	17 %	1.89 ± 0.23	118	5.4	15 %
Y110A	0.37	2.6 ± 0.1	4 %	1.07 ± 0.09	67 %	2.5	7 %
WT	0.55	64.6 ± 3.4	100	1.14 ± 0.12	100	56.6	100 %
Y110F	0.55	52.7 ± 2.8	82 %	1.46 ± 0.14	128	36.1	64 %
Y110H	0.55	14.0 ± 0.3	22 %	1.89 ± 0.06	166	7.4	13 %
Y110A	0.55	3.6 ± 0.4	6 %	1.25 ± 0.24	110	2.9	5 %
WT	0.74	72.9 ± 3.4	100	1.10 ± 0.10	100	66.5	100 %
Y110F	0.74	63.4 ± 4.9	87 %	1.32 ± 0.19	120	48.0	72 %
Y110H	0.74	16.0 ± 1.1	22 %	1.64 ± 0.18	149	9.7	15 %
Y110A	0.74	5.6 ± 0.2	8 %	1.52 ± 0.12	138	3.7	6 %
ScGrx7	[GSH] (mM)	$k_{cat}^{app(HEDS)}^a$		$K_m^{app(HEDS)}^a$		$k_{cat}^{app}/K_m^{app(HEDS)}$	
		(s ⁻¹)		(mM)		(mM ⁻¹ s ⁻¹)	
WT	0.3	34.1 ± 4.1	100	0.92 ± 0.18	100	36.9	100 %
Y110F	0.3	31.2 ± 15.8	91 %	1.78 ± 1.20	193	17.5	47 %
Y110H	0.3	10.2 ± 1.9	30 %	2.27 ± 0.53	245	4.5	12 %
Y110A	0.3	1.7 ± 0.3	5 %	1.10 ± 0.33	120	1.5	4 %
WT	0.5	63.9 ± 4.1	100	1.33 ± 0.12	100	47.8	100 %
Y110F	0.5	78.5 ± 31	123	3.40 ± 1.58	256	23.1	48 %
Y110H	0.5	13.8 ± 1.6	22 %	2.02 ± 0.30	152	6.9	14 %
Y110A	0.5	2.0 ± 0.3	3 %	0.67 ± 0.18	50 %	3.0	6 %
WT	1.0	81.1 ± 8.9	100	0.90 ± 0.16	100	90.1	100 %
Y110F	1.0	104.4 ± 19.4	129	2.59 ± 0.59	288	40.2	45 %
Y110H	1.0	20.4 ± 0.8	25 %	1.65 ± 0.15	183	12.3	14 %
Y110A	1.0	4.5 ± 0.9	6 %	0.79 ± 0.26	88 %	5.8	6 %
WT	1.5	90.0 ± 12.5	100	0.82 ± 0.19	100	110	100 %
Y110F	1.5	138.9 ± 28.9	154	2.85 ± 0.71	348	48.8	44 %
Y110H	1.5	25.8 ± 3.6	29 %	1.77 ± 0.32	216	14.6	13 %
Y110A	1.5	4.2 ± 0.1	5 %	0.61 ± 0.02	74 %	6.8	6 %

^a Mean ± s.d. from Michaelis-Menten plots of three independent protein purifications. Percentages are relative to wild-type enzyme. P-values are listed in Supplementary Table 11 'Statistics'.

Supplementary Table 4. Comparison of estimated true k_{cat} and K_m values and Dalziel coefficients Φ_1 and Φ_2 of wild-type ScGrx7 and D144X, E147X and R153X mutants.

ScGrx7	GSSCys assay					
	$1/\Phi_1^a$ (M⁻¹s⁻¹)	$1/\Phi_2^a$ (M⁻¹s⁻¹)	$k_{\text{cat}} \text{ (GSSCys)}$ (s⁻¹)	$k_{\text{cat}} \text{ (GSH)}^a$ (s⁻¹)	$K_m \text{ (GSSCys)}^a$ (μM)	$K_m \text{ (GSH)}^a$ (μM)
WT	7.1×10^5	2.8×10^5	213	206	257	744
D144A	5.7×10^5	3.0×10^5	161	151	250	488
D144K	5.9×10^5	4.7×10^5	591	161	760	590
E147A	7.1×10^5	2.9×10^5	259	370	314	926
E147K	7.6×10^5	7.0×10^5	263	332	280	300
R153A	2.8×10^5	2.7×10^5	125	168	404	293
R153E	1.4×10^5	1.4×10^5	72	113	491	807

^a Estimated Dalziel coefficients, k_{cat} and K_m values were obtained from Supplementary Fig. 8 (D144X), Supplementary Fig. 10 (E147X) and Supplementary Fig. 12 (R153X). The true k_{cat} and K_m values have to be interpreted with care because of the proximity of the intersection points to the origin of the graphs.

Supplementary Table 5. Selected k_{cat}^{app} and K_m^{app} values from GSSCys assays with ScGrx7 wild-type enzyme and D144X and E147X mutants obtained from Supplementary Figs. 7 and 9.

ScGrx7	[GSSCys]	$k_{cat}^{app(GSH)}$ ^a		$K_m^{app(GSH)}$ ^a		$k_{cat}^{app}/K_m^{app(GSH)}$	
	(μM)	(s^{-1})		(μM)		($mM^{-1}s^{-1}$)	
WT	25	16.2 \pm 0.2	100	67.5 \pm 4.4	100	240	100 %
D144A	25	13.0 \pm 0.1	80 %	68.6 \pm 2.6	102	190	79 %
D144K	25	10.9 \pm 0.1	67 %	25.2 \pm 1.2	37 %	433	180 %
E147A	25	17.0 \pm 0.1	105	77.6 \pm 2.3	115	219	91 %
E147K	25	18.0 \pm 0.3	111	47.4 \pm 4.9	70 %	379	158 %
WT	50	30.4 \pm 0.4	100	120 \pm 5.6	100	253	100 %
D144A	50	23.1 \pm 0.2	76 %	103 \pm 4.2	86 %	225	89 %
D144K	50	24.9 \pm 0.4	82 %	64.0 \pm 5.6	53 %	389	154 %
E147A	50	32.3 \pm 0.5	106	145 \pm 0.5	121	223	88 %
E147K	50	34.4 \pm 0.6	113	87.2 \pm 6.5	73 %	395	156 %
WT	100	53.3 \pm 0.9	100	211 \pm 11.1	100	253	100 %
D144A	100	40.0 \pm 1.0	75 %	194 \pm 16.4	92 %	214	85 %
D144K	100	42.2 \pm 0.7	79 %	82.6 \pm 6.2	38 %	511	202 %
E147A	100	60.4 \pm 1.0	113	237 \pm 12.4	112	255	101 %
E147K	100	67.3 \pm 0.8	126	139 \pm 6.3	66 %	486	192 %
WT	150	68.0 \pm 2.4	100	244 \pm 27.1	100	279	100 %
D144A	150	58.7 \pm 1.3	86 %	275 \pm 18.1	113	214	77 %
D144K	150	58.2 \pm 1.7	86 %	138 \pm 13.1	56 %	422	151 %
E147A	150	82.9 \pm 1.3	122	344 \pm 14.0	141	241	86 %
E147K	150	77.2 \pm 1.4	114	142 \pm 9.2	58 %	543	195 %
ScGrx7	[GSH]	$k_{cat}^{app(GSSCys)}$ ^a		$K_m^{app(GSSCys)}$ ^a		$k_{cat}^{app}/K_m^{app(GSSCys)}$	
	(μM)	(s^{-1})		(μM)		($mM^{-1}s^{-1}$)	
WT	50	13.3 \pm 0.5	100	22.1 \pm 3.3	100	603	100 %
D144A	50	16.0 \pm 0.8	120	44.4 \pm 6.0	201	360	60 %
D144K	50	22.7 \pm 0.8	171	50.2 \pm 4.9	227	453	75 %
E147A	50	13.6 \pm 0.4	102	25.8 \pm 2.5	117	526	87 %
E147K	50	30.9 \pm 1.3	232	60.9 \pm 6.0	276	508	84 %
WT	100	23.2 \pm 0.7	100	36.4 \pm 3.1	100	639	100 %
D144A	100	26.2 \pm 0.9	112	62.7 \pm 5.3	172	418	65 %
D144K	100	41.3 \pm 4.4	178	89.2 \pm 19.5	245	463	72 %
E147A	100	25.8 \pm 1.8	111	41.1 \pm 8.0	113	629	98 %
E147K	100	57.5 \pm 2.2	248	104 \pm 7.9	287	550	86 %
WT	200	45.8 \pm 2.6	100	70.7 \pm 9.0	100	648	100 %
D144A	200	42.3 \pm 4.4	92 %	89.3 \pm 19.1	126	473	73 %
D144K	200	95.2 \pm 5.3	208	213 \pm 18.1	301	446	69 %
E147A	200	45.0 \pm 1.4	98 %	70.4 \pm 4.9	100	640	99 %
E147K	200	77.9 \pm 3.3	170	117 \pm 9.2	165	665	103 %
WT	1000	114 \pm 13.0	100	155 \pm 29.9	100	735	100 %
D144A	1000	122 \pm 12.5	107	252 \pm 37.3	163	485	66 %
D144K	1000	182 \pm 37.1	160	377 \pm 103	243	483	66 %
E147A	1000	139 \pm 7.3	122	189 \pm 15.6	122	737	100 %
E147K	1000	363 \pm 33.2	318	509 \pm 54.2	328	714	97 %

^a Mean \pm s.d. from Michaelis-Menten plots of three independent protein purifications. Percentages are relative to wild-type enzyme. P-values are listed in Supplementary Table 11 'Statistics'.

Supplementary Table 6. Selected $k_{\text{cat}}^{\text{app}}$ and K_m^{app} values from GSSCys assays with ScGrx7 wild-type enzyme and R153X mutants obtained from Supplementary Fig. 11.

ScGrx7	[GSSCys]	$k_{\text{cat}}^{\text{app}}_{(\text{GSH})}{}^a$		$K_m^{\text{app}}_{(\text{GSH})}{}^a$		$k_{\text{cat}}^{\text{app}}/K_m^{\text{app}}_{(\text{GSH})}$	
	(μM)	(s^{-1})		(μM)		($\text{mM}^{-1}\text{s}^{-1}$)	
WT	25	16.2 \pm 0.2	100	67.5 \pm 4.4	100	240	100 %
R153A	25	6.6 \pm 0.1	41 %	32.8 \pm 2.0	49 %	201	84 %
R153E	25	3.5 \pm 0.0	22 %	27.1 \pm 2.8	40 %	128	53 %
WT	50	30.4 \pm 0.4	100	120 \pm 5.6	100	253	100 %
R153A	50	12.9 \pm 0.1	42 %	56.2 \pm 2.7	47 %	230	91 %
R153E	50	6.6 \pm 0.1	22 %	54.3 \pm 3.4	45 %	122	48 %
WT	100	53.3 \pm 0.9	100	211 \pm 11.1	100	253	100 %
R153A	100	24.2 \pm 0.3	45 %	110 \pm 4.8	52 %	221	87 %
R153E	100	13.4 \pm 0.1	25 %	101 \pm 4.3	48 %	133	53 %
WT	150	68.0 \pm 2.4	100	244 \pm 27.1	100	279	100 %
R153A	150	31.6 \pm 0.6	46 %	118 \pm 8.0	48 %	268	96 %
R153E	150	17.0 \pm 0.2	25 %	130 \pm 6.2	53 %	131	47 %
ScGrx7	[GSH]	$k_{\text{cat}}^{\text{app}}_{(\text{GSSCys})}{}^a$		$K_m^{\text{app}}_{(\text{GSSCys})}{}^a$		$k_{\text{cat}}^{\text{app}}/K_m^{\text{app}}_{(\text{GSSCys})}$	
	(μM)	(s^{-1})		(μM)		($\text{mM}^{-1}\text{s}^{-1}$)	
WT	50	13.3 \pm 0.5	100	22.1 \pm 3.3	100	603	100 %
R153A	50	14.1 \pm 0.3	106	66.5 \pm 3.5	306	212	35 %
R153E	50	8.1 \pm 1.5	61 %	64.1 \pm 27.3	290	126	21 %
WT	100	23.2 \pm 0.7	100	36.4 \pm 3.1	100	639	100 %
R153A	100	22.5 \pm 1.2	97 %	88.5 \pm 9.5	243	254	40 %
R153E	100	11.9 \pm 2.0	51 %	82.7 \pm 30.3	227	144	23 %
WT	200	45.8 \pm 2.6	100	70.7 \pm 9.0	100	648	100 %
R153A	200	37.1 \pm 1.2	81 %	135 \pm 7.6	191	276	43 %
R153E	200	19.5 \pm 2.6	43 %	136 \pm 32.2	192	144	22 %
WT	1000	114 \pm 13.0	100	155 \pm 29.9	100	735	100 %
R153A	1000	79.0 \pm 5.8	69 %	270 \pm 28.2	174	293	40 %
R153E	1000	52.2 \pm 4.1	46 %	332 \pm 19.0	214	145	20 %

^a Mean \pm s.d. from Michaelis-Menten plots of three independent protein purifications. Percentages are relative to wild-type enzyme. P-values are listed in Supplementary Table 11 'Statistics'.

Supplementary Table 7. Comparison of estimated true k_{cat} and K_m values and Dalziel coefficients Φ_1 and Φ_2 of wild-type ScGrx7 ScGrx7^{WP}, ScGrx7^{loop}, ScGrx7^{WP+loop} as well as HsGrx5, HsGrx5^{RR}, HsGrx5^{loop} and HsGrx5^{RR+loop}.

GSSCys assay						
ScGrx7	$1/\Phi_1^a$ (M ⁻¹ s ⁻¹)	$1/\Phi_2^a$ (M ⁻¹ s ⁻¹)	$k_{\text{cat}}(\text{GSSCys})^c$ (s ⁻¹)	$k_{\text{cat}}(\text{GSH})^a$ (s ⁻¹)	$K_m(\text{GSSCys})^a$ (μM)	$K_m(\text{GSH})^a$ (μM)
WT	7.8×10^5	3.3×10^5	492	334	427	1479
RR→WP	1.7×10^5	2.8×10^5	312	496	2953	1134
loop	5.8×10^3	1.9×10^3	1.9	1.5	262	1013
WP+loop	1.1×10^3	1.5×10^3	0.4	0.7	694	265

GSSCys assay						
HsGrx5 ^c	$1/\Phi_1^b$ (M ⁻¹ s ⁻¹)	$1/\Phi_2^b$ (M ⁻¹ s ⁻¹)	$k_{\text{cat}}(\text{GSSCys})^t$ (s ⁻¹)	$k_{\text{cat}}(\text{GSH})^b$ (s ⁻¹)	$K_m(\text{GSSCys})^b$ (μM)	$K_m(\text{GSH})^b$ (mM)
WT	/	/	/	/	/	/
WP→RR	/	/	/	/	/	/
loop	1.8×10^3	4.6×10^3	∞	∞	∞	∞
RR+loop	74	/	/	/	/	/

^a Estimated Dalziel coefficients, k_{cat} and K_m values were obtained from Supplementary Fig. 14. The true k_{cat} and K_m values have to be interpreted with care because of the proximity of the intersection points to the origin of the graphs.

^b Estimated Dalziel coefficients, k_{cat} and K_m values were obtained from Supplementary Fig. 16. The true k_{cat} values have to be interpreted with care because of the proximity of the intersection points to the origin of the graphs.

^c Except for HsGrx5^{loop}, the activities of the HsGrx5 constructs were very similar to the NADPH consumption of negative controls (with an activity tendency HsGrx5^{RR+loop} > HsGrx5 > HsGrx5^{RR}).

Supplementary Table 8. Selected k_{cat}^{app} and K_m^{app} values from GSSCys assays with wild-type ScGrx7, ScGrx7^{WP}, ScGrx7^{loop} and ScGrx7^{WP+loop} obtained from Supplementary Fig. 13.

ScGrx7	[GSSCys] (μ M)	$k_{cat}^{app(GSH)}$ ^a (s ⁻¹)		$K_m^{app(GSH)}$ ^a (μ M)		$k_{cat}^{app}/K_m^{app(GSH)}$ (mM ⁻¹ s ⁻¹)		
WT	25	18.4	\pm 1.1	100	78.5	\pm 34	100	275 100 %
RR \rightarrow WP	25	4.18	\pm 0.66	23 %	32.6	\pm 11	42 %	138 50 %
loop	25	0.14	\pm 0.01	0.8	89.0	\pm 9.7	113	1.5 0.6 %
WP+loop	25	0.025	\pm	0.1	23.2	\pm 4.8	30 %	1.1 0.4 %
WT	50	35.4	\pm 1.0	100	126	\pm 42	100	308 100 %
RR \rightarrow WP	50	8.12	\pm 0.66	23 %	50.6	\pm 9.4	40 %	163 53 %
loop	50	0.22	\pm 0.03	0.6	158	\pm 8.8	125	1.4 0.5 %
WP+loop	50	0.05	\pm	0.1	46.9	\pm 2.0	37 %	1.1 0.3 %
WT	100	67.4	\pm 3.9	100	222	\pm 9.4	100	305 100 %
RR \rightarrow WP	100	15.7	\pm 1.4	23 %	81.4	\pm 17	37 %	197 65 %
loop	100	0.42	\pm 0.11	0.6	247	\pm 59	111	1.7 0.6 %
WP+loop	100	0.098	\pm	0.1	81.2	\pm 25	37 %	1.2 0.4 %
WT	150	79.9	\pm 27	100	286	\pm 45	100	273 100 %
RR \rightarrow WP	150	26.0	\pm 2.0	33 %	124	\pm 25	43 %	214 78 %
loop	150	0.65	\pm 0.14	0.8	350	\pm 25	122	1.8 0.7 %
WP+loop	150	0.12	\pm 0.02	0.2	87.0	\pm 21	30 %	1.5 0.5 %
ScGrx7	[GSH] (μ M)	$k_{cat}^{app(GSSCys)}$ ^a (s ⁻¹)		$K_m^{app(GSSCys)}$ ^a (μ M)		$k_{cat}^{app}/K_m^{app(GSSCys)}$ (mM ⁻¹ s ⁻¹)		
WT	50	22.0	\pm 1.3	100	49.6	\pm 15	100	475 100 %
RR \rightarrow WP	50	13.2	\pm 1.1	60 %	100	\pm 6.1	202	132 28 %
loop	50	0.11	\pm 0.01	0.5	30.7	\pm 6.0	62 %	3.8 0.8 %
WP+loop	50	0.066	\pm 0.02	0.3	69.4	\pm 13	140	1.0 0.2 %
WT	200	56.0	\pm 7.9	100	84.0	\pm 28	100	696 100 %
RR \rightarrow WP	200	41.2	\pm 5.6	74 %	281	\pm 43	335	147 21 %
loop	200	0.31	\pm 0.06	0.6	76.4	\pm 3.8	91 %	4.0 0.6 %
WP+loop	200	0.13	\pm 0.04	0.2	150	\pm 40	179	0.9 0.1 %
WT	500	139	\pm 20	100	193	\pm 37	100	727 100 %
RR \rightarrow WP	500	128	\pm 36	92 %	750	\pm 190	389	170 23 %
loop	500	0.61	\pm 0.11	0.4	120	\pm 34	62 %	5.3 0.7 %
WP+loop	500	0.25	\pm 0.02	0.2	242	\pm 36	125	1.0 0.1 %
WT	1000	239	\pm 54	100	320	\pm 91	100	757 100 %
RR \rightarrow WP	1000	175	\pm 51	73 %	1036	\pm 377	324	173 23 %
loop	1000	0.94	\pm 0.38	0.4	170	\pm 5.8	53 %	5.5 0.7 %
WP+loop	1000	0.69	\pm 0.12	0.3	631	\pm 38	197	1.1 0.1 %

^a Mean \pm s.d. from Hanes plots of three independent protein purifications. Percentages are relative to wild-type enzyme. P-values are listed in Supplementary Table 11 'Statistics'.

Supplementary Table 9. Selected k_{cat}^{app} and K_m^{app} values from GSSCys assays with HsGrx5, HsGrx5^{RR}, HsGrx5^{loop} and HsGrx5^{RR+loop} obtained from Supplementary Fig. 15.

HsGrx5	[GSSCys] (μ M)	$k_{cat}^{app(GSH)}$ ^a (s^{-1})	$K_m^{app(GSH)}$ ^a (μ M)	$k_{cat}^{app}/K_m^{app(GSH)}$ ($mM^{-1}s^{-1}$)
WT	25	/	0 %	/
WP \rightarrow RR	25	/	0 %	/
loop	25	0.046 \pm	100	10.2 \pm 5.3
RR+loop	25	/	0 %	/
WT	50	0.004 \pm	<5 %	/
WP \rightarrow RR	50	/	0 %	/
loop	50	0.083 \pm	100	17.7 \pm 8.9
RR+loop	50	0.004 \pm	5 %	25.4 \pm 47
WT	100	0.003 \pm	<2 %	/
WP \rightarrow RR	100	/	0 %	/
loop	100	0.18 \pm 0.05	100	47.6 \pm 30
RR+loop	100	0.016 \pm	9 %	127 \pm 87
WT	150	0.003 \pm	<1 %	/
WP \rightarrow RR	150	/	0 %	/
loop	150	0.27 \pm 0.02	100	59.9 \pm 15
RR+loop	150	0.019 \pm	7 %	174 \pm 91
HsGrx5	[GSH] (μ M)	$k_{cat}^{app(GSSCys)}$ ^a (s^{-1})	$K_m^{app(GSSCys)}$ ^a (μ M)	$k_{cat}^{app}/K_m^{app(GSSCys)}$ ($mM^{-1}s^{-1}$)
WT	50	/	0 %	/
WP \rightarrow RR	50	/	0 %	/
loop	50	0.24 \pm 0.00	100	156 \pm 19
RR+loop	50	/	0 %	/
WT	200	/	0 %	/
WP \rightarrow RR	200	/	0 %	/
loop	200	0.88 \pm 0.06	100	563 \pm 58
RR+loop	200	/	0 %	/
WT	500	/	0 %	/
WP \rightarrow RR	500	/	0 %	/
loop	500	4.33 \pm 0.21	100	2703 \pm 119
RR+loop	500	/	0 %	/
WT	1000	/	0 %	/
WP \rightarrow RR	1000	/	0 %	/
loop	1000	1.08 \pm 6.3	100	765 \pm
RR+loop	1000	/	0 %	/

^a Mean \pm s.d. from Hanes plots of three independent protein purifications. Percentages are relative to HsGrx5^{loop}. P-values are listed in Supplementary Table 11 'Statistics'.

^b Except for HsGrx5^{loop}, the activities of the HsGrx5 constructs were very similar to the consumption of negative controls (with an activity tendency HsGrx5^{RR+loop} > HsGrx5 > HsGrx5^{RR}).

Supplementary Table 10. List of mutagenesis and subcloning primers.

Primer	Sequence (codons, mutations and restriction sites highlighted)
ScGrx7/Y110A/s	5'-GCAAGACTGGCTGCCAG <u>C</u> TAGCAAAAAACTGAAAGC-3'
ScGrx7/Y110A/as	5'-GCTTCAGTTTTGCT <u>A</u> G <u>C</u> GGCAGCCAGTCTGC-3'
ScGrx7/Y110F/s	5'-GCAAGACTGGCTGCC <u>A</u> TTAGCAAAAAACTGAAAGC-3'
ScGrx7/Y110F/as	5'-GCTTCAGTTTTGCT <u>A</u> ATGGCAGCCAGTCTGC-3'
ScGrx7/Y110H/s	5'-GCAAGACTGGCTGCC <u>C</u> ATAGCAAAAAACTGAAAGC-3'
ScGrx7/Y110H/as	5'-GCTTCAGTTTTGCT <u>A</u> TGTGGCAGCCAGTCTGC-3'
ScGrx7/D144A/s	5'-CACACAAAAGAA <u>CTACAAG<u>CCC</u></u> CAGATTGAAAAAGTC <u>ACTGG</u> -3'
ScGrx7/D144A/as	5'-CCAGTGACTTTCAATCT <u>G<u>GG</u>CTTG</u> AGTTCTTTGTGTG-3'
ScGrx7/D144K/s	5'-CACACAAAAGAA <u>CTACAA<u>AA</u>ACAGATTGAAAAAGTC<u>ACTGG</u>-3'</u>
ScGrx7/D144K/as	5'-CCAGTGACTTTCAATCT <u>G<u>TTT</u>GTAGTTCTTTGTGTG</u> -3'
ScGrx7/D147A/s	5'-GA <u>CTACAAGACCAGATT<u>G<u>CAAA</u>AGTC</u>ACTGGTAGGAGAAC-3'</u>
ScGrx7/D147A/as	5'-GTTCTCCTACCAGTGACT <u>TT<u>TG</u>CAATCTGGTCTTGTAGTC</u> -3'
ScGrx7/D147K/s	5'-GA <u>CTACAAGACCAGATT<u>AAA<u>AGTC</u>ACTGGTAGGAGAAC-3'</u></u>
ScGrx7/D147K/as	5'-GTTCTCCTACCAGTGACT <u>TT<u>TAATCTGGTCTTGTAGTC</u></u> -3'
ScGrx7/R153A/s	5'-GAAAAAGTC <u>ACTGGTAGGG<u>CAACAGT</u>CCC<u>AAACGTTATCATC</u>-3'</u>
ScGrx7/R153A/as	5'-GATGATAACGTTGGACT <u>GT<u>CC</u>CTACCAGTGACTTTTC</u> -3'
ScGrx7/R153E/s	5'-GAAAAAGTC <u>ACTGGTAGGG<u>AAACAGT</u>CCC<u>AAACGTTATCATC</u>-3'</u>
ScGrx7/R153E/as	5'-GATGATAACGTTGGACT <u>GT<u>CC</u>CTACCAGTGACTTTTC</u> -3'
ScGrx7/BamHI/s	5'-GAT <u>CGGATCC</u> GT <u>TAACGA</u> AT <u>CA</u> TC <u>ACTACACATC</u> -3'
ScGrx7/HindIII/as	5'-GAT <u>CAAG<u>CTT</u>CATT<u>AA</u>AG<u>CA</u>G<u>ATTCTG</u>ATT<u>GAGAATTAG</u>-3'</u>
HsGrx5/BamHI/s	5'-GAT <u>CGGATCC</u> G <u>CTGGT</u> T <u>CTGGT</u> G <u>CTGGT</u> GG-3'
HsGrx5/HindIII/as	5'-GAT <u>CAAG<u>CTT</u>CATT<u>AT</u>TT<u>GA</u>AT<u>CT</u>G<u>ATCTT</u>CTTT-3'</u>
HsGrx5 ^{Loop} /G68P/s	5'-GAAGACAGGAT <u>GT<u>CC</u></u> AT <u>TTCTAACGCTG</u> -3'
HsGrx5 ^{Loop} /G68P/as	5'-CAGCGTTAG <u>AAA<u>AT</u>GG</u> AC <u>AT</u> CC <u>GT</u> CTTC-3'
HsGrx5/R97Q/s	5'-GATGATCCAGA <u>ATT<u>G<u>CAAC</u>AGG</u>TATTAAAG</u> -3'
HsGrx5/ R97Q /as	5'-CTTTAATAC <u>CTTG<u>TTG</u>CAATTCTGGATCATC</u> -3'

Supplementary Table 11. Statistical analysis of k_{cat}^{app} and K_m^{app} values from the indicated measurements of ScGrx7. P-values from one way ANOVA analysis followed by a Holm-Sidak test were calculated in SigmaPlot 13 ($P > 0.05$: ns; $P \leq 0.05$: *; $P \leq 0.01$: **, $P \leq 0.001$: ***).

A) GSSCys assay ScGrx7 Y110X (Fig. 2, Supplementary Fig. 2 and Supplementary Table 2)

A1.1) $k_{cat}^{app(GSSCys)}$ @ 50 μM GSH

Comparison		P-value
WT	→ Y110F	0.019
WT	→ Y110H	<0.001
WT	→ Y110A	<0.001
Y110F	→ Y110H	<0.001
Y110F	→ Y110A	<0.001
Y110H	→ Y110A	<0.001

A2.1) $k_{cat}^{app(GSH)}$ @ 25 μM GSSCys

Comparison		P-value
WT	→ Y110F	0.017
WT	→ Y110H	<0.001
WT	→ Y110A	<0.001
Y110F	→ Y110H	<0.001
Y110F	→ Y110A	<0.001
Y110H	→ Y110A	<0.001

A1.2) $k_{cat}^{app(GSSCys)}$ @ 100 μM GSH

Comparison		P-value
WT	→ Y110F	0.101
WT	→ Y110H	0.033
WT	→ Y110A	<0.001
Y110F	→ Y110H	0.004
Y110F	→ Y110A	<0.001
Y110H	→ Y110A	<0.001

A2.2) $k_{cat}^{app(GSH)}$ @ 50 μM GSSCys

Comparison		P-value
WT	→ Y110F	<0.001
WT	→ Y110H	<0.001
WT	→ Y110A	<0.001
Y110F	→ Y110H	<0.001
Y110F	→ Y110A	<0.001
Y110H	→ Y110A	0.001

A1.3) $k_{cat}^{app(GSSCys)}$ @ 200 μM GSH

Comparison		P-value
WT	→ Y110F	0.070
WT	→ Y110H	0.009
WT	→ Y110A	<0.001
Y110F	→ Y110H	0.001
Y110F	→ Y110A	<0.001
Y110H	→ Y110A	0.012

A2.3) $k_{cat}^{app(GSH)}$ @ 100 μM GSSCys

Comparison		P-value
WT	→ Y110F	0.001
WT	→ Y110H	<0.001
WT	→ Y110A	<0.001
Y110F	→ Y110H	<0.001
Y110F	→ Y110A	<0.001
Y110H	→ Y110A	0.001

A1.4) $k_{cat}^{app(GSSCys)}$ @ 1000 μM GSH

Comparison		P-value
WT	→ Y110F	0.413
WT	→ Y110H	0.013
WT	→ Y110A	0.002
Y110F	→ Y110H	0.032
Y110F	→ Y110A	0.004
Y110H	→ Y110A	0.199

A2.4) $k_{cat}^{app(GSH)}$ @ 150 μM GSSCys

Comparison		P-value
WT	→ Y110F	<0.001
WT	→ Y110H	<0.001
WT	→ Y110A	<0.001
Y110F	→ Y110H	<0.001
Y110F	→ Y110A	0.004
Y110H	→ Y110A	<0.001

A3.1) $K_m^{app(GSSCys)}$ @ 50 μM GSH

Comparison		P-value	
WT	→ Y110F	0.991	ns
WT	→ Y110H	0.011	*
WT	→ Y110A	0.032	*
Y110F	→ Y110H	0.013	*
Y110F	→ Y110A	0.041	*
Y110H	→ Y110A	0.520	ns

A4.1) $K_m^{app(GSH)}$ @ 25 μM GSSCys

Comparison		P-value	
WT	→ Y110F	0.004	**
WT	→ Y110H	<0.001	***
WT	→ Y110A	0.001	***
Y110F	→ Y110H	0.001	***
Y110F	→ Y110A	0.223	ns
Y110H	→ Y110A	0.004	**

A3.2) $K_m^{app(GSSCys)}$ @ 100 μM GSH

Comparison		P-value	
WT	→ Y110F	0.807	ns
WT	→ Y110H	<0.001	***
WT	→ Y110A	0.237	ns
Y110F	→ Y110H	<0.001	***
Y110F	→ Y110A	0.236	ns
Y110H	→ Y110A	0.006	**

A4.2) $K_m^{app(GSH)}$ @ 50 μM GSSCys

Comparison		P-value	
WT	→ Y110F	0.355	ns
WT	→ Y110H	0.001	***
WT	→ Y110A	0.151	ns
Y110F	→ Y110H	<0.001	***
Y110F	→ Y110A	0.051	ns
Y110H	→ Y110A	0.012	*

A3.3) $K_m^{app(GSSCys)}$ @ 200 μM GSH

Comparison		P-value	
WT	→ Y110F	0.747	ns
WT	→ Y110H	0.012	*
WT	→ Y110A	0.283	ns
Y110F	→ Y110H	0.016	*
Y110F	→ Y110A	0.317	ns
Y110H	→ Y110A	0.111	ns

A4.3) $K_m^{app(GSH)}$ @ 100 μM GSSCys

Comparison		P-value	
WT	→ Y110F	0.949	ns
WT	→ Y110H	0.003	**
WT	→ Y110A	0.072	ns
Y110F	→ Y110H	0.003	**
Y110F	→ Y110A	0.096	ns
Y110H	→ Y110A	0.071	ns

A3.4) $K_m^{app(GSSCys)}$ @ 1000 μM GSH

Comparison		P-value	
WT	→ Y110F	0.114	ns
WT	→ Y110H	0.672	ns
WT	→ Y110A	0.214	ns
Y110F	→ Y110H	0.310	ns
Y110F	→ Y110A	0.667	ns
Y110H	→ Y110A	0.379	ns

A4.4) $K_m^{app(GSH)}$ @ 150 μM GSSCys

Comparison		P-value	
WT	→ Y110F	0.608	ns
WT	→ Y110H	<0.001	***
WT	→ Y110A	0.017	*
Y110F	→ Y110H	<0.001	***
Y110F	→ Y110A	0.012	*
Y110H	→ Y110A	0.002	**

B) HEDS assay ScGrx7 Y110X (Supplementary Figs. 4 and 5 and Supplementary Table 3)**B1.1) $k_{cat}^{app(HEDS)}$ @ 300 μM GSH**

Comparison		P-value	
WT	\rightarrow Y110F	0.596	ns
WT	\rightarrow Y110H	0.007	**
WT	\rightarrow Y110A	0.001	***
Y110F	\rightarrow Y110H	0.011	*
Y110F	\rightarrow Y110A	0.002	**
Y110H	\rightarrow Y110A	0.262	ns

B2.1) $k_{cat}^{app(GSH)}$ @ 0.18 mM HEDS

Comparison		P-value	
WT	\rightarrow Y110F	<0.001	***
WT	\rightarrow Y110H	<0.001	***
WT	\rightarrow Y110A	<0.001	***
Y110F	\rightarrow Y110H	<0.001	***
Y110F	\rightarrow Y110A	<0.001	***
Y110H	\rightarrow Y110A	0.139	ns

B1.2) $k_{cat}^{app(HEDS)}$ @ 500 μM GSH

Comparison		P-value	
WT	\rightarrow Y110F	0.223	ns
WT	\rightarrow Y110H	<0.001	***
WT	\rightarrow Y110A	<0.001	***
Y110F	\rightarrow Y110H	<0.001	***
Y110F	\rightarrow Y110A	<0.001	***
Y110H	\rightarrow Y110A	0.196	ns

B2.2) $k_{cat}^{app(GSH)}$ @ 0.37 mM HEDS

Comparison		P-value	
WT	\rightarrow Y110F	<0.001	***
WT	\rightarrow Y110H	<0.001	***
WT	\rightarrow Y110A	<0.001	***
Y110F	\rightarrow Y110H	<0.001	***
Y110F	\rightarrow Y110A	<0.001	***
Y110H	\rightarrow Y110A	0.005	**

B1.3) $k_{cat}^{app(HEDS)}$ @ 1000 μM GSH

Comparison		P-value	
WT	\rightarrow Y110F	0.298	ns
WT	\rightarrow Y110H	0.011	*
WT	\rightarrow Y110A	0.004	**
Y110F	\rightarrow Y110H	0.003	**
Y110F	\rightarrow Y110A	0.001	***
Y110H	\rightarrow Y110A	0.325	ns

B2.3) $k_{cat}^{app(GSH)}$ @ 0.55 mM HEDS

Comparison		P-value	
WT	\rightarrow Y110F	0.010	**
WT	\rightarrow Y110H	<0.001	***
WT	\rightarrow Y110A	<0.001	***
Y110F	\rightarrow Y110H	<0.001	***
Y110F	\rightarrow Y110A	<0.001	***
Y110H	\rightarrow Y110A	0.010	**

B1.4) $k_{cat}^{app(HEDS)}$ @ 1500 μM GSH

Comparison		P-value	
WT	\rightarrow Y110F	0.033	*
WT	\rightarrow Y110H	0.012	*
WT	\rightarrow Y110A	0.003	**
Y110F	\rightarrow Y110H	<0.001	***
Y110F	\rightarrow Y110A	<0.001	***
Y110H	\rightarrow Y110A	0.218	ns

B2.4) $k_{cat}^{app(GSH)}$ @ 0.74 mM HEDS

Comparison		P-value	
WT	\rightarrow Y110F	0.057	ns
WT	\rightarrow Y110H	<0.001	***
WT	\rightarrow Y110A	<0.001	***
Y110F	\rightarrow Y110H	<0.001	***
Y110F	\rightarrow Y110A	<0.001	***
Y110H	\rightarrow Y110A	0.081	ns

B3.1) $K_m^{app(HEDS)}$ @ 300 μM GSH

Comparison		P-value	
WT	→ Y110F	0.511	ns
WT	→ Y110H	0.511	ns
WT	→ Y110A	0.511	ns
Y110F	→ Y110H	0.511	ns
Y110F	→ Y110A	0.511	ns
Y110H	→ Y110A	0.511	ns

B4.1) $K_m^{app(GSH)}$ @ 0.18 mM HEDS

Comparison		P-value	
WT	→ Y110F	0.966	ns
WT	→ Y110H	0.966	ns
WT	→ Y110A	0.966	ns
Y110F	→ Y110H	0.966	ns
Y110F	→ Y110A	0.966	ns
Y110H	→ Y110A	0.966	ns

B3.2) $K_m^{app(HEDS)}$ @ 500 μM GSH

Comparison		P-value	
WT	→ Y110F	0.182	ns
WT	→ Y110H	0.182	ns
WT	→ Y110A	0.182	ns
Y110F	→ Y110H	0.182	ns
Y110F	→ Y110A	0.182	ns
Y110H	→ Y110A	0.182	ns

B4.2) $K_m^{app(GSH)}$ @ 0.37 mM HEDS

Comparison		P-value	
WT	→ Y110F	0.884	ns
WT	→ Y110H	0.525	ns
WT	→ Y110A	0.159	ns
Y110F	→ Y110H	0.470	ns
Y110F	→ Y110A	0.156	ns
Y110H	→ Y110A	0.022	*

B3.3) $K_m^{app(HEDS)}$ @ 1000 μM GSH

Comparison		P-value	
WT	→ Y110F	0.039	*
WT	→ Y110H	0.289	ns
WT	→ Y110A	0.816	ns
Y110F	→ Y110H	0.305	ns
Y110F	→ Y110A	0.033	*
Y110H	→ Y110A	0.293	ns

B4.3) $K_m^{app(GSH)}$ @ 0.55 mM HEDS

Comparison		P-value	
WT	→ Y110F	0.443	ns
WT	→ Y110H	0.057	ns
WT	→ Y110A	0.621	ns
Y110F	→ Y110H	0.277	ns
Y110F	→ Y110A	0.594	ns
Y110H	→ Y110A	0.084	ns

B3.4) $K_m^{app(HEDS)}$ @ 1500 μM GSH

Comparison		P-value	
WT	→ Y110F	0.037	*
WT	→ Y110H	0.250	ns
WT	→ Y110A	0.723	ns
Y110F	→ Y110H	0.261	ns
Y110F	→ Y110A	0.026	*
Y110H	→ Y110A	0.272	ns

B4.4) $K_m^{app(GSH)}$ @ 0.74 mM HEDS

Comparison		P-value	
WT	→ Y110F	0.146	ns
WT	→ Y110H	0.146	ns
WT	→ Y110A	0.146	ns
Y110F	→ Y110H	0.146	ns
Y110F	→ Y110A	0.146	ns
Y110H	→ Y110A	0.146	ns

C) GSSCys assay ScGrx7 D144X (Fig. 4, Supplementary Fig. 7 and Supplementary Table 5)

C1.1) $k_{cat}^{app(GSSCys)}$ @ 50 μM GSH				C3.1) $K_m^{app(GSSCys)}$ @ 50 μM GSH			
Comparison P-value				Comparison P-value			
WT → D144A	0.040	*		WT → D144A	0.035	*	
WT → D144K	<0.001	***		WT → D144K	0.020	*	
D144A → D144K	0.001	***		D144A → D144K	0.437	ns	
C1.2) $k_{cat}^{app(GSSCys)}$ @ 100 μM GSH				C3.2) $K_m^{app(GSSCys)}$ @ 100 μM GSH			
Comparison P-value				Comparison P-value			
WT → D144A	0.453	ns		WT → D144A	0.034	*	
WT → D144K	0.008	**		WT → D144K	0.005	**	
D144A → D144K	0.013	*		D144A → D144K	0.066	ns	
C1.3) $k_{cat}^{app(GSSCys)}$ @ 200 μM GSH				C3.3) $K_m^{app(GSSCys)}$ @ 200 μM GSH			
Comparison P-value				Comparison P-value			
WT → D144A	0.576	ns		WT → D144A	0.443	ns	
WT → D144K	<0.001	***		WT → D144K	0.002	**	
D144A → D144K	<0.001	***		D144A → D144K	0.003	**	
C1.4) $k_{cat}^{app(GSSCys)}$ @ 1000 μM GSH				C3.4) $K_m^{app(GSSCys)}$ @ 1000 μM GSH			
Comparison P-value				Comparison P-value			
WT → D144A	0.682	ns		WT → D144A	0.119	ns	
WT → D144K	0.038	*		WT → D144K	0.018	*	
D144A → D144K	0.043	*		D144A → D144K	0.112	ns	
C2.1) $k_{cat}^{app(GSH)}$ @ 25 μM GSSCys				C4.1) $K_m^{app(GSH)}$ @ 25 μM GSSCys			
Comparison P-value				Comparison P-value			
WT → D144A	<0.001	***		WT → D144A	0.813	ns	
WT → D144K	<0.001	***		WT → D144K	<0.001	***	
D144A → D144K	<0.001	***		D144A → D144K	<0.001	***	
C2.2) $k_{cat}^{app(GSH)}$ @ 50 μM GSSCys				C4.2) $K_m^{app(GSH)}$ @ 50 μM GSSCys			
Comparison P-value				Comparison P-value			
WT → D144A	<0.001	***		WT → D144A	0.056	ns	
WT → D144K	<0.001	***		WT → D144K	<0.001	***	
D144A → D144K	0.012	*		D144A → D144K	0.004	**	
C2.3) $k_{cat}^{app(GSH)}$ @ 100 μM GSSCys				C4.3) $K_m^{app(GSH)}$ @ 100 μM GSSCys			
Comparison P-value				Comparison P-value			
WT → D144A	<0.001	***		WT → D144A	0.366	ns	
WT → D144K	<0.001	***		WT → D144K	<0.001	***	
D144A → D144K	0.131	ns		D144A → D144K	0.001	***	
C2.4) $k_{cat}^{app(GSH)}$ @ 150 μM GSSCys				C4.4) $K_m^{app(GSH)}$ @ 150 μM GSSCys			
Comparison P-value				Comparison P-value			
WT → D144A	0.027	*		WT → D144A	0.325	ns	
WT → D144K	0.032	*		WT → D144K	0.020	*	
D144A → D144K	0.855	ns		D144A → D144K	0.009	**	

D) GSSCys assay ScGrx7 E147X (Fig. 4, Supplementary Fig. 9 and Supplementary Table 5)

D1.1) $k_{cat}^{app(GSSCys)}$ @ 50 μM GSH				D3.1) $K_m^{app(GSSCys)}$ @ 50 μM GSH			
Comparison		P-value		Comparison		P-value	
WT → E147A	0.999	ns		WT → E147A	0.550	ns	
WT → E147K	<0.001	***		WT → E147K	0.002	**	
E147A → E147K	<0.001	***		E147A → E147K	0.002	**	
D1.2) $k_{cat}^{app(GSSCys)}$ @ 100 μM GSH				D3.2) $K_m^{app(GSSCys)}$ @ 100 μM GSH			
Comparison		P-value		Comparison		P-value	
WT → E147A	0.317	ns		WT → E147A	0.641	ns	
WT → E147K	<0.001	***		WT → E147K	0.001	***	
E147A → E147K	<0.001	***		E147A → E147K	0.001	***	
D1.3) $k_{cat}^{app(GSSCys)}$ @ 200 μM GSH				D3.3) $K_m^{app(GSSCys)}$ @ 200 μM GSH			
Comparison		P-value		Comparison		P-value	
WT → E147A	0.840	ns		WT → E147A	0.984	ns	
WT → E147K	<0.001	***		WT → E147K	0.012	*	
E147A → E147K	<0.001	***		E147A → E147K	0.018	*	
D1.4) $k_{cat}^{app(GSSCys)}$ @ 1000 μM GSH				D3.4) $K_m^{app(GSSCys)}$ @ 1000 μM GSH			
Comparison		P-value		Comparison		P-value	
WT → E147A	0.427	ns		WT → E147A	0.539	ns	
WT → E147K	<0.001	***		WT → E147K	0.002	**	
E147A → E147K	<0.001	***		E147A → E147K	0.001	***	
D2.1) $k_{cat}^{app(GSH)}$ @ 25 μM GSSCys				D4.1) $K_m^{app(GSH)}$ @ 25 μM GSSCys			
Comparison		P-value		Comparison		P-value	
WT → E147A	0.054	ns		WT → E147A	0.125	ns	
WT → E147K	0.006	**		WT → E147K	0.025	*	
E147A → E147K	0.058	ns		E147A → E147K	0.005	**	
D2.2) $k_{cat}^{app(GSH)}$ @ 50 μM GSSCys				D4.2) $K_m^{app(GSH)}$ @ 50 μM GSSCys			
Comparison		P-value		Comparison		P-value	
WT → E147A	0.037	*		WT → E147A	0.042	*	
WT → E147K	0.004	**		WT → E147K	0.025	*	
E147A → E147K	0.042	*		E147A → E147K	0.003	**	
D2.3) $k_{cat}^{app(GSH)}$ @ 100 μM GSSCys				D4.3) $K_m^{app(GSH)}$ @ 100 μM GSSCys			
Comparison		P-value		Comparison		P-value	
WT → E147A	0.003	**		WT → E147A	0.122	ns	
WT → E147K	<0.001	***		WT → E147K	0.005	**	
E147A → E147K	0.002	**		E147A → E147K	0.002	**	
D2.4) $k_{cat}^{app(GSH)}$ @ 150 μM GSSCys				D4.4) $K_m^{app(GSH)}$ @ 150 μM GSSCys			
Comparison		P-value		Comparison		P-value	
WT → E147A	0.003	**		WT → E147A	0.008	**	
WT → E147K	0.021	*		WT → E147K	0.016	*	
E147A → E147K	0.063	ns		E147A → E147K	<0.001	***	

E) GSSCys assay ScGrx7 R153X (Fig. 5, Supplementary Fig. 11 and Supplementary Table 6)

E1.1) $k_{cat}^{app(GSSCys)}$ @ 50 μM GSH				E3.1) $K_m^{app(GSSCys)}$ @ 50 μM GSH			
Comparison P-value				Comparison P-value			
WT → R153A	0.549	ns		WT → R153A	0.043	*	
WT → R153E	0.013	*		WT → R153E	0.036	*	
R153A → R153E	0.010	**		R153A → R153E	0.857	ns	
E1.2) $k_{cat}^{app(GSSCys)}$ @ 100 μM GSH				E3.2) $K_m^{app(GSSCys)}$ @ 100 μM GSH			
Comparison P-value				Comparison P-value			
WT → R153A	0.710	ns		WT → R153A	0.039	*	
WT → R153E	0.004	**		WT → R153E	0.043	*	
R153A → R153E	0.004	**		R153A → R153E	0.713	ns	
E1.3) $k_{cat}^{app(GSSCys)}$ @ 200 μM GSH				E3.3) $K_m^{app(GSSCys)}$ @ 200 μM GSH			
Comparison P-value				Comparison P-value			
WT → R153A	0.033	*		WT → R153A	0.015	*	
WT → R153E	<0.001	***		WT → R153E	0.021	*	
R153A → R153E	0.003	**		R153A → R153E	0.950	ns	
E1.4) $k_{cat}^{app(GSSCys)}$ @ 1000 μM GSH				E3.4) $K_m^{app(GSSCys)}$ @ 1000 μM GSH			
Comparison P-value				Comparison P-value			
WT → R153A	0.125	ns		WT → R153A	0.008	**	
WT → R153E	0.005	**		WT → R153E	0.011	*	
R153A → R153E	0.021	*		R153A → R153E	0.970	ns	
E2.1) $k_{cat}^{app(GSH)}$ @ 25 μM GSSCys				E4.1) $K_m^{app(GSH)}$ @ 25 μM GSSCys			
Comparison P-value				Comparison P-value			
WT → R153A	<0.001	***		WT → R153A	<0.001	***	
WT → R153E	<0.001	***		WT → R153E	<0.001	***	
R153A → R153E	<0.001	***		R153A → R153E	0.255	ns	
E2.2) $k_{cat}^{app(GSH)}$ @ 50 μM GSSCys				E4.2) $K_m^{app(GSH)}$ @ 50 μM GSSCys			
Comparison P-value				Comparison P-value			
WT → R153A	<0.001	***		WT → R153A	<0.001	***	
WT → R153E	<0.001	***		WT → R153E	<0.001	***	
R153A → R153E	<0.001	***		R153A → R153E	0.760	ns	
E2.3) $k_{cat}^{app(GSH)}$ @ 100 μM GSSCys				E4.3) $K_m^{app(GSH)}$ @ 100 μM GSSCys			
Comparison P-value				Comparison P-value			
WT → R153A	<0.001	***		WT → R153A	<0.001	***	
WT → R153E	<0.001	***		WT → R153E	<0.001	***	
R153A → R153E	<0.001	***		R153A → R153E	0.454	ns	
E2.4) $k_{cat}^{app(GSH)}$ @ 150 μM GSSCys				E4.4) $K_m^{app(GSH)}$ @ 150 μM GSSCys			
Comparison P-value				Comparison P-value			
WT → R153A	<0.001	***		WT → R153A	0.005	**	
WT → R153E	<0.001	***		WT → R153E	0.006	**	
R153A → R153E	<0.001	***		R153A → R153E	0.611	ns	

Supplementary Table 12. Statistical analysis of AUC (OxD*sec) values from the indicated measurements of ScGrx7. P-values from one way ANOVA analysis followed by a Holm-Sidak test were calculated in SigmaPlot 13 (P > 0.05 : ns; P ≤ 0.05 : *; P ≤ 0.01 : **, P ≤ 0.001 : ***).

A) roGFP2 assay ScGrx7 C108S and unfused roGFP2 (Fig. 7b)

A1) AUC (OxD*sec) @ 20 µM H ₂ O ₂				A4) AUC (OxD*sec) @ 200 µM H ₂ O ₂			
Comparison		P-value		Comparison		P-value	
WT	→ C108S	0.381	ns	WT	→ C108S	0.002	**
WT	→ roGFP2	0.305	ns	WT	→ roGFP2	0.002	**
C108S	→ roGFP2	0.888	ns	C108S	→ roGFP2	0.727	ns
A2) AUC (OxD*sec) @ 50 µM H ₂ O ₂				A5) AUC (OxD*sec) @ 500 µM H ₂ O ₂			
Comparison		P-value		Comparison		P-value	
WT	→ C108S	0.235	ns	WT	→ C108S	<0.001	***
WT	→ roGFP2	0.177	ns	WT	→ roGFP2	<0.001	***
C108S	→ roGFP2	0.221	ns	C108S	→ roGFP2	0.323	ns
A3) AUC (OxD*sec) @ 100 µM H ₂ O ₂				A6) AUC (OxD*sec) @ 1000 µM H ₂ O ₂			
Comparison		P-value		Comparison		P-value	
WT	→ C108S	0.070	ns	WT	→ C108S	<0.001	***
WT	→ roGFP2	0.071	ns	WT	→ roGFP2	<0.001	***
C108S	→ roGFP2	0.942	ns	C108S	→ roGFP2	0.595	ns

B) roGFP2 assay ScGrx7 K105X (Fig. 7c)

B1) AUC (OxD*sec) @ 20 µM H ₂ O ₂				B3) AUC (OxD*sec) @ 100 µM H ₂ O ₂			
Comparison		P-value		Comparison		P-value	
WT	→ K105R	0.273	ns	WT	→ K105R	0.069	ns
WT	→ K105A	0.210	ns	WT	→ K105A	0.102	ns
WT	→ K105Y	0.647	ns	WT	→ K105Y	0.213	ns
WT	→ K105E	0.985	ns	WT	→ K105E	0.048	*
K105R	→ K105A	0.843	ns	K105R	→ K105A	0.202	ns
K105R	→ K105Y	0.134	ns	K105R	→ K105Y	0.011	*
K105R	→ K105E	0.400	ns	K105R	→ K105E	0.393	ns
K105A	→ K105Y	0.092	ns	K105A	→ K105Y	0.074	ns
K105A	→ K105E	0.629	ns	K105A	→ K105E	0.651	ns
K105Y	→ K105E	0.400	ns	K105Y	→ K105E	0.031	*
B2) AUC (OxD*sec) @ 50 µM H ₂ O ₂				B4) AUC (OxD*sec) @ 200 µM H ₂ O ₂			
Comparison		P-value		Comparison		P-value	
WT	→ K105R	0.227	ns	WT	→ K105R	0.003	**
WT	→ K105A	0.184	ns	WT	→ K105A	0.050	*
WT	→ K105Y	0.225	ns	WT	→ K105Y	0.013	*
WT	→ K105E	0.214	ns	WT	→ K105E	<0.001	***
K105R	→ K105A	0.330	ns	K105R	→ K105A	0.090	ns
K105R	→ K105Y	0.607	ns	K105R	→ K105Y	0.070	ns
K105R	→ K105E	0.629	ns	K105R	→ K105E	0.043	*
K105A	→ K105Y	0.198	ns	K105A	→ K105Y	0.257	ns
K105A	→ K105E	0.400	ns	K105A	→ K105E	0.003	**
K105Y	→ K105E	0.629	ns	K105Y	→ K105E	0.007	**

B5) AUC (OxD*sec) @ 500 µM H₂O₂

Comparison		P-value	
WT	→ K105R	0.004	**
WT	→ K105A	0.002	**
WT	→ K105Y	0.024	*
WT	→ K105E	<0.001	***
K105R	→ K105A	0.482	ns
K105R	→ K105Y	0.013	*
K105R	→ K105E	0.002	**
K105A	→ K105Y	<0.001	***
K105A	→ K105E	<0.001	***
K105Y	→ K105E	<0.001	***

B6) AUC (OxD*sec) @ 1000 µM H₂O₂

Comparison		P-value	
WT	→ K105R	0.002	**
WT	→ K105A	0.003	**
WT	→ K105Y	0.004	**
WT	→ K105E	<0.001	***
K105R	→ K105A	0.874	ns
K105R	→ K105Y	0.450	ns
K105R	→ K105E	<0.001	***
K105A	→ K105Y	0.665	ns
K105A	→ K105E	<0.001	***
K105Y	→ K105E	<0.001	***

C) roGFP2 assay ScGrx7 Y110X (Fig. 7d)

C1) AUC (OxD*sec) @ 20 µM H₂O₂

Comparison		P-value	
WT	→ Y110F	0.438	ns
WT	→ Y110H	0.150	ns
WT	→ Y110A	0.299	ns
Y110F	→ Y110H	0.705	ns
Y110F	→ Y110A	0.245	ns
Y110H	→ Y110A	0.200	ns

C4) AUC (OxD*sec) @ 200 µM H₂O₂

Comparison		P-value	
WT	→ Y110F	0.669	ns
WT	→ Y110H	0.043	*
WT	→ Y110A	0.003	**
Y110F	→ Y110H	0.003	**
Y110F	→ Y110A	<0.001	***
Y110H	→ Y110A	0.003	**

C2) AUC (OxD*sec) @ 50 µM H₂O₂

Comparison		P-value	
WT	→ Y110F	0.515	ns
WT	→ Y110H	0.423	ns
WT	→ Y110A	0.256	ns
Y110F	→ Y110H	0.205	ns
Y110F	→ Y110A	0.140	ns
Y110H	→ Y110A	0.400	ns

C5) AUC (OxD*sec) @ 500 µM H₂O₂

Comparison		P-value	
WT	→ Y110F	0.857	ns
WT	→ Y110H	0.064	ns
WT	→ Y110A	0.006	**
Y110F	→ Y110H	0.105	ns
Y110F	→ Y110A	0.028	*
Y110H	→ Y110A	0.100	ns

C3) AUC (OxD*sec) @ 100 µM H₂O₂

Comparison		P-value	
WT	→ Y110F	0.466	ns
WT	→ Y110H	0.452	ns
WT	→ Y110A	0.178	ns
Y110F	→ Y110H	0.198	ns
Y110F	→ Y110A	0.080	ns
Y110H	→ Y110A	0.483	ns

C6) AUC (OxD*sec) @ 1000 µM H₂O₂

Comparison		P-value	
WT	→ Y110F	0.035	*
WT	→ Y110H	0.303	ns
WT	→ Y110A	0.003	**
Y110F	→ Y110H	0.027	*
Y110F	→ Y110A	0.003	**
Y110H	→ Y110A	0.012	*

D) roGFP2 assay ScGrx7 D144X (Fig. 7e)**D1) AUC (OxD*sec) @ 20 µM H₂O₂**

Comparison		P-value	
WT	→ D144A	0.411	ns
WT	→ D144K	0.578	ns
D144K	→ D144A	0.285	ns

D4) AUC (OxD*sec) @ 200 µM H₂O₂

Comparison		P-value	
WT	→ D144A	0.086	ns
WT	→ D144K	0.026	*
D144K	→ D144A	0.969	ns

D2) AUC (OxD*sec) @ 50 µM H₂O₂

Comparison		P-value	
WT	→ D144A	0.626	ns
WT	→ D144K	0.840	ns
D144K	→ D144A	0.441	ns

D5) AUC (OxD*sec) @ 500 µM H₂O₂

Comparison		P-value	
WT	→ D144A	0.583	ns
WT	→ D144K	0.800	ns
D144K	→ D144A	0.780	ns

D3) AUC (OxD*sec) @ 100 µM H₂O₂

Comparison		P-value	
WT	→ D144A	0.689	ns
WT	→ D144K	0.965	ns
D144K	→ D144A	0.757	ns

D6) AUC (OxD*sec) @ 1000 µM H₂O₂

Comparison		P-value	
WT	→ D144A	0.106	ns
WT	→ D144K	0.748	ns
D144K	→ D144A	0.302	ns

E) roGFP2 assay ScGrx7 E147X (Fig. 7e)**E1) AUC (OxD*sec) @ 20 µM H₂O₂**

Comparison		P-value	
WT	→ E147A	0.624	ns
WT	→ E147K	0.686	ns
E147A	→ E147K	0.807	ns

E4) AUC (OxD*sec) @ 200 µM H₂O₂

Comparison		P-value	
WT	→ E147A	0.517	ns
WT	→ E147K	0.229	ns
E147A	→ E147K	0.997	ns

E2) AUC (OxD*sec) @ 50 µM H₂O₂

Comparison		P-value	
WT	→ E147A	0.443	ns
WT	→ E147K	0.523	ns
E147A	→ E147K	0.748	ns

E5) AUC (OxD*sec) @ 500 µM H₂O₂

Comparison		P-value	
WT	→ E147A	0.069	ns
WT	→ E147K	0.073	ns
E147A	→ E147K	0.491	ns

E3) AUC (OxD*sec) @ 100 µM H₂O₂

Comparison		P-value	
WT	→ E147A	0.392	ns
WT	→ E147K	0.577	ns
E147A	→ E147K	0.154	ns

E6) AUC (OxD*sec) @ 1000 µM H₂O₂

Comparison		P-value	
WT	→ E147A	0.050	*
WT	→ E147K	0.080	ns
E147A	→ E147K	0.886	ns

F) roGFP2 assay ScGrx7 R153X and E170A (Fig. 7f)**F1) AUC (OxD*sec) @ 20 µM H₂O₂**

Comparison		P-value	
WT	→ R153A	0.629	ns
WT	→ R153E	0.178	ns
R153A	→ R153E	0.545	ns
WT	→ E170A	0.119	ns

F4) AUC (OxD*sec) @ 200 µM H₂O₂

Comparison		P-value	
WT	→ R153A	0.015	*
WT	→ R153E	0.009	**
R153A	→ R153E	0.140	ns
WT	→ E170A	0.008	**

F2) AUC (OxD*sec) @ 50 µM H₂O₂

Comparison		P-value	
WT	→ R153A	0.316	ns
WT	→ R153E	0.207	ns
R153A	→ R153E	0.164	ns
WT	→ E170A	0.182	ns

F5) AUC (OxD*sec) @ 500 µM H₂O₂

Comparison		P-value	
WT	→ R153A	0.058	ns
WT	→ R153E	0.113	ns
R153A	→ R153E	0.574	ns
WT	→ E170A	0.010	**

F3) AUC (OxD*sec) @ 100 µM H₂O₂

Comparison		P-value	
WT	→ R153A	0.200	ns
WT	→ R153E	0.120	ns
R153A	→ R153E	0.242	ns
WT	→ E170A	0.108	ns

F6) AUC (OxD*sec) @ 1000 µM H₂O₂

Comparison		P-value	
WT	→ R153A	0.287	ns
WT	→ R153E	0.221	ns
R153A	→ R153E	0.525	ns
WT	→ E170A	0.006	**

G) roGFP2 assay ScGrx7 interconversion mutants with DTT pretreatment (Fig. 7g)**G1) AUC (OxD*sec) @ 20 µM H₂O₂**

Comparison		P-value	
WT	→ roGFP2	0.083	ns
WT	→ C108S	0.044	*
WT	→ WP	0.229	ns
WT	→ loop	0.198	ns
WT	→ WP+loop	0.037	*
WP	→ roGFP2	0.982	ns
WP	→ C108S	0.985	ns
WP	→ loop	0.887	ns
WP	→ WP+loop	0.599	ns
loop	→ roGFP2	0.862	ns
loop	→ C108S	0.796	ns
loop	→ WP+loop	0.412	ns
WP+loop	→ roGFP2	0.196	ns
WP+loop	→ C108S	0.181	ns
roGFP2	→ C108S	0.863	ns

G3) AUC (OxD*sec) @ 100 µM H₂O₂

Comparison		P-value	
WT	→ roGFP2	0.002	*
WT	→ C108	<0.001	***
WT	→ WP	0.002	**
WT	→ loop	0.001	**
WT	→ WP+loop	0.003	**
WP	→ roGFP2	0.762	ns
WP	→ C108S	0.595	ns
WP	→ loop	0.739	ns
WP	→ WP+loop	0.830	ns
loop	→ roGFP2	0.880	ns
loop	→ C108S	0.998	ns
loop	→ WP+loop	0.613	ns
WP+Loop	→ roGFP2	0.643	ns
WP+Loop	→ C108S	0.500	ns
roGFP2	→ C108S	0.610	ns

G2) AUC (OxD*sec) @ 50 µM H₂O₂

Comparison		P-value	
WT	→ roGFP2	0.106	ns
WT	→ C108S	0.043	*
WT	→ WP	0.318	ns
WT	→ loop	0.108	ns
WT	→ WP+oop	0.089	ns
WP	→ roGFP2	0.475	ns
WP	→ C108S	0.273	ns
WP	→ loop	0.602	ns
WP	→ WP+loop	0.383	ns
loop	→ roGFP2	0.793	ns
loop	→ C108S	0.472	ns
loop	→ WP+loop	0.569	ns

G4) AUC (OxD*sec) @ 200 µM H₂O₂

Comparison		P-value	
WT	→ roGFP2	0.007	*
WT	→ C108S	0.002	**
WT	→ WP	0.009	**
WT	→ loop	0.002	**

WT	\rightarrow WP+loop	0.007	**	loop	\rightarrow C108S	0.319	ns
WP	\rightarrow roGFP2	0.994	ns	loop	\rightarrow WP+loop	0.452	ns
WP	\rightarrow C108S	0.844	ns	WP+loop	\rightarrow roGFP2	0.060	ns
WP	\rightarrow loop	0.592	ns	WP+loop	\rightarrow C108S	0.041	*
WP	\rightarrow WP+loop	0.691	ns	roGFP2	\rightarrow C108S	0.631	ns
loop	\rightarrow roGFP2	0.512	ns				
loop	\rightarrow C108S	0.359	ns				
loop	\rightarrow WP+loop	0.881	ns				G6) AUC (OxD*sec) @ 1000 μ M H ₂ O ₂
WP+loop	\rightarrow roGFP2	0.575	ns				
WP+loop	\rightarrow C108S	0.420	ns				Comparison P-value
roGFP2	\rightarrow C108S	0.717	ns	WT	\rightarrow roGFP2	<0.001	***
				WT	\rightarrow C108	<0.001	***
				WT	\rightarrow WP	0.003	**
				WT	\rightarrow loop	<0.001	***
				WT	\rightarrow WP+loop	<0.001	***
				WP	\rightarrow roGFP2	0.418	ns
				WP	\rightarrow C108S	0.435	ns
				WP	\rightarrow loop	0.074	ns
				WP	\rightarrow WP+loop	0.106	ns
				loop	\rightarrow roGFP2	0.081	ns
				loop	\rightarrow C108S	0.013	*
				loop	\rightarrow WP+loop	0.733	ns
				WP+loop	\rightarrow roGFP2	0.076	ns
				WP+loop	\rightarrow C108S	0.011	*
				roGFP2	\rightarrow C108S	0.636	ns

H) roGFP2 assay ScGrx5 interconversion mutants (Fig. 7h)**H1) AUC (OxD*sec) @ 20 μ M H₂O₂**

Comparison		P-value	
WT	\rightarrow RR	0.990	ns
WT	\rightarrow loop	0.725	ns
WT	\rightarrow RR+loop	0.223	ns
RR	\rightarrow loop	0.700	ns
RR	\rightarrow RR+loop	0.057	ns
loop	\rightarrow RR+loop	0.629	ns

H4) AUC (OxD*sec) @ 200 μ M H₂O₂

Comparison		P-value	
WT	\rightarrow RR	0.414	ns
WT	\rightarrow loop	0.700	ns
WT	\rightarrow RR+loop	0.606	ns
RR	\rightarrow loop	0.530	ns
RR	\rightarrow RR+loop	0.986	ns
loop	\rightarrow RR+loop	0.493	ns

H2) AUC (OxD*sec) @ 50 μ M H₂O₂

Comparison		P-value	
WT	\rightarrow RR	0.793	ns
WT	\rightarrow loop	0.839	ns
WT	\rightarrow RR+loop	0.649	ns
RR	\rightarrow loop	0.876	ns
RR	\rightarrow RR+loop	0.262	ns
loop	\rightarrow RR+loop	0.857	ns

H5) AUC (OxD*sec) @ 500 μ M H₂O₂

Comparison		P-value	
WT	\rightarrow RR	0.100	ns
WT	\rightarrow loop	0.883	ns
WT	\rightarrow RR+loop	0.844	ns
RR	\rightarrow loop	0.068	ns
RR	\rightarrow RR+loop	0.046	*
loop	\rightarrow RR+loop	0.680	ns

H3) AUC (OxD*sec) @ 100 μ M H₂O₂

Comparison		P-value	
WT	\rightarrow RR	0.684	ns
WT	\rightarrow loop	0.614	ns
WT	\rightarrow RR+loop	0.794	ns
RR	\rightarrow loop	0.690	ns
RR	\rightarrow RR+loop	0.445	ns
loop	\rightarrow RR+loop	1.000	ns

H6) AUC (OxD*sec) @ 1000 μ M H₂O₂

Comparison		P-value	
WT	\rightarrow RR	0.700	ns
WT	\rightarrow loop	0.188	ns
WT	\rightarrow RR+loop	0.315	ns
RR	\rightarrow loop	0.047	*
RR	\rightarrow RR+loop	0.036	*
loop	\rightarrow RR+loop	0.382	ns

I) roGFP2 assay ScGrx5 interconversion mutants with DTT pretreatment (Fig. 7i)**I1) AUC (OxD*sec) @ 20 µM H₂O₂**

Comparison	P-value						
WT →roGFP2	0.084	ns	loop	→loop+G68P+R97Q	0.226	ns	
WT →loop	0.362	ns	loop+G68P	→roGFP2	0.088	ns	
WT →loop+G68P	0.044	*	loop+G68P	→RR+loop	0.597	ns	
WT →RR+loop	0.070	ns	loop+G68P	→RR+loop+G68P	0.226	ns	
WT →RR+loop+G68P	0.090	ns	loop+G68P	→loop+G68P+R97Q	0.470	ns	
WT →loop+G68P+R97Q	0.035	**	RR+loop	→roGFP2	0.030	*	
loop →roGFP2	0.872	ns	RR+loop	→RR+loop+G68P	0.226	ns	
loop →loop+G68P	0.442	ns	RR+loop	→loop+G68P+R97Q	0.399	ns	
loop →RR+loop	0.776	ns	RR+loop+G68P	→roGFP2	0.270	ns	
loop →RR+loop+G68P	0.676	ns	RR+loop+G68P	→loop+G68P+R97Q	0.316	ns	
loop →loop+G68P+R97Q	0.416	ns	loop+G68P+R97Q	→roGFP2	0.264	ns	
loop+G68P →roGFP2	0.217	ns					
loop+G68P →RR+loop	0.308	ns					
loop+G68P →RR+loop+G68P	0.564	ns					
loop+G68P →loop+G68P+R97Q	0.963	ns					
RR+loop →roGFP2	0.700	ns					
RR+loop →RR+loop+G68P	0.754	ns					
RR+loop →loop+G68P+R97Q	0.244	ns					
RR+loop+G68P →roGFP2	0.586	ns					
RR+loop+G68P →loop+G68P+R97Q	0.514	ns					
loop+G68P+R97Q →roGFP2	0.162	ns					

I2) AUC (OxD*sec) @ 50 µM H₂O₂

Comparison	P-value						
WT →roGFP2	0.092	ns	loop	→loop+G68P+R97Q	0.049	*	
WT →loop	0.524	ns	loop+G68P	→roGFP2	0.027	*	
WT →loop+G68P	0.157	ns	loop+G68P	→RR+loop	0.799	ns	
WT →RR+loop	0.050	*	loop+G68P	→RR+loop+G68P	0.547	ns	
WT →RR+loop+G68P	0.192	ns	loop+G68P	→loop+G68P+R97Q	0.089	ns	
WT →loop+G68P+R97Q	0.044	**	RR+loop	→roGFP2	0.143	ns	
loop →roGFP2	0.147	ns	RR+loop	→RR+loop+G68P	0.760	ns	
loop →loop+G68P	0.230	ns	RR+loop	→loop+G68P+R97Q	0.135	ns	
loop →RR+loop	0.597	ns	RR+loop+G68P →roGFP2	0.101	ns		
loop →RR+loop+G68P	0.327	ns	RR+loop+G68P →loop+G68P+R97Q	0.189	ns		
loop →loop+G68P+R97Q	0.065	ns	loop+G68P+R97Q →roGFP2	0.033	*		
loop+G68P →roGFP2	0.473	ns					
loop+G68P →RR+loop	0.597	ns					
loop+G68P →RR+loop+G68P	0.657	ns					
loop+G68P →loop+G68P+R97Q	0.764	ns					
RR+loop →roGFP2	0.144	ns					
RR+loop →RR+loop+G68P	0.295	ns					
RR+loop →loop+G68P+R97Q	0.744	ns					
RR+loop+G68P →roGFP2	0.796	ns					
RR+loop+G68P →loop+G68P+R97Q	0.370	ns					
loop+G68P+R97Q →roGFP2	0.142	ns					

I3) AUC (OxD*sec) @ 100 µM H₂O₂

Comparison	P-value						
WT →roGFP2	0.575	ns	loop	→loop+G68P+R97Q	0.012	*	
WT →loop	0.889	ns	loop+G68P	→roGFP2	0.023	*	
WT →loop+G68P	0.107	ns	loop+G68P	→RR+loop	0.045	*	
WT →RR+loop	0.103	ns	loop+G68P	→RR+loop+G68P	0.269	ns	
WT →RR+loop+G68P	0.301	ns	loop+G68P	→loop+G68P+R97Q	0.015	*	
WT →loop+G68P+R97Q	0.234	ns	RR+loop	→roGFP2	0.002	ns	
loop →roGFP2	0.544	ns	RR+loop	→RR+loop+G68P	0.979	ns	
loop →loop+G68P	0.123	ns	RR+loop	→loop+G68P+R97Q	0.079	ns	
loop →RR+loop	0.135	ns	RR+loop+G68P →roGFP2	0.065	ns		
loop →RR+loop+G68P	0.319	ns	RR+loop+G68P →loop+G68P+R97Q	0.191	ns		
			loop+G68P+R97Q →roGFP2	0.004	**		

I6) AUC (OxD*sec) @ 1000 µM H₂O₂

Comparison		P-value			P-value		
WT	→roGFP2	0.010	**	loop+G68P	→roGFP2	<0.001	***
WT	→loop	0.723	ns	loop+G68P	→RR+loop	0.004	**
WT	→loop+G68P	0.013	*	loop+G68P	→RR+loop+G68P	0.002	**
WT	→RR+loop	0.002	**	loop+G68P	→loop+G68P+R97Q	0.099	ns
WT	→RR+loop+G68P	<0.001	***	RR+loop	→roGFP2	<0.001	***
WT	→loop+G68P+R97Q	0.032	*	RR+loop	→RR+loop+G68P	0.021	*
loop	→roGFP2	0.025	*	RR+loop	→loop+G68P+R97Q	0.399	ns
loop	→loop+G68P	0.014	*	RR+loop+G68P	→roGFP2	<0.001	***
loop	→RR+loop	0.002	**	RR+loop+G68P	→loop+G68P+R97Q	0.682	ns
loop	→RR+loop+G68P	0.001	**	loop+G68P+R97Q	→roGFP2	0.010	**
loop	→loop+G68P+R97Q	0.029	*				

J) roGFP2 assay ScGrx7 interconversion mutants (Supplementary Fig. 17)

J1) AUC (OxD*sec) @ 20 µM H₂O₂

Comparison		P-value
WT	→ WP	0.803
WT	→ loop	0.396
WT	→ WP+loop	0.401
WP	→ loop	0.448
WP	→ WP+loop	0.250
loop	→ WP+loop	0.828

J5) AUC (OxD*sec) @ 500 µM H₂O₂

Comparison		P-value
WT	→ WP	0.036
WT	→ loop	0.008
WT	→ WP+loop	0.008
WP	→ loop	0.034
WP	→ WP+loop	0.117
loop	→ WP+loop	0.794

J2) AUC (OxD*sec) @ 50 µM H₂O₂

Comparison		P-value
WT	→ WP	0.230
WT	→ loop	0.189
WT	→ WP+loop	0.172
WP	→ loop	0.555
WP	→ WP+loop	0.427
loop	→ WP+loop	0.700

J6) AUC (OxD*sec) @ 1000 µM H₂O₂

Comparison		P-value
WT	→ WP	<0.001
WT	→ loop	0.002
WT	→ WP+loop	0.003
WP	→ loop	0.051
WP	→ WP+loop	0.102
loop	→ WP+loop	0.828

J3) AUC (OxD*sec) @ 100 µM H₂O₂

Comparison		P-value
WT	→ WP	<0.001
WT	→ loop	<0.001
WT	→ WP+loop	0.100
WP	→ loop	0.939
WP	→ WP+loop	0.808
loop	→ WP+loop	0.678

J4) AUC (OxD*sec) @ 200 µM H₂O₂

Comparison		P-value
WT	→ WP	0.005
WT	→ loop	0.035
WT	→ WP+loop	0.038
WP	→ loop	0.873
WP	→ WP+loop	0.664
loop	→ WP+loop	0.716

Supplementary Table 13. Statistical analysis of the fraction of bound states from the MD simulations of ScGrx7.^a

Comparison		p-value	
WT	K105R	0.155	ns
WT	K105E	0.043	*
WT	E147K	0.153	ns
K105R	K105E	0.052	ns
K105R	E147K	0.806	ns
K105E	E147K	0.065	ns

^a See also Fig. 8a. P-values are derived from a two-tailed t-test assuming unequal variances. ($p < 0.05$: *; $p \geq 0.05$: ns)

Supplementary Table 14. Correlation analysis of the S-S-distance vs. S-S-S-angle from the MD simulations of ScGrx7.^a

ScGrx7	R²	p-value
WT	0.01	0.851
K105R	0.42	< 0.001
K105E	0.07	0.293
E147K	0.08	0.001

^a See also Fig. 8e.

Supplementary Table 15. ScGrx7 residues forming contacts with GS⁻ during MD simulations.

ScGrx7 Residue ^a	Contact fraction ^b			
	WT	K105R	K105E	E147K
K 105	0.09	0.18	0.04	0.08
T 106	0.26	0.26	0.21	0.28
G 107	0.27	0.31	0.20	0.26
γE SSG	0.23	0.17	0.26	0.31
C SSG	0.11	0.20	0.03	0.12
G SSG	0.19	0.22	0.10	0.29
P 109	0.25	0.29	0.18	0.20
Y 110	0.17	0.14	0.10	0.11
K 112	0.44	0.42	0.38	0.40
K 113	0.40	0.39	0.34	0.39
K 115	0.33	0.42	0.21	0.35
A 116	0.27	0.22	0.24	0.25
T 119	0.15	0.14	0.11	0.13
N 120	0.22	0.19	0.19	0.19
S 125	0.16	0.15	0.13	0.14
V 130	0.22	0.31	0.10	0.24
E 132	0.26	0.35	0.17	0.29
R 135	0.42	0.47	0.30	0.44
K 140	0.16	0.15	0.11	0.18
E 147	0.09	0.05	0.06	0.47
G 151	0.13	0.11	0.20	0.43
R 152	0.17	0.14	0.33	0.46
R 153	0.15	0.11	0.10	0.38
T 154	0.29	0.17	0.28	0.67
T 163	0.12	0.13	0.21	0.19
S 164	0.07	0.06	0.20	0.21
G 166	0.05	0.07	0.12	0.25
T 169	0.17	0.12	0.21	0.19
E 170	0.14	0.10	0.24	0.23
K 176	0.17	0.19	0.14	0.15
K 185	0.15	0.16	0.14	0.16
K 186	0.18	0.26	0.18	0.26
D 189	0.12	0.19	0.13	0.15
T 193	0.18	0.17	0.16	0.17
K 195	0.21	0.22	0.24	0.24

^a Residue number of the contacting residue. SSG γE, C, and G represent the γ-glutamyl, cysteinyl, and glycyl moiety of the bound disulfide glutathione, respectively. Only residues that have a fraction of 0.15 or higher in at least one of the ScGrx7 systems are shown.

^b Fraction of the simulation time in which a contact between any GS⁻ molecule and the residue was present.

2.2. Zimmermann et al., 2021, *Free Radical Biology and Medicine*

An intracellular assay for activity screening and characterization of glutathione-dependent oxidoreductases.

Zimmermann, J.[§], Oestreicher, J. [§], Geissel, F., Deponte, M. and Morgan, B.

Free Radical Biology and Medicine. 2021 June; 172, 340-349

DOI: 10.1016/j.freeradbiomed.2021.06.016

[§] Equally contributing authors

Reprinted from *Free Radical Biology and Medicine*: Zimmermann, J., Oestreicher, J., Geissel, F., Deponte, M. and Morgan, B. *An intracellular assay for activity screening and characterization of glutathione-dependent oxidoreductases*. 172, 340-349 © (2021), with permission from Elsevier (*Free Radical Biology and Medicine*, Society of Redox Biology and Medicine).

All rights reserved.



Contents lists available at ScienceDirect

Free Radical Biology and Medicine

journal homepage: www.elsevier.com/locate/freeradbiomed

Original article

An intracellular assay for activity screening and characterization of glutathione-dependent oxidoreductases

Jannik Zimmermann ^{a,1}, Julian Oestreicher ^{a,1}, Fabian Geissel ^b, Marcel Deponte ^{b,*,*}, Bruce Morgan ^{a,*}^a Institute of Biochemistry, Centre for Human and Molecular Biology (ZHMB), Saarland University, 66123 Saarbrücken, Germany^b Faculty of Chemistry, Department of Biochemistry, University of Kaiserslautern, Kaiserslautern, Germany

ARTICLE INFO

ABSTRACT

Keywords:

Glutaredoxin
roGFP2
Glutathione transport
GSNO
Enzyme activity

The thioredoxin fold superfamily is highly diverse and contains many enzymatically active glutathione-dependent thiol-disulfide oxidoreductases, for example glutaredoxins and protein disulfide isomerases. However, many thioredoxin fold proteins remain completely uncharacterized, their cellular function is unknown, and it is unclear if they have a redox-dependent enzymatic activity with glutathione or not. Investigation of enzymatic activity traditionally involved time-consuming *in vitro* characterization of recombinant proteins, limiting the capacity to study novel mechanisms and structure-function relationships. To accelerate our investigation of glutathione-dependent oxidoreductases, we have developed a high-throughput and semi-quantitative assay in yeast. We combined overexpression of the glutathione transporter *OPT1* with genetic fusion constructs between glutathione-dependent oxidoreductases and redox-sensitive green fluorescent protein 2 (roGFP2) to allow the rapid characterization of enzymatic activity with physiological substrates. We show that the kinetics of roGFP2 oxidation by glutathione disulfide correlate well with the *in vitro*-determined activity of the genetically fused glutaredoxins or mutants thereof. Our assay thus allows direct screening of glutaredoxin activity and rapid investigation of structure-function relationships. We also demonstrate that our assay can be used to monitor roGFP2 oxidation by S-nitrosoglutathione (GSNO). We show that glutaredoxins efficiently catalyze oxidation of roGFP2 by GSNO in both live yeast cells and *in vitro*. In summary, we have established a novel assay for activity screening and characterization of glutathione-dependent oxidoreductases.

1. Introduction

The thioredoxin fold superfamily contains a large number of proteins [1,2]. Many members of this family function as enzymatically active thiol-disulfide oxidoreductases or thiol peroxidases, including glutaredoxins, thioredoxins, peroxiredoxins, glutathione peroxidases and protein disulfide isomerases. Other family members are redox-inactive, for example Fe–S cluster-binding glutaredoxins or glutathione transferases [3,4]. Numerous proteins in the thioredoxin superfamily remain uncharacterized and their cellular function is unclear. Often, it is not known if they are enzymatically active or not and, if so, with which substrates [1].

Much of our knowledge regarding the enzymatic activity, mechanism, and structure function-relationships of thioredoxin superfamily

proteins has come from classical protein biochemistry and enzyme kinetics assays performed *in vitro* with recombinant proteins. Nonetheless, many members of the thioredoxin superfamily, for example class III glutaredoxins, have not been possible to purify as recombinant protein to allow for *in vitro* assays to be performed. Therefore, there is a need for novel assays to increase the speed of screening for activity in novel proteins of interest and mutants thereof and to facilitate analyses of proteins that cannot be purified and tested *in vitro*.

We recently developed novel yeast-based assays, using genetic fusion constructs between enzymes and redox-sensitive green fluorescent protein (roGFP2) to allow for the semi-quantitative, high-throughput screening of thiol peroxidase and glutaredoxin activity [5–7]. The kinetics of roGFP2 oxidation were shown to depend upon the activity of the genetically fused glutaredoxin or thiol peroxidase thus allowing for

* Corresponding author.

** Corresponding author.

E-mail addresses: deponte@chemie.uni-kl.de (M. Deponte), bruce.morgan@uni-saarland.de (B. Morgan).¹ These authors contributed equally.

<https://doi.org/10.1016/j.freeradbiomed.2021.06.016>

Received 12 May 2021; Accepted 14 June 2021

Available online 17 June 2021

0891-5849/© 2021 Elsevier Inc. All rights reserved.

semi-quantitative comparison of enzyme activity based on roGFP2 oxidation kinetics [5,6]. We recently employed these approaches, for example in a comparison of enzymatically-active and inactive glutaredoxins, enabling us to identify four protein regions that together contribute to the enzymatic activity of glutaredoxins [5]. Furthermore, roGFP2 fusion constructs, expressed in yeast cells, were used to show that monothiol glutaredoxins can efficiently catalyze roGFP2 oxidation and reduction [7]. Ultimately, *in cellulo* analyses may also permit measurement of the impact of post-translational modifications on redox enzyme activity, which can be extremely challenging to study *in vitro*. A proof-of-principle of this concept was recently provided in the context of monitoring hyperoxidation of the thiol peroxidase *PfAOP* from *Plasmodium falciparum* inside live yeast cells [6].

To date, roGFP2 fusion construct-expressing yeast cells were typically treated with hydrogen peroxide (H_2O_2) to induce the formation of glutathione disulfide (GSSG), which in turn leads to Grx-dependent roGFP2 oxidation. Nonetheless, there are several limitations of this assay, including the high concentrations of external H_2O_2 required to induce roGFP2 oxidation and the unclear mechanism by which H_2O_2 directly or indirectly leads to GSSG formation in yeast. To overcome these issues and to further expand the range of possibilities for *in vivo* screening of redox enzyme activity, here we report on the development of a novel assay allowing for the monitoring of glutaredoxin activity inside living cells in response to a natural substrate, i.e. GSSG. This assay is based upon the overexpression of the gene encoding the plasma membrane glutathione transporter Opt1/Hgt1 in a yeast strain deleted for the genes encoding glutathione reductase, Glt1, and the two active cytosolic dithiol glutaredoxins, Grx1 and Grx2, ($\Delta grx1\Delta grx1\Delta grx2$) [5]. In this genetic background we show that (i) cytosolic roGFP2-Grx fusion constructs respond sensitively to exogenous GSSG, (ii) the kinetics of roGFP2 oxidation depend upon the activity of the genetically fused glutaredoxin, and (iii) the relative roGFP2 oxidation kinetics correlate well with previously determined *in vitro* kinetics and H_2O_2 -dependent *in vivo* roGFP2-Grx oxidation kinetics. Furthermore, we find that this assay can be used to monitor roGFP2 oxidation in response to S-nitroso-glutathione (GSNO). We reveal that GSNO efficiently drives roGFP2 oxidation in a Grx and Opt1-dependent manner, whereas the GSNO reductase Sfa1 had no effect on the GSNO-dependent roGFP2 oxidation. *In vitro* stopped-flow analyses subsequently revealed efficient Grx-mediated catalysis of GSNO-dependent roGFP2 oxidation.

2. Materials and methods

2.1. Growth of yeast cells

All experiments were performed in a *Saccharomyces cerevisiae* YPH499 (*MATa ura3-52 lys2-801_amber ade2-101_ochre trp1-Δ63 his3-Δ200 leu2-Δ1*) yeast strain background [8] unless otherwise stated. Cells were grown in Hartwell complete (HC) media with 2% glucose as carbon source as described previously [6,9]. Appropriate amino acids were omitted when necessary for plasmid selection.

2.2. Transformation of yeast cells

Yeast cells were transformed using a lithium acetate (LiAc)-based method [10]. Briefly, cells were harvested from an overnight culture grown in YPD (1% yeast extract, 2% peptone, 2% glucose) medium, washed once with 1 ml of sterile milliQ-H₂O and resuspended in 100 μl One-Step-Transformation Buffer consisting of 40% polyethylene glycol (*Sigma Aldrich*), 0.2 M lithium acetate (*Sigma Aldrich*) and 0.1 M dithiothreitol (DTT) (*AppliChem*). Subsequently, 5 μl salmon-sperm DNA (ssDNA) (*Sigma Aldrich*) and 300 ng of plasmid DNA were added and cells were incubated at 45 °C with vigorous shaking for 30 min before being streaked out onto HC plates lacking the appropriate amino acid for plasmid selection. Plates were then incubated at 30 °C for 2 days.

2.3. Construction of yeast strains

The $\Delta grx1::natNT2 \Delta grx1::hphNT1 \Delta grx2::kanMX4$ yeast strain used throughout this study was generated previously [5]. To generate a further deletion of *SFA1* in this background a combination of standard homologous recombination-based approach [11] and tetrad dissection was used to generate $\Delta grx1::natNT2 \Delta grx1::hphNT1 \Delta grx2::kanMX4 \Delta sfa1::kanMX4$. Briefly, *SFA1* was replaced in a YPH500 *MATa ura3-52 lys2-801_amber ade2-101_ochre trp1-Δ63 his3-Δ200 leu2-Δ1* strain by transformation of a PCR product amplified from a pre-existing BY4742 *Δsfa1::kanMX4* strain using primers designed to anneal ~500 bp up- and down-stream of the *SFA1* locus. The subsequent YPH500 *Δsfa1::kanMX4* was confirmed by PCR, using primers designed to anneal ~1000 bp up- and down-stream of the *SFA1* locus. The YPH500 *Δsfa1::kanMX4* strain was transformed with an empty p416TEF plasmid to introduce a functional *URA3* gene and subsequently was mated with a YPH499 $\Delta grx1::natNT2 \Delta grx1::hphNT1 \Delta grx2::kanMX4$ strain on YPD agar plates. Subsequently, to select for diploid cells, cells were re-streaked on HC agar plates lacking uracil and supplemented with cloNAT, thus selecting both for the presence of a *natNT2* resistance cassette and a *URA3* gene, which can only be found together in mated diploid cells. After two rounds of diploid selection, and one round of growth in YPD medium, cells were transferred to sporulation medium, consisting of 1% potassium acetate, 0.1% yeast extract and 0.05% glucose, and incubated for 5 days with shaking at 23 °C. Subsequently, 1 ml of culture was centrifuged, washed with 1 ml of sterile milliQ H₂O, and resuspended in 1 ml of 1 M D-sorbitol. Following the addition of ~2 mg of zymolyase 20T (21,900 U/g) tetrads were incubated at 30 °C for 15 min to digest the ascii. Subsequently, 40 μl of treated cells were transferred to a YPD plate and tetrads were dissected using a dissection microscope (*Singer Instruments*). Spores were grown for 3 days and streaked onto antibiotic plates for determination of the spore genotype. Appropriate colonies were confirmed by PCR for all loci as described previously. By tetrad dissection we were able to obtain a $\Delta grx1::hphNT1 \Delta grx2::kanMX4 \Delta sfa1::kanMX4$ strain. *GLR1* was subsequently deleted in this background by homologous recombination using a *natNT2* resistance cassette. All gene deletions were confirmed by PCR using primers to either bind 500 bp up- and down-stream of the gene or primers that bind into the *natNT2* resistance cassette. Finally, cells were plated on HC medium containing 0.1% 5-fluoroorotic acid to counter-select against any cells still containing a p416TEF plasmid.

2.4. Cloning of plasmids

Most plasmids used in this study were published previously [5,7]. To generate p415TEF *OPT1* the *OPT1* coding sequence was PCR amplified from yeast genomic DNA using the forward primer 5'-CTGGACCAC-TAGTATGAGTACCATTTATAGGGAG-3' and the reverse primer 5'-GTCCTATGAGTCGACTTACCACTATTATC-3' designed to insert restriction sites up-stream (*SpeI*) and down-stream (*Sall*) of the gene. Subsequently, the gene was cloned into an empty p415TEF plasmid and confirmed by sequencing (*Eurofins genomics*). For purification of recombinant roGFP2, the sequence encoding roGFP2 was PCR-amplified from a p416TEF *ROGFP2-PfAOP* plasmid [6] using forward primer 5'-GATCCCATGGCTAGCGAGITC-3' and reverse primer 5'-GATCCCT-GAGTTATACAATTCCATCCATACCCAATG-3'. The PCR product was digested and cloned into the *NcoI* and *XbaI* restriction sites of the expression vector pET28 yielding pET28 *ROGFP2*. The correct sequence was confirmed after plasmid minipreparation by analytical restriction digests and by sequencing both strands (*GATC Biotech*).

2.5. Fluorescence-based roGFP2 measurements

Reduction-oxidation sensitive green fluorescent protein 2 (roGFP2) contains two cysteine residues on adjacent β-strands of the GFP β-barrel, directly next to the GFP chromophore. These cysteine residues can form

an intramolecular disulfide bond, which in turn changes the protonation state of the chromophore. The anionic chromophore predominant in reduced roGFP2 exhibits an excitation maximum at ~490 nm, with emission at 510 nm. The neutral chromophore, predominant in oxidized roGFP2, has an excitation maximum at ~400 nm, with emission at 510 nm. The degree of roGFP2 oxidation (OxD) can be calculated according to equation (1) using 20 mM diamide (*Sigma Aldrich*) and 100 mM DTT to generate fully oxidized and fully reduced controls respectively.

Equation (1):

$$O \times D_{roGFP2} = \frac{(I_{400\text{sample}} * I_{480\text{red}}) - (I_{400\text{red}} * I_{480\text{sample}})}{(I_{400\text{sample}} * I_{480\text{red}}) - (I_{400\text{sample}} * I_{480\text{ox}}) + (I_{400\text{ox}} * I_{480\text{sample}}) - (I_{400\text{red}} * I_{480\text{sample}})} \quad (1)$$

Yeast strains used in this study harbor roGFP2 or genetic fusions between roGFP2 and a glutaredoxin expressed in every case from a p416TEF plasmid. Furthermore, they are co-transformed with either an empty p415TEF plasmid or a p415TEF *OPT1* plasmid, encoding a plasma membrane-localized glutathione transporter [12]. A preculture was grown overnight to stationary phase in HC medium lacking uracil and leucine for plasmid selection and containing 2% glucose as carbon source. Strains were then diluted in fresh selective medium and grown for another 19 h to an $OD_{600} \approx 3$. Subsequently, 1.5 OD_{600} units of cells were harvested (where 1 OD_{600} unit equals 1 ml of culture with an $OD_{600} = 1$), resuspended in 1fresh HC medium (lacking leucine and uracil) to a density of 7.5 OD_{600} units/ml and transferred to a flat-bottomed 96-well plate. Cells were then treated with either 100 mM DTT or 20 mM diamide as reduced and oxidized controls respectively or treated with H₂O₂ (*Sigma Aldrich*) at concentrations ranging from 0 to 1000 μ M or GSSG (*Sigma Aldrich*) or GSNO (*Cayman Chemical*) at concentrations ranging from 0 to 100 μ M. Cells transformed with an empty p416TEF plasmid were used for fluorescence background subtraction. Sensor oxidation after treatment was followed over ~15 min using a *BMG Labtech CLARIOstar* fluorescence plate reader.

2.6. DTNB-based whole cell assay

Whole cell glutathione was analyzed using a modified version of a 5,5'-dithiobis-2-nitrobenzoic acid (DTNB) recycling assay as described previously [13]. YPH499 $\Delta glr1\Delta gx1\Delta gx2$ cells, co-transformed with either an empty p415TEF or p415TEF *OPT1* and an empty p416TEF plasmid, were grown in HC medium lacking leucine and uracil for plasmid selection to an $OD_{600} \approx 3.5$. At this point 50 OD_{600} units were harvested to serve as an untreated control. Subsequently, GSSG was added directly to the yeast cell cultures at final concentrations of 0, 25 and 50 μ M. Cultures were incubated at 30 °C, with shaking and 50 OD_{600} unit samples were collected at 5, 15 and 30 min after GSSG addition. All samples were isolated by centrifugation at 1000g for 3 min at room temperature, washed once with 15 ml sterile milliQ H₂O, resuspended in 250 μ l ice-cold SSA/HCl buffer (1.3% sulfosalicylic acid, 8 mM HCl) and stored on ice to be processed together at the end of the experiment. In all samples, ~500 μ l of 0.5 mm glass-beads were then added and cells were mechanically lysed by using a Disruptor Genie (*Scientific industries*) for 3 min, followed by the addition of 100 μ l SSA/HCl buffer and disruption for a further 5 min. After lysis glass beads were removed and cell lysates were collected by centrifugation at 1000g for 3 min. Lysates were kept on ice and incubated for 15 min to allow for protein precipitation. Finally, samples were centrifuged at 16000g for 15 min at 4 °C to remove cell debris and precipitated protein. For determination of "total" cellular glutathione content (defined as GSH + GSSG, where one molecule of GSSG represents two GSH equivalents), 20 μ l of sample was diluted

1:100 in KPE buffer (100 mM potassium phosphate, 5 mM ethylenediaminetetraacetic acid (EDTA), pH 7.5) and transferred to a 96-well plate before the addition of 120 μ l of a 2 mg/ml DTNB and 2 mg/ml NADPH solution. For whole cell glutathione quantification, 20 μ l of serial diluted GSH standards (0.4–26 μ M) were used.

For measurements of the total GSSG content, 100 μ l sample and diluted GSSG standards (0.4–26 μ M) were incubated with 2 μ l 20% (v/v) 2-vinylpyridine in ethanol to alkylate all GSH in the sample. Subsequently, 40 μ l of 1 M MES/Tris pH 7 buffer were added to all samples

and standards to raise the pH, before incubation for 1 h at room temperature. Finally, 20 μ l of samples and standards were mixed with 120 μ l of the DTNB/NADPH mix in a 96-well plate.

For both total glutathione and GSSG measurements, the reaction was started by the addition of glutathione reductase. The change in absorbance of samples and standards at 412 nm was monitored using a *BMG Labtech CLARIOstar*. 'Total' glutathione and GSSG concentrations were determined according to GSH and GSSG concentration standard curves.

2.7. Production and purification of recombinant proteins

Escherichia coli strain BL21 (DE3) was transformed with plasmid pET28 ROGFP2 and selected with kanamycin. Overnight expression of roGFP2 in 1 L LB medium at 16 °C was induced with 0.5 mM isopropyl β-D-thiogalactopyranoside at an OD_{600} of 0.7. Cells were transferred to an ice-water bath, chilled for 10 min, harvested by centrifugation (15 min, 4000g at 4 °C), resuspended in 15 ml ice-cold phosphate buffer (20 mM imidazole, 300 mM NaCl, 50 mM Na₂HPO₄, pH 8.0 at 4 °C) and stored at –20 °C. The thawed suspension was stirred for 1 h on ice with DNaseI and 15 mg lysozyme, followed by sonication and centrifugation (30 min, 10000g at 4 °C). The supernatant was loaded on a column containing 0.5 ml equilibrated nickel-nitrilotriacetic acid agarose (*Qiagen*). Bound C-terminally LEH₆-tagged roGFP2 was washed with 15 column volumes of phosphate buffer and eluted with 1.5 column volumes of ice-cold elution buffer containing 200 mM imidazole, 300 mM NaCl, 50 mM Na₂HPO₄, pH 8.0 at 4 °C. Recombinant N-terminally MRGSH₆GS-tagged PfGrx-C88S and PfGrx-C32S/C88S were produced in *E. coli* strain XI.1-blue using plasmids pQE30 PfGRX-C32S/C88S and pQE30 PfGRX-C88S as described previously [14,15]. Protein eluates containing either purified recombinant roGFP2, PfGrx-C88S or PfGrx-C32S/C88S were incubated for 1 h with 5 mM DTT on ice. Samples were desalted with stopped flow buffer (1 mM EDTA, 100 mM Tris, pH 8.0 at 25 °C) using a PD10 column (*Merck*) and the protein concentration was determined spectrophotometrically at 280 nm using calculated molar extinction coefficients of 9970 and 21890 M^{–1}cm^{–1} for PfGrx and roGFP2, respectively.

2.8. Stopped-flow kinetic measurements

The reaction between GSNO and freshly purified recombinant roGFP2, PfGrx-C88S or PfGrx-C32S/C88S was monitored at 25 °C in a thermostatted SX-20 spectrophluorometer (*Applied Photophysics*). A stock of 20 mM GSNO was prepared freshly in stopped-flow buffer using a molar extinction coefficient $\epsilon_{334\text{nm}}$ of 800 M^{–1}cm^{–1} [16]. The first syringe contained 2 μ M reduced roGFP2 with or without 2 μ M reduced PfGrx-C88S or PfGrx-C32S/C88S in stopped-flow buffer. The second syringe contained 2–200 μ M GSNO in stopped-flow buffer. The roGFP2 fluorescence ($\lambda_{\text{exc}} = 484$ nm, total emission) was detected for up to 500 s after mixing. The averaged fluorescence from three biological replicates

was fitted using the *Applied Photophysics Pro-Data SX* software. Best results were obtained for linear fits of the initial change of fluorescence. Rate constants k_{obs} were subsequently plotted against the substrate concentration in SigmaPlot 13.0, yielding a linear curve for roGFP2 and

hyperbolic curves for the mixture of roGFP2 and *PfGrx-C88S* or *PfGrx-C32S/C88S*. Slopes from linear fits at low and high substrate concentrations of these blots yielded approximate second-order rate constants k_1 and k_2 , respectively.

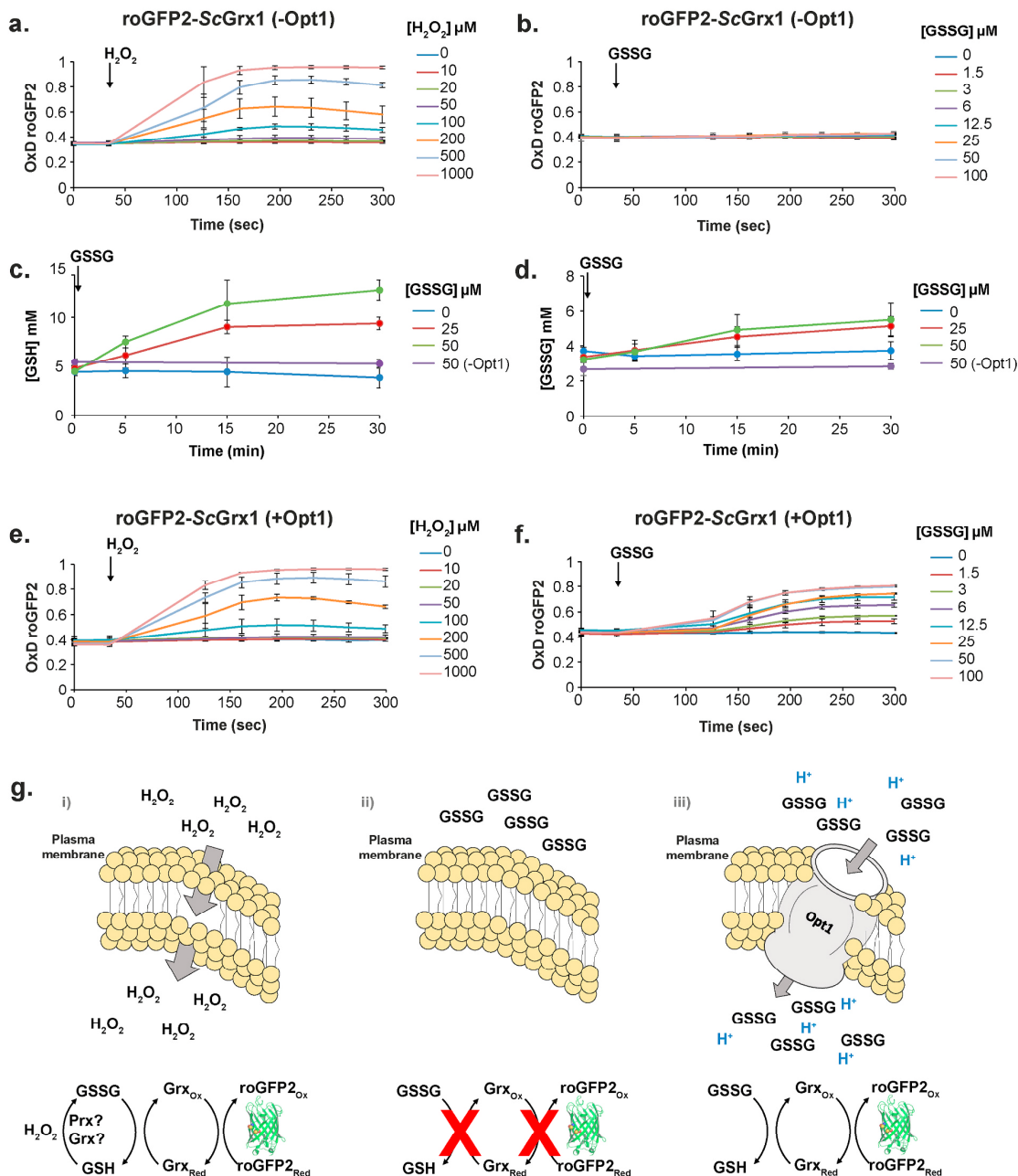


Fig. 1. OPT1 overexpression facilitates cytosolic roGFP2-ScGrx1 oxidation in response to exogenous GSSG.

Cytosolic roGFP2-ScGrx1 oxidation was monitored in YPH499 $\Delta grl1 \Delta grx1 \Delta grx2$ cells following the addition of a. exogenous H_2O_2 or b. exogenous GSSG at the indicated concentrations. c,d. Cellular GSH and GSSG content were measured in YPH499 $\Delta grl1 \Delta grx1 \Delta grx2$ cells containing p415TEF *OPT1* and p416TEF empty vectors at the indicated timepoints after the addition of 0 μM, 25 μM or 50 μM GSSG. GSH and GSSG content were also measured at 0 and 30 min in cells without *OPT1* overexpression as a control. Cytosolic roGFP2-ScGrx1 oxidation was monitored in YPH499 $\Delta grl1 \Delta grx1 \Delta grx2$ cells containing a p415TEF *OPT1* plasmid following the addition of e. exogenous H_2O_2 or f. exogenous GSSG at the indicated concentrations. g. Schematic illustration of the experimental setup. i) Exogenous H_2O_2 readily diffuses across the plasma membrane leading to GSSG formation and subsequently to oxidation of Grx-coupled roGFP2. ii) GSSG is not capable of crossing the plasma membrane. Therefore, roGFP2-ScGrx1 is not responsive to the exogenous addition of GSSG. iii) Overexpression of the proton-coupled symporter, *OPT1*, allows for rapid transport of exogenous GSSG into the cytosol and to subsequent roGFP2-ScGrx1 oxidation. In all figures errors bars represent the standard deviation of at least three independent repeats.

3. Results

3.1. OPT1 overexpression permits roGFP2 oxidation by exogenous GSSG

We asked if it was possible to develop a yeast and roGFP2-based assay that retains the advantages of high-throughput screening as previously described [5–7,17], whilst allowing Grx activity to be monitored in response to a physiological substrate, i.e. GSSG. Nonetheless, it is not possible to directly titrate with GSSG as, in contrast to H_2O_2 , GSSG is membrane impermeable and the plasma membrane-localized GSH/GSSG transporter, Opt1/Hgt1 [12,18], does not permit sufficient GSSG entry under normal conditions (Fig. 1a and b) [19,20].

It was previously shown that overexpression of *OPT1* allows for rapid import and accumulation of intracellular glutathione upon application of exogenous GSH or GSSG [19,20]. We thus asked if we could use *OPT1* overexpression in $\Delta ghr1\Delta grx1\Delta grx2$ cells as a tool to allow us to monitor the activity of glutaredoxins in response to exogenous GSSG. To this end we transformed $\Delta ghr1\Delta grx1\Delta grx2$ cells with a p415TEF *OPT1* plasmid. We subsequently monitored the change in cellular glutathione content over time in response to the addition of 25 or 50 μM GSSG to test that the system was working as previously reported in our genetic background. We observed a rapid, almost three-fold, increase in cellular GSH content following the addition of exogenous GSSG (Fig. 1c). Cellular GSSG content increased slightly after 30 min, whilst no increase in cellular GSSG content was observed after 30 min in control cells without *OPT1* overexpression (Fig. 1d). These observations are consistent with previous reports of the robustness of cytosolic glutathione redox homeostasis [21] and show that the majority of imported GSSG is rapidly reduced to GSH despite the absence of *GLR1*.

We next asked whether cytosolic GSSG levels would increase enough to promote roGFP2 oxidation. To this end, we transformed $\Delta ghr1\Delta grx1\Delta grx2 + p415TEF$ empty and $\Delta ghr1\Delta grx1\Delta grx2 + p415TEF OPT1$ cells with either p416TEF *ROGFP2* or p416TEF *ROGFP2-ScGrx1* plasmids and monitored the roGFP2 response to the exogenous addition of H_2O_2 and GSSG. Unfused roGFP2, i.e. without any genetically linked glutaredoxin, was unresponsive to both exogenous H_2O_2 and GSSG at

concentrations up to 1000 μM and 100 μM respectively (Supplementary Fig. 1a and b). In contrast, in the context of a genetic fusion with Grx1 from *S. cerevisiae*, i.e. roGFP2-*ScGrx1*, we observed roGFP2 oxidation in response to both exogenous H_2O_2 (Fig. 1e) and GSSG (Fig. 1f). Unlike for GSSG, the response to H_2O_2 was independent of *OPT1* expression (compare Fig. 1a and e). These results confirm the Grx-dependence of roGFP2 oxidation [21–26] and reveal sensitive and concentration-dependent roGFP2 oxidation in response to exogenous GSSG at concentrations from 0 to 100 μM (Fig. 1g). In summary, our data show that overexpression of *OPT1* enables Grx-dependent oxidation of cytosolic roGFP2 in response to exogenous GSSG.

3.2. RoGFP2 oxidation kinetics correlate with glutaredoxin activity

We next asked if roGFP2 oxidation kinetics in response to exogenous GSSG correlate with the activity of the genetically fused glutaredoxin, as we have previously shown is the case when using H_2O_2 as the oxidant [5]. To test this, we first turned to fusion constructs between roGFP2 and redox active and redox inactive glutaredoxins, as well as loss- and gain-of-function mutants thereof [5]. We thus transformed $\Delta ghr1\Delta grx1\Delta grx2 + p415TEF OPT1$ cells with p416TEF plasmids encoding either roGFP2-*ScGrx7*, roGFP2-*ScGrx7-K105E*, roGFP2-*HsGrx5* or roGFP2-*HsGrx5-Active* (in which residues G60 to Q66 are removed and replaced by TG, as well as containing the mutations G68P, R97Q and C122S). We subsequently monitored roGFP2 oxidation in each case in response to the addition of H_2O_2 from 0 to 1000 μM (Supplementary Fig. 2) or GSSG from 0 to 100 μM (Fig. 2). We observed rapid oxidation of the roGFP2-*ScGrx7* construct in a GSSG concentration-dependent manner (Fig. 2a), whilst the roGFP2 fusion construct containing the poorly active *ScGrx7-K105E* construct was barely responsive at any GSSG concentration tested (Fig. 2b). No roGFP2 oxidation was seen in the fusion with the redox inactive, Fe-S cluster-binding glutaredoxin, *HsGrx5* (Fig. 2c), whereas some response was observed for the roGFP2 fusion with the enzymatically active *HsGrx5* mutant, *HsGrx5-Active* (Fig. 2d). However, as also previously observed [5], the roGFP2 moiety in this mutant construct is more than

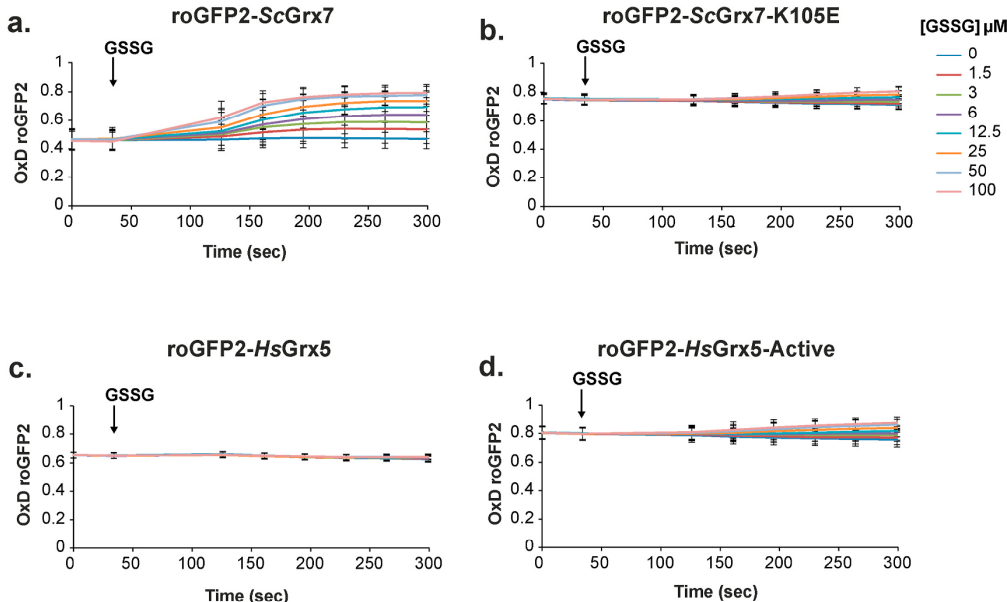


Fig. 2. RoGFP2 oxidation in response to exogenous GSSG requires the presence of an enzymatically active glutaredoxin.

a-d. The indicated roGFP2 fusion constructs were expressed in $\Delta ghr1\Delta grx1\Delta grx2$ cells containing a p415TEF *OPT1* plasmid. RoGFP2 oxidation was monitored following the addition of exogenous GSSG at the indicated concentrations. In all figures error bars represent the standard deviation of at least three independent repeats.

80% oxidized at steady state, which strongly limits further possible roGFP2 oxidation (Fig. 2d). Importantly, the pattern of responses to GSSG was very similar to that observed in response to exogenous H₂O₂ for all constructs (Supplementary Fig. 2).

To overcome the problem of high steady-state roGFP2 oxidation in the roGFP2-HsGrx5 construct, we asked if a DTT pre-treatment, which we previously developed [5], would also be compatible with our Opt1/GSSG assay and allow us to monitor responses in situations where steady-state roGFP2 oxidation is high. Immediately prior to GSSG addition, we treated all cells with 50 mM DTT for 4 min, followed by centrifugation and resuspension in fresh growth medium to remove excess DTT. Subsequently, we monitored roGFP2 oxidation in response to the addition of exogenous GSSG or H₂O₂ (as a control), as above (Fig. 3). We observed almost no response of the roGFP2-HsGrx5 construct to either exogenous H₂O₂ or GSSG, consistent with its lack of enzymatic activity (Fig. 3a and b). In contrast, we were now able to observe oxidation of the roGFP2-HsGrx5-Active construct in response to both exogenous H₂O₂, as previously reported [5], and to GSSG (Fig. 3c and d). Interestingly, at least ten-fold lower GSSG concentrations were sufficient to induce a similar roGFP2 oxidation compared to H₂O₂, and we were able to observe a better concentration dependence of roGFP2 oxidation in response to GSSG. Furthermore, while H₂O₂ treatments required 200–1000 μM H₂O₂, which also resulted in some background oxidation of unfused roGFP2, a linear and robust concentration-dependent response was observed between 1.5 and 100 μM GSSG (Fig. 3e and f).

To further test whether the Opt1/GSSG assays would allow a semi-quantitative analysis of glutaredoxin activity, we tested roGFP2 fusion

constructs with a series of mutants that we have previously shown to exhibit a step-wise change in activity, namely ScGrx7, ScGrx7-Y110F, ScGrx7-Y110H, and ScGrx7-Y110A [5]. We transformed $\Delta grl1\Delta grx1\Delta grx2$ + p415TEF OPT1 cells with p416TEF plasmids encoding the respective roGFP2 fusion constructs and monitored roGFP2 oxidation in response to exogenous GSSG (Fig. 4). We observed a slight increase in the rate of oxidation of the roGFP2-ScGrx7-Y110F construct compared to roGFP2-ScGrx7 (Fig. 4a,b,e), followed by a stepwise decrease in the oxidation kinetics of the roGFP2-ScGrx7-Y110H and roGFP2-ScGrx7-Y110A constructs respectively (Fig. 4c,d,e). These differences in roGFP2 oxidation are consistent with the previously determined differences in activity of these recombinant mutants *in vitro*, and in the context of roGFP2 responses of the corresponding fusion constructs in yeast cells following H₂O₂ treatment [5]. We thus conclude that our Opt1-based assay allows for semi-quantitative screening of glutaredoxin activity, inside living cells, in direct response to a physiological substrate, i.e. GSSG.

3.3. Monitoring roGFP2 oxidation by exogenous GSNO

Finally, we were interested to see if our assay would allow us to investigate the cellular response to other glutathione derivatives. To this end, we investigated the response to GSNO. Interestingly, we observed a sensitive, Opt1- and Grx-dependent roGFP2 response to exogenous GSNO addition (Fig. 5a–c). No response to GSNO was observed in the absence of a fused Grx (Fig. 5a) or in the absence of Opt1 (Fig. 5b). We were thus interested to use this system to learn more about the mechanism of GSNO-mediated protein thiol oxidation *in vivo*. Previous

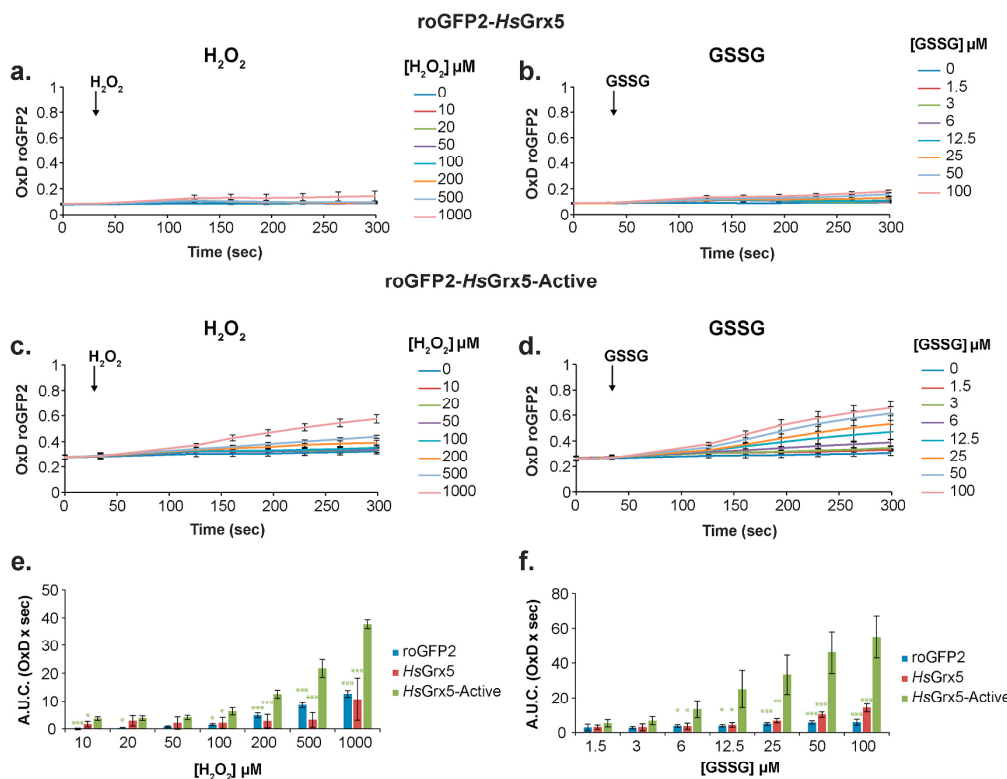


Fig. 3. DTT pre-treatment permits monitoring of constructs with high steady state oxidation.

Cytosolic roGFP2-HsGrx5 probe responses were measured in a $\Delta grl1\Delta grx1\Delta grx2$ cells expressing OPT1 from a p415TEF plasmid in response to a. exogenous H₂O₂ or b. exogenous GSSG applied at the indicated concentrations after DTT pre-treatment and subsequent washout. c,d. as for a,b., but with cells expressing roGFP2-HsGrx5-Active. To quantify roGFP2 responses, the integrated area under the curve (A.U.C.) was calculated for the first 270 s of the probe response to c. exogenous H₂O₂ or f. exogenous GSSG. In all figures errors bars represent the standard deviation of at least three independent repeats. P-values were calculated using a one-way ANOVA followed by a Tukey's HSD test. *P ≤ 0.05, **P ≤ 0.01, ***P ≤ 0.005.

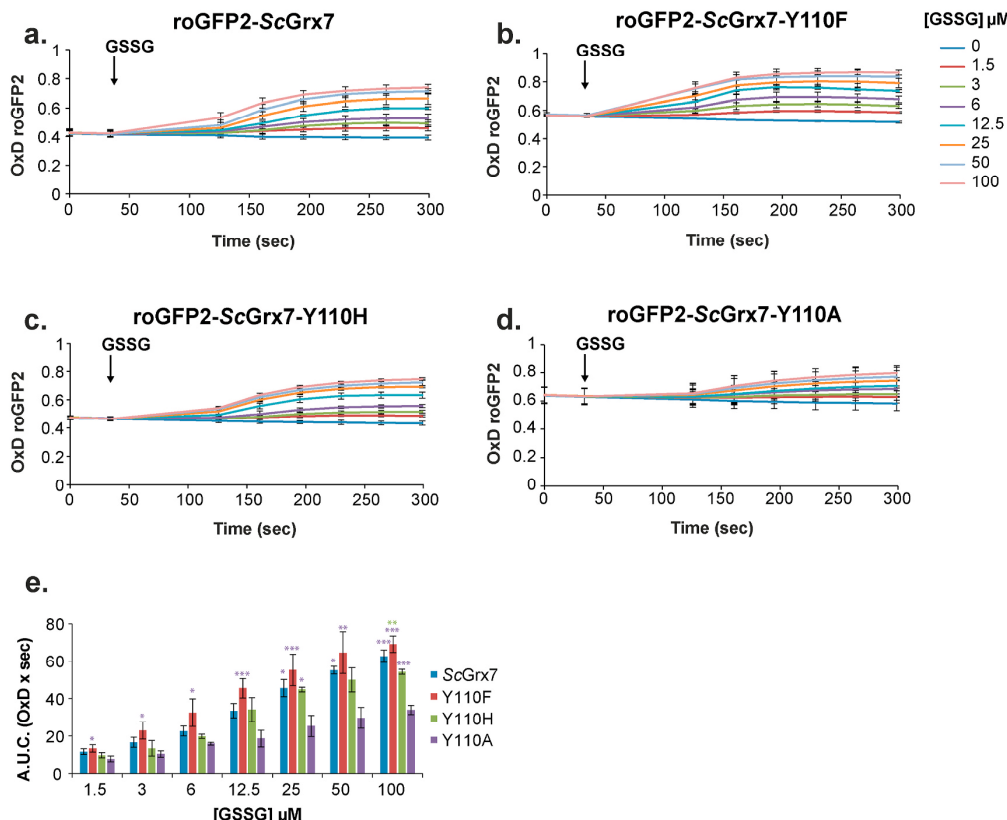


Fig. 4. RoGFP2 oxidation can be used as a semi-quantitative measure of glutaredoxin activity.

a-d. The indicated roGFP2 fusion constructs were expressed in $\Delta glr1\Delta grx1\Delta grx2$ cells containing a p415TEF *OPT1* plasmid. RoGFP2 oxidation in all cases was measured in response to the addition of exogenous GSSG at the indicated concentrations. e. The integrated area under the curve (A.U.C.) was calculated for the first 270 s of the probe response. In all figures errors bars represent the standard deviation of at least three independent repeats. P-values were calculated using a one-way ANOVA followed by a Tukey's HSD test. * $P \leq 0.05$, ** $P \leq 0.01$, *** $P \leq 0.005$.

reports have suggested that the alcohol and formaldehyde dehydrogenase, Sfa1, can function as a GSNO reductase, mediating the rapid conversion of GSNO into GSSG [27]. This led us to hypothesize that GSNO-dependent roGFP2 oxidation may be indirect, i.e. via the production of GSSG. To test this hypothesis, we compared roGFP2-ScGrx1 responses in $\Delta glr1\Delta grx1\Delta grx2$ + p415TEF *OPT1* and $\Delta glr1\Delta grx1\Delta grx2\Delta sfa1$ + p415TEF *OPT1* backgrounds. The loss of *SFA1* did not significantly decrease the roGFP2-ScGrx1 response to GSNO at any concentration tested. On the contrary, with 25 and 100 μM exogenous GSNO, we even observed an apparent slight but significant increase in the roGFP2-ScGrx1 response in the absence of *SFA1* (Fig. 5c–e). Thus, our results indicate that *SFA1* is not required for roGFP2 oxidation in response to GSNO. As a control, we observed that the roGFP2-ScGrx1 response to exogenous GSSG was also independent of the presence of *SFA1* (Fig. 5e and Supplementary Fig. 3). To gain further insight into the mechanism of GSNO-dependent roGFP2 oxidation, we turned to *in vitro* stopped-flow kinetic measurements. GSNO was mixed with either recombinant roGFP2 alone or roGFP2 in combination with the model glutaredoxin *PfGrx* from *Plasmodium falciparum* [15,28,29]. Our analysis revealed that GSNO can directly oxidize roGFP2, with a second order rate constant of $8.6 \times 10^2 M^{-1} s^{-1}$ (Fig. 6a). Interestingly, in the presence of either monothiol *PfGrx-C32S/C88S* or dithiol *PfGrx-C88S*, hyperbolic kinetics were observed, with approximate rate constants at low GSNO concentrations (k_1) of $(1.7 \pm 0.2) \times 10^4 M^{-1} s^{-1}$ and $(7.3 \pm 1.5) \times 10^3 M^{-1} s^{-1}$ and approximate rate constants at high GSNO concentrations (k_2) of $(8.7 \pm 0.3) \times 10^2 M^{-1} s^{-1}$ and $(7.2 \pm 0.4) \times 10^2 M^{-1} s^{-1}$ respectively (Fig. 6b and c). These data indicate that in addition to a

slower, direct oxidation of roGFP2 by GSNO, there is a ten to twenty times faster Grx-dependent oxidation of roGFP2. At high GSNO concentrations, the Grx-dependent oxidation shows saturation behavior, which is masked by the non-enzymatic background reaction between roGFP2 and GSNO. Furthermore, in yeast cells, both dithiol roGFP2-PfGrx and monothiol roGFP2-PfGrx-C32S constructs responded sensitively to GSNO addition (Fig. 6d-f) and to GSSG as a control (Supplementary Fig. 4). Our data thus indicate that both a monothiol and a dithiol glutaredoxin *PfGrx* and the non-related *ScGrx1* can catalyze the GSNO-dependent oxidation of roGFP2. We suggest that in yeast cells, where genetic fusion increases the effective Grx concentration by ~1000-fold from the perspective of the roGFP2 [24], Grx-dependent catalysis underlies roGFP2 oxidation by GSNO.

4. Discussion

Here we report on the development of a novel, cell-based assay, that facilitates the rapid screening of glutaredoxin activity and structure-function relationships in response to GSSG and GSNO. This system is based on the use of roGFP2 fusion constructs expressed in yeast with deletion of the genes encoding glutathione reductase and the two redox-active cytosolic glutaredoxins to facilitate sensitive and specific roGFP2 oxidation. Finally, in this genetic background we overexpressed the gene encoding the plasma membrane transporter Opt1/Hgt1 to promote rapid import of exogenous glutathione derivatives. In principle, this assay should be readily employable to test the ability of any thioredoxin fold superfamily protein to engage in glutathione-dependent catalysis,

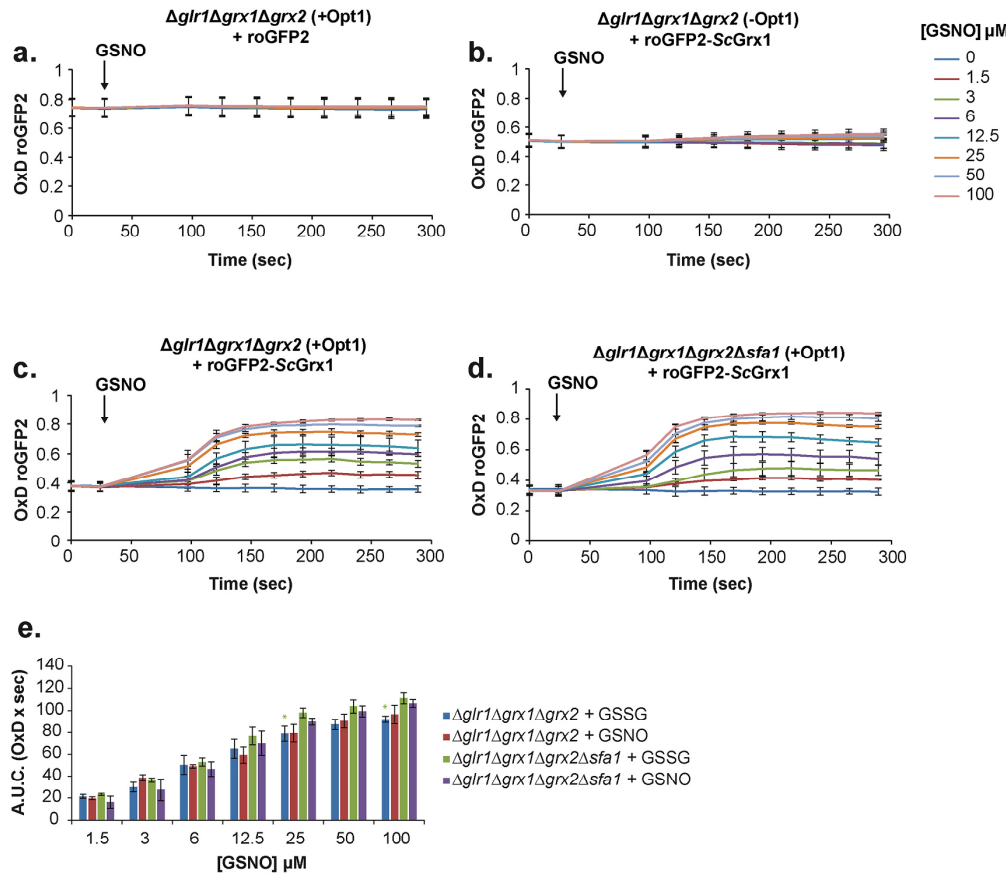


Fig. 5. Exogenous GSNO oxidizes roGFP2 in an Opt1- and Grx-dependent manner.

a. RoGFP2-ScGrx1 oxidation was measured in $\Delta grl1\Delta grx1\Delta grx2$ cells containing an empty p415TEF plasmid in response to exogenous GSNO applied at the indicated concentrations. b. RoGFP2 and c. roGFP2-ScGrx1 oxidation was monitored in $\Delta grl1\Delta grx1\Delta grx2$ cells containing a p415TEF OPT1 plasmid in response to exogenous GSNO applied at the indicated concentrations. d. RoGFP2-ScGrx1 oxidation was monitored in $\Delta grl1\Delta grx1\Delta grx2\Delta sfa1$ cells containing a p415TEF OPT1 plasmid in response to exogenous GSNO applied at the indicated concentrations. e. The integrated A.U.C. was calculated for the first 270 s of the probe response. In all figures errors bars represent the standard deviation of at least three independent repeats. P-values were calculated using a one-way ANOVA followed by a Tukey's HSD test. *P ≤ 0.05, **P ≤ 0.01, ***P ≤ 0.005.

provided that the protein in question can also transfer oxidation to roGFP2. Some obvious candidates for activity and structure-function analyses could include the more than 20 human protein disulfide isomerases, for which glutathione interactions have been reported but, in comparison to other glutathione-dependent redox enzymes, remain to be characterized in much more detail [30–33]. Arguably, in the context of glutathione-dependent catalysis, protein disulfide isomerases are the most poorly understood glutathione-dependent oxidoreductases. A better understanding of the mechanism of GSH and GSSG interaction with PDIs may allow the development of mutants with modified interactions with glutathione. This might finally allow us to untangle the role of glutathione within the ER about which much discussion still remains [31,32,34–37].

The assay that we report here has the advantage of allowing direct titration of the enzyme substrate, i.e. glutathione derivatives. However, it is not the only cell-based assay that has recently been developed to screen the enzymatic activity of thioredoxin fold superfamily proteins. We recently reported an cell viability rescue assay that allows the qualitatively screening for enzyme activity in terms of the ability to reduce ribonucleotide reductase, methionine sulfoxide reductase and phosphoadenosine phosphosulfate (PAPS) reductase [7]. Furthermore, a recent study extended this concept to bacteria, screening the ability of over 100 uncharacterized thioredoxin fold proteins to functionally

rescue $\Delta dsbA$, $\Delta dsbC$ and $\Delta trxA$ *E. coli* mutants [1]. We do not expect cell-based assays to ever completely replace classical *in vitro* enzyme kinetic studies, instead we see them as a complementary approach that has particular utility in screening and the identification of interesting proteins and mutants thereof, for more detailed follow-up studies *in vitro*. Another advantage and future application of our assay could be the analysis of glutathione structure-function relationships. Glutathione interacts with a variety of enzymes via its charged amino and carboxylate groups [3]. Using synthetic glutathione analogs in our assay could help to unravel the relevance of each functional group for a variety of enzymes, provided that the analogs or its mixed disulfides with glutathione are transported by Opt1.

The overexpression of OPT1 allows for efficient transport of both GSSG and GSNO into cells and the study of their impact on roGFP2 oxidation. We observed very similar roGFP2 oxidation sensitivity to GSSG and GSNO with several different genetically fused glutaredoxins. This surprising observation led us to question more deeply the mechanism of GSNO-dependent roGFP2 oxidation. The $K_{0.5}$ of Opt1 for GSSG was reported to be $92 \pm 17 \mu M$ [18], whilst it is not known for GSNO. Nonetheless, given that the $K_{0.5}$ for GSH was reported to be very similar to GSSG at $76 \pm 17 \mu M$ [18], it seems reasonable to assume that Opt1 will have a similar affinity for GSNO. Assuming that GSSG and GSNO enter the cells with similar efficiency, how then does GSNO lead to

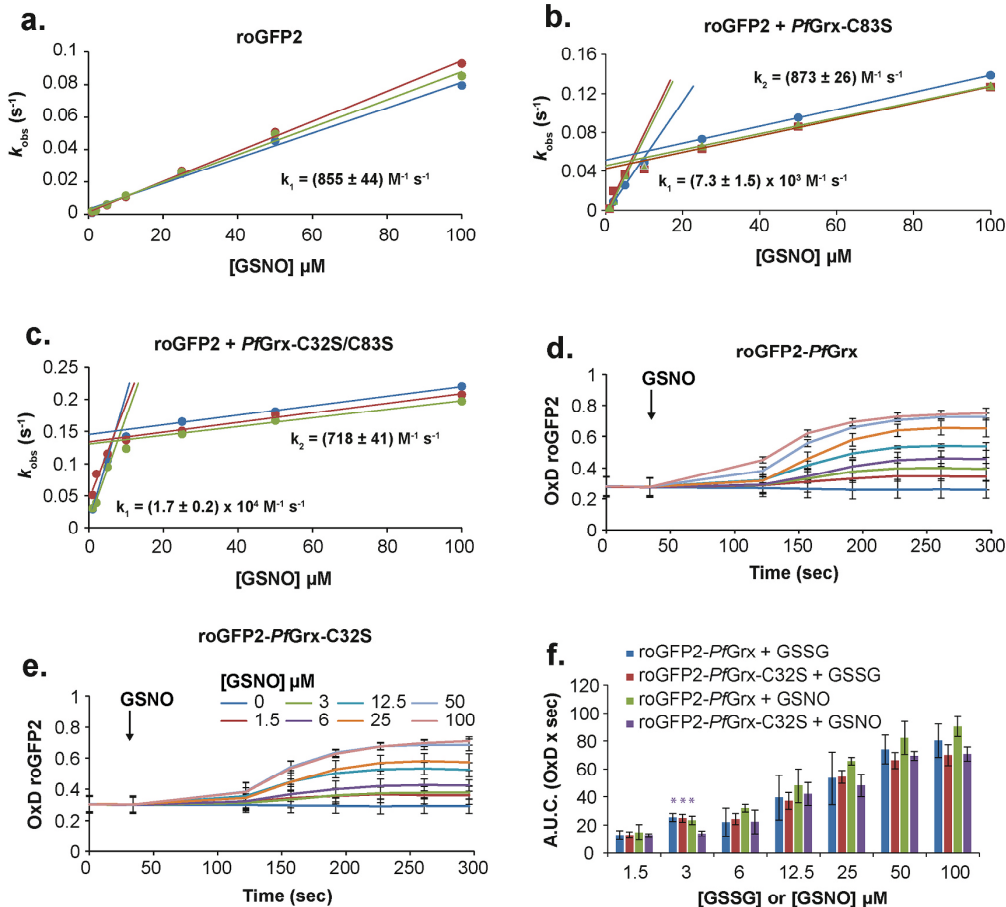


Fig. 6. Monothiol and dithiol glutaredoxins catalyze GSNO-dependent roGFP2 oxidation.

Stopped-flow fluorimetry was used to monitor the oxidation of reduced recombinant roGFP2 by GSNO *in vitro* in a. the absence of recombinant glutaredoxins, b. in the presence of the reduced dithiol glutaredoxin *PfGrx-C88S* and c. in the presence of the reduced monothiol mutant *PfGrx-C32S/C88S*. While direct roGFP2 oxidation kinetics revealed a linear GSNO concentration-dependence, the presence of recombinant *PfGrx* resulted in apparent hyperbolic curves, suggesting a substrate saturation. Approximate rate constants with *PfGrx* were therefore determined at low (k_1) and high (k_2) GSNO concentrations. Data from three independent biological replicates are shown. The response of d. roGFP2-*PfGrx* and e. roGFP2-*PfGrx-C32S* was monitored in *Aglr1Δgrx1Δgrx2* cells containing a p415TEF *OPT1* plasmid in response to exogenous GSNO applied at the indicated concentrations. f. Related to Fig. 6d and e and Supplementary Fig. 4a and b. The integrated A.U.C. was calculated for the first 270 s of the probe response. In all figures errors bars represent the standard deviation of at least three independent repeats. P-values were calculated using a one-way ANOVA followed by a Tukey's HSD test. *P ≤ 0.05, **P ≤ 0.01, ***P ≤ 0.005.

roGFP2 oxidation? One obvious hypothesis would be that the formaldehyde reductase, Sfa1 (also known as alcohol dehydrogenase 5), which also functions as a GSNO reductase [27], would efficiently convert GSNO to GSSG. GSSG would then drive the Grx-dependent oxidation of roGFP2. However, we observed that deleting *SFA1* had no detectable impact upon GSNO-mediated roGFP2 oxidation. Subsequent *in vitro* studies showed that glutaredoxins can directly catalyze the oxidation of roGFP2 by GSNO. Although the rate enhancement was small, i.e. only 10–20 fold, in the context of a genetic fusion, where the effective glutaredoxin concentration is increased by ~1000-fold from the perspective of the roGFP2, this would likely explain the strict Grx-dependence of GSNO-mediated roGFP2 oxidation.

Our observations raise the question of the precise mechanism of glutaredoxin mediated GSNO oxidation. One possibility is that glutaredoxins can function as *S*-transnitrosylases, catalyzing the transfer of an NO group from GSNO to roGFP2. To the best of our knowledge, no such function has been reported for a glutaredoxin to date [38], although mammalian glutaredoxin isoforms were recently reported to be able to function as *S*-denitrosylases [39]. Should a glutaredoxin-catalyzed *S*-transnitrosylation reaction underlie roGFP2 oxidation by GSNO,

then presumably the final step of the reaction would be the formation of an intramolecular disulfide in roGFP2 together with the release of nitroxyl (HNO). A possible alternative might be that GSNO leads to *S*-glutathionylation of the Grx and HNO release. This could occur if the sulfur atom of the GSNO were the target of the nucleophilic attack of the Grx active site cysteine instead of the nitrogen atom of the GSNO. Such a scenario seems more likely considering the conservation of the glutathione scaffold-site and the reaction geometry with glutathione substrates [5,29,40]. In this case, the subsequent reactions leading to the oxidation of roGFP2 would be the same as for GSSG, i.e. transfer of the *S*-glutathionylation from the glutaredoxin to roGFP2 followed by the formation of a roGFP2 disulfide bond and release of GSH. In support of this latter hypothesis, it was previously shown that GSNO leads to *S*-glutathionylation of GrxS12 from *Populus tremula × tremuloides* [41]. The presence of the glutathione scaffold-site in combination with the reaction geometry might indeed explain why GSNO leads to *S*-glutathionylation of glutaredoxins whereas for other known targets it is thought to induce *N*-nitrosylation. These questions and hypotheses will be certainly exciting to investigate further in future studies.

In conclusion, we have developed an in-cell assay that allows high-

throughput, semi-quantitative screening of glutaredoxin activity in response to the physiological substrates GSSG and GSNO.

Acknowledgements

B.M. and M.D. acknowledge generous funding from the Deutsche Forschungsgemeinschaft (DFG) in the framework of the SPP1710 program (MO-2774/2-1 and DE1431/8-2). We thank Robin Schumann for cloning of pET28 ROGFP2.

Appendix A. Supplementary data

Supplementary data to this article can be found online at <https://doi.org/10.1016/j.freeradbiomed.2021.06.016>.

Author contributions

B.M. and M.D. conceived the study, helped design the experiments and wrote the manuscript. J.Z., J.O. and F.G. performed experiments, analyzed data and helped write the manuscript.

References

- [1] S. Nileski, M. Varatnitskaya, T. Masuch, A. Kusnezowa, M. Gellert, A.F. Baumann, N. Lupilov, W. Kusnezow, M.H. Koch, M. Eisenacher, et al., Functional metagenomics of the thioredoxin superfamily, *J. Biol. Chem.* 296 (2021) 100247.
- [2] J.L. Pan, J.C. Bardwell, The origami of thioredoxin-like folds, *Protein Sci.* 15 (2006) 2217–2227.
- [3] M. Deponte, Glutathione catalysis and the reaction mechanisms of glutathione-dependent enzymes, *Biochim. Biophys. Acta* 1830 (2013) 3217–3266.
- [4] M. Deponte, The incomplete glutathione puzzle: just guessing at numbers and figures? *Antioxidants Redox Signal.* 27 (2017) 1130–1161.
- [5] L. Liedgens, J. Zimmermann, L. Waschenbach, F. Geissel, H. Laporte, H. Gohlke, B. Morgan, M. Deponte, Quantitative assessment of the determinant structural differences between redox-active and inactive glutaredoxins, *Nat. Commun.* 11 (2020) 1725.
- [6] V. Staudacher, M. Trujillo, T. Diederichs, T.P. Dick, R. Radi, B. Morgan, M. Deponte, Redox-sensitive GFP fusions for monitoring the catalytic mechanism and inactivation of peroxiredoxins in living cells, *Redox Biol.* 14 (2018) 549–556.
- [7] J. Zimmermann, J. Oestreicher, S. Hess, J.M. Hermann, M. Deponte, B. Morgan, One cysteine is enough: a monothiol Grx can functionally replace all cytosolic Trx and diithiol Grx, *Redox Biol.* 36 (2020) 101598.
- [8] R.S. Sikorski, P. Hietter, A system of shuttle vectors and yeast host strains designed for efficient manipulation of DNA in *Saccharomyces cerevisiae*, *Genetics* 122 (1989) 19–27.
- [9] B. Morgan, M.C. Sobotta, T.P. Dick, Measuring E(GSH) and H2O2 with roGFP2-based redox probes, *Free Radic. Biol. Med.* 51 (2011) 1943–1951.
- [10] R.D. Gietz, R.A. Woods, Transformation of yeast by lithium acetate/single-stranded carrier DNA/polyethylene glycol method, *Methods Enzymol.* 350 (2002) 87–96.
- [11] C. Janke, M.M. Magiera, N. Rathfelder, C. Taxis, S. Reber, H. Maekawa, A. Moreno-Borchart, G. Doenges, E. Schwob, E. Schieberl, et al., A versatile toolbox for PCR-based tagging of yeast genes: new fluorescent proteins, more markers and promoter substitution cassettes, *Yeast* 21 (2004) 947–962.
- [12] A. Bourbouloux, P. Shahi, A. Chakladar, S. Delrot, A.K. Bachhawat, Hgt1p, a high affinity glutathione transporter from the yeast *Saccharomyces cerevisiae*, *J. Biol. Chem.* 275 (2000) 13259–13265.
- [13] I. Rahman, A. Kode, S.K. Biswas, Assay for quantitative determination of glutathione and glutathione disulfide levels using enzymatic recycling method, *Nat. Protoc.* 1 (2006) 3159–3165.
- [14] M. Urscher, S.S. More, R. Alisch, R. Vince, M. Deponte, Tight-binding inhibitors efficiently inactivate both reaction centers of monomeric Plasmodium falciparum glyoxalase 1, *FEBS J.* 279 (2012) 2568–2578.
- [15] C.F. Djuika, S. Fiedler, M. Schnolzer, C. Sanchez, M. Lanzer, M. Deponte, Plasmodium falciparum antioxidant protein as a model enzyme for a special class of glutaredoxin/glutathione-dependent peroxiredoxins, *Biochim. Biophys. Acta* 1830 (2013) 4073–4090.
- [16] S.P. Singh, J.S. Wishnok, M. Keshive, W.M. Deen, S.R. Tannenbaum, The chemistry of the S-nitrosoglutathione/glutathione system, *Proc. Natl. Acad. Sci. U. S. A.* 93 (1996) 14428–14433.
- [17] B. Morgan, K. Van Laer, T.N. Owusu, D. Ezerina, D. Pastor-Flores, P.S. Ampsonah, A. Tursch, T.P. Dick, Real-time monitoring of basal H2O2 levels with peroxiredoxin-based probes, *Nat. Chem. Biol.* 12 (2016) 437–443.
- [18] H. Osawa, G. Stacey, W. Gassmann, ScOPT1 and AtOPT4 function as proton-coupled oligopeptide transporters with broad but distinct substrate specificities, *Biochem. J.* 393 (2006) 267–275.
- [19] A.J. Ponsero, A. Igbaria, M.A. Darch, S. Miled, C.E. Outten, J.R. Winther, G. Palais, B. D'Autreux, A. Delaunay-Moisan, M.B. Toledano, Endoplasmic reticulum transport of glutathione by Sec61 is regulated by Ero1 and bip, *Mol. Cell.* 67 (2017) 962–973, e965.
- [20] C. Kumar, A. Igbaria, B. D'Autreux, A.G. Planson, C. Junot, E. Godat, A. K. Bachhawat, A. Delaunay-Moisan, M.B. Toledano, Glutathione revisited: a vital function in iron metabolism and ancillary role in thiol-redox control, *EMBO J.* 30 (2011) 2044–2056.
- [21] B. Morgan, D. Ezerina, T.N. Amoako, J. Riemer, M. Seedorf, T.P. Dick, Multiple glutathione disulfide removal pathways mediate cytosolic redox homeostasis, *Nat. Chem. Biol.* 9 (2013) 119–125.
- [22] M. Gutschner, A.L. Pauleau, L. Marty, T. Brach, G.H. Wabnitz, Y. Samstag, A. J. Meyer, T.P. Dick, Real-time imaging of the intracellular glutathione redox potential, *Nat. Methods* 5 (2008) 553–559.
- [23] A.J. Meyer, T. Brach, L. Marty, S. Kreys, N. Rouhier, J.P. Jacquot, R. Hell, Redox-sensitive GFP in *Arabidopsis thaliana* is a quantitative biosensor for the redox potential of the cellular glutathione redox buffer, *Plant J.* 52 (2007) 973–986.
- [24] A.J. Meyer, T.P. Dick, Fluorescent protein-based redox probes, *Antioxidants Redox Signal.* 13 (2010) 621–650.
- [25] H. Ostergaard, C. Tachibana, J.R. Winther, Monitoring disulfide bond formation in the eukaryotic cytosol, *J. Cell Biol.* 166 (2004) 337–345.
- [26] M. Schwarzenbauer, T.P. Dick, A.J. Meyer, B. Morgan, Dissecting redox biology using fluorescent protein sensors, *Antioxidants Redox Signal.* 24 (2016) 680–712.
- [27] L. Liu, A. Hausladen, M. Zeng, L. Que, J. Heitman, J.S. Stamler, A metabolic enzyme for S-nitrosothiol conserved from bacteria to humans, *Nature* 410 (2001) 490–494.
- [28] P. Begas, V. Staudacher, M. Deponte, Systematic re-evaluation of the bis(2-hydroxyethyl)disulfide (HEDS) assay reveals an alternative mechanism and activity of glutaredoxins, *Chem. Sci.* 6 (2015) 3788–3796.
- [29] P. Begas, L. Liedgens, A. Moseler, A.J. Meyer, M. Deponte, Glutaredoxin catalysis requires two distinct glutathione interaction sites, *Nat. Commun.* 8 (2017) 14835.
- [30] A.K. Lappi, L.W. Ruddock, Reexamining of the role of interplay between glutathione and protein disulfide isomerase, *J. Mol. Biol.* 409 (2011) 238–249.
- [31] C.E. Jessop, N.J. Bulleid, Glutathione directly reduces an oxidoreductase in the endoplasmic reticulum of mammalian cells, *J. Biol. Chem.* 279 (2004) 55341–55347.
- [32] S. Chakravarthi, N.J. Bulleid, Glutathione is required to regulate the formation of native disulfide bonds within proteins entering the secretory pathway, *J. Biol. Chem.* 279 (2004) 39872–39879.
- [33] R.P.P. Neves, P.A. Fernandes, M.J. Ramos, Mechanistic insights on the reduction of glutathione disulfide by protein disulfide isomerase, *Proc. Natl. Acad. Sci. U. S. A.* 114 (2017) E4724–E4733.
- [34] S. Tsunoda, E. Avezov, Z. Zryanova, T. Konno, L. Mendes-Silva, E. Pinho Melo, H. P. Harding, D. Ron, Intact protein folding in the glutathione-depleted endoplasmic reticulum implicates alternative protein thiol reductants, *Elife* 3 (2014) e03421.
- [35] M.B. Toledano, M.E. Huang, The unfinished puzzle of glutathione physiological functions, an old molecule that still retains many enigmas, *Antioxidants Redox Signal.* 27 (2017) 1127–1129.
- [36] A. Delaunay-Moisan, A. Ponsero, M.B. Toledano, Reexamining the function of glutathione in oxidative protein folding and secretion, *Antioxidants Redox Signal.* 27 (2017) 1178–1199.
- [37] C. Hwang, A.J. Sinskey, H.F. Lodish, Oxidized redox state of glutathione in the endoplasmic reticulum, *Science* 257 (1992) 1496–1502.
- [38] E. Kalinina, M. Novichkova, Glutathione in protein redox modulation through S-glutathionylation and S-nitrosylation, *Molecules* 26 (2021).
- [39] X. Ren, R. Sengupta, J. Lu, J.O. Lundberg, A. Holmgren, Characterization of mammalian glutaredoxin isoforms as S-denitrosylases, *FEBS Lett.* 593 (2019) 1799–1806.
- [40] E. Eckers, M. Bien, V. Stroobant, J.M. Herrmann, M. Deponte, Biochemical characterization of diithiol glutaredoxin 8 from *Saccharomyces cerevisiae*: the catalytic redox mechanism redux, *Biochemistry* 48 (2009) 1410–1423.
- [41] M. Zaffagnini, M. Bedhomme, C.H. Marchand, J.R. Couturier, X.H. Gao, N. Rouhier, P. Trost, S.P. Lemaire, Glutaredoxin s12: unique properties for redox signaling, *Antioxidants Redox Signal.* 16 (2012) 17–32.

2.2.1. Supplementary information

An intracellular assay for activity screening and characterization of glutathione-dependent oxidoreductases.

Zimmermann, J.[§], Oestreicher, J. [§], Geissel, F., Deponte, M. and Morgan, B.

Free Radical Biology and Medicine 2021 June; 172, 340-349

DOI: 10.1016/j.freeradbiomed.2021.06.016

[§] Equally contributing authors

Reprinted from *Free Radical Biology and Medicine*: Zimmermann, J., Oestreicher, J., Geissel, F., Deponte, M. and Morgan, B. *An intracellular assay for activity screening and characterization of glutathione-dependent oxidoreductases*. 172, 340-349 © (2021), with permission from Elsevier (*Free Radical Biology and Medicine*, Society of Redox Biology and Medicine).

All rights reserved.

Supplementary Information

A novel assay for the *in vivo* characterization of glutathione-dependent enzymes

Jannik Zimmermann^{1†}, Julian Oestreicher^{1†}, Fabian Geissel², Marcel Deponte^{2*} and Bruce Morgan^{1*}

Affiliations:

¹ Institute of Biochemistry, Centre for Human and Molecular Biology (ZHMB), Saarland University, 66123 Saarbrücken, Germany

² Faculty of Chemistry, Department of Biochemistry, University of Kaiserslautern, Kaiserslautern, Germany

[†] These authors contributed equally.

*To whom correspondence should be addressed

Prof. Dr. Bruce Morgan

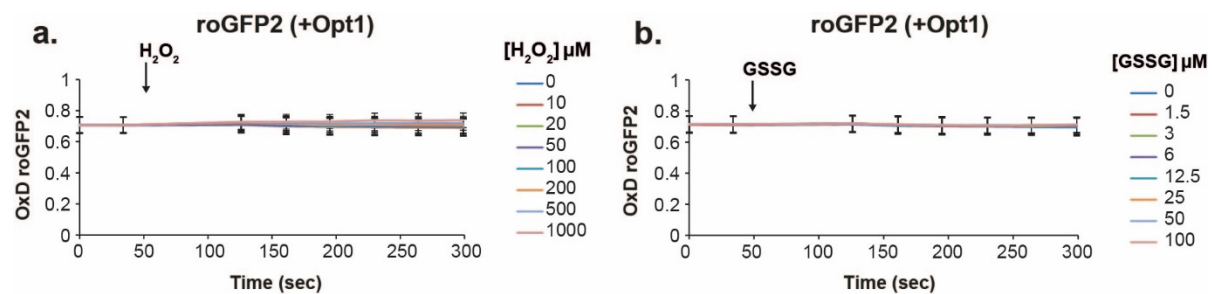
Tel.: +49-631-205-2885

Email: [bruce.morgan@uni-saarland.de](mailto;bruce.morgan@uni-saarland.de)

Prof. Dr. Marcel Deponte

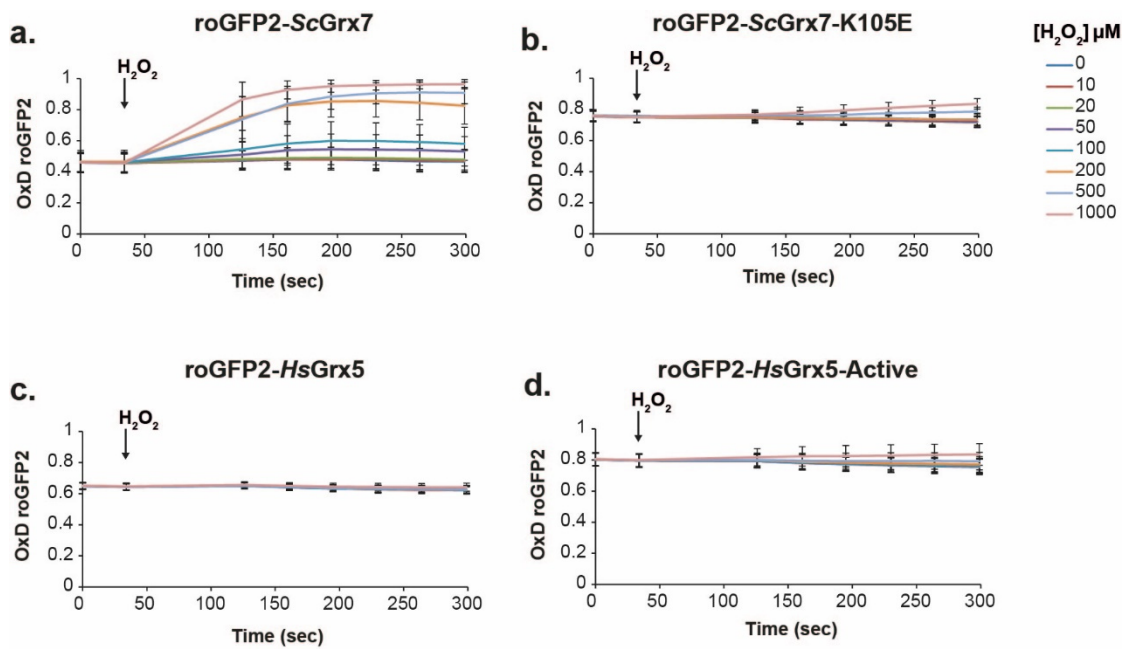
Tel.: +49-6841-205-4060

Email: deponte@chemie.uni-kl.de



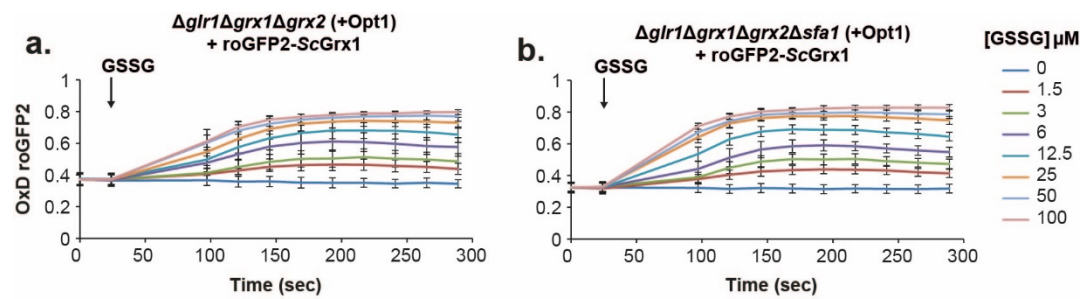
Supplementary Figure 1. Redox-active glutaredoxins are required to facilitate roGFP2 oxidations by exogenous H₂O₂ or GSSG

RoGFP2 oxidation was monitored in YPH499 Δ grl1 Δ grx1 Δ grx2 cells containing a p415TEF OPT1 plasmid following the addition of **a.** exogenous H₂O₂ or **b.** exogenous GSSG at the indicated concentrations.



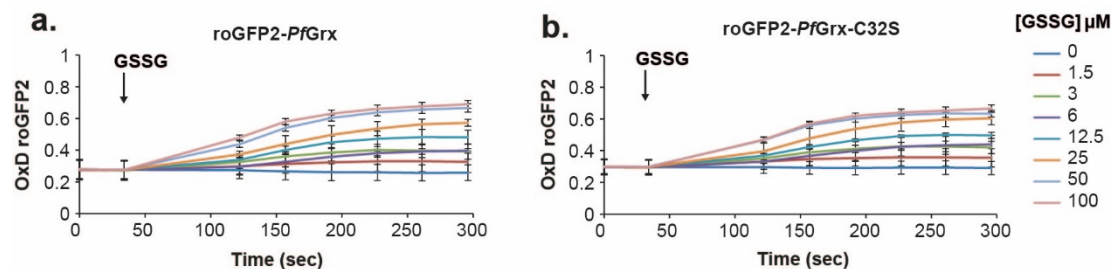
Supplementary Figure 2. RoGFP2 oxidation is dependent upon the presence of a catalytically active glutaredoxin.

a-d. The indicated roGFP2 fusion constructs were expressed in YPH499 $\Delta glr1\Delta grx1\Delta grx2$ cells containing a p415TEF *OPT1* plasmid. RoGFP2 oxidation was monitored following the addition of exogenous H_2O_2 at the indicated concentrations.



Supplementary Figure 3. SFA1 does not affect the response to roGFP2-ScGrx1 to exogenous GSSG

RoGFP2-ScGrx1 oxidation was measured in **a.** $\Delta glr1\Delta grx1\Delta grx2$ or **b.** $\Delta glr1\Delta grx1\Delta grx2\Delta sfa1$ cells, both transformed with a p415TEF *OPT1* plasmid, following the addition of exogenous GSSG at the indicated concentrations.



Supplementary Figure 4. A monothiol mutant of PfGrx efficiently catalyzes roGFP2 oxidation in response to exogenous GSSG treatment.

The oxidation of **a.** roGFP2-PfGrx and **b.** roGFP2-PfGrx-C32S was monitored in $\Delta glr1\Delta grx1\Delta grx2$ cells, containing a p415TEF OPT1 plasmid, following the addition of exogenous GSSG at the indicated concentrations.

Supplementary Table 1. Yeast strains used in this study

Genotype	Source	Figure
YPH499 $\Delta glr1::natNT2 \Delta grx1::hphNT1 \Delta grx2::kanMX4$ + p415TEF empty + p416TEF empty	Liedgens 2020 This study	1c,d
YPH499 $\Delta glr1::natNT2 \Delta grx1::hphNT1 \Delta grx2::kanMX4$ + p415TEF OPT1 + p416TEF empty	Liedgens 2020 This study	1a-f; 2; 3a-d; 4a-d; 5a-d; 6d,e
YPH499 $\Delta glr1::natNT2 \Delta grx1::hphNT1 \Delta grx2::kanMX4$ + p415TEF empty + p416TEF roGFP2-ScGrx1	Liedgens 2020 This study	1a,b; 5b
YPH499 $\Delta glr1::natNT2 \Delta grx1::hphNT1 \Delta grx2::kanMX4$ + p415TEF OPT1 + p416TEF roGFP2-ScGrx1	Liedgens 2020 This study	1e,f; 5c; S3a
YPH499 $\Delta glr1::natNT2 \Delta grx1::hphNT1 \Delta grx2::kanMX4$ + p415TEF OPT1 + p416TEF roGFP2	Liedgens 2020 This study	5a; S1
YPH499 $\Delta glr1::natNT2 \Delta grx1::hphNT1 \Delta grx2::kanMX4$ + p415TEF OPT1 + p416TEF roGFP2-ScGrx7	Liedgens 2020 This study	2a; 4a; S2a
YPH499 $\Delta glr1::natNT2 \Delta grx1::hphNT1 \Delta grx2::kanMX4$ + p415TEF OPT1 + p416TEF roGFP2-ScGrx7-K105E	Liedgens 2020 This study	2b; S2b
YPH499 $\Delta glr1::natNT2 \Delta grx1::hphNT1 \Delta grx2::kanMX4$ + p415TEF OPT1 + p416TEF roGFP2-ScGrx7-Y110F	Liedgens 2020 This study	4b
YPH499 $\Delta glr1::natNT2 \Delta grx1::hphNT1 \Delta grx2::kanMX4$ + p415TEF OPT1 + p416TEF roGFP2-ScGrx7-Y110H	Liedgens 2020 This study	4c
YPH499 $\Delta glr1::natNT2 \Delta grx1::hphNT1 \Delta grx2::kanMX4$ + p415TEF OPT1 + p416TEF roGFP2-ScGrx7-Y110A	Liedgens 2020 This study	4d
YPH499 $\Delta glr1::natNT2 \Delta grx1::hphNT1 \Delta grx2::kanMX4$ + p415TEF OPT1 + p416TEF roGFP2-HsGrx5	Liedgens 2020 This study	2c; 3,b; S2c
YPH499 $\Delta glr1::natNT2 \Delta grx1::hphNT1 \Delta grx2::kanMX4$ + p415TEF OPT1 + p416TEF roGFP2-HsGrx5-Active	Liedgens 2020 This study	2d; 3c,d; S2d
YPH499 $\Delta glr1::natNT2 \Delta grx1::hphNT1 \Delta grx2::kanMX4$ + p415TEF OPT1 + p416TEF roGFP2-PfGrx	Liedgens 2020 This study	6d; S4a
YPH499 $\Delta glr1::natNT2 \Delta grx1::hphNT1 \Delta grx2::kanMX4$ + p415TEF OPT1 + p416TEF roGFP2-PfGrx-C32S	Liedgens 2020 This study	6e; S4b
YPH499 $\Delta glr1::natNT2 \Delta grx1::hphNT1 \Delta grx2::kanMX4$ $\Delta sfa1::kanMX4$ + p415TEF OPT1 + p416TEF roGFP2-ScGrx1	This study	5d; S3b

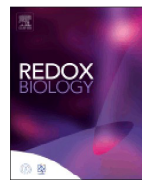
2.3. Zimmermann et al., 2020, *Redox Biology*

One cysteine is enough: A monothiol Grx can functionally replace all cytosolic Trx and dithiol Grx.

Zimmermann, J., Oestreicher, J., Hess, S., Herrmann, J.M., Deponte, M. and Morgan, B.
Redox Biology. 2020 May; 101598
DOI: 10.1016/j.redox.2020.101598

Reprinted from *Redox Biology*: Zimmermann, J., Oestreicher, J., Hess, S., Herrmann, J.M., Deponte, M. and Morgan, B. *One cysteine is enough: A monothiol Grx can functionally replace all cytosolic Trx and dithiol Grx.* 101598 © (2020), with permission from Elsevier (*Redox Biology, Society of Redox Biology and Medicine*).

All rights reserved.



One cysteine is enough: A monothiol Grx can functionally replace all cytosolic Trx and dithiol Grx



Jannik Zimmermann^a, Julian Oestreicher^a, Steffen Hess^b, Johannes M. Herrmann^b, Marcel Deponte^{c,**,}, Bruce Morgan^{a,*}

^a Institute of Biochemistry, Zentrum für Human- und Molekulärbiologie (ZHMB), Saarland University, Saarbrücken, Germany

^b Cell Biology, University of Kaiserslautern, Kaiserslautern, Germany

^c Faculty of Chemistry, Department of Biochemistry, University of Kaiserslautern, Kaiserslautern, Germany

ARTICLE INFO

Keywords:
 Glutaredoxins
 Protein disulfide
 Redox catalysis
 roGFP2
 Thioredoxins

ABSTRACT

Glutaredoxins are small proteins of the thioredoxin superfamily that are present throughout life. Most glutaredoxins fall into two major subfamilies. Class I glutaredoxins are glutathione-dependent thiol-disulfide oxidoreductases whilst class II glutaredoxins coordinate Fe–S clusters. Class I glutaredoxins are typically dithiol enzymes with two active-site cysteine residues, however, some enzymatically active monothiol glutaredoxins are also known. Whilst both monothiol and dithiol class I glutaredoxins mediate protein deglutathionylation, it is widely claimed that only dithiol glutaredoxins are competent to reduce protein disulfide bonds. In this study, using a combination of yeast ‘viability rescue’, growth, and redox-sensitive GFP-based assays, we show that two different monothiol class I glutaredoxins can each facilitate the reduction of protein disulfide bonds in ribonucleotide reductase, methionine sulfoxide reductase and roGFP2. Our observations thus challenge the generalization of the dithiol mechanism for glutaredoxin catalysis and raise the question of why most class I glutaredoxins have two active-site cysteine residues.

1. Introduction

Glutaredoxins are glutathione-interacting members of the thioredoxin superfamily and are found throughout life. Glutaredoxins can be broadly separated into two highly abundant major subfamilies, termed class I and II glutaredoxins, as well as less prevalent smaller subfamilies [1,2]. Class I glutaredoxins are enzymatically active thiol-disulfide oxidoreductases that use reduced glutathione (GSH) as a co-substrate to facilitate disulfide reduction [3–5]. Class II glutaredoxins bind Fe–S clusters and usually have little or no oxidoreductase activity [6–8]. Class I glutaredoxins, together with thioredoxins, are important for reducing disulfide bonds that are formed as part of the catalytic mechanism of several cytosolic and nuclear enzymes including ribonucleotide reductase [9,10], peroxiredoxins (Prx) [11–15], methionine sulfoxide reductase [16,17], arsenate reductase [18], sulfiredoxin [19] and 3'-phosphoadenosine 5'-phosphosulfate reductase (PAPS reductase) [20,21] (Fig. 1a). Furthermore, class I glutaredoxins can reduce regulatory protein disulfide bonds, for example in the transcription factor OxyR [22] and the collapsin response mediator protein 2 [23,24]. The relative importance of the thioredoxins and glutaredoxins for protein

disulfide reduction appears to vary between different substrates and different organisms. Whilst, ribonucleotide reductase from *Escherichia coli* can be reduced by either thioredoxins or the *E. coli* Grx1 [9,10], PAPS reductase in yeast can only be reduced by thioredoxins [25].

Class I glutaredoxins typically contain two active-site cysteine residues, for example in a CPYC motif [1,5]. However, there are examples of class I glutaredoxins that have only one active-site cysteine residue yet are enzymatically active in *in vitro* assays [26–30]. In contrast, class II glutaredoxins usually contain one active-site cysteine residue, for example in a CGFS motif [2]. The terms ‘dithiol’ and ‘monothiol’ glutaredoxin have sometimes been used as alternative names for class I and class II glutaredoxins. However, given that examples of both monothiol and dithiol class I glutaredoxins are known, here we use the terms ‘monothiol’ and ‘dithiol’ strictly to delineate between glutaredoxins containing either one or two active-site cysteine residues respectively.

Interestingly, several *in vitro* studies have demonstrated that dithiol class I glutaredoxins mutated for their second cysteine residue retain enzymatic activity or become even more active [12,31–35]. This raises the question of why most class I glutaredoxins have two active-site cysteine residues. In general, glutaredoxins can catalyze both protein

* Corresponding author.

** Corresponding author.

E-mail addresses: deponte@chemie.uni-kl.de (M. Deponte), bruce.morgan@uni-saarland.de (B. Morgan).

<https://doi.org/10.1016/j.redox.2020.101598>

Received 7 April 2020; Received in revised form 20 May 2020; Accepted 26 May 2020

Available online 31 May 2020

2213-2317/ © 2020 The Authors. Published by Elsevier B.V. This is an open access article under the CC BY-NC-ND license (<http://creativecommons.org/licenses/by-nc-nd/4.0/>).

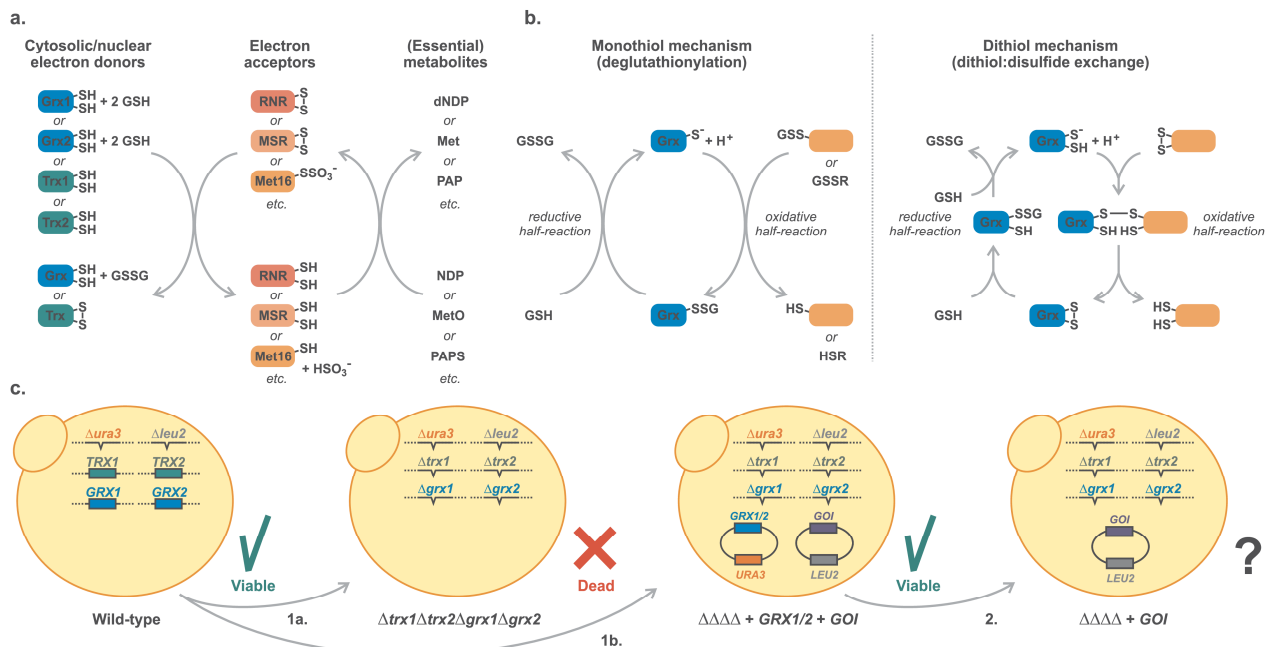


Fig. 1. Relevance and analysis of the cytosolic glutaredoxin and thioredoxin systems in yeast.

a. *Saccharomyces cerevisiae* has two major cytosolic thiol-disulfide oxidoreductase systems consisting of two thioredoxins (Trx1/2) as well as two dithiol class I glutaredoxins (Grx1/2) and reduced glutathione (GSH). Both systems donate electrons to a variety of enzymes such as ribonucleotide reductases (RNR), methionine sulfoxide reductases (MSR) and PAPS reductase (Met16). These and other enzymes catalyze the reduction of nucleoside diphosphates (NDP), methionine sulfoxide (MetO), 3'-phosphoadenosine 5'-phosphosulfate (PAPS) or other metabolites, yielding, for example, essential precursors for DNA or protein synthesis. b. One cysteine residue of class I glutaredoxins suffices to catalyze the reduction of glutathionylated substrates (left panel). In contrast, protein disulfide reduction has been claimed to require both active-site cysteine residues of class I glutaredoxins (right panel). c. Plasmid-shuffling experiments allow rapid structure-function analyses of a gene of interest (GOI) in yeast. First, relevant genes are knocked out (1a.). To ensure viability and to test the function of the GOI, yeast cells are complemented with an episomal copy of an essential gene as well as the GOI on another plasmid (1b.). After negative selection against the plasmid with the essential gene, cell growth fully relies on the GOI and can only occur if it functionally replaces the essential gene (2.).

deglutathionylation and protein disulfide reduction (Fig. 1b). Protein deglutathionylation can theoretically occur via a dithiol or a monothiol mechanism involving either both cysteine residues or only the more N-terminal of the active-site cysteine residues respectively. However, numerous studies showed that the monothiol reaction is more efficient: The dithiol mechanism is therefore usually considered as a side reaction for deglutathionylation reactions [1,12,33,34,36,37]. In contrast to protein deglutathionylation, protein disulfide reduction was widely claimed to require both active-site cysteine residues and to occur via a dithiol mechanism as reported for *E. coli* ribonucleotide reductase and PAPS reductase [21,38] as well as poplar PrxII and human Prx3 [13,39] (Fig. 1b). Nonetheless, mammalian ribonucleotide reductase can be reduced by a monothiol mechanism [32]. Furthermore, recent *in vitro* studies with a metal-binding domain as a protein disulfide substrate also challenged the dithiol mechanism and suggested an alternative monothiol mechanism that includes a GSH-dependent reduction of Grx-SS-protein disulfide bonds [37]. In summary, the reduction of protein disulfide bonds has been postulated to occur via a dithiol mechanism and to necessitate the presence of two active-site cysteine residues in glutaredoxins. However, for eukaryotic glutaredoxins this dogma is predominantly based on *in vitro* studies that were shown to depend upon the recombinant proteins being studied.

The budding yeast, *Saccharomyces cerevisiae*, contains two cytosolic thioredoxins and two enzymatically active cytosolic dithiol class I glutaredoxins [40] (Fig. 1a). A third dithiol glutaredoxin, Grx8, is a poorly active hybrid protein that neither belongs to the class I nor class II glutaredoxins [41]. Yeast also contain three further redox-inactive, monothiol class II glutaredoxins, Grx3, Grx4 and Grx5 [6,8], as well as two enzymatically active monothiol class I glutaredoxins, Grx6 and

Grx7, which are targeted to the secretory pathway [26,28]. However, none of these latter five glutaredoxins are relevant for the efficient reduction of cytosolic or nuclear redox proteins.

A yeast strain deleted for both cytosolic thioredoxins and both cytosolic dithiol class I glutaredoxins, $\Delta trx1\Delta trx2\Delta grx1\Delta grx2$, is not viable [40]. However, all four possible triple deletion mutants are viable, demonstrating that retaining any single cytosolic thioredoxin or class I glutaredoxin is enough to maintain yeast viability. We reasoned that the ability of yeast to survive and grow with one single glutaredoxin would allow us to test the capacity of a monothiol class I glutaredoxin to support disulfide reduction of several protein substrates inside living cells (Fig. 1c). We found that both a cytosol-targeted variant of the naturally occurring monothiol glutaredoxin Grx7 as well as the engineered monothiol glutaredoxin, Grx2 C64S, can support the growth of yeast cells deleted for both cytosolic thioredoxins and both cytosolic dithiol class I glutaredoxins. Furthermore, the growth rate of these cells was indistinguishable from that of cells rescued by a dithiol glutaredoxin. These results reveal that a monothiol glutaredoxin must, at minimum, support efficient reduction of yeast ribonucleotide reductase. We furthermore show that monothiol glutaredoxins can mediate reduction of methionine sulfoxide reductase and the non-physiological protein disulfide in redox-sensitive green fluorescent protein 2 (roGFP2). In conclusion, we demonstrate that different enzymatically active monothiol glutaredoxins can support the efficient reduction of multiple different protein disulfides inside living cells. Our observations require a major re-think of current hypotheses on the relevance of the widely conserved active-site second cysteine residue and the dithiol mechanism as well as the physiological functions of monothiol and dithiol class I glutaredoxins in general.

2. Results

2.1. A monothiol class I glutaredoxin can sustain viability of a $\Delta trx1\Delta trx2\Delta grx1\Delta grx2$ strain

To test whether a monothiol class I glutaredoxin can support efficient protein disulfide bond reduction in living yeast cells, we first generated the triple deletion strain $\Delta trx1\Delta trx2\Delta grx2$. Subsequently, we transformed this strain with a p416TEF plasmid encoding roGFP2-Grx2, a genetic fusion construct between roGFP2 and yeast Grx2. Finally, in this background we deleted *GRX1* to create the quadruple mutant $\Delta trx1\Delta trx2\Delta grx1\Delta grx2 + p416TEF\ roGFP2-GRX2$. The quadruple mutant was confirmed by PCR analysis and by growth on agar plates supplemented with appropriate antibiotics or with dropout of specific amino acids and nucleobases (Figs. S1a and b).

We next utilized a plasmid shuffling strategy [42] to test the capacity of different dithiol and monothiol glutaredoxins to maintain cell viability (Fig. 1c). We transformed the $\Delta trx1\Delta trx2\Delta grx1\Delta grx2 + p416TEF\ roGFP2-GRX2$ strain with p415TEF expression plasmids encoding the yeast dithiol class I glutaredoxins Grx1 and Grx2 as positive controls and the enzymatically inactive human monothiol class II glutaredoxin *HsGrx5* or an empty plasmid as negative controls. Finally, we also transformed with a p415TEF plasmid encoding the enzymatically active yeast monothiol class I glutaredoxin Grx7. Grx2 and Grx7 were cloned without their mitochondrial targeting sequence and signal sequence respectively to allow for cytosolic localization. All strains grew well on Hartwell's Complete (HC) agar plates as well as on HC plates lacking leucine and uracil to select for retention of both plasmids (Fig. 2a). We next investigated growth on HC media containing 5-fluoroorotic acid (5-FOA). The p416TEF plasmid contains a *URA3* gene to allow for auxotrophic selection. *URA3* encodes an orotidine 5-phosphate decarboxylase, which can also decarboxylate 5-fluoroorotic acid-5'-monophosphate to 5-fluorouridine-5'-monophosphate a toxic metabolite that kills cells [43]. Thus, in the presence of 5-FOA, cells can only grow if they have lost the p416TEF *roGFP2-GRX2* plasmid, which can only occur if the glutaredoxin encoded on the p415TEF plasmid can sustain cell viability. Cells transformed with an empty p415TEF plasmid were unable to grow on HC + 5-FOA media (Fig. 2a). Cells transformed with a p415TEF plasmid encoding class II *HsGrx5* were also inviable, whilst cells containing p415TEF plasmids encoding either Grx1 or Grx2 grew well (Fig. 2a). Intriguingly, cells transformed with p415TEF encoding the monothiol class I glutaredoxin, Grx7, also grew well on 5-FOA-containing plates (Fig. 2a).

To demonstrate that our observation is general for enzymatically active monothiol glutaredoxins and not specific to Grx7, we repeated the above experiment with a monothiol mutant of yeast Grx2. We observed that $\Delta trx1\Delta trx2\Delta grx1\Delta grx2$ cells containing a p415TEF plasmid encoding Grx2 with a CPYS active-site motif, i.e. Grx2 C64S, were able to grow in the presence of 5-FOA (Fig. 2b). In contrast, cells containing p415TEF plasmids encoding either Grx2 C61S or Grx2 C61S, C64S mutants were unable to grow in the presence of 5-FOA but grew well on HC plates, thus confirming the essentiality of the N-terminal active-site cysteine residue (Fig. 2b). Furthermore, we observed no difference in growth of Grx7 or Grx2 C64S rescued yeast when, instead of the strong constitutive TEF promoter, we used either the much weaker, constitutive, ADH promoter [44] (Fig. S2a) or the endogenous Grx2 promoter and terminator (Fig. S2b). Thus, the rescue of yeast viability by monothiol class I glutaredoxins is not a peculiarity of 'overexpression' or extreme protein concentrations.

To further validate our results, we performed similar experiments in liquid media. Specifically, we inoculated $\Delta trx1\Delta trx2\Delta grx1\Delta grx2 + p416TEF\ roGFP2-GRX2$ strains, which were transformed with p415TEF plasmids encoding Grx1, Grx2, *HsGrx5* or Grx7, into HC medium supplemented with 0.1% 5-FOA (Fig. 2c). Consistent with the growth on agar plates, we observed no growth of cells containing a p415TEF empty vector or of cells containing a p415TEF plasmid encoding

HsGrx5. Interestingly, an *HsGrx5* mutant, which we have recently engineered to be enzymatically active (*HsGrx5 Loop + G68P + R97Q*) [45], was also unable to restore growth on 5-FOA plates (Figs. S3a and b). On the contrary, $\Delta trx1\Delta trx2\Delta grx1\Delta grx2$ cells containing Grx1, Grx2 or Grx7 grew well (Fig. 2c), whereas cells containing Grx7 C108S, which lacks the active-site cysteine residue, could not grow on either agar plates or in liquid culture (Figs. S3a and b). The long lag phase is due to the selection mechanism of 5-FOA. Only cells that have by chance lost the p416TEF plasmid will be able to grow in the presence of 5-FOA, thus the actual number of cells in the culture that will be able to divide at the beginning of the growth assay is very low. For Grx2 cysteine mutants we also observed the same growth pattern in liquid cultures as we had observed on agar plates. Cells containing Grx2 or Grx2 C64S grew well, whilst cells expressing Grx2 C61S or Grx2 C61S, C64S did not grow (Fig. 2d). Finally, we subjected $\Delta trx1\Delta trx2\Delta grx1\Delta grx2 + p416TEF\ roGFP2-GRX2$ cells, transformed with p415TEF plasmids encoding either Grx1, Grx2, Grx2 C64S or Grx7, to two rounds of selection on 5-FOA to ensure complete loss of the p416TEF *roGFP2-GRX2* plasmid. We then grew the resultant $\Delta trx1\Delta trx2\Delta grx1\Delta grx2 + p415TEF\ GRX1, GRX2, GRX2 C64S$ or *GRX7* strains on HC media. We observed no difference in growth irrespective of whether the cells contained a monothiol or dithiol class I glutaredoxin (Fig. 2e). Therefore, our observations clearly demonstrate that a monothiol class I glutaredoxin can replace all the essential functions of cytosolic thioredoxins and dithiol class I glutaredoxins. Finally, as a further control, we also tested the ability of thioredoxin cysteine mutants to restore growth. Specifically, we streaked $\Delta trx1\Delta trx2\Delta grx1\Delta grx2 + p416TEF\ roGFP2-GRX2$ strains, transformed with p415TEF vectors encoding either Trx1, Trx2, Trx2 C34S or Trx2 C31S, C34S, onto both HC agar plates and HC plates supplemented with 5-FOA. All strains grew well on HC plates, whilst only strains with either Trx1 or Trx2 were able to grow in the presence of 5-FOA confirming the essentiality of both thioredoxin active-site cysteine residues in accordance with a dithiol mechanism (Fig. S3c). We were also interested to test if protein disulfide isomerases (PDIs) could rescue growth of the $\Delta trx1\Delta trx2\Delta grx1\Delta grx2$ strain. This is plausible as PDIs can reduce protein disulfide bonds and can themselves be reduced by GSH [46]. However, none of the protein disulfide isomerases Pdi1, Mpd1 or Mpd2 could rescue growth on agar plates (Fig. S3d). In summary, we demonstrate that monothiol class I glutaredoxins can fulfil all essential protein disulfide bond reduction required for sustaining yeast viability and growth.

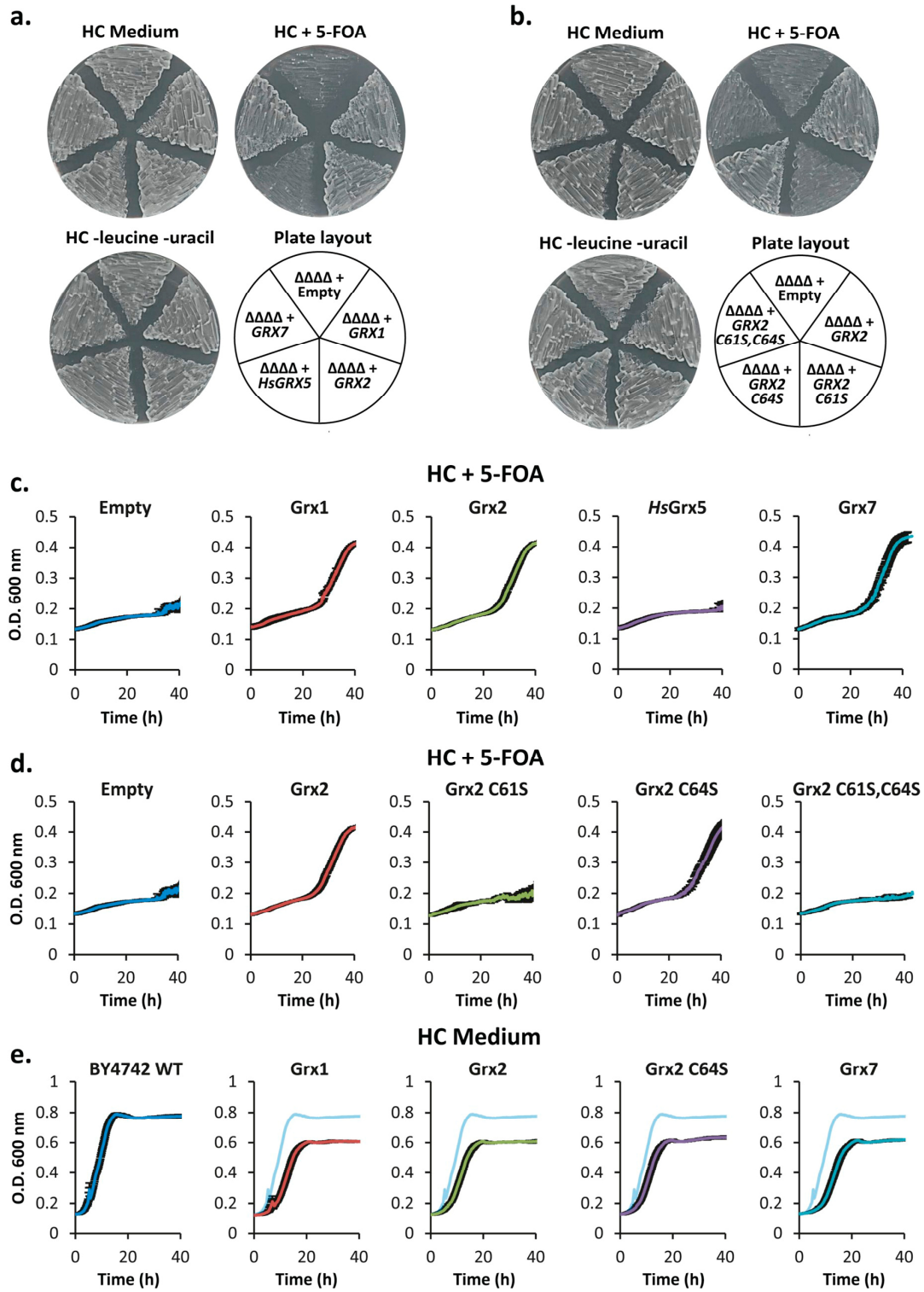
2.2. Monothiol class I glutaredoxins can reduce methionine sulfoxide reductase

The rescue of yeast viability and growth by monothiol class I glutaredoxins demonstrates that, at minimum, these enzymes must facilitate the reduction of ribonucleotide reductase. It is unclear whether reduction of any other cytosolic/nuclear protein disulfide is essential for yeast viability. Nonetheless, there are several protein disulfides that require reduction as part of their normal catalytic mechanism and we were interested to see whether a monothiol class I glutaredoxin could reduce these protein disulfides. One of these proteins is PAPS reductase, which is responsible for reducing activated sulfate to sulfite. This is an important step in the assimilation of inorganic sulfate to produce, for example, methionine and cysteine. Previous studies have shown that yeast deleted for both cytosolic thioredoxins are auxotrophic for methionine and it is therefore assumed that glutaredoxins are unable to reduce yeast PAPS reductase [25]. Our assays supported these observations. BY4742WT, a methionine prototroph, grew well on solid or liquid HC media without methionine and served as a control (Fig. 3a and b). In contrast, BY4742 $\Delta trx1\Delta trx2$, $\Delta trx1\Delta trx2\Delta grx1$ and $\Delta trx1\Delta trx2\Delta grx2$ strains could not grow on either solid or liquid HC media without methionine (Figs. S4a and b). Furthermore, the methionine auxotrophic strain, BY4741, as well as BY4742

$\Delta trx1\Delta trx2\Delta grx1\Delta grx2$ strains with p415TEF plasmids encoding either Grx1, Grx2, Grx2 C64S or Grx7 also showed no growth on either solid or liquid HC media lacking methionine (Fig. 3a and b). We conclude that neither a dithiol nor monothiol class I glutaredoxin is capable of

supporting sulfate assimilation in the absence of thioredoxins, most likely because glutaredoxins cannot mediate reduction of yeast PAPS reductase.

The methionine auxotrophy of our BY4742 $\Delta trx1\Delta trx2\Delta grx1\Delta grx2$



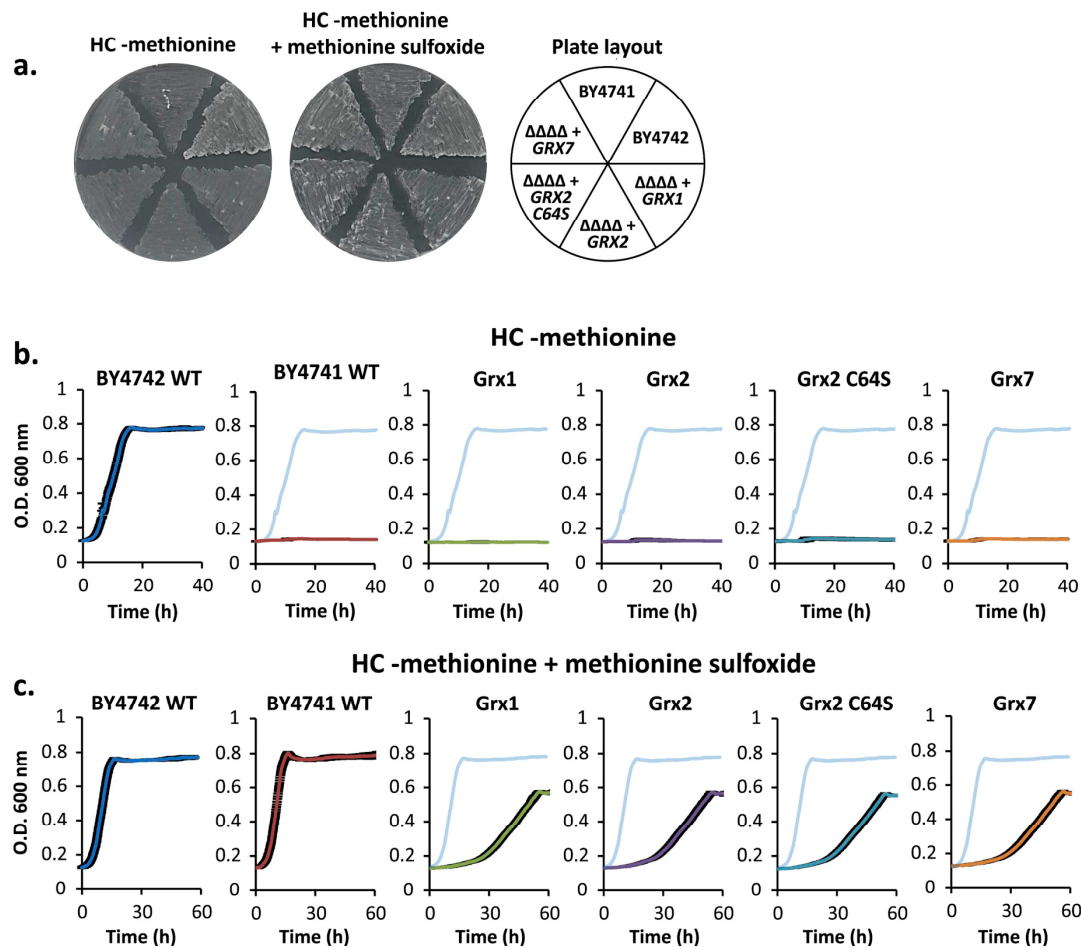
(caption on next page)

Fig. 2. A single monothiol class I glutaredoxin can sustain viability of $\Delta trx1\Delta trx2\Delta grx1\Delta grx2$ yeast strains.

a. BY4742 $\Delta trx1\Delta trx2\Delta grx1\Delta grx2$ cells containing a p416TEF *roGFP2-GRX2* were transformed with p415TEF plasmids encoding either Grx1, Grx2, HsGrx5 or Grx7. Cells were streaked onto either HC plates, HC + 0.1 g/l 5-FOA or HC without leucine and uracil. Plates were grown for 48 h at 30 °C. b. As in (a.) except that cells were transformed with p415TEF plasmids encoding either Grx2 or one of the mutants Grx2 C61S, Grx2 C64S, Grx2 C61S, C64S. c. and d. BY4742 $\Delta trx1\Delta trx2\Delta grx1\Delta grx2$ cells containing a p416TEF *roGFP2-GRX2* plasmid as well as p415TEF plasmids for the expression of the indicated glutaredoxins, as in (a.) and (b.), were inoculated in HC medium supplemented with 0.1 g/l 5-FOA to an initial OD₆₀₀ = 0.1. Cultures were subsequently grown in a round-bottomed 96-well plate with continuous shaking at 30 °C. e. BY4742 $\Delta trx1\Delta trx2\Delta grx1\Delta grx2$ cells containing a p416TEF *roGFP2-GRX2* plasmid and p415TEF plasmids encoding either Grx1, Grx2, Grx2 C64S or Grx7 underwent two rounds of selection on HC plates supplemented with 0.1 g/l 5-FOA to ensure complete loss of the p416TEF plasmid. Subsequently, these cells were inoculated to an initial OD₆₀₀ = 0.1 and were grown in a round-bottomed 96-well plate with continuous shaking at 30 °C. BY4742WT cells were also grown for comparison. The growth curve of the BY4742WT is shown in all other panels in light blue. Error bars in all panels represent the standard error for three experimental repeats. (For interpretation of the references to colour in this figure legend, the reader is referred to the Web version of this article.)

strains, due to the absence of a functional thioredoxin, nonetheless afforded us the opportunity to genetically test the reduction of another protein disulfide, namely in methionine sulfoxide reductases. Previous studies have shown that methionine auxotrophic yeast strains with functional methionine sulfoxide reductases can grow using methionine sulfoxide as a source of methionine [47,48]. It was reported that a $\Delta trx1\Delta trx2$ yeast strain cannot grow on methionine sulfoxide [47,48]. This is supported by *in vitro* studies on methionine sulfoxide reductases suggesting that 2-Cys methionine sulfoxide reductases, which form an

intramolecular disulfide bond, are exclusively reduced by thioredoxins [17]. Nonetheless, in our experiments, BY4742 $\Delta trx1\Delta trx2$, $\Delta trx1\Delta trx2\Delta grx1$ and $\Delta trx1\Delta trx2\Delta grx2$ strains all grew, albeit relatively slowly, on both solid and liquid HC medium supplemented with 0.24 mM methionine sulfoxide in place of methionine (Figs. S4a and c). This observation therefore allowed us to test whether a monothiol class I glutaredoxin can also sustain growth on methionine sulfoxide. To this end, we tested the growth of $\Delta trx1\Delta trx2\Delta grx1\Delta grx2$ cells transformed with p415TEF plasmids encoding either Grx1, Grx2, Grx2 C64S or Grx7

**Fig. 3. A monothiol class I glutaredoxin can reduce methionine sulfoxide reductase.**

a. BY4742 $\Delta trx1\Delta trx2\Delta grx1\Delta grx2$ cells containing a p415TEF plasmid, for the expression of the indicated glutaredoxins, were streaked either onto HC plates lacking methionine or HC plates supplemented with 0.24 mM L-methionine sulfoxide. Plates were incubated for 48 h at 30 °C. BY4741WT (methionine auxotroph) and BY4742WT (methionine prototroph) cells were included as controls. b. and c. Cells as used in (a.) were inoculated to an initial OD₆₀₀ = 0.1 in either HC medium without methionine or IIC medium supplemented with 0.24 mM L-methionine sulfoxide and were grown in a round-bottomed 96-well plate with continuous shaking at 30 °C. The growth curve of BY4742WT cells was reproduced in all panels in light blue. Error bars in all panels represent the standard error for three experimental repeats. (For interpretation of the references to colour in this figure legend, the reader is referred to the Web version of this article.)

on both solid and liquid HC media containing 0.24 mM methionine sulfoxide (Fig. 3a,c). Interestingly, all strains grew at a similar rate to the $\Delta trx1\Delta trx2$ strain (compare Fig. 2c with Fig. S4c), suggesting that monothiol and dithiol class I glutaredoxins can reduce yeast methionine sulfoxide reductase(s) with equal efficiency. In summary, we demonstrate that monothiol class I glutaredoxins can support growth on methionine sulfoxide, which is strongly consistent with the conclusion that monothiol glutaredoxins can reduce yeast methionine sulfoxide reductase(s).

2.3. The cytosolic glutathione pool remains highly reduced in rescued $\Delta trx1\Delta trx2\Delta grx1\Delta grx2$ strains

It has previously been demonstrated that the yeast dithiol glutaredoxins, Grx1 or Grx2 can mediate the equilibration between the roGFP2 thiol-disulfide redox couple and the 2GSH/GSSG redox couple under steady-state conditions [49]. Therefore, the degree of roGFP2 oxidation is a quantitative noninvasive real-time measure of the glutathione redox potential provided that suitable glutaredoxins are present to mediate the equilibration [50–52]. We were thus interested to see whether the monothiol glutaredoxins, Grx2 C64S and Grx7 could also equilibrate roGFP2 with the glutathione pool, which would require that they can efficiently oxidize and reduce roGFP2. To address this question, we transformed $\Delta trx1\Delta trx2\Delta grx1\Delta grx2$ cells rescued by p415TEF plasmids encoding either Grx1, Grx2, Grx2 C64S or Grx7 with a p416TEF plasmid encoding roGFP2. We then used a plate-reader assay to monitor the degree of roGFP2 oxidation in these strains (Fig. 4a–d). Interestingly, average roGFP2 oxidation in $\Delta trx1\Delta trx2\Delta grx1\Delta grx2$ cells with Grx1, Grx2 or Grx2 C64S was less than 20% in each case. This result clearly demonstrates that the cytosolic glutathione pool remains highly reduced in these strains, with a glutathione redox potential of ≤ -295 mV. Furthermore, the roGFP2 sensor in all three strains responded very similarly to the exogenous addition of H₂O₂ (Fig. 4a–d), indicating that the monothiol glutaredoxin, Grx2 C64S, is capable of mediating roGFP2 oxidation and reduction, with similar efficiency to dithiol glutaredoxins. Interestingly, the steady-state oxidation of roGFP2 in Grx7 cells, at ~40%, was higher than in the other strains, although the roGFP2 reporter did readily respond to exogenous H₂O₂. This result may either indicate that the cytosolic glutathione redox potential is indeed higher in this strain or could indicate that Grx7 is less efficient in roGFP2 reduction than in roGFP2 oxidation. An imbalance in reduction versus oxidation alone could not change the thermodynamics of roGFP2 oxidation. However, other proteins such as peroxidases, can slowly oxidize roGFP2 and could drive accumulation of oxidized roGFP2 over time [53] if such oxidation could not be efficiently reduced by Grx7. To gain further insight into this question, we expressed genetic fusion constructs between roGFP2 and either Grx2 or Grx7. In such a direct fusion, the effective concentration of glutaredoxin ‘perceived’ by the roGFP2 reporter will be increased by ~1000-fold and thus may compensate for kinetic limitations [50]. Indeed, in the context of both the roGFP2-Grx2 and roGFP2-Grx7 fusion constructs, the steady-state average roGFP2 oxidation was approximately 10% and both probes responded readily to exogenous H₂O₂ (Fig. 4e and f). Thus, we demonstrate that two different monothiol class I glutaredoxins, Grx2 C64S and Grx7, can mediate rapid oxidation and reduction of roGFP2 inside living cells, although Grx7 seems to be less efficient at reducing roGFP2. Furthermore, our results demonstrate that even in cells lacking both cytosolic thioredoxins and both cytosolic dithiol class I glutaredoxins, the cytosolic glutathione pool remains highly reduced in the presence of a monothiol class I glutaredoxin.

In $\Delta trx1\Delta trx2\Delta grx1\Delta grx2$ cells expressing either Grx2 C64S or Grx7, reduction of every cytosolic disulfide bond presumably oxidizes two molecules of GSH, which serves as the electron donor. We therefore asked whether this led to a detectable increase in cellular GSSG content. In any strain in which the genes encoding both Trx1 and Trx2 were

deleted, we did indeed observe a large increase in cellular GSSG content, consistent with GSH/Grx becoming the predominant or even sole source of disulfide reductive power (Fig. 4g). As the roGFP2 reporter indicated that the cytosolic glutathione pool remained highly reduced, the ‘extra’ GSSG is presumably stored in the vacuole as we have previously shown [49]. We also observed that ‘total’ cellular glutathione (defined as GSH + GSSG) levels increased in $\Delta trx1\Delta trx2$ cells, which is consistent with previous reports [54], as well as in $\Delta trx1\Delta trx2\Delta grx1$ and $\Delta trx1\Delta trx2\Delta grx2$ cells (Fig. 4h). Intriguingly, the presence of either Grx1, Grx2 or Grx7 in $\Delta trx1\Delta trx2\Delta grx1\Delta grx2$ cells restored ‘total’ cellular glutathione levels to those found in wild-type cells although the reason for this is unclear. This effect was not observed in cells expressing Grx2 C64S (Fig. 4h). In summary, we show that the cytosolic glutathione pool remains highly reduced in cells lacking both cytosolic thioredoxins and a glutaredoxin. The extra ‘demand’ on the glutathione pool is reflected in increased cellular GSSG, which is presumably stored in the vacuole. Finally, we demonstrate that a monothiol class I glutaredoxin allows efficient roGFP2-based sensing of the glutathione redox potential.

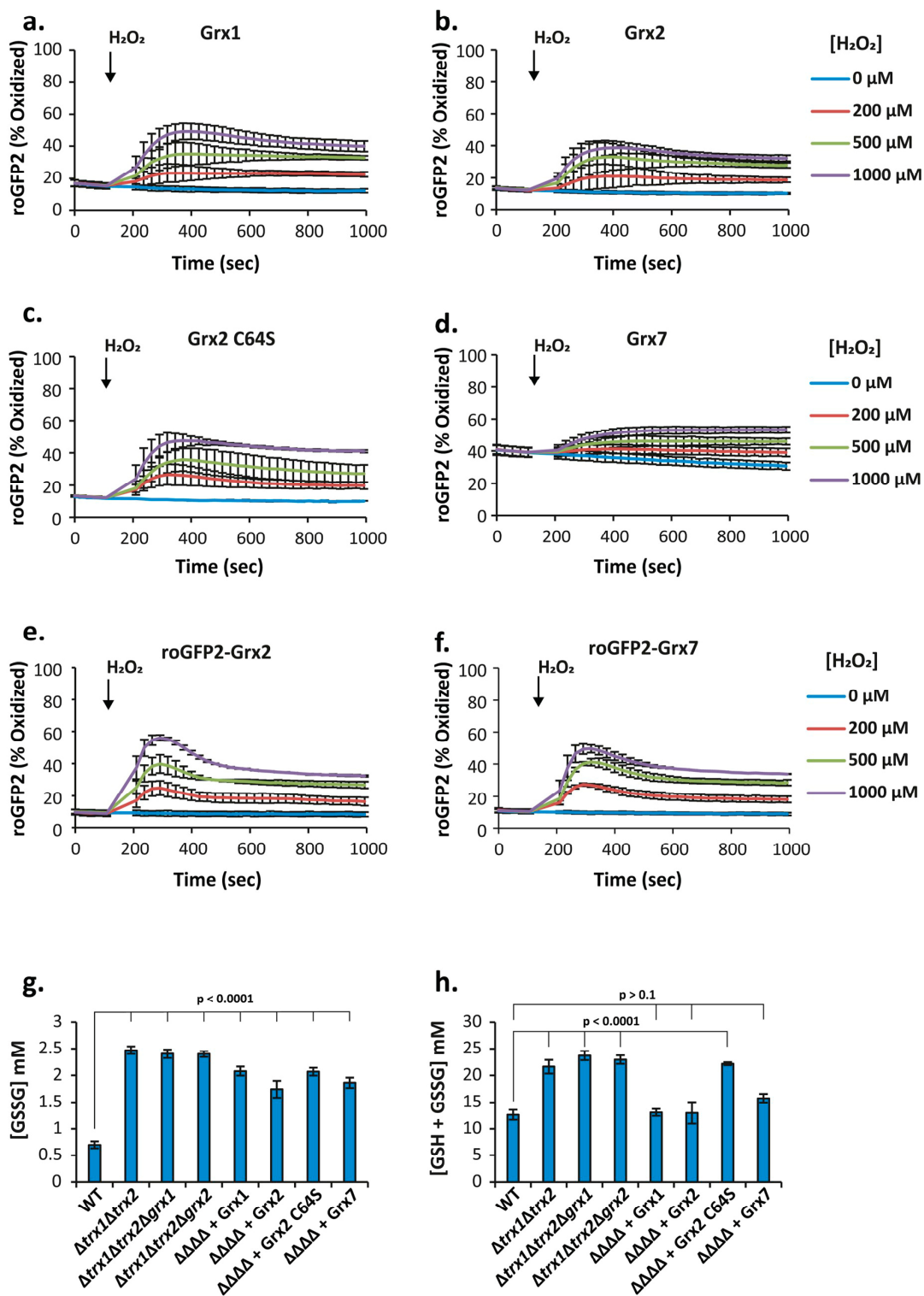
3. Discussion

Why do most class I glutaredoxins have two active-site cysteine residues even though monothiol mutants are usually more active as deglutathionylating enzymes *in vitro*? It is frequently reported that glutaredoxin-mediated protein disulfide reduction requires a dithiol mechanism, and this was indeed shown for *E. coli* ribonucleotide reductase and PAPS reductase [21,38,55,56]. Nonetheless, many other *in vitro* studies with non-glutathione protein disulfide substrates, some of which are frequently cited as examples for a dithiol mechanism, appear to lack the crucial control experiment with GSH and a monothiol class I glutaredoxin to exclude a monothiol mechanism [18,22,23]. In the presence of GSH, a monothiol mechanism might indeed be highly relevant, as demonstrated *in vitro* for the reduction of protein disulfide bonds in mammalian ribonucleotide reductase and the metal-binding domain of the ATPase HMA4 [32,37] as well as the non-glutathione model substrate bis(2-hydroxyethyl)disulfide [45,57,58]. Furthermore, monothiol class I glutaredoxins were recently shown to efficiently oxidize roGFP2 inside living cells and to permit roGFP2-dependent redox measurements [45]. Here we demonstrate that monothiol class I glutaredoxins can also efficiently reduce roGFP2.

Importantly, we found that two different monothiol class I glutaredoxins, Grx7 and Grx2 C64S, with a natural and an engineered CPYS active-site motif respectively, maintained viability of yeast strains lacking all endogenous cytosolic thioredoxins and dithiol class I glutaredoxins. Indeed, the growth rates of yeast strains rescued with monothiol or dithiol class I glutaredoxins were virtually indistinguishable. Considering the subcellular localization of yeast Grx1 and Grx2 [59,60] and of their functional replacements, we conclude that the dithiol mechanism is dispensable for essential reductions of known and unknown cytosolic and nuclear protein disulfide substrates in yeast. Thus, yeast ribonucleotide reductase can be reduced via a monothiol mechanism *in vivo* in accordance with the *in vitro* data for mammalian ribonucleotide reductase [32]. Our data also imply that other protein disulfides can be efficiently reduced by a monothiol class I glutaredoxin. This includes the proteins methionine sulfoxide reductase and roGFP2. However, PAPS reductase cannot be reduced by either a monothiol or dithiol glutaredoxin. Whether the dithiol mechanism is also dispensable in other eukaryotes remains to be shown. Nonetheless, at this stage we cannot fully exclude that the dithiol mechanism might become essential under alternative experimental conditions, for example due to absent compensatory mechanisms or altered glutaredoxin concentrations [61]. For example, according to the ‘cysteine resolving model’, the second cysteine residue might resolve kinetically trapped glutaredoxin species with unreactive Grx-SSG or Grx-SS-protein conformations that cannot efficiently react with GSH because of steric or

geometric constraints [1,5,41]. Such trapped glutaredoxin species are not restricted to substrates or hypothetical redox signaling partners but might include unspecific Grx-SS-protein disulfides that accumulate under certain conditions, such as observed in pull-down experiments with mutant monothiol class I glutaredoxins [62–64]. The physiological

impact of these trapped species might depend on the total glutaredoxin concentration, although different promoter strengths had no impact on our growth assays under the chosen conditions. In summary, we found that a single monothiol class I glutaredoxin suffices for yeast cell viability and that the dithiol mechanism is dispensable for essential



(caption on next page)

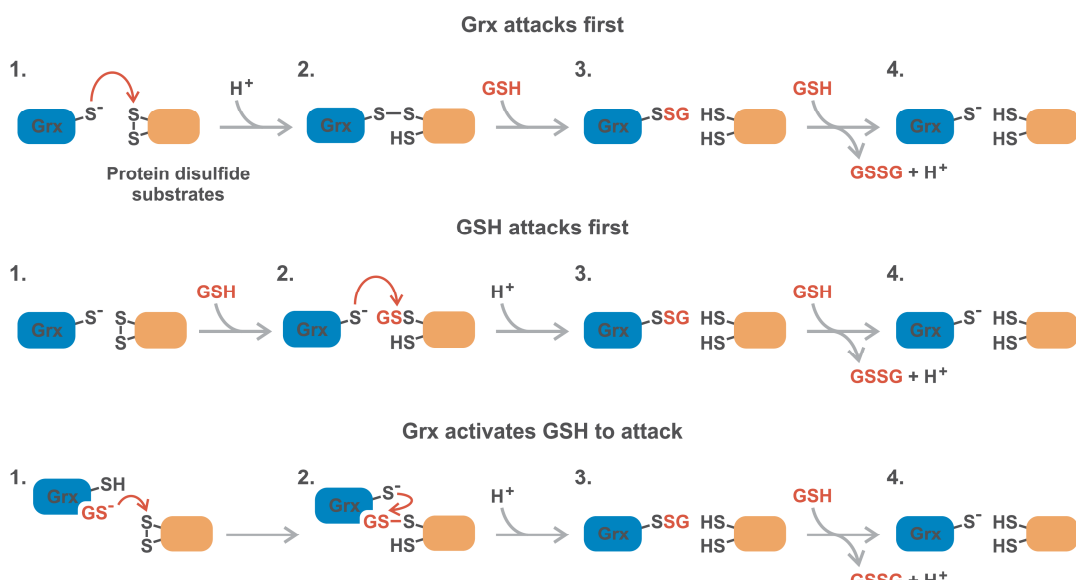
Fig. 4. The glutathione redox potential is highly reduced in $\Delta trx1\Delta trx2\Delta grx1\Delta grx2$ yeast cells.

BY4742 $\Delta trx1\Delta trx2\Delta grx1\Delta grx2$ cells containing a p416TEF plasmid encoding roGFP2 and a p415TEF plasmid encoding either a. Grx1, b. Grx2, c. Grx2 C64S or d. Grx7 were resuspended to an $OD_{600} = 7.5$ in 100 mM MES-Tris pH 6 and transferred into wells of a flat-bottomed 96-well plate. H_2O_2 was added at the concentrations indicated and the change in roGFP2 oxidation was monitored with a fluorescence plate-reader-based assay. e. BY4742 $\Delta trx1\Delta trx2\Delta grx1\Delta grx2$ cells containing an empty p416TEF plasmid as well as a p415TEF plasmid encoding either, e. roGFP2-Grx2 or f. roGFP2-Grx7 were treated as described for panels a-d. RoGFP2 oxidation was likewise monitored following addition of H_2O_2 at the indicated concentrations. g. 'Total' glutathione assay. For each of the strains described in a-d, as well as BY4742WT, $\Delta trx1\Delta trx2$, $\Delta trx1\Delta trx2\Delta grx1$ and $\Delta trx1\Delta trx2\Delta grx2$ strains, a DTNB-based assay was used to measure 'total' glutathione (GSH and GSSG; reported as GSH equivalents) in lysates produced from 50 OD_{600} units of these cells, where 1 OD_{600} unit represents 1 ml of culture with an $OD_{600} = 1$. h. As for g., but with an adapted protocol to monitor GSSG levels in cell lysates. P-values were determined by a one-way ANOVA analysis followed by a Tukey's test.

glutaredoxin catalysis. The second active-site cysteine residue in dithiol class I glutaredoxins might have conserved (non-essential) functions other than the reduction of ribonucleotide reductase. One of these alternative functions that remains to be addressed in future studies is a hypothetical role as a resolving cysteine for trapped glutaredoxin species.

How can a monothiol glutaredoxin reduce a protein disulfide substrate? We consider three of several non-exclusive mechanistic models. a) The monothiol class I glutaredoxin itself performs the initial nucleophilic attack on the protein disulfide bond (Fig. 5a). This would result in a transient intermolecular disulfide between the glutaredoxin and the protein substrate. In this scenario GSH reduces the intermolecular Grx-SS-protein disulfide. Theoretically, GSH could either attack (i) the glutaredoxin sulfur atom, yielding a glutathionylated glutaredoxin and the reduced protein substrate, or (ii) the sulfur atom of the protein substrate, yielding a glutathionylated protein, which is subsequently deglutathionylated by the glutaredoxin. Both reaction sequences result in glutathionylated glutaredoxin (step 3 in Fig. 5a). The glutathionylated glutaredoxin subsequently reacts with a second GSH molecule yielding GSSG. A direct reaction between a monothiol class I glutaredoxin and substrate seems very likely because this part of the reaction is identical to the dithiol mechanism. Pathway (i) has

previously been suggested for the reduction of HMA4 [37], whereas pathway (ii) takes the reaction geometry into account and is supported by the kinetic patterns with the model substrate bis(2-hydroxyethyl) disulfide [45,57,58]. b) GSH non-enzymatically reacts with the protein disulfide substrate (Fig. 5b). The glutathionylated protein is subsequently deglutathionylated following a regular monothiol mechanism. While the second part of this reaction sequence is in perfect agreement with numerous *in vitro* studies (e.g. Ref. [33,36]), the rate constant for the first part of the reaction sequence depends on the protein disulfide substrate. This rate constant is probably too small for most substrates to be significant [61]. c) In a variation of the latter mechanism, glutaredoxins or a glutathione transferase may deprotonate and activate GSH, to increase its nucleophilicity for the initial attack on the protein disulfide (Fig. 5c). GSH activation is a common principle in the structurally related glutathione transferases, some of which can reduce disulfide bonds or sulfenic acids [5]. A prediction of this mechanism is that the GSH-mediated reduction of protein disulfides, resulting in glutathionylated proteins, could be catalyzed in the presence of a glutaredoxin without a cysteine residue provided that GSH activation can still occur. It will be exciting to test this possibility, perhaps in the context of future *in vitro* studies.

**Fig. 5. Plausible mechanisms for reduction of protein disulfides by a monothiol glutaredoxin.**

a. Glutaredoxin attacks first. Here the nucleophilic active-site cysteine of the glutaredoxin attacks one of the sulfur atoms of the protein disulfide, leading to the formation of an intermolecular disulfide bond between the protein and the glutaredoxin. GSH would then act to resolve this intermolecular disulfide, thereby directly or indirectly generating a glutathionylated glutaredoxin. This can be reduced by a second molecule of GSH yielding GSSG. b. GSH attacks first. In this model, GSH performs an uncatalyzed nucleophilic attack on the protein disulfide resulting in a glutathionylated protein. The active-site, nucleophilic cysteine of a monothiol glutaredoxin can then attack the sulfur atom of the glutathione moiety resulting in the glutathionylation of the glutaredoxin. Finally, another GSH would be required to regenerate reduced glutaredoxin, thereby producing GSSG. c. Glutaredoxin (or another protein) activates GSH to attack. Here GSH is activated by glutaredoxin leading to deprotonation of the GSII moiety, possibly by acid-base catalysis. The GS⁻ anion then serves as an efficient nucleophile to attack one of the sulfur atoms of the target protein disulfide bond. This would lead to the glutathionylation of the protein. The deglutathionylation can then proceed by a classic monothiol glutaredoxin mechanism as described for a. and b.

4. Materials and methods

4.1. Growth of yeast strains

All yeast strains were generated in a BY4742 (his3Δ1 leu2Δ0 lys2Δ0 ura3Δ0) background unless otherwise indicated (Supplementary Table 1.). For all experiments cells were grown in Hartwell (HC) media supplemented with 2% glucose as carbon source. Amino acids were dropped out for plasmid selection and supplements were added as indicated.

4.2. Construction of yeast strains

A standard homologous recombination protocol was used to create gene deletions [65]. Antibiotic resistant cassettes were amplified by PCR using primers designed to have 50–60 base-pairs of homology to the genomic regions immediately up- and downstream of the gene to be deleted. *GRX1* and *GRX2* were deleted in a BY4742 *Δtrx1Δtrx2* background [53]. For *GRX1* deletion, the primers S1-*GRX1*-FWD 5'-AATTATCAAATAGACAAACCTCAGAAGGAAAAAAATCGTACGGCTGCAGGTCGAC-3' and S2-*GRX1*-REV 5'-TATAAACCTGTGCGATGGAAAAAAACTTTGCTGCCCTTAATCGATGAATTGAGCTCG-3' were used to amplify a *natNT2* cassette from a pFA6-*natNT2* plasmid. For *GRX2* deletion, the primers S1-*GRX2*-FWD 5'-ATTAACGGACACTCCAACACTGTTATATATGTTTCATGCGTAGCGCTGCAGGTCGAC-3' and S2-*GRX2*-REV 5'-TGTAAATATTATGAAGGGATATTAGCGTAATTAAACTAATCGATGAATTGAGCTCG-3' were used to amplify an *hphNT1* cassette from a pFA6-*hphNT1* plasmid. The PCR products of these reactions were transformed into yeast cells using a standard lithium acetate/polyethyleneglycol-based protocol. Briefly, yeast cells were harvested and resuspended in One-Step-Transformation buffer containing 40% polyethylene glycol, 0.2 M lithium acetate and 0.1 M Dithiothreitol (DTT) followed by addition of 10 µl of salmon testes single-strand DNA and PCR-product/plasmid DNA. Cells were then incubated at 45 °C for 30 min with continuous shaking and subsequently transferred to appropriate YPD plates for selection. Gene deletions were confirmed by PCR on genomic DNA using primers designed to bind to chromosomal regions approximately 400 base pairs up- and downstream of the gene of interest and by plating on HC agar plates supplemented with the appropriate antibiotics.

4.3. Cloning and plasmid construction

Genes encoded on p415TEF, p416TEF or prs315 plasmids as used in this study were PCR-amplified from either pre-existing plasmids or genomic DNA. Genomic DNA was always extracted from BY4742WT cells. Briefly, cells were vortexed in 30 µl 0.2% SDS and boiled at 96 °C for 10 min. Subsequently, cells were vortexed again followed by centrifugation at 18000g for 1 min. One µl of supernatant was used as DNA-template in the PCR-reaction-mix.

GRX1 was amplified from genomic DNA using the forward primer 5'-CATGGGATCCACCAGGTATCTAAGAAACTATCAAGCAC-3' and reverse primer 5'-CTAGCTGAGTTAAATTGCAAGAATAGGTCTAACAAATTC-3' and subsequently cloned into an empty p415TEF plasmid using BamHI and XhoI restriction sites. *GRX2* was amplified by PCR from p416TEF *roGFP2-GRX2* [49] using the forward primer 5'-CATGTCTAGACCATGGTATCCCAGGAAACAGTTGCTCAC-3' and reverse primer 5'-CTAGCTGAGGTGACGGTATCGATAAGCTCTATTG-3'. Please note that *GRX2* harbors two in-frame start codons for either mitochondrial translocation or cytosolic expression. *GRX2* was amplified without the mitochondrial targeting sequence and cloned into an empty p415TEF plasmid using XbaI and XhoI restriction sites. *HsGRX5* and *HsGRX5* Active (Loop + G68P + R97Q) gene sequences with codons optimized for *Saccharomyces cerevisiae* expression were amplified from either p416TEF *roGFP2-HsGRX5* or p416TEF *roGFP2-HsGRX5* Active (Loop + G68P + R97Q) plasmids [45] using the forward primer 5'-CGTAGTGGGATCCACCATGGCTGGTCTGGTGC-3' and the reverse primer 5'-CAGTGCAGTATTGTTGAATCTTGATCTTCTTTCATC-3' and subcloned into an empty

p415TEF plasmid using BamHI and XhoI restriction sites. Please note that all *HsGRX5* constructs lack the mitochondrial pre-sequence and start with a methionine followed by residue Ala32. *GRX7* and *GRX7C108S* sequences were PCR-amplified from either p416TEF *roGFP2-GRX7* or p416TEF *roGFP2-GRX7C108S* plasmids [45] using the forward primer 5'-CGTAGTGGGATCCACCAGGTAACTG-3' and the reverse primer 5'-CAGTGCAGTATTGCG-3' and subsequently cloned into an empty p415TEF plasmid using BamHI and XhoI restriction sites. *GRX7* was cloned without the secretory pathway-targeting signal-sequence to ensure cytosolic localization. Gene sequences for *roGFP2-GRX2* and *roGFP2-GRX7* were subcloned from p416TEF *roGFP2-GRX2* [49] and p416TEF *roGFP2-GRX7* [45] plasmids into empty p415TEF plasmids using XbaI and XhoI restriction-sites. *TRX1* was amplified from genomic DNA using the forward primer 5'-CATGGGATCCACCAGGTAACTG-3' and reverse primer 5'-CTAGCTGAGTAAAGCA-3' and *TRX2* was amplified from genomic DNA using the forward primer 5'-CATGGGATCCACCAGGTAACTG-3' and reverse primer 5'-CTAGCTGAGTAAAGCA-3'. Both genes were cloned into empty p415TEF plasmids using BamHI and XhoI restriction sites. *PDI1*, *MPD1* and *MPD2* were each amplified from genomic DNA. *PDI1* was amplified using the forward primer 5'-CTAGCGGATCCACCAGTAAACAGAGGCTGTGGCCCTG-3' and reverse primer 5'-GCATGACTCGAGTTAAATGGCATCTTCTCGTCAGCCA-3'. *MPD1* was amplified using the forward primer 5'-CAGAATGGATCCACCATGCAAACACTTACGATTCGATCCTCATATATCAGAG-3' and reverse primer 5'-CAGTTCCTCGAGTTACCTGTTCTGAGGAGGAATGGTTCTT-3'. *MPD2* was amplified using the forward primer 5'-CAGTCTGGATCCACCATGAGTAACTACTGTTACCTGCTTCTATGTG-3'. All sequences were amplified lacking both the N-terminal signal-sequence and the C-terminal HDEL-sequence to ensure cytosolic localization and were cloned into empty p415TEF plasmids using BamHI and XhoI restriction sites.

GRX2 and *GRX2C64S* were subcloned from p415TEF *GRX2* and p415TEF *GRX2 C64S* plasmids into an empty p415ADH vector using XbaI and XhoI restriction sites to generate the p415ADH *GRX2* and p415ADH *GRX2 C64S* plasmids. *GRX7* was subcloned from a p415TEF *GRX7* plasmid to an empty p415 ADH plasmid using BamHI and XhoI restriction sites to generate p415ADH *GRX7*.

For the construction of the prs315 *GRX2* plasmid, the promotor region 839 bp up-stream of the *GRX2* start codon was PCR-amplified from genomic DNA using the forward primer 5'-CATGTCTAGAGTGTGCACAAAGATATCGATAACCCGTTGC-3' and the reverse primer 5'-CTAGGGATCCAAACAAATATAACAGTAGTTGGAGTG-3' and subsequently cloned into an empty prs315 vector using XbaI and BamHI restriction sites. In a second cloning step *GRX2* with its endogenous terminator was amplified from genomic DNA from the second ATG start codon, i.e. lacking the mitochondrial targeting sequence using the forward primer 5'-CATGGGATCCACCATGGTATCCCAGGAAACAGTTGCTCAC-3' and the reverse primer 5'-CTAGAAGCTCTCAGACGAAATTAGCGGGTCTATTGG-3' binding 171 bp down-stream of the *GRX2* stop codon. Subsequently, the PCR product was ligated into the previously created prs315 *GRX2* Promotor vector using BamHI and HindIII restriction sites to generate prs315 *GRX2* with endogenous promoter and terminator. Site-directed mutagenesis was subsequently performed on the prs315 *GRX2* plasmid using the *GRX2C64S* forward primer 5'-CATACTGCCCTTACAGTAAAGCTACTITG-3' and the *GRX2C64S* reverse primer 5'-CAAAGTAGCTTACTGTAAGGGCAGTATG-3' to generate prs315 *GRX2 C64S*. All constructs were confirmed by sequencing (Eurofins Genomics).

4.4. Site-directed mutagenesis

The p415TEF *GRX2* plasmid was used as a template for mutation of Cys61 to serine using the *GRX2C61S* forward primer 5'-GCAAAGACA TACTCGCCTTACTGTAAAG-3' and the *GRX2C61S* reverse primer 5'-CTTTACAGTAAGGGCAGTATGCTTTGC-3'. Cys64 was mutated to

serine using p415TEF *GRX2* as template together with the *GRX2C64S* forward primer 5'-CATACTGCCCTTACAGTAAAGCTACTTG-3' and the *GRX2C64S* reverse primer 5'-CAAAGTAGCTTACTGTAAGGGCAGT ATG-3'. Subsequently, the newly generated p415TEF *GRX2C64S* was used as template to generate the double cysteine mutant p415TEF *GRX2C61S, C64S* using the forward primer 5'-GCAAAGACATACTCTC CTTACAGTAAAGC-3' and the reverse primer 5'-GCTTTACTGTAAGGA GAGTATGTCTTGC-3'. Mutation of either *TRX2* Cys34 alone or both Cys31 and Cys34 to serine was performed using p415TEF *TRX2* as a template in combination with the primers *TRX2C34S* forward 5'-GGT GTGGGCCATCTAAAATGATTGC-3' and *TRX2C34S* reverse 5'-GCAATC ATTTAGATGGCCACACC-3' or *TRX2C31S, C34S* forward 5'-GCCAC ATGGCTCTGGGCCATCTAAAATGATTGC-3' and *TRX2C31S, C34S* reverse 5'-GCAATCATTAGATGGCCCAGACCATGTGGC-3'. All site-directed mutagenesis was performed using a standard PCR-based protocol with an S7 Fusion Polymerase (Biozym). Methylated template DNA was digested by *DpnI* (NEB), followed by transformation into chemically competent *E. coli* Top 10 cells and subsequent plasmid extraction. Mutations were confirmed by sequencing (Eurofins Genomics).

4.5. 5-FOA-based 'plasmid-shuffling' assays

In *Δtrx1Δtrx2Δgrx1Δgrx2* yeast cells, cell viability was initially maintained by the presence of a p416TEF roGFP2-*GRX2* plasmid. This strain was subsequently transformed with p415TEF plasmids for the expression of different enzymes including glutaredoxins, thioredoxins, protein disulfide isomerases and mutants thereof. Briefly, cells were harvested and resuspended in One-Step-Transformation buffer as described previously. Following the addition of 5 µl salmon testes single-strand-DNA and ~400 ng plasmid DNA, cells were incubated shaking at 45 °C for 30 min and subsequently plated onto appropriate HC plates for plasmid selection. Following transformation of the p415TEF plasmid cells were rigorously selected by two rounds of growth on HC plates without leucine and uracil. Subsequently, cells were streaked onto HC plates supplemented with 0.1% 5-fluoroorotic acid (5-FOA, Zymo Research) and incubated for 48 h at 30 °C. 5-FOA is only converted into toxic 5-fluorouracil in cells harboring a functional *URA3*. Therefore, 5-FOA is used as counter-selection for cells expressing a p416TEF plasmid. In other words, growth of *Δtrx1Δtrx2Δgrx1Δgrx2* cells on 5-FOA containing plates can only occur if the protein encoded on the p415TEF plasmid is capable of supporting cell viability. For further experiments strains growing on 5-FOA plates were re-streaked again and subsequently inoculated in HC medium lacking uracil to ensure all cells lost the p416TEF plasmid. In that way *Δtrx1Δtrx2Δgrx1Δgrx2 + p415TEF GRX2/GRX2/GRX2C64S/GRX7/roGFP2-GRX2/roGFP2-GRX7* strains were generated.

4.6. Intracellular measurements of roGFP2 oxidation

Redox-sensitive GFP2 (roGFP2) contains two cysteine residues on opposing β-strands directly adjacent to the GFP chromophore. These two cysteines residues can form a disulfide bond, which leads to a change in chromophore protonation (predominantly anionic in the reduced roGFP and predominantly neutral in the oxidized roGFP). The anionic chromophore has a fluorescence excitation maximum around 490 nm whilst for the neutral chromophore fluorescence excitation has a maximum around 400 nm. For both chromophores states fluorescence emission is around 510 nm. Thus, the fluorescence excitation ratio directly correlates to the degree of roGFP2 oxidation, which can be determined according to equation (1):

$$\text{OxD}_{\text{roGFP2}} = \frac{(I_{400\text{sample}} * I_{480\text{red}}) - (I_{400\text{red}} * I_{480\text{sample}})}{(I_{400\text{sample}} * I_{480\text{red}}) - (I_{400\text{sample}} * I_{480\text{ox}})} + \frac{(I_{400\text{ox}} * I_{480\text{sample}}) - (I_{400\text{red}} * I_{480\text{sample}})}{(I_{400\text{ox}} * I_{480\text{sample}}) - (I_{400\text{red}} * I_{480\text{sample}})} \quad (1)$$

All yeast strains in this study express either roGFP2 or genetic

fusions between roGFP2 and glutaredoxins from either p415TEF or p416TEF plasmids. RoGFP2 was synthesized with codons optimized for expression in yeast as described previously [49,53], as was *HsGrx5*. For roGFP2 assays, cells were grown in HC medium lacking uracil and leucine for plasmid selection at 30 °C to an OD₆₀₀ ≈ 3.5. Subsequently, 1.5 OD₆₀₀ units of cells were harvested and resuspended in 200 µl of 100 mM MES/Tris pH 6 and transferred to the well of a flat-bottomed 96-well plate. The 96-well plates were centrifuged at 15 g for 5 min to form a loose cell pellet at the bottom of each well.

For each strain samples treated with either 20 mM diamide or 100 mM DTT served as fully oxidized and fully reduced roGFP2 controls, respectively. These controls enable the determination of the degree of oxidation (OxD), according to Equation (1). RoGFP2 fluorescence was monitored using a BMG Labtech CLARIOstar fluorescence plate-reader. For dynamics measurements, roGFP2 fluorescence was monitored for ~15 min following the addition of exogenous H₂O₂ at the concentrations indicated [51].

4.7. Whole cell lysate GSH and GSSG measurements

The concentration of GSH and GSSG in yeast cells lysates was performed using a modified version of a 5,5'-dithiobis-2-nitrobenzoic acid (DTNB) assay as described previously [66]. Yeast cultures were grown in HC medium lacking uracil and leucine for plasmid selection until they reached an OD₆₀₀ ≈ 3.5. At this stage, fifty OD₆₀₀ units of cells (where 1 OD₆₀₀ unit equals 1 ml of culture with an OD₆₀₀ = 1) were harvested by centrifugation at 1000g for 3 min at 25 °C. Cells were washed once with 10 ml of Milli-Q H₂O, re-harvested by centrifugation and finally resuspended in 250 µl SSA buffer (1.3% sulfosalicylic acid, 8 mM HCl). Cells were lysed by addition of 0.5 mm glass-beads and subsequent shaking using a Disruptor Genie cell homogenizer (Carl Roth GmbH and Co, Karlsruhe, Germany) at 4 °C. A further 100 µl of SSA buffer was added and samples disrupted for a further 5 min. The resultant cell lysate was incubated on ice for 15 min to precipitate proteins followed by centrifugation at 16000g for 15 min at 4 °C.

To determine the 'total' glutathione concentration in the lysate (defined as GSH + GSSG, where one molecule of GSSG represents two GSH equivalents), 5 µl of supernatant was mixed with 995 µl ice-cold KPE buffer (100 mM potassium phosphate, 5 mM ethylenediaminetetraacetic acid [EDTA] pH 7.5). To determine GSSG levels, 100 µl supernatant was treated with 2 µl 20% (v/v) 2-vinylpyridine in ethanol and 40 µl 1 M MES/Tris pH 7.0 to raise the pH and alkylate GSH. Samples were incubated for 1 h at 25 °C. Both 'total' glutathione samples and GSSG samples were subsequently measured using a DTNB-recycling assay. For 'total' glutathione samples, 20 µl of the cell lysates was taken for the DTNB assay. For GSSG samples, 2 µl of sample was taken and adjusted to 20 µl with ice-cold KPE buffer. Next, for all samples were transferred to wells of a 96-well plate. To the samples, 120 µl KPE buffer containing 2 mg/ml NADPH and 2 mg/ml DTNB was added. Reactions were started by the addition of 0.16 U glutathione reductase. Absorbance change at 412 nm was measured using a BMG Labtech CLARIOstar plate-reader. 'Total' glutathione and GSSG concentrations were determined according to GSH and GSSG concentration standard curves.

4.8. Growth curves

Precultures for plasmid-shuffling experiments were grown in HC lacking leucine and uracil for plasmid selection, while precultures for all other experiments were grown in HC medium. Precultures were diluted to OD₆₀₀ = 0.5 in fresh media and grown for a further 4 h at 30 °C. Subsequently, 1 OD₆₀₀ unit of cells were harvested, washed and resuspended in 1 ml of distilled water. Aliquots of 10 µl of the cell suspension were added to 90 µl of the appropriate HC-medium in a 96-well plate. Cells were incubated with continuous shaking at 30 °C using a BioTek-Microplate Reader. The OD₆₀₀ was automatically recorded

every 10 min for at least 40 h. All growth curves were repeated at least 3 times.

Author contributions

B.M. and M.D. conceived the study, helped design and supervise the experiments, analyzed and interpreted experimental data and wrote the manuscript. J.M.H supervised experiments and helped to write the paper. J.Z. helped design and perform experiments, analyzed data and helped to write the manuscript. J.O. performed the measurements of glutathione content in cell lysates. S.H. performed all growth curve experiments.

Declaration of competing interest

The authors declare that they have no known competing financial interests or personal relationships that could have appeared to influence the work reported in this paper.

Acknowledgements

B.M., M.D. and J.M.H. acknowledge generous support from the DFG Priority Program SPP1710 (MO 2774/2-1 and DE 1431/8-2 and HE2803/8-2). We thank Jun.-Prof. Dr. Letícia Prates Roma for helpful comments on this manuscript.

Appendix A. Supplementary data

Supplementary data to this article can be found online at <https://doi.org/10.1016/j.redox.2020.101598>.

References

- [1] L. Liedgens, M. Deponte, The catalytic mechanism of glutaredoxins, in: Leopold Flohé (Ed.), *Glutathione*, CRC Press, 2019, pp. 251–261 ISBN 9780815365327.
- [2] J. Couturier, J.P. Jacquot, N. Rouhier, Evolution and diversity of glutaredoxins in photosynthetic organisms, *Cell. Mol. Life Sci.* 66 (2009) 2539–2557.
- [3] C.H. Lillig, C. Berndt, A. Holmgren, Glutaredoxin systems, *Biochim. Biophys. Acta* 1780 (2008) 1304–1317.
- [4] J.J. Mieyal, M.M. Gallogly, S. Qanungo, E.A. Sabens, M.D. Shelton, Molecular mechanisms and clinical implications of reversible protein S-glutathylation, *Antioxidants Redox Signal.* 10 (2008) 1941–1988.
- [5] M. Deponte, Glutathione catalysis and the reaction mechanisms of glutathione-dependent enzymes, *Biochim. Biophys. Acta* 1830 (2013) 3217–3266.
- [6] E. Herrero, M.A. de la Torre-Ruiz, Monothiol glutaredoxins: a common domain for multiple functions, *Cell. Mol. Life Sci.* 64 (2007) 1518–1530.
- [7] J. Couturier, J. Przybyla-Toscano, T. Roret, C. Didierjean, N. Rouhier, The roles of glutaredoxins ligating Fe-S clusters: sensing, transfer or repair functions? *Biochim. Biophys. Acta* 1853 (2015) 1513–1527.
- [8] C.E. Outten, A.N. Albel, Iron sensing and regulation in *Saccharomyces cerevisiae*: ironing out the mechanistic details, *Curr. Opin. Microbiol.* 16 (2013) 662–668.
- [9] A. Holmgren, Glutathione-dependent synthesis of deoxyribonucleotides. Purification and characterization of glutaredoxin from *Escherichia coli*, *J. Biol. Chem.* 254 (1979) 3664–3671.
- [10] A. Holmgren, F. Aslund, Glutaredoxin, *Methods Enzymol.* 252 (1995) 283–292.
- [11] A.V. Peskin, P.F. Pace, J.B. Behring, I.N. Paton, M. Soethoudt, M.M. Bachschmid, C.C. Winterburn, Glutathionylation of the active site cysteines of peroxiredoxin 2 and recycling by glutaredoxin, *J. Biol. Chem.* 291 (2016) 3053–3062.
- [12] C.F. Djuitka, S. Fiedler, M. Schnolzer, C. Sanchez, M. Lanzer, M. Deponte, Plasmodium falciparum antioxidant protein as a model enzyme for a special class of glutaredoxin/glutathione-dependent peroxiredoxins, *Biochim. Biophys. Acta* 1830 (2013) 4073–4090.
- [13] E.M. Hanschmann, M.E. Lonn, L.D. Schutte, M. Funke, J.R. Godoy, S. Ettrner, C. Hudemann, C.H. Lillig, Both thioredoxin 2 and glutaredoxin 2 contribute to the reduction of the mitochondrial 2-Cys peroxiredoxin Prx3, *J. Biol. Chem.* 285 (2010) 40699–40705.
- [14] F. Pauwels, B. Vergauwen, F. Vanrobaeys, B. Devreese, J.J. Van Beeumen, Purification and characterization of a chimeric enzyme from *Haemophilus influenzae* Rd that exhibits glutathione-dependent peroxidase activity, *J. Biol. Chem.* 278 (2003) 16658–16666.
- [15] N. Rouhier, E. Gelhaye, P.E. Sautiere, A. Brun, P. Laurent, D. Tagu, J. Gerard, E. de Fay, Y. Meyer, J.P. Jacquot, Isolation and characterization of a new peroxiredoxin from poplar sieve tubes that uses either glutaredoxin or thioredoxin as a proton donor, *Plant Physiol.* 127 (2001) 1299–1309.
- [16] H.Y. Kim, Glutaredoxin serves as a reductant for methionine sulfoxide reductases with or without resolving cysteine, *Acta Biochim. Biophys. Sin.* 44 (2012) 623–627.
- [17] L. Tarrago, E. Laugier, M. Zaffagnini, C. Marchand, P. Le Marechal, N. Rouhier, S.D. Lemaire, P. Rey, Regeneration mechanisms of *Arabidopsis thaliana* methionine sulfoxide reductases B by glutaredoxins and thioredoxins, *J. Biol. Chem.* 284 (2009) 18963–18971.
- [18] L. Lopez-Maury, A.M. Sanchez-Riego, J.C. Reyes, F.J. Florencio, The glutathione/glutaredoxin system is essential for arsenate reduction in *Synechocystis* sp. strain PCC 6803, *J. Bacteriol.* 191 (2009) 3534–3543.
- [19] S. Boukhenouna, H. Mazon, G. Branlant, C. Jacob, M.B. Toledano, S. Rahuel-Clermont, Evidence that glutathione and the glutathione system efficiently recycle 1-cys sulfiredoxin in vivo, *Antioxidants Redox Signal.* 22 (2015) 731–743.
- [20] C. Berndt, J.D. Schwenn, C.H. Lillig, The specificity of thioredoxins and glutaredoxins is determined by electrostatic and geometric complementarity, *Chem. Sci.* 6 (2015) 7049–7058.
- [21] C.H. Lillig, A. Prior, J.D. Schwenn, F. Aslund, D. Ritz, A. Vlamis-Gardikas, A. Holmgren, New thioredoxins and glutaredoxins as electron donors of 3'-phosphoadenylsulfate reductase, *J. Biol. Chem.* 274 (1999) 7695–7698.
- [22] M. Zheng, F. Aslund, G. Storz, Activation of the OxyR transcription factor by reversible disulfide bond formation, *Science* 279 (1998) 1718–1721.
- [23] M. Gellert, S. Venz, J. Mitlohner, C. Cott, E.M. Hanschmann, C.H. Lillig, Identification of a dithiol-disulfide switch in collapsin response mediator protein 2 (CRMP2) that is toggled in a model of neuronal differentiation, *J. Biol. Chem.* 288 (2013) 35117–35125.
- [24] L. Brautigam, L.D. Schutte, J.R. Godoy, T. Prozorovski, M. Gellert, G. Hauptmann, A. Holmgren, C.H. Lillig, C. Berndt, Vertebrate-specific glutaredoxin is essential for brain development, *Proc. Natl. Acad. Sci. U. S. A.* 108 (2011) 20532–20537.
- [25] E.G. Muller, Thioredoxin deficiency in yeast prolongs S phase and shortens the G1 interval of the cell cycle, *J. Biol. Chem.* 266 (1991) 9194–9202.
- [26] N. Mesecke, A. Spang, M. Deponte, J.M. Herrmann, A novel group of glutaredoxins in the *cis*-Golgi critical for oxidative stress resistance, *Mol. Biol. Cell* 19 (2008) 2673–2680.
- [27] N. Mesecke, S. Mittler, E. Eckers, J.M. Herrmann, M. Deponte, Two novel monothiol glutaredoxins from *Saccharomyces cerevisiae* provide further insight into iron-sulfur cluster binding, oligomerization, and enzymatic activity of glutaredoxins, *Biochemistry* 47 (2008) 1452–1463.
- [28] A. Izquierdo, C. Casas, A. Muñehoff, C.H. Lillig, E. Herrero, *Saccharomyces cerevisiae* Grx6 and Grx7 are monothiol glutaredoxins associated with the early secretory pathway, *Karyotyp.* Cell 7 (2008) 1415–1426.
- [29] J. Couturier, C.S. Koh, M. Zaffagnini, A.M. Winger, J.M. Gualberto, C. Corbier, P. Decottignies, J.P. Jacquot, S.D. Lemaire, C. Didierjean, et al., Structure-function relationship of the chloroplastic glutaredoxin S12 with an atypical WCSYS active site, *J. Biol. Chem.* 284 (2009) 9299–9310.
- [30] M. Zaffagnini, M. Bedhomme, C.H. Marchand, J.R. Couturier, X.H. Gao, N. Rouhier, P. Trost, S.P. Lemaire, Glutaredoxin S12: unique properties for redox signaling, *Antioxidants Redox Signal.* 16 (2012) 17–32.
- [31] O. Björnberg, H. Ostergaard, J.R. Winther, Mechanistic insight provided by glutaredoxin within a fusion to redox-sensitive yellow fluorescent protein, *Biochemistry* 45 (2006) 2362–2371.
- [32] F. Zahedi Avval, A. Holmgren, Molecular mechanisms of thioredoxin and glutaredoxin as hydrogen donors for Mammalian S phase ribonucleotide reductase, *J. Biol. Chem.* 284 (2009) 8233–8240.
- [33] M.M. Gallogly, D.W. Starke, A.K. Leonberg, S.M. Ospina, J.J. Mieyal, Kinetic and mechanistic characterization and versatile catalytic properties of mammalian glutaredoxin 2: implications for intracellular roles, *Biochemistry* 47 (2008) 11144–11157.
- [34] Y. Yang, S. Jao, S. Nanduri, D.W. Starke, J.J. Mieyal, J. Qin, Reactivity of the human thioltransferase (glutaredoxin) C7S, C25S, C78S, C82S mutant and NMR solution structure of its glutathionyl mixed disulfide intermediate reflect catalytic specificity, *Biochemistry* 37 (1998) 17145–17156.
- [35] Y.F. Yang, W.W. Wells, Identification and characterization of the functional amino acids at the active center of pig liver thioltransferase by site-directed mutagenesis, *J. Biol. Chem.* 266 (1991) 12759–12765.
- [36] S.A. Gravina, J.J. Mieyal, Thioltransferase is a specific glutathionyl mixed disulfide oxidoreductase, *Biochemistry* 32 (1993) 3368–3376.
- [37] A.A. Ukwela, A.I. Bush, A.G. Wedd, Z. Xiao, Glutaredoxins employ parallel monothiol-dithiol mechanisms to catalyze thiol-disulfide exchanges with protein disulfides, *Chem. Sci.* 9 (2018) 1173–1183.
- [38] J.H. Bushweller, F. Aslund, K. Wuthrich, A. Holmgren, Structural and functional characterization of the mutant *Escherichia coli* glutaredoxin (C14—S) and its mixed disulfide with glutathione, *Biochemistry* 31 (1992) 9288–9293.
- [39] F. Gama, C. Brehelein, E. Gelhaye, Y. Meyer, J.P. Jacquot, P. Rey, N. Rouhier, Functional analysis and expression characteristics of chloroplastic Prx IIIE, *Physiol. Plantarum* 133 (2008) 599–610.
- [40] T. Draculic, I.W. Dawes, C.M. Grant, A single glutaredoxin or thioredoxin gene is essential for viability in the yeast *Saccharomyces cerevisiae*, *Mol. Microbiol.* 36 (2000) 1167–1174.
- [41] E. Eckers, M. Bien, V. Stroobant, J.M. Herrmann, M. Deponte, Biochemical characterization of dithiol glutaredoxin 8 from *Saccharomyces cerevisiae*: the catalytic redox mechanism redux, *Biochemistry* 48 (2009) 1410–1423.
- [42] R.S. Sikorski, J.D. Boeke, In vitro mutagenesis and plasmid shuffling: from cloned gene to mutant yeast, *Methods Enzymol.* 194 (1991) 302–318.
- [43] J.D. Boeke, F. LaCroute, G.R. Fink, A positive selection for mutants lacking ornithine-5-phosphate decarboxylase activity in yeast: 5-fluoro-orotic acid resistance, *Mol. Gen. Genet.* 197 (1984) 345–346.
- [44] D. Mumberg, R. Muller, M. Funk, Yeast vectors for the controlled expression of

- heterologous proteins in different genetic backgrounds, *Gene* 156 (1995) 119–122.
- [45] L. Liedgens, J. Zimmermann, L. Wäschenbach, F. Geissel, H. Laporte, H. Gohlke, B. Morgan, M. Deponte, Quantitative assessment of the determinant structural differences between redox-active and inactive glutaredoxins, *Nat. Commun.* 11 (2020) 1725.
- [46] N.J. Bulleid, L. Ellgaard, Multiple ways to make disulfides, *Trends Biochem. Sci.* 36 (2011) 485–492.
- [47] F. Vignols, C. Brehelin, Y. Surdin-Kerjan, D. Thomas, Y. Meyer, A yeast two-hybrid knockout strain to explore thioredoxin-interacting proteins *in vivo*, *Proc. Natl. Acad. Sci. U. S. A.* 102 (2005) 16729–16734.
- [48] N. Mouahed, D. Thomas, L. Verdoucq, P. Monfort, Y. Meyer, In vivo functional discrimination between plant thioredoxins by heterologous expression in the yeast *Saccharomyces cerevisiae*, *Proc. Natl. Acad. Sci. U. S. A.* 95 (1998) 3312–3317.
- [49] B. Morgan, D. Ezerina, T.N. Amoako, J. Riemer, M. Seedorf, T.P. Dick, Multiple glutathione disulfide removal pathways mediate cytosolic redox homeostasis, *Nat. Chem. Biol.* 9 (2013) 119–125.
- [50] A.J. Meyer, T.P. Dick, Fluorescent protein-based redox probes, *Antioxidants Redox Signal.* 13 (2010) 621–650.
- [51] B. Morgan, M.C. Sobotta, T.P. Dick, Measuring E(GSH) and H₂O₂ with roGFP2-based redox probes, *Free Radic. Biol. Med.* 51 (2011) 1943–1951.
- [52] M. Schwarlander, T.P. Dick, A.J. Meyer, B. Morgan, Dissecting redox biology using fluorescent protein sensors, *Antioxidants Redox Signal.* 24 (2016) 680–712.
- [53] B. Morgan, K. Van Laer, T.N. Owusu, D. Ezerina, D. Pastor-Flores, P.S. Amponsah, A. Tursch, T.P. Dick, Real-time monitoring of basal H₂O₂ levels with peroxiredoxin-based probes, *Nat. Chem. Biol.* 12 (2016) 437–443.
- [54] E.G. Muller, A glutathione reductase mutant of yeast accumulates high levels of oxidized glutathione and requires thioredoxin for growth, *Mol. Biol. Cell* 7 (1996) 1805–1813.
- [55] A. Vlamis-Gardikas, A. Holmgren, Thioredoxin and glutaredoxin isoforms, *Methods Enzymol.* 347 (2002) 286–296.
- [56] C.H. Lillig, C. Berndt, Glutaredoxins in thiol/disulfide exchange, *Antioxidants Redox Signal.* 18 (2013) 1654–1665.
- [57] P. Begas, L. Liedgens, A. Moseler, A.J. Meyer, M. Deponte, Glutaredoxin catalysis requires two distinct glutathione interaction sites, *Nat. Commun.* 8 (2017) 14835.
- [58] P. Begas, V. Staudacher, M. Deponte, Systematic re-evaluation of the bis(2-hydroxyethyl)disulfide (HEDS) assay reveals an alternative mechanism and activity of glutaredoxins, *Chem. Sci.* 6 (2015) 3788–3796.
- [59] J.R. Pedrajas, P. Porras, E. Martínez-Galisteo, C.A. Padilla, A. Miranda-Vizcute, J.A. Barcena, Two isoforms of *Saccharomyces cerevisiae* glutaredoxin 2 are expressed *in vivo* and localize to different subcellular compartments, *Biochem. J.* 364 (2002) 617–623.
- [60] K. Kojer, V. Peleh, G. Calabrese, J.M. Herrmann, J. Riemer, Kinetic control by limiting glutaredoxin amounts enables thiol oxidation in the reducing mitochondrial intermembrane space, *Mol. Biol. Cell* 26 (2015) 195–204.
- [61] M. Deponte, The incomplete glutathione puzzle: just guessing at numbers and figures? *Antioxidants Redox Signal.* 27 (2017) 1130–1161.
- [62] L.D. Schutte, S. Baumüller, B. Weis, C. Hudemann, E.M. Hanschmann, C.H. Lillig, Identification of potential protein dithiol-disulfide substrates of mammalian Grx2, *Biochim. Biophys. Acta* 1830 (2013) 4999–5005.
- [63] N. Rouhier, A. Villarejo, M. Srivastava, E. Gelhaye, O. Keech, M. Droux, I. Finkemeier, G. Samuelsson, K.J. Dietz, J.P. Jacquot, et al., Identification of plant glutaredoxin targets, *Antioxidants Redox Signal.* 7 (2005) 919–929.
- [64] N. Sturm, E. Jortzik, B.M. Mailu, S. Koncarevic, M. Deponte, K. Forchhammer, S. Rahlf, K. Becker, Identification of proteins targeted by the thioredoxin superfamily in *Plasmodium falciparum*, *PLoS Pathog.* 5 (2009) e1000383.
- [65] C. Janke, M.M. Magiera, N. Rathfelder, C. Taxis, S. Reber, H. Maekawa, A. Moreno-Borchart, G. Doenges, E. Schwob, E. Schiebel, et al., A versatile toolbox for PCR-based tagging of yeast genes: new fluorescent proteins, more markers and promoter substitution cassettes, *Yeast* 21 (2004) 947–962.
- [66] I. Rahman, A. Kode, S.K. Biswas, Assay for quantitative determination of glutathione and glutathione disulfide levels using enzymatic recycling method, *Nat. Protoc.* 1 (2006) 3159–3165.

2.3.1. Supplementary information

One cysteine is enough: A monothiol Grx can functionally replace all cytosolic Trx and dithiol Grx.

Zimmermann, J., Oestreicher, J., Hess, S., Herrmann, J.M., Deponte, M. and Morgan, B.
Redox Biology. 2020 May; 101598
DOI: 10.1016/j.redox.2020.101598

Reprinted from *Redox Biology*: Zimmermann, J., Oestreicher, J., Hess, S., Herrmann, J.M., Deponte, M. and Morgan, B. *One cysteine is enough: A monothiol Grx can functionally replace all cytosolic Trx and dithiol Grx.* 101598 © (2020), with permission from Elsevier (*Redox Biology, Society of Redox Biology and Medicine*).

All rights reserved.

Supplementary Information

One cysteine is enough: A monothiol Grx can functionally replace all cytosolic Trx and dithiol Grx

Jannik Zimmermann¹, Julian Oestreicher¹, Steffen Hess², Johannes M Herrmann², Marcel Deponte^{3,*}
Bruce Morgan^{1,*}

Affiliations:

¹ Institute of Biochemistry, Zentrum für Human- und Molekularbiologie (ZHMB), Saarland University,
Saarbrücken, Germany

² Cell Biology, University of Kaiserslautern, Kaiserslautern, Germany

³ Faculty of Chemistry, Department of Biochemistry, University of Kaiserslautern, Kaiserslautern,
Germany

*To whom correspondence should be addressed

Prof. Dr. Bruce Morgan

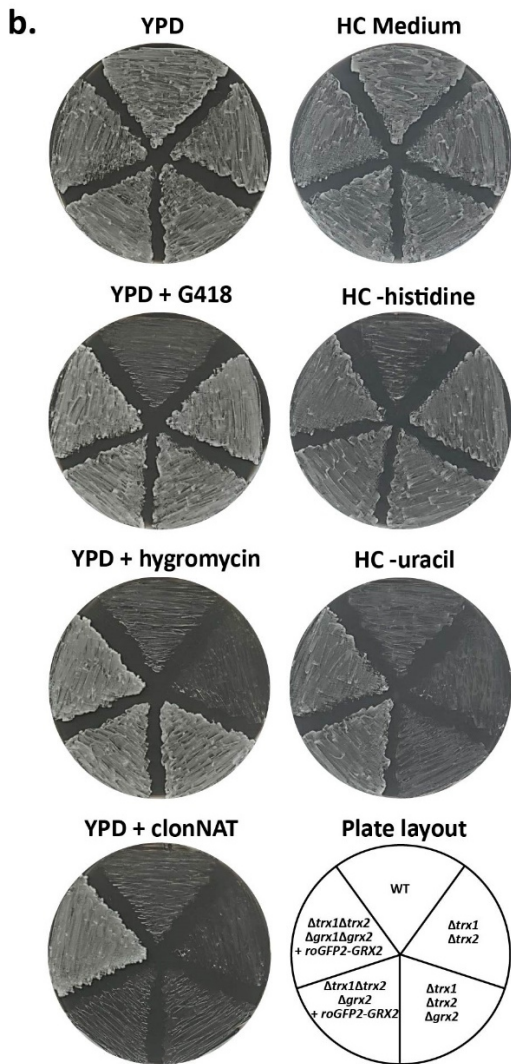
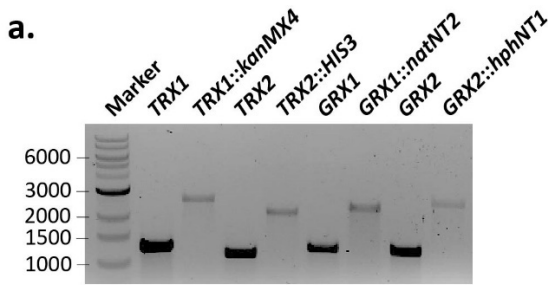
Tel.: +49-681-302-3339

Email: bruce.morgan@uni-saarland.de

Prof. Dr. Marcel Deponte

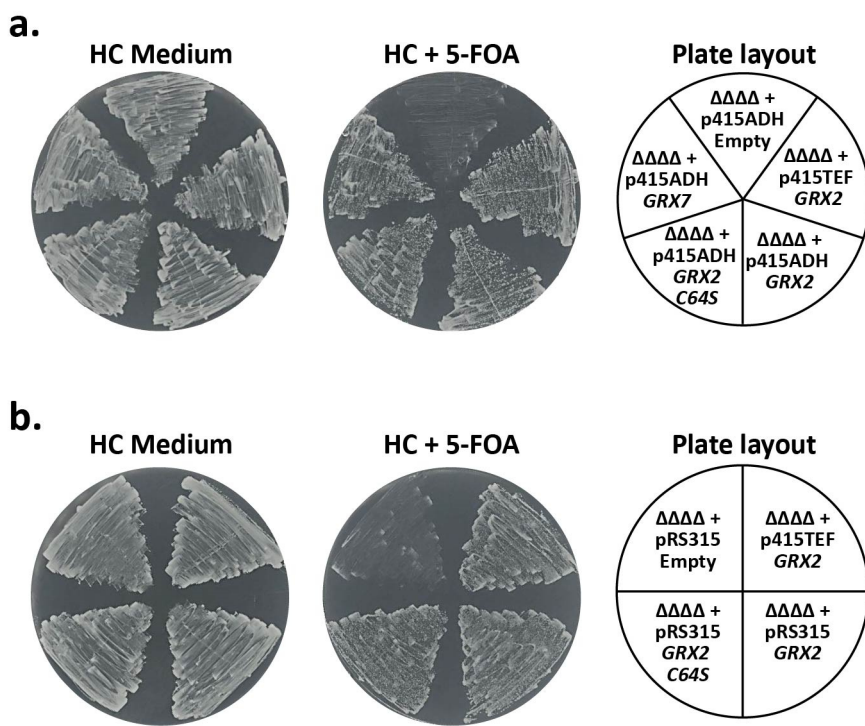
Tel.: +49-6841-205-4060

Email: deponte@chemie.uni-kl.de



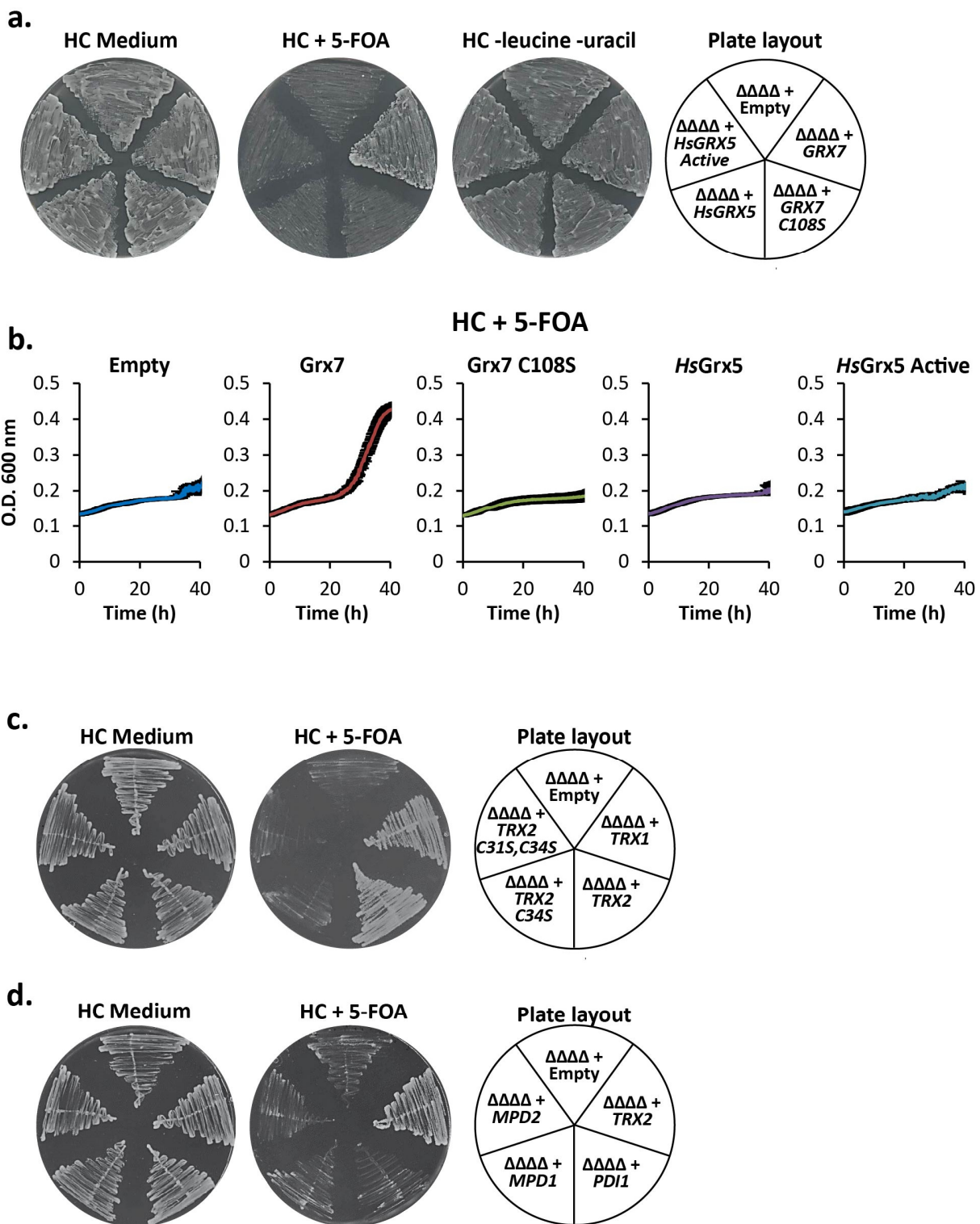
Supplementary Figure 1. Generation of a BY4742 $\Delta trx1\Delta trx2\Delta grx1\Delta grx2$ strain.

a. The $\Delta trx1\Delta trx2\Delta grx1\Delta grx2$ strain was constructed in a $\Delta trx1\Delta trx2$ background. First the *GRX2* gene was deleted. Subsequently, the $\Delta trx1\Delta trx2\Delta grx2$ strain was transformed with a p416TEF *roGFP2-GRX2* plasmid. Finally, in this background, *GRX1* was deleted. Confirmation PCRs were performed on the genomic DNA isolated from the $\Delta trx1\Delta trx2\Delta grx1\Delta grx2$ + p416TEF *roGFP2-GRX2* strain to confirm correct deletion and replacement by the appropriate antibiotic resistance cassette at all loci. *TRX1* was replaced by a *kanMX4* cassette, *TRX2* by a *HIS3* gene, *GRX1* by a *natNT2* cassette and *GRX2* by an *hphNT1* cassette. **b.** The strains indicated in the plate layout were streaked onto different agar plates as indicated. All strains grew as expected based on their auxotrophic and antibiotic resistance markers.



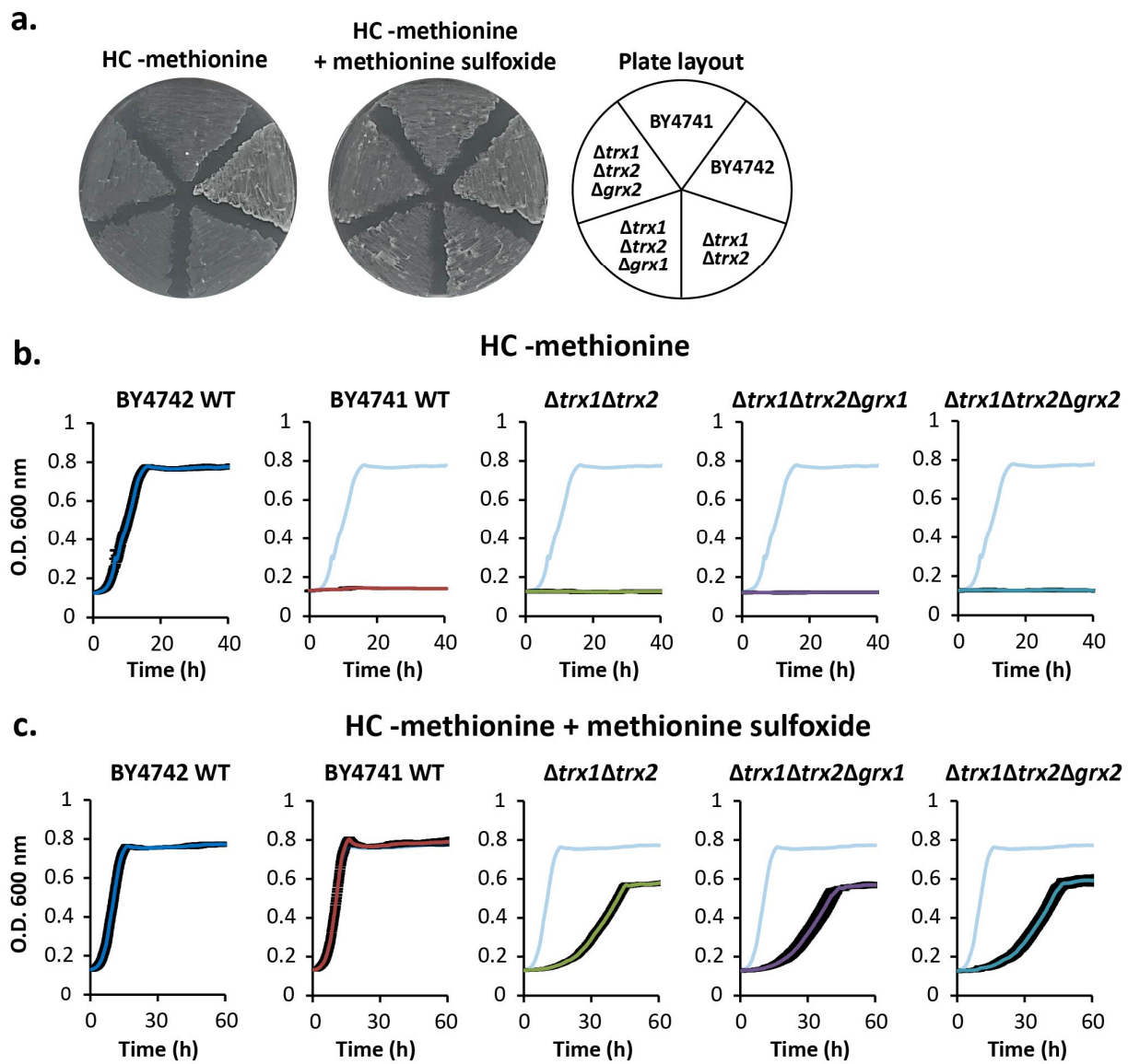
Supplementary Figure 2. Grx2 C64S rescues viability of a $\Delta trx1\Delta trx2\Delta grx1\Delta grx2$ strain when expressed from an ADH, TEF or endogenous promoter.

a. BY4742 $\Delta trx1\Delta trx2\Delta grx1\Delta grx2$ cells containing a p416TEF plasmid encoding roGFP2-Grx2 and a p415TEF plasmid encoding Grx2 under the control of a TEF promoter, or Grx2, Grx2 C64S and Grx7 under the control of an ADH promoter, were streaked onto HC plates as well as HC plates containing 0.1 g/l 5-FOA and incubated for 48 hours at 30°C. **b.** BY4742 $\Delta trx1\Delta trx2\Delta grx1\Delta grx2$ cells containing a p416TEF plasmid encoding roGFP2-Grx2 and a p415TEF plasmid encoding Grx2 or pRS315 plasmids encoding either Grx2 or Grx2C64S with their endogenous promoter and terminator, as well as an empty pRS315 plasmid control.



Supplementary Figure 3. Monothiol thioredoxins and PDIs cannot support protein disulfide reduction.

a. BY4742 Δ tr_x1 Δ tr_x2 Δ gr_x1 Δ gr_x2 cells containing a p416TEF plasmid encoding roGFP2-Grx2 and a p415TEF plasmid encoding either Grx7, Grx7 C108S, HsGrx5, an enzymatically active HsGrx5 mutant (HsGrx5 Active) or an empty p415TEF plasmid, were streaked onto HC plates as well as HC plates containing 0.1 g/l 5-FOA and incubated for 48 hours at 30°C. **b.** The strains described in (a.) were inoculated into HC liquid media supplemented with 0.1 g/l 5-FOA to an initial OD₆₀₀ = 0.1. Cells were grown with continuous shaking at 30°C. **c.** BY4742 Δ tr_x1 Δ tr_x2 Δ gr_x1 Δ gr_x2 cells containing a p416TEF plasmid encoding roGFP2-Grx2 and a p415TEF plasmid encoding either Trx1, Trx2, Trx2 C34S or Trx2 C31S,C34S were streaked onto HC plates as well as HC plates containing 0.1 g/l 5-FOA and incubated for 48 hours at 30°C. **d.** BY4742 Δ tr_x1 Δ tr_x2 Δ gr_x1 Δ gr_x2 cells containing a p416TEF plasmid encoding roGFP2-Grx2 and a p415TEF plasmid encoding either Trx2, Pdi1, Mpd1 or Mpd2 were streaked onto HC plates as well as HC plates containing 0.1 g/l 5-FOA and incubated for 48 hours at 30°C.



Supplementary Figure 4. Monothiol glutaredoxins can support reduction of yeast 2-Cys methionine sulfoxide reductase.

a. BY4741 WT, BY4742 WT, $\Delta trx1\Delta trx2$, $\Delta trx1\Delta trx2\Delta grx1$ and $\Delta trx1\Delta trx2\Delta grx2$ cells were streaked onto HC agar plates either lacking methionine or supplemented with 0.24 mM methionine sulfoxide as indicated. Plates were incubated at 30°C for 48 hours. **b.** The strains described in (a.) were inoculated into liquid HC media either **b.** lacking methionine or **c.** supplemented with 0.24 mM L-methionine sulfoxide to an initial $OD_{600} = 0.1$, and grown with continuous shaking at 30°C.

Supplementary Table 1. Yeast strains used in this study

Genotype	Source	Figure
BY4741 MATα his3Δ1 leu2Δ0 met15Δ0 ura3Δ0	Euroscarf	3a,b,c; S4a,b,c
BY4742 MATα his3Δ1 leu2Δ1 lys2Δ0 ura3Δ0	Euroscarf	2e; 3a,b,c; 4g,h; S1a,b; S4a,b,c
BY4742 Δ$trx1::kanMX4$ Δ$trx2::HIS3$	Carlsberg laboratory	3a,b,c; 4g,h; S1b; S4a,b,c
BY4742 Δ$trx1::kanMX4$ Δ$trx2::HIS3$ Δ$grx1::hphNT1$	This study	3a,b,c; 4g,h; S1b; S4a,b,c
BY4742 Δ$trx1::kanMX4$ Δ$trx2::HIS3$ Δ$grx2::hphNT1$	This study	3a,b,c; 4g,h; S1b; S4a,b,c
BY4742 Δ$trx1::kanMX4$ Δ$trx2::HIS3$ Δ$grx2::hphNT1$ + p416TEF roGFP2-Grx2	This study	S1b
BY4742 Δ$trx1::kanMX4$ Δ$trx2::HIS3$ Δ$grx1::natNT2$ Δ$grx2::hphNT1$ + p416TEF roGFP2-Grx2	This study	S1a,b
BY4742 Δ$trx1::kanMX4$ Δ$trx2::HIS3$ Δ$grx1::natNT2$ Δ$grx2::hphNT1$ + p416TEF roGFP2-Grx2 + p415TEF Empty	This study	2a,b,c,d; S3a,b,c,d
BY4742 Δ$trx1::kanMX4$ Δ$trx2::HIS3$ Δ$grx1::natNT2$ Δ$grx2::hphNT1$ + p416TEF roGFP2-Grx2 + p415TEF Grx1	This study	2a,c
BY4742 Δ$trx1::kanMX4$ Δ$trx2::HIS3$ Δ$grx1::natNT2$ Δ$grx2::hphNT1$ + p416TEF roGFP2-Grx2 + p415TEF Grx2	This study	2a,b,c,d
BY4742 Δ$trx1::kanMX4$ Δ$trx2::HIS3$ Δ$grx1::natNT2$ Δ$grx2::hphNT1$ + p416TEF roGFP2-Grx2 + p415TEF HsGrx5	This study	2a,c; S3a,b
BY4742 Δ$trx1::kanMX4$ Δ$trx2::HIS3$ Δ$grx1::natNT2$ Δ$grx2::hphNT1$ + p416TEF roGFP2-Grx2 + p415TEF Grx7	This study	1a,c; S3a,b
BY4742 Δ$trx1::kanMX4$ Δ$trx2::HIS3$ Δ$grx1::natNT2$ Δ$grx2::hphNT1$ + p416TEF roGFP2-Grx2 + p415TEF Grx2 C61S	This study	2b,d
BY4742 Δ$trx1::kanMX4$ Δ$trx2::HIS3$ Δ$grx1::natNT2$ Δ$grx2::hphNT1$ + p416TEF roGFP2-Grx2 + p415TEF Grx2 C64S	This study	2b,d
BY4742 Δ$trx1::kanMX4$ Δ$trx2::HIS3$ Δ$grx1::natNT2$ Δ$grx2::hphNT1$ + p416TEF roGFP2-Grx2 + p415TEF Grx2 C61S,C64S	This study	2b,d
BY4742 Δ$trx1::kanMX4$ Δ$trx2::HIS3$ Δ$grx1::natNT2$ Δ$grx2::hphNT1$ + p416TEF roGFP2-Grx2 + p415TEF Grx7 C108S	This study	S3a,b
BY4742 Δ$trx1::kanMX4$ Δ$trx2::HIS3$ Δ$grx1::natNT2$ Δ$grx2::hphNT1$ + p416TEF roGFP2-Grx2 + p415TEF HsGrx5-Active (Loop+G68P+R97Q)	This study	S3a,b
BY4742 Δ$trx1::kanMX4$ Δ$trx2::HIS3$ Δ$grx1::natNT2$ Δ$grx2::hphNT1$ + p416TEF roGFP2-Grx2 + p415TEF Trx1	This study	S3c
BY4742 Δ$trx1::kanMX4$ Δ$trx2::HIS3$ Δ$grx1::natNT2$ Δ$grx2::hphNT1$ + p416TEF roGFP2-Grx2 + p415TEF Trx2	This study	S3c,d

BY4742 Δtr₁::kanMX4 Δtr₂::HIS3 Δgrx1::natNT2 Δ grx2::hphNT1 + p416TEF roGFP2-Grx2 + p415TEF Trx2 C34S	This study	S3c,d
BY4742 Δtr₁::kanMX4 Δtr₂::HIS3 Δgrx1::natNT2 Δ grx2::hphNT1 + p416TEF roGFP2-Grx2 + p415TEF Trx2 C31S,C34S	This study	S3c,d
BY4742 Δtr₁::kanMX4 Δtr₂::HIS3 Δgrx1::natNT2 Δ grx2::hphNT1 + p416TEF roGFP2-Grx2 + p415TEF Pdi1	This study	S3c,d
BY4742 Δtr₁::kanMX4 Δtr₂::HIS3 Δgrx1::natNT2 Δ grx2::hphNT1 + p416TEF roGFP2-Grx2 + p415TEF Mpd1	This study	S3c,d
BY4742 Δtr₁::kanMX4 Δtr₂::HIS3 Δgrx1::natNT2 Δ grx2::hphNT1 + p416TEF roGFP2-Grx2 + p415TEF Mpd2	This study	S3c,d
BY4742 Δtr₁::kanMX4 Δtr₂::HIS3 Δgrx1::natNT2 Δ grx2::hphNT1 + p415TEF Grx1	This study	2e; 3a,b,c
BY4742 Δtr₁::kanMX4 Δtr₂::HIS3 Δgrx1::natNT2 Δ grx2::hphNT1 + p415TEF Grx2	This study	2e; 3a,b,c
BY4742 Δtr₁::kanMX4 Δtr₂::HIS3 Δgrx1::natNT2 Δ grx2::hphNT1 + p415TEF Grx2 C64S	This study	2e; 3a,b,c
BY4742 Δtr₁::kanMX4 Δtr₂::HIS3 Δgrx1::natNT2 Δ grx2::hphNT1 + p415TEF Grx7	This study	2e; 3a,b,c
BY4742 Δtr₁::kanMX4 Δtr₂::HIS3 Δgrx1::natNT2 Δ grx2::hphNT1 + p416TEF Empty + p415TEF Grx2	This study	4a,b,c,d,e,f
BY4742 Δtr₁::kanMX4 Δtr₂::HIS3 Δgrx1::natNT2 Δ grx2::hphNT1 + p416TEF roGFP2 + p415TEF Grx1	This study	4a,g,h
BY4742 Δtr₁::kanMX4 Δtr₂::HIS3 Δgrx1::natNT2 Δ grx2::hphNT1 + p416TEF roGFP2 + p415TEF Grx2	This study	4b,g,h
BY4742 Δtr₁::kanMX4 Δtr₂::HIS3 Δgrx1::natNT2 Δ grx2::hphNT1 + p416TEF roGFP2 + p415TEF Grx2 C64S	This study	4c,g,h
BY4742 Δtr₁::kanMX4 Δtr₂::HIS3 Δgrx1::natNT2 Δ grx2::hphNT1 + p416TEF roGFP2 + p415TEF Grx7	This study	4d,g,h
BY4742 MATα his3Δ1 leu2Δ1 lys2Δ0 ura3Δ0 + p416TEF roGFP2 + p415TEF Empty	This study	4g,h
BY4742 Δtr₁::kanMX4 Δtr₂::HIS3 + p416TEF roGFP2 + p415TEF Empty	This study	4g,h
BY4742 Δtr₁::kanMX4 Δtr₂::HIS3 Δgrx1::hphNT1 + p416TEF roGFP2 + p415TEF Empty	This study	4g,h
BY4742 Δtr₁::kanMX4 Δtr₂::HIS3 Δgrx2::hphNT1 + p416TEF roGFP2 + p415TEF Empty	This study	4g,h
BY4742 Δtr₁::kanMX4 Δtr₂::HIS3 Δgrx1::natNT2 Δ grx2::hphNT1 + p415TEF roGFP2-Grx2 + p416TEF Empty	This study	4e
BY4742 Δtr₁::kanMX4 Δtr₂::HIS3 Δgrx1::natNT2 Δ grx2::hphNT1 + p415TEF roGFP2-Grx7 + p416TEF Empty	This study	4f

BY4742 Δtr₁::kanMX4 Δtr₂::HIS3 Δgr_{x1}::natNT2	This study	S2a
Δ gr _{x2} ::hphNT1 + p416TEF roGFP2-Grx2		
+ p415ADH Empty		
BY4742 Δtr₁::kanMX4 Δtr₂::HIS3 Δgr_{x1}::natNT2	This study	S2a
Δ gr _{x2} ::hphNT1 + p416TEF roGFP2-Grx2		
+ p415ADH Grx2		
BY4742 Δtr₁::kanMX4 Δtr₂::HIS3 Δgr_{x1}::natNT2	This study	S2a
Δ gr _{x2} ::hphNT1 + p416TEF roGFP2-Grx2		
+ p415ADH Grx2 C64S		
BY4742 Δtr₁::kanMX4 Δtr₂::HIS3 Δgr_{x1}::natNT2	This study	S2a
Δ gr _{x2} ::hphNT1 + p416TEF roGFP2-Grx2		
+ p415ADH Grx7		
BY4742 Δtr₁::kanMX4 Δtr₂::HIS3 Δgr_{x1}::natNT2	This study	S2b
Δ gr _{x2} ::hphNT1 + p416TEF roGFP2-Grx2		
+ pRS315 Empty		
BY4742 Δtr₁::kanMX4 Δtr₂::HIS3 Δgr_{x1}::natNT2	This study	S2b
Δ gr _{x2} ::hphNT1 + p416TEF roGFP2-Grx2		
+ pRS315 Prom. _{GRX2} ::Grx2::Term. _{GRX2}		
BY4742 Δtr₁::kanMX4 Δtr₂::HIS3 Δgr_{x1}::natNT2	This study	S2b
Δ gr _{x2} ::hphNT1 + p416TEF roGFP2-Grx2		
+ pRS315 Prom. _{GRX2} ::Grx2 C64S::Term. _{GRX2}		

2.4. Amponsah *et al.*, 2021, *Nature Chemical Biology*

Peroxiredoxins couple metabolism and cell division in an ultradian cycle.

Amponsah, P.S., Yahya, G., **Zimmermann, J.**, Mai, M., Mergel, S., Mühlhaus, T., Storchova, Z. and Morgan, B.

Nature Chemical Biology. 2021 February, 17(4), 477-484

DOI: 10.1038/s41589-020-00728-9

Reprinted from *Nature Chemical Biology*: Amponsah, P.S., Yahya, G., Zimmermann, J., Mai, M., Mergel, S., Mühlhaus, T., Storchova. Z. and Morgan, B. Peroxiredoxins couple metabolism and cell division in an ultradian cycle. 17(4), 477-484 © (2021), with permission from Nature Springer (*Nature Chemical Biology*).

All rights reserved.



Peroxiredoxins couple metabolism and cell division in an ultradian cycle

Prince Saforo Amponsah^{1,2}, Galal Yahya^{3,4}, Jannik Zimmermann^{1,2}, Marie Mai^{1,2}, Sarah Mergel¹, Timo Mühlhaus⁵, Zuzana Storchova^{1,4} and Bruce Morgan^{1,2}✉

Redox cycles have been reported in ultradian, circadian and cell cycle-synchronized systems. Redox cycles persist in the absence of transcription and cyclin-CDK activity, indicating that cells harbor multiple coupled oscillators. Nonetheless, the causal relationships and molecular mechanisms by which redox cycles are embedded within ultradian, circadian or cell division cycles remain largely elusive. Yeast harbor an ultradian oscillator, the yeast metabolic cycle (YMC), which comprises metabolic/redox cycles, transcriptional cycles and synchronized cell division. Here, we reveal the existence of robust cycling of H₂O₂ and peroxiredoxin oxidation during the YMC and show that peroxiredoxin inactivation disrupts metabolic cycling and abolishes coupling with cell division. We find that thiol-disulfide oxidants and reductants predictably modulate the switching between different YMC metabolic states, which in turn predictably perturbs cell cycle entry and exit. We propose that oscillatory H₂O₂-dependent protein thiol oxidation is a key regulator of metabolic cycling and its coordination with cell division.

Circadian clocks play an important role in adapting organismal physiology in anticipation of daily environmental changes and in the temporal compartmentalization of cellular processes^{1,2}. The circadian clock is also frequently found to be robustly coupled to cell division³. Circadian clocks are well understood to be controlled by transcription translation feedback loops (TTFLs). Nonetheless, the existence of TTFL-independent circadian clocks has been recognized for several decades^{4–7}. The concept of TTFL-independent clocks was recently generalized and extended to mammalian systems by the discovery of circadian and ultradian oscillations in the level of hyperoxidized peroxiredoxin proteins—peroxiredoxins in which the active-site cysteine residue is oxidized to a sulfinic (SO₂H) or sulfonic acid (SO₃H)—in representative organisms from all three domains of life^{8–13}. These observations suggest the existence of a universally conserved, metabolism-based, timekeeping mechanism that possibly precedes the more recently evolved TTFL-based clocks found in many organisms. However, it remains unclear if peroxiredoxins play an active role in cellular timekeeping or are merely convenient reporters of clock activity.

Budding yeast (*Saccharomyces cerevisiae*) do not have a circadian clock, but do maintain an ultradian cycle that is known as the yeast metabolic cycle (YMC)¹⁴. The YMC encompasses metabolic and transcriptional cycles as well as synchronized cell division. The most obvious feature of the YMC is an oscillation in oxygen consumption between phases of low oxygen consumption (LOC) and high oxygen consumption (HOC)¹⁴ (Fig. 1a). Furthermore, the levels of many metabolites and more than 50% of gene transcripts also oscillate during the YMC^{14,15}. In the YMC, cell division is synchronized with, and probably gated by, metabolic cycles^{16–19}. Interestingly, several studies have indicated that redox processes play an important role in YMC regulation^{14,15,20}, and cycles of peroxiredoxin hyperoxidation have recently been reported⁸. The YMC thus represents a convenient model system to investigate the role of peroxiredoxins in cellular timekeeping and in the coupling of cell division to metabolic cycles.

Peroxiredoxins, which are thiol peroxidases, are among the most H₂O₂-reactive proteins in the cell and are well understood to play an important role in the removal of cellular H₂O₂²¹. Peroxiredoxins harbor an extremely H₂O₂-reactive cysteine residue, termed the peroxidatic cysteine (C_p). Peroxidatic cysteine residues can react with H₂O₂ with a second-order rate constant in the range of 10⁵–10⁸ M^{−1} s^{−1} to form a cysteine sulfenic acid (SOH). The cysteine sulfenic acid group then typically reacts with another thiol to form a disulfide bond. In the case of typical and atypical 2-Cys peroxiredoxins, this second thiol is provided by a protein cysteine residue termed the resolving cysteine (C_R)²². In the context of their normal catalytic cycle, the peroxiredoxin disulfide bond is usually reduced by thioredoxin, thereby allowing for a new round of H₂O₂ reduction. However, in situations of high peroxide concentration it is possible for the C_p sulfenic acid to react with further molecules of peroxide before it can react with the C_R, leading to the formation of C_p sulfinic or sulfonic acid groups. This is referred to as hyperoxidation and results in inactivation of peroxiredoxin catalytic activity²³.

Here, using a genetically encoded roGFP2-Tsa2ΔC_R sensor, we show that there are cyclical changes in H₂O₂ levels and peroxiredoxin disulfide formation during the YMC. We reveal that switching between LOC and HOC can be predictably controlled by thiol-disulfide oxidation and reduction and demonstrate that peroxiredoxins are essential for coupling cell division to metabolic cycles. Disrupting YMC progression with thiol oxidants or reductants strongly disrupts cell cycle entry and exit, leading, for example, to de novo cell cycle initiation, irrespective of completion of the preceding round of cell division. In summary, our findings indicate that peroxiredoxins are important regulators of YMC progression and of the coupling of metabolic cycles with cell division.

Results

H₂O₂ levels oscillate during the YMC. We first sought to monitor H₂O₂ levels during the YMC. To this end, we employed a genetically

¹Cellular Biochemistry, Technische Universität Kaiserslautern, Kaiserslautern, Germany. ²Institute of Biochemistry, Centre for Human and Molecular Biology (ZHMB), Saarland University, Saarbrücken, Germany. ³Department of Microbiology and Immunology, School of Pharmacy, Zagazig University, Zagazig, Egypt. ⁴Department of Molecular Genetics, Technische Universität Kaiserslautern, Kaiserslautern, Germany. ⁵Computational Systems Biology, Technische Universität Kaiserslautern, Kaiserslautern, Germany. ✉e-mail: bruce.morgan@uni-saarland.de

ARTICLES

NATURE CHEMICAL BIOLOGY

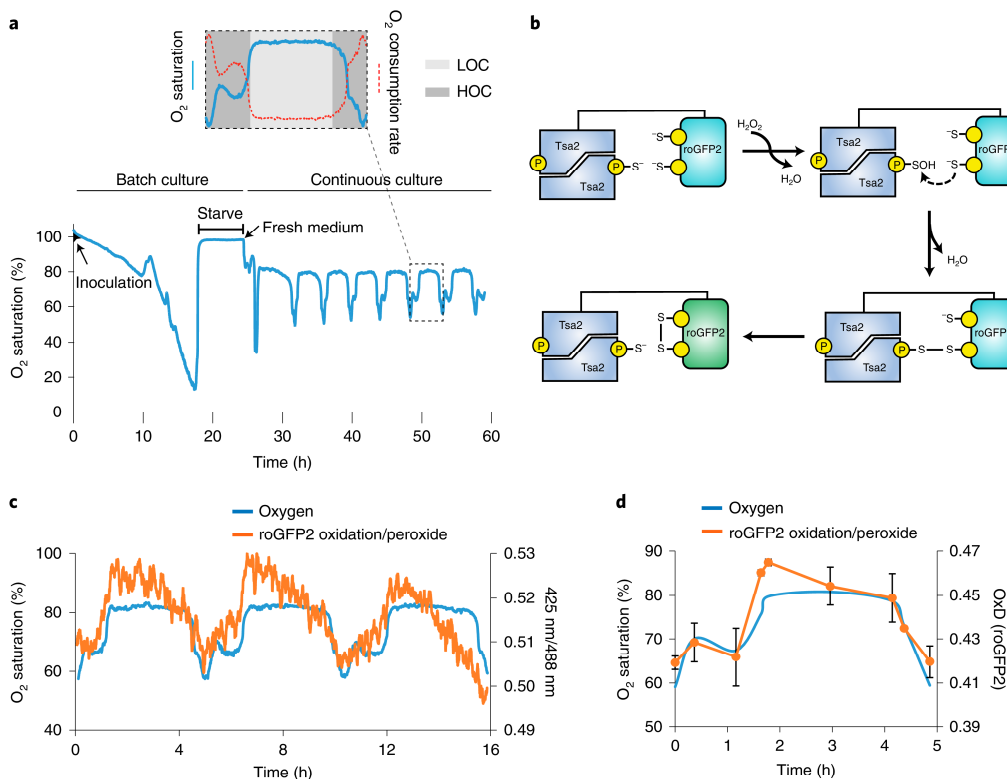


Fig. 1 | H₂O₂ levels and peroxiredoxin oxidation oscillate during the YMC. **a**, Oxygen trace showing the procedure for establishing YMC-synchronized continuous cultures. The dashed red line illustrates the predicted concomitant change in cellular oxygen consumption. **b**, Diagram to illustrate the mechanism of the roGFP2-Tsa2ΔC_R sensor, which is based on the principle of a peroxiredoxin redox relay. **c**, Representative trace of dissolved oxygen levels and roGFP2 fluorescence excitation ratio over three complete YMC cycles ($n=3$ independent experiments in which roGFP2-Tsa2ΔC_R responses were recorded for three complete cycles in independent YMC-synchronized cultures; Supplementary Fig. 2b). **d**, The degree of roGFP2-Tsa2ΔC_R oxidation measured in samples removed from a YMC-synchronized culture at the indicated time points ($n=3$ independent experiments in which samples at each time point were measured in cells from independent YMC-synchronized cultures). Data are presented as mean \pm s.d.

encoded roGFP2-Tsa2ΔC_R probe²⁴. RoGFP2-Tsa2ΔC_R has previously been used for the real-time monitoring of basal cellular H₂O₂ levels in yeast cells and thus is well suited for monitoring potential changes in H₂O₂ during the YMC (Fig. 1b). We integrated the coding sequence for roGFP2-Tsa2ΔC_R into the genome of the prototrophic yeast strain CEN.PK 113-1A (Supplementary Fig. 1). This strain has a genome that combines elements of standard laboratory yeast strains with wild and industrial yeasts²⁵. Importantly, this CEN.PK strain, in common with other wild yeast isolates, can establish robust YMC synchrony¹⁶, which has not been achieved with common laboratory yeast strains such as BY4742 and W303¹⁴. CEN.PK 113-1A, with a genetically integrated roGFP2-Tsa2ΔC_R probe, was grown in continuous culture to establish YMC synchrony as previously described¹⁴ (Fig. 1a). Changes in culture oxygen saturation have previously been shown to be directly inversely proportional to changes in cellular oxygen consumption²⁶ (Fig. 1a).

Using an online monitoring system to continuously record changes in roGFP2 fluorescence (Supplementary Fig. 2a) we found that probe oxidation oscillates during the YMC (Fig. 1c and Supplementary Fig. 2b). RoGFP2 oxidation peaked at the entry into the LOC phase, while a reduction of roGFP2 correlated with the switch to the HOC phase (see Methods for a definition of the HOC and LOC phases). We further confirmed the dynamic probe observations by removing samples from the fermentor at defined time points, ‘trapping’ the probe thiol redox state with the thiol

alkylating agent *N*-ethylmaleimide (NEM) and subsequently determining the degree of probe oxidation (OxD) using a fluorescence plate reader-based protocol (Fig. 1d and Supplementary Fig. 2c)²⁷. Autocorrelation analysis of the online monitoring data revealed a clear periodicity in the oxygen and roGFP2 signals (Extended Data Fig. 1a–c). An overlay of the autocorrelations shows a strong phase synchrony, confirmed by linear regression of the minimum and maximum points (Extended Data Fig. 1d). In summary, we demonstrate the existence of cyclical changes in H₂O₂ levels during the YMC.

High peroxide levels trigger switching to the HOC phase. Exogenously applied H₂O₂ can trigger phase-shifting of the YMC¹⁸. Application of either 5 mM H₂O₂ or 1 mM *tert*-butylhydroperoxide (*t*-BuOOH) to our YMC-synchronized cultures recapitulated this result (Supplementary Fig. 3a,b). Addition of either compound at the beginning of the LOC phase triggered a rapid and premature switch to the HOC phase. For further experiments we preferentially used *t*-BuOOH, which reacts efficiently with most thiol peroxidases but not with catalase. This eliminates catalase-mediated oxygen production upon H₂O₂ disproportionation, which interfered with our oxygen measurements (Supplementary Fig. 3a). Adding lower concentrations of H₂O₂ or *t*-BuOOH had no discernible effect on YMC cycling (Supplementary Fig. 3a,b). Online monitoring of roGFP2-Tsa2ΔC_R probe oxidation revealed that 0.1 mM and 0.5 mM

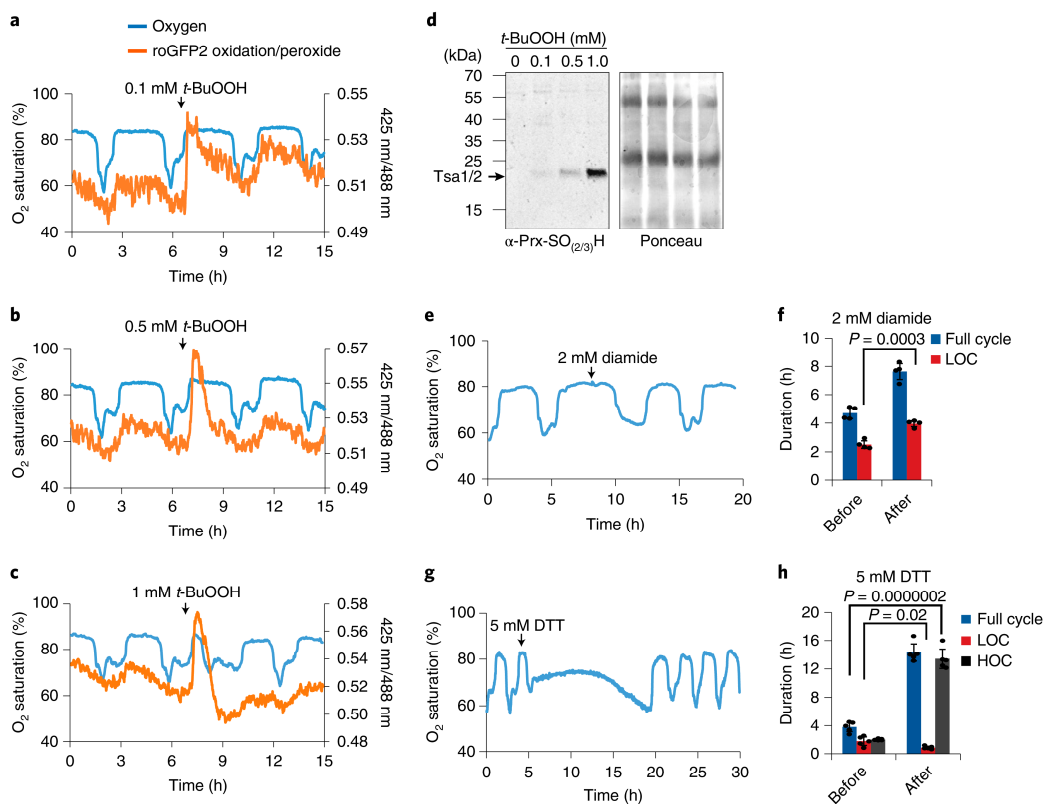


Fig. 2 | The YMC is redox-regulated and controlled by peroxiredoxins. **a–c**, Representative response of a roGFP2-Tsa2ΔC_R probe in YMC-synchronized cultures treated with 0.1 mM (a), 0.5 mM (b) or 1 mM (c) t-BuOOH ($n=3$ experiments in which the indicated concentration of t-BuOOH was added to independent YMC-synchronized cultures; Supplementary Fig. 4). **d**, Representative western blot for hyperoxidized endogenous Tsa1/Tsa2 following application of t-BuOOH to continuous cultures at the indicated concentrations ($n=3$ experimental repeats). **e**, Representative oxygen trace showing the response of the YMC to the addition of 2 mM diamide towards the end of the LOC ($n=4$ experiments in which diamide was added to independent YMC-synchronized cultures; Supplementary Fig. 7a). **f**, Related to **e** and Supplementary Fig. 7a, the average YMC period (defined as the period between the points of lowest dissolved oxygen saturation) and average LOC period for the cycle immediately before diamide treatment and the cycle in which diamide was added towards the end of the LOC phase. **g**, Representative oxygen trace showing the response of the YMC to the addition of 5 mM DTT at the beginning of the LOC phase ($n=4$ experiments in which DTT was added to independent YMC-synchronized cultures; Supplementary Fig. 7b). **h**, Related to **g** and Supplementary Fig. 7b, the average YMC period (defined as the period between the points of lowest dissolved oxygen saturation) and average high oxygen consumption (HOC) period, for the cycle immediately before DTT treatment and the cycle in which DTT was added at the beginning of LOC. Data are presented as mean \pm s.d. *P* values are derived from an unpaired two-tailed Student's *t*-test.

t-BuOOH induced transient probe oxidation, which appeared to recover during LOC, before the switch to HOC (Fig. 2a,b and Supplementary Fig. 4a,b). In both cases, the sensor remained responsive to further treatment with H₂O₂ (Supplementary Fig. 5a). By contrast, addition of 1 mM t-BuOOH at the beginning of the LOC phase induced a transient oxidation of the roGFP2-Tsa2ΔC_R probe, after which it became almost fully reduced and unresponsive to further treatment with H₂O₂ (Fig. 2c and Supplementary Figs. 4c and 5a). These observations are strongly indicative of hyperoxidation-based inactivation of the Tsa2 moiety of the roGFP2-Tsa2ΔC_R probe upon 1 mM t-BuOOH treatment as the Tsa2-mediated transfer of oxidation from H₂O₂ to roGFP2 is blocked^{24,28} (Supplementary Fig. 5b). This conclusion was supported by western blotting with an antibody against hyperoxidized typical 2-Cys peroxiredoxins, which showed hyperoxidation of endogenous Tsa1/2 after addition of 1 mM t-BuOOH at the beginning of the LOC phase (Fig. 2d). Therefore, peroxide can trigger premature switching from LOC to HOC but only if added at concentrations high enough to induce hyperoxidation of typical 2-Cys peroxiredoxins.

Thiol oxidation regulates metabolic cycling. Our observations intriguingly suggested that peroxiredoxins may indeed be involved in regulating metabolic switching in the YMC, possibly by regulating the thiol-disulfide redox state on specific regulatory proteins. To test this hypothesis, we investigated the consequences of adding thiol oxidants and reductants at defined time points during the YMC. First, we monitored the impact of adding the thiol oxidant *N,N,N',N'*-tetramethylazodicarboxamide (diamide) at the beginning of the LOC phase and found that diamide prolonged the LOC in a concentration-dependent manner (Supplementary Fig. 6a–c). Real-time monitoring revealed that recovery of the oxidation state of the roGFP2-Tsa2ΔC_R probe following diamide treatment was relatively rapid and that switching to HOC was only observed after a recovery in probe oxidation (Supplementary Fig. 6a–c). When diamide was applied toward the end of the LOC phase, we were able to substantially delay the switch to HOC (Fig. 2e,f and Supplementary Fig. 7a). Real-time monitoring of roGFP2-Tsa2ΔC_R oxidation again revealed that switching to HOC coincided with roGFP2 reduction (Extended Data Fig. 2). On the contrary,

ARTICLES

NATURE CHEMICAL BIOLOGY

addition of 5 mM 1,4-dithiothreitol (DTT), a disulfide reductant, at the beginning of the LOC triggered a rapid switch to HOC and substantially extended the duration of the HOC phase (Fig. 2g,h and Supplementary Fig. 7b). Thus, we conclude that thiol oxidation, on one or more proteins, is an important regulator of LOC/HOC switching.

Peroxiredoxins are important for YMC cycling. We next monitored the impact of peroxiredoxin deletion on the YMC. Consistent with a previous report⁸, we found that deletion of the two cytosolic typical 2-Cys peroxiredoxins, Tsa1 and Tsa2, led to perturbation of the YMC and a substantially shorter YMC period (Extended Data Fig. 3a,d–f). Previous studies have indicated that there is considerable functional redundancy between the eight different thiol peroxidases in yeast²⁹. We therefore also investigated the impact of deleting the genes encoding the cytosolic atypical 2-Cys peroxiredoxin, Ahp1, and the mitochondrial matrix 1-Cys peroxiredoxin, Prx1 (Extended Data Fig. 3b,c,e,f). We observed that *AHP1* deletion also disrupted the YMC, whereas *PRX1* deletion had no statistically significant effect in our experimental set-up. Next, we asked about the consequences of deleting *TSA1* and *TSA2* in combination with *AHP1*. Surprisingly, we were unable to generate either $\Delta tsa1\Delta ahp1$ or $\Delta tsa1\Delta tsa2\Delta ahp1$ deletion strains in the CEN.PK 113-1A background using a homologous recombination-based gene deletion approach. In subsequent mating, sporulation and tetrad dissection experiments, we were unable to obtain a viable spore containing deletion of both *TSA1* and *AHP1* from any of the 33 tetrads dissected (Extended Data Fig. 4a–d). These observations indicate that combined deletion of *TSA1* and *AHP1* is lethal in the CEN.PK background. This contrasts with the common laboratory yeast strain, BY4742, where all eight thiol peroxidases can be deleted without any effect on viability²⁹. The difference between CEN.PK and BY4742 cannot be explained simply by differences in auxotrophic markers, as a BY4742 $\Delta tsa1\Delta ahp1$ strain transformed with a pHLUK plasmid³⁰ to replace all auxotrophic markers remained fully viable (Supplementary Fig. 8).

To assess the effect on the YMC of the combined loss of *TSA1* and *AHP1*, we genomically fused *AHP1* with an auxin regulable degron in a $\Delta tsa1\Delta tsa2$ background, allowing for the rapid degradation of Ahp1 following supplementation with the auxin hormone indole-3-acetic acid (IAA; Supplementary Fig. 9a). Drop dilution growth assays, performed on yeast extract peptone dextrose (YPD) plates supplemented with either 0.2 mM IAA or 0.1% DMSO as vehicle control, demonstrated that depletion of Ahp1 in a $\Delta tsa1$ or $\Delta tsa1\Delta tsa2$ background is detrimental for growth, while depletion in wild-type or $\Delta tsa2$ background is not (Supplementary Fig. 9b). Addition of 0.1 mM IAA to cultures of wild-type cells did not affect the YMC period, whereas the YMC period in wild-type cells containing Ahp1 with a fused auxin degron was substantially shortened (Fig. 3a,b and Supplementary Fig. 9c,d). Addition of IAA to $\Delta tsa1\Delta tsa2$ cells containing Ahp1 with a fused auxin degron led to a further decrease in YMC period (Fig. 3a,b and Supplementary Fig. 9e). It is important to point out that IAA addition decreases, but does not completely deplete, Ahp1 levels (Supplementary Fig. 9f). Our results thus indicate that there is functional redundancy between the different peroxiredoxins with respect to YMC control, supporting the conclusion that peroxiredoxins are crucial for YMC regulation.

Peroxiredoxins couple cell division to metabolic cycling. In the YMC, cell division is tightly coupled to the oscillatory metabolic state¹⁷ and the switch into the HOC phase has been reported to gate cell cycle entry^{16,31,32}. We therefore next asked whether peroxiredoxins also affect the coordination of cell division with the metabolic cycles. To test this, we collected samples from cultures of YMC-synchronized wild-type and $\Delta tsa1\Delta tsa2$ cells at defined time

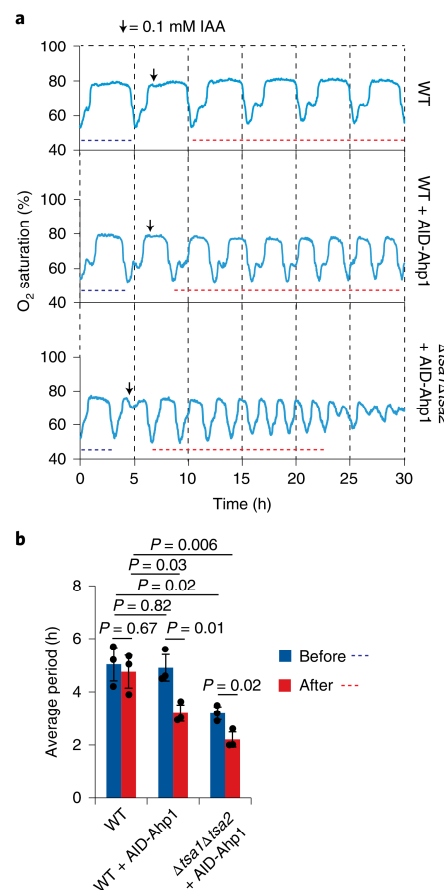


Fig. 3 | Peroxiredoxins are essential for robust YMC cycling.

a, Representative oxygen traces showing the effect of treating YMC-synchronized cultures of wild-type cells or wild-type and $\Delta tsa1\Delta tsa2$ cells expressing Ahp1 genetically fused to an auxin-inducible degron, with 0.1 mM IAA (auxin); Supplementary Fig. 9. **b**, Average YMC period, defined as the period between the points of lowest oxygen saturation, before and after addition of 0.1 mM auxin at the beginning of LOC in **a**. The YMC period before IAA addition was determined as the average period over the range indicated by the blue dashed line. The YMC period after auxin addition was defined as the average period over the time indicated by the red dashed line. The results are from $n=3$ experiments in which auxin was added to independent YMC-synchronized cultures. Data are presented as mean \pm s.d. *P* values are derived from an unpaired two-tailed Student's *t*-test.

points, immediately fixed the collected cells in ethanol and stained with propidium iodide to enable flow cytometry-based monitoring of DNA content (Fig. 4a–d and Supplementary Fig. 10). As a control, and as previously reported¹⁴, in wild-type cells we observed an initiation of DNA replication coinciding with the transition from the point of highest oxygen consumption in HOC back to LOC (Fig. 4a and Supplementary Fig. 11a,b,d,e,g,h). These data were supported by determining the budding index (the fraction of cells containing buds) at different points of the YMC, which showed increased bud formation correlating with the onset of DNA synthesis (Fig. 4b and Supplementary Fig. 11c,f,i). However, in $\Delta tsa1\Delta tsa2$ cells we observed a complete loss of cell cycle synchrony and a complete absence of coupling between cell division and the metabolic cycle (Fig. 4c,d and Supplementary Fig. 12a,b,d,e,g,h). Counting of

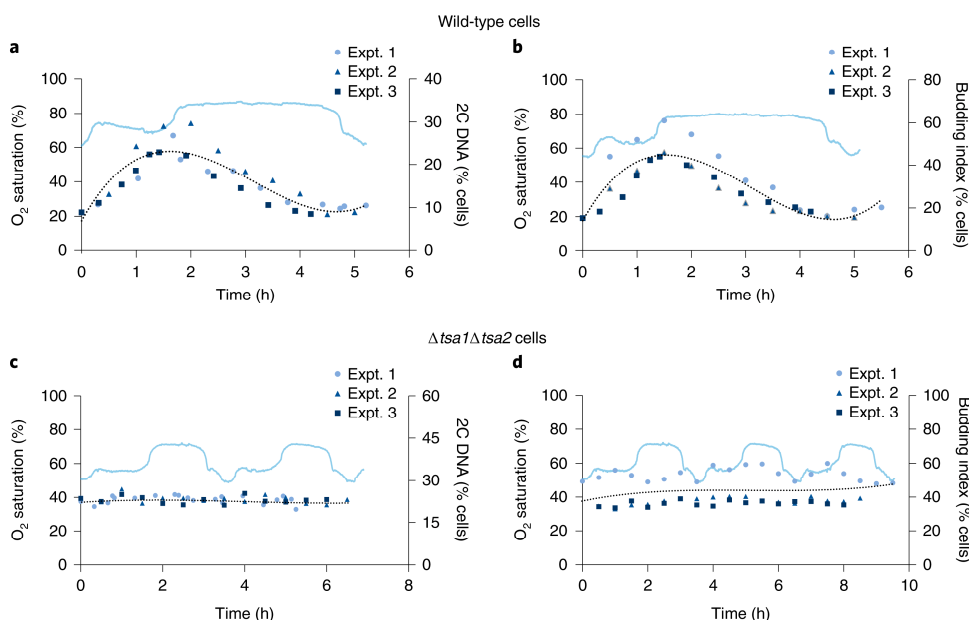


Fig. 4 | Peroxiredoxins are required for coupling cell division and metabolic cycles. **a**, Change in DNA content during the YMC for wild-type cells (Supplementary Figs. 10 and 11). The results are from $n=3$ experiments with independent YMC-synchronized cultures. The light blue line represents the dissolved oxygen trace from one experimental repeat and is displayed for guidance only. Individual datasets are shown in Supplementary Fig. 11b,e,h. **b**, Change in the budding index during the YMC of wild-type cells. This experiment was performed three times with independent YMC-synchronized cultures. The light blue line represents the dissolved oxygen trace from one experimental repeat and is displayed for guidance only. Individual datasets are shown in Supplementary Fig. 11c,f,i. **c**, Change in DNA content during the YMC for $\Delta tsal\Delta tsa2$ cells. Results are from $n=3$ experiments performed with independent YMC-synchronized cultures. The light blue line represents the dissolved oxygen trace from one experimental repeat and is displayed for guidance only. Individual datasets are shown in Supplementary Fig. 12b,e,h. **d**, Change in the budding index during the YMC of $\Delta tsal\Delta tsa2$ yeast cells. This experiment was performed three times with independent YMC-synchronized cultures. The light blue line represents the dissolved oxygen trace from one experimental repeat and is displayed for guidance only. The black lines represent the fits of a 3rd order polynomial function. Individual datasets are shown in Supplementary Fig. 12c,f,i. Datasets were best fitted with a third-order polynomial function, which reflects the expected number of inflection points during the YMC cycle.

the budding index also revealed an equal number of budding cells at every stage of the YMC from which samples were taken from $\Delta tsal\Delta tsa2$ cultures (Fig. 4d and Supplementary Fig. 12c,f,i). A third-order polynomial function, which reflects the expected number of inflection points in the number of cells with 2C DNA during the YMC, fitted well to our three datasets with wild-type cells but presented as a flat line in the datasets with $\Delta tsal\Delta tsa2$ cells. These observations show that the strong coupling between metabolic cycles and cell division strictly requires the presence of the typical 2-Cys peroxiredoxins, Tsa1 and Tsa2. Moreover, our identification of a molecular switch that couples metabolic cycles with cell division supports the conclusion that metabolic cycles are independent of cell division^{17,33}.

Thiol redox compounds disrupt cell cycle entry and exit. Our observations that (1) application of thiol oxidants and reductants allows us to predictably manipulate switching between LOC and HOC and (2) metabolic cycles are independent of cell division afforded the opportunity to investigate the importance of metabolic cycling for regulating cell cycle progression. Specifically, we asked how thiol redox compounds affect the coupling of cell division to metabolic cycles. First, we treated YMC-synchronized cultures with either 5 mM DTT or 2 mM diamide, which delay switching from HOC to LOC or from LOC to HOC, respectively. Subsequently, we collected samples at defined time points after DTT or diamide addition and applied either flow cytometry-based monitoring of DNA content or determined the budding index (Fig. 5a–f and Supplementary Figs. 13

and 14). Interestingly, following DTT addition, which held the culture in the HOC phase for more than 10 h, we observed a continuous increase in the number of cells with 2C DNA content (Fig. 5a and Supplementary Fig. 13b,e,h). Strikingly, starting ~4 h after the addition of DTT, we observed the appearance of cells with >2C DNA content (Fig. 5b and Supplementary Fig. 13b,e,h). Microscopic analysis revealed the increasing occurrence of budding cells and cells with two buds (Fig. 5c,d and Extended Data Fig. 5). Given that the occurrence of a new bud is synchronized with initiation of DNA replication in budding yeast³⁴, this observation suggests that artificial extension of HOC drives cells to initiate a new cell cycle, that is, to pass the Start checkpoint, irrespective of whether they have completed the preceding cell cycle. This leads to the accumulation of cells with two buds and to the observation of increasing DNA content in flow cytometry analyses. These observations also suggest that switching back to LOC is important for completion of cell division.

By contrast, upon diamide treatment, the switch to HOC was delayed by ~2 h, as was the initiation of cell division (Fig. 5e,f and Supplementary Fig. 14). Western blot against Sic1, a cyclin-dependent kinase inhibitor that robustly blocks S-phase initiation and has to be degraded at the G1–S transition³⁵, shows that, upon diamide treatment and the subsequent delay of the LOC–HOC switch, cells are trapped in G1 phase (Supplementary Fig. 15). Accordingly, Clb2, a B-type cyclin that accumulates during G2 and M phase and becomes fully degraded during G1 phase, was found to decrease to non-detectable levels shortly before diamide treatment and did not reappear during the time course of our experiment

ARTICLES

NATURE CHEMICAL BIOLOGY

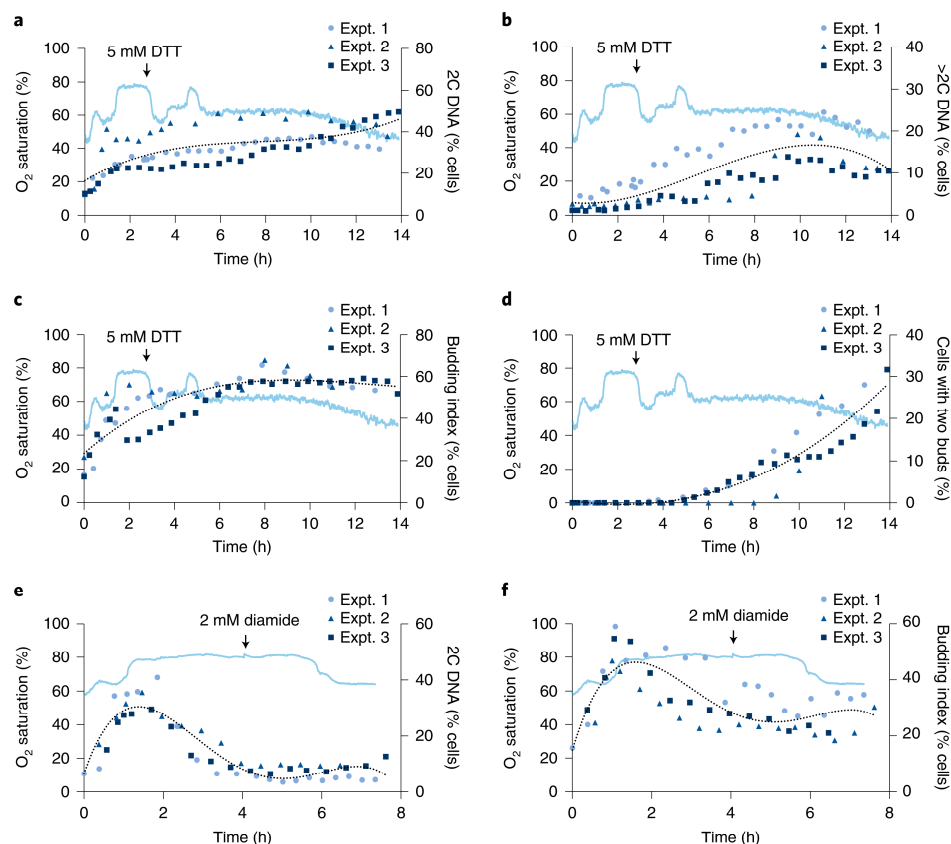


Fig. 5 | Metabolic switching is crucial for triggering cell cycle entry and exit. **a,b**, Change in cells with 2C DNA content (**a**) and cells with >2C DNA content (**b**) in YMC-synchronized cultures of wild-type cells following treatment with 5 mM DTT. This experiment was performed three times with independent YMC-synchronized cultures. Individual datasets are shown in Supplementary Fig. 13b,e,h. **c,d**, Change in budding index (cells with one or more bud) (**c**) and percentage of cells with two buds (**d**) in YMC-synchronized cultures of wild-type cells following DTT treatment. This experiment was performed three times with independent YMC-synchronized cultures. Individual datasets are shown in Supplementary Fig. 13c,f,i. **e,f**, Change in DNA content (**e**) and budding index (**f**) following diamide treatment of YMC-synchronized cultures of wild-type cells. Experiments were performed three times with independent YMC-synchronized cultures. Individual datasets are shown in Supplementary Fig. 14. In all panels, the light blue line represents the dissolved oxygen trace from one experimental repeat and is displayed for guidance only. Datasets were best fitted with a third-order polynomial function, which reflects the expected number of inflection points during the YMC cycle.

(Supplementary Fig. 15). These results thus further support our finding that LOC ‘locks’ cells in G1 phase. In summary, switching to HOC seems to be a prerequisite for initiation of cell cycle start, that is, passing the G1/S checkpoint. On the contrary, switching to LOC is required for completion of cell division.

Discussion

Using a combination of an ultra-sensitive, genetically encoded peroxide sensor, roGFP2-Tsa2ΔC_R, together with an ‘in-house’-constructed online monitoring system, we were able to unequivocally demonstrate the existence of oscillations in cytosolic H₂O₂ during the YMC. Importantly, as roGFP2-Tsa2ΔC_R is based on the endogenous yeast peroxiredoxin Tsa2, the data also reveal that the changes in H₂O₂ are of sufficient magnitude to affect the thiol oxidation state of a yeast peroxiredoxin, which in turn transfers oxidation to roGFP2. Thus, our findings demonstrate the existence of physiologically relevant, cyclical changes in the thiol-disulfide oxidation state of peroxiredoxins and peroxiredoxin substrate proteins, that is, changes that are part of the normal peroxiredoxin catalytic cycle. In our system, we were not able to detect cycles of hyperoxidation, as have been reported previously^{9–11}.

We found that thiol oxidants and reductants predictably modulate the switching between the LOC and HOC phases of the YMC. The thiol oxidant diamide prevented switching from LOC to HOC, while the thiol reductant DTT mediated rapid LOC-to-HOC switching and induced a prolonged HOC phase. Intriguingly, we found that exogenous application of H₂O₂ or *t*-BuOOH, at a concentration high enough to induce hyperoxidation of endogenous peroxiredoxins, also induced rapid switching from LOC to HOC. In combination, our data strongly support the existence of at least one redox-regulated protein that regulates metabolic switching during the YMC. However, our data also raise the question of how to reconcile the similar effects of an oxidant (H₂O₂ or *t*-BuOOH) and a reductant (DTT). We believe the answer to this problem lies in understanding how protein thiols are oxidized by H₂O₂.

There are two main models for explaining H₂O₂-dependent protein thiol oxidation: the floodgate model and the peroxiredoxin redox relay model. The consequences of peroxiredoxin inactivation for oxidation of H₂O₂ target proteins in each model are completely opposite. In the floodgate model, peroxiredoxin inactivation would lead to increased target protein oxidation, whereas in a peroxiredoxin redox relay, target proteins would become insensitive to

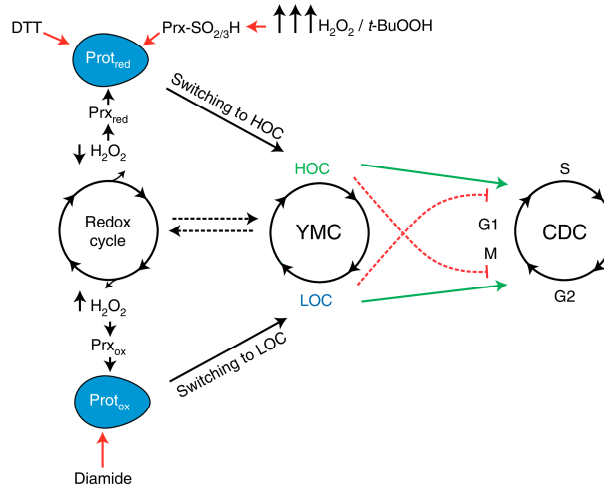


Fig. 6 | Model showing the role of peroxiredoxins in the YMC. Model showing the proposed role of peroxiredoxins in the regulation of metabolic cycling and coupling with cell division. Red arrows indicate non-physiological treatments that have been used in this study to test the model. CDC, cell division cycle.

oxidation or even become reduced. This latter conclusion is well supported by experimental observations. For example, two recent studies showed that peroxiredoxin hyperoxidation is important for maintaining a reduced cytosolic thioredoxin pool and a reduced mitochondrial glutathione pool respectively, under acute H₂O₂ challenge^{36,37}. Our observations that (1) we were unable to detect any peroxiredoxin hyperoxidation in the context of a 'normal' YMC cycle and (2) artificial induction of peroxiredoxin hyperoxidation mimicked the effect of disulfide reductants led us to favor a peroxiredoxin redox relay-dependent regulation of YMC cycling. In other words, we propose that the similar effects of peroxiredoxin hyperoxidation-inducing concentrations of peroxide and DTT are not consistent with a floodgate mechanism and can best be described by a peroxiredoxin redox relay in which the protein(s) regulating LOC-HOC switching are redox-regulated by H₂O₂ in a peroxiredoxin-dependent manner. However, we do not rule out the possibility of less direct peroxiredoxin-dependent control of target protein thiol oxidation, for example via peroxiredoxin-dependent control of thioredoxin oxidation, with thioredoxins ultimately interacting with target proteins.

If, indeed, peroxiredoxin redox relays are important for regulating YMC cycling, what might be the target proteins of these relays? Indirect evidence suggests that there are many unidentified targets of peroxiredoxin redox relays. For example, it has been reported that ~50% of all yeast transcripts respond to H₂O₂; however, this genome-wide transcriptional response is almost completely dependent on the presence of thiol peroxidases, including peroxiredoxins²⁹. Furthermore, a recent study suggested that there are also many targets of peroxiredoxin redox relays in mammalian cells³⁸. Nonetheless, so far, very few bona fide peroxiredoxin target proteins are known^{39,40}. Exceptions in yeast include the transcription factor Yap1, which is oxidized and thereby regulated by the glutathione peroxidase-like protein Orp1⁴¹. Furthermore, it was recently reported that Tsa1 can regulate redox modifications on the yeast protein kinase A subunit Tpk1⁴². The general stress-responsive transcription factor Msn2 is a target of PKA, and Msn2 deletion has been shown to strongly disrupt YMC cycling, particularly the switching from LOC to HOC⁴³. Other targets of PKA include the general heat shock response transcription factor Hsf1 and

metabolic enzymes, such as Pfk2, encoding phosphofructokinase. Thus, one exciting possibility is that peroxiredoxins, via redox regulation of PKA, enable cells to regulate a wide range of transcriptional and metabolic processes in response to changing H₂O₂ levels. The underlying mechanistic connections and their relevance, for example for coupling with the cell cycle, will be particularly interesting to investigate in the future.

Another interesting feature of the YMC is that the metabolic cycles are closely coupled with synchronized cell division^{8,14,33,44}. Typically, during each cycle of the YMC, ~30% of the cells in the population are observed to divide synchronously^{14,18}. Far from being a peculiarity of the YMC, it is becoming increasingly clear that cell division can be, and often is, coupled to the circadian clock in organisms ranging from bacteria to humans³. The YMC is thus a powerful model system in which to study potential roles of peroxiredoxins in clock function and the coupling of rhythmic, clock-associated metabolism to cell division.

Previous studies have suggested that cell division may involve several coupled but nonetheless independent oscillators, in addition to the classic and well understood cyclin-CDK system. There is evidence, for example, for the existence of cyclin-CDK-independent transcriptional and metabolic cycles^{17,45–47}. Additionally, it was recently suggested that metabolic cycles are crucial for regulating cell cycle entry and exit^{16,17}. However, the mechanistic connections between metabolic cycles and cell division remains completely unclear. Our data show that maintaining cells in the LOC phase, for example with diamide treatment, prevents cell cycle entry—that is, passing the G1-S/Start checkpoint—based on the stability of the G1 marker protein Sic1, the absence of DNA replication and the absence of de novo bud formation. On the contrary, forcing a prolonged switch to HOC, for example with DTT treatment, prevents completion of cell division, while still allowing for a second round of de novo cell cycle initiation as determined by measuring DNA content and the appearance of a second bud. It is currently unclear at what stage cell division is arrested in these conditions. However, we noted that one of the two buds always lacked DNA, despite an increased DNA content measured by flow cytometry. This may suggest that mitosis is blocked and therefore that the cell cycle is arrested at the G2-M checkpoint, without preventing initiation of a second cell cycle. It will be exciting to gain a more detailed understanding of these processes in future studies.

In our study, we also reveal that peroxiredoxins are crucial both for the stable oscillation of the YMC and for the coupling between metabolic cycles and cell division. Following deletion of the genes encoding the two cytosolic typical 2-Cys peroxiredoxins, Tsa1 and Tsa2, the YMC persisted, albeit in a perturbed manner. However, we observed cells to divide completely asynchronously from the metabolic cycles and from each other. This is particularly interesting, as deletion of peroxiredoxins is associated with an increased genomic mutation rate and increased incidence of cancer in higher organisms^{48,49}. These phenotypes are typically attributed to supposedly higher levels of reactive oxygen species in peroxiredoxin-deficient cells. However, an attractive alternate hypothesis arising from our study is that, in the absence of peroxiredoxins, the uncoupling of cell division from metabolism allows cells to divide at 'inappropriate' times, with respect, for example, to metabolite availability and the prevailing metabolic conditions. This is an area that will also be particularly interesting to investigate more closely in the future.

In summary, we have provided a mechanistic explanation for the role of peroxiredoxins in cellular timekeeping. Furthermore, we have identified a molecular mechanism coupling cell division with YMCs by demonstrating that perturbation of both peroxiredoxins and the cellular thiol redox state allows for uncoupling of cell division from metabolic cycles. These observations lend further support to the assertion that metabolic switching is a key regulator of cell cycle entry and exit¹⁷ (Fig. 6). Our observations do not detract

ARTICLES

NATURE CHEMICAL BIOLOGY

from the known and well-understood importance of cyclin-CDK networks for the control of cell division⁵⁰. Rather, they indicate that cell division involves multiple independent, albeit probably highly coupled, oscillators, including metabolic, transcriptional and cyclin-CDK cycles^{17,45–47}. Untangling the molecular mechanistic details of these oscillators and their modes of crosstalk and synchronization, where peroxiredoxins clearly have an important role, represents an exciting challenge for the future.

Online content

Any methods, additional references, Nature Research reporting summaries, source data, extended data, supplementary information, acknowledgements, peer review information; details of author contributions and competing interests; and statements of data and code availability are available at <https://doi.org/10.1038/s41589-020-00728-9>.

Received: 26 September 2019; Accepted: 22 December 2020;

Published online: 11 February 2021

References

- Takahashi, J. S. Transcriptional architecture of the mammalian circadian clock. *Nat. Rev. Genet.* **18**, 164–179 (2017).
- Dunlap, J. C. Molecular bases for circadian clocks. *Cell* **96**, 271–290 (1999).
- Gaucher, J., Montellier, E. & Sassone-Corsi, P. Molecular cogs: interplay between circadian clock and cell cycle. *Trends Cell Biol.* **28**, 368–379 (2018).
- Nakajima, M. et al. Reconstitution of circadian oscillation of cyanobacterial KaiC phosphorylation in vitro. *Science* **308**, 414–415 (2005).
- Tomita, J., Nakajima, M., Kondo, T. & Iwasaki, H. No transcription–translation feedback in circadian rhythm of KaiC phosphorylation. *Science* **307**, 251–254 (2005).
- Sweeney, B. M., Tuffli, C. F. Jr & Rubin, R. H. The circadian rhythm in photosynthesis in *Acetabularia* in the presence of actinomycin D, puromycin and chloramphenicol. *J. Gen. Physiol.* **50**, 647–659 (1967).
- Woolum, J. C. A re-examination of the role of the nucleus in generating the circadian rhythm in *Acetabularia*. *J. Biol. Rhythms* **6**, 129–136 (1991).
- Causton, H. C., Feeney, K. A., Ziegler, C. A. & O'Neill, J. S. Metabolic cycles in yeast share features conserved among circadian rhythms. *Curr. Biol.* **25**, 1056–1062 (2015).
- Edgar, R. S. et al. Peroxiredoxins are conserved markers of circadian rhythms. *Nature* **485**, 459–464 (2012).
- O'Neill, J. S. & Reddy, A. B. Circadian clocks in human red blood cells. *Nature* **469**, 498–503 (2011).
- O'Neill, J. S. et al. Circadian rhythms persist without transcription in a eukaryote. *Nature* **469**, 554–558 (2011).
- Cho, C. S., Yoon, H. J., Kim, J. Y., Woo, H. A. & Rhee, S. G. Circadian rhythm of hyperoxidized peroxiredoxin II is determined by hemoglobin autoxidation and the 20S proteasome in red blood cells. *Proc. Natl Acad. Sci. USA* **111**, 12043–12048 (2014).
- Henslee, E. A. et al. Rhythmic potassium transport regulates the circadian clock in human red blood cells. *Nat. Commun.* **8**, 1978 (2017).
- Tu, B. P., Kudlicki, A., Rowicka, M. & McKnight, S. L. Logic of the yeast metabolic cycle: temporal compartmentalization of cellular processes. *Science* **310**, 1152–1158 (2005).
- Tu, B. P. et al. Cyclic changes in metabolic state during the life of a yeast cell. *Proc. Natl Acad. Sci. USA* **104**, 16886–16891 (2007).
- Burnetti, A. J., Aydin, M. & Buchler, N. E. Cell cycle start is coupled to entry into the yeast metabolic cycle across diverse strains and growth rates. *Mol. Biol. Cell* **27**, 64–74 (2016).
- Papagiannakis, A., Niebel, B., Wit, E. C. & Heinemann, M. Autonomous metabolic oscillations robustly gate the early and late cell cycle. *Mol. Cell* **65**, 285–295 (2017).
- Chen, Z., Odstrcil, E. A., Tu, B. P. & McKnight, S. L. Restriction of DNA replication to the reductive phase of the metabolic cycle protects genome integrity. *Science* **316**, 1916–1919 (2007).
- Klevecz, R. R., Bolen, J., Forrest, G. & Murray, D. B. A genomewide oscillation in transcription gates DNA replication and cell cycle. *Proc. Natl Acad. Sci. USA* **101**, 1200–1205 (2004).
- Lloyd, D., Lemar, K. M., Salgado, L. E., Gould, T. M. & Murray, D. B. Respiratory oscillations in yeast: mitochondrial reactive oxygen species, apoptosis and time; a hypothesis. *FEMS Yeast Res.* **3**, 333–339 (2003).
- Zeida, A. et al. Catalysis of peroxide reduction by fast reacting protein thiols. *Chem. Rev.* **119**, 10829–10855 (2019).
- Perkins, A., Nelson, K. J., Parsonage, D., Poole, L. B. & Karplus, P. A. Peroxiredoxins: guardians against oxidative stress and modulators of peroxide signaling. *Trends Biochem. Sci.* **40**, 435–445 (2015).
- Veal, E. A., Underwood, Z. E., Tomalin, L. E., Morgan, B. A. & Pillay, C. S. Hyperoxidation of peroxiredoxins: gain or loss of function? *Antioxid. Redox Signal.* **28**, 574–590 (2018).
- Morgan, B. et al. Real-time monitoring of basal H₂O₂ levels with peroxiredoxin-based probes. *Nat. Chem. Biol.* **12**, 437–443 (2016).
- Nijkamp, J. F. et al. De novo sequencing, assembly and analysis of the genome of the laboratory strain *Saccharomyces cerevisiae* CEN.PK113-7D, a model for modern industrial biotechnology. *Microb. Cell Fact.* **11**, 36 (2012).
- Murray, D. B. et al. in *Systems Biology of Metabolic and Signaling Networks* (eds Aon, M. et al.) 323–349 (Springer, 2014).
- Morgan, B., Sobotta, M. C. & Dick, T. P. Measuring E(GSH) and H₂O₂ with roGFP2-based redox probes. *Free Radic. Biol. Med.* **51**, 1943–1951 (2011).
- Staudacher, V. et al. Redox-sensitive GFP fusions for monitoring the catalytic mechanism and inactivation of peroxiredoxins in living cells. *Redox Biol.* **14**, 549–556 (2018).
- Fomenko, D. E. et al. Thiol peroxidases mediate specific genome-wide regulation of gene expression in response to hydrogen peroxide. *Proc. Natl Acad. Sci. USA* **108**, 2729–2734 (2011).
- Mulleder, M., Campbell, K., Matsarskaia, O., Eckerstorfer, F. & Ralsler, M. *Saccharomyces cerevisiae* single-copy plasmids for auxotrophy compensation, multiple marker selection, and for designing metabolically cooperating communities. *F1000Res.* **5**, 2351 (2016).
- Ewald, J. C. How yeast coordinates metabolism, growth and division. *Curr. Opin. Microbiol.* **45**, 1–7 (2018).
- Zhao, G., Chen, Y., Carey, L. & Futcher, B. Cyclin-dependent kinase co-ordinates carbohydrate metabolism and cell cycle in *S. cerevisiae*. *Mol. Cell* **62**, 546–557 (2016).
- Slavov, N., Macinskis, J., Caudy, A. & Botstein, D. Metabolic cycling without cell division cycling in respiring yeast. *Proc. Natl Acad. Sci. USA* **108**, 19090–19095 (2011).
- Williamson, D. H. The timing of deoxyribonucleic acid synthesis in the cell cycle of *Saccharomyces cerevisiae*. *J. Cell Biol.* **25**, 517–528 (1965).
- Schneider, B. L., Yang, Q. H. & Futcher, A. B. Linkage of replication to start by the Cdk inhibitor Sic1. *Science* **272**, 560–562 (1996).
- Brown, J. D. et al. A peroxiredoxin promotes H₂O₂ signaling and oxidative stress resistance by oxidizing a thioredoxin family protein. *Cell Rep.* **5**, 1425–1435 (2013).
- Calabrese, G. et al. Hyperoxidation of mitochondrial peroxiredoxin limits H₂O₂-induced cell death in yeast. *EMBO J.* **38**, e101552 (2019).
- Stöcker, S., Maurer, M., Ruppert, T. & Dick, T. P. A role for 2-Cys peroxiredoxins in facilitating cytosolic protein thiol oxidation. *Nat. Chem. Biol.* **14**, 148–155 (2018).
- Sobotta, M. C. et al. Peroxiredoxin-2 and STAT3 form a redox relay for H₂O₂ signaling. *Nat. Chem. Biol.* **11**, 64–70 (2015).
- Jarvis, R. M., Hughes, S. M. & Ledgerwood, F. C. Peroxiredoxin 1 functions as a signal peroxidase to receive, transduce, and transmit peroxide signals in mammalian cells. *Free Radic. Biol. Med.* **53**, 1522–1530 (2012).
- Delaunay, A., Pfleiderer, D., Barrault, M. B., Vinh, J. & Toledano, M. B. A thiol peroxidase is an H₂O₂ receptor and redox-transducer in gene activation. *Cell* **111**, 471–481 (2002).
- Roger, F. et al. Peroxiredoxin promotes longevity and H₂O₂-resistance in yeast through redox-modulation of protein kinase A. *eLife* **9**, e60346 (2020).
- Kuang, Z., Pinglay, S., Ji, H. & Boeke, J. D. Msn2/4 regulate expression of glycolytic enzymes and control transition from quiescence to growth. *eLife* **6**, 29938 (2017).
- Silverman, S. J. et al. Metabolic cycling in single yeast cells from unsynchronized steady-state populations limited on glucose or phosphate. *Proc. Natl Acad. Sci. USA* **107**, 6946–6951 (2010).
- Haase, S. B. & Reed, S. I. Evidence that a free-running oscillator drives G1 events in the budding yeast cell cycle. *Nature* **401**, 394–397 (1999).
- Orlando, D. A. et al. Global control of cell-cycle transcription by coupled CDK and network oscillators. *Nature* **453**, 944–947 (2008).
- Simmons Kovacs, L. A. et al. Cyclin-dependent kinases are regulators and effectors of oscillations driven by a transcription factor network. *Mol. Cell* **45**, 669–679 (2012).
- Iraqi, I. et al. Peroxiredoxin Tsai1 is the key peroxidase suppressing genome instability and protecting against cell death in *Saccharomyces cerevisiae*. *PLoS Genet.* **5**, e1000524 (2009).
- Nystrom, T., Yang, J. & Molin, M. Peroxiredoxins, gerontogenes linking aging to genome instability and cancer. *Genes Dev.* **26**, 2001–2008 (2012).
- Morgan, D. O. Principles of CDK regulation. *Nature* **374**, 131–134 (1995).

Publisher's note Springer Nature remains neutral with regard to jurisdictional claims in published maps and institutional affiliations.

© The Author(s), under exclusive licence to Springer Nature America, Inc. 2021

Methods

Yeast strains. All experiments were performed in a CEN.PK 113-1A strain background unless otherwise stated. Gene deletion strains (Supplementary Table 1) were created using a standard, homologous recombination-based gene deletion approach. All deletion strains were confirmed by polymerase chain reaction (PCR) on isolated genomic DNA using primers designed to anneal 100–200 base pairs up- and downstream of the gene of interest.

Establishment of continuous culture. A Biostat A fermentor (Sartorius Stedim Systems) was used for all continuous culture experiments. Fermentor runs were initiated by the addition of a 20-ml starter culture, which had been grown to stationary phase in YPD medium at 30 °C. The culture working volume was 800 ml. The fermentor was run at a constant temperature of 30 °C, with a constant pH of 3.4 maintained by automated addition of 10% (wt/vol) NaOH. The culture was continuously aerated at 11 min⁻¹ with stirring at 530 r.p.m. After growth to stationary phase as a batch culture, continuous culture was initiated by the addition of growth medium at a constant dilution rate of 0.05 h⁻¹.

The growth medium consisted of 10 g l⁻¹ glucose, 1 g l⁻¹ yeast extract (Becton Dickinson), 5 g l⁻¹ (NH₄)₂SO₄, 2 g l⁻¹ KH₂PO₄, 0.5 g l⁻¹ MgSO₄·7H₂O, 0.1 g l⁻¹ CaCl₂·2H₂O, 0.02 g l⁻¹ FeSO₄·7H₂O, 0.01 g l⁻¹ ZnSO₄·7H₂O, 0.005 g l⁻¹ CuSO₄·5H₂O, 0.001 g l⁻¹ MnCl₂·4H₂O, 2.5 ml 70% H₂SO₄ and 0.5 ml l⁻¹ Antifoam 204 (Sigma). Medium components and trace metals were separately prepared, sterilized and reconstituted to a total volume of 5 l. Briefly, a solution consisting of 1 g l⁻¹ yeast extract (Becton Dickinson), 5 g l⁻¹ (NH₄)₂SO₄, 2 g l⁻¹ KH₂PO₄, 0.5 g l⁻¹ MgSO₄·7H₂O and 0.1 g l⁻¹ CaCl₂·2H₂O was prepared to the appropriate volume and autoclaved. To this solution were added the appropriate amounts of separately autoclaved 100 g l⁻¹ glucose solution and 70% H₂SO₄ solution. ZnSO₄·7H₂O, CuSO₄·5H₂O and MnCl₂·4H₂O were prepared as a 1,000× trace metal stock and separately autoclaved. Finally, FeSO₄·7H₂O was dissolved to 10 mg ml⁻¹ in water, sterile-filtered and the appropriate amount added to the medium mix, together with the appropriate volume of Antifoam 204.

We defined HOC as starting at the time point at which the running average oxygen saturation, determined as the mean of the preceding five data points, dropped below 80% of the immediately preceding oxygen maximum relative to the next oxygen minimum. LOC was therefore determined as starting at the time at which the running average oxygen saturation, determined as the mean of the preceding five data points, increased above a value of 80% of the immediately preceding oxygen minimum relative to the next oxygen maximum.

Construction of genetically integrated roGFP2-Tsa2ΔC_R expressing strain. The Prx-based H₂O₂ sensor, roGFP2-Tsa2ΔC_R, was modified for integration and expression from the yeast genome. Briefly, the coding sequence for roGFP2-Tsa2ΔC_R was genetically fused to the kanMX4 resistance cassette and the strong constitutive promoter, GPD, both derived from a pYM-N14 plasmid. The complete construct was assembled in a p415TEF plasmid and confirmed by sequencing (Supplementary Fig. 1a). The entire KanMX4-GPD-roGFP2-Tsa2ΔC_R construct was then amplified by PCR using the primers Fwd, CCATTAAAT-TCCACCTTCGGATTTTTGTCAAATCTCTAACTCTCAATTCCCCGGATCCA-TCTGCCGAATGCGTAGCTGCAGGTCGAC and Rev, CGTTCTGTCAATCTAACGACTTGAAAGATTACAGGACTTTTTTCTCTACTGTATTTCCTCGTAGAGTGGTACCGCCGCAAATAAG, which were designed to have overhangs complementary to a noncoding genome region between the *HXT6* and *HXT7* genes. The PCR product was transformed into yeast for homologous recombination, positive colonies were selected on YPD plates supplemented with G418, and confirmed by PCR of the genomic DNA.

Online monitoring of roGFP2-Tsa2ΔC_R. To enable the continuous ‘online’ monitoring of roGFP2-Tsa2ΔC_R fluorescence, we developed an in-house system. Briefly, a peristaltic pump was used to continuously pump culture from the fermentor through a flow cell (Type 71-F, Starna) inserted into a JASCO FP-6500 spectrofluorimeter. Fluorescence was measured at fixed excitation wavelengths of 425 nm and 488 nm with emission monitored at 510 nm. The excitation and emission bandwidths were set to 5 nm. A measurement was recorded every 30 s.

NEM-based alkylation for degree of oxidation of roGFP2-Tsa2ΔC_R. To monitor changes in roGFP2-Tsa2ΔC_R oxidation during the YMC, an NEM-based probe oxidation ‘trapping’ method was used. Briefly, cells were removed from the culture vessel at the indicated time points. Aliquots of 450 µl were immediately added to separate Eppendorf tubes containing either 50 µl of 1 M NEM (that is, 100 mM final), 50 µl of 1 M DTT (that is, 100 mM final) or 50 µl of 0.2 M diamide (that is, 20 mM final). The samples were incubated at room temperature for 10 min. Cells were subsequently collected by centrifugation at 900g for 3 min and resuspended in 100 mM MES-Tris pH 6.0 buffer containing 10 mM NEM. Cells were then transferred to a 96-well plate and probe oxidation was measured using a BMG Labtech CLARIOstar fluorescence plate reader operated with standard BMG Labtech software, version 5.20 R3. Data were subsequently analyzed with standard BMG Labtech CLARIOstar MARS data analysis software, version 3.10 R2. All data were subsequently exported to Microsoft Excel 2019. The degree of sensor oxidation was determined according to equation (1), as previously described,

based on the fluorescence emission intensity at 510 nm with excitation at both 405 nm and 488 nm for the fully oxidized, fully reduced and control samples, respectively^{24,27,51}:

$$\text{OxD}_{\text{roGFP2}} = \frac{(I_{405\text{sample}} \times I_{488\text{red}}) - (I_{405\text{red}} \times I_{488\text{sample}})}{(I_{405\text{sample}} \times I_{488\text{red}}) + (I_{405\text{ox}} \times I_{488\text{ox}}) + (I_{405\text{red}} \times I_{488\text{sample}})} \quad (1)$$

Yeast mating, sporulation and tetrad dissection. A CEN.PK 113-1A $\Delta tsa1\Delta tsa2$ strain was crossed with its *MATA* counterpart, CEN.PK 113-7D, which had been deleted for *AHPI*. The resultant diploid cells were selected and enriched by growth on YPD plates supplemented with G418, nourseothricin and hygromycin. These cells were subsequently inoculated into 10 ml of fresh YPD medium and incubated overnight with shaking at 150 r.p.m., 30 °C. Next, 500 µl of YPD culture was collected by centrifugation at 900g for 3 min and resuspended in 10 ml of sporulation medium (10 g l⁻¹ potassium acetate, 1 g l⁻¹ yeast extract, 0.5 g l⁻¹ glucose). The cell suspension was further incubated at 30 °C for four days to allow for sporulation. A 500 µl volume of sporulated cell suspension were collected by centrifugation at 900g for 3 min and resuspended in 100 µl of 1.2 M sorbitol buffer supplemented with zymolase and incubated for 15 min at room temperature. Zymolase-treated cells were further diluted 1:50 in 1.2 M sorbitol buffer and a few microliters of the suspension transferred onto the side of a dried YPD plate under sterile conditions. The plate was dried for a further 10 min and tetrads dissected using a tetrad dissection microscope. Dissected tetrads were incubated at 30 °C for 48 h and characterized by growth on appropriate antibiotic containing medium.

Construction of yeast strains capable of conditional Ahp1 depletion via an auxin-inducible degron system. A plasmid construct of both the auxin-inducible degron and *Arabidopsis thaliana* F-box protein, transport inhibitor response 1 (*AtTir1*), was a generous gift from B. Schwappach. The construct was modified and amplified by PCR for genomic integration and fusion to the N terminus of *AHPI*. Positive clones were selected on YPD agar supplemented with G418 and verified by PCR. Sensitivity to auxin was determined by spotting serial dilutions of exponentially growing yeast cultures on YPD plates containing the indicated concentration of auxin.

Protein extraction and western blot. For the detection of hyperoxidized peroxiredoxins, 2.0 optical density at 600 nm (OD₆₀₀) units of cells were collected from the fermentor 30 min after *t*-BuOOH treatment and immediately treated with 100 mM NEM for 10 min at room temperature. The cells were isolated by centrifugation at 1,000g for 3 min, resuspended in 100 µl of 100 mM NaOH and incubated for 10 min at room temperature, then centrifuged at 900g for 3 min, resuspended in 15 µl of lysis buffer (50 mM HEPES, pH 8.0, 50 mM NaCl, 1% SDS, 10 µM EDTA, 20 mM NEM) and mixed with 15 µl of 2× non-reducing sodium dodecyl sulfate polyacrylamide gel electrophoresis (SDS-PAGE) sample loading buffer. For western blots against Myc- and FLAG-tagged proteins as well as against Sic1, Clb2 and Rps23, 1.0 OD₆₀₀ units of cells were collected at the indicated time points, resuspended in lysis buffer and mixed with an equal volume of 2× reducing SDS-PAGE sample loading buffer. All western blot samples were heated to 98 °C for 10 min, centrifuged at 17,000g for 2 min and the lysate loaded onto a 16% SDS-PAGE gel. Gels were run at 25 mA for 2 h and transferred onto polyvinylidene fluoride membranes at 200 mA for 1.5 h. Membranes were blocked with 5% (wt/vol) milk in Tris-buffered saline for 1 h. The membranes were subsequently incubated overnight with either rabbit anti-Prx-SO₃⁻H (Abfrontier, LF-PA0004) diluted 1:1,000, mouse anti-FLAG M2 (Sigma-Aldrich, F3165) diluted 1:500, mouse anti-Myc 9E11 (MAI-16637, Invitrogen) diluted 1:500, guinea pig α-Sic1 (gift from B. Luke) diluted 1:1,000, rabbit α-Clb2 (gift from B. Luke) diluted 1:500 or mouse α-Rps23 (Santa Cruz, Sc-100837) diluted 1:1,000 antibodies at 4 °C. Membranes were washed and then incubated with the respective horseradish peroxidase (HRP)-conjugated secondary antibodies (HRP-conjugated anti-rabbit and anti-mouse, R&D Systems, HAF008 and HAF007, respectively, or anti-guinea pig, a gift from B. Luke) at room temperature for 1 h at a dilution of 1:10,000 in each case.

Flow cytometry analysis of DNA content. Aliquots of 1.0 OD₆₀₀ units of fermenter cultures (~1 × 10⁷ cells) were collected at 6,000g for 1 min. Cells were resuspended and fixed in 1 ml of 70% (vol/vol) ethanol at 4 °C overnight. Fixed cells were then pelleted at 6,000g for 1 min and washed with Milli-Q water. Cells were subsequently resuspended in 250 µl of FxCycle PI/RNase staining solution (Life Technologies, #F10797), incubated at room temperature in the dark for 30 min and then stored at 4 °C for 72 h. Samples were sonicated at 30% amplitude for 20 s and run on an Attune flow cytometer. Data analyses were performed using the FlowJo software, version 10. Samples were gated for single cells and a histogram of cell count against propidium iodide (PI) intensity was plotted. The percentages of cells with 1C DNA and 2C DNA content were determined as follows. The percentage of cells with 1C DNA content was determined as the number of cells with a PI staining intensity from 0–2.7 × 10⁵ as a percentage of the total number of cells analyzed. The percentage of cells with 2C DNA content was determined as the number of cells with a PI staining intensity from 2.7 × 10⁵–4.5 × 10⁵ as a percentage

ARTICLES

NATURE CHEMICAL BIOLOGY

of the total number of cells analyzed. The percentage of cells with >2C DNA content was determined as the number of cells with a PI staining intensity from $>4.5 \times 10^5$ as a percentage of the total number of cells analyzed.

Budding index determination and DNA visualization by DAPI staining and microscopy. Fermenter culture samples were collected at the indicated times and fixed with 70% (vol/vol) ethanol at 4 °C for 30 min. Cells were washed twice with 1× PBS. Budded and non-budded cells in several random fields were scored to calculate the budding index. To visualize DNA, DAPI was added to the collected cells at a final concentration of 1 µg ml⁻¹ in PBS and incubated in the dark for 10 min. Cells were then washed and resuspended in PBS for visualization. Cells were visualized with a fully automated Zeiss inverted microscope (AxioObserver Z1) equipped with the CSU-X1 spinning disk confocal head (Yokogawa). Image acquisition was performed using a CoolSnap HQ camera (Roper Scientific) and a ×40 air or ×63 oil objective under the control of SlideBook software, version 6.0.6 (Intelligent Imaging Innovations).

Correlation analysis. Autocorrelation of the roGFP2 and oxygen signals was calculated using FSharp Version 4.3 with FSharp Stats package Version 0.2 (<https://github.com/CSBiology/FSharp.Stats>) to account for the individual shapes during oscillation. Subsequent regression analysis of the extreme values in autocorrelation space was performed to test for phase correlation. The significance was tested by analysis of variance.

Reporting Summary. Further information on research design is available in the Nature Research Reporting Summary linked to this Article.

Data availability

All datasets generated or analyzed during this study are included in this Article and its Supplementary Information. Source data are provided with this paper.

References

51. Meyer, A. J. & Dick, T. P. Fluorescent protein-based redox probes. *Antioxid. Redox Signal.* **13**, 621–650 (2010).

Acknowledgements

B.M. acknowledges generous financial support from the Deutsche Forschungsgemeinschaft in the framework of the SPP1710 (MO 2774/2-1) and IRTG1830 programmes, as well as funding from the Technische Universität Kaiserslautern Nachwuchsring and the Forschungsinitiative Rhineland-Pfalz BioComp. G.Y.M. is funded by the Georg Forster Research Fellowship, awarded from the Alexander von Humboldt Foundation. We thank W. Zachariae (Max Planck Institute of Biochemistry) for providing the Clb2 antibody and B. Luke (Institute of Molecular Biology) for providing the Sic1 antibody. We thank T. Dick, J. Herrmann, J. Riemer, L. Prates Roma and F. Hannemann for invaluable discussions and for helpful and insightful comments on the manuscript. We thank V. Nehr for valuable technical assistance.

Author contributions

B.M., P.S.A. and Z.S. designed all experiments and wrote the manuscript. P.S.A., J.Z., M.M. and S.M. performed metabolic cycle and online roGFP2-Tsa2ΔC_R-based measurements, as well as experiments to assess the impact of redox compounds on oxygen and roGFP2-Tsa2ΔC_R cycling. They also performed the experiments to assess the impact of genetic and chemical perturbation of the YMC on cell division using flow cytometry-based analysis of DNA content. P.S.A. performed tetrad dissection and the experiments associated with auxin degron-based regulation of peroxiredoxin level. G.Y. performed all budding index experiments and western blot analyses of cell cycle markers. P.S.A., T.M. and B.M. performed the correlation analyses and statistical analyses of all datasets. All authors contributed to data interpretation.

Competing interests

The authors declare no competing interests.

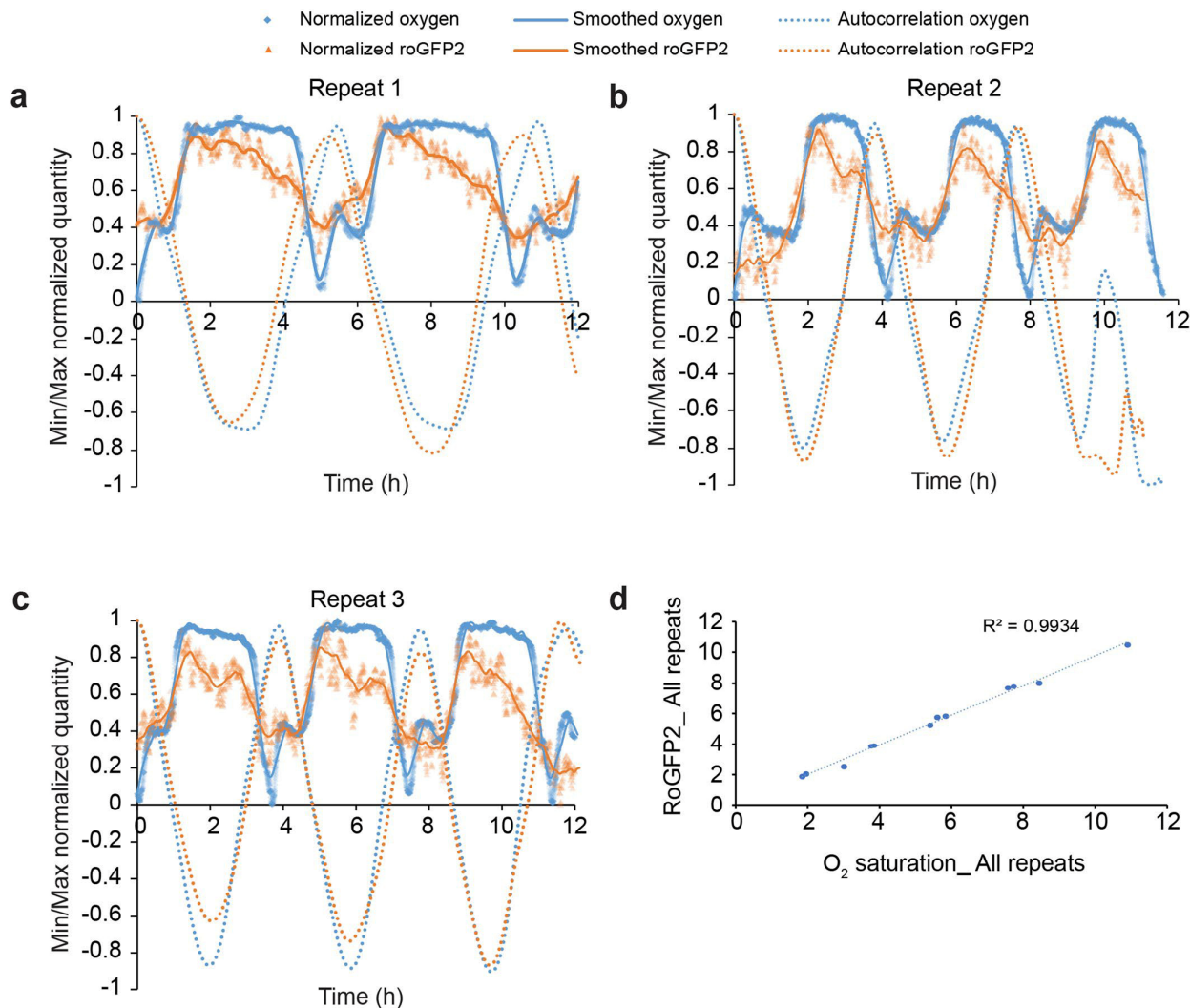
Additional information

Extended data is available for this paper at <https://doi.org/10.1038/s41589-020-00728-9>.

Supplementary information The online version contains supplementary material available at <https://doi.org/10.1038/s41589-020-00728-9>.

Correspondence and requests for materials should be addressed to B.M.

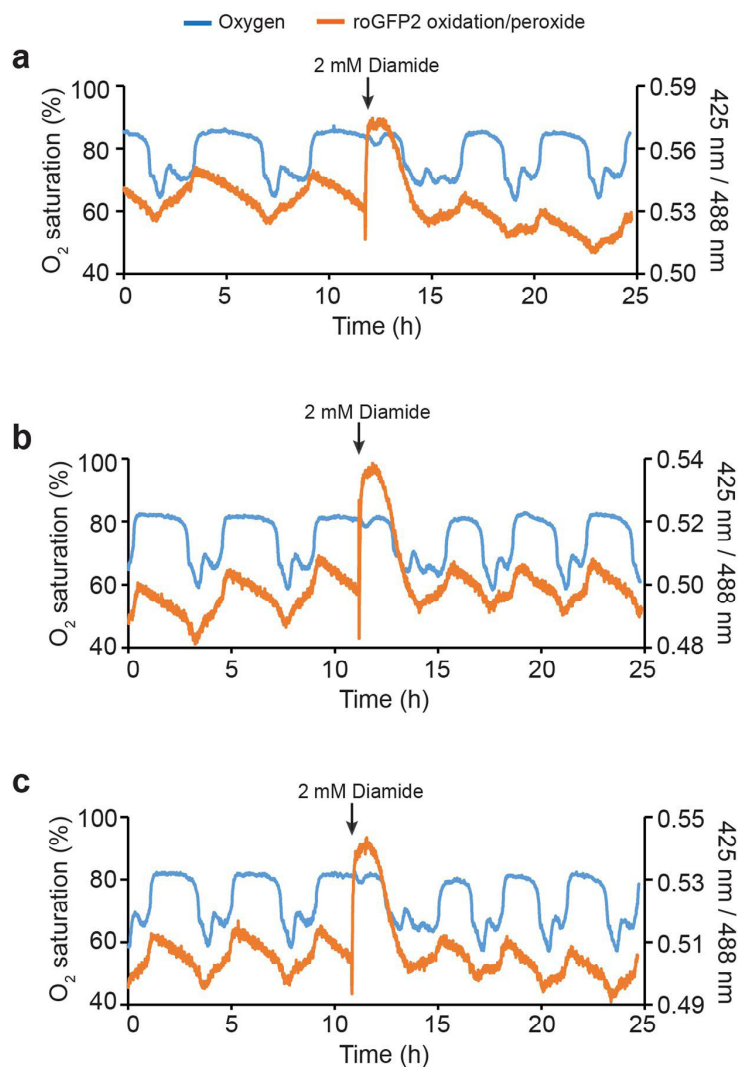
Reprints and permissions information is available at www.nature.com/reprints.



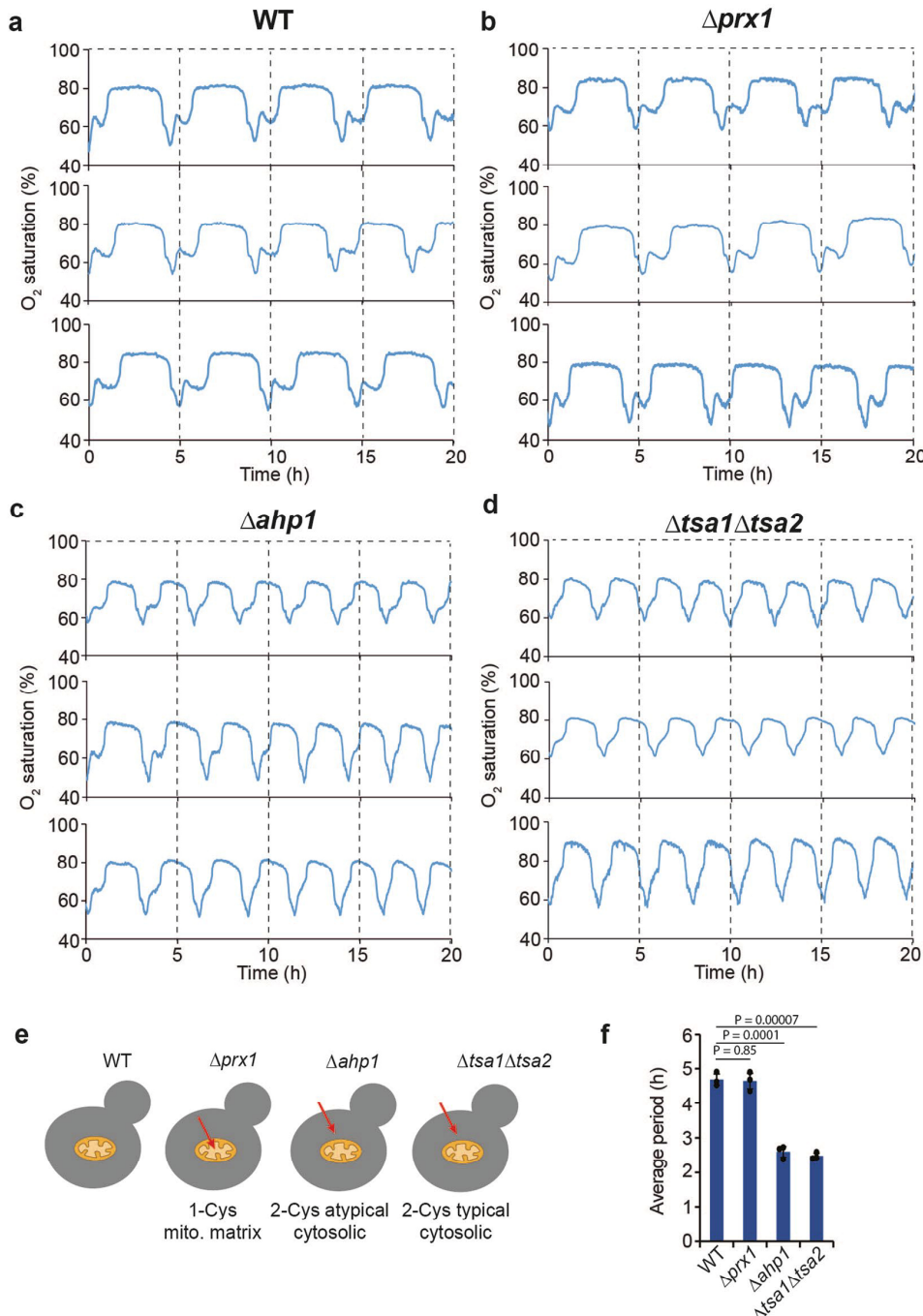
Extended Data Fig. 1 | Oxygen consumption and cytosolic H₂O₂ levels oscillate in phase. **a–c**, The media oxygen saturation and roGFP2-Tsa2ΔC_R oxidation was monitored for three complete cycles in three independent YMC-synchronized cultures of wild-type cells (datasets presented in Fig. 1c and Supplementary Fig. 2b). Autocorrelation analysis of the oxygen and roGFP2-Tsa2ΔC_R oxidation revealed robust and in-phase periodicity of the two signals. **d**, Plot showing time points of the oxygen saturation and roGFP2-Tsa2ΔC_R oxidation minima and maxima. Data were fitted by linear regression and significance, as tested by a two-sided ANOVA, revealed $p \approx 0$ (4.9×10^{-324}).

ARTICLES

NATURE CHEMICAL BIOLOGY



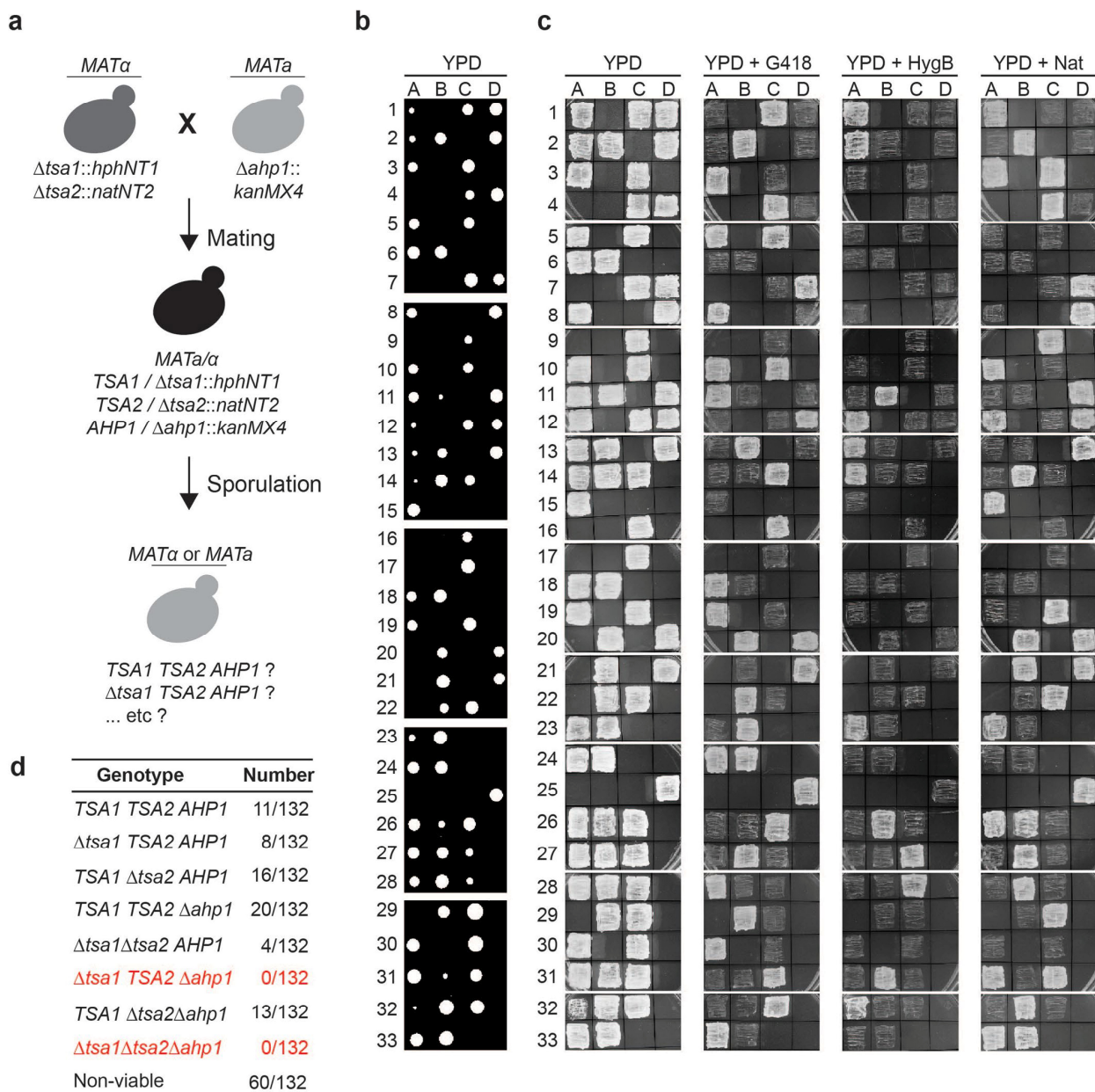
Extended Data Fig. 2 | LOC to HOC switching correlates with probe reduction after diamide treatment. **a–c**, RoGFP2-Tsa2ΔC_R probe oxidation following the addition of 2 mM diamide towards the end of LOC phase in three independent YMC-synchronized cultures.



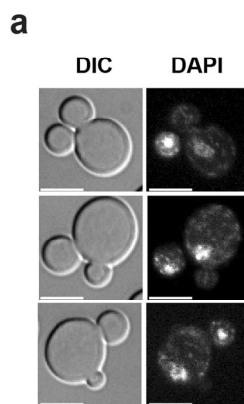
Extended Data Fig. 3 | Peroxiredoxin deletion perturbs the YMC. **a-d**, Oxygen traces to show YMC cycling in either wild-type cells or cells deleted for the genes encoding the indicated peroxiredoxins. Each trace is derived from a completely independent YMC-synchronized culture. **e**, Cartoon illustrating the subcellular localization of the peroxiredoxins presented in **a-d**. **f**, Graph showing the average YMC periods determined from the datasets presented in **a-d**. $n=3$ independent YMC-synchronized cultures. Error bars, mean \pm s.d. P values are derived from an unpaired two-tailed Student's t-test.

ARTICLES

NATURE CHEMICAL BIOLOGY



Extended Data Fig. 4 | Combined deletion of *AHP1* and *TSA1* is lethal in CEN.PK yeast. **a**, Scheme illustrating the mating, sporulation and tetrad dissection procedure. **b**, Images of tetrad dissection plates for all 33 tetrads dissected. **c**, Images showing growth of cells from all recovered viable spores on media containing the indicated antibiotics to assess for the presence of the antibiotic resistance cassettes used for gene deletion. **d**, Table showing the eight possible genotypes and the number of spores recovered with each genotype.



Extended Data Fig. 5 | A prolonged switch to HOC phase leads to accumulation of cells with two buds. **a,** Representative microscopy images of DAPI stained cells with 2 buds, isolated from YMC-synchronized cultures ~10 hours after addition of 5 mM DTT, the scale bar represents 2 μ M. n=3 independent experimental repeats.

2.4.1. Supplementary information

Amponsah, et al., 2021, *Nature Chemical Biology*

Peroxiredoxins couple metabolism and cell division in an ultradian cycle.

Amponsah, P.S., Yahya, G., **Zimmermann, J.**, Mai, M., Mergel, S., Mühlhaus, T., Storchova, Z. and Morgan, B.

Nature Chemical Biology. 2021 February, 17(4), 477-484

DOI: 10.1038/s41589-020-00728-9

Reprinted from *Nature Chemical Biology*: Amponsah, P.S., Yahya, G., Zimmermann, J., Mai, M., Mergel, S., Mühlhaus, T., Storchova. Z. and Morgan, B. Peroxiredoxins couple metabolism and cell division in an ultradian cycle. 17(4), 477-484 © (2021), with permission from Nature Springer (*Nature Chemical Biology*).

All rights reserved.

Supplementary Information

Peroxiredoxins couple metabolism and cell division in an ultradian cycle

Prince Saforo Amponsah^{1,2}, Galal Yahya^{3,4}, Jannik Zimmermann², Marie Mai², Sarah Mergel¹, Timo Mühlhaus⁵, Zuzana Storchova⁴ and Bruce Morgan^{2*}

Affiliations:

¹ Cellular Biochemistry, Technische Universität Kaiserslautern, 67663 Kaiserslautern, Germany

² Institute of Biochemistry, Centre for Human and Molecular Biology (ZHMB), Saarland University, 66123 Saarbrücken, Germany

³ Department of Microbiology and Immunology, School of Pharmacy, Zagazig University, Egypt.

⁴ Department of Molecular Genetics, Technische Universität Kaiserslautern, 67663 Kaiserslautern, Germany

⁵ Computational Systems Biology, Technische Universität Kaiserslautern, 67663 Kaiserslautern, Germany

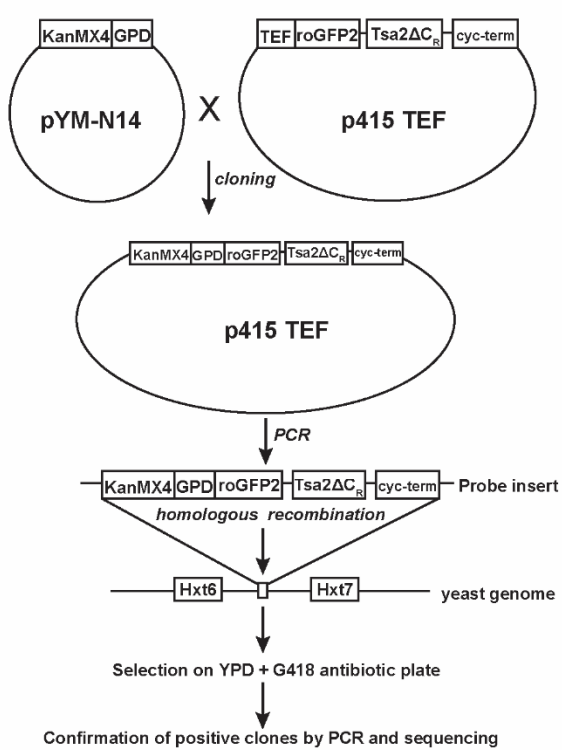
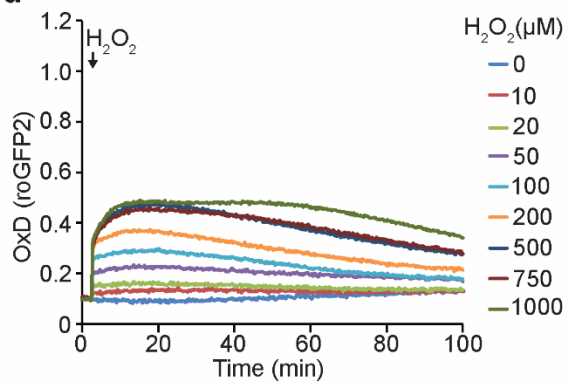
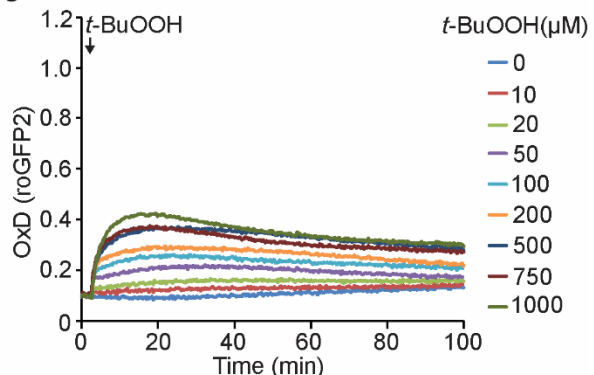
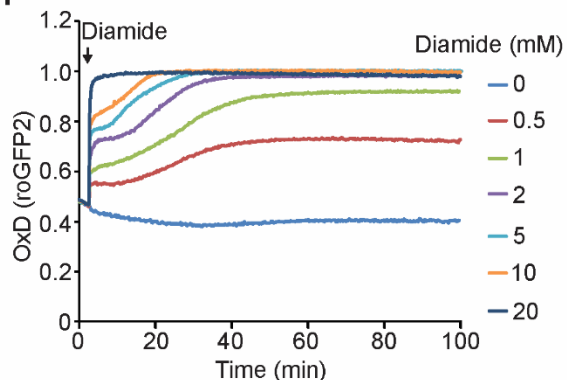
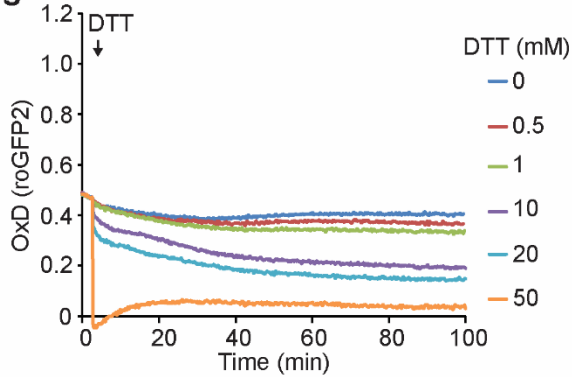
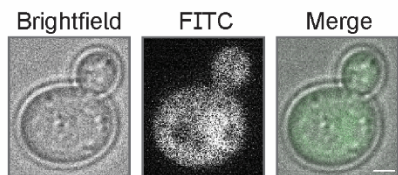
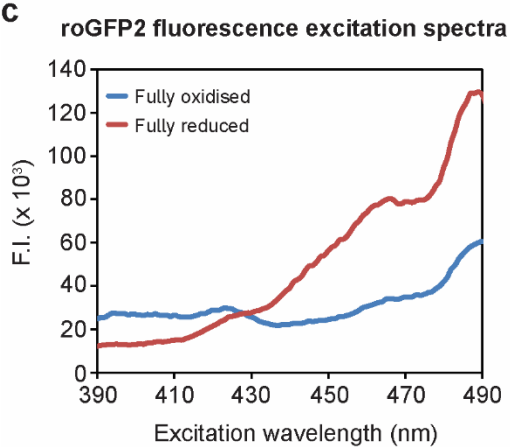
*To whom correspondence should be addressed

Prof. Dr. Bruce Morgan

Tel.: +49-631-205-2885

Email: bruce.morgan@uni-saarland.de

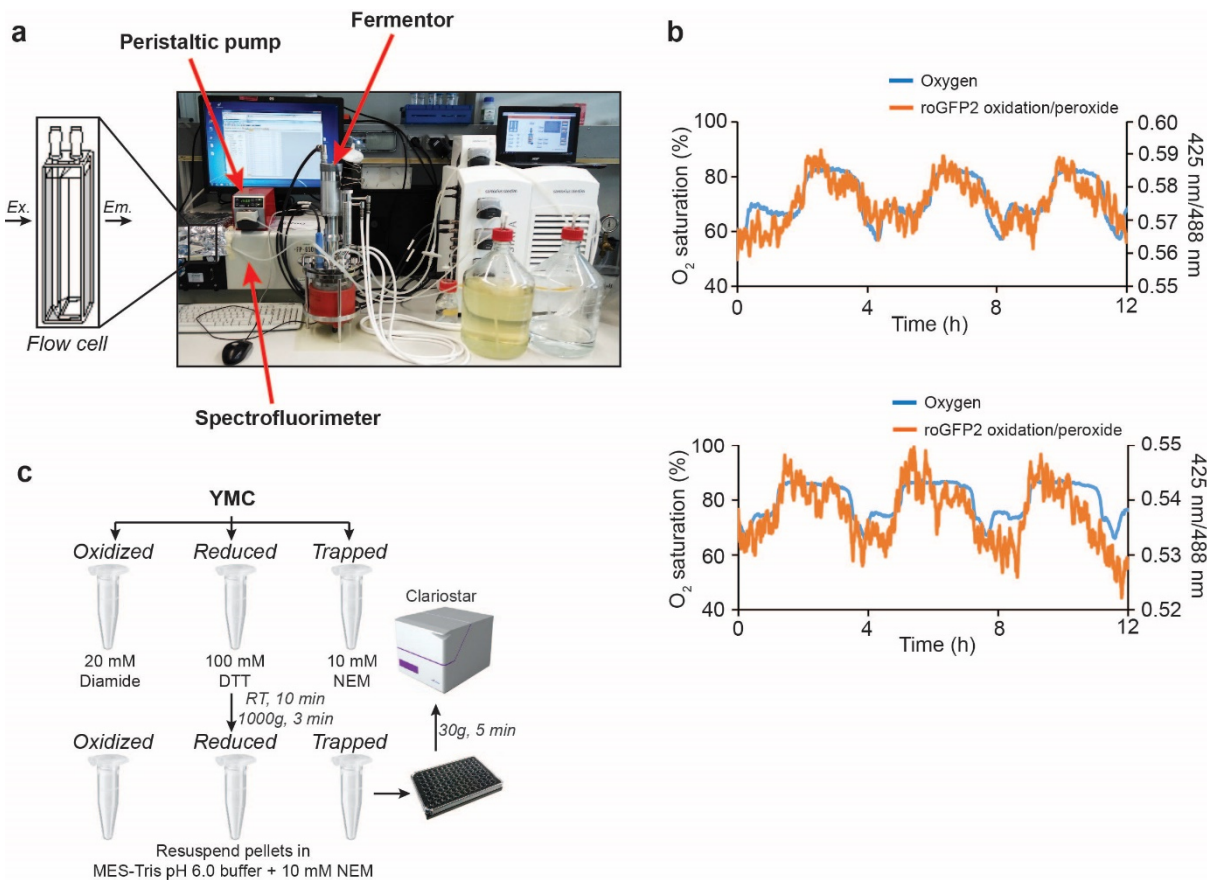
Supplementary Figure 1.

a**d****e****f****g****b****c**

Supplementary Fig. 1. Characterization of the genomically integrated roGFP2-Tsa2ΔC_R probe

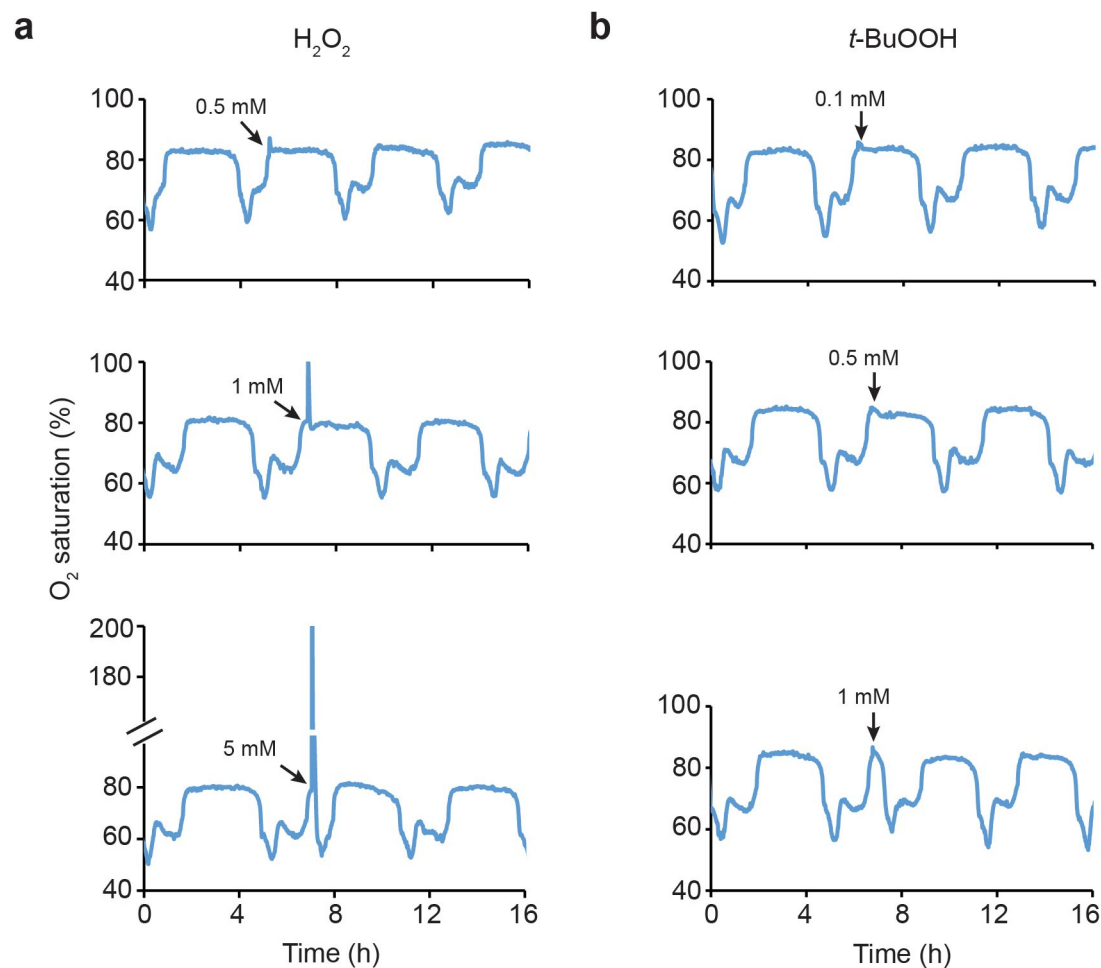
(a) Scheme illustrating the generation of CEN.PK strain with a genomically integrated construct for roGFP2-Tsa2ΔC_R probe expression. (b) Representative fluorescence microscopic image to show the cytosolic localization of roGFP2-Tsa2ΔC_R probe, the scale bar represents 2 μM. (c) Fluorescence excitation spectra of CEN.PK cells expressing roGFP2-Tsa2ΔC_R. Fully oxidized and fully reduced spectra were obtained by treating the cells with 20 mM diamide and 100 mM DTT respectively. (d) Response of the roGFP2-Tsa2ΔC_R probe, expressed in CEN.PK cells, to the addition of H₂O₂ at the indicated concentrations. (e) Response of the roGFP2-Tsa2ΔC_R probe, expressed in CEN.PK cells, to the addition of *t*-BuOOH at the indicated concentrations. (f) Response of the roGFP2-Tsa2ΔC_R probe, expressed in CEN.PK cells, to the addition of diamide at the indicated concentrations. (g) Response of the roGFP2-Tsa2ΔC_R probe, expressed in CEN.PK cells, to the addition of DTT at the indicated concentrations.

Supplementary Figure 2.



Supplementary Fig. 2. Procedures for monitoring of roGFP2-Tsa2 Δ C_R oxidation during the YMC.

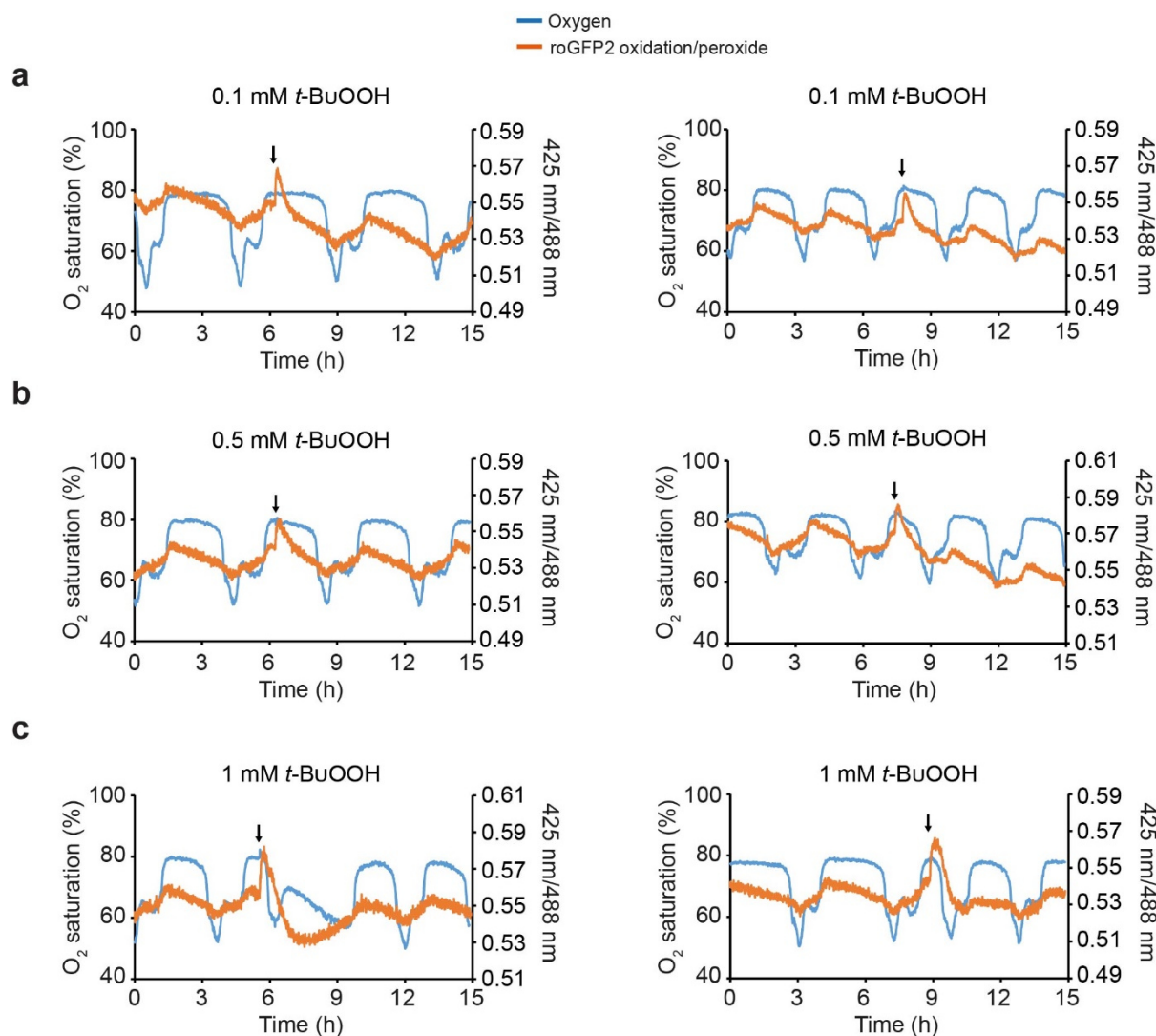
(a) Labelled photograph showing the coupled fermentor–spectrofluorimeter setup used for the online monitoring of roGFP2-Tsa2 Δ C_R oxidation. (b) Two further experimental repeats of the dataset in Fig. 1c. (c) Scheme illustrating the procedure for fluorescence plate-reader-based monitoring of roGFP2-Tsa2 Δ C_R oxidation.

Supplementary Figure 3.

Supplementary Fig. 3. High concentrations of H_2O_2 or $t\text{-BuOOH}$ promote LOC to HOC switching

(a) H_2O_2 and (b) $t\text{-BuOOH}$ was added to YMC-synchronized cultures of wild-type cells at the indicated concentrations.

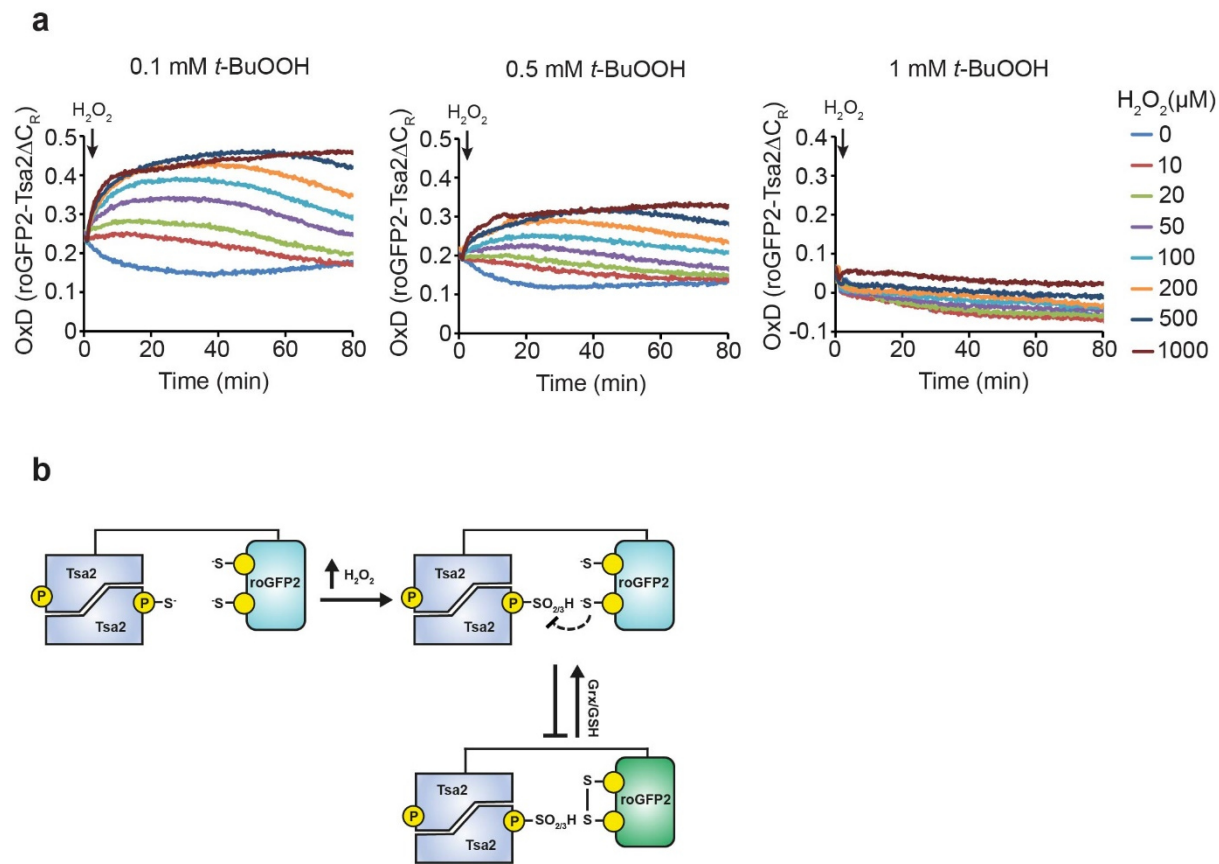
Supplementary Figure 4.



Supplementary Fig. 4. Peroxide levels recover before the switch to HOC

(a–c) Two further experimental repeats of the experiment presented in **Fig. 2a–c**, showing the impact on O₂ saturation and roGFP2-Tsa2ΔC_R oxidation of the addition of (a) 0.1 mM, (b) 0.5 mM and (c) 1 mM $t\text{-BuOOH}$.

Supplementary Figure 5.

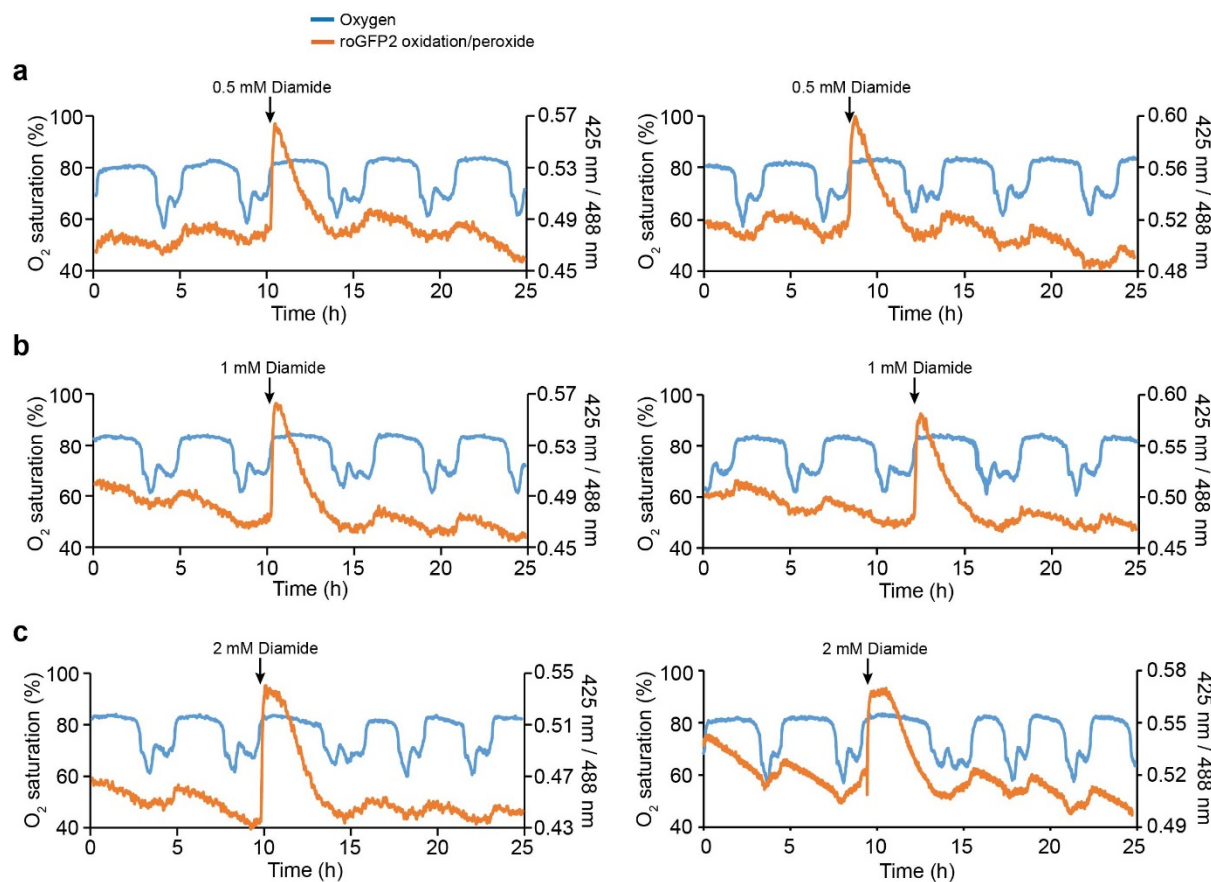


Supplementary Fig. 5. Peroredoxin hyperoxidation correlates with peroxide induced LOC to HOC switching.

(a) Samples were isolated from YMC-synchronized cultures 30 minutes after *t*-BuOOH addition at the indicated concentrations. Probe oxidation and response to subsequent treatment with H_2O_2 at the indicated concentrations were monitored in a fluorescence plate-reader. Related to **Fig. 2a–c** and **Supplementary Fig. 5.** (b) Scheme illustrating how peroxiredoxin hyperoxidation leads to roGFP2 reduction. Upon hyperoxidation of the peroxidatic cysteine to either a sulfinic (SO_2H) or sulfonic (SO_3H) acid, oxidation can no longer be transferred to roGFP2. If roGFP2 is already oxidized when the

attached peroxiredoxin is hyperoxidized it will tend to become reduced due to reduction of the roGFP2 disulfide via GSH and glutaredoxins.

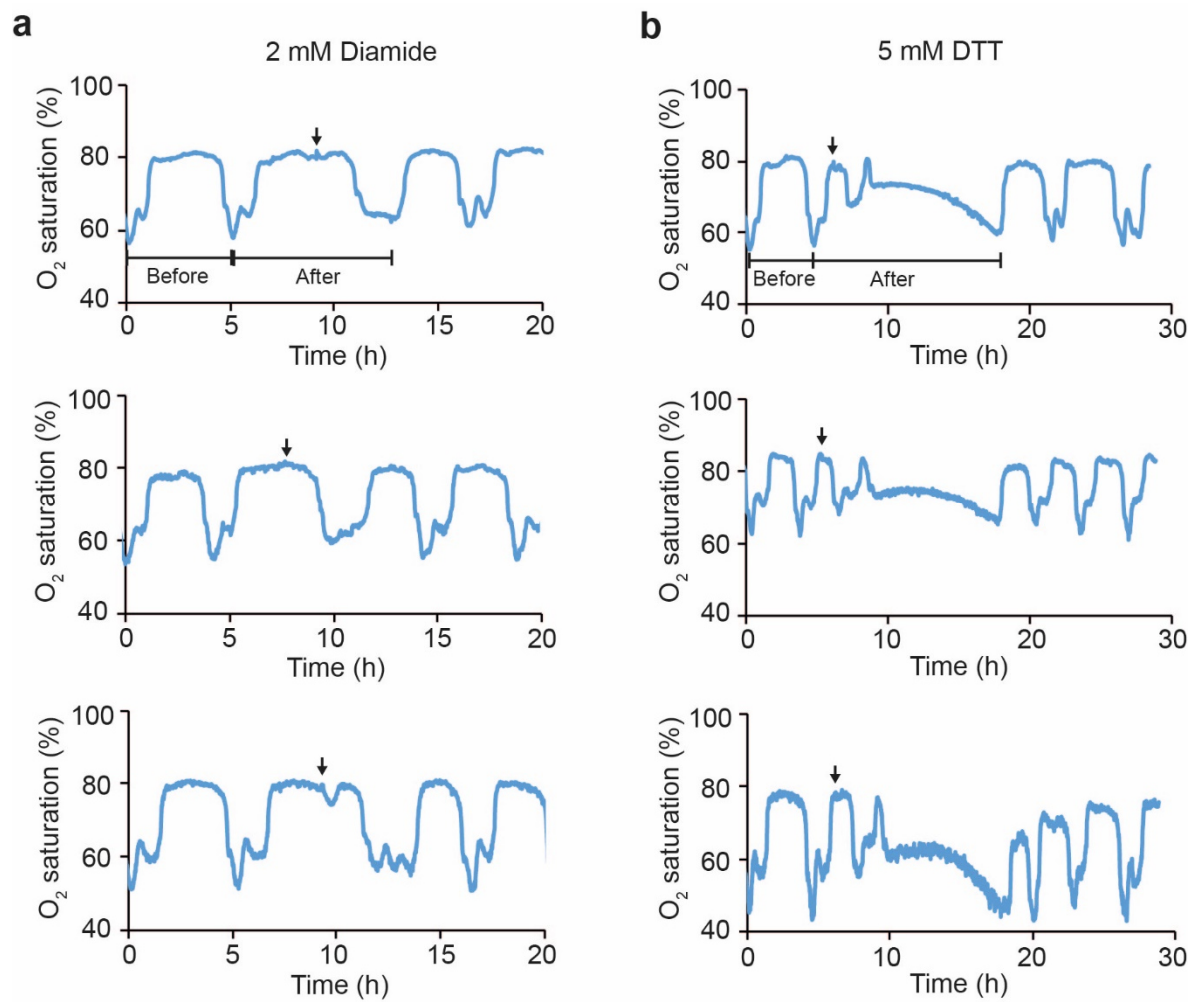
Supplementary Figure 6.



Supplementary Fig. 6. A thiol oxidant extends the LOC phase

(a) Two independent experimental repeats showing the response of independent YMC-synchronized cultures of wild-type cells, as monitored by oxygen consumption, together with the response of a genetically integrated roGFP2-Tsa2 Δ C_R probe, to diamide added at a final concentration of (a) 0.5 mM, (b) 1 mM and (c) 2 mM.

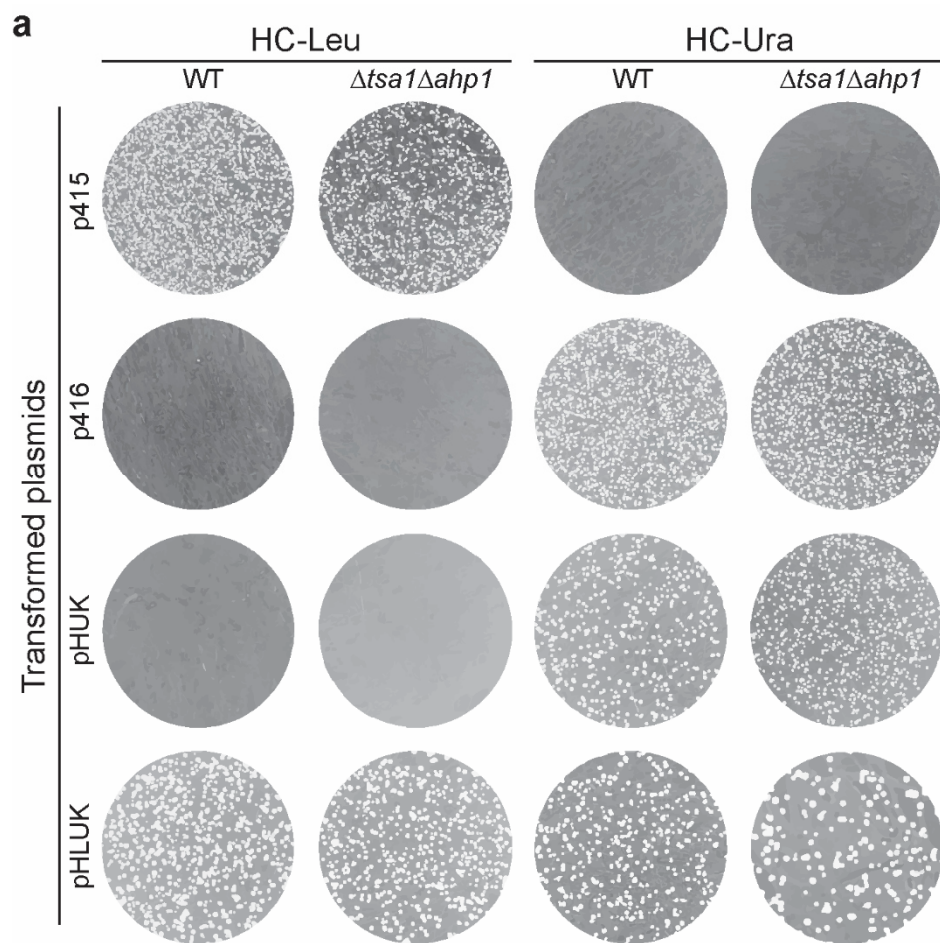
Supplementary Figure 7.



Supplementary Fig. 7. Thiol oxidation regulates LOC to HOC switching

Corresponding to **Fig. 2e–h**. Three further experimental repeats showing the impact of (a) 2 mM diamide or (b) 5 mM DTT addition at the indicated time-points to YMC-synchronized cultures of wild-type cells.

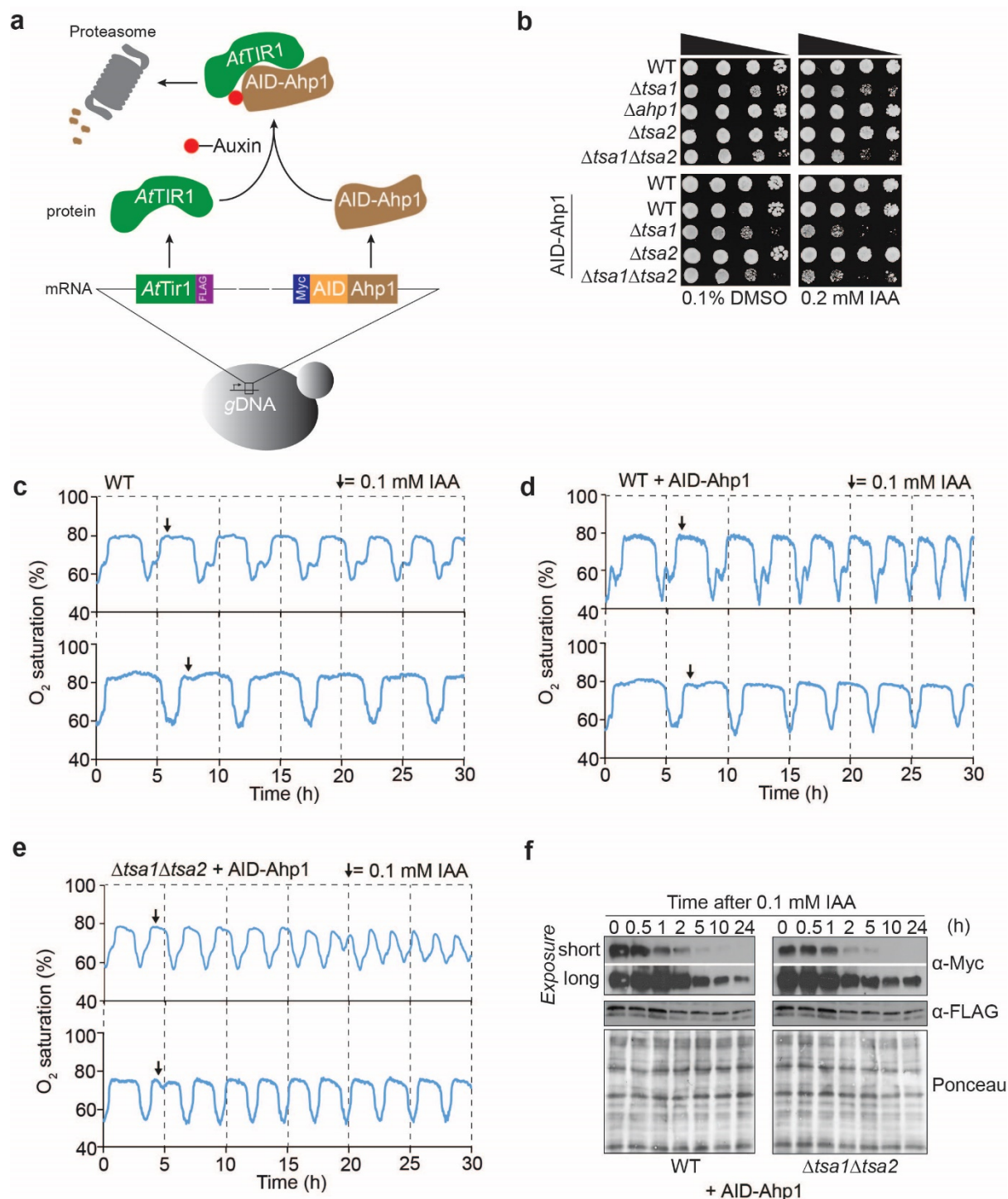
Supplementary Figure 8.



Supplementary Fig. 8. BY4742 $\Delta tsa1\Delta ahp1$ cells are viable irrespective of auxotrophic markers

(a) Images of colonies of BY4742 $\Delta tsa1\Delta ahp1$ cells formed on indicated selective plates following transformation with the indicated plasmids. Note: BY4742 cells are uracil and leucine auxotrophs. Therefore, cells transformed with p416 and pHUK plasmids, which both harbor *URA3* as a selective marker, would not be expected to grow on media lacking leucine. Likewise, cells transformed with p415 (*LEU2* as selective marker) should not grow on plates lacking uracil. These conditions therefore serve as controls. BY4742 $\Delta tsa1\Delta ahp1$ cells transformed with a pHLUK plasmid to replace all four auxotrophic markers grows well on media lacking with leucine or uracil.

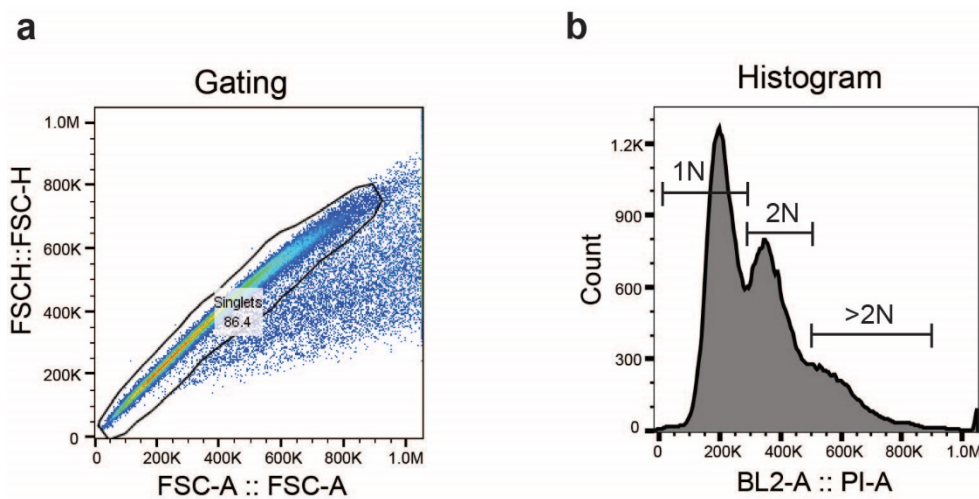
Supplementary Figure 9.



Supplementary Fig. 9. Auxin induced degradation of Ahp1 in $\Delta ts\alpha 1\Delta ts\alpha 2$ cells induces a poor growth phenotype.

(a) Cartoon illustrating the mechanism of the auxin-regulable degron fused to Ahp1. (b) Drop dilution assay showing the growth of the indicated yeast strains on YPD plates containing either 0.1% DMSO as a vehicle control or 0.2 mM indole-3-acetic acid (IAA). (c–e) Two further experimental repeats of the data presented in **Fig. 3a**. (f) Western blot with an anti-MYC antibody to assess the degradation of Ahp1 following IAA addition to a YMC-synchronized culture. Representative image of 2 independent experimental repeats.

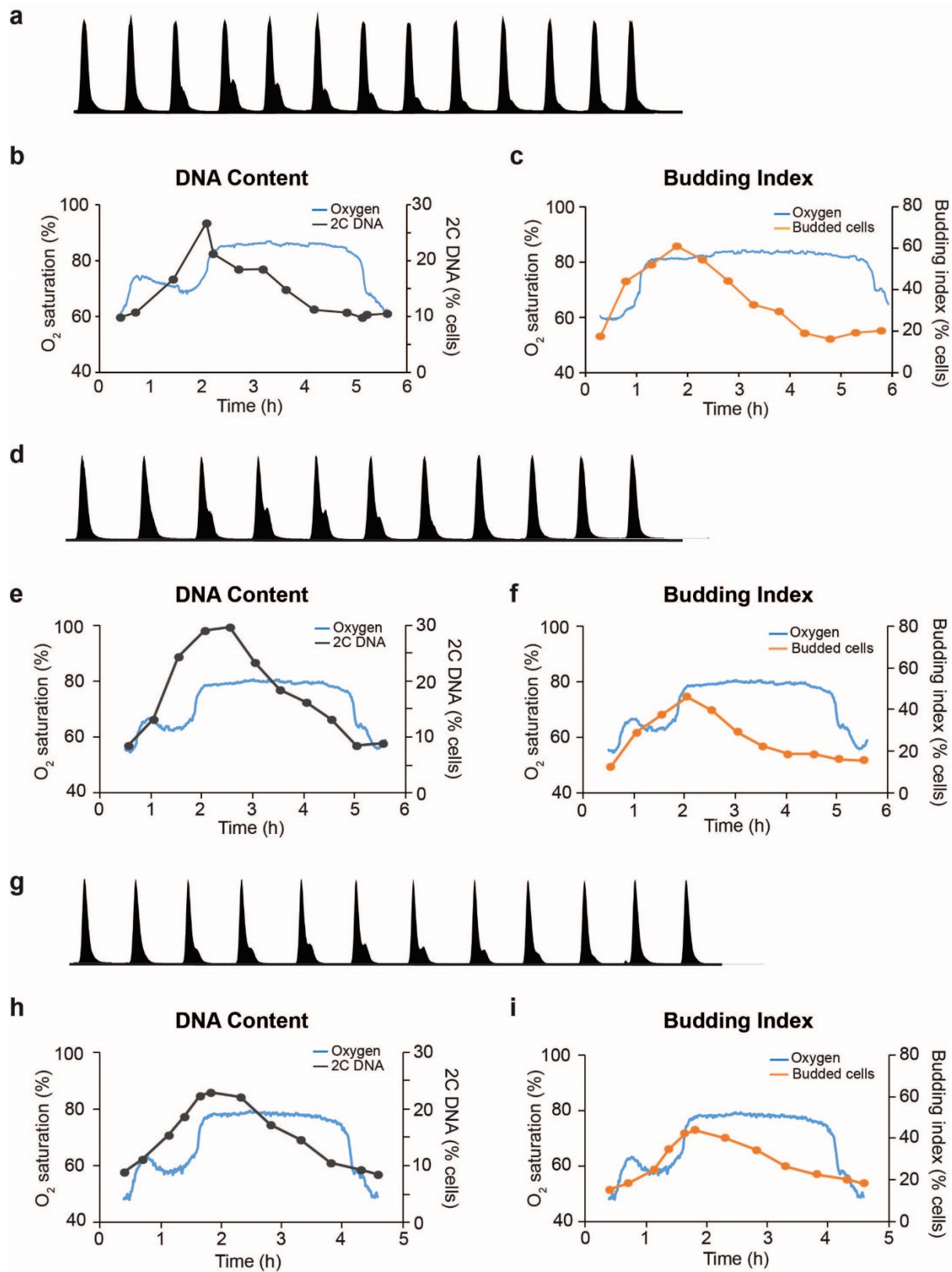
Supplementary Figure 10.



Supplementary Fig. 10. Gating and analysis strategy for flow cytometry data.

(a) The represented gating strategy was used to select for singlets by monitoring forward scatter area (FSC-A) vs. forward scatter height (FSC-H). (b) Propidium iodide fluorescence intensity in these cells was then used to determine DNA content based on the following criteria. The percentages of cells with 1C DNA and 2C DNA content were determined as follows. The percentage of cells with 1C DNA content was determined as the number of cells with a PI staining intensity from $0\text{--}2.7 \times 10^5$ as a percentage of the total number of cells analyzed. The percentage of cells with 2C DNA content was determined as the number of cells with a PI staining intensity from $2.7 \times 10^5\text{--}4.5 \times 10^5$ as a percentage of the total number of cells analyzed. The percentage of cells with >2C DNA content was determined as the number of cells with a PI staining intensity from $>4.5 \times 10^5$ as a percentage of the total number of cells analyzed

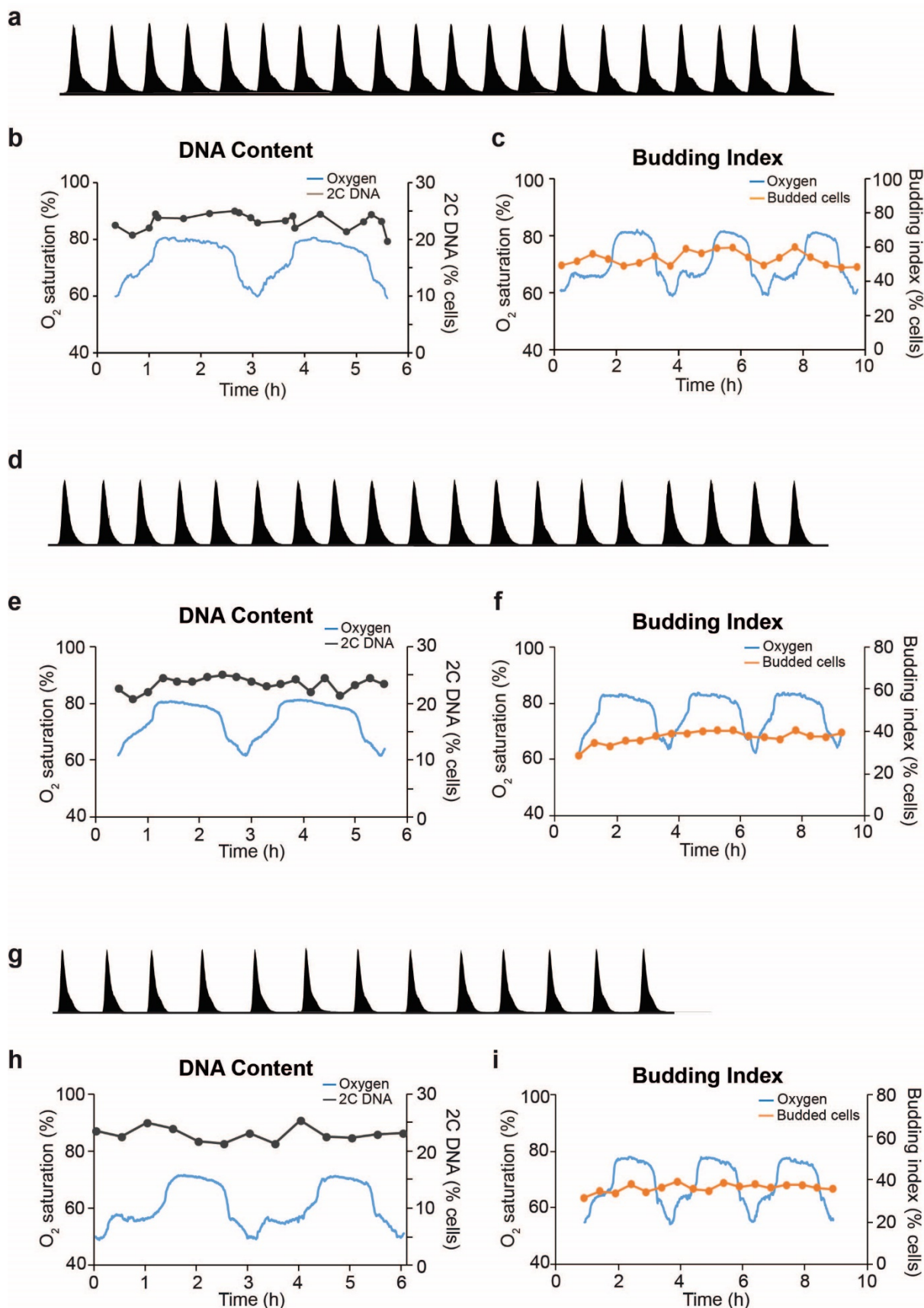
Supplementary Figure 11.



Supplementary Fig. 11. Cell division is coupled to the yeast metabolic cycle

Corresponds to the data presented in **Fig. 4a,b**. Three independent, YMC-synchronized cultures of wild-type cells were analyzed for DNA content (a,b,d,e,g,h) and budding index (c,f,i) at the points during the YMC as indicated.

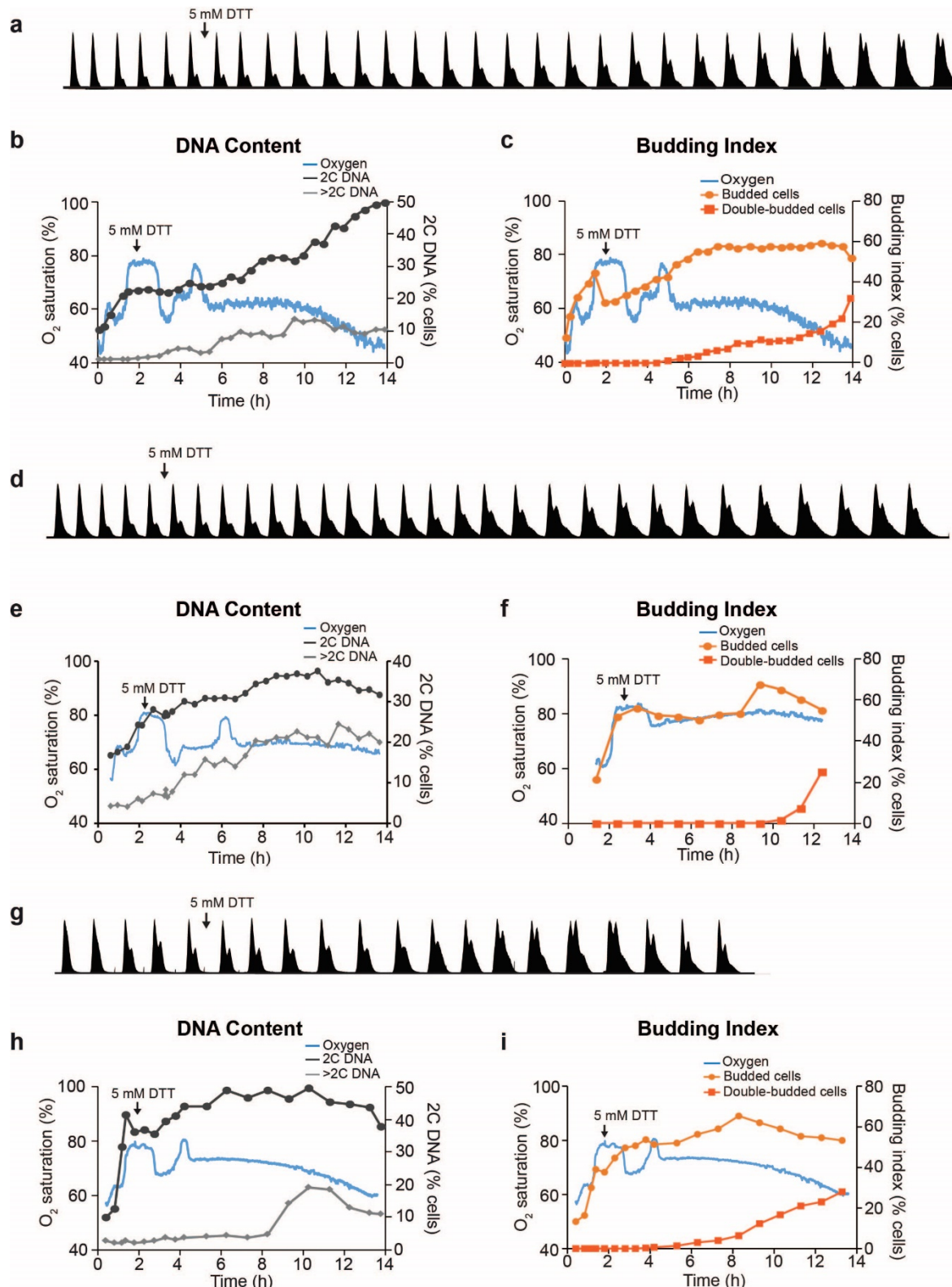
Supplementary Figure 12.



Supplementary Fig. 12. Cell division is uncoupled from metabolic cycling in $\Delta tsa1\Delta tsa2$ cells

Corresponds to the data presented in **Fig. 4c,f**. Three independent, YMC-synchronized cultures of $\Delta tsa1\Delta tsa2$ cells were analyzed for DNA content (a,b,d,e,g,h) and budding index (c,f,i) at the points during the YMC as indicated.

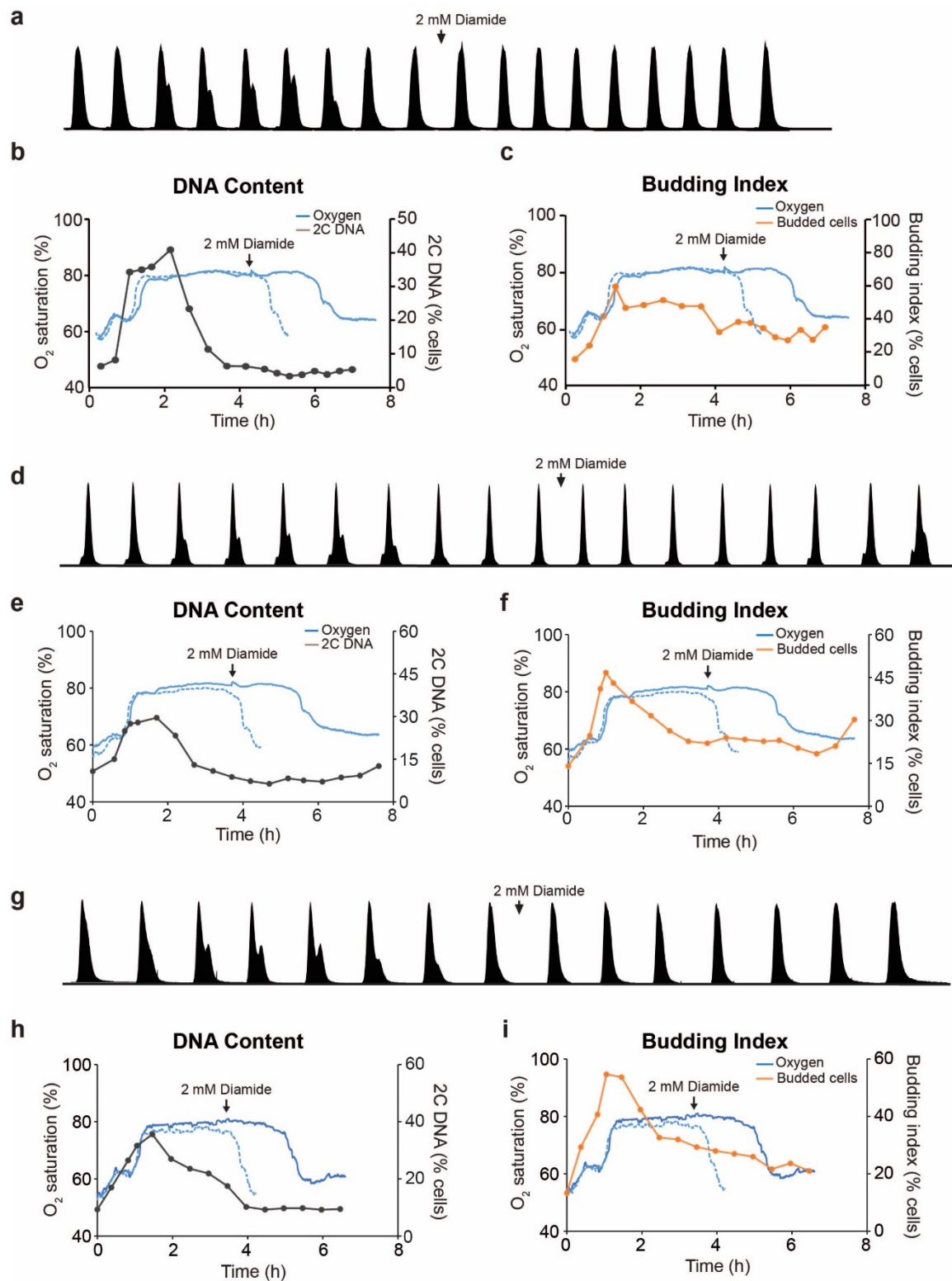
Supplementary Figure 13.



Supplementary Fig. 13. Maintaining cells in HOC phase prevents cell cycle completion

Corresponds to the data presented in **Fig. 5a–d**. 5 mM DTT was added to three independent YMC-synchronized cultures of wild-type cells at the indicated time-points. Cultures were subsequently analyzed to assess DNA content and budding index.

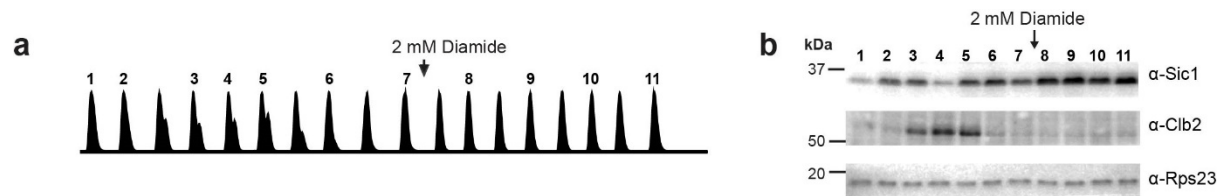
Supplementary Figure 14.



Supplementary Fig. 14. Prevention of LOC to HOC switching blocks cell cycle initiation

Corresponds to the data presented in **Fig. 5e,f.** 2 mM diamide was added to three independent YMC-synchronized cultures of wild-type cells at the indicated time-points. Cultures were subsequently analyzed to assess DNA content and budding index.

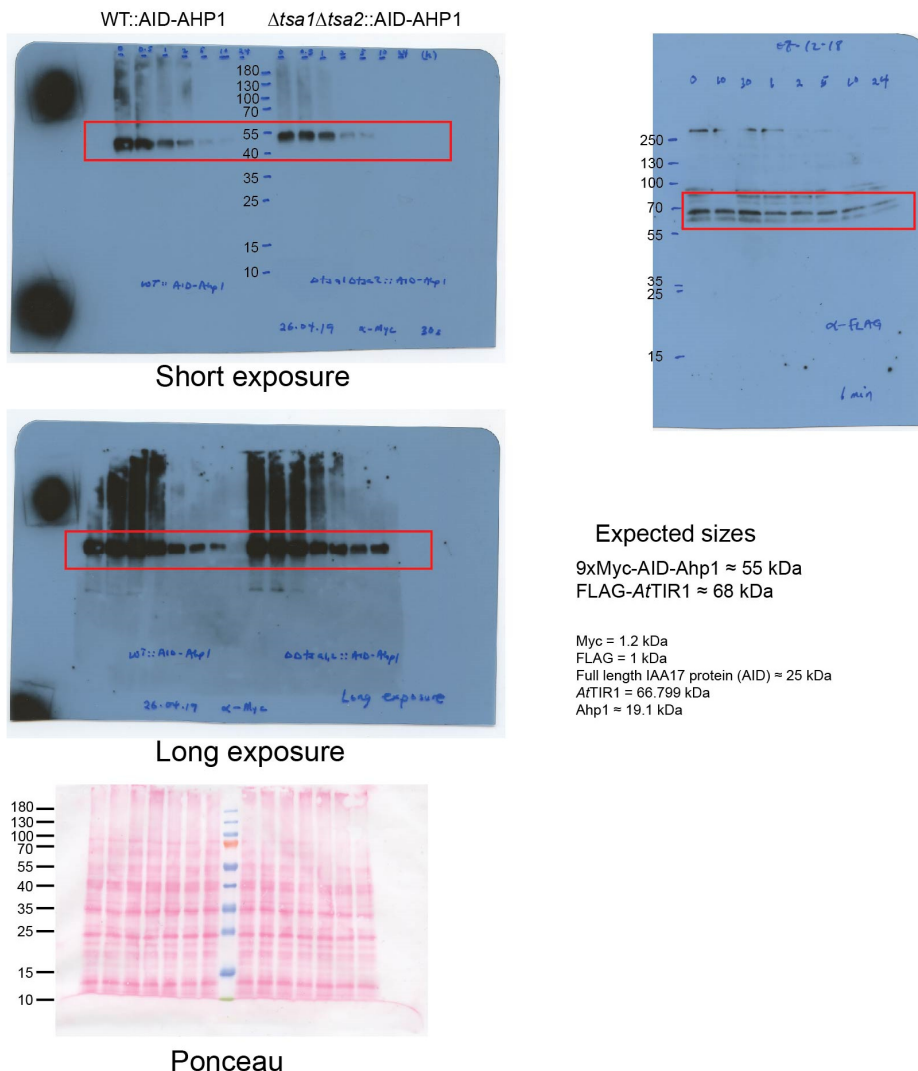
Supplementary Figure 15.



Supplementary Fig. 15. Cell cycle start markers confirm that cell cycle start is inhibited after diamide treatment

a,b) Representative Western blot using anti-Sic1 and anti-Clb2 antibodies. Rps23 was used as a loading control. Samples analyzed were the same as those used in **Supplementary Fig. 19a,b**. The numbering on the western blot corresponds to the flow cytometry histograms in panel a, indicating the analyzed samples. n=3 independent experimental repeats.

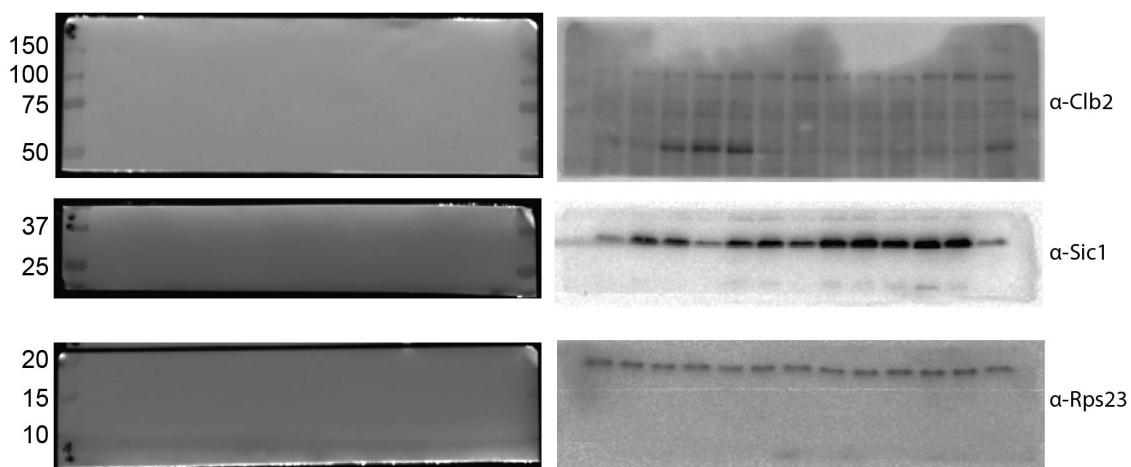
Supplementary Figure 16.

a

Expected sizes

9xMyc-AID-Ahp1 \approx 55 kDa
 α -FLAG-AtTIR1 \approx 68 kDa

Myc = 1.2 kDa
 α -FLAG = 1 kDa
 Full length IAA17 protein (AID) \approx 25 kDa
 AtTIR1 = 66.799 kDa
 Ahp1 \approx 19.1 kDa

b

Supplementary Figure 16. Source Data for Supplementary Figures

a) Unprocessed western blots and ponceau-stained membrane relating to Supplementary Fig. 13f. **b)** Unprocessed western blots relating to Supplementary Fig. 20b.

Supplementary Table 1. Yeast strains used in this study

Genotype	Source
CEN.PK113-1A <i>MATα</i>	Kind gift from P. Kötter, Frankfurt
CEN.PK113-7D <i>MATa</i>	Kind gift from P. Kötter, Frankfurt
CEN.PK113-1A $\Delta prx1::hphNT1$	This study
CEN.PK113-1A $\Delta tsa1::hphNT1$	This study
CEN.PK113-1A $\Delta tsa2::natNT2$	This study
CEN.PK113-1A $\Delta tsa1::hphNT1 \Delta tsa2::natNT2$	This study
CEN.PK113-1A $\Delta ahp1::hphNT1$	This study
CEN.PK113-1A <i>kanMX4-P_{GPD}-roGFP2-Tsa2ΔC_R</i>	This study
CEN.PK113-7D $\Delta ahp1::kanMX4$	This study
CEN.PK113-1A <i>At-Tir1-FLAG-Myc-kanMX4-AID-AHP1</i>	This study
CEN.PK113-1A $\Delta tsa1::hphNT1 \Delta tsa2::natNT2 At-Tir1-FLAG-Myc-kanMX4-AID-AHP1$	This study
BY4741 <i>MATa his3Δ1 leu2Δ0 met15Δ0 ura3Δ0</i>	Euroscarf
BY4742 <i>MATα his3Δ1 leu2Δ0 lys2Δ0 ura3Δ0</i>	Euroscarf
BY4742 $\Delta tsa1::kanMX4 \Delta ahp1::hphNT1$	This study

3. General discussion and perspective

Thioredoxin superfamily enzyme analyses are typically performed *in vitro* using recombinant proteins. However, *in vitro* protein characterization is time-consuming and labor-intensive, especially when studying multiple proteins or different mutants in parallel. Consequently, many thioredoxin fold enzymes remain uncharacterized. Their redox activity and substrate preference are often largely unknown. Thus far, certain members could not be purified as recombinant proteins e.g., class III glutaredoxins from land plants, not allowing for an *in vitro* analysis. To overcome these limitations, this dissertation is dedicated to the development, application and refinement of novel yeast- and fluorescence-based approaches. These methods would complement existing *in vitro* analyses and improve the characterization of thioredoxin superfamily proteins. The demands on these novel assays are (i.) rapid, high throughput-like screening of various proteins with their (ii.) physiological substrates in a (iii.) cellular environment, without the need of initial protein purification.

3.1. Development of a fluorescence-based screen to monitor glutaredoxin activity

in vivo

It has recently been demonstrated that the fluorescence readout of roGFP2 is suitable for monitoring aspects of the peroxiredoxin-dependent catalysis of *PfAOP* from the malaria parasite *Plasmodium falciparum* (Staudacher *et al.*, 2018). The authors used wild-type *S. cerevisiae* cells, expressing fusions between roGFP2 and *PfAOP* or mutants thereof in the cytosol. This study provided several novel findings. (i.) Upon treatment with *tert*-butyl hydroperoxide (*t*-BuOOH), relative differences in roGFP2 oxidation kinetics between multiple *PfAOP* fusion constructs correlated with their activity determined *in vitro* (Staudacher *et al.*, 2015). (ii.) They reported sensitivity to hyperoxidation upon application of *t*-BuOOH and H₂O₂ for different mutants *in vivo*. Monitoring H₂O₂-mediated inactivation of *PfAOP* with roGFP2 was particularly interesting. Steady-state kinetic measurements with H₂O₂ *in vitro* were not possible as a result of direct and effective inactivation of the enzyme. (iii.) In their experimental setup, roGFP2 serves as an alternative substrate for oxidation by *PfAOP*. Thus, the kinetics of roGFP2 oxidation were directly dependent on the enzyme activity. However, the application of this approach to examine other thioredoxin superfamily proteins remains to be confirmed. Thus, investigation of roGFP2-based enzyme analyses has been extended to other proteins, namely active class I and inactive class II glutaredoxins. ScGrx7 serves as a model protein for active class I glutaredoxins for many reasons.

ScGrx7 has already been studied *in vitro* in the laboratory of Prof. Dr. Marcel Deponte at the University of Kaiserslautern (Begas *et al.*, 2015; Begas *et al.*, 2017). Quantitative data for *ScGrx7* and many mutants thereof were already collected and could serve as an important benchmark for results obtained in yeast. *ScGrx7* is a class I glutaredoxin with particularly interesting characteristics. Unlike its paralog, *ScGrx6*, it does not bind Fe-S clusters. *ScGrx7* and inactive class II glutaredoxins share the same active site -CxxS- arrangement. This raises the question as to which other structural differences determine presence or absence of activity in either of the classes. Consequently, the catalytic mechanism of monothiol class I *ScGrx7* depends on a single cysteine residue. This simplifies analyses of their redox catalysis and mechanism due to absence of alternative reactions with other cysteine residues.

Fusions between roGFP2 and *ScGrx7*, or any subsequent mutants thereof, were generated and expressed in the cytosol of yeast cells (see publication 2.1.). The natural glutaredoxin substrate, GSSG, is essential for glutaredoxin-dependent roGFP2 oxidation. Thus, it must be provided in sufficient amounts to not limit the reaction. To induce glutathione oxidation and readily perturb the cytosolic 2GSH/GSSG redox couple, H₂O₂ was exogenously applied at different concentrations. In this experimental setup, H₂O₂ diffuses into the cell leading to accumulation of GSSG. Equilibration of roGFP2 with the change in endogenous GSSG levels is dependent on the activity of the fused *ScGrx7* moiety. Notably, formation of GSSG upon addition of H₂O₂ is most likely indirect. An accumulation of GSSG resulting from the reaction between H₂O₂ and 2GSH is thermodynamically possible. However, *in vitro* studies have shown rate constants below 30 M⁻¹ s⁻¹ (Winterbourn *et al.*, 1999). As yeast do not harbor *bona fide* glutathione peroxidases, thiol peroxidases alongside glutathione transferases and glutaredoxins are most likely the major sources of GSSG upon the H₂O₂ treatment (Collinson *et al.*, 2002; Peskin *et al.*, 2016; Calabrese *et al.*, 2019; Zimmermann *et al.*, unpublished). Their rate constants with H₂O₂ or GSH are several orders of magnitude higher and would therefore mediate the formation of GSSG.

Development of the roGFP2-based screen involved characterization of probe behavior in the cytosol of yeast cells. Wild-type yeast cells however, as used in the study of Staudacher and colleagues in 2018, were not suitable for measurements of *ScGrx7*-dependent roGFP2 oxidation. Minor roGFP2 responses, following the H₂O₂ application, indicate rapid GSSG reduction (**Figure 7A**; Morgan *et al.*, 2011). H₂O₂ and GSSG can be readily reduced by cytosolic thioredoxin and glutathione reductases in wild-type cells. Both enzymes limit the aforementioned necessary supply of GSSG in sufficient amounts. Deletion of the gene encoding the glutathione reductase (*ScGLR1*) was necessary for sensitizing the cytosolic glutathione pool to the H₂O₂ treatment (**Figure 7B**). In accordance with previous studies, steady-state oxidation increases in *Δglr1* yeast strains, which directly reflects increased cytosolic GSSG levels (Morgan *et al.*, 2011). However, unfused roGFP2 and fusion of roGFP2

to the inactive $\text{ScGrx7}^{\text{C}108\text{S}}$ also seemed to equilibrate to the change in GSSG, independently of the activity of the fused moiety. This is problematic for the enzyme activity readout, as roGFP2 oxidation was not exclusively mediated by ScGrx7. Cytosolic dithiol class I glutaredoxins i.e., the endogenous ScGrx1 and ScGrx2 , are known to equilibrate roGFP2 with the 2GSH/GSSG redox couple (Björnberg *et al.*, 2006). It is important to note that equilibration of roGFP2 by cytosolic glutaredoxins involve ScGrx1 and ScGrx2 , but not the third cytosolic glutaredoxin, ScGrx8 . ScGrx8 structurally differs from classical dithiol glutaredoxins and remains largely uncharacterized (Eckers *et al.*, 2009; Tang *et al.*, 2014). Therefore, all following discussions about cytosolic glutaredoxins exclude ScGrx8 unless explicitly stated otherwise.

To enhance the specificity of roGFP2 oxidation, genes encoding ScGrx1 and ScGrx2 were deleted in a Δglr1 background in order to obtain the $\Delta\text{glr1}\Delta\text{grx1}\Delta\text{grx2}$ yeast strain. This yeast strain fulfills the requirements for rapid perturbation of the cytosolic glutathione pool, as well as specific roGFP2 oxidation mediated by the fused glutaredoxin (**Figure 7C**; publication 2.1., Figure 7a).

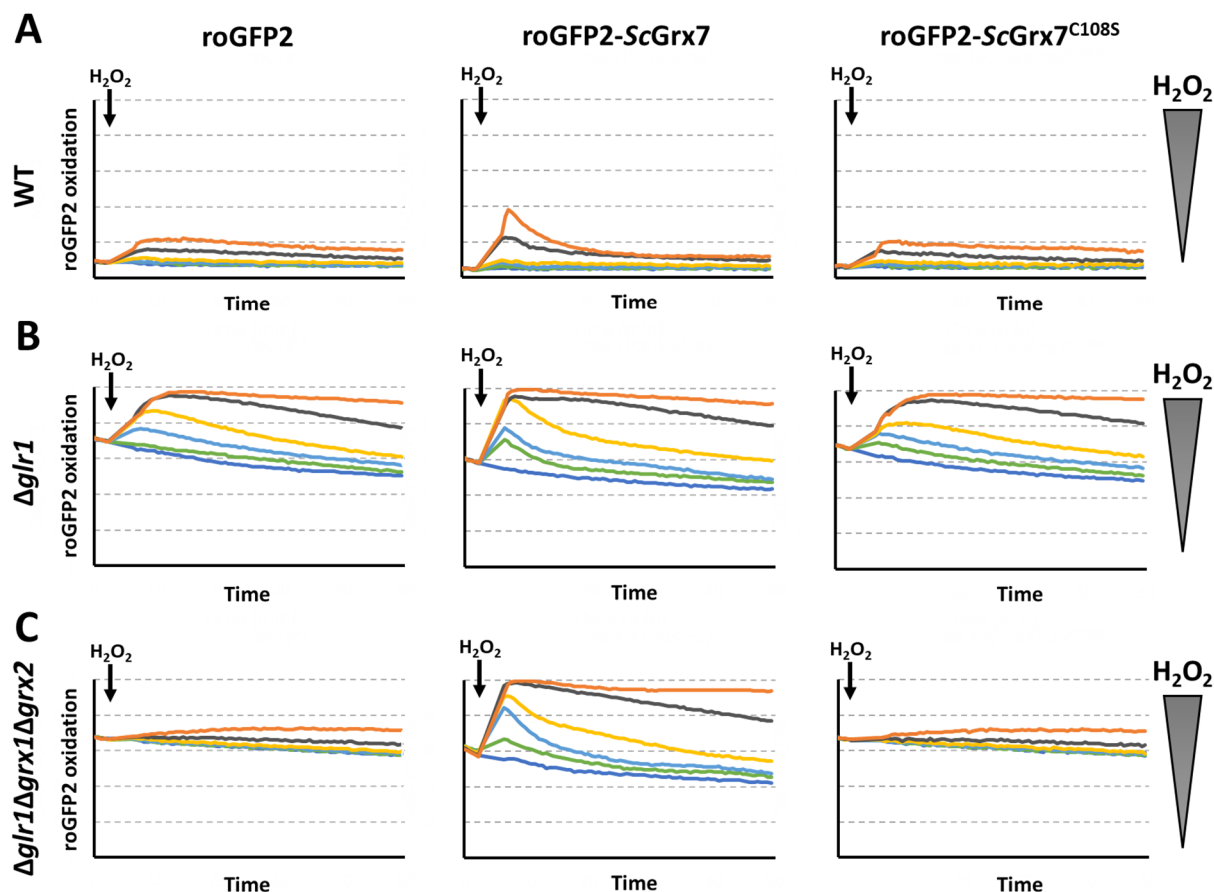


Figure 7. Development of a screen to monitor ScGrx7 activity. Unfused roGFP2, roGFP2-ScGrx7 and catalytically inactive roGFP2-ScGrx7 $^{\text{C}108\text{S}}$ were expressed in (A) wild-type (WT), (B) Δglr1 or (C) $\Delta\text{glr1}\Delta\text{grx1}\Delta\text{grx2}$ yeast cells. Genes were deleted to allow for rapid perturbation of the glutathione pool (Δglr1) in combination with specific, ScGrx7 -dependent roGFP2 oxidation ($\Delta\text{grx1}\Delta\text{grx2}$) upon application of different H_2O_2 concentrations.

Differences between the unfused or the inactive negative control roGFP2-ScGrx7^{C108S} and the active roGFP2-ScGrx7 can be clearly seen in triple deletion yeast cells (**Figure 7C**). However, many subsequent mutations in ScGrx7 led to slightly elevated or reduced activity, which was difficult to decipher directly from the corresponding roGFP2 response curves. Therefore, the integrated area under the OxD-curve was calculated after baseline subtraction (0 µM H₂O₂ treatment) as shown previously (Staudacher *et al.*, 2018), allowing a semi-quantitative readout of the roGFP2 oxidation kinetics (see publication 2.1., Figure 7b). Initial refinements of the approach involved increasing the temporal resolution in order to observe even slight differences in roGFP2 oxidation kinetics between constructs. Thus, the fluorescence plate reader was adjusted to minimize the time for scanning each well. Using a multichannel pipette allowed for the simultaneous treatment of up to twelve wells. Future improvements of this method might include measurements in 96- or even 384-well plates with automated application of H₂O₂ or other substrates.

Equilibration of roGFP2 with the 2GSH/GSSG redox couple requires its efficient and reversible oxidation and reduction. The glutaredoxin moiety in the roGFP2-ScGrx7 fusion mediates this equilibration in the absence of endogenous dithiol glutaredoxins in $\Delta grl1\Delta grx1\Delta grx2$ deletion cells. Consequently, monothiol ScGrx7 can use roGFP2 as a disulfide substrate. This is particularly interesting as it is often postulated that protein disulfide reduction, according to the traditional model for glutaredoxin catalysis, requires a dithiol mechanism (**Figure 1A**). Examples are reported for *E. coli* ribonucleotide reductase, PAPS reductase and human PRDX3 (Bushweller *et al.*, 1992; Lillig *et al.*, 1999; Hanschmann *et al.*, 2010). Reduction of disulfides by monothiol ScGrx7 and engineered monothiol ScGrx2^{C64S} have been investigated in a detailed follow-up study and will be discussed in following sections (see publication 2.3.).

Interestingly, in absence of suitable glutaredoxins facilitating the equilibration, steady-states are comparably high. What mediates high steady-state oxidation in $\Delta grl1\Delta grx1\Delta grx2$ deletion cells expressing unfused roGFP2 or inactive roGFP2-ScGrx7^{C108S}? In this case, roGFP2 is most likely directly oxidized by GSSG. However, other proteins might also mediate slow roGFP2 oxidation e.g., peroxiredoxins. Experimental evidence was collected by expressing a fusion between roGFP2 and the peroxiredoxin ScTsa2ΔC_R in $\Delta grx1\Delta grx2$ deletion cells. Under these conditions, roGFP2 was fully oxidized at steady-state (Morgan *et al.*, 2016). After peroxiredoxin-mediated roGFP2 oxidation, endogenous dithiol glutaredoxins were necessary for roGFP2 reduction. In 2004, Østergaard and colleagues used a pulse-chase experimental setup with radioactively labeled ³⁵S in order to demonstrate that cytosolic rxYFP is oxidized, albeit slowly but continuously in a $\Delta grl1\Delta grx1\Delta grx2$ yeast deletion (Østergaard *et al.*, 2004).

De novo synthesis of reduced proteins after the washout of ^{35}S is not a factor in the pulse-chase experiment as they are not radioactively labeled. However, *de novo* synthesis of reduced proteins as well as cellular degradation of oxidized roGFP2 might affect the steady-state oxidation in fluorescence measurements. This, in combination with slow, direct oxidation of roGFP2, might explain the elevated sensor oxidation. To further investigate this possibility in future experiments, roGFP2 could be expressed under the control of an inducible promoter. Following the washout of the inductor, direct roGFP2 oxidation could be followed over time using a fluorescence plate reader to exclude *de novo* synthesis of reduced sensor proteins.

In summary, the cytosol of yeast cells was used as a *test-tube* to develop an in-cell screening system. In this model, (i.) $\Delta\text{grl1}\Delta\text{grx1}\Delta\text{grx2}$ yeast cells allowed for perturbation of the glutathione pool and specificity of roGFP2 oxidation. (ii.) The exogenous application of H_2O_2 induced changes in endogenous GSSG levels, (iii.) while high temporal resolution enabled monitoring of roGFP2 equilibration to the changes in endogenous GSSG levels i.e., the oxidation kinetics. (iv.) 96-well plate-based measurements enabled the simultaneous screening of multiple constructs and conditions.

3.2. Establishment of a roGFP2-based screen to monitor ScGrx7 structure-function relationships

Active class I glutaredoxins harbor a glutathione-scaffold site and a glutathione-activator site for the reaction with either the glutathionylated substrate or GSH as the reductant (**Figure 2**). To further identify and characterize contributing residues to both sites, the activity of selected point mutants within conserved protein regions were analyzed using the roGFP2-based approach (see publication 2.1., Figure 1b,d and 7c-f). For validation and establishment of the novel fluorescence-based screen, the same mutants were also analyzed *in vitro*. This allowed for direct comparison between the results obtained from both approaches. In other words, do relative differences in the roGFP2 oxidation kinetics between certain constructs correlate with the corresponding *in vitro* data?

Generally, results obtained *in vivo*, using the roGFP2 fluorescence readout, correlated well with the corresponding *in vitro* kinetics for the oxidative half-reaction using GSSCys as a glutathionylated substrate (Begas *et al.*, 2017; publication 2.1., Figure 2,4,5). Oxidation of roGFP2 by the fused ScGrx7 in the yeast-based assay requires both half-reactions. First the glutaredoxin thiolate attacks GSSG resulting in glutathionylated ScGrx7 (oxidative half-reaction), which then glutathionylates roGFP2 (reductive half-reaction). Subsequently, roGFP2 forms an intramolecular disulfide bond changing its spectral properties (**Figure 4**).

Which of these half-reactions is rate-limiting and thus determines the kinetics of roGFP2 oxidation? The constructs roGFP2-ScGrx7^{R153A} (point mutation in the basic loop following Helix 3) and roGFP2-ScGrx7^{E170A} (point mutation within Helix 4) served as controls for the glutathione-scaffold site (see publication 2.1., Figure 7f). *In vitro*, both mutations affected the oxidative but not the reductive half-reaction (Begas *et al.*, 2017 and publication 2.1., Figure 5). Accordingly, slower oxidation kinetics for roGFP2-ScGrx7^{R153A} and roGFP2-ScGrx7^{E170A} *in vivo* indicated rate-limitation of the oxidative half-reaction. In other words, glutathionylation of the ScGrx7 moiety by GSSG dictated the kinetics of roGFP2 oxidation, rather than glutathionylation and subsequent disulfide bond formation on roGFP2.

This is particularly interesting, as the opposite was postulated for analyses of fusions between roGFP2 and *PfAOP* or mutants thereof (Staudacher *et al.*, 2018). In this study, the pattern of roGFP2 oxidation kinetics correlated with the rate-limiting reductive half-reaction of *PfAOP* with GSH *in vitro*. Given the high reactivity of thiol peroxidases towards peroxides, an extremely efficient oxidative half-reaction could explain the rate-limiting reduction of *PfAOP* by roGFP2. However, a rate-limiting reduction by roGFP2 would not necessarily result in differences in the roGFP2 oxidation kinetics, as long as the mutations do not directly affect the interaction with roGFP2 as a substrate. The selected mutants in this study were postulated to cause local unfolding of the active site. This could promote GSH-dependent reduction *in vitro*. It is also possible that this would make the sulfenic acid in oxidized *PfAOP* more accessible to a nucleophilic attack performed by roGFP2.

In the roGFP2-based screen, charge inversion mutation in ScGrx7^{K105E} had the strongest effect leading to almost full inactivation (see publication 2.1., Figure 7c). The conserved, positively charged lysine residue and the -CPYS- active site in ScGrx7 are separated by a short threonine-glycine- (TG-) loop. In other active class I glutaredoxins, these motifs are separated by similar two amino acid loops. Hence, a role of Lys105 in stabilization of the thiolate anion seems evident according to calculations performed on human GRX1 or experiments on the corresponding lysine in NrdH-redoxin from *Corynebacterium glutamicum* (Jao *et al.*, 2006; Van Laer *et al.*, 2014). Interestingly, the thiol pK_a in ScGrx7^{K105E} changes only moderately, implying other important functions e.g., stabilization of the glutathionylated enzyme. Replacement with uncharged alanine in ScGrx7^{K105A} or tyrosine in ScGrx7^{K105Y} affected both half-reactions *in vitro*. This further suggests that Lys105 plays a role in the reaction of the glutathionylated enzyme with GSH (Begas *et al.*, 2015). Relevance of the conserved, positively charged lysine residue to the glutathione activator site was also shown for *Trypanosoma brucei* Grx1. In *TbGrx1*, a tryptophan residue replaces the lysine nearby the active site. In accordance with the model for the glutathione activator site, *TbGrx1* was not reduced by GSH (Manta *et al.*, 2019).

The active site tyrosine mutant $\text{ScGrx7}^{\text{Y}110\text{F}}$ indicated that the hydroxyl group is dispensable for the glutathione-dependent catalysis. Intriguingly, even a slight gain-of-function was reported for this mutant. However, exchanging the aromatic side chain with either the imidazole ring in the corresponding histidine mutant ($\text{ScGrx7}^{\text{Y}110\text{H}}$) or replacement of the bulky side chain by alanine ($\text{ScGrx7}^{\text{Y}110\text{A}}$) led to an incremental decrease of activity. The side chain might play an important structural role by keeping the glutathionyl moiety of the glutathionylated enzyme in the correct orientation. Again, data obtained *in vivo*, using the roGFP2-based assay, correlated well with the corresponding *in vitro* data for the oxidative half-reaction (see publication 2.1., Figure 2 and 7d).

Liedgens et al., 2020

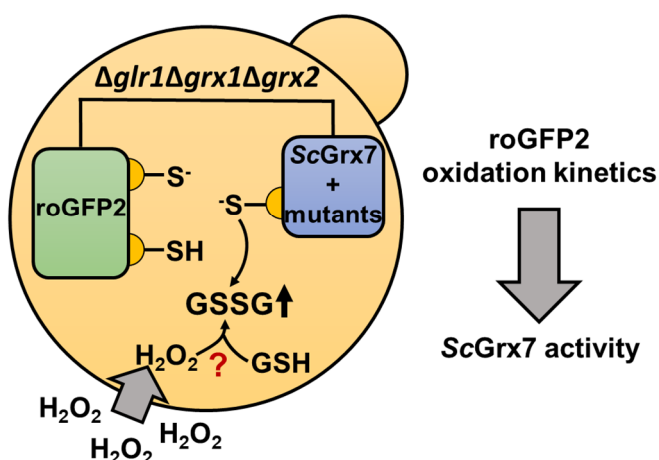


Figure 8. Schematic summary of the contributing publication 2.1. Assessment of the oxidoreductase activity of ScGrx7 and mutants thereof using genetic fusions to roGFP2. Application of H_2O_2 leads to GSSG production. Glutaredoxin-mediated roGFP2 oxidation upon GSSG accumulation directly correlates with the activity of the protein in question. Relative differences in roGFP2 oxidation kinetics between several mutants further correlated with the corresponding *in vitro* data. (Zimmermann, Morgan, unpublished)

In summary, comparing the results obtained *in vivo* with the corresponding *in vitro* data demonstrated: (i.) Suitability of the roGFP2 oxidation kinetics as a measure of glutaredoxin activity. (ii.) Faithful replication of ScGrx7 structure-function relationships *in vivo* and (iii.) rapid screening of multiple mutants without the need of initial protein purification (Figure 8). With this proof-of-principle in place, the system was applied to extend this study. Having identified and characterized important protein areas, accounting for the oxidoreductase activity in ScGrx7, is it now possible to interconvert active class I and inactive class II glutaredoxins?

3.3. Interconversion analyses of redox-active and -inactive glutaredoxins

In order to further validate the contribution of certain areas to the oxidoreductase activity in active class I glutaredoxins, interconversion analyses were performed. Interestingly, ScGrx7 and inactive class II glutaredoxins harbor the same -CxxS- active site arrangement. If a single cysteine residue in the active site can account for the oxidoreductase activity in ScGrx7, which other motifs determine presence or absence of activity in different glutaredoxins? Conserved motifs and residues from ScGrx7 were introduced individually or in combination to inactive class II human GRX5 (*HsGrx5*) for conversion into an active glutaredoxin and *vice versa*.

Striking structural features in redox-inactive *HsGrx5* are (i.) the elongated GTPEQPQ-loop that separates the conserved lysine residue from the active site and (ii.) a conserved tryptophan-proline (WP) motif in the loop following Helix 3 (see publication 2.1., Figure 1d). Interestingly, roGFP2-ScGrx7^{loop} (where the short TG-loop is replaced by the GTPEQPQ-loop), roGFP2-ScGrx7^{WP} (where two arginine residues are replaced by the WP-motif) and a combination of both in roGFP2-ScGrx7^{loop+WP} showed almost full sensor oxidation at steady-state (**Figure 9B**). Consequently, they were robust against further oxidation upon the addition of H₂O₂. Therefore, it was not possible to conclude inactivation of ScGrx7 as a result of the mutations using the standard approach.

What is the reason for this high steady-state oxidation? The answer to this question is not yet completely clear. Usually, when reporting the glutathione redox potential (E_{GSH}), roGFP2 is fused to human or yeast Grx1. The reason for this is, that Grx1 can efficiently equilibrate roGFP2 with the 2GSH/GSSG redox couple. As previously stated, equilibration requires both, reversible oxidation and reduction of the roGFP2 moiety by Grx1. When fusing roGFP2 to different glutaredoxin mutants with altered enzymatic properties e.g., either impaired or accelerated oxidative or reductive half-reactions, equilibration might be affected. In other words, a glutaredoxin mutant might still be able to glutathionylate roGFP2, but loses the ability to use oxidized roGFP2 as a substrate. Similarly, *Arabidopsis thaliana* GrxS15 was demonstrated to oxidize roGFP2 with GSSG but could not reduce it with GSH *in vitro* (Begas *et al.*, 2015; Moseler *et al.*, 2015). This is not a problem *per se*, as the screen is not intended to monitor E_{GSH} . In this case however, most roGFP2 molecules would be oxidized at steady-state. This would limit any further roGFP2 oxidation upon treatment with H₂O₂ and therefore prevent the essential monitoring of the oxidation kinetics. To overcome the problem of high steady-state oxidation and test the activity of aforementioned mutants, a sensitizing dithiothreitol (DTT) assay was developed (**Figure 9A**). DTT is a strong disulfide reductant. Yeast cells were shortly incubated with DTT to reduce all roGFP2 molecules. The chemical reduction of roGFP2 before the addition of H₂O₂ decreases the steady-state oxidation.

This in turn increases the dynamic range and allows for monitoring of oxidation kinetics upon the treatment with H₂O₂.

Using this approach, roGFP2-ScGrx7^{loop}, roGFP2-ScGrx7^{WP} and roGFP2-ScGrx7^{loop+WP} were around 10-20% oxidized at steady-state and remained unresponsive towards the addition of H₂O₂. In contrast, the roGFP2-ScGrx7 positive control responded similarly to previous measurements without DTT pre-treatment. With the exception of the roGFP2-ScGrx7^{WP} construct, this inactivation was in agreement with the corresponding *in vitro* data. *In vitro*, ScGrx7^{WP} displayed only a decelerated oxidative half-reaction while the reductive half-reaction was largely unaffected. This suggests that interaction with GSH is not impaired. A lack of activity *in vivo* could be attributed to the bulky WP-motif blocking the interaction with roGFP2. Thus, insertion of the long GTPEQPQ-loop alone, or in combination with the conserved WP-motif, led to a loss of oxidoreductase activity in ScGrx7 *in vitro* and *in vivo* (see publication 2.1., Figure 6 and 7g).

Vice versa, the corresponding mutations were also introduced to the Fe-S cluster binding protein, HsGrx5, and redox activity of the roGFP2 fusion was tested *in vivo*. However, roGFP2-HsGrx5^{loop} (where the elongated GTPEQPQ-loop is replaced by short TG-loop), roGFP2-HsGrx5^{RR} (where the WP-motif is replaced by two arginine residues) and roGFP2-HsGrx5^{loop+RR} were all barely active, suggesting that these motifs alone are not sufficient to convert HsGrx5 into an oxidoreductase (see publication 2.1., Figure 7h).

More than 15 combinations of specific point mutations in roGFP2-HsGrx5^{loop} and roGFP2-HsGrx5^{loop+RR} were created by site-directed mutagenesis. Subsequently, these constructs were rapidly characterized *in vivo* using the roGFP2-based screen in combination with the DTT pre-treatment protocol. With the system established and previous comparisons to corresponding *in vitro* data, the fluorescence-based system was solely used for the characterization of additional mutants. Gain of oxidoreductase activity was detected for the roGFP2-HsGrx5^{loop} construct with an additional mutation within the active site, where the conserved glycine (-CGFS-) was mutated to proline (-CPFS-). The gain-of-function of the glycine-to-proline mutation could be explained by proline preventing Fe-S cluster coordination due to reduced flexibility of the protein backbone (Johansson *et al.*, 2007). An additional mutation of the Helix 3 arginine residue to the conserved glutamine further increased the roGFP2 oxidation kinetics. The resulting HsGrx5^{loop+G68P+R97Q} (hereinafter referred to as HsGrx5^{Active}) was almost as active as ScGrx7 at high H₂O₂ concentrations (**Figure 9C**; see publication 2.1., Figure 7i).

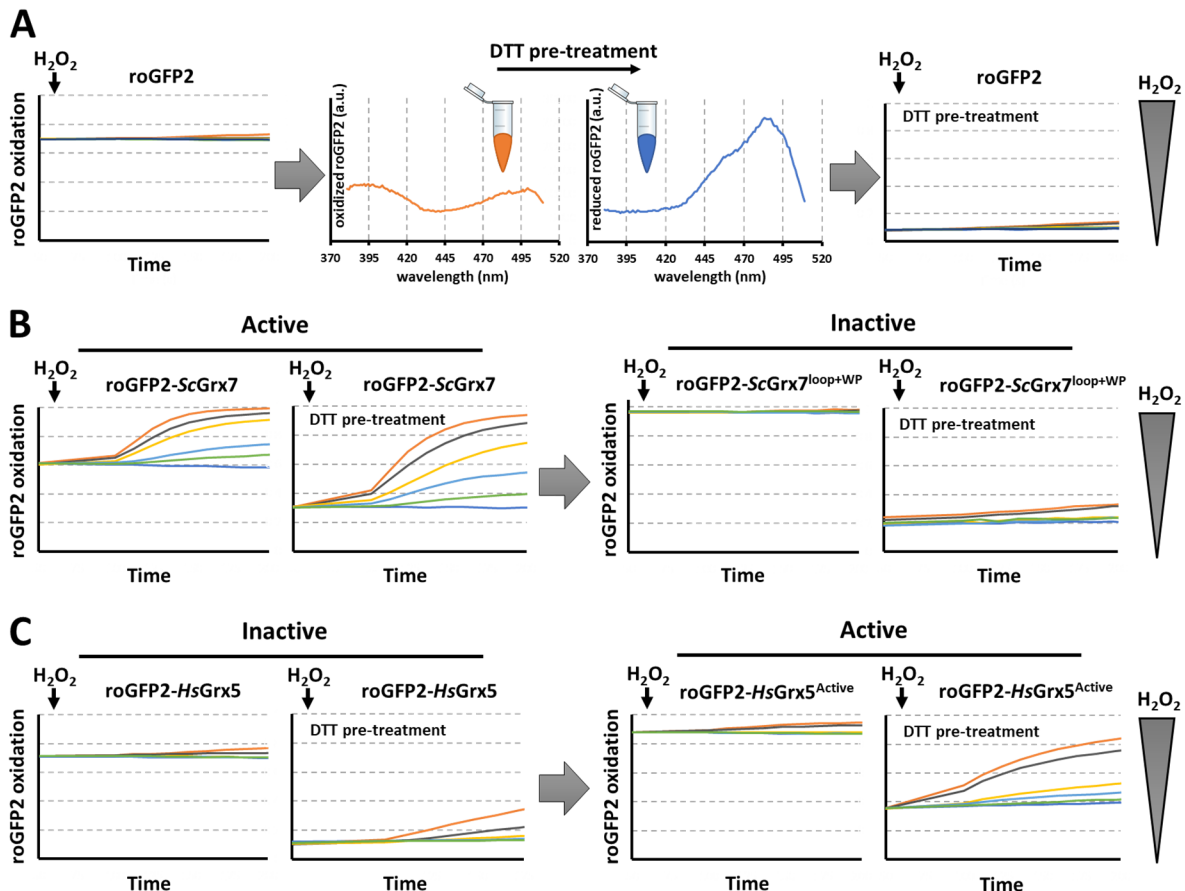


Figure 9. DTT pre-treatment allows for monitoring of the roGFP2 oxidation kinetics when steady-state oxidation is high. (A) Response of unfused roGFP2 before and after the DTT pre-treatment. DTT reduces the roGFP2 steady-state oxidation as indicated by the excitation spectra. High steady-states in **(B)** roGFP2-ScGrx7^{loop+WP} and **(C)** roGFP2-HsGrx5^{Active} prevent further oxidation after H₂O₂ treatment. Using the DTT assay, loss-of-function in ScGrx7^{loop+WP} and gain-of-function in HsGrx5^{Active} was monitored. Responses of roGFP2-ScGrx7 and roGFP2-HsGrx5 serve as positive and negative controls, respectively. (see publication 2.1., Figure 7, Supplementary Figure 17).

These results are in agreement with another interconversion study, published shortly after, by Trnka and colleagues. They used purified roGFP2 *in vitro* and Zebrafish embryos as an *in vivo* model. Accordingly, their *HsGrx5^{loop}* mutant (inserting the short class I-loop from *HsGrx2* adjacent to the active site) showed significant gain-of-function for the oxidation and reduction of roGFP2 *in vitro*. For *in vivo* analyses of the engineered mutants, the mitochondrial class II Grx5 from Zebrafish was knocked down. This significantly decreased viability of the zebrafish embryos. They complemented the loss by the expression of different recombinant proteins and mutants. While *HsGrx5* rescued the survival rate, the activated *HsGrx5^{loop}* mutant was unable to complement for the *knockdown* of endogenous Grx5. This indicates uncoupling from its former role in Fe-S cluster biogenesis and trafficking. Opposingly, *HsGrx2^{loop}* (with the elongated class II-loop), which lost almost all its oxidoreductase activity in the roGFP2 assay, restored the viability of the embryos to the same extent as *HsGrx5* (Trnka *et al.*, 2020). Based on these results it was postulated that the loop-motif adjacent to the active site switches the function of glutaredoxins from oxidoreductases to Fe-S transferases or *vice versa*. Consequently, the loop-motif acts as an on/off switch for oxidoreductase activity.

In publication 2.1., replacement of the elongated GTPEQPQ-loop by the short TG-loop proved necessary for the conversion of *HsGrx5* into a redox active glutaredoxin (see publication 2.1., Figure 7h,i). However, oxidation kinetics in *HsGrx5^{loop}* were only slightly increased. Multiple protein areas together were shown to contribute to the oxidoreductase activity. These findings were further investigated in an unpublished follow-up study. Amongst other thioredoxin superfamily enzymes, active class I *HsGrx1* and mutants thereof were also tested as fusion constructs with roGFP2. Interestingly, the oxidation kinetics of roGFP2 in the *HsGrx1^{loop}* mutant were slower compared to the wild-type enzyme, albeit not absent. It would be interesting to investigate whether other mutations in combination could fully inactivate *HsGrx1^{loop}*. Altogether, these studies show that the loop is a determinant structural difference for both classes but does not alone account for the interconversion of class I and class II glutaredoxins.

Surprisingly, *ScGrx7* and *HsGrx5^{Active}* did not just respond to the H₂O₂ treatment in a concentration dependent manner, but also showed elevated steady-state oxidation despite the DTT pre-treatment when compared to the inactive negative controls (**Figure 9B,C**). This can probably be attributed to active glutaredoxins oxidizing roGFP2 during the washing and subsequent centrifugation steps. This is an interesting observation and counterintuitive, as the addition of a strong reductant shows oxidation of roGFP2 shortly after it has been washed out. Most likely, residual cytosolic GSSG is rapidly sensed by the roGFP2-Grx fusion. This also depends upon the activity of the glutaredoxin moiety and explains the lower roGFP2 steady-state when fused to less active glutaredoxin mutants. A possible alternative explanation could be the activity of yeast endoplasmic reticulum oxidoreductin 1 (*ScEro1*). *ScEro1* is an important enzyme involved in oxidative protein folding in the ER. It re-oxidizes the protein disulfide isomerase 1 (*ScPdi1*), which facilitates the oxidation of client proteins during oxidative protein folding (Frands *et al.*, 1999). Usually, *ScPdi1* donates electrons to *ScEro1*. *ScEro1* harbors several regulatory cysteines, which are important for sensing the redox state of *ScPdi1* (Tavender *et al.*, 2010). In its active, reduced form, *ScEro1* shuffles electrons to molecular oxygen using FAD as a cofactor, generating H₂O₂ (Zito, 2015). In the presence of DTT, regulatory cysteine residues of *ScEro1* remain reduced allowing a continuous transfer of electrons leading to accumulation of H₂O₂. Peroxide formation by *ScEro1* can indeed be increased as a result of a DTT treatment (Gross *et al.*, 2006; Tavender *et al.*, 2010). H₂O₂ might then diffuse into the cytosol where it leads to generation of GSSG as described previously. This could explain why roGFP2 fused to active or activated glutaredoxins (*ScGrx7* or *HsGrx5^{Active}*) display a higher steady-state oxidation and consequently respond sensitively to changes in GSSG compared to inactive glutaredoxins or unfused roGFP2. Considering both possibilities, not only probe responses to exogenously added H₂O₂, but also the steady-state oxidation after DTT pre-treatment indicate the conversion of *HsGrx5* into an active glutaredoxin, which could potentially serve as a further measure for oxidoreductase activity.

The developed system might enable new possibilities in characterization of other thioredoxin superfamily proteins. (i.) With the gained knowledge about the structural determinant differences between redox-active and -inactive glutaredoxins, it is possible to examine other proteins that might use glutathione as a substrate. For instance, glutathione is present in the ER, but its role in certain processes, such as oxidative protein folding, remains largely elusive. Therefore, it would be interesting to see if ER proteins e.g., protein disulfide isomerase are able to interact with glutathione as indicated previously (Molteni *et al.*, 2004; Delaunay-Moisan *et al.*, 2017). Genetic fusions between roGFP2 and ScPdi1 or HsPDI1 have already been generated, and demonstrated glutathione-dependent oxidoreductase activity of these proteins. Protein disulfide isomerasers are particularly interesting because they harbor multiple thioredoxin fold domains. Again, site-directed mutagenesis and subsequent rapid screening in the cytosol of yeast cells could be used to dissect the structural motifs, enabling them the interaction with either the glutathionylated substrate or reduced glutathione. (ii.) Furthermore, such an approach might enable the characterization of proteins in a cellular, yeast-based ‘test-tube’ that could not yet be analyzed *in vitro*. An example being land plant-specific class III glutaredoxins, also known as CC-type or ROXY glutaredoxins (Couturier *et al.*, 2009; Patterson *et al.*, 2016). Genetic analyses point towards functions in development and pathogen defense (Meyer *et al.*, 2012). Comprehensive biochemical characterization however, are still missing due to difficulties in purifying recombinant proteins (Couturier *et al.*, 2010; Couturier *et al.*, 2013). Expressing roGFP2 fusions in yeast seemed possible from preliminary experiments. However, neither the wild-type protein nor putative gain-of-function mutants were active in the fluorescence-based assay (data not shown). (iii.) An activity screening assay within living cells could also enable analyses of post-translational modifications (PTM). Insights were already gained in *PfOAP* regarding its accessibility to hyperoxidation (Staudacher *et al.*, 2018). Monitoring H₂O₂-dependent inactivation was only possible *in vivo* using fusions to roGFP2. PTMs in the context of thiol peroxidase hyperoxidation were also investigated in yeast mitochondria (Calabrese *et al.*, 2019) as well as in continuous, synchronized fermenter cultures (see publication 2.4.) using roGFP2-based sensors. Analyses of PTMs in general is challenging *in vitro* with recombinant proteins. Therefore, future studies in yeast might also involve effects on the protein activity upon other PTMs e.g., phosphorylation of non-catalytic residues in peroxidases (Woo *et al.*, 2010; Lim *et al.*, 2015; Rawat *et al.*, 2013).

In summary, combination of site-directed mutagenesis and rapid roGFP2-based screening for activity, provides new possibilities for analyses of structure-function relationships and catalytic mechanisms in thioredoxin superfamily proteins. This novel approach enables rapid screening of multiple conditions, different proteins and mutants using genetically engineered yeast cells. Certain proteins or mutants can then further be subjected for quantitative follow-up

characterization *in vitro*. In future experiments this approach will certainly be expanded to more members of the thioredoxin superfamily.

3.4. *ScOPT1* overexpression allows for direct application of GSSG

Following the development and application of the novel roGFP2-based approach, remaining questions were addressed in follow-up studies. Application of H₂O₂ as an indirect substrate harbors two major limitations. (i.) The requirement of application of high H₂O₂ concentrations to induce sufficient formation of GSSG and (ii.) the unknown mechanism in which GSSG is directly or indirectly formed (**Figure 8,10A**). Especially, given the possibility that the glutaredoxin in the genetic fusion to roGFP2 might participate in GSSG production in the absence of endogenous cytosolic ScGrx1 and ScGrx2. Applying a natural glutaredoxin substrate would thus significantly improve the approach and would further rule out contribution of any unknowns about GSSG formation upon the H₂O₂ treatment in the assay.

Unlike H₂O₂, GSSG cannot freely cross the plasma membrane. Its transport into yeast cells is facilitated by the proton-coupled glutathione symporter ScOpt1/ScHgt1 (Bourbouloux *et al.*, 2000; Osawa *et al.*, 2006). Despite of its endogenous expression, application of exogenous GSSG instead of H₂O₂ did not result in glutaredoxin-mediated roGFP2 oxidation. This indicates, that ScOpt1 expression levels did not allow for sufficient GSSG transport into the cell (see publication 2.2., Figure 1a,b). Overexpression of this transporter however, was shown to permit rapid import of GSH and GSSG (Kumar *et al.*, 2011; Ponsero *et al.*, 2017). This raised the question if overexpression of *ScOPT1* in $\Delta grl1\Delta grx1\Delta grx2$ yeast cells would allow for monitoring the oxidoreductase activity of glutaredoxins with their natural substrate, GSSG. Thus, yeast cells were co-transformed with two plasmids, the first encoding ScOpt1 and the second plasmid encoding a genetic fusion between roGFP2 and ScGrx1. Indeed, roGFP2 responded readily to exogenous GSSG in an ScOpt1- and glutaredoxin-dependent manner (**Figure 10B**; see publication 2.2., Figure 1f). The results were further supported by elevated glutathione levels measured in whole cell lysates after GSSG treatment (see publication 2.2., Figure 1c,d).

To prove the suitability of the new assay for monitoring glutaredoxin structure-function relationships, a series of previously characterized mutants of *ScGrx7* and *HsGrx5* were tested (see publication 2.1 Figure 7 and publication 2.2 Figure 2, 3, 4). The results clearly show that roGFP2 oxidation kinetics depend on the activity of the fused glutaredoxin moiety. This assay is also compatible with the sensitizing DTT pre-treatment. It was possible to corroborate previous results using this assay. *HsGrx5*^{Active}, the class II glutaredoxin mutant which exhibits

oxidoreductase activity, already responded to concentrations of GSSG, which were ten times lower than those of H₂O₂ in the standard assay (see publication 2.2., Figure 3). Again, this demonstrated the necessity of high H₂O₂ concentrations to induce sufficient glutathione oxidation in the standard assay. Moreover, GSSG treatment enabled a better concentration-dependent resolution i.e., a more linear response-pattern. Differences between roGFP2-HsGrx5 and roGFP2-HsGrx5^{Active} could only be seen when using high concentrations of H₂O₂ between 100 µM and 1000 µM (publication 2.2., Figure 3e,f). Statistical significance in the optimized assay was shown for GSSG concentrations as low as 6 µM. As mentioned previously, there is a possibility that the glutaredoxin in the fusion contributes to GSSG production e.g., by reducing thiol peroxidases after the H₂O₂ treatment. It is possible that HsGrx5^{Active} is unable to, or competes less efficiently for the reduction of peroxidases. This means, that less GSSG might be generated, especially towards less excessive peroxide amounts i.e., mid-to-low range H₂O₂ concentrations. This could explain the relatively quick drop of roGFP2 oxidation kinetics between 500 µM and 200 µM H₂O₂ (**Figure 9C**, compare the grey and yellow lines in the right panel, see also publication 2.1., Figure 7i). In contrast, there is a more linear decrease when applying GSSG directly, and not relying on H₂O₂-dependent GSSG formation (see publication 2.2., Figure 3d,f).

An assay that enables import and sensing of GSSG, would presumably allow for testing other glutathione derivatives *in vivo* accordingly (**Figure 10B**). GSNO showed similar ScOpt1- and glutaredoxin-dependent roGFP2 oxidation kinetics in comparison to GSSG. Intriguingly, responses to both substrates were almost indistinguishable. This suggests either an indirect roGFP2 oxidation by rapid conversion of GSNO into GSSG, or that glutaredoxins are capable of reacting comparably well with either substrate. Regarding the first possibility, previous studies have suggested that the formaldehyde dehydrogenase ScSfa1 can also function as a reductase for GSNO (Liu *et al.*, 2001). In order to test the effect of a putative rapid conversion into GSSG, the quadruple deletion strain $\Delta\text{gfr1}\Delta\text{grx1}\Delta\text{grx2}\Delta\text{sfa1}$ was generated. However, responses of roGFP2-ScGrx1 to GSNO were not affected by the additional gene deletion, suggesting that GSNO might directly react with the glutaredoxin (see publication 2.2., Figure 5c,d). To further analyze this reaction, *in vitro* stopped-flow kinetic measurements were performed. Interestingly, GSNO-mediated oxidation was not solely depending on glutaredoxins. In accordance with previous observations, GSNO could directly oxidize roGFP2 (Müller *et al.*, 2017). This was not observed *in vivo* and the reason for this remains unclear (see publication 2.2., Figure 5a). *In vitro*, GSNO-mediated oxidation of roGFP2 could be accelerated by addition of either monothiol or dithiol glutaredoxins (see publication 2.2., Figure 6b,c). The use of genetic fusion constructs *in vivo* but not *in vitro* might partially explain the strict glutaredoxin-dependency. Together with the *in vitro* data, results point towards a direct reaction between GSNO and the glutaredoxin.

This raises the question for the mechanism of GSNO-dependent oxidation of the glutaredoxin moiety. Either, the glutaredoxin thiolate nucleophilically attacks the nitrogen atom in GSNO, and therefore functions as an S-transnitrosylase, or the sulfur atom is the target. In the latter case, the reactions leading to roGFP2 oxidation would be identical for both, GSNO and GSSG (**Figure 4**). This could explain the similarity in roGFP2 oxidation kinetics with both substrates. Such a mechanism was postulated for poplar GrxS12, where GSNO addition led to S-glutathionylation (Zaffagnini *et al.*, 2012). Future studies might untangle the exact mechanism of the glutaredoxin-dependent reaction of GSNO with roGFP2 *in vivo*.

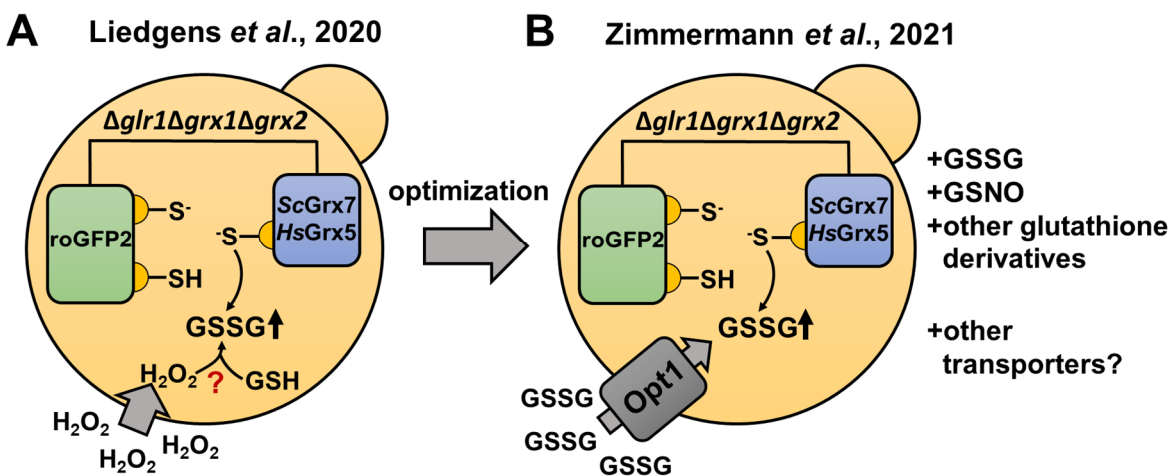


Figure 10. Schematic summary of the contributing publications 2.1. and 2.2. (A) Fluorescence-based approaches were developed and applied to monitor structure-function relationships of active class I and inactive class II glutaredoxins. (B) To avoid indirect GSSG formation upon H_2O_2 application, the system presented in (A) was refined by overexpression of *ScOPT1*. *ScOPT1* facilitates the import of the natural glutaredoxin substrate, GSSG, and other glutathione derivatives. The approach could be expanded to the expression of other transporters for the import of alternative metabolites or substrates. (Zimmermann, Morgan, unpublished)

The presented approaches can be applied to investigate other thioredoxin superfamily proteins in future studies. Interestingly, the human thioredoxin-related protein of 14 kDa (*HsTRP14*) is an efficient S-denitrosylase (Pader *et al.*, 2014; Espinosa, Arnér, 2019). This thioredoxin superfamily protein was also tested in a fusion to roGFP2 in a thus far unpublished study. *HsTRP14* could not oxidize roGFP2 after the exogenous H_2O_2 treatment and subsequent GSSG formation. Although it remains to be tested with direct titration of GSSG, the preliminary results strongly suggest that *HsTRP14* does not, or at least inefficiently, interact with GSSG as a substrate. However, at this experimental stage, impaired interaction with roGFP2 cannot be excluded. Nonetheless, it would still be interesting to see if the application of GSNO, using the *ScOPT1* overexpression assay, could lead to S-nitrosylation of *HsTRP14*. The subsequent transfer of the NO group to roGFP2 could then result in disulfide bond formation under release of nitroxyl (HNO). Such an experiment would provide an example that allows for testing certain

proteins with respect to their specific substrate preference, which might differ from that of glutathione-dependent enzymes.

Having a transporter that facilitates the import of sufficient amounts of GSSG or GSNO as alternative substrates, might also allow for the application of other glutathione derivatives. This would enable testing for the reaction with alternative substrates. Such an assay might also permit the characterization of enzymes with unknown substrates. In this case, the import of a certain substrate into the cytosol would depend upon the capability of ScOpt1 to facilitate the transfer of this molecule. However, overexpression of other transporters could also be attempted. A putative candidate would be the cystine-specific transporter from *Candida glabrata* CYN1 (Yadav, Bachhawat, 2011). Again, this would relate to *HsTRP14*, which has shown the ability to also efficiently reduce *L*-cystine *in vitro*, even via a monothiol mechanism in an engineered cysteine mutant (Pader et al., 2014). Interestingly, engineered monothiol thioredoxins are usually inactive (see publication 2.3.), pointing towards specified functions of *HsTRP14*. Given that cysteinylated *HsTRP14* is accessible to the nucleophilic attack by the roGFP2 thiolate, this reaction could presumably be monitored using the fluorescence-based assay.

A similar approach would also be particularly interesting for the characterization of the third, cytosolic glutaredoxin in yeast i.e., ScGrx8. ScGrx8 was barely active with HEDS *in vitro* (Eckers et al., 2009; Tang et al., 2014). In a fusion to roGFP2, it was unresponsive to H₂O₂ and subsequent GSSG formation, even after decreasing the steady-state oxidation using the sensitizing DTT-assay (data not shown). Interestingly, ScGrx8 and *HsTRP14* share an unusual -SWCPDC- motif. Therefore, they might also have similar substrates, which could explain the absence of significant oxidoreductase activity with GSSG *in vivo* and HEDS *in vitro*. Application of GSNO using the ScOpt1 overexpression assay, or an expression of the cystine transporter CgCYN1 might permit alternative assays to investigate the elusive function of ScGrx8 *in vivo*.

Altogether, it has been shown that the new assay can be used as an optimized screen for monitoring activity of oxidoreductases. Preliminary, unpublished data show suitability of the approach for structure-function analyses of other thioredoxin superfamily proteins. Providing a fine-tuned environment that allows for perturbations in GSSG and specific probe responses, activity and structure-function analyses can be assessed semi-quantitatively *in vivo* (see publication 2.1.). In order to optimize this assay and developing a more '*in vitro*-like' experimental setup, the plasma membrane glutathione transporter, ScOPT1, was overexpressed. The transporter facilitated the import of the natural glutaredoxin substrate i.e., GSSG and other glutathione derivatives such as GSNO (**Figure 10**; see publication 2.2.). Furthermore, the dynamic range of probe responses can be increased with a brief DTT

pre-treatment. Using the disulfide reductant DTT decreased the roGFP2 steady-state oxidation. Although this assay was not necessary for all measurements, it provided invaluable data for characterization of mutants that could oxidize but not, or at least inefficiently, reduce roGFP2 (see publication 2.1. and publication 2.2.).

3.5. Monitoring oxidoreductase-mediated reduction of endogenous proteins

Monothiol ScGrx7 was previously shown to be able to equilibrate roGFP2 with the glutathione redox couple. Equilibration requires reversible glutathionylation of roGFP2 and reduction of its disulfide bond. This was particularly interesting, because according to the traditional model of the glutathione-dependent glutaredoxin catalysis, it has often been claimed that reduction of disulfide substrates requires a dithiol mechanism (**Figure 1A**). However, there are already known exceptions e.g., reduction of the mammalian ribonucleotide reductase or oxidation of rxYFP by an engineered monothiol ScGrx1 (Zahedi Avval, Holgrem, 2009; Björnberg *et al.*, 2006). *In vitro*, quantitative assessment of the glutaredoxin-mediated reduction often involves oxidized model proteins e.g., ribonucleotide reductase or 3'-phosphoadenylylsulfate (PAPS) reductase (Bushweller *et al.*, 1992; Deponte, 2013). Therefore, it would be interesting to develop a yeast-based assay that allows to assess if monothiol glutaredoxins can in fact mediate the reduction of these disulfide substrates *in vivo*.

Interestingly, yeast cells lacking both cytosolic thioredoxins (ScTrx1, ScTrx2) and the two active class I dithiol glutaredoxins (ScGrx1, ScGrx2) are inviable. The reason for this is an inability to perform the essential reduction of disulfides in certain proteins including ribonucleotide reductase or PAPS reductase in absence of methionine in the growth medium (see publication 2.3. Figure 1a). However, a single thioredoxin or glutaredoxin is enough to maintain viability, making all four possible triple deletions viable (Draculic *et al.*, 2000). This enabled to test if certain proteins are able to complement the absence of endogenous ScTrx1, ScTrx2, ScGrx1 and ScGrx2, and therefore maintain viability of the yeast deletion strain. In other words, the cytosol of $\Delta trx1\Delta trx2\Delta grx1\Delta grx2$ yeast cells, where reduction of essential endogenous proteins solely depends upon the protein in question, is suitable for monitoring the reduction capacity of monothiol glutaredoxins and possibly other thioredoxin superfamily enzymes.

To clarify the opportunities this novel in-cell approach provides for testing specific protein disulfide reduction, the following section briefly describes the proceeding of strain generation and plasmid shuffling. First, $\Delta trx1\Delta trx2\Delta grx2$ cells were complemented by the transformation and expression of *ScGRX2* from a p416TEF plasmid harboring *URA3*. *URA3* encodes for the

orotidine-5'-monophosphate decarboxylase, which is critical for plasmid selection. Genomic *ScGRX1* was then deleted using a homologous recombination-based method (see publication 2.3., Supplementary Figure 1). Hence, viability of the resulting quadruple deletion yeast strain, $\Delta trx1\Delta trx2\Delta grx1\Delta grx2$, fully relies on *ScGrx2* encoded on the p416TEF plasmid. Noteworthy, $\Delta trx1\Delta trx2\Delta grx1\Delta grx2 + p416TEF$ (roGFP2-) *ScGRX2* does not require growth on uracil-lacking medium for plasmid selection. Stable plasmid integration is ensured by lethality of the quadruple deletion yeast strain in the absence of this plasmid. Subsequently, these cells were transformed with a second plasmid harboring a *LEU2* gene (p415TEF) for plasmid selection and importantly also the oxidoreductase in question. Eventually, cells were streaked out on Hartwell Complete (HC) plates containing 0.1% 5-FOA (see publication 2.3., Figure 1c). 5-FOA is used for counter-selection against cells harboring the *URA3* gene. Cells expressing *URA3* convert non-toxic 5-FOA into toxic 5-flurouracil, which then becomes incorporated into the RNA, leading to cell death. This means that only those cells survive on 5-FOA, that can afford losing the p416TEF (*URA3*) plasmid and therefore contain a protein encoded on the second plasmid (*LEU2*), which complements the loss of endogenous thioredoxins and glutaredoxins. Using the plasmid shuffling-based approach allows for rapidly testing the capacity for reduction of essential protein disulfides of all proteins in question (**Figure 11**).

It was demonstrated that any of the four deleted enzymes could restore viability of the quadruple deletion yeast strain, while cells transformed with an empty p415TEF plasmid alone did not grow on 5-FOA-containing plates (see publication 2.3., Figure 2 and Supplementary Figure 3). Strikingly, cells transformed with a plasmid encoding monothiol class I *ScGrx7* or engineered monothiol *ScGrx2^{C64S}* (now containing the *ScGrx7*-like -CPYS- active site motif) were also able to grow, even at similar rates as cells rescued by dithiol *ScGrx1* or *ScGrx2*. However, monothiol *HsGrx5*, the class II glutaredoxin previously used, did not rescue growth. The result strongly suggests that active class I monothiol glutaredoxins can, at minimum, perform the essential reduction of disulfide bonds in ribonucleotide reductase. This indicates that the second active site cysteine residue in dithiol glutaredoxins is dispensable for the essential reduction of known and unknown protein disulfides in yeast.

Interestingly, previous *in vitro* studies have demonstrated that engineered -CxxS-glutaredoxins i.e., dithiol glutaredoxins mutated for their second active site cysteine residue, are as active or become even more active than their dithiol counterparts (Yang *et al.*, 1991; Djika *et al.*, 2013). Thus, it raises the question why most active class I glutaredoxins possess two active site cysteine residues. One possible explanation is given by the cysteine-resolving model (Deponte, 2013). After the oxidative half-reaction, the glutathionyl moiety of the glutathionylated enzyme might block the 'glutathione activator site' for the reaction with GSH (Grx-S-SG) (**Figure 2**).

Glutaredoxins could possibly also become trapped in a permanent disulfide to substrates or target proteins (Grx-S-S-substrate/protein). In either case, unfavorable conformational states between both moieties might then prevent the reaction with GSH. The glutaredoxin thus becomes unreactive. In such a scenario, the second cysteine residue could nucleophilically attack the intermolecular disulfide bond and resolve or free the trapped species. Unfortunately, it is unclear how efficient the reduction of ribonucleotide reductase or other putative essential disulfides must be in order to maintain viability of this yeast strain. Physiological relevance of the cysteine resolving model could also be covered by the overexpression of the protein from the plasmid. In such a scenario it is necessary that a fraction of monothiol glutaredoxins must reduce ribonucleotide reductase without becoming trapped to ensure viability of the yeast strain. To exclude that the rescuing effects of monothiol glutaredoxins are not an artifact of the overexpression from a strong and constitutive promoter, a weaker, and also the endogenous promoter of *ScGRX2* were tested. Irrespective of this, the strains expressing monothiol or dithiol class I glutaredoxins grew similarly and survived on plates containing 5-FOA (see publication 2.3., Supplementary Figure 2).

Interestingly, *HsGrx5^{Active}*, which could efficiently oxidize roGFP2 (see publication 2.1 and 2.2) could not support viability of the quadruple deletion yeast strain (see publication 2.3., Supplementary Figure 3). A high steady-state oxidation in the roGFP2 assay also suggests a less efficient reduction of roGFP2 as a disulfide substrate. Therefore, assessment of this fusion construct required a sensitizing DTT pre-treatment. Even though it is possible that *HsGrx5^{Active}* might not interact with roGFP2 or ribonucleotide reductase as an appropriate substrate, another explanation could be general incapability of disulfide bond reduction in this mutant. Considering the observations from both approaches, the results together suggest a gain-of-function in *HsGrx5^{Active}* towards the oxidative half-reaction with GSSG and the subsequent oxidation of target proteins e.g., roGFP2. However, roGFP2 and ribonucleotide reductase cannot or may be used less efficiently as disulfide substrates by this mutant.

Besides the essential reduction of ribonucleotide reductase in the shuffling-based screen, reduction of other protein disulfides was investigated, using the $\Delta trx1\Delta trx2\Delta grx1\Delta grx2$ yeast cells as a ‘test-tube’. Reduction of disulfide bonds was analyzed in PAPS reductase, methionine sulfoxide reductase and roGFP2. Viable yeast strains containing plasmids encoding mono- or dithiol glutaredoxins were streaked onto HC plates without methionine. In accordance with *in vitro* studies and previous studies in yeast (Muller, 1991), neither monothiol nor dithiol glutaredoxins were able to reduce the disulfide bond in PAPS-reductase. This in turn halted any growth on methionine lacking plates and suggests that PAPS-reductase is exclusively reduced by thioredoxins (see publication 2.3., Figure 3). The methionine auxotrophy of *TRX1* and *TRX2* deficient yeast cells made testing for disulfide reduction in 2-Cys methionine sulfoxide reductases possible.

Although several studies reported reduction exclusively by thioredoxins (Vignols *et al.*, 2005; Tarrago *et al.*, 2009) and therefore inability to use methionine sulfoxide as the sole sulfur source, cells grew slowly in HC medium supplemented with methionine sulfoxide (see publication 2.3., Figure 3; Mouahed *et al.*, 1998). Thus, thioredoxins probably mediate the reduction of 2-Cys methionine sulfoxide reductase *in vivo*. However, dithiol and monothiol class I glutaredoxins are able to take over this function, albeit they react more slowly.

Zimmermann *et al.*, 2020

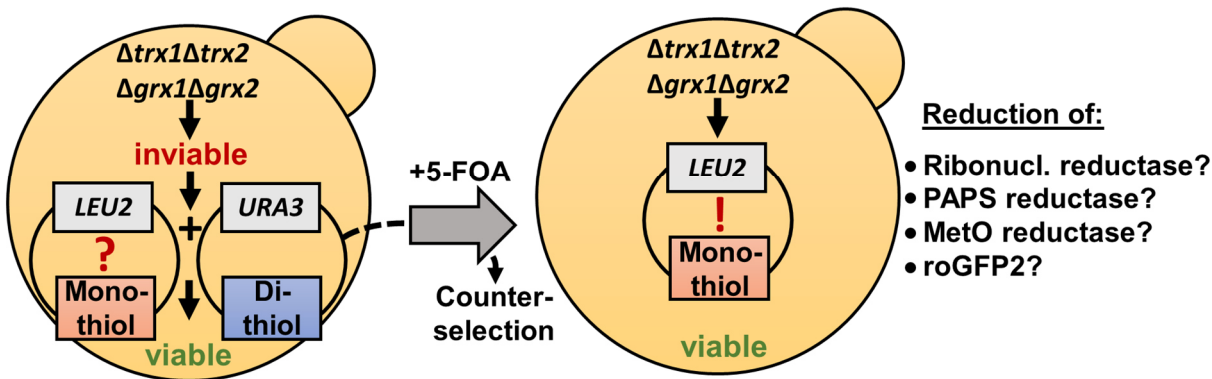


Figure 11. Schematic summary of the contributing publication 2.3. Yeast-based viability and growth assays enable testing for the capability of disulfide bond reduction in selected proteins, including the essential reduction of ribonucleotide reductase or of non-essential disulfide substrates PAPS reductase, MetO reductase and roGFP2.

In summary, a system was developed which enabled the monitoring of disulfide bond reduction in selected proteins, mediated by the oxidoreductase in question. This novel in-cell approach can be used in combination with the previously discussed semi-quantitative roGFP2-based screen. Using both methods make it possible to cover more aspects of the oxidoreductase catalysis for a more comprehensive understanding of oxidoreductase-mediated oxidation and reduction of target proteins (**Figure 11**). In future experiments, further activation of *HsGrx5*^{Active} could be attempted in order to combat the incapability to reduce disulfide target proteins. Activation of this part of the catalytic cycle would also require further knowledge about the 'glutathione activator site' and contribution of other residues towards the reductive half-reaction of glutaredoxins. Future experiments with different proteins or mutants in combination with side-by-side *in vitro* characterization will certainly extend the understanding of different thioredoxin superfamily members. After promising *in vivo* analyses using the roGFP2-based screen and successful plasmid shuffling, the protein could then be subjected to further *in vitro* analyses. Another interesting approach to characterize the reduction of disulfide substrates would be a *N,N,N',N'*-tetramethylazadiacaboxamide (diamide) pre-treatment (Kojer *et al.*, 2009). Rather than decreasing the steady-state oxidation as seen in the DTT pre-treatment, diamide would fully oxidize all roGFP2 molecules. Reduction of the disulfide bond in roGFP2 by the fused oxidoreductase could then be monitored over time. Although this approach would be restricted to roGFP2 as the sole disulfide substrate, the reduction could again be determined semi-quantitatively.

For example, the ‘area under the curve’ between the basal oxidation/reduction of unfused roGFP2 and the reduction kinetics of a certain roGFP2 fusion could serve as a measure. This would be particularly interesting, as some thioredoxin superfamily proteins potentially have minimal reducing activity, which might not suffice to maintain viability of the quadruple deletion yeast strain.

3.6. Using roGFP2-Tsa2 Δ C_R to assess peroxiredoxin-mediated coupling between metabolism and cell division

Fusions between roGFP2 and glutaredoxins or peroxiredoxins were first used to measure E_{GSH} or qualitative changes in H₂O₂, respectively. Thus far, novel yeast- and roGFP2-based approaches to study oxidoreductase activity have been discussed. However, in the study of a former colleague, Prince Amponsah, other members of the thioredoxin superfamily, namely peroxiredoxins, were investigated using a different approach. In a fermenter-based setup, the role of peroxiredoxins in cellular time-keeping was investigated.

Biological clocks are ubiquitous throughout life. These clocks usually underly cyclic transcriptional, translational and metabolic changes. However, there are examples for circadian cycles independent of so-called transcription-translation feedback loops. Interestingly, cycles of peroxiredoxin hyperoxidation were shown in human red blood cells in ~24-hour periods. As mature red blood cells do not harbor nuclei, this observation indicates that these redox cycles can occur independent of transcription and translation (Cho *et al.*, 2014). This raises the question as to what mediates the coupling of these oscillators to the circadian clock? *S. cerevisiae* does not possess a circadian, but rather an ultradian clock i.e., periodic oscillations shorter than 24 hours. During these ultradian cycles, periodic changes in oxygen consumption occur, which has been termed the ‘yeast metabolic cycle’ (YMC). They are present in synchronized, continuous and glucose-limited cultures. In this study, the H₂O₂ sensor roGFP2-Tsa2 Δ C_R was applied to monitor H₂O₂-fluctuations, aiming for a better understanding of redox cycles during the YMC. Therefore, a fermenter- and flow-cell-based setup was used. Permanent sampling and parallel fluorescence measurements in a spectrofluorimeter enabled simultaneous monitoring of oxygen saturation in the medium and peroxide-dependent oxidation of roGFP2-Tsa2 Δ C_R (see publication 2.4., Supplementary Figure 2).

Robust cycles in H₂O₂ were reported by periodic, reversible oxidation and reduction of the redox sensor. Interestingly, phases of high roGFP2 oxidation correlated with LOC, while reduction of the sensor occurred when switching to HOC (see publication 2.4., Figure 1).

These correlations were later confirmed using the novel peroxide sensor, HyPer7 (data not shown). Although HyPer7 is presumably less sensitive than roGFP2-Tsa2 Δ C_R (Kritsiligkou *et al.*, 2021; Cubas *et al.*, 2021), it is brighter and might therefore be advantageous in future studies for monitoring H₂O₂ oscillations during the YMC. However, the redox relay within roGFP2-Tsa2 Δ C_R proved invaluable for further experiments as discussed below (**Figure 5B**).

A correlation between oxygen consumption and H₂O₂ cycles suggests that high intracellular peroxide levels might lead to phase switching. To further investigate this observation, H₂O₂ was added to the culture. When applied at high concentrations, an immediate phase-shift to HOC could be observed, as previously shown (Chen *et al.*, 2007). Unfortunately, H₂O₂ disproportionation by catalases interfered with the oxygen consumption readout leading to an immediate increase in dissolved oxygen within the fermenter vessel. Therefore, the organic oxidant *t*-BuOOH was subsequently used instead of H₂O₂. Treatment of the culture with 1 mM *t*-BuOOH confirmed a LOC to HOC phase shift.

What led to the rapid phase-switching upon addition of high peroxide concentrations? Interestingly, samples from the fermenter vessel after oxidant treatment revealed that roGFP2-Tsa2 Δ C_R was unresponsive to any further peroxide treatment. This indicated hyperoxidation of the Tsa2 Δ C_R moiety to sulfinic (SO₂H) or sulfonic (SO₃H) acids. Hyperoxidation prevents further roGFP2 oxidation in the redox relay due to inactivation of the peroxidase (**Figure 3B**, **Figure 12**). Suitability of roGFP2-based peroxide sensors for monitoring hyperoxidation was already shown in previous studies (Staudacher *et al.*, 2018, Calabrese *et al.*, 2019; Zimmermann *et al.*, unpublished). Hyperoxidation of the sensor moiety in the fusion implies hyperoxidation of endogenous peroxiredoxins, which was confirmed by western blotting using antibodies against hyperoxidized peroxiredoxins. These results suggest that peroxiredoxins can act as putative regulators for metabolic switching. To further investigate LOC-HOC switching in dependence on the cellular thiol-disulfide redox state, thiol oxidants and reductants were applied directly into the fermenter vessel. Addition of the oxidant diamide to the beginning or even end of LOC substantially prolonged this phase. Importantly, switching to HOC again coincided with reduction of the roGFP2-Tsa2 Δ C_R sensor (see publication 2.4., Extended Data Figure 2). Opposingly, addition of the thiol reductant DTT led to immediate switching to HOC (see publication 2.4., Figure 2 g,h and Supplementary Figure 7b). Together these results indicate predictable metabolic switching upon thiol oxidation or reduction.

How can the similar effects of the reductant DTT and hyperoxidation-inducing concentrations of peroxide be explained? It is possible that endogenous peroxiredoxins function in a redox relay, in which target proteins are redox-regulated by H₂O₂ via peroxiredoxins, similar to that of the roGFP2-Tsa2 Δ C_R sensor as discussed previously (**Figure 5B**). Inactivation of

peroxiredoxins by hyperoxidation does not allow for oxidation of putative target proteins. To exclude less direct peroxiredoxin-dependent effects in these processes, it would be extremely interesting to test variants of peroxidases that are less accessible to hyperoxidation. In other words, would LOC to HOC switching still occur in absence of peroxiredoxin inactivation? This would require replacement of endogenous thiol peroxidases with hyperoxidation-insensitive variants. Such variants were shown for the malaria parasite peroxiredoxin *PfAOP^{L109M}*, which was less accessible to hyperoxidation upon H₂O₂ and *t*-BuOOH treatment (Staudacher *et al.*, 2018). In yeast, mitochondrial ScPrx1 was also engineered to be less sensitive to hyperoxidation (ScPrx1^{P233stop}) (Calabrese *et al.*, 2019). In both cases, these effects were monitored using roGFP2-based probes.

Amponsah *et al.*, 2021

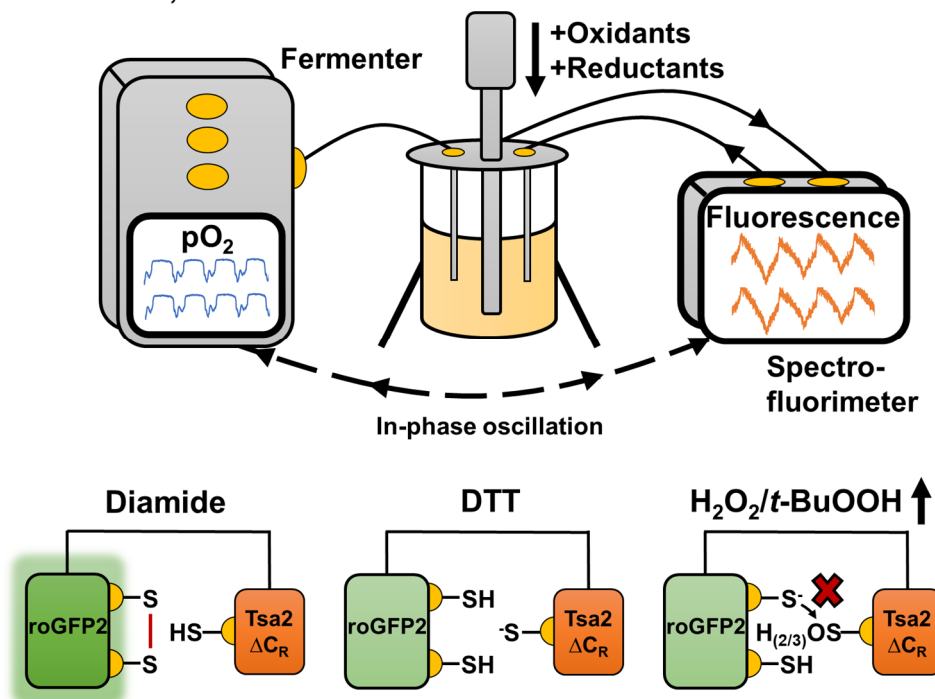


Figure 12. Schematic summary of the contributing publication 2.4. Expression of roGFP2-Tsa2 ΔC_R enabled simultaneous monitoring of metabolic and peroxide cycles. Application of oxidants and reductants can further predictably manipulate the YMC, possibly via peroxiredoxin-dependent control of thiol oxidation in target proteins.

Manipulating the YMC with oxidants or reductants further perturbed cell cycle entry and exit. Coupling to the cell division cycle (CDC) was monitored by sampling at different stages throughout the YMC, and through subsequent analysis of the DNA content by flow-cytometry or counting of budding cells. In *S. cerevisiae*, appearance of new buds and S-phase initiation is synchronized (Williamson, 1965). Chemical perturbation with diamide inhibited entry into the cell cycle and cells were trapped in the G1-phase (see publication 2.4., Supplementary Figure 15). This was indicated by low DNA content and the occurrence of less budding cells in samples extracted from the fermenter vessel (see publication 2.4., Figure 5e,f). Opposingly, the strong reductant DTT not only prevented an exit from the cell cycle, but also

initiated a second round of the cell cycle (see publication 2.4., Figure 6). Interestingly, cells were detected with even more than one bud.

What is the role of peroxiredoxins in coupling metabolism and CDC? In absence of endogenous ScTsa1 and ScTsa2 i.e., $\Delta tsa1\Delta tsa2$ deletion cells, cyclic oxygen consumption was still observed, however with significantly shorter periods. Measurements of DNA content and budding index however revealed uncoupling of cell cycle and cell division from metabolic cycles in this strain (see publication 2.4., Figure 4). This is particularly interesting as increased spontaneous genomic mutations were reported in cells lacking *TSA1* (Wong *et al.*, 2004; Iraqui *et al.*, 2009; Kaya *et al.*, 2014). Furthermore, in higher organisms, cells lacking peroxiredoxins showed an increased probability of cancer (Nyström *et al.*, 2012). Other general phenotypes of thiol peroxidase deletion cells e.g., growth defects or increased sensitivity to chemical treatments, are often attributed to decreased peroxide scavenging, which leads to increased intracellular H₂O₂ levels. Rather than increased cellular peroxide levels, an alternative hypothesis arising from this study is the potential role of peroxiredoxins in the regulation of cell cycle under limited metabolite availability. Perturbation of their redox state or their complete absence might impair peroxiredoxin-mediated signaling and therefore initiate cell cycle and division at unfavorable metabolic conditions. Limitation of metabolites for replication during S-phase might then lead to failure in DNA synthesis and potential occurrence of genomic mutations.

In summary, it was shown that roGFP2-based H₂O₂ sensors are suitable for monitoring peroxide cycles in a continuous and synchronized culture. The results further indicate a strong correlation between metabolic cycling and the endogenous thiol-disulfide redox state of peroxiredoxins. Thus, peroxiredoxins were shown to be important for stable oscillations in oxygen consumption and coupling of these metabolic cycles to cell cycle and division. Future experiments will certainly aim to characterize the target of peroxiredoxin-mediated oxidation in the postulated redox relay. It was recently reported that ScTsa1 can regulate the activity of the protein kinase A (PKA) subunit Tpk1 via oxidation (Roger *et al.*, 2020). The stress-responsive transcription factor, ScMsn2, is a known target of PKA. Remarkably, metabolic cycles in ScMSN2 deletion cells were shown to be heavily perturbed (Kuang *et al.*, 2017). PKA has many other known and putative targets. Therefore, it might be possible that ScTsa1 regulates metabolic switching and coupling to cell cycle by modulating the PKA activity. Furthermore, it will certainly be interesting to monitor potential oscillations of NADPH during the YMC. If cycles of NADPH were monitored, they would potentially cycle opposing to oxygen consumption and importantly, endogenous H₂O₂ levels. This would suggest an increased NADPH demand during cell cycle and division and at stages where peroxide concentrations are high. Development of appropriate sensors and experiments in the near future will certainly contribute to the understanding of peroxiredoxin-mediated redox regulation in the YMC.

References

- Adachi, T., Pimentel, D. R., Heibeck, T., Hou, X., Lee, Y. J., Jiang, B., Ido, Y., & Cohen, R. A. (2004). S-glutathiolation of Ras mediates redox-sensitive signaling by angiotensin II in vascular smooth muscle cells. *The Journal of biological chemistry*, 279(28), 29857–29862.
- Albrecht, S. C., Sobotta, M. C., Bausewein, D., Aller, I., Hell, R., Dick, T. P., & Meyer, A. J. (2014). Redesign of genetically encoded biosensors for monitoring mitochondrial redox status in a broad range of model eukaryotes. *Journal of biomolecular screening*, 19(3), 379–386.
- Amponsah, P. S., Yahya, G., Zimmermann, J., Mai, M., Mergel, S., Mühlhaus, T., Storchova, Z., & Morgan, B. (2021). Peroxiredoxins couple metabolism and cell division in an ultradian cycle. *Nature chemical biology*, 17(4), 477–484.
- Back, P., De Vos, W. H., Depuydt, G. G., Matthijssens, F., Vanfleteren, J. R., & Braeckman, B. P. (2012). Exploring real-time *in vivo* redox biology of developing and aging *Caenorhabditis elegans*. *Free radical biology & medicine*, 52(5), 850–859.
- Begas, P., Liedgens, L., Moseler, A., Meyer, A. J., & Deponte, M. (2017). Glutaredoxin catalysis requires two distinct glutathione interaction sites. *Nature communications*, 8, 14835.
- Begas, P., Staudacher, V., & Deponte, M. (2015). Systematic re-evaluation of the bis(2-hydroxyethyl)disulfide (HEDS) assay reveals an alternative mechanism and activity of glutaredoxins. *Chemical science*, 6(7), 3788–3796.
- Belousov, V. V., Fradkov, A. F., Lukyanov, K. A., Staroverov, D. B., Shakhbazov, K. S., Terskikh, A. V., & Lukyanov, S. (2006). Genetically encoded fluorescent indicator for intracellular hydrogen peroxide. *Nature methods*, 3(4), 281–286.
- Björnberg, O., Østergaard, H., & Winther, J. R. (2006). Mechanistic insight provided by glutaredoxin within a fusion to redox-sensitive yellow fluorescent protein.
- Bodvard, K., Peeters, K., Roger, F., Romanov, N., Igbaria, A., Welkenhuysen, N., Palais, G., Reiter, W., Toledano, M. B., Käll, M., & Molin, M. (2017). Light-sensing via hydrogen peroxide and a peroxiredoxin. *Nature communications*, 8, 14791.
- Boeke, J. D., Trueheart, J., Natsoulis, G., & Fink, G. R. (1987). 5-Fluoroorotic acid as a selective agent in yeast molecular genetics. *Methods in enzymology*, 154, 164–175.
- Botstein, D., Chervitz, S. A., & Cherry, J. M. (1997). Yeast as a model organism. *Science (New York, N.Y.)*, 277(5330), 1259–1260.
- Bourbouloux, A., Shahi, P., Chakladar, A., Delrot, S., & Bachhawat, A. K. (2000). Hgt1p, a high affinity glutathione transporter from the yeast *Saccharomyces cerevisiae*. *The Journal of biological chemistry*, 275(18), 13259–13265.
- Bushweller, J. H., Aslund, F., Wüthrich, K., & Holmgren, A. (1992). Structural and functional characterization of the mutant *Escherichia coli* glutaredoxin (C14----S) and its mixed disulfide with glutathione. *Biochemistry*, 31(38), 9288–9293.
- Cabiscol, E., & Levine, R. L. (1996). The phosphatase activity of carbonic anhydrase III is reversibly regulated by glutathiolation. *Proceedings of the National Academy of Sciences of the United States of America*, 93(9), 4170–4174.

- Calabrese, G., Peker, E., Amponsah, P. S., Hoehne, M. N., Riemer, T., Mai, M., Bienert, G. P., Deponte, M., Morgan, B., & Riemer, J. (2019). Hyperoxidation of mitochondrial peroxiredoxin limits H₂O₂-induced cell death in yeast. *The EMBO journal*, 38(18), e101552.
- Carmona, M., de Cubas, L., Bautista, E., Moral-Blanch, M., Medraño-Fernández, I., Sitia, R., Boronat, S., Ayté, J., & Hidalgo, E. (2019). Monitoring cytosolic H₂O₂ fluctuations arising from altered plasma membrane gradients or from mitochondrial activity. *Nature communications*, 10(1), 4526.
- Carvalho, A. P., Fernandes, P. A., & Ramos, M. J. (2006). Similarities and differences in the thioredoxin superfamily. *Progress in biophysics and molecular biology*, 91(3), 229–248.
- Causton, H. C., Feeney, K. A., Ziegler, C. A., & O'Neill, J. S. (2015). Metabolic Cycles in Yeast Share Features Conserved among Circadian Rhythms. *Current biology: CB*, 25(8), 1056–1062.
- Chae, H. Z., Chung, S. J., & Rhee, S. G. (1994). Thioredoxin-dependent peroxide reductase from yeast. *The Journal of biological chemistry*, 269(44), 27670–27678.
- Chae, H. Z., Robison, K., Poole, L. B., Church, G., Storz, G., & Rhee, S. G. (1994). Cloning and sequencing of thiol-specific antioxidant from mammalian brain: alkyl hydroperoxide reductase and thiol-specific antioxidant define a large family of antioxidant enzymes. *Proceedings of the National Academy of Sciences of the United States of America*, 91(15), 7017–7021.
- Chen, Z., Odstrcil, E. A., Tu, B. P., & McKnight, S. L. (2007). Restriction of DNA replication to the reductive phase of the metabolic cycle protects genome integrity. *Science (New York, N.Y.)*, 316(5833), 1916–1919.
- Cho, C. S., Yoon, H. J., Kim, J. Y., Woo, H. A., & Rhee, S. G. (2014). Circadian rhythm of hyperoxidized peroxiredoxin II is determined by hemoglobin autoxidation and the 20S proteasome in red blood cells. *Proceedings of the National Academy of Sciences of the United States of America*, 111(33), 12043–12048.
- Collinson, E. J., Wheeler, G. L., Garrido, E. O., Avery, A. M., Avery, S. V., & Grant, C. M. (2002). The yeast glutaredoxins are active as glutathione peroxidases. *The Journal of biological chemistry*, 277(19), 16712–16717.
- Couturier, J., Didierjean, C., Jacquot, J. P., & Rouhier, N. (2010). Engineered mutated glutaredoxins mimicking peculiar plant class III glutaredoxins bind iron-sulfur centers and possess reductase activity. *Biochemical and biophysical research communications*, 403(3-4), 435–441.
- Couturier, J., Jacquot, J. P., & Rouhier, N. (2009). Evolution and diversity of glutaredoxins in photosynthetic organisms. *Cellular and molecular life sciences: CMLS*, 66(15), 2539–2557.
- Couturier, J., Jacquot, J. P., & Rouhier, N. (2013). Toward a refined classification of class I dithiol glutaredoxins from poplar: biochemical basis for the definition of two subclasses. *Frontiers in plant science*, 4, 518.
- Couturier, J., Przybyla-Toscano, J., Roret, T., Didierjean, C., & Rouhier, N. (2015). The roles of glutaredoxins ligating Fe-S clusters: Sensing, transfer or repair functions? *Biochimica et biophysica acta*, 1853(6), 1513–1527.

- Cubas, L., Pak, V. V., Belousov, V. V., Ayté, J., & Hidalgo, E. (2021). The Mitochondria-to-Cytosol H₂O₂ Gradient Is Caused by Peroxiredoxin-Dependent Cytosolic Scavenging. *Antioxidants (Basel, Switzerland)*, 10(5), 731.
- Daudi, A., & O'Brien, J. A. (2012). Detection of Hydrogen Peroxide by DAB Staining in *Arabidopsis* Leaves. *Bio-protocol*, 2(18), e263.
- Delaunay, A., Pflieger, D., Barrault, M. B., Vinh, J., & Toledano, M. B. (2002). A thiol peroxidase is an H₂O₂ receptor and redox-transducer in gene activation. *Cell*, 111(4), 471–481.
- Delaunay-Moisan, A., Ponsero, A., & Toledano, M. B. (2017). Reexamining the Function of Glutathione in Oxidative Protein Folding and Secretion. *Antioxidants & redox signaling*, 27(15), 1178–1199.
- Deponte, M. (2013). Glutathione catalysis and the reaction mechanisms of glutathione-dependent enzymes. *Biochimica et biophysica acta*, 1830(5), 3217–3266.
- Discola, K. F., de Oliveira, M. A., Rosa Cussiol, J. R., Monteiro, G., Bárcena, J. A., Porras, P., Padilla, C. A., Guimarães, B. G., & Netto, L. E. (2009). Structural aspects of the distinct biochemical properties of glutaredoxin 1 and glutaredoxin 2 from *Saccharomyces cerevisiae*. *Journal of molecular biology*, 385(3), 889–901.
- Djuika, C. F., Fiedler, S., Schnölzer, M., Sanchez, C., Lanzer, M., & Deponte, M. (2013). Plasmodium falciparum antioxidant protein as a model enzyme for a special class of glutaredoxin/glutathione-dependent peroxiredoxins. *Biochimica et biophysica acta*, 1830(8), 4073–4090.
- Djuika, C. F., Staudacher, V., Sanchez, C. P., Lanzer, M., & Deponte, M. (2017). Knockout of the peroxiredoxin 5 homologue PFAOP does not affect the artemisinin susceptibility of Plasmodium falciparum. *Scientific reports*, 7(1), 4410.
- Dooley, C. T., Dore, T. M., Hanson, G. T., Jackson, W. C., Remington, S. J., & Tsien, R. Y. (2004). Imaging dynamic redox changes in mammalian cells with green fluorescent protein indicators. *The Journal of biological chemistry*, 279(21), 22284–22293.
- Draculic, T., Dawes, I. W., & Grant, C. M. (2000). A single glutaredoxin or thioredoxin gene is essential for viability in the yeast *Saccharomyces cerevisiae*. *Molecular microbiology*, 36(5), 1167–1174.
- D'Autréaux, B., & Toledano, M. B. (2007). ROS as signalling molecules: mechanisms that generate specificity in ROS homeostasis. *Nature reviews. Molecular cell biology*, 8(10), 813–824.
- Eckers, E., Bien, M., Stroobant, V., Herrmann, J. M., & Deponte, M. (2009). Biochemical characterization of dithiol glutaredoxin 8 from *Saccharomyces cerevisiae*: the catalytic redox mechanism redux. *Biochemistry*, 48(6), 1410–1423.
- Edgar, R. S., Green, E. W., Zhao, Y., van Ooijen, G., Olmedo, M., Qin, X., Xu, Y., Pan, M., Valekunja, U. K., Feeney, K. A., Maywood, E. S., Hastings, M. H., Baliga, N. S., Merrow, M., Millar, A. J., Johnson, C. H., Kyriacou, C. P., O'Neill, J. S., & Reddy, A. B. (2012). Peroxiredoxins are conserved markers of circadian rhythms. *Nature*, 485(7399), 459–464.
- Elledge, S. J., Zhou, Z., & Allen, J. B. (1992). Ribonucleotide reductase: regulation, regulation, regulation. *Trends in biochemical sciences*, 17(3), 119–123.

- Enyedi, B., Zana, M., Donkó, Á., & Geiszt, M. (2013). Spatial and temporal analysis of NADPH oxidase-generated hydrogen peroxide signals by novel fluorescent reporter proteins. *Antioxidants & redox signaling*, 19(6), 523–534.
- Escoria, W., & Forsburg, S. L. (2018). Tetrad Dissection in Fission Yeast. *Methods in molecular biology (Clifton, N.J.)*, 1721, 179–187.
- Espinosa, B., & Arnér, E. (2019). Thioredoxin-related protein of 14 kDa as a modulator of redox signalling pathways. *British journal of pharmacology*, 176(4), 544–553.
- Forsburg S. L. (2001). The art and design of genetic screens: yeast. *Nature reviews. Genetics*, 2(9), 659–668.
- Frandsen, A. R., & Kaiser, C. A. (1999). Ero1p oxidizes protein disulfide isomerase in a pathway for disulfide bond formation in the endoplasmic reticulum. *Molecular cell*, 4(4), 469–477.
- Ghaemmaghami, S., Huh, W. K., Bower, K., Howson, R. W., Belle, A., Dephoure, N., O'Shea, E. K., & Weissman, J. S. (2003). Global analysis of protein expression in yeast. *Nature*, 425(6959), 737–741.
- Goffeau, A., Barrell, B. G., Bussey, H., Davis, R. W., Dujon, B., Feldmann, H., Galibert, F., Hoheisel, J. D., Jacq, C., Johnston, M., Louis, E. J., Mewes, H. W., Murakami, Y., Philippson, P., Tettelin, H., & Oliver, S. G. (1996). Life with 6000 genes. *Science (New York, N.Y.)*, 274(5287), 546–567.
- Gorelenkova Miller, O., & Mieyal, J. J. (2019). Critical Roles of Glutaredoxin in Brain Cells—Implications for Parkinson's Disease. *Antioxidants & redox signaling*, 30(10), 1352–1368.
- Gough, D. R., & Cotter, T. G. (2011). Hydrogen peroxide: a Jekyll and Hyde signalling molecule. *Cell death & disease*, 2(10), e213.
- Grant C. M. (2001). Role of the glutathione/glutaredoxin and thioredoxin systems in yeast growth and response to stress conditions. *Molecular microbiology*, 39(3), 533–541.
- Gross, E., Sevier, C. S., Heldman, N., Vitu, E., Bentzur, M., Kaiser, C. A., Thorpe, C., & Fass, D. (2006). Generating disulfides enzymatically: reaction products and electron acceptors of the endoplasmic reticulum thiol oxidase Ero1p. *Proceedings of the National Academy of Sciences of the United States of America*, 103(2), 299–304.
- Gutscher, M., Pauleau, A. L., Marty, L., Brach, T., Wabnitz, G. H., Samstag, Y., Meyer, A. J., & Dick, T. P. (2008). Real-time imaging of the intracellular glutathione redox potential. *Nature methods*, 5(6), 553–559.
- Gutscher, M., Sobotta, M. C., Wabnitz, G. H., Ballikaya, S., Meyer, A. J., Samstag, Y., & Dick, T. P. (2009). Proximity-based protein thiol oxidation by H₂O₂-scavenging peroxidases. *The Journal of biological chemistry*, 284(46), 31532–31540.
- Hall, A., Nelson, K., Poole, L. B., & Karplus, P. A. (2011). Structure-based insights into the catalytic power and conformational dexterity of peroxiredoxins. *Antioxidants & redox signaling*, 15(3), 795–815.
- Hanschmann, E. M., Lönn, M. E., Schütte, L. D., Funke, M., Godoy, J. R., Eitner, S., Hudemann, C., & Lillig, C. H. (2010). Both thioredoxin 2 and glutaredoxin 2 contribute to the reduction of the mitochondrial 2-Cys peroxiredoxin Prx3. *The Journal of biological chemistry*, 285(52), 40699–40705.

- Hanson, G. T., Aggeler, R., Oglesbee, D., Cannon, M., Capaldi, R. A., Tsien, R. Y., & Remington, S. J. (2004). Investigating mitochondrial redox potential with redox-sensitive green fluorescent protein indicators. *The Journal of biological chemistry*, 279(13), 13044–13053.
- Hashimoto, F., & Hayashi, H. (1990). Significance of catalase in peroxisomal fatty acyl-CoA beta-oxidation: NADH oxidation by acetoacetyl-CoA and H₂O₂. *Journal of biochemistry*, 108(3), 426–431.
- Heller, J., Meyer, A. J., & Tudzynski, P. (2012). Redox-sensitive GFP2: use of the genetically encoded biosensor of the redox status in the filamentous fungus *Botrytis cinerea*. *Molecular plant pathology*, 13(8), 935–947.
- Herrero, E., & de la Torre-Ruiz, M. A. (2007). Monothiol glutaredoxins: a common domain for multiple functions. *Cellular and molecular life sciences: CMLS*, 64(12), 1518–1530.
- Herrero, E., Ros, J., Tamarit, J., & Bellí, G. (2006). Glutaredoxins in fungi. *Photosynthesis research*, 89(2-3), 127–140.
- Hirayama, J., Cho, S., & Sassone-Corsi, P. (2007). Circadian control by the reduction/oxidation pathway: catalase represses light-dependent clock gene expression in the zebrafish. *Proceedings of the National Academy of Sciences of the United States of America*, 104(40), 15747–15752.
- Hofmann, B., Hecht, H. J., & Flohé, L. (2002). Peroxiredoxins. *Biological chemistry*, 383(3-4), 347–364.
- Holmgren A. (1976). Hydrogen donor system for Escherichia coli ribonucleoside-diphosphate reductase dependent upon glutathione. *Proceedings of the National Academy of Sciences of the United States of America*, 73(7), 2275–2279.
- Holmgren, A., & Aslund, F. (1995). Glutaredoxin. *Methods in enzymology*, 252, 283–292.
- Holmgren, A., Söderberg, B. O., Eklund, H., & Brändén, C. I. (1975). Three-dimensional structure of Escherichia coli thioredoxin-S2 to 2.8 Å resolution. *Proceedings of the National Academy of Sciences of the United States of America*, 72(6), 2305–2309.
- Höög, J. O., Jörnvall, H., Holmgren, A., Carlquist, M., & Persson, M. (1983). The primary structure of Escherichia coli glutaredoxin. Distant homology with thioredoxins in a superfamily of small proteins with a redox-active cystine disulfide/cysteine dithiol. *European journal of biochemistry*, 136(1), 223–232.
- Hung, Y. P., Albeck, J. G., Tantama, M., & Yellen, G. (2011). Imaging cytosolic NADH-NAD(+) redox state with a genetically encoded fluorescent biosensor. *Cell metabolism*, 14(4), 545–554.
- Iraqi, I., Kienda, G., Soeur, J., Faye, G., Baldacci, G., Kolodner, R. D., & Huang, M. E. (2009). Peroxiredoxin Tsa1 is the key peroxidase suppressing genome instability and protecting against cell death in *Saccharomyces cerevisiae*. *PLoS genetics*, 5(6), e1000524.
- Ivleva, N. B., Bramlett, M. R., Lindahl, P. A., & Golden, S. S. (2005). LdpA: a component of the circadian clock senses redox state of the cell. *The EMBO journal*, 24(6), 1202–1210.
- Izquierdo, A., Casas, C., Mühlenhoff, U., Lillig, C. H., & Herrero, E. (2008). *Saccharomyces cerevisiae* Grx6 and Grx7 are monothiol glutaredoxins associated with the early secretory pathway. *Eukaryotic cell*, 7(8), 1415–1426.

- Jacobson, F. S., Morgan, R. W., Christman, M. F., & Ames, B. N. (1989). An alkyl hydroperoxide reductase from *Salmonella typhimurium* involved in the defense of DNA against oxidative damage. Purification and properties. *The Journal of biological chemistry*, 264(3), 1488–1496.
- Jang, H. H., Lee, K. O., Chi, Y. H., Jung, B. G., Park, S. K., Park, J. H., Lee, J. R., Lee, S. S., Moon, J. C., Yun, J. W., Choi, Y. O., Kim, W. Y., Kang, J. S., Cheong, G. W., Yun, D. J., Rhee, S. G., Cho, M. J., & Lee, S. Y. (2004). Two enzymes in one; two yeast peroxiredoxins display oxidative stress-dependent switching from a peroxidase to a molecular chaperone function. *Cell*, 117(5), 625–635.
- Janke, C., Magiera, M. M., Rathfelder, N., Taxis, C., Reber, S., Maekawa, H., Moreno-Borchart, A., Doenges, G., Schwob, E., Schieber, E., & Knop, M. (2004). A versatile toolbox for PCR-based tagging of yeast genes: new fluorescent proteins, more markers and promoter substitution cassettes. *Yeast (Chichester, England)*, 21(11), 947–962.
- Jao, S. C., English Ospina, S. M., Berdis, A. J., Starke, D. W., Post, C. B., & Mieyal, J. J. (2006). Computational and mutational analysis of human glutaredoxin (thioltransferase): probing the molecular basis of the low pKa of cysteine 22 and its role in catalysis. *Biochemistry*, 45(15), 4785–4796.
- Johansson, C., Kavanagh, K. L., Gileadi, O., & Oppermann, U. (2007). Reversible sequestration of active site cysteines in a 2Fe-2S-bridged dimer provides a mechanism for glutaredoxin 2 regulation in human mitochondria. *The Journal of biological chemistry*, 282(5), 3077–3082.
- Kaya, A., Lobanov, A. V., Gerashchenko, M. V., Koren, A., Fomenko, D. E., Koc, A., & Gladyshev, V. N. (2014). Thiol peroxidase deficiency leads to increased mutational load and decreased fitness in *Saccharomyces cerevisiae*. *Genetics*, 198(3), 905–917.
- Knop, M., Siegers, K., Pereira, G., Zachariae, W., Winsor, B., Nasmyth, K., & Schieber, E. (1999). Epitope tagging of yeast genes using a PCR-based strategy: more tags and improved practical routines. *Yeast (Chichester, England)*, 15(10B), 963–972.
- Kojer, K., Bien, M., Gangel, H., Morgan, B., Dick, T. P., & Riemer, J. (2012). Glutathione redox potential in the mitochondrial intermembrane space is linked to the cytosol and impacts the Mia40 redox state. *The EMBO journal*, 31(14), 3169–3182.
- Kondratov, R. V., Kondratova, A. A., Gorbacheva, V. Y., Vykhovanets, O. V., & Antoch, M. P. (2006). Early aging and age-related pathologies in mice deficient in BMAL1, the core component of the circadian clock. *Genes & development*, 20(14), 1868–1873.
- Kritsiligkou, P., Shen, T. K., & Dick, T. P. (2021). A comparison of Prx- and OxyR-based H₂O₂ probes expressed in *S. cerevisiae*. *The Journal of biological chemistry*, 297(1), 100866. Advance online publication.
- Kuang, Z., Pinglay, S., Ji, H., & Boeke, J. D. (2017). Msn2/4 regulate expression of glycolytic enzymes and control transition from quiescence to growth. *eLife*, 6, e29938.
- Kumar, C., Igbaria, A., D'Autreux, B., Planson, A. G., Junot, C., Godat, E., Bachhawat, A. K., Delaunay-Moisant, A., & Toledano, M. B. (2011). Glutathione revisited: a vital function in iron metabolism and ancillary role in thiol-redox control. *The EMBO journal*, 30(10), 2044–2056.

- Langford, T. F., Huang, B. K., Lim, J. B., Moon, S. J., & Sikes, H. D. (2018). Monitoring the action of redox-directed cancer therapeutics using a human peroxiredoxin-2-based probe. *Nature communications*, 9(1), 3145.
- Liedgens, L., Zimmermann, J., Wäschenbach, L., Geissel, F., Laporte, H., Gohlke, H., Morgan, B., & Deponte, M. (2020). Quantitative assessment of the determinant structural differences between redox-active and inactive glutaredoxins. *Nature communications*, 11(1), 1725.
- Lillig, C. H., Berndt, C., & Holmgren, A. (2008). Glutaredoxin systems. *Biochimica et biophysica acta*, 1780(11), 1304–1317.
- Lillig, C. H., Berndt, C., Vergnolle, O., Lönn, M. E., Hudemann, C., Bill, E., & Holmgren, A. (2005). Characterization of human glutaredoxin 2 as iron-sulfur protein: a possible role as redox sensor. *Proceedings of the National Academy of Sciences of the United States of America*, 102(23), 8168–8173.
- Lillig, C. H., Prior, A., Schwenn, J. D., Aslund, F., Ritz, D., Vlamis-Gardikas, A., & Holmgren, A. (1999). New thioredoxins and glutaredoxins as electron donors of 3'-phosphoadenylylsulfate reductase. *The Journal of biological chemistry*, 274(12), 7695–7698.
- Lim, J. M., Lee, K. S., Woo, H. A., Kang, D., & Rhee, S. G. (2015). Control of the pericentrosomal H₂O₂ level by peroxiredoxin I is critical for mitotic progression. *The Journal of cell biology*, 210(1), 23–33.
- Liu, H., & Zhang, J. (2019). Yeast Spontaneous Mutation Rate and Spectrum Vary with Environment. *Current biology : CB*, 29(10), 1584–1591.e3.
- Liu, L., Hausladen, A., Zeng, M., Que, L., Heitman, J., & Stamler, J. S. (2001). A metabolic enzyme for S-nitrosothiol conserved from bacteria to humans. *Nature*, 410(6827), 490–494.
- Liu, W., Li, L., Ye, H., Chen, H., Shen, W., Zhong, Y., Tian, T., & He, H. (2017). From *Saccharomyces cerevisiae* to human: The important gene co-expression modules. *Biomedical reports*, 7(2), 153–158.
- Lu, J., & Holmgren, A. (2014). The thioredoxin antioxidant system. *Free radical biology & medicine*, 66, 75–87.
- Lu, J., & Holmgren, A. (2014). The thioredoxin superfamily in oxidative protein folding. *Antioxidants & redox signaling*, 21(3), 457–470.
- Manta, B., Möller, M. N., Bonilla, M., Deambrosi, M., Grunberg, K., Bellanda, M., Comini, M. A., & Ferrer-Sueta, G. (2019). Kinetic studies reveal a key role of a redox-active glutaredoxin in the evolution of the thiol-redox metabolism of trypanosomatid parasites. *The Journal of biological chemistry*, 294(9), 3235–3248.
- Martin J. L. (1995). Thioredoxin--a fold for all reasons. *Structure (London, England: 1993)*, 3(3), 245–250.
- Maughan, S. C., Pasternak, M., Cairns, N., Kiddie, G., Brach, T., Jarvis, R., Haas, F., Nieuwland, J., Lim, B., Müller, C., Salcedo-Sora, E., Kruse, C., Orsel, M., Hell, R., Miller, A. J., Bray, P., Foyer, C. H., Murray, J. A., Meyer, A. J., & Cobbett, C. S. (2010). Plant homologs of the *Plasmodium falciparum* chloroquine-resistance transporter, PfCRT, are required for glutathione homeostasis and stress responses. *Proceedings of the National Academy of Sciences of the United States of America*, 107(5), 2331–2336.

- Mesecke, N., Mittler, S., Eckers, E., Herrmann, J. M., & Deponte, M. (2008). Two novel monothiol glutaredoxins from *Saccharomyces cerevisiae* provide further insight into iron-sulfur cluster binding, oligomerization, and enzymatic activity of glutaredoxins. *Biochemistry*, 47(5), 1452–1463.
- Meyer, A. J., & Dick, T. P. (2010). Fluorescent protein-based redox probes. *Antioxidants & redox signaling*, 13(5), 621–650.
- Meyer, Y., Belin, C., Delorme-Hinoux, V., Reichheld, J. P., & Riondet, C. (2012). Thioredoxin and glutaredoxin systems in plants: molecular mechanisms, crosstalks, and functional significance. *Antioxidants & redox signaling*, 17(8), 1124–1160.
- Mieyal, J. J., Gallogly, M. M., Qanungo, S., Sabens, E. A., & Shelton, M. D. (2008). Molecular mechanisms and clinical implications of reversible protein S-glutathionylation. *Antioxidants & redox signaling*, 10(11), 1941–1988.
- Mohanty, J. G., Jaffe, J. S., Schulman, E. S., & Raible, D. G. (1997). A highly sensitive fluorescent micro-assay of H₂O₂ release from activated human leukocytes using a dihydroxyphenoxazine derivative. *Journal of immunological methods*, 202(2), 133–141.
- Mohr, S., Hallak, H., de Boitte, A., Lapetina, E. G., & Brüne, B. (1999). Nitric oxide-induced S-glutathionylation and inactivation of glyceraldehyde-3-phosphate dehydrogenase. *The Journal of biological chemistry*, 274(14), 9427–9430.
- Moltensi, S. N., Fassio, A., Ciriolo, M. R., Filomeni, G., Pasqualetto, E., Fagioli, C., & Sitia, R. (2004). Glutathione limits Ero1-dependent oxidation in the endoplasmic reticulum. *The Journal of biological chemistry*, 279(31), 32667–32673.
- Morgan, B., Ezeriña, D., Amoako, T. N., Riemer, J., Seedorf, M., & Dick, T. P. (2013). Multiple glutathione disulfide removal pathways mediate cytosolic redox homeostasis. *Nature chemical biology*, 9(2), 119–125.
- Morgan, B., Sobotta, M. C., & Dick, T. P. (2011). Measuring $E_{(GSH)}$ and H₂O₂ with roGFP2-based redox probes. *Free radical biology & medicine*, 51(11), 1943–1951.
- Morgan, B., Van Laer, K., Owusu, T. N., Ezeriña, D., Pastor-Flores, D., Amponsah, P. S., Tursch, A., & Dick, T. P. (2016). Real-time monitoring of basal H₂O₂ levels with peroxiredoxin-based probes. *Nature chemical biology*, 12(6), 437–443.
- Moseler, A., Aller, I., Wagner, S., Nietzel, T., Przybyla-Toscano, J., Mühlenhoff, U., Lill, R., Berndt, C., Rouhier, N., Schwarzländer, M., & Meyer, A. J. (2015). The mitochondrial monothiol glutaredoxin S15 is essential for iron-sulfur protein maturation in *Arabidopsis thaliana*. *Proceedings of the National Academy of Sciences of the United States of America*, 112(44), 13735–13740.
- Mouaheb, N., Thomas, D., Verdoucq, L., Monfort, P., & Meyer, Y. (1998). *In vivo* functional discrimination between plant thioredoxins by heterologous expression in the yeast *Saccharomyces cerevisiae*. *Proceedings of the National Academy of Sciences of the United States of America*, 95(6), 3312–3317.
- Muller E. G. (1991). Thioredoxin deficiency in yeast prolongs S phase and shortens the G1 interval of the cell cycle. *The Journal of biological chemistry*, 266(14), 9194–9202.

- Mühlenhoff, U., Molik, S., Godoy, J. R., Uzarska, M. A., Richter, N., Seubert, A., Zhang, Y., Stubbe, J., Pierrel, F., Herrero, E., Lillig, C. H., & Lill, R. (2010). Cytosolic monothiol glutaredoxins function in intracellular iron sensing and trafficking via their bound iron-sulfur cluster. *Cell metabolism*, 12(4), 373–385.
- Müller, A., Schneider, J. F., Degrossoli, A., Lupilova, N., Dick, T. P., & Leichert, L. I. (2017). Systematic *in vitro* assessment of responses of roGFP2-based probes to physiologically relevant oxidant species. *Free radical biology & medicine*, 106, 329–338.
- Nagai, S., & Black, S. (1968). A thiol-disulfide transhydrogenase from yeast. *The Journal of biological chemistry*, 243(8), 1942–1947.
- Nelson, K. J., Knutson, S. T., Soito, L., Klomsiri, C., Poole, L. B., & Fetrow, J. S. (2011). Analysis of the peroxiredoxin family: using active-site structure and sequence information for global classification and residue analysis. *Proteins*, 79(3), 947–964.
- Netto, L., de Oliveira, M. A., Monteiro, G., Demasi, A., Cussiol, J., Discola, K. F., Demasi, M., Silva, G. M., Alves, S. V., Faria, V. G., & Horta, B. B. (2007). Reactive cysteine in proteins: protein folding, antioxidant defense, redox signaling and more. *Comparative biochemistry and physiology : CBP*, 146(1-2), 180–193.
- Nilewski, S., Varatnitskaya, M., Masuch, T., Kusnezowa, A., Gellert, M., Baumann, A. F., Lupilov, N., Kusnezow, W., Koch, M. H., Eisenacher, M., Berkmen, M., Lillig, C. H., & Leichert, L. I. (2021). Functional metagenomics of the thioredoxin superfamily. *The Journal of biological chemistry*, 296, 100247.
- Nyström, T., Yang, J., & Molin, M. (2012). Peroxiredoxins, gerontogenes linking aging to genome instability and cancer. *Genes & development*, 26(18), 2001–2008.
- Ogusucu, R., Rettori, D., Munhoz, D. C., Netto, L. E., & Augusto, O. (2007). Reactions of yeast thioredoxin peroxidases I and II with hydrogen peroxide and peroxy nitrite: rate constants by competitive kinetics. *Free radical biology & medicine*, 42(3), 326–334.
- O'Neill, J. S., & Reddy, A. B. (2011). Circadian clocks in human red blood cells. *Nature*, 469(7331), 498–503.
- O'Neill, J. S., van Ooijen, G., Dixon, L. E., Troein, C., Corellou, F., Bouget, F. Y., Reddy, A. B., & Millar, A. J. (2011). Circadian rhythms persist without transcription in a eukaryote. *Nature*, 469(7331), 554–558.
- Osawa, H., Stacey, G., & Gassmann, W. (2006). ScOPT1 and AtOPT4 function as proton-coupled oligopeptide transporters with broad but distinct substrate specificities. *The Biochemical journal*, 393(Pt 1), 267–275.
- Østergaard, H., Henriksen, A., Hansen, F. G., & Winther, J. R. (2001). Shedding light on disulfide bond formation: engineering a redox switch in green fluorescent protein. *The EMBO journal*, 20(21), 5853–5862.
- Østergaard, H., Tachibana, C., & Winther, J. R. (2004). Monitoring disulfide bond formation in the eukaryotic cytosol. *The Journal of cell biology*, 166(3), 337–345.
- Pader, I., Sengupta, R., Cebula, M., Xu, J., Lundberg, J. O., Holmgren, A., Johansson, K., & Arnér, E. S. (2014). Thioredoxin-related protein of 14 kDa is an efficient L-cystine reductase and S-denitrosylase. *Proceedings of the National Academy of Sciences of the United States of America*, 111(19), 6964–6969.

- Pak, V. V., Ezeriña, D., Lyublinskaya, O. G., Pedre, B., Tyurin-Kuzmin, P. A., Mishina, N. M., Thauvin, M., Young, D., Wahni, K., Martínez Gache, S. A., Demidovich, A. D., Ermakova, Y. G., Maslova, Y. D., Shokhina, A. G., Eroglu, E., Bilan, D. S., Bogeski, I., Michel, T., Vriz, S., Messens, J., Belousov, V. V. (2020). Ultrasensitive Genetically Encoded Indicator for Hydrogen Peroxide Identifies Roles for the Oxidant in Cell Migration and Mitochondrial Function. *Cell metabolism*, 31(3), 642–653.e6.
- Papazian H. P. (1952). The Analysis of Tetrad Data. *Genetics*, 37(2), 175–188.
- Patterson, K., Walters, L. A., Cooper, A. M., Olvera, J. G., Rosas, M. A., Rasmusson, A. G., & Escobar, M. A. (2016). Nitrate-Regulated Glutaredoxins Control Arabidopsis Primary Root Growth. *Plant physiology*, 170(2), 989–999.
- Peskin, A. V., Low, F. M., Paton, L. N., Maghzal, G. J., Hampton, M. B., & Winterbourn, C. C. (2007). The high reactivity of peroxiredoxin 2 with H₂O₂ is not reflected in its reaction with other oxidants and thiol reagents. *The Journal of biological chemistry*, 282(16), 11885–11892.
- Peskin, A. V., Pace, P. E., Behring, J. B., Paton, L. N., Soethoudt, M., Bachschmid, M. M., & Winterbourn, C. C. (2016). Glutathionylation of the Active Site Cysteines of Peroxiredoxin 2 and Recycling by Glutaredoxin. *The Journal of biological chemistry*, 291(6), 3053–3062.
- Perkins, A., Nelson, K. J., Parsonage, D., Poole, L. B., & Karplus, P. A. (2015). Peroxiredoxins: guardians against oxidative stress and modulators of peroxide signaling. *Trends in biochemical sciences*, 40(8), 435–445.
- Ponsero, A. J., Igbaria, A., Darch, M. A., Miled, S., Outten, C. E., Winther, J. R., Palais, G., D'Autréaux, B., Delaunay-Moisan, A., & Toledano, M. B. (2017). Endoplasmic Reticulum Transport of Glutathione by Sec61 Is Regulated by Ero1 and Bip. *Molecular cell*, 67(6), 962–973.e5.
- Rastogi, R. P., Singh, S. P., Häder, D. P., & Sinha, R. P. (2010). Detection of reactive oxygen species (ROS) by the oxidant-sensing probe 2',7'-dichlorodihydrofluorescein diacetate in the cyanobacterium *Anabaena variabilis* PCC 7937. *Biochemical and biophysical research communications*, 397(3), 603–607.
- Rawat, S. J., Creasy, C. L., Peterson, J. R., & Chernoff, J. (2013). The tumor suppressor Mst1 promotes changes in the cellular redox state by phosphorylation and inactivation of peroxiredoxin-1 protein. *The Journal of biological chemistry*, 288(12), 8762–8771.
- Reddy, A. B., & Rey, G. (2014). Metabolic and nontranscriptional circadian clocks: eukaryotes. *Annual review of biochemistry*, 83, 165–189.
- Rhee S. G. (2016). Overview on Peroxiredoxin. *Molecules and cells*, 39(1), 1–5
- Robinson, K. M., Janes, M. S., Pehar, M., Monette, J. S., Ross, M. F., Hagen, T. M., Murphy, M. P., & Beckman, J. S. (2006). Selective fluorescent imaging of superoxide *in vivo* using ethidium-based probes. *Proceedings of the National Academy of Sciences of the United States of America*, 103(41), 15038–15043.
- Rodríguez-Manzaneque, M. T., Tamarit, J., Bellí, G., Ros, J., & Herrero, E. (2002). Grx5 is a mitochondrial glutaredoxin required for the activity of iron/sulfur enzymes. *Molecular biology of the cell*, 13(4), 1109–1121.

- Roger, F., Picazo, C., Reiter, W., Libiad, M., Asami, C., Hanzén, S., Gao, C., Lagniel, G., Welkenhuysen, N., Labarre, J., Nyström, T., Grøtli, M., Hartl, M., Toledano, M. B., & Molin, M. (2020). Peroxiredoxin promotes longevity and H₂O₂-resistance in yeast through redox-modulation of protein kinase A. *eLife*, 9, e60346.
- Sobotta, M. C., Liou, W., Stöcker, S., Talwar, D., Oehler, M., Ruppert, T., Scharf, A. N., & Dick, T. P. (2015). Peroxiredoxin-2 and STAT3 form a redox relay for H₂O₂ signaling. *Nature chemical biology*, 11(1), 64–70.
- Song, J. J., & Lee, Y. J. (2003). Differential role of glutaredoxin and thioredoxin in metabolic oxidative stress-induced activation of apoptosis signal-regulating kinase 1. *The Biochemical journal*, 373(Pt 3), 845–853.
- Sousa, S. F., Neves, R., Waheed, S. O., Fernandes, P. A., & Ramos, M. J. (2019). Structural and mechanistic aspects of S-S bonds in the thioredoxin-like family of proteins. *Biological chemistry*, 400(5), 575–587.
- Staudacher, V., Djukica, C. F., Koduka, J., Schlossarek, S., Kopp, J., Büchler, M., Lanzer, M., & Deponte, M. (2015). Plasmodium falciparum antioxidant protein reveals a novel mechanism for balancing turnover and inactivation of peroxiredoxins. *Free radical biology & medicine*, 85, 228–236.
- Staudacher, V., Trujillo, M., Diederichs, T., Dick, T. P., Radi, R., Morgan, B., & Deponte, M. (2018). Redox-sensitive GFP fusions for monitoring the catalytic mechanism and inactivation of peroxiredoxins in living cells. *Redox biology*, 14, 549–556.
- Tairum, C. A., Jr, de Oliveira, M. A., Horta, B. B., Zara, F. J., & Netto, L. E. (2012). Disulfide biochemistry in 2-cys peroxiredoxin: requirement of Glu50 and Arg146 for the reduction of yeast Tsa1 by thioredoxin. *Journal of molecular biology*, 424(1-2), 28–41.
- Tang, Y., Zhang, J., Yu, J., Xu, L., Wu, J., Zhou, C. Z., & Shi, Y. (2014). Structure-guided activity enhancement and catalytic mechanism of yeast grx8. *Biochemistry*, 53(13), 2185–2196.
- Tao, R., Zhao, Y., Chu, H., Wang, A., Zhu, J., Chen, X., Zou, Y., Shi, M., Liu, R., Su, N., Du, J., Zhou, H. M., Zhu, L., Qian, X., Liu, H., Loscalzo, J., & Yang, Y. (2017). Genetically encoded fluorescent sensors reveal dynamic regulation of NADPH metabolism. *Nature methods*, 14(7), 720–728.
- Tarrago, L., Laugier, E., Zaffagnini, M., Marchand, C., Le Maréchal, P., Rouhier, N., Lemaire, S. D., & Rey, P. (2009). Regeneration mechanisms of *Arabidopsis thaliana* methionine sulfoxide reductases B by glutaredoxins and thioredoxins. *The Journal of biological chemistry*, 284(28),
- Tavender, T. J., & Bulleid, N. J. (2010). Molecular mechanisms regulating oxidative activity of the Ero1 family in the endoplasmic reticulum. *Antioxidants & redox signaling*, 13(8), 1177–1187.
- Tavender, T. J., & Bulleid, N. J. (2010). Peroxiredoxin IV protects cells from oxidative stress by removing H₂O₂ produced during disulphide formation. *Journal of cell science*, 123(Pt 15), 2672–2679.
- Teixeira, F., Tse, E., Castro, H., Makepeace, K., Meinen, B. A., Borchers, C. H., Poole, L. B., Bardwell, J. C., Tomás, A. M., Southworth, D. R., & Jakob, U. (2019). Chaperone activation and client binding of a 2-cysteine peroxiredoxin. *Nature communications*, 10(1), 659.

- Trnka, D., Engelke, A. D., Gellert, M., Moseler, A., Hossain, M. F., Lindenberg, T. T., Pedroletti, L., Odermatt, B., de Souza, J. V., Bronowska, A. K., Dick, T. P., Mühlhoff, U., Meyer, A. J., Berndt, C., & Lillig, C. H. (2020). Molecular basis for the distinct functions of redox-active and FeS-transferring glutaredoxins. *Nature communications*, 11(1), 3445.
- Trujillo, M., Ferrer-Sueta, G., Thomson, L., Flohé, L., & Radi, R. (2007). Kinetics of peroxiredoxins and their role in the decomposition of peroxynitrite. *Sub-cellular biochemistry*, 44, 83–113.
- Tu, B. P., Kudlicki, A., Rowicka, M., & McKnight, S. L. (2005). Logic of the yeast metabolic cycle: temporal compartmentalization of cellular processes. *Science (New York, N.Y.)*, 310(5751), 1152–1158.
- Tu, B. P., Mohler, R. E., Liu, J. C., Dombek, K. M., Young, E. T., Synovec, R. E., & McKnight, S. L. (2007). Cyclic changes in metabolic state during the life of a yeast cell. *Proceedings of the National Academy of Sciences of the United States of America*, 104(43), 16886–16891.
- Van Laer, K., Oliveira, M., Wahni, K., & Messens, J. (2014). The concerted action of a positive charge and hydrogen bonds dynamically regulates the pKa of the nucleophilic cysteine in the NrdH-redoxin family. *Protein science: a publication of the Protein Society*, 23(2), 238–242.
- Veal, E. A., Underwood, Z. E., Tomalin, L. E., Morgan, B. A., & Pillay, C. S. (2018). Hyperoxidation of Peroxiredoxins: Gain or Loss of Function? *Antioxidants & redox signaling*, 28(7), 574–590.
- Vignols, F., Bréhélin, C., Surdin-Kerjan, Y., Thomas, D., & Meyer, Y. (2005). A yeast two-hybrid knockout strain to explore thioredoxin-interacting proteins *in vivo*. *Proceedings of the National Academy of Sciences of the United States of America*, 102(46), 16729–16734.
- Vilella, F., Alves, R., Rodríguez-Manzaneque, M. T., Bellí, G., Swaminathan, S., Sunnerhagen, P., & Herrero, E. (2004). Evolution and cellular function of monothiol glutaredoxins: involvement in iron-sulphur cluster assembly. *Comparative and functional genomics*, 5(4), 328–341.
- Wach, A., Brachat, A., Pöhlmann, R., & Philipsen, P. (1994). New heterologous modules for classical or PCR-based gene disruptions in *Saccharomyces cerevisiae*. *Yeast (Chichester, England)*, 10(13), 1793–1808.
- Williamson D. H. (1965). The timing of deoxyribonucleic acid synthesis in the cell cycle of *Saccharomyces cerevisiae*. *The Journal of cell biology*, 25(3), 517–528.
- Wingert, R. A., Galloway, J. L., Barut, B., Foott, H., Fraenkel, P., Axe, J. L., Weber, G. J., Dooley, K., Davidson, A. J., Schmid, B., Paw, B. H., Shaw, G. C., Kingsley, P., Palis, J., Schubert, H., Chen, O., Kaplan, J., Zon, L. I., & Tübingen 2000 Screen Consortium (2005). Deficiency of glutaredoxin 5 reveals Fe-S clusters are required for vertebrate haem synthesis. *Nature*, 436(7053), 1035–1039.
- Winterbourn C. C. (2008). Reconciling the chemistry and biology of reactive oxygen species. *Nature chemical biology*, 4(5), 278–286.
- Winterbourn C. C. (2013). The biological chemistry of hydrogen peroxide. *Methods in enzymology*, 528, 3–25.

- Winterbourn, C. C., & Metodiewa, D. (1999). Reactivity of biologically important thiol compounds with superoxide and hydrogen peroxide. *Free radical biology & medicine*, 27(3-4), 322–328.
- Wolfe, K. H., & Shields, D. C. (1997). Molecular evidence for an ancient duplication of the entire yeast genome. *Nature*, 387(6634), 708–713.
- Wong, C. M., Siu, K. L., & Jin, D. Y. (2004). Peroxiredoxin-null yeast cells are hypersensitive to oxidative stress and are genomically unstable. *The Journal of biological chemistry*, 279(22), 23207–23213.
- Woo, H. A., Yim, S. H., Shin, D. H., Kang, D., Yu, D. Y., & Rhee, S. G. (2010). Inactivation of peroxiredoxin I by phosphorylation allows localized H₂O₂ accumulation for cell signaling. *Cell*, 140(4), 517–528.
- Wood, Z. A., Poole, L. B., & Karplus, P. A. (2003). Peroxiredoxin evolution and the regulation of hydrogen peroxide signaling. *Science (New York, N.Y.)*, 300(5619), 650–653.
- Wood, Z. A., Schröder, E., Robin Harris, J., & Poole, L. B. (2003). Structure, mechanism and regulation of peroxiredoxins. *Trends in biochemical sciences*, 28(1), 32–40. yeast genome. *Nature*, 387(6634), 708–713.
- Yadav, A. K., & Bachhawat, A. K. (2011). CgCYN1, a plasma membrane cystine-specific transporter of *Candida glabrata* with orthologues prevalent among pathogenic yeast and fungi. *The Journal of biological chemistry*, 286(22), 19714–19723.
- Yang, Y. F., & Wells, W. W. (1991). Identification and characterization of the functional amino acids at the active center of pig liver thioltransferase by site-directed mutagenesis. *The Journal of biological chemistry*, 266(19), 12759–12765.
- Yoshida, Y., Iigusa, H., Wang, N., & Hasunuma, K. (2011). Cross-talk between the cellular redox state and the circadian system in *Neurospora*. *PloS one*, 6(12), e28227.
- Zaffagnini, M., Bedhomme, M., Marchand, C. H., Couturier, J. R., Gao, X. H., Rouhier, N., Trost, P., & Lemaire, S. P. (2012). Glutaredoxin s12: unique properties for redox signaling. *Antioxidants & redox signaling*, 16(1), 17–32.
- Zahedi Avval, F., & Holmgren, A. (2009). Molecular mechanisms of thioredoxin and glutaredoxin as hydrogen donors for Mammalian s phase ribonucleotide reductase. *The Journal of biological chemistry*, 284(13), 8233–8240.
- Zeyl C. (2004). Capturing the adaptive mutation in yeast. *Research in microbiology*, 155(4), 217–223.
- Zhao, Y., Hu, Q., Cheng, F., Su, N., Wang, A., Zou, Y., Hu, H., Chen, X., Zhou, H. M., Huang, X., Yang, K., Zhu, Q., Wang, X., Yi, J., Zhu, L., Qian, X., Chen, L., Tang, Y., Loscalzo, J., & Yang, Y. (2015). SoNar, a Highly Responsive NAD+/NADH Sensor, Allows High-Throughput Metabolic Screening of Anti-tumor Agents. *Cell metabolism*, 21(5), 777–789.
- Zhao, Y., Jin, J., Hu, Q., Zhou, H. M., Yi, J., Yu, Z., Xu, L., Wang, X., Yang, Y., & Loscalzo, J. (2011). Genetically encoded fluorescent sensors for intracellular NADH detection. *Cell metabolism*, 14(4), 555–566.

Zimmermann, J. & Morgan, B. (*unpublished*). Chapter: Thiol-based redox probes
Alvarez, B., Comini, M., Salinas, G., Trujillo, M., Redox Chemistry and Biology of Thiols.
Elsevier, currently under revision

Zimmermann, J., Laporte, H., Amponsah, P.S., Michalk, C., Sukmann, T., Oestreicher, J.,
Tursch, A., Owusu, T., Prates Roma, L., Riemer, J. & Morgan, B. (*unpublished*). Tsa1 is the
dominant peroxide scavenger and a major source of H₂O₂-dependent GSSG production in
yeast.

Zimmermann, J., Oestreicher, J., Geissel, F., Deponte, M., & Morgan, B. (2021). An
intracellular assay for activity screening and characterization of glutathione-dependent
oxidoreductases. *Free radical biology & medicine*, 172, 340–349.

Zimmermann, J., Oestreicher, J., Hess, S., Herrmann, J. M., Deponte, M., & Morgan, B. (2020).
One cysteine is enough: A monothiol Grx can functionally replace all cytosolic Trx and dithiol
Grx. *Redox biology*, 36, 101598.

Zito E. (2015). ERO1: A protein disulfide oxidase and H₂O₂ producer. *Free radical biology &
medicine*, 83, 299–304.